INEEL/EXT-02-01210

Environmental Systems Research Analysis FY 2002 Annual Report

David L. Miller, Program Manager
Peter M. Castle, Deputy Program Manager
Steven J. Piet, Deputy Program Manager

January 2003

Idaho National Engineering and Environmental Laboratory
Bechtel BWXT Idaho, LLC

INEEL/EXT-02-01210

Environmental Systems Research Analysis
FY 2002 Annual Report

David L. Miller, Program Manager
Peter M. Castle, Deputy Program Manager
Steven J. Piet, Deputy Program Manager

January 2003

Idaho National Engineering and Environmental Laboratory
Idaho Falls, Idaho 83415

Prepared for the
U.S. Department of Energy
Office of Environmental Management
Under DOE Idaho Operations Office
Contract DE-AC07-99ID13727

Environmental Systems Research Analysis
FY 2002 Annual Report

INTRODUCTION

Welcome to the FY 2002 annual report of the Environmental Systems Research and Analysis (ESRA) program. The ESRA program was initiated in mid-FY 1998 to support the technical needs of Environmental Management (EM) through science and engineering research. Those technical needs have been identified by the INEEL, other DOE sites (through their Site Technology Coordinating Groups), and various site-specific and complexwide road-mapping efforts. Focused on EM's mission, the ESRA program is performing the needed ground work for the technical foundations that will deal with both current and anticipated technical issues in disposition, remediation, and waste management. The ESRA program is structured to perform both core research and problem-driven research. Core research is more basic, focusing on understanding environmental processes, developing new tools, and collecting data. Problem-driven research is more complex, focusing on application. The ESRA program largely focuses on problems relevant to the INEEL, but most of the research results apply more broadly to the DOE complex in general. An overarching goal of the program is to build capabilities that can address current as well as future EM technical issues.

The objectives of the ESRA program for FY 2002 involved two main tasks: the Environmental Systems Research (ESR) task, the research portion of the program, and the Complexwide Science and Technology Integration task, which focuses on technical planning and integration in support of the EM's R&D Strategy, Environmental Quality (EQ) Portfolio, and Portfolio Adequacy Analyses. This report describes the ESR task. The ESR task addresses two global technical areas relevant to EM: Subsurface Science and Waste Management Science. These technical areas are further divided into five thematic areas (See Figure 1).

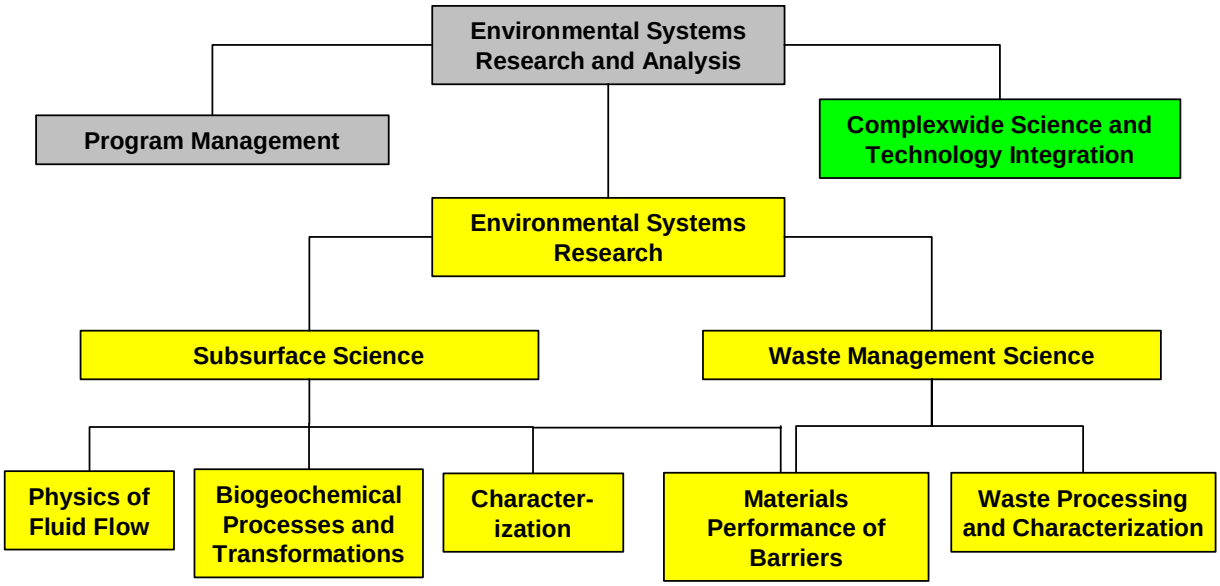

Figure 1. ESRA Program structure.

The three thematic areas for subsurface science, which are based on an assessment of research needs, are as follows:

- *Physics of Fluid Flow*. This research develops improved understanding of and predictive capability for the subsurface movement of fluids with particular focus on vadose zone processes.

- *Biogeochemical Processes and Transformaions*. This research quantifies the role of naturally occurring subsurface biogeochemical processes in contaminant fate and mobility.

- *Subsurface Characterization*. This research develops and applies new tools to characterize subsurface flow and contaminant distribution and movement.

The two thematic areas for waste management science are as follows:

- *Material Performance of Barriers*. This research develops models and investigates materials degradation mechanisms and their impact on the long-term ability of materials to isolate radionuclides and other contaminants from the environment and the population.

- *Waste Processing and Characterization*. This area builds on the INEEL's world class nuclear spectroscopy based nondestructive assay/examination (NDA/NDE) capabilities, and augments the advancement of subsurface characterization and monitoring techniques as well as enhancing waste package characterization. There is also an examination of the effects of high ionic strength on the thermodynamics and physical properties of non-ideal solutions. High level waste processing and subsurface migration are strongly influenced by these parameters.

The program structure and content of this report differs from that of FY 2001. The Waste Management Science portion was strengthened in the middle of FY 2002 by the addition of four new, peer reviewed research tasks. The Subsurface Science portion of the program did not have a stand-alone modeling task in FY 2002; modeling was an integral part of a number of the tasks.

The first chapter in this report describes the Water Integration Project, which lists the results of an April Value Engineering Workshop with respect to subsurface technical issues that need to be resolved. The participants included federal and state regulators, various stakeholders, and operations related individuals. We listed those issues below to provide a context for the research described in the other chapters of this report:

- Mechanisms and parameters describing adsorption of contaminants onto INEEL materials have not been adequately developed or measured.

- Knowledge of stratigraphic and structural controls on flow patterns in the vadose zone and the aquifer is limited.

- Available field data are of insufficient quality and quantity for use in predictive simulation.

- Conceptual models are often inadequate for prediction because they do not incorporate necessary physical and biogeochemical processes.

- Chemistry of the near-field environment, such as oxidation-reduction potential and solubility effects, may significantly affect the release and the rate of migration.

- Knowledge of flow direction and temporal behavior in the aquifer is limited.

- Conditions leading to facilitated transport are unknown.

- Preferred pathways are not detected or monitored, and there is relatively little information available.

- Contaminant inventory uncertainties.

- Various sources of uncertainty and their relative impact on the predictability of transport are unknown and currently unqualified.

In addition to the results of the value engineering activity, the Water Integration Project carried out interviews with many personnel who had experience in operations to compile a consensus list of technical issues. The results are presented here for the same purpose listed above:

- Plutonium geochemistry/transport
- Carbon-14 research
- Actinide geochemistry research
- K_d value research
- Development of better monitoring methods
- Source term research
- Flow characterization methods
- Development of models and codes
- Research on caps/barriers/grouting/ remediation methods
- Studies of long term degradation of landfill covers in arid environments.

It will be seen while reading the chapters in the Subsurface Science section of this report that the research tasks are related to one or more of the needs or issues appearing in these two lists. The majority of the tasks in the Waste Processing and Characterization activity were chosen by Operations from a list of proposals that had passed a technical peer review.

Throughout the report various INEEL facilities and waste area groups (WAGs) are mentioned. Figure 2 is a map of the INEEL site with the major facilities shown. Table 1 lists which facilities are associated with the WAGs.

The ESRA research portfolio has been assembled to address some of the technical issues associated with some of facilities mentioned above. The following chapters describe the research activities and results from FY 2002.

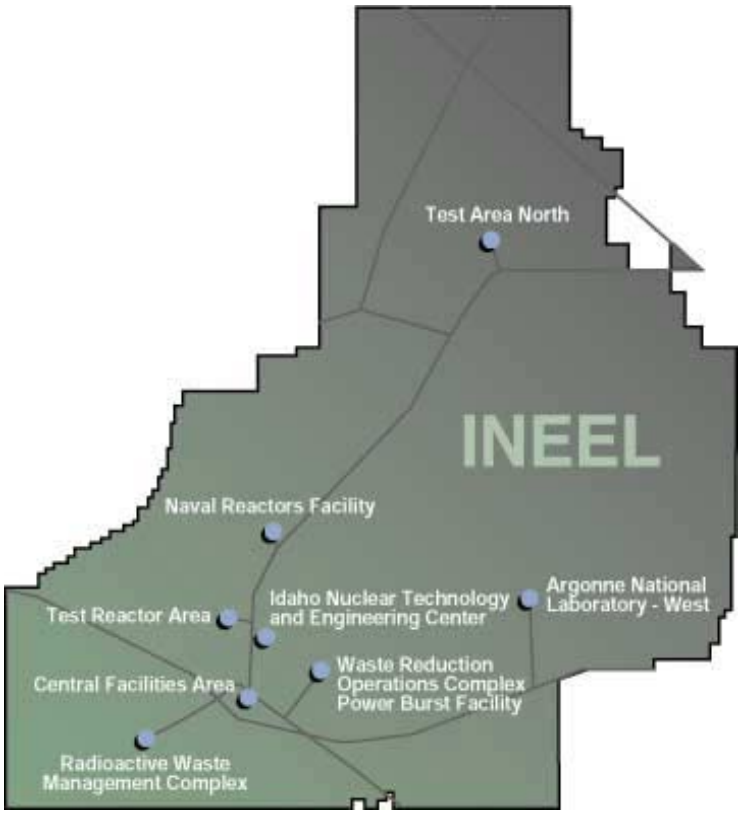

Figure. 2 INEEL site map.

Table 1. WAGs and Facilities

Waste Area Group	Location
WAG 1	Test Area North (TAN)
WAG 2	Test Reactor Area (TRA)
WAG 3	Idaho Nuclear Technology and Engineering Center (INTEC)
WAG 4	Central Facilities Area (CFA)
WAG 5	Power Burst Facility/Auxiliary Reactor Area (PBF/ARA)
WAG 6	Experimental Breeder Reactor No. 1 (EBR-I)
WAG 7	Radioactive Waste Management Complex (RWMC)
WAG 8	Naval Reactors Facility (NRF)
WAG 9	Argonne National Laboratory (ANL/EBR-II)
WAG 10	Miscellaneous (Misc)

CONTENTS

Introduction i

Subsurface Science 1

Water Integration Project 3

"Next Generation" Predictive Models of Vadose Zone Flow and Transport 15

Spatial and Temporal Characterization of the Vadose Zone 41

Mesoscale Investigations of Vadose Zone Carbon Cycles 61

Geomicrobiology of Subsurface Environments 87

Interfacial Processes Controlling Fate and Mobility of Actinides, Fission Products, and Other Contaminants 113

Biogeochemical Controls on the Migration of Cesium in the Rhizosphere (Water Integration Project) 159

Borehole Probe Development 183

Geocentrifuge Research Laboratory Development 195

Waste Management 201

Advanced Concepts of Nuclear Physics Applied to DOE's Mission 203

Biocorrosion 223

Corrosion of Neutron Absorbing Materials 237

Near-Surface Engineered Environmental Barrier Integrity 249

Alternative Waste Stabilization Technologies 289

Non-Ideal Solution Thermodynamics 317

Inorganic Supports for Binding Ammonium Molybdophosphate (AMP) to Produce Ion Exchange Sorbents for Removal of Cesium-137 from Acidic Nuclear Waste 331

Subsurface Science

Water Integration Project

Douglas Burns, Paul Wichlacz, and Roger Scott

SUMMARY

In FY 2002, ESRA funds supported start-up of technical activities conducted by the INEEL Water Integration Project. The project was formed by DOE to establish a basis for integrating and coordinating the acquisition of existing and new knowledge about the subsurface characteristics of the Eastern Snake River Plain. During the year the project (a) compiled, analyzed, and compared the several evolving conceptual models of the INEEL subsurface region; (b) revised and used the INEEL Vadose Zone/Ground Water Roadmap to identify and prioritize uncertainties in understanding of vadose zone and ground water characteristics at the INEEL; and (c) matched the uncertainties with the science and technology needs of INEEL Operations. The project helped the INEEL Hydrogeologic Data Repository make user access and data retrieval more efficient.

PROJECT DESCRIPTION

Introduction

The mission of the water integration project is to establish a basis for integrating and coordinating present and future activities that characterize, monitor, and remediate the ground water and vadose zone of Eastern Idaho Snake River Plain.

In early FY 2002, the water integration project established a set of objectives to accomplish its 3-year mission. These objectives were to:

- Produce a single, comprehensive, conceptual model of the subsurface that can be used to strategically plan future ground water and vadose zone research activities at the INEEL.
- Establish science strategies that align subsurface research and development (R&D) with operations' needs, and produce research data that supports credible, sustainable risk-based decisions.
- Establish an internet-based system that encompasses available subsurface data and information that users can access with their desktop computers, comprehensively search, and download to meet their needs.
- Develop a tool to calculate facilitywide cumulative risk and the contribution of individual sources to that risk for Environmental Management Operations use in determining appropriate remedial actions.
- Identify actions necessary to maximize the usefulness of INEEL ground water monitoring data for research and for environmental compliance needs.
- Identify metrics that INEEL water and vadose zone project managers can use to monitor and consistently report project performance sitewide.
- Demonstrate the value of collaborative stakeholder participation in strengthening the technical basis for strategic decisions related to INEEL ground water/vadose zone projects.

During FY 2002, the ESRA program funded activities associated with the first three objectives; therefore, this report focuses on those activities.

Approach

As the project got underway, it adopted a fundamental premise that, "participation by a wide range of stakeholders will improve the final project results." This premise applies to internal as well as external stakeholders. The project's activities can affect and be affected by many groups and individuals: livestock and crop producers, industries, community residents, and state and local government officials. Also interested and affected are: Native American tribal members and governments, state and federal regulators, public interest groups, the Department of Energy and its sister federal agencies, and

INEEL research, operations, and facility management personnel.

Since its inception, the project has involved stakeholders in key project decisions by routinely practicing open, transparent decision-making that provides opportunities for them to develop and weight decision criteria and establish priorities. Although they are funded separately from the ESRA program, key stakeholder involvement activities are inseparable from and fundamental to meeting the project's technical objectives.

Technical Tasks

INEEL Subregional Conceptual Model

In August 2002, the project took the first step toward achieving its objective to produce a single, comprehensive, conceptual model of the subsurface underlying the INEEL subregion when it published the draft *INEEL Subregional Conceptual Model Report Volume 1*.

The project adopted the National Research Council's definition of a conceptual model: "…an evolving hypothesis identifying the important features, processes, and events controlling fluid flow and contaminant transport of consequence at a specific field site in the context of a recognized problem."[1] Presently, several subregional conceptual models are under development at the INEEL. Facility-specific conceptual models have also been described as part of environmental restoration activities at the INEEL.

The Volume 1 report, which compiles and compares the evolving models, exposed many areas of convergence and some areas of divergence among the models, and significant data gaps in all the models.

Model Convergence

Conceptual models of ground water flow and contaminant transport at the INEEL include the description of the geologic framework, matrix hydraulic properties, and inflows and outflows. They also define contaminant source term and transport mechanisms.

The geologic framework of the INEEL subregion is described by the geometry of the system, stratigraphic units within the system, and structural features that affect ground water flow and contaminant transport. These elements define geohydrologic units that make up the Snake River Plain aquifer (SRPA).

Model Boundaries. The United States Geological Survey (USGS) conceptual model encompasses approximately 1,920 mi^2 of the Eastern Snake River Plain (see Figure 1).[a] The Waste Area Group (WAG) 10 model includes the USGS area and additional areas to the northeast and southeast (see Figure 2).[2] Both conceptual models are bounded to the northwest by the Pioneer Mountains, Lost River Range, and Lemhi Mountains, and to the southeast by ground water flow paths determined from aquifer water-level contours. The up gradable extent of the USGS model is a water-level contour that includes the northeastern boundary of the INEEL. The WAG 10 model includes more of the Mud Lake area to take advantage of previous estimates of underflow into the subregion. Both conceptual models extend 25 miles to the southwest of the INEEL, a distance sufficient to include known concentrations of contaminant tracers.

Geohydrologic Units. Conceptual models have utilized a stratigraphic data set to define geohydrologic units within the INEEL subregion. This data set, compiled from geophysical logs and cores from boreholes, correlates the thick, complex stack of basalt flows across the subregion. Conceptual models generally concur that the upper geohydrologic unit consists of a section of highly fractured, multiple, thin basalt flows and sedimentary interbeds. Beneath this unit is an already (aerially) extensive, thick, unfractured basalt flow that rises above the water table southwest of the INEEL. The bottom unit consists of a thick section of slightly- to moderately-altered basalt.

---

a. D. J. Ackerman, S. R. Anderson, L. C. Davis, B. R. Orr, G. W. Rattray, and J. P. Rousseau, "A Conceptual Model of Flow in the Snake River Plain Aquifer at and Near the Idaho National Engineering and Environmental Laboratory with Implications for Contaminant Transport," U.S. Geological Survey-Resources Investigation Report (in preparation).

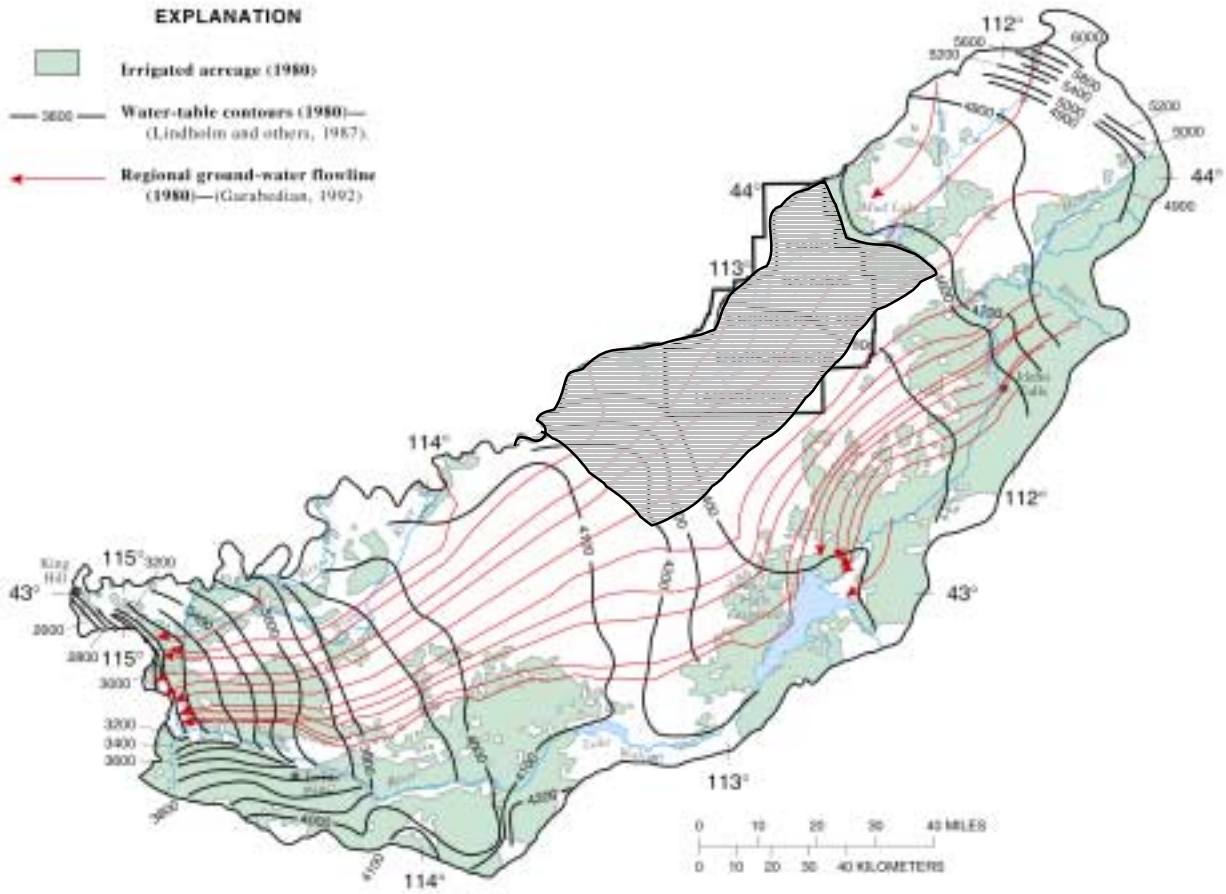

Figure 1. Extent of the USGS INEEL subregional conceptual model, eastern SRPA, Idaho.[a] The gray area is the USGS conceptual model area

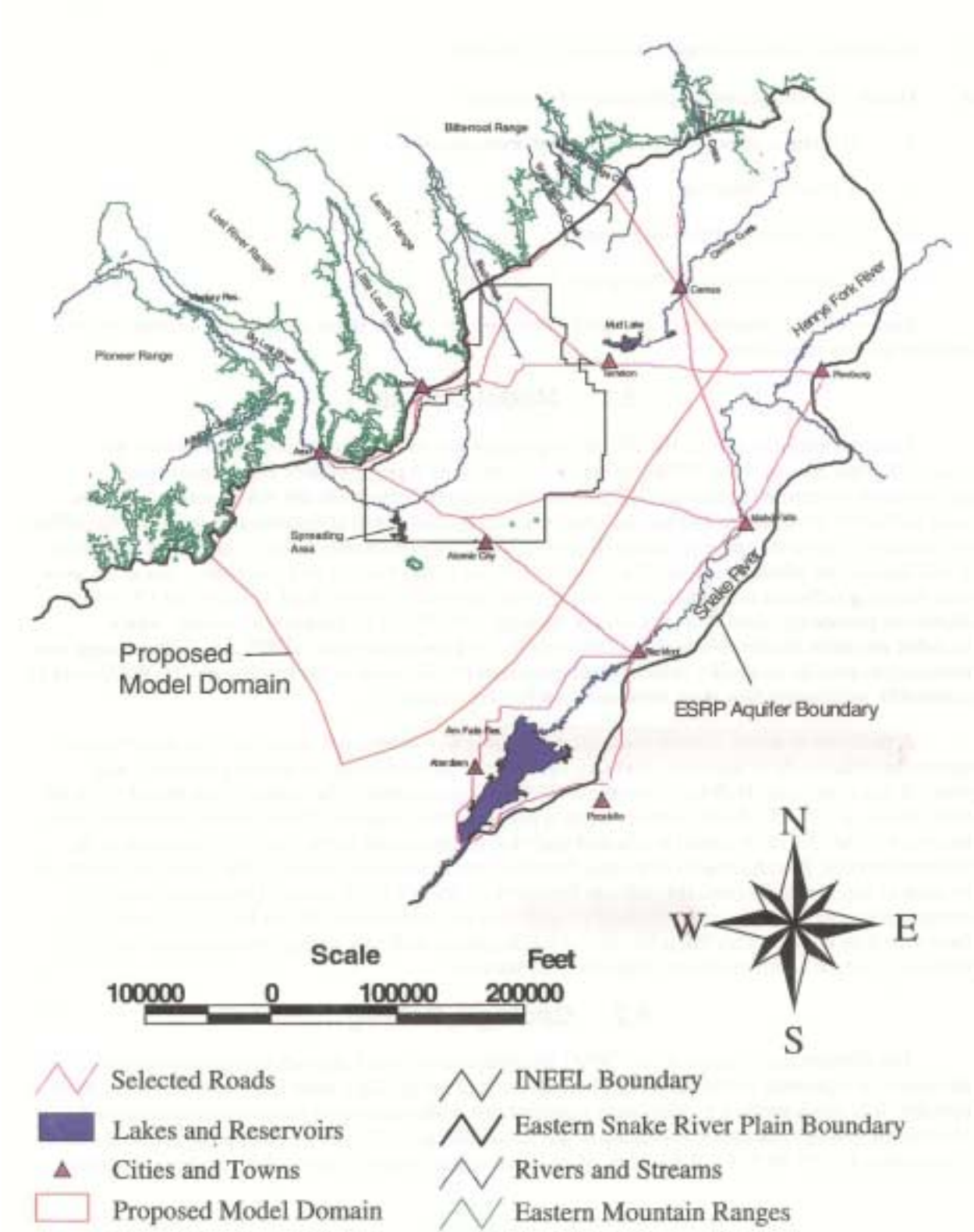

Figure 2. Extent of WAG 10 conceptual model of the INEEL subregion.[2]

Subregional conceptual models concur that structural features across the plain affect ground-water flow and contaminant transport. Structural uplift and subsidence has modified the orientation of geohydrologic units. Volcanic rift features, including vent corridors, locally affect the distribution of hydraulic properties of the aquifer.

Hydraulic Properties. Matrix hydraulic properties of the basalt and interbed sediments of the Eastern Snake River Plain include hydraulic conductivity (the measure of the capability of these rocks to transmit water) and the storage coefficient (the measure of the capability of these rocks to store water). The subregional and facility-specific conceptual models all note a large range in hydraulic conductivity from tests in the SRPA and vadose zone. The hydraulic conductivity estimates from aquifer tests in 114 aquifer wells at the INEEL ranged from 0.01 to 32,000 ft/day. A similar range was observed in wells completed in perched water bodies. The distribution of hydraulic conductivity in the INEEL subregion is not defined by any of the subregional or facility-specific conceptual models because of heterogeneities attributed to the complex, layered system of overlapping basalt flows and the occurrence of volcanic vent corridors that significantly affect hydraulic conductivity. Subregional estimates of the storage coefficient range from 5–20%. Facility-specific estimates, calculated using inverse numerical models of hydraulic and chemical information, range from 3–6%.

Ground Water Flow. The configuration of the subregional ground-water-flow field depends on flows into and out of the subregion. These flows occur as underflow from regional and tributary basin systems, flow across the base of the aquifer, and recharge from infiltrating precipitation and stream flow.

Underflow into and out of the INEEL subregion is estimated indirectly in conceptual models from gradient and hydraulic property information. Underflow estimates into the subregion are within 5% of each other (1,225 and 1,298 ft^3/s). Based on limited gradient and hydraulic-property information The USGS model estimates about 2,350 ft^3/s of underflow from the region.

Conceptual models concur that small flows probably enter the SRPA flow system across the base of the aquifer. The USGS model estimates that approximately 44 ft^3/s of flow may enter the aquifer throughout the subregion. The WAG 10 model infers from temperature data that flows may be larger in some areas.

Subregional and facility-specific estimates of recharge from aerial precipitation are derived from tracer and other studies. The USGS conceptual model estimates that recharge from aerial precipitation is 0.02 to 0.04 ft/year with a maximum recharge contribution of about 70 ft^3/s over the entire subregion. The WAG 10 conceptual model uses similar estimates for aerial recharge and suggests that direct precipitation on the plain locally recharges the aquifer to a limited degree, particularly when snow melts rapidly in the spring. The net effect of recharge from precipitation on contaminant transport is probably very small when compared to other sources of inflow and is a less important consideration than more concentrated sources such as stream flow infiltration.

Subregional conceptual models concur on the magnitude of underflow into the SRPA from contributing mountain basins to the northwest. The USGS calculates that 361 ft^3/s of underflow enters the aquifer from the Big Lost River basin, 226 ft^3/s of underflow enters the aquifer from the Little Lost River basin, and 102 ft^3/s of underflow enters the aquifer from the Birch Creek basin. These estimates are derived from mean annual basin yield calculations and stream flow data. The WAG 10 estimates incorporate a 25% uncertainty into the USGS estimates.

Model Divergence

Aquifer Thickness. Several hypotheses have been developed concerning the effective thickness of the SRPA at the INEEL. The USGS model has defined the effective thickness from electrical resistivity and borehole data to be as much as 2,500 ft in the eastern part of the subregion and as much as 4,000 ft in the southwestern part. The WAG 10 model has developed two alternatives using aquifer-temperature and electrical-resistivity data. The “thick” aquifer interpretation uses colder temperature data and includes a north-trending

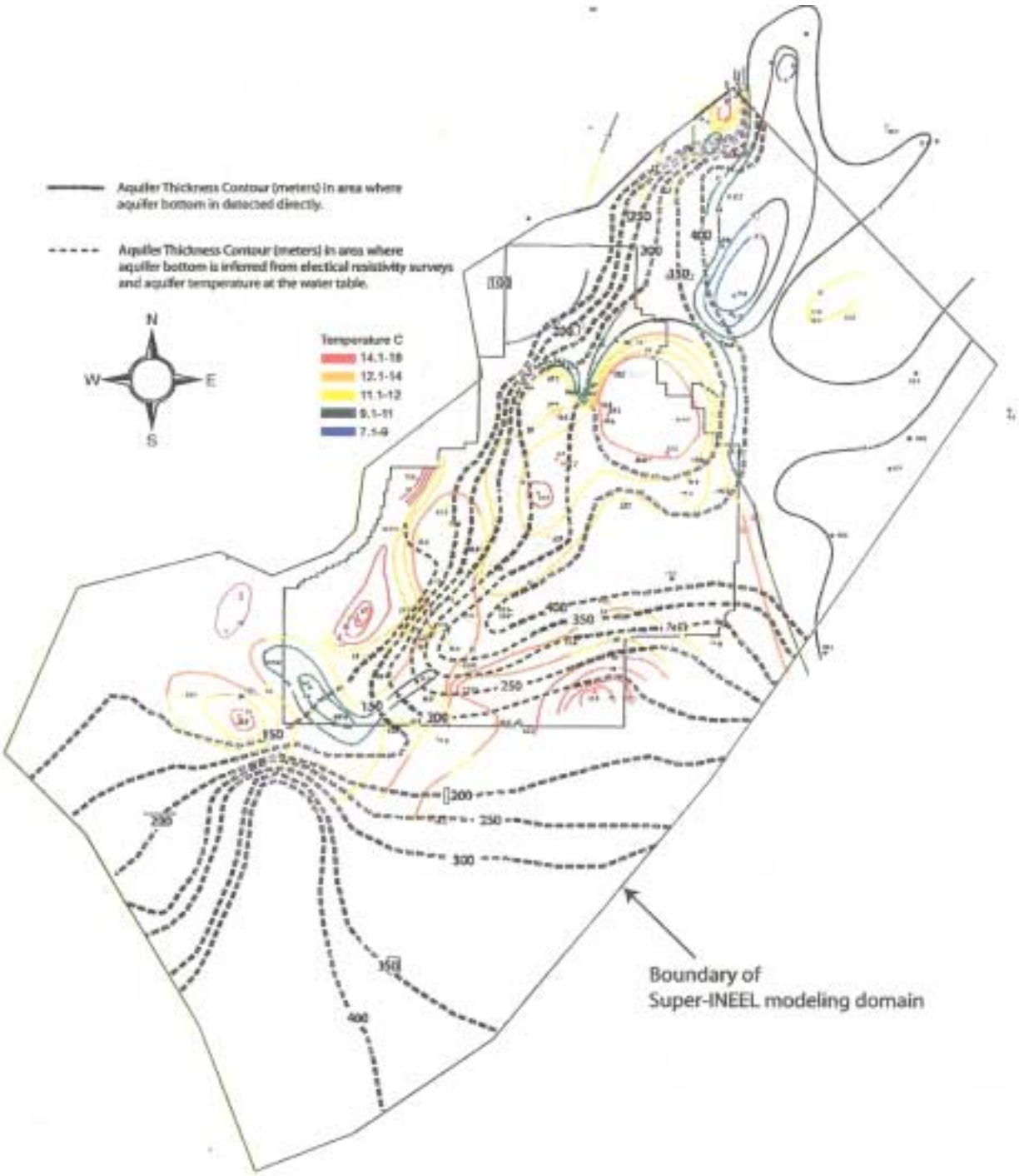

Figure 3. WAG 10 thick aquifer interpretation for the INEEL subregion (Arnett and Smith, 2001).

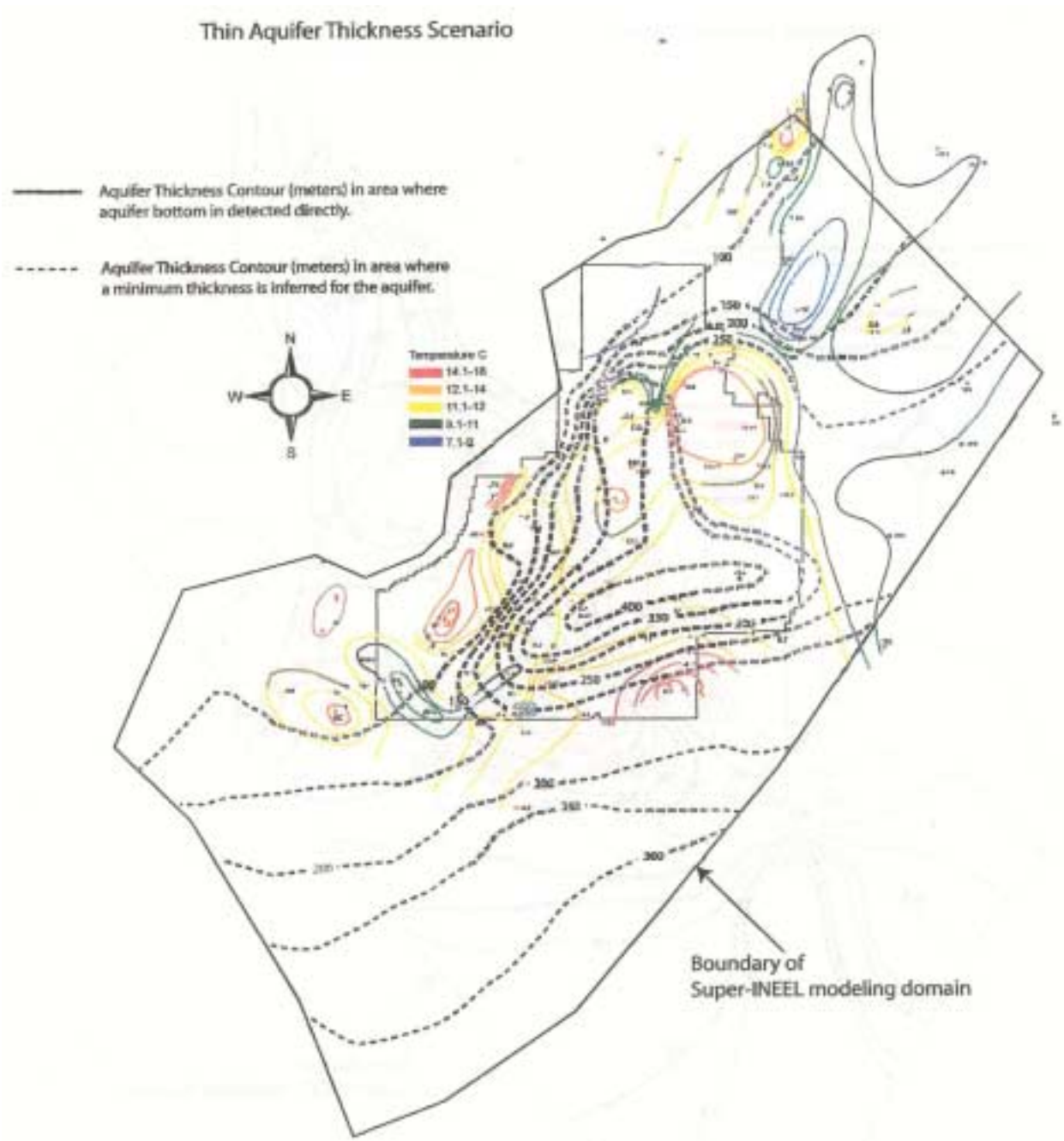

Figure 4. WAG 10 thin aquifer interpretation for the INEEL subregion (Arnett and Smith, 2001).

zone in which the thickness exceeds 1,300 ft with a maximum thickness of 1,700 ft (see Figure 3). The "thin" aquifer interpretation minimizes aquifer thickness, with thickness ranging from 328–1,300 ft (see Figure 4). Facility-specific models have generally focused efforts on the upper 250 ft of saturation.

Significant Gaps in Present Models

Episodic Recharge. Historically, large volumes of water have been recharged to the SRPA in response to episodic runoff from the Big Lost River drainage basin. Recharge has occurred along the channel of the Big Lost River and in the INEEL spreading areas near sources of

INEEL-derived contaminants. This source of large episodic recharge has locally affected hydrologic conditions in the vadose zone and aquifer. However, the effect of this recharge on contaminant transport is not well understood. The USGS tracer test conducted in the INEEL spreading areas in 1999 demonstrated that rapid, lateral flow can occur in the vadose zone in response to episodic recharge. Subregional and WAG specific studies (in proximity to episodic effects of stream flow recharge) recognize that more information is required to adequately assess the effects of episodic recharge on flow and contaminant migration.

Contaminant Transport. The migration of contaminants within the vadose zone and SRPA is controlled by the source term and by mechanisms that enhance or impede transport. The migration of contaminants is defined by the distribution of those contaminants in water within the aquifer and vadose zone.

The source term includes a definition of the inventory of contaminants of concern and the mechanism for release. Contaminants have been released to the subsurface through injection wells, infiltration ponds, spills, and as waste materials buried at disposal sites. Little site-specific data regarding contaminant chemical forms and mechanisms of release have been incorporated into INEEL conceptual models.

Contaminant transport within the INEEL subregion is controlled by chemical speciation, adsorption, complexation, facilitated transport, and other chemical and physical processes. Few studies have been conducted that describe the specific contaminant-water-rock interactions that are known to occur in similar terrain. WAG specific studies, with a few exceptions, rely on generalized knowledge of chemical behavior. Little site-specific data regarding contaminant chemical forms or mechanisms of release have been incorporated into INEEL conceptual models.

Path Forward

This project will build on the descriptive data produced in Fiscal Year 2002 to integrate the evolving conceptual models into a comprehensive conceptual model of the Eastern Snake River Plain's INEEL Subregion. Through a series of workshops involving external and internal stakeholders and independent scientific peers, the project will attempt to achieve consensus on the features of the comprehensive model. The model will visually depict the biogeochemical and hydrologic activities important in the transport of contaminants on and off the INEEL site toward potential down gradient receptors. Significant gaps in the model and its most uncertain aspects, coupled with the highest priority operations needs for science and technology, will guide development of future subsurface science strategies.

Funds from sources other than the ERSA program will support continued conceptual model development.

Science Strategies

This project developed Revision 2 of the *INEEL Vadose Zone/Ground Water Roadmap* (the Roadmap) to determine gaps in knowledge and capabilities for the vadose zone and ground water at the INEEL, and to ensure that ongoing and planned S&T activities will meet INEEL operations and S&T needs in the coming years. Revising the Roadmap is the first step in achieving the Project's objective to insure that the INEEL's long-term S&T strategy is aligned with site programs, that it takes advantage of progress made to date, and that it can assist in meeting site operations milestones and budgets. Establishing science strategies will facilitate monitoring, characterization, prediction, and assessment activities to reduce the uncertainties in long-term risk predictions, assist in risk management decisions, and ensure that long-term stewardship of contaminated sites at the INEEL is achieved.

Ten Highest Priority Uncertainties

To determine gaps in knowledge, the project engaged scientists and engineers knowledgeable in geosciences, flow and transport modeling, source term issues, and surface and ground-water issues to prepare a listing of uncertainties. These uncertainties represent gaps in knowledge and capabilities for the vadose zone and ground water at the INEEL. Twenty-five uncertainties were

identified from the first roadmap document,[3] and an uncertainties validation meeting held in March 2002.

In April 2002, 25 people participated in a facilitated value engineering (VE) session to prioritize the uncertainties. This group represented public stakeholders, federal and state regulators, INEEL State Oversight, the United States Geological Survey, DOE Headquarters, DOE-ID, and BBWI. They brought diverse backgrounds to the session, including concerned public, INEEL Operations, geoscience research, flow and transport modeling, geochemistry, contaminant experts, applied geosciences, agriculture, academia, and project management. These 25 people spent 2 days discussing the uncertainties, developing criteria to be used in the prioritization, and prioritizing the uncertainties. All data from the 2 days were documented.[4]

The VE session prioritized all 25 uncertainties. Prioritization scores ranged from 15.85–7.29. The following list summarizes the 10 highest priority uncertainties and their scores (in order of priority):

1. Mechanisms and parameters describing adsorption of contaminants onto INEEL materials have not been adequately developed or measured. (score 15.85)

2. Knowledge of stratigraphic and structural controls on flow patterns in the vadose zone and the aquifer is limited. (score 15.49)

3. Available field data are of insufficient quality and quantity for use in predictive simulation. (score 15.25)

4. Conceptual models are often inadequate for prediction because they do not incorporate necessary physical and biogeochemical processes. (score 14.88)

5. Chemistry of the near-field environment (e.g. the oxidation-reduction potential and solubility effects) may significantly affect the release and the rate of migration. (score 14.77)

6. Knowledge of flow direction and temporal behavior in the aquifer is limited. (score 14.43)

7. Conditions leading to facilitated transport are unknown. (score 14.19)

8. Preferred pathways are not detected or monitored, and there is relatively little information available. (score 14.12)

9. Contaminant inventory uncertainties (score 14.02)

10. Various sources of uncertainty and their relative impact on the predictability of transport are unknown and currently unqualified. (score 13.90)

Identification of Specific Operational Needs

As part of the road-mapping activity, project staff interviewed approximately 50 people with INEEL operations expertise and knowledge of the need to meet regulatory milestones and provide for long-term monitoring of the site. The roadmap report contains detailed results of the interviews. It also matches the detailed, specific needs with technical need, Waste Area Group need, and what uncertainty the R&D would help to solve. The categories of major operational needs are summarized as follows (in no particular priority):

- Plutonium geochemistry/transport
- Carbon-14 research
- Actinide geochemistry research
- K_d value research
- Development of better monitoring methods
- Source-term research
- Flow characterization methods
- Development of models and codes

- Research on caps, barriers, grouting, and remediation methods

- Studies of long term degradation of landfill covers in arid environments.

In September 2002, the project sponsored a second VE session to focus on and prioritize the operational needs. With few exceptions, the same participants who attended the April 2002 VE session participated. The raw data report from that session is still being prepared.

Path Forward

Continued development of subsurface science strategies will be funded from sources other than the ESRA program. This project will use the prioritized uncertainties and operational needs to develop subsurface science strategies and define the hypotheses (research questions) that need to be tested to implement those strategies. The project will also write test plans for incorporation into calls for research proposals through which the research necessary to implement the strategies will be performed. The strategies, research questions, and calls for proposals will be validated by internal and external stakeholders and independent technical peers .

Subsurface Information Electronic Library

Over the more than 50-year history of the INEEL, many different entities have generated a massive amount of data related to the Snake River Plain's subsurface characteristics. The INEEL Hydrogeologic Data Repository (IHDR) houses geologic and hydrologic information on the region, the Eastern Snake River Plain, and the SRPA.

Information Available

Well and Drill Hole Information. Geophysical logs; borehole videos; lithologic, stratigraphic, structural, and petrographic information; and a comprehensive survey of individual well history, completion, and monitoring.

Maps. Well location, topographic, physiographic, soil, facility, infrastructure, contaminant plumes, land use, irrigation withdrawal, aquifer characteristics, geologic, and geophysical.

Historical Data. INEEL historical water quality and water level data, historical waste inventory, and historical vadose zone studies.

Snake River Plain. Evolution, structure, tectonics, stratigraphy, faulting, geology, physiography, geophysics, magnetics, gravity, stress-state, heat flow, geochemistry, isotopes, lithology, petrology, glacial history, volcanic rift zones, regional seismic and volcanic history, and hazards assessment.

Aquifer Characteristics. Hydraulic parameters of basalts and interbeds, basalt and sedimentary interbed relationships, aquifer contaminant chemistry data, site hydrogeology, ground water system features, ground-water use, contaminant plumes, water quality, water level.

Surface Water Information. Surface water hydrology, stream flow characteristics, meteorology.

Soil Characterization and Sediment Property. Mechanical properties, soil types, INEEL soils and vegetation, soil erosion, sediment transport and deposition, geotechnical site investigations.

Formats and Access

These data, created in a variety of forms, were archived according to requirements specific to the projects that produced them, and the information storage technologies available at the time. The holdings in the IHDR include more than 2,700 contractor reports, journal articles, state and federal agency reports, which are catalogued in a searchable bibliographic media-specific database, and much of the resource is available electronically. Other data, such as some geophysical and lithologic well logs, borehole videos, and maps, have been available only in graphic or paper formats.

The IHDR has been a valuable resource for subsurface data and information. However, past funding constraints have not allowed the

repository to adopt the recent technological advances in information storage and access. Users have been required to submit an electronic form requesting searches by IHDR personnel, or to search electronically or physically at the Idaho Falls repository. As a result, users have spent inordinate amounts of time accessing and searching subsurface data. Upgrading access to and search capabilities of the IHDR with presently available technologies will significantly reduce the amount of time users spend to obtain needed subsurface data and information.

To be readily available, some archived subsurface data must be converted to formats that make them retrievable through modern internet-based information management technologies. Project planners and managers, as well as researchers, must be able to search existing subsurface data with confidence that they will find all available pertinent data, and that data can be appropriately referenced according to its source. To achieve this aim, a single subsurface data architecture must be established, with common standards and nomenclature.

Ultimately, this project intends to establish an internet-based system encompassing available subsurface data and information that users can access with their desktop computers, comprehensively search, and download to meet their needs.

This objective will be realized by linking existing databases and other sources of subsurface information, defining a scope of information and data needed for subsurface science research, and integrating new data, technology, and information into a flexible, expandable system.. The system will be modified or expanded or both as needs and technologies evolve.

Activities in FY 2002 made users' access to subsurface data more comprehensive and convenient, and took the following significant steps toward establishing an internet-based system:

- Approximately 70% of the IHDR was scanned, interpreted by optical character recognition (OCR) technology, and indexed for full-text search capability.
- Access to the system is now available through a viewer, which is available by request. Initially established to accommodate five users simultaneously, access has been doubled to allow 10 users at once.
- Well information in multiple formats has been linked through unique identifiers for searching, retrieval, downloading, and printing.
- Software was purchased that will enable people to access the IHDR holdings on the INEEL intranet.
- Migration of the system search engine to standard query language began, to maximize interface capabilities with other major information systems at the INEEL.
- Custom integration code writing was completed to link the bibliographic multimedia system to the imaging and full-text search system.
- The capacity for performing all functions was increased, including scanning, OCR technology, searching, retrieving, copying, emailing imaged documents (electronic copy to image capability).
- Software was acquired to capture and modify images in obsolete formats such as well files graphics, import obsolete graphical formats, and migrate files to current configuration.

Path Forward

ESRA funding for subsurface data integration ended with FY 2002. As other funds sources become available, the planned path forward for this project includes developing a web page meeting the INEEL internal web page standards and developing, implementing and codifying a recognized process for information to be directed into the system, making it available on the website. A cross reference system will be established to make well searches more transparent. The repository will continue to

expand its multimedia holdings as appropriate data and information are identified.

ACCOMPLISHMENTS

ESRA funds allowed this project to take significant steps in establishing a basis for integrating and coordinating present and future activities that characterize, monitor and remediate the Eastern Idaho Snake River Plain's ground water and vadose zone. During FY 2002 the project:

- Identified areas of convergence and divergence and significant gaps in subsurface knowledge among the evolving INEEL subregional conceptual models of the Snake River Plain vadose zone and aquifer.

- Identified and prioritized the key uncertainties, or gaps in knowledge or capabilities, regarding INEEL subsurface geology and ground water.

- Identified and prioritized the operational needs for science and technology to support INEEL environmental remediation activities, and began a process to integrate these with key uncertainties, which will be input to a set of sitewide subsurface research strategies.

- Made available approximately 70% of the INEEL Hydrogeologic Data Repository's holdings by electronic, full-text search, allowing 10 users to access the system simultaneously—double the previous capacity.

Publications

U.S. Department of Energy, INEEL *Subregional Conceptual Model Report Volume 1,* "Summary of Existing Knowledge of Natural and Anthropogenic Influences Governing Subsurface Contaminant Transport in the INEEL Subregion of the Snake River Plain (Draft)," Idaho National Engineering and Environmental Laboratory, INEEL/EXT-02-00987, Revision A, Idaho Falls, ID. 2002.

U.S. Department of Energy, "Development of the FY-02 Supplement of the INEEL Site-Wide Vadose Zone/Ground water Roadmap," Idaho National Engineering and Environmental Laboratory, INEEL/EXT-02-01038-DRAFT, Idaho Falls, ID. 2002.

REFERENCES

1. National Research Council, *Conceptual models of flow and transport in the fractured vadose zone*, Washington, D.C., National Academy Press, 2001, p. 12.

2. R. C. Arnett and R. P. Smith, *WAG 10 Ground water Modeling Strategy and Conceptual Model,* Idaho National Engineering and Environmental Laboratory, Bechtel BWXT Idaho, LLC, INEEL/EXT-01-00768, 2001.

3. Bechtel BWXT Idaho, LLC, *Uncertain Predictions of Contaminant Behavior At INEEL: A Roadmap for Addressing Current Limitations Through Vadose Zone Studies*, INEEL/EXT-2001-552, September 2001.

4. Bechtel BWXT Idaho, LLC, *Raw data report and meeting record from the Vadose Zone/Ground water Uncertainties Prioritization Meeting, April 2 and 3, 2002*, INEEL/EXT-02-00529, 2002.

"Next Generation" Predictive Models of Vadose Zone Flow and Transport

T. R. Wood, D. L. Stoner; K. Baker, G. Heath, R. A. LaViolette, T. R. McJunkin, R. C. Starr, K. Noah, R. K. Podgorney, and F. White (INEEL); D. Peak (Utah State University); R. J. Glass (Sandia National Laboratories); J. Fairley and M. J. Nicholl (University of Idaho); R. D. Stedtfeld and T. L. Tyler (Idaho State University); D. Lebreque (MultiPhase Technologies, LLC); and P. Chiappini (Ziccardi Productions)

SUMMARY

The ability to predict the transport of radionuclides, chlorinated hydrocarbons, metals, and other pollutants in the subsurface, particularly in fractured rock vadose zones, is both a requirement and a challenge for subsurface environmental policy. Recent monitoring efforts at a number of locations suggest that fractures can accelerate contaminant transport in the subsurface.[1–4] Not only did contaminant transport rates exceed predicted rates by several orders of magnitude, but also the contaminant detection events were episodic in nature. Subsequent field and laboratory experiments have verified that variable or episodic fluid flow and contaminant transport does occur.[5–9] Based on what is already known about fluid flow and contaminant transport, we propose that fractured rock vadose zones are complex and dynamic systems. We also suggest that the variable flow of water observed in fractured rock systems is due to the dynamical interaction of the physical, chemical, and biological properties of the system. A paradigm shift is required to account for the effects that the interacting parameters have in producing the dynamic behavior of water flow and contaminant transport in subsurface environments. Accordingly, the development and application of methodologies that account for the full dynamics in unsaturated flow and transport processes will lead us to improved numerical simulations for fractured rock vadose zones. Scientifically sound and integrated experimental, theoretical, and mathematical studies will be necessary to describe the impacts of complex system behavior on contaminant fate and transport. The development of appropriate mathematical tools to diagnose the existence of complexity is an important aspect of this effort. The fusion of mathematics with traditional characterization technologies, such as chemistry, geology, hydrology, microbiology, and with new mathematical tools is essential for the development of a new conceptual framework for the mechanisms that underlie liquid flow and contaminant transport. This project is investigating the role of complex, interacting hydrological, geochemical, and biological parameters in producing the dynamic behavior of contaminants in subsurface environments. Mesoscale test beds are the unifying experimental framework upon which system identification tools, sensing methods, and conceptual models are developed. The mathematical tools under development are to be used for the diagnosis of system characteristics, and will provide the basis for predictive modeling.

PROJECT DESCRIPTION

Three general tasks were performed during FY 2002: experiments, real vadose zone studies, and modeling. These tasks and their subtasks are described in this report.

Experiments

Fracture Intersections as Integrators for Unsaturated Flow

Recent laboratory experiments have shown that a steady application of fluid to the top of an unsaturated fracture-matrix network can produce dynamic preferential pathways, with flow fluctuating both along individual paths, and between alternate pathways.[10] The magnitude of the observed fluctuations was larger than could be explained by pulsation or dripping along gravity-driven fingers within individual fractures.[11,12] It was hypothesized that these larger fluctuations could be caused by fracture intersections acting as hysteretic gates. In this conceptual model, fracture intersections form capillary barriers that accumulate flow from above, and then release the

integrated volume when the barrier is breached. Our simple experiment considered unsaturated flow across an intersection between vertical and horizontal fractures. Results show that behavior within the system transitions between two flow-rate-dependent regimes. At higher flow rates, we observed a viscous stabilized regime in which flow was not influenced by the intersection. However, at low rates of supply, pulsed flow in the upper fracture was integrated by the intersection and released into the lower fracture as less frequent pulses of larger magnitude.

We fabricated a simple intersection between vertical and horizontal fractures by stacking four blocks of rock (see Figure 1). An array of four optical sensors was employed to monitor fracture flow both above and below the intersection. Each sensor was formed by positioning a light emitting diode (LED) and a photoelectric cell on opposite sides of the 5-cm- wide fracture (see Figure 1). With the fracture empty, the light path between a photocell and corresponding LED was unimpeded. Water spanning the fracture aperture (in contact with both fracture walls) decreased light transmission, and thus, output from the photocell (see Figure 2). Two optical sensors were located in the upper vertical fracture (24 cm and 7 cm above the intersection), and two in the lower vertical fracture (4 cm and 23 cm below the intersection). The intersection itself was left unobstructed to facilitate visual observation.

Figure 1 illustrates how the four $5 \times 7 \times 30$-cm blocks of porous limestone were clamped within a frame to form a 60-cm-high vertical fracture bisected by a 14-cm-long horizontal fracture. Four LEDs were mounted on the plastic sheeting as shown, with their output directed into the vertical fracture. Each LED was paired with a photocell located on the opposite side of the vertical fracture (hidden in this view). Water was supplied to the fracture using a peristaltic pump; inflow and outflow rates were measured gravimetrically, with both reservoirs placed on electronic balances.

The waveforms shown in Figure 2 are characteristic of measured behavior over 15-second intervals at three different flow rates. Individual voltage traces for the sensors have been shifted vertically for presentation: 1 (top, black),

Error! Objects cannot be created from editing field codes.

Figure 1. Experimental system.

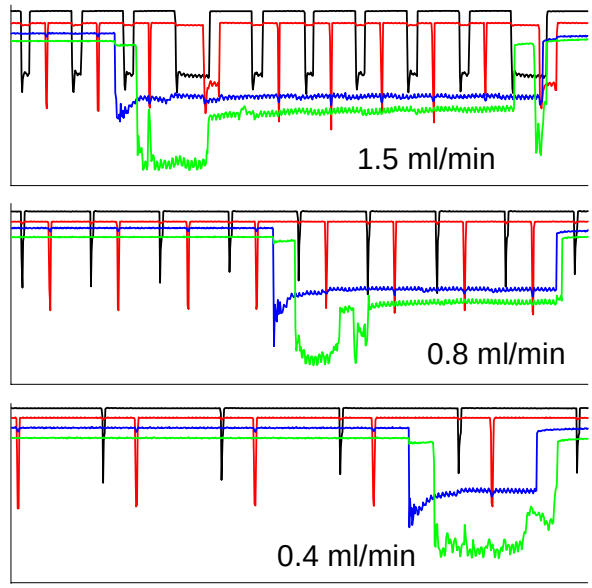

Figure 2. Optical sensor data.

2 (red), 3 (blue), 4 (bottom, green).The degree of deflection from baseline voltage is unchanged from the original range of ~0.2–0.5 V. At 0.4 mL/min, the voltage signal from the 3rd sensor (blue) drops suddenly, then slowly rises to a constant level before sharply returning to baseline. This signal represents a pulse of water that thins out along its trailing edge to form a tail. As shown in Figure 2, the length of the tail increased with the flow rate. At higher flow rates (>2 mL/min), the tail reached sufficient length to form a tendril of fluid conducting flow along the fracture plane. Su et al. (Reference 12) reported a similar transition from pulsed flow to a stable tendril for gravity-driven unsaturated flow between parallel glass plates with a step change in aperture. The bottommost sensor (green) shows more erratic behavior, where a long pulse is closely followed by one or more much shorter pulses (1.5 mL/min).

To characterize flow behavior according to the data streams from the optical sensors, we defined pulse interval as the elapsed time from the leading edge of one pulse to the leading edge of the following pulse. We also defined pulse width as the elapsed time between the leading edge and

trailing edge of an individual pulse. Figure 3 shows each of these measures as a function of flow rate for sensor 3, located 4 cm below the fracture intersection.

Both data sets in Figure 3 are shown on log-log axes to accommodate the wide range of observed data; for clarity, supply flow is shown on the vertical axis. At the highest flow rate considered, behavior was stable (pulse interval = pulse width) with flow occurring as a tendril. As flow decreases, the flowing tendril becomes unstable, breaking and reforming at temporal scales that range over four orders of magnitude. At yet lower flows, pulse interval shows two modes before settling into a single mode that increases with decreasing flow rate. Pulse width shows similar variability at high flow rates before converging to a single value at low flow. As we stepped down the flow rate, the tendril below the intersection became unstable. At ~2 mL/min, snapping and reforming of the tendril became increasingly frequent; during this time, pulse interval and pulse width varied over orders of magnitude. As the flow rate was dropped below ~2 mL/min, we observed a transition from tendrils to pulses, where long pulses at sensor 3 were often immediately followed by one or more short pulses. Below this transition, and down to the smallest flow rates considered, pulse widths remained relatively constant, with a mean of ~3–4 s; pulse interval steadily increased over the same range of flow rates. This combination of a relatively constant pulse width and a negative correlation between flow rate and pulse interval suggest that at low flow rates, conditions for discharge at the intersection involved a finite storage volume.

In the low flow regime, flow was integrated when our simple intersection acted as a capillary

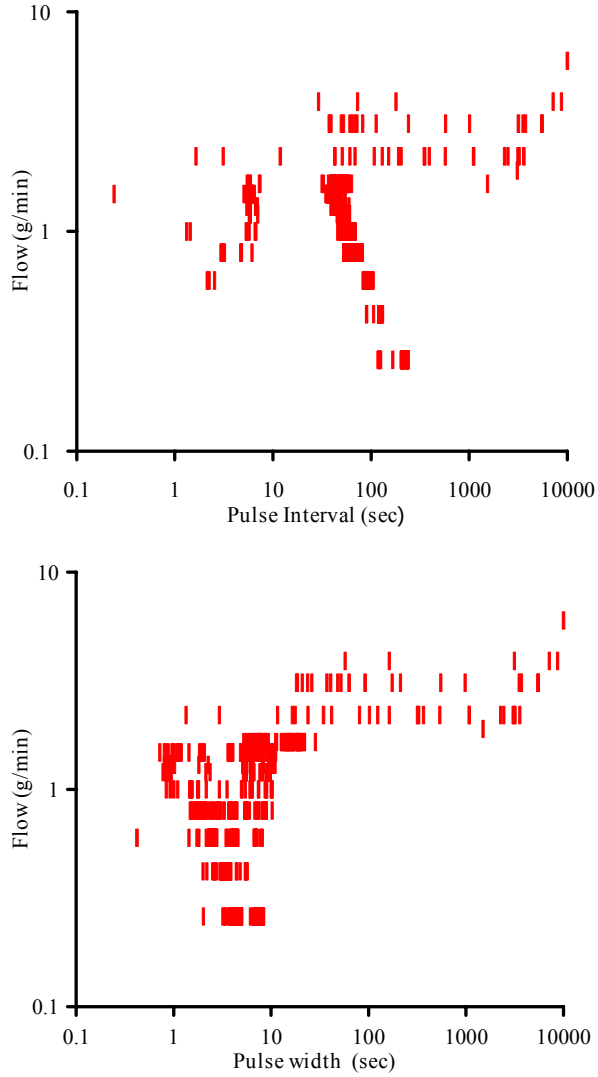

Figure 3. Characteristic measures as a function of flow.

barrier, causing water to pool. Visual observation shows that accumulation and discharge of water at the intersection followed a six-step process (see Figure 4a–f), during which two capillary barriers are breached: (1)Following a discharge event, both horizontal fractures are partially filled, and a small pool of fluid is left above the intersection. Initially, the menisci of these three fluid bodies are not in contact with one another. Because of small differences in aperture geometry, the pool in the right-hand horizontal fracture abuts the intersection, while the pool in the left-hand fracture is retracted. (2) The surface of the pool above the intersection rises with continued addition of water. Increased fluid pressure causes

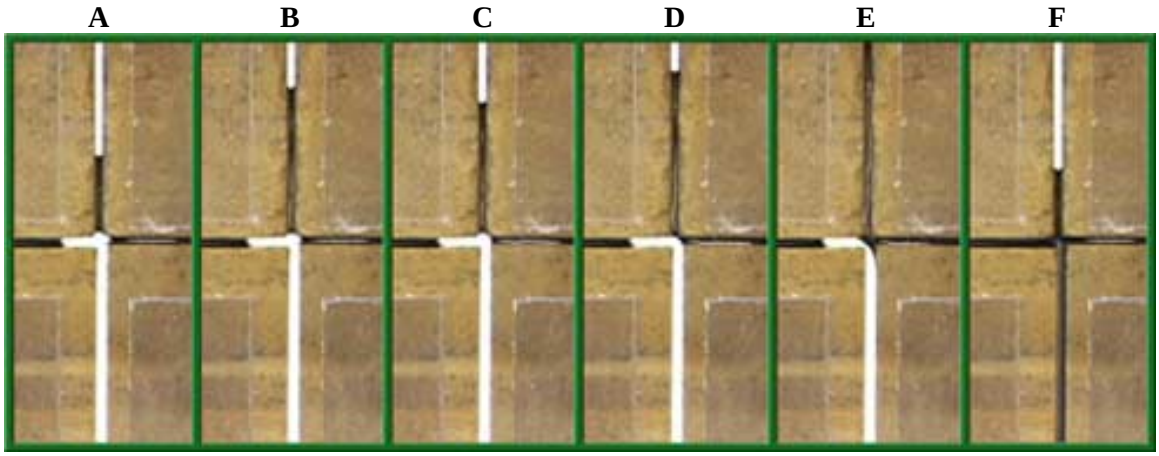

Figure 4. Intersection invasion process

the meniscus along the bottom of the pool to move downward until it connects with fluid in the right-hand fracture, breaching the first capillary barrier. (3) The upper surface of the pool drops slightly as water flows into the right-hand fracture. (4) When storage in the right-hand fracture is filled, the upper surface of the pool again begins to rise. Increased fluid pressure causes the meniscus connecting the upper and right- hand fractures to grow downward into the intersection (5) When this lower meniscus touches the upper corner of the lower left hand brick, the second capillary barrier is breached (image shown is just prior to contact). Note that the fluid pressure (pool height) required to breach this second capillary barrier is greater than for the first (step b). (6) Water rapidly fills the intersection, invading the lower fracture as a gravity-driven finger. The pool above the intersection decreases to a minimum as water flows out of storage in both the upper and horizontal fractures. The finger thins to a tendril as water is depleted. The thinning tendril eventually "snaps " vacating the intersection to produce a condition similar, but not necessarily identical to, that at the beginning of the process (step a). The sequence of steps is then repeated. Clearly, the degree of integration at an intersection will be strongly dependent on the oscillatory storage volume (maximum-minimum) at the capillary barrier. Interestingly, three integrating reservoirs were linked in our experiment.

Figure 4 shows the intersection invasion process as a series of six time-lapsed images of fluid accumulation and discharge that occurred over an ~40-second period at a flow rate of 1 mL/min. Each image shows a 3.5-cm-high by 1.8-cm-wide region about the intersection; dark areas within the fractures are occupied by water, while the light areas are empty. Coupling between pools above the intersection and in the horizontal fracture (left and right), allowed a larger degree of integration than would have occurred with any of the individual pools.

Conclusions. At low flow rates, we find that a simple idealized fracture intersection acts to integrate unsaturated flow, taking a high frequency, low volume inflow and transforming it into a low frequency, high volume outflow. Observation shows that this integration is accomplished by the build up and discharge of fluid, as a sequence of two capillary barriers at the intersection are first established and then breached. The integration volume appears to be well defined, with a small range of fluctuation. As flow rate increases and viscous forces become important, pulsating flow transitions to a stable configuration where the intersection no longer behaves as a gate. Our experiment focused on a simple intersection with only one aperture distribution. During our design phase, we have also seen other interesting behavior generated by fracture intersections, including: multiple tendrils, snap off into the horizontal fracture, migrating tendrils, and spontaneous switching between tendril and dripping behavior at a constant flow rate. Furthermore, we only considered a limited range

of flow rates much smaller (0.23–8 mL/min) than those expected for saturated flow under unit gradient conditions (~600 mL/min). Although we observed a viscous stabilized regime at the upper range of the flows we considered, it is possible that viscous forces may act to destabilize unsaturated flows of greater magnitude. The interplay between system parameters and this rich behavior promises to be an area of fertile research. However, the critical discovery is that individual fracture intersections can act to integrate unsaturated flow. This behavior has strong implications with respect to the development of justifiable conceptual models for fluid flow and contaminant transport in unsaturated fractured rock.

Fluid Behavior in a Mesoscale Fracture Network—30 Brick Experiments

The purpose of this experiment is to study the behavior of water flow through variably saturated fractured rock at the mesoscale under controlled laboratory conditions. These experiments are designed to increase our understanding of the flow processes in fractured rock environments and to bridge the gap between field and bench scale studies. We define the mesoscale as the physical and temporal experimental scale at which the coupling or interdependence of chemical, biological, and physical processes can be observed. Thus, the actual physical scale for a mesoscale experiment depends on the processes of interest and experimental objectives. The mesoscale is large enough to exhibit behavior representative of the interaction of many smaller scale processes, yet small enough that controlling and monitoring the system to examine the effects of individual or multiple variables is possible. We are conducting mesoscale physical model studies to collect sufficient data to document and understand the system dynamics control the boundary conditions and describe and control the system heterogeneity.

The physical model was a wall of 24 or 30 limestone bricks stacked six bricks wide by four to five bricks high. It was constructed to simulate a simple fracture network and to examine the advance of an infiltrating wetting front as it traverses multiple fractures and fracture intersections. Each brick was approximately 30.5 cm tall × 7 cm wide × 5 cm thick. The wall was supported in a model assembly frame, which in turn was supported on a large balance system. The general approach was to introduce water at the top of the model at several of the five vertical fractures, to observe the pattern of water flowing through the fracture network and imbibing into the bricks, and to perform a mass balance for water. Fiberglass wicks (0.635-cm diameter) were placed underneath the bottom row of bricks at each of the five fractures to convey water exiting the simulated fractures to an outflow measuring system. The experimental apparatus included systems for (a) injecting controlled amounts of water into the top of the model; (b) measuring the amount of water exiting the bottom of the model; (c) measuring the amount of water stored in the limestone bricks; (d) measuring the relative humidity within and outside of the experiment; (e) measuring the distribution of barometric pressure within the experiment and the lab itself; (f) monitoring the temperature in and around the experiment; (g) monitoring for seismic anomalies in the laboratory that may trigger unstable flow; and (h) a system for collecting video images of the front of the model to document the wetting process.

The following example of data sets illustrates the wetting and flow processes. Two images of the limestone brick wall collected at different times in the same experiment show wet regions of the bricks as a darker color (see Figure 5). The same flux of water was supplied to each vertical fracture at the top of the model, yet penetration of water varied between different fractures. Flow converged with depth, with water being conducted through all five vertical fractures in the uppermost row, four in the second and third rows, and a different set of four vertical fractures in the bottom row. Convergence of flow with depth and spontaneous changes in flow paths were observed.

We used data from the mass measurement system to examine the dynamics of flow and fracture/matrix interactions. As shown in Figure 6, the total discharge from the system and the rate of change of mass storage in the matrix (shown normalized) showed little change after approximately 1,500 minutes of testing. After this time, the rate of combined mass flux out of the system maintained a near maximum value while

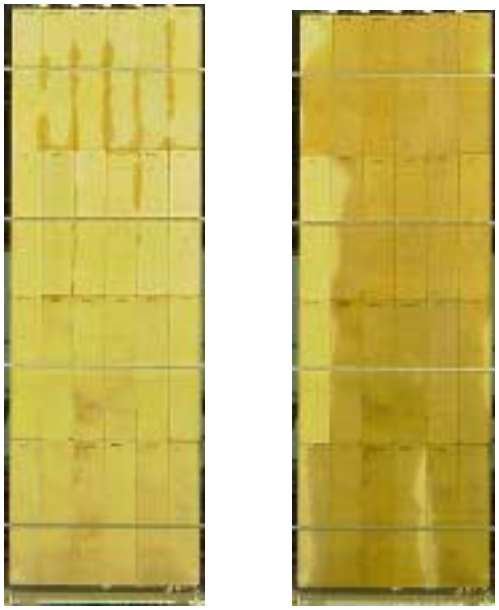

A B

Figure 5. Time-lapse images of the front of the bricks from one of the tests. Image A was taken 1 hr after starting water flow; image B, 15 hrs after.

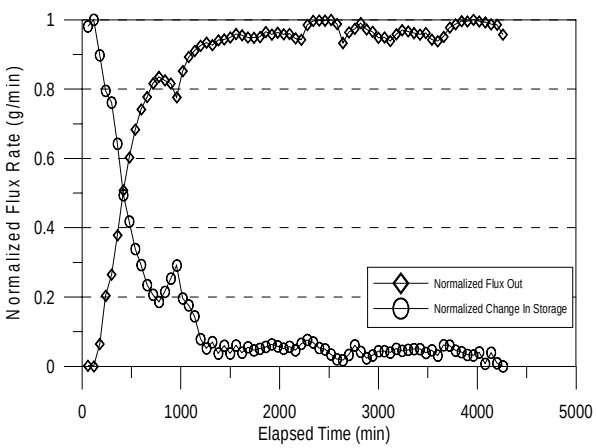

Figure 6. Time course of normalized flux rate of water out of and change of water stored in the brick matrix.

the matrix no longer imbibed a significant amount of mass. One interesting event occurred at approximately 900 minutes of elapsed test time, shown by the spike in the flux into the matrix and drop in the flux out of the system. We postulate that this was in response to a new flow path being generated in the system, exposing the flowing water to dryer areas within the rock matrix, and hence, more water was taken into storage by the system. This observation can be confirmed by examining Figure 7, which shows the cumulative mass out of each fracture and the corresponding fluxes, respectively. This figure clearly shows that the flux out of Drain 4 suddenly began at this time, while flux out of Drain 5 showed a rapid decrease. More interestingly however, was the fact that after approximately 1,500 minutes of testing the cumulative flux out of the system and flux into storage remained relatively constant, indicating the system had reached a pseudo steady-state condition, yet the fluctuations in flux continued to occur among the individual fractures. For example, after 1,500 minutes, the flux into Drain 5 showed a continual increase, seemingly at the expense of Drain 4. In addition, at approximately 2,800 minutes, the flux into Drain 5 suddenly increased by over 0.3 g/min while a decrease was observed in Drains 1 and 2 (see Figure 5). These data strongly suggest dynamical switching of flow paths in the system after it had seemingly reached steady state. The measurements of discharge from the bottom of the vertical fractures show that the flow was not uniformly distributed among vertical fractures despite a uniform flow provided to the top of each fracture. Furthermore, the flow from individual fractures varied over time. Changes in flow from individual vertical fractures over time suggest that dynamical behavior occurred in this system during these 3-day tests. Longer tests are planned to fully evaluate the dynamical behavior and its cause(s).

Longer-term tests (approximately 30 days) are now being conducted to observe trends in data over longer time scales. The results of all experiments are being compared with conventional numerical models as described below.

Impact of Microorganisms on the Dynamics of Unsaturated Flow within Fractures

Microorganisms are widespread in the environment and their presence in the deep subsurface terrestrial ecosphere is no exception.[14-20] Understanding the impact of microbiota on fluid flow in ground water and subsurface environments is of significance because of the importance of the water resources, contaminant transport issues, and the potential use of microorganisms for in situ processes such as mineral dissolution and

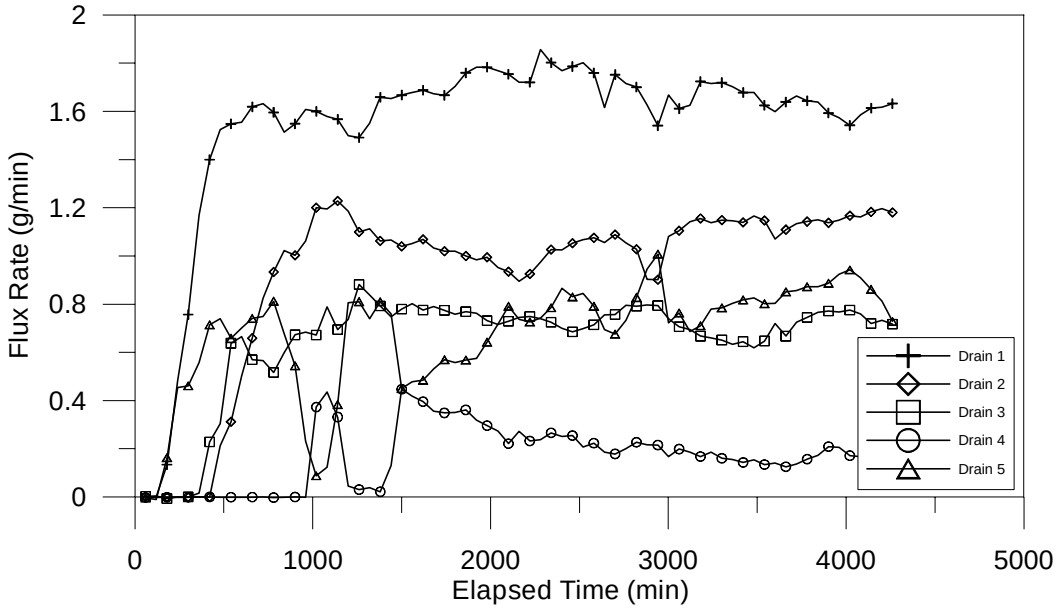

Figure 7. Fluxes out of individual fractures.

recovery, microbially enhanced oil recovery, and remediation technologies.[21–23] Studies at the INEEL demonstrated the occurrence of converging and spontaneously changing flow paths within mesoscale, laboratory test beds (see Reference 8) that could account for the large, dynamical flow fluctuations observed in field and laboratory studies,[24] and the rapid transport, as well as the intermittent detection of contaminants in monitoring wells hundreds to thousands of meters (see References 5–9) from potential contaminant sources. A closer look at the dynamics within fractures revealed that fracture intersections acted as integrators that transformed the regular flow behavior observed above the intersection into large irregularly occurring pulses below that intersection.[25,26] To our knowledge, the role of microorganisms in generating or triggering dynamical in-fracture behavior of unsaturated flow in the fractured-rock systems had not been previously evaluated, although it has been mentioned as a possible cause of variation in flow behavior (see Reference 24).

In this study, an experimental system (see Figure 8) comprised of limestone blocks and a ground water bacterial isolate were used to evaluate the impact of microorganisms on fluid behavior within fractures. This ground water isolate is of interest because of the potential use of microorganisms for the in situ generation of barriers to contain contaminants in the subsurface. Four blocks (25 cm × 6.6 cm × 5 cm) were configured to make a vertical fracture (50.2 × 5 × 0.07 cm) that was intersected at a right angle by a horizontal fracture (13.4 × 5 × 0.1 cm). To monitor the behavior of water within the fracture, five optical sensors were installed external to the vertical fracture, two were installed above the fracture intersection, two below, and one at the intersection. Each optical sensor consisted of a light emitting diode as the light source and a photocell to detect the light passing through the fracture. The presence of fluid was detected as a decrease in light transmission as the fluid passed by each detector. Drop interval (the period of time between succeeding drops at the same detector) and drop width (the period of time it took for a water drop or stream to pass by each detector) data was collected for each of the five detectors during each data acquisition period. Liquids were introduced via a single needle at the top of the fracture at a rate of 0.5 mL/min. Deionized water, which had been chemically equilibrated with the limestone rock, was the control medium into which cells, cells with 0.01% yeast extract, cells with 0.1% yeast extract, and cells with 0.1% yeast extract and 30 mM urea were added. For the equilibrated water, drop intervals and drop widths above the fracture intersection were ~1 second and

<0.1 second, respectively. Drop intervals and widths at and below the fracture intersection were ~100 seconds and ~10 seconds, respectively. The addition of cells or cells with 0.01% yeast extract had little effect on drop intervals and drop widths above the fracture intersection (see Figure 9). At and below the intersection, however, drop intervals increased to ~500 seconds and drop widths to ~10 seconds. Later, with the addition of 0.1% yeast extract or 0.1% with urea, drop interval and drop width immediately increased at locations above the fracture intersection and again within 24 hours continuous streaming was observed. For the lower sensors, drop interval and drop width initially decreased, followed by continuous streaming the day after the 0.1% yeast extract and urea was added to the system. The dynamics of drop behavior in fracture systems is a complex process that is impacted by the presence of bacteria, nutrient amendments and the fracture configuration.

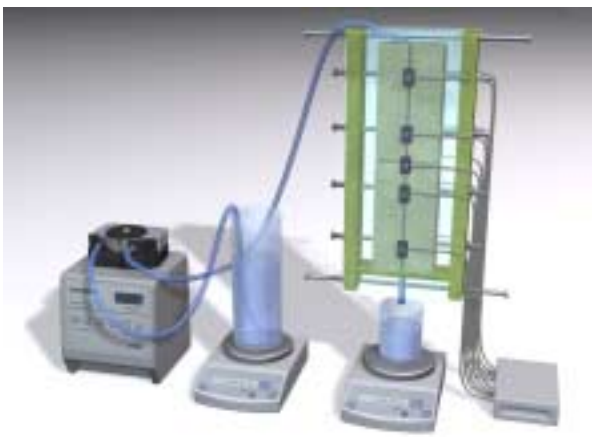

Figure 8. An experimental apparatus consisting of four limestone blocks configured as intersecting fractures. Light emitting diodes and detectors were used to monitor drip events, drop interval and drop width within the fractures.

Convergent Flow Observed in a Laboratory-Scale Unsaturated Fracture System

It was recognized in the last decade that flow in unsaturated fractured media with a low-permeability matrix might not always be diffusive (continuously spreading in the directions orthogonal to the direction of infiltration). Instead,

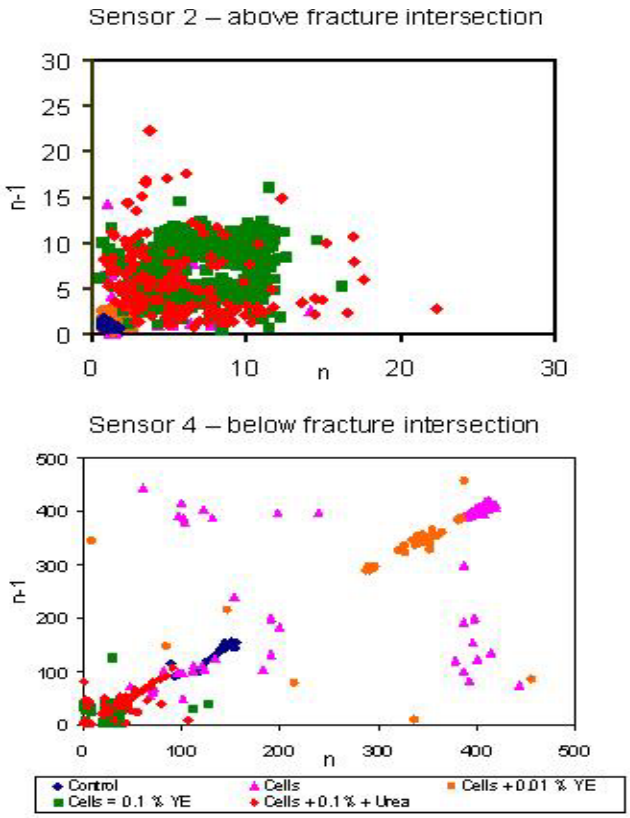

Figure 9. Phase plots of drop intervals within a fracture system showing the impact of bacteria and nutrient amendments on fluid flow within fractures. Sensors 2 and 4 are above and below the fracture intersection, respectively.

it was proposed, via a thought experiment, that the flow might focus or converge, even in the absence of strong heterogeneity, ultimately flowing down only a few fractures in an otherwise pervasively fractured rock formation.[27] Diffusive behavior is expected from the traditional volume-averaged porous-continuum model of flow physics, wherein any irregularities within the flow field would be attributed to heterogeneities in the material properties. Figure 10 illustrates these two circumstances. For the diffusive case, the flow creates the one-dimensional saturation profiles that spread throughout the matrix. For the convergent case, discrete flow paths combine with depth.

The presence of focused or convergent flow within unsaturated rock formations has been suggested in the literature.[28] A variety of evidence shows rapid and deep penetration of meteoric water in fractured vadose zones,[29,30] as well as

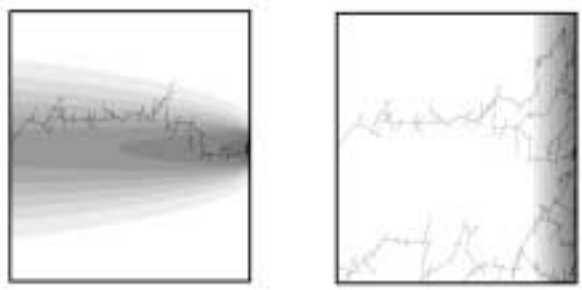

Figure 10. Convergent flow observed in a laboratory-scale unsaturated fracture system.

infield-scale[31] and other laboratory-scale infiltration experiments.[32] Nevertheless, the direct observation of convergent flow has been elusive. The thought experiment proposed by Glass (see Reference 31), led us to conduct the experiments where flow in a fractured unsaturated media could be observed.

The experimental system employed 12 limestone bricks (each nominally 30 × 7 × 5 cm) to form a vertical plane 90 cm high and 28 cm wide, with three rows of four bricks. The gaps between the bricks play the role of fractures. The bricks were held together with a horizontal compressive load. The entire system was encased in transparent plastic, which reduced evaporation. Irregularities in the brick surfaces due to saw cuts employed in fabrication led to variable apertures within the fracture network. Where four bricks came together, an intersection was formed with additional irregularities due to imperfections along the corners of the bricks. The surrogate for ground water was tap water chemically equilibrated with the limestone bricks. This water then was supplied to needles at the top of the network, at equal rates (1 mL/min) to each of the three fractures. Fiberglass wicks 30 cm long were connected to the bottom of the vertical fractures; therefore, the suction applied to the bottom was equivalent to a hanging column the height of one brick. Loadcells were employed for both the supply and recovery bottles for each fracture to verify the in-flow rate. Figure 11 shows a schematic of the apparatus.

Five configurations were constructed in which the bricks for each were randomly permuted within the geometry specified above—three rows of four bricks in a vertical plane (see Figure 11).

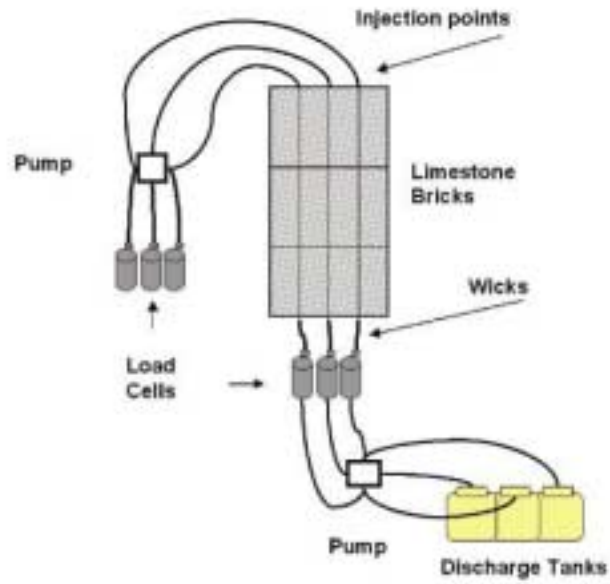

Figure 11. Schematic of laboratory-scale unsaturated fracture system.

Eight experiments were performed (one on each of four configurations and four on the other configuration) as discussed below. The bricks were thoroughly air-dried at the start of each experiment. The infiltration process was recorded with time-lapse video. Within 24 hours, all bricks in all arrangements were wet. A sequence of frames (spanning over 9 hours) in one of the arrangements with converging flow is shown in Figure 12. One sees a stop-and-go dynamic as the water moves through the network to break-through (less than 2 hrs). Water moves rapidly down to an intersection and then waits. At least one horizontal fracture at an intersection is spanned, and then, after a further wait, water continues downward but now often as a combined flow from two fractures above. After breakthrough (greater than 2.6 hrs), the bricks continue to wet from the water flowing within the fractures, and occasionally, additional fractures begin to carry some flow.

Of the five permuted configurations tested, three displayed convergence at the scale of the experiment. One of the three arrangements that displayed converging flow was retested three times, without rearrangement, after drying each time. All four of those tests displayed similar converging flow.

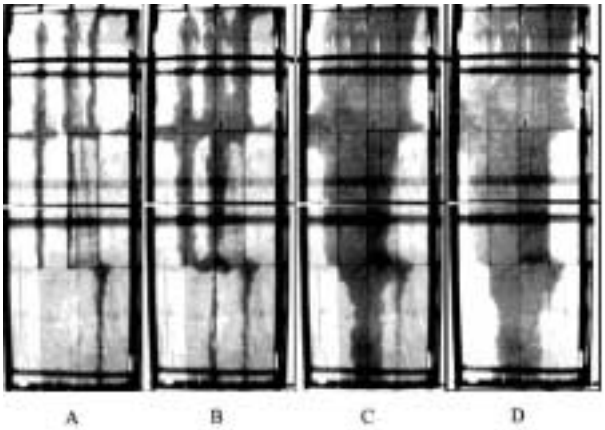

Figure 12. The infiltration process recorded with time-lapse video over 9 hours in one of the eight experiments.

Even with only five independent samples (corresponding to the five permutations of the bricks), a quantitative estimate of the uncertainty in the mean occurrence of converging flow can be achieved via the bootstrap method.[33] The bootstrap with exact enumeration gives for the mean occurrence of converging flow at the 80% confidence level. Therefore, the occurrence of converging flow is at least as statistically significant as the occurrence of uniform flow in these experiments.

The cause of convergent, or focused flow has been attributed to pathway integration by capillary barriers. Multiple pathways from above are combined in the pool above a capillary barrier. When this barrier breaches, it tends to do so at a single location from which the integrated flow emanates. In our experiment, the intersections of the horizontal and vertical fractures between bricks act as capillary barriers. Subsequent to breaching the intersection, the water was observed to enter one of the two horizontal fractures, fill it, and then breach the lower vertical fracture and continue downward. It is this added behavior of the horizontal fractures during the intersection invasion process that results in convergence. Where two vertical fractures are connected by a filled horizontal fracture, the combined flow tends to enter the vertical fracture that breaches first, leaving the other vertical fracture empty. The sequential application of this process with depth causes continued pathway convergence. For convergence to continue with depth, pathways must come into contact via capillary barriers of increasing scale, but this requirement is likely to be fulfilled for a wide variety of fractured systems.

In conclusion, the results of this study support the conjecture of Glass et al. (see Reference 27) An additional focusing can occur if a horizontal fracture is already filled when water reaches the intersection from above. From the geometrical arguments employed elsewhere for pores,[34] the pressure to breach the barrier will be lowered in this case; thus, facilitating the spanning of the intersection to the horizontal fracture that was initially filled, and causing the capture of a lagging pathway by a leader (see Reference 31).[35] Converging flow was observed in a laboratory-scale fracture network, apparently for the first time. The mechanism for local convergence within the fracture network is due to the behavior of fractures and fracture intersections as flow conduits and distributed capillary barriers, respectively.

Small-Scale ERT Monitoring of Fluid Flow in Fractured Rocks

The Electrical Resistivity Tomography (ERT) method is an adaptation of the traditional surface resistivity geophysical method. Where traditional resistivity surveys use a relatively small number of measurements collected along a single line using a single specific electrode pattern or array, ERT employs the collection of large, high-density data sets using two- or three-dimensional arrays of electrodes. Our objective for this experiment was to develop methods of making small-scale (centimeter to tens of centimeter) measurements of fractured systems. The primary goal is to improve these methods to allow them to support hydrological research at this scale. A useful property of ERT is that the methodology is scalable, meaning it can be applied to a wide range of dimensions ranging from core-sample studies to scales that are on the order of hundreds of meters. Although theory allows for ERT measurements at any scale, problems are encountered in making very small-scale measurements. As we decrease the scale of the system, we also must decrease the size of the electrodes. Small electrodes have large contact resistance (they do not connect well to the earth or model) that in turn decreases the strength of the injected electric current and increases the electrical

noise. Thus the design of electrode systems is a significant challenge for very small systems.

The imaging of ERT data depends on the development of a sophisticated inverse algorithm to reconstruct three-dimensional (3-D) conductivity distributions from electrical resistance measurements. The results presented here used the 3-D inverse algorithm described by LaBrecque and Casale (see Reference 35), which is an anisotropic version of the finite-difference formulation of Dey and Morrison.[36] The algorithm uses the so-called Occam's inversion method,[37] and seeks to find the smoothest possible solution that still fits the data within a specified a-priori value (see Reference 35).[38] An iterative approach is used that compares the data with calculated responses that would occur if the anisotropic electrical conductivity and corresponding distribution of electric source currents from the last version of the modeled earth were true. The relationship between the various parameters is based on Ohms law, which relates current, resistance, and electrical potential.

The experiments used the simplified physical model of a fracture system shown in Figure 13. The model was built using 24 limestone blocks arranged in a rectangle (Images 13a and b). Each of the blocks is approximately 30 cm long by 7 cm wide by 5 cm thick. The individual blocks were held tightly together using a series of clamps. Each electrode was made from four stainless-steel, self-tapping, screws arranged in a 2.54 cm (1-in.) square pattern (Image 13c). The screws are 2.5 cm (1 in.) long, 6.35 mm (1/4 in.) in diameter, and were inserted into 6 mm holes that had been filled with conductive electrolytic gel (Spectra 360). The screws tap themselves into the limestone.

Twelve electrodes were spaced at 10 cm (4 in.) along each side of the model. Four

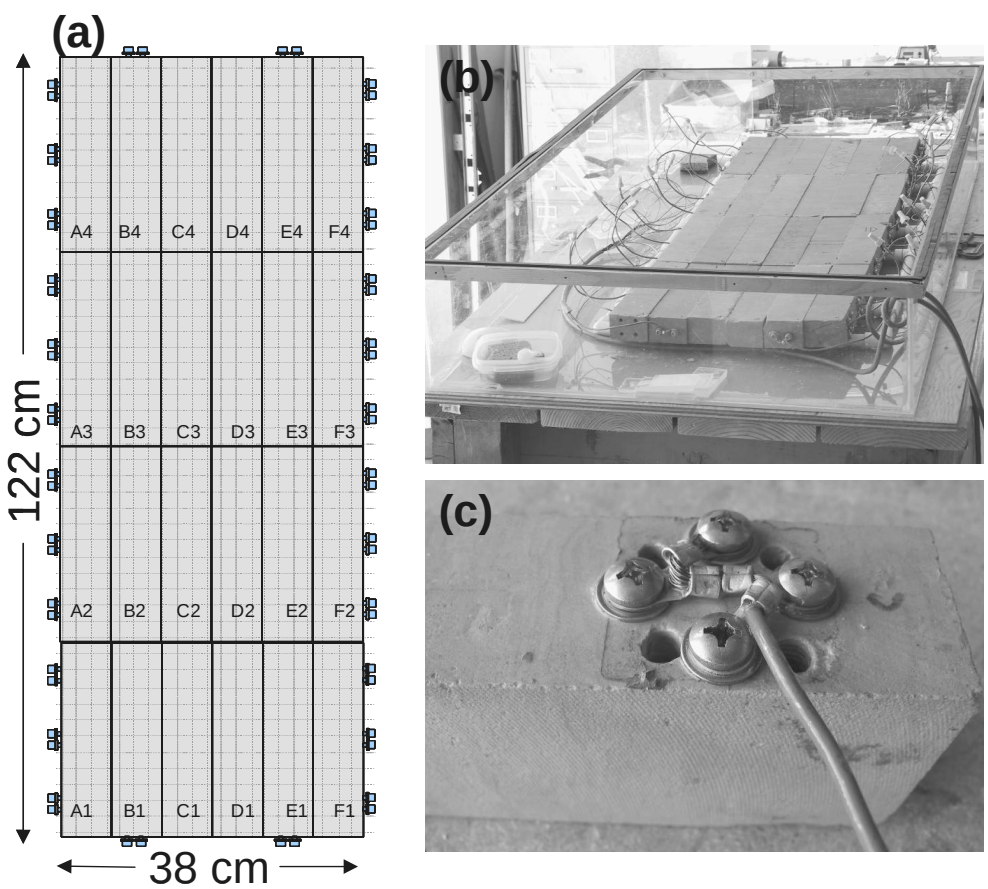

Figure 13. Simplified physical model of a fracture system enclosed in a Plexiglas box.

additional electrodes were placed in the top and bottom of the model by inserting a pair of stainless steel screws into holes drilled into the ends of bricks. The entire apparatus was enclosed in a Plexiglas box (Image 13b) to control water loss and humidity. We conducted experiments in which a single, known variable was changed.

Resistive (dry) fractures were made by placing a piece of vinyl 0.5 mm thick in one of the joints between two or more bricks. Conductive (wet) fractures were created by injecting a small quantity of water into the center of one of the joints between the bricks. Dye was added to the injected water to find if the water "wicked" along the fracture due to capillary forces. "Background" data were collected before and after each experiment. Generally, it required less than 1 hour to complete a given experiment, so there should have been very little change in the system except in and adjacent to the fracture.

Before assembling the model, the blocks were soaked in tap water overnight then assembled as shown in Figure 13. Data were collected using a common separation for transmit and receive electrode pairs. Since each electrode pair consists of two electrical poles, and since these dipoles are the same size, this electrode configuration is called a "dipole-dipole" array. In this case, the size of the dipoles (dipole-length) was a brick-circumference-based 10 cm length. Since each dipole-length does not contain another electrode (adjacent electrodes are employed), this dipole-length is often generically referred to as "skip 0" or "dipole-length 1."

Our experiments fall into two groups: resistive fractures, in which a piece of vinyl is used to create a near-perfect resistor, and conductive fractures, in which water is added. Each of these experiments presented unique challenges to data collection and processing. For resistive features, the presence of the target radically changes the electric current flow within the model. The results were completely electrically isolated. The resistivity of [su] is highly nonlinear, and thus present difficulties in both forward and inverse modeling. In the most extreme case, portions of the model can be [ch] a region would be indeterminate. Although they would not be completely undetermined, we would expect to see difficulties in imaging regions that are partly, but not totally isolated from the rest of the model, such as when multiple resistive fractures were present or the resistor was near the edges of the mesh.A vinyl resistor was added between the bricks, as indicated by the region shown in the hatched box (see Figure 14). Each image in Figure 14 shows the percent change between the background and image of the model with a resistive target. Resistivities along the fracture increase by up to a factor of 2,000. The extreme contrast of the resistor generated some variability in results as indicated; however, the main point of the experiment was to prove that the inversion would correctly locate a resistive fracture. For a vertically directed resistive target that is near the center of the model (Images 14a and b), the anomalies in the images agree fairly well with the true locations of the fractures. However, when the target is moved to the fractures along the edge of the model (Image 14c), the image of the resistor tends to be shifted inward towards the center of the model. Although the routine correctly located horizontal fractures, the anomalies tended to be short and thick rather than elongated (Image 14d).

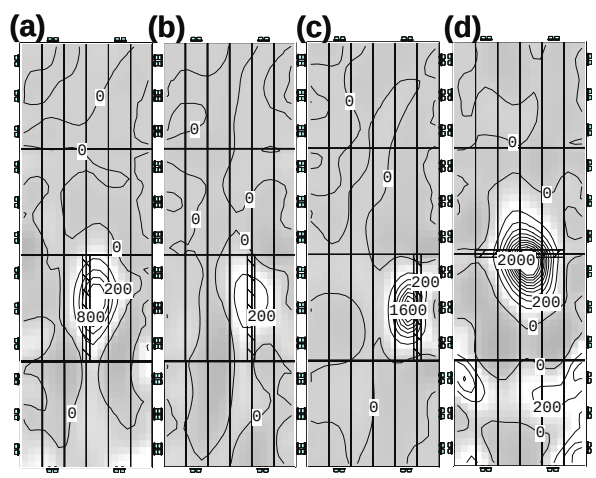

Figure 14. ERT images of "resistive fractures" located (a) center (b) offset from the center (c) near the edge, and (d) horizontal. Contours are percent difference from background.

The conductive targets are much more amenable to our existing forward and inverse modeling. However, the anomalies were much smaller amplitude. To image the subtle change in resistivity produced in the conductive experiments,

we found it necessary to use the difference processing techniques (see Reference 6). Figure 15 illustrates the application of this processing to one of the more difficult targets. Images 15a and 15b show the resistivity images made, without any special processing, for data collected before and after injecting 10 cc of water along the vertical fracture at the bottom center of the image. Because the resistivities vary on a steep gradient, extending over a broad range of values, it is difficult to compare the two images. With Occam's inversion, we trade off image resolution versus data fit. Thus small changes in the quantity or quality of the data can result in differences in resolution of anomalous features. When we compare images, any change in resolution between images will cause artifacts to appear on the flanks of the anomalies. When we compare the first two images, we see a number of these artifacts throughout the image (Image 15c). Using the difference inversion (Image 15d) eliminates most of the artifacts.

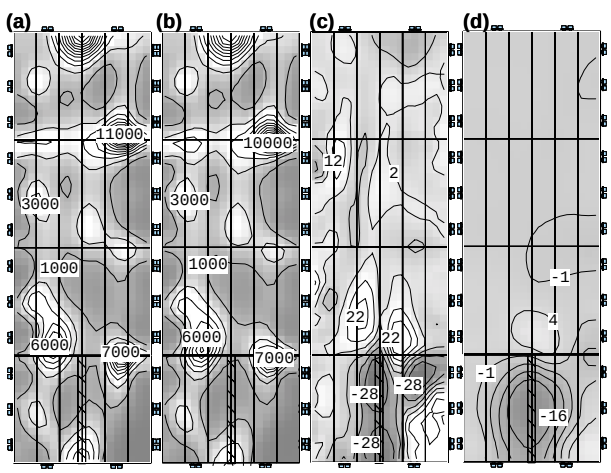

Figure 15. ERT images illustrating the processing progression; (a) background data; (b) raw "C1-D1" data; (c) percent difference between images in (a) and (b); (d) percent difference between the difference inverted and background images.

Figure 16, compares the ability of ERT to locate conductive targets in different parts of the model. In each case, ten cubic centimeters of water were added along the surface of the fracture in the region shown as the hatched box. The background data were collected before adding water, and the water-added data were collected within 10 minutes of water addition. The individual images in Figure 16 show the percent change from background. Note that imaged resistivities along the fracture decrease by only 20–30%; yet the routine is clearly able to identify and properly locate the area of water addition. The imaging method is able to correctly locate the targets for most cases. However, the resolution is far better for fractures near the center of the mesh than near the edges.

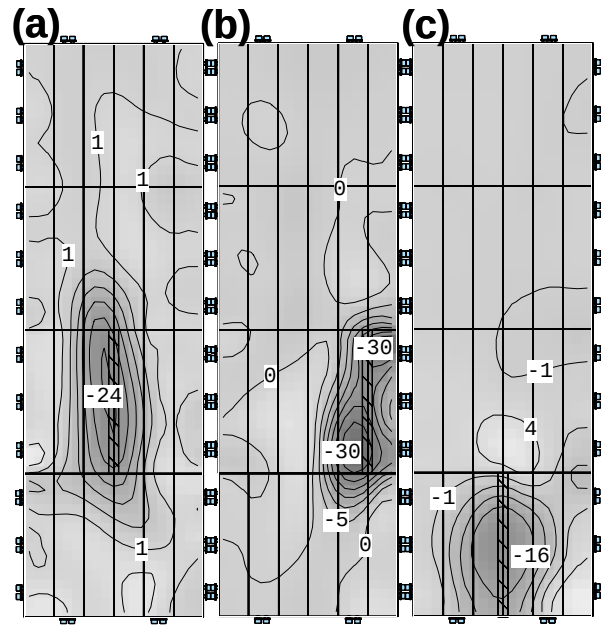

Figure 16. ERT images of "conductive fractures" located at (a) C2-D2, (b) D2-E2, and (c) DC1-D1. Data have been difference inverted and units are percent difference from background.

The ability of ERT to accurately resolve conductive and resistive fractures in homogenous background has been demonstrated. The interpretation is complicated by the fact both the limestone blocks and the fractures between the blocks showed a great deal of variability in resistivity prior to emplacing any targets. This can be compensated for by careful experiments in which only a single variable is changed but the large variability of the background resistivity can make comparisons of the images difficult.

Evaluation of Real Vadose Zones for Complexity

The ground water beneath the Radioactive Waste Management Complex (RWMC) (see Figure 17) is

monitored quarterly and undergoes field, laboratory, and statistical detection confirmation protocols. The statistical protocols assume that contaminants would be released in a uniform manner and disperse evenly through the vadose zone to the aquifer. The statistical methods were applied to historical data to determine if past analytical detections were significantly higher than background contamination levels, and if the observed data supported the assumed conceptual site model for flow. The resulting conclusions were that only some of the analytical detections were significantly higher than background—supporting the need for statistical as well as field and laboratory comparisons of the data, and that observed data supported the assumed conceptual site model for flow. The resulting conclusions were that only some of the analytical detections were significantly higher than background—supporting the need for statistical as well as field and laboratory comparisons of the data, and that the observed data did not support the flow model. If the assumed model were correct, then contamination would be pervasive instead of intermittent. An alternative flow model, avalanches of flow through preferential flow paths, might support such intermittent statistical detections. Further work includes rigorous comparison of historical monitoring data to simulated preferential flow path data, and possibly, development of statistical methods that are appropriate under this new assumed model.

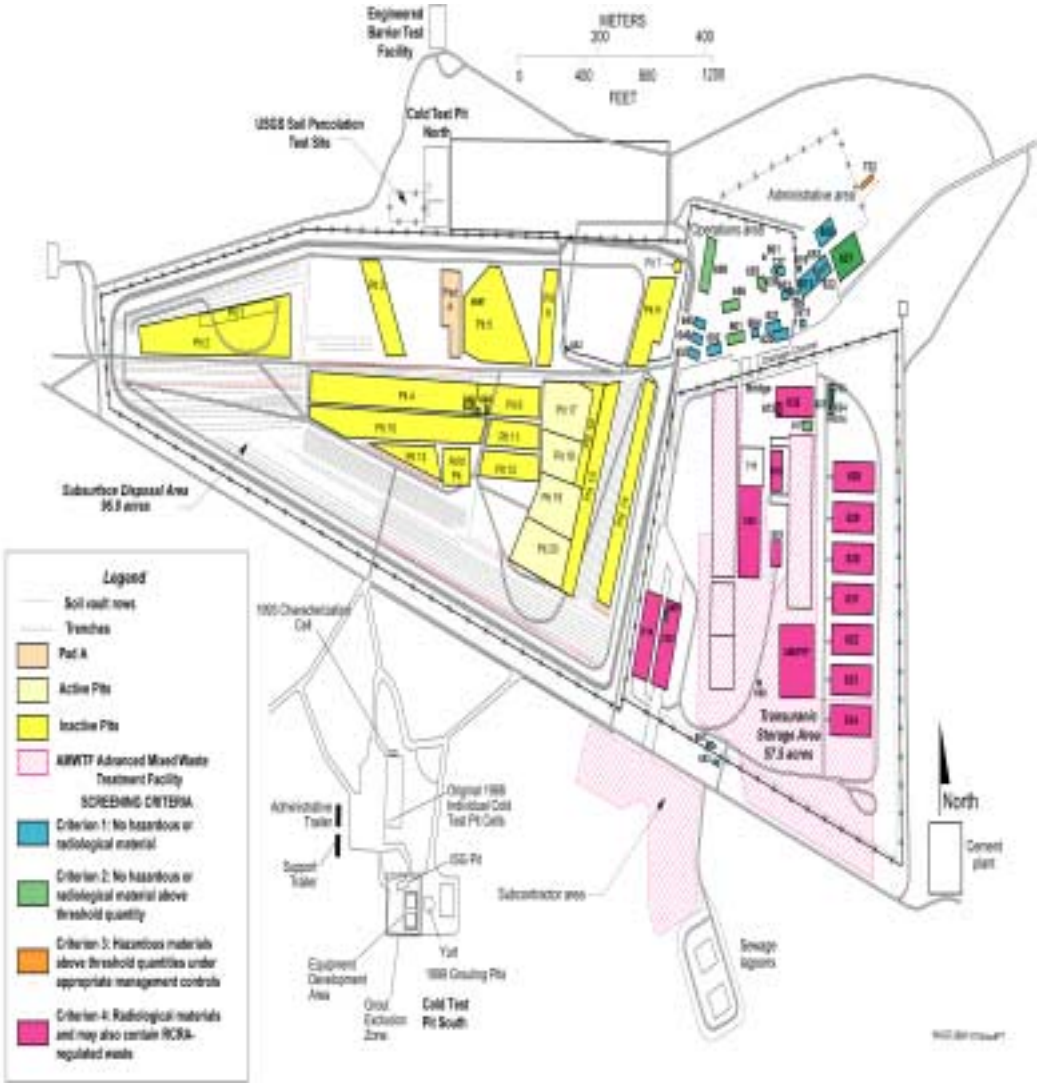

Figure 17. The Radioactive Waste Management Complex.

The data validation protocol historically used to detect radionuclides in ground water was error-prone based on the assumed conceptual site model. Analytical detections were discounted at the next sampling round, which conflicts with the assumption of diffusive flow. These false-positives cause undue public concern and political upheaval. The protocol depends solely on analytical precision, not statistical comparison between ground water well samples and back-ground status. Since weapons were tested in the area, background levels greater than zero are expected. Also, since detection decisions were made with respect to sample-specific values (minimum detectable activity and standard deviation) no probability of an incorrect decision could be calculated.

Statistical methods allow discrimination between detectable background levels and contamination in the ground water at specified rates of false-positive and false-negative decisions. A false-positive decision is made if detection is declared when there is no contamination. A false-negative decision is made if true contamination fails to be detected in the sample. Each new result is compared to the background distribution so a false-positive and false-negative (assuming an elevated value) rates can be fixed.

The radionuclide ground water monitoring at the RWMC has four characteristics to consider when developing a data validation protocol. First, since the local gradient is indeterminate, the relative position of the monitoring wells to the source is unknown. Without up-gradient and down-gradient wells, no direct comparison can be made and validation is made on an intrawell basis. Second, there is no predisposal data, so that current status cannot be compared to historically clean status. Third, multiple wells are sampled and a decision about the RWMC is based on results from all wells. The acceptable error rate on the sitewide decision must account for the many well-specific decisions. Finally, the radionuclide data do not contain ND placeholders, although nondetect values are reported. The data consist of values with qualifiers indicating the analytical detection status based on analytical precision, MDAs, and comparison with field blank results (Figure 18). This allows more rigorous data analysis, but differs from most published approaches.

Three approaches were applied to historical data; a combination control chart, and two types of prediction limits. The control chart is a combination[39] of the Shewart Control Chart,[40] developed to discover large deviations from the expected level, and the CUSUM Control Chart,[41] developed to discover gradual changes over time. Prediction limits are used to discover large deviations only.

In order to compare the three methods to the current approach, each was applied to the historical database for plutonium-238 and americium 241 from 16 monitoring wells from 7/1996 to 4/2001. In order to apply the methods, a background status was determined. A background database was parsed from the historical database and the methods applied to all values.

The frequency of detections was compared for each method. Since none of the historic results were confirmed on the next sampling round we assumed no true positive detections. Based on that assumption, we calculated false-positive rates. Note that false-negative rates could not be calculated under this assumption since there were no true positives. The method with the fewest sample detections was deemed best under the assumed conceptual site model. This assumed conceptual model is based upon slowly moving diffusive plumes, which does not and cannot account for intermittent, spiky contaminant concentrations measured at monitoring wells.

The combined control chart is the recommended method since it performed best on the historical data and also has desirable properties. It had the fewest detections overall, and none for values that were analytically undetectable. It has a trigger for both large sudden shifts and gradual changes. It is sequential in nature, as are the measurements. It is also more robust to nonnormality than the parametric prediction limits. The nonparametric prediction limit method is appropriate for wells with little historical data, but false positive rates are high and soon outlives its usefulness when data is available to estimate the mean and variance. The parametric prediction limit is not robust to lack of normality.

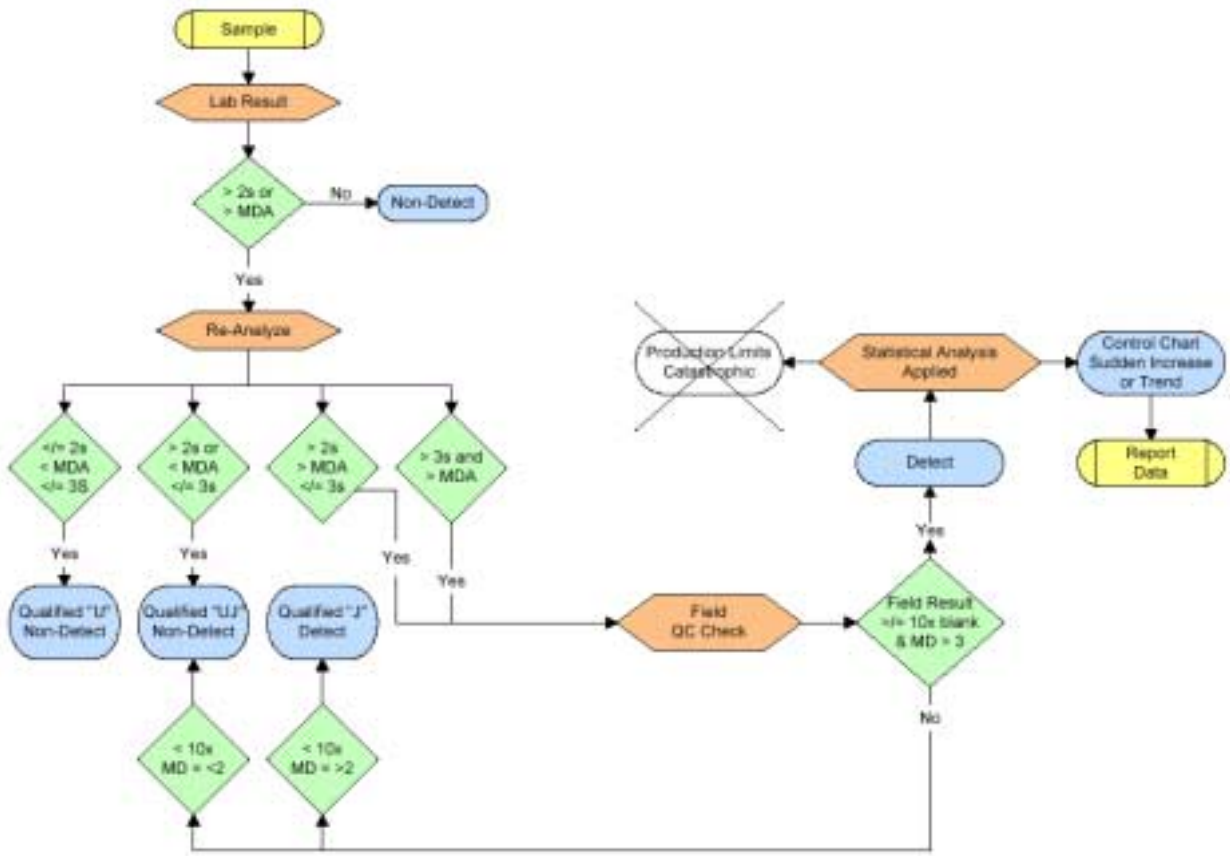

Figure 18. Flowchart of proposed monitoring data validation process.

The combined control chart method and analyses performed on the INEEL monitoring data address criticisms made of the EPA guidance.[42–45] The first criticism of the EPA guidance is that many wells are sampled for many constituents and there is not adequate guidance on controlling the facility-wide false-positive rate for all of these tests while retaining a suitable true-positive rate. The guidance does not even suggest what appropriate rates are. In our proposed method, the facility-wide false-positive rate is reduced by the resampling practice. Average run lengths characterize the performance instead of false-positive and false-negative rates.

The second criticism is that there is no guidance on determining and dealing with spatial relationships among wells. The spatial relationship of the INEEL monitoring data was investigated and discounted. Tests for differences among wells were insignificant (Kruskal-Wallis, $p = 0.6$ for Am-241 and $p = 0.9$ for Pu-238) and the variogram (distance and variance between pairs of sites at that approximate distance) was level indicating no spatial correlation. The third criticism is that the measurement error is unaccounted for by current methods. The measurement error was investigated and found to be the same as the sample variance, indicating that no additional variance component was necessary in this INEEL monitoring data. The measurement variance (uncertainty value, σ) is considered in our validation protocol by previous decisions made on the sample data (see Figure 18), using advice from Currie.[46] The fourth criticism is that repeated sampling too close in time may induce temporal correlation, and hence violate independence assumptions. When re-sampling is advocated in the guidance, a time lag has not been recommended. It has been shown[42,44] that, depending on the system, at least a month between samples is necessary to obtain independent results. Since we have no data to refute this claim, the proposed method includes this recommendation.

Another recommendation is to average reanalysis values when appropriate. Samples are reanalyzed if they exceed 2σ and the MDA. Averaging of reanalyses provides a better estimate of the concentration. Only results that have the same data qualifiers should be averaged. The assumption of a diffusive flow model supports the hypothesis that the historical analytical detections are high values but within the range of background status. The interbedded basalt flows and soil may affect flow differently than assumed by the conceptual site model. A different flow model might support a different hypothesis for the data. For instance a pipe model or preferential flow model might support the high values as representing sporadic contamination of the aquifer. This could be explored using experimental and simulated data. The effect of sampling frequency could also be explored (under various flow assumptions) using this data. Work on this is forthcoming.

Modeling Variable Flow Networks with Self-Organized Dynamics

Computational analysis conducted in FY 2001 indicated that the variable flow rates in fractured rock vadose zones could be accounted for with concepts based on self-organized dynamics. The computational analysis was based on field data collected during the Hell's Half Acre (HHA) study. In this study a series of small-scale (1 m) infiltration tests showed highly variable flow rates, which were apparently unrelated to the water head in the infiltration pond.[47] Water had been maintained at constant pressure at the surface of a bed of fractured basaltic rock and allowed to percolate downward, through a fracture to an open chamber about 1 m or so below (see Figure 19). Droplets form at various sites on the underside of the basalt flow and drip at irregular intervals into the cavity. Detachment of drops was monitored by a collection of piezoelectric sensors and drops were collected to measure total flow mass. Mean-field theories predict that, under the relatively fixed boundary conditions of this experiment, steady flow will eventually be attained. On the contrary, steady flow was never observed in the HHA data.

HHA flow rate data exhibit strong fluctuations that, most likely, are not due to some low-dimensional process. The HHA drop interval data show even greater variability. If one examines the frequency of occurrence of drop intervals of different sizes in the HHA data, one finds an approximate power law relationship. Power law behavior is often symptomatic of an underlying process that lacks a characteristic length or time scale. One circumstance in which power laws can arise is when a spatio-temporal system is decomposable into a network of subsystems with a wide range of sizes.[48] Because of the heterogeneity of cracks in fractured media, flow in fractured rock is a natural candidate for being such a system. In particular, we propose that flow of liquid through channels in fractured rock can be expected to episodically turn on and off as conditions of channel wetting, channel blockage, bubble formation, and the like vary. We expect that such fluctuations can result in flow networks with a self-organizing character. The simplest example of this is that flow, stopped in one channel for whatever reason, can stop flow both above and below that channel.

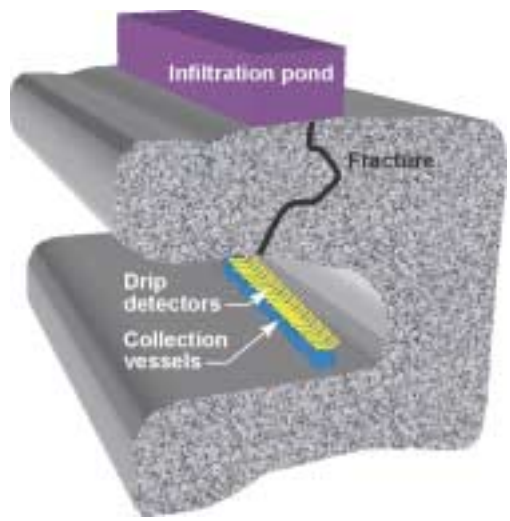

Figure 19. Schematic of experimental set up at the Hell's Half Acre field research site.

A simple pipe network model, the geometry of which is shown in Figure 20, captured the essence of such self-organized fluctuations in fluid flow. The computational model produced flow rates and drop intervals that are remarkably similar to those seen in the HHA data (see Figures 21 and 22). While none of this proves that variability in flow in fractured rock is an example of self-organized dynamics, the similarities between model and field measurements are extraordinarily suggestive.

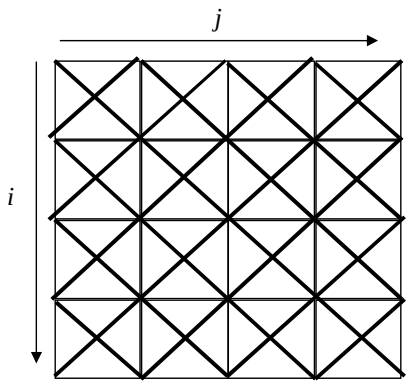

Figure 20. Pipe network model.

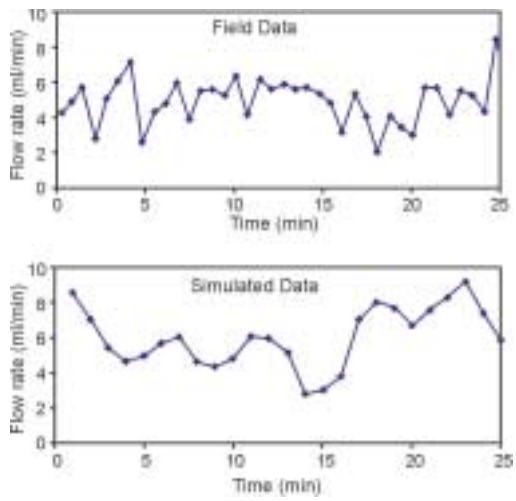

Figure 21. (Top) Flow rate from the Hell's Half Acre field study; (Bottom) Flow rate for the simple pipe network simulation.

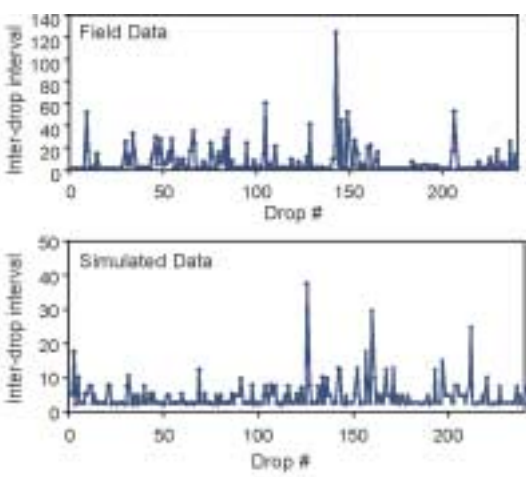

Figure 22. (top) Drop interval for the Hell's Half Acre data set; (bottom) drop interval for the simple pipe network simulation.

In FY 2002 the pipe network model was extended to show that a relationship could exist between variable water flow and intermittent detection of radioactive contaminants in monitoring wells. During field monitoring, water is collected every 3 months from a series of wells encircling the waste management sites. Occasionally and infrequently, elevated concentrations of radioisotopes are found in one of the wells—rarely in the same well on successive measurements. The modified pipe network model (see Figure 23) is intended to represent a hot spot of concentrated contaminants somewhere in the middle of the bed of fractured rock. Whenever a fully connected path happens to pass through that node, water flow can carry the contaminant to one of several wells below. Subsurface flow is assumed to refresh each well at some continuous rate. The aggregated and monitored results from this model (see Figure 24) are suggestive of the intermittent detections observed at the INEEL (see Figure 25).

Modeling Using Conventional Continuum Numerical Codes

The results of the laboratory tests were simulated using the integral finite difference model TOUGH2,[49,50] configured with the EOS9 (Richard's Equation) module. The computational grid was discretized to allow discrete fracture simulations of the model domain by assigning appropriate elements with properties representative of the fracture domain; alternatively, an equivalent continuum approach could be implemented by assigning a single property set to all computational grid blocks. Influx to model was accomplished by prescribing a mass-generation rate of 0.3 mL/min divided equally between three elements in the top boundary, whose locations corresponded to the fracture elements in the experiment and Discrete Fracture Model (DFM) simulations. A constant pressure boundary allowed effluent from the bottom boundary of the model to exit the simulation domain unhindered. This was believed to be representative of the actual experimental conditions, as the presence of wicks in the fractures prevented the formation of a capillary barrier at this boundary.

The laboratory tests were simulated using both Equivalent Continuum and Discrete Fracture

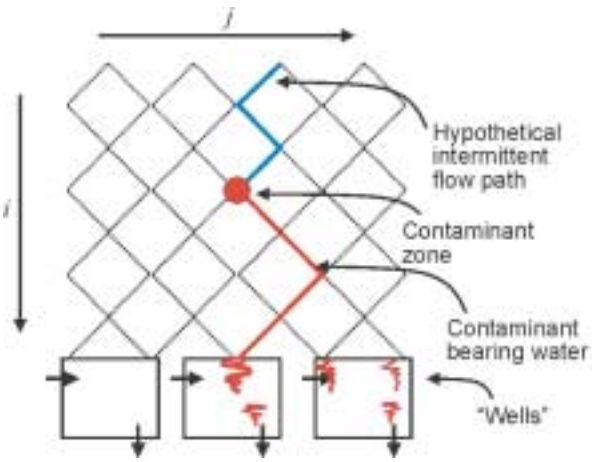

Figure 23. Conceptual model for a 2-dimensional pipe array depicting a contaminant zone, hypothetical flow path, and monitoring "wells."

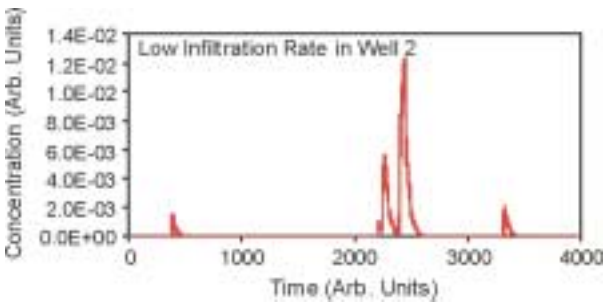

Figure 24. Results of simulations that were based on a 2-dimensional pipe network, a "hot spot" of contaminants and monitoring "wells."

models (ECM and DFM, respectively). Although the flow properties of the matrix blocks were well-characterized, the properties for the factures were somewhat more difficult to ascertain. As a first approximation, the measured fracture apertures were used to calculate permeability using the parallel-plate solution and theoretical air-entry pressures from capillary theory. Although the brick faces were quite smooth, it has been shown that the parallel-plate model tends to over-estimate fracture permeability.[51] Studies were therefore performed to examine the sensitivity of the model to changes in the calculated values of fracture absolute permeability and air-entry pressure, and it was determined that a one (for air-entry pressure) or two (for permeability) order of magnitude change resulted in only minimal differences to the simulation outcome.

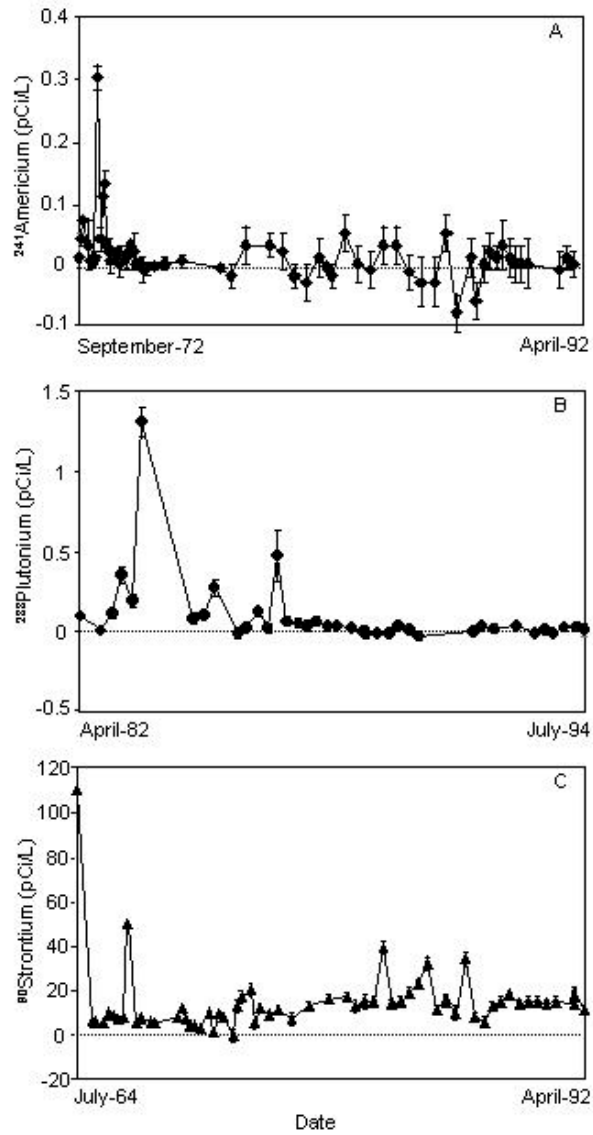

Figure 25. Intermittent subsurface flow detections observed at the INEEL

For DFM simulations, the matrix and fracture properties as described above were used without adjustment. An "effective," single-media property set for the ECM simulations was derived by the generally-accepted method of using harmonically- and arithmetically-averaged permeability in the directions normal (horizontal) and parallel (vertical) to the flow gradient. Because the volume of the matrix greatly exceeded the volume of fractures, other domain properties (such as the air-entry pressure, porosity, etc.) were taken directly from the measured values for the matrix. Sensitivity studies showed that, within reasonable

limits, the values of the assigned parameters exerted minimal effect on the simulation results. Following a set of "blind" simulations that attempted to replicate the laboratory experiments using the model parameters as developed above, a second set of simulations was undertaken to "calibrate" the model. Because the DFM conceptual model was deemed better suited to reproducing the observed behavior, calibration was limited to DFM simulations.

Quantitative comparisons were made between observed and simulated behavior for cumulative mass of water discharged from the test domain, and effluent breakthrough time at the bottom boundary of the test apparatus. Figure 26 shows the results of this comparison graphically. As indicated in the figure, both the ECM and DFM "blind" simulations compared poorly with the experimental observations. Both models predicted arrival of the wetting front at the bottom boundary of the model domain approximately 3.5×10^4s after the onset of injection, over-predicting the observed breakthrough time (~8×10^3s) by about a factor of four. The DFM, however, showed some slight improvement over the ECM simulations for late-time estimates of effluent mass leaving the model domain. Although both models substantially under-predicted cumulative mass discharged from the model boundary, the model input and output functions for the DFM were within a few percent of each other, minimizing the discrepancy between simulation and observation. In contrast, the ECM simulations continued to predict a large differential between input and output functions for an extended period of time following breakthrough. As a result, the discrepancy between observed and simulated cumulative discharge from the bottom boundary increased throughout the duration of the ECM simulations.

In the case of the DFM, examination of the model behavior prior to arrival of the wetting front at the bottom boundary of the model indicated that the discrepancy between observation and simulation arises because the simulated behavior of the wetting front in the fractures is significantly different from the experiment. To adjust for this error, a series of calibration simulations were performed with the intention of matching cumulative mass of effluent, and breakthrough

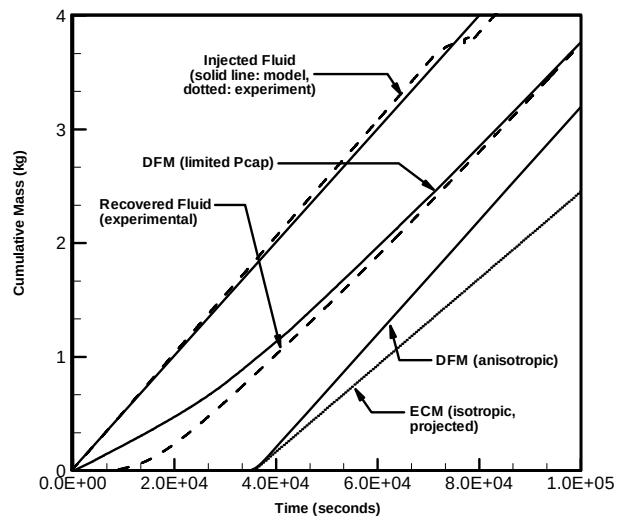

Figure 26. Comparison of simulation results with experimental observations of inflow and outflow across model boundaries.

time of effluent at the bottom boundary. Initial tests indicated that model results were sensitive to the value chosen for the fracture m parameter, but manipulation of this parameter alone produced only marginal improvements in performance. Subsequent testing demonstrated that the strength of the fracture/matrix interaction exerted controlling influence on model behavior. By manipulating these two factors in combination, reasonable agreement was obtained between simulation results and experimental observations.

All five laboratory tests demonstrated a consistent set of behavioral characteristics, including: nonuniform wetting of the matrix blocks, focusing of flow paths with increasing distance from the upper boundary, and wetting of the matrix significantly lagging passage of the wetting front in the fractures. In contrast to the behavior observed in the laboratory experiments, both uncalibrated models consistently demonstrate uniform, diffuse flow, and wetting front advance at approximately equal rates in the fractures and the matrix.

It is not necessary for a model to replicate all the behaviors of the modeled system; for instance, nonuniform wetting of the matrix blocks probably makes a relatively small contribution to the experiment/model discrepancies, at least for flow

processes. However, the focusing of flow paths with distance from the boundary, and the rapid advance of the wetting front in the fractures relative to the matrix, exert controlling influence on the outcome of the tests, and the contrasting behavior demonstrated by the uncalibrated models underlies the discrepancies between simulations and observations. Although the behavior of the uncalibrated models differs significantly from experimental observations, it is congruent with expectations based on early conceptual models of flow in fractured porous media.

Since the commonly used conceptual models of flow in unsaturated, heterogeneous media have been shown to be inaccurate under controlled conditions, it is assumed that some important physical process has been neglected in their formulation. A scaling analysis is currently being undertaken to estimate the order of magnitude of the missing term in the mathematical description of unsaturated flow. The objective of this analysis is to infer the origin of the missing term by comparing its magnitude in diverse experimental settings. If successful, this will result in substantially improved accuracy of numerical simulations in unsaturated, fractured media.

ACCOMPLISHMENTS

Experimental Test Bed

- Designed and built multiple single fracture intersection models for studying the physics of flow, and published a paper on the same.
- Designed and built single fracture intersection model for studying the effects of microbial growth on fracture flow, and presented a poster on the same.
- Designed and built apparatus for testing the effects of air entrapment/air entry of flow in Snake River Plain Basalts, and presented a poster on the same.
- Designed and built mesoscale fractured rock weighing lysimeter for evaluating flow in fracture network, and gave a presentation of the same.

Sensors and Data Acquisition

- Evaluated electrical resistivity tomography as a method in fractured rock, and submitted a paper on the same.
- Designed and built miniature tensiometers for use in fractured rock environments.
- Designed and built optical sensors for imaging droplet movement in fractured rock experiments.

Mathematical Analysis and Conceptual Model Formulation

- Modeled the Hell's Half Acre field data with self-organized dynamics.
- Constructed and tested a new self-organized criticality (SOC) model in collaboration with R. J. Glass. The SOC model, different from Peak's self-organized dynamics (SOD) model, accounts for intermittent flow in fractures with minimal assumptions. The SOC model, in conjunction with the SOD model, is expected to provide an explanation for experimental results, and the foundation for a new theory for flow in fractured media.

Technical

- Seven peer-reviewed journal articles
- Eleven technical presentations and posters.

Publications

Glass, R. J., M. J. Nicholl, and S. E. Pringle, Unsaturated flow through a fracture-matrix-network: A first experiment. "Bridging the Gap between Measurement and Modeling in Heterogeneous Media," *International Association of Hydrology, Ground water Symposium, Berkeley, March 25–29, 2002 Conference proceedings*.

Glass, R. J., S. E. Pringle, M. J. Nicholl, and T. R. Wood. "Unsaturated Flow Through a Fracture-Matrix-Network: Dynamic Pathways in

Mesoscale Laboratory Experiments" *Water Resources Research,* In Press.

LaViolette, R. A., and G. D. Redden, Comment on "Modeling the Mass-Action Expression for Bidentate Adsorption," *Environ. Sci. Tech.*, Vol. 36, 2002, p. 2279.

LaViolette, R. A., and R. A. Harris, "Chiral Fluctuations in Achiral Clusters and Liquids via Molecular Dynamics Simulations," *J. Chem. Phys.*, Vol. 116 7104, 2002, (highlighted in *Virtual J. Biol. Phys. Res*. Vol. 3, April 15, 2002.)

LaViolette, R. A., R. J. Glass, T. R. Wood, T. R. McJunkin, K. S. Noah, R. K. Podgorney, R. C. Starr, and D. L. Stoner, "Convergent Flow Observed in a Laboratory-Scale Unsaturated Fracture System," accepted for publication in *Geophysical Research Letters,* 2002.

Tolle, C. R., R. A. LaViolette, H. B. Smartt, K. L. Kenney, D. P. Pace, J. W. James, A. D. Watkins, T. R. Wood, and D. L. Stoner, "Is There Evidence of Determinism in Droplet Detachment Within the Gas Metal Arc Welding Process?," *6th Intl. Conf. on Trends in Welding Res*., (Paper 2.6, ASM/AWS, 2002).

Wood, T. R., D. L. Stoner, R. A. LaViolette, D. Peak, "Forum: A Discussion of Complexity and the Prediction of Contaminant Transport in Fractured Rock Vadose Zones, Environmental Management."

Wood, T. R., M. J. Nicholl, and R. J. Glass, "Fracture Intersections as Integrators for Unsaturated Flow," in press, in *Geophysical Research Letters*, 2002.

Presentations and Posters

Fairley, J. A., T. R. Wood, and T. R. McJunkin, "Comparison of Numerical Modeling Results with Laboratory Experiments of Flow in Unsaturated, Fractured Rock," Abstract accepted, *2001 Fall meeting of the American Geophysical Union, San Francisco, CA, December 10–14, 2001*.

Glass, R. J., and T. R. Wood, "Transport Within the Earth's Vadose Zone: Process Based Issues for Scaling," Abstract accepted, *2001 Fall meeting of the American Geophysical Union, San Francisco, CA, December 10–14, 2001*.

Glass, R. J., S. E. Pringle, and M. J. Nicholl, "Unsaturated Flow through a Fracture-Matrix-Network: Laboratory Experiments at the Meter Scale," Abstract accepted, *Fall 2001 Annual Meeting of the Geological Society of America, Boston, MA, November 1–10, 2001*.

LaBrecque, D. J., R. Sharpe, T. R. Wood, and G. Heath, 2002, "Considerations for Small-Scale ERT Monitoring of Fluid Flow in Fractured Rocks," *Spectrum 2002 Conference, 9th Biennial International Conference on Nuclear and Hazardous Waste Management, August 4–8, 2002, Reno, Nevada*.

LaViolette, R. A., "Obstacles to Realistic Models of Contaminant Fate in the Subsurface," Abstract accepted, *2001 Fall meeting of the American Geophysical Union, San Francisco, CA, December 10–14, 2001*.

Noah, K. S., T. R. McJunkin, R. K. Podgorney, R. C. Starr, R. J. Glass, R. A. LaViolette, D. L. Stoner, F. J. White, and T. R. Wood, 2002 "Automated Acquisition and Control of Water Flow in an Unsaturated Rock Mesoscale Experiment," *Spectrum 2002 Conference, 9th Biennial International Conference on Nuclear and Hazardous Waste Management, August 4–8, 2002, Reno, Nevada*.

Peak, D., R. Datwyler, N. Rasmussen, P. Simonson, T. Wood, T. Stoops, 2002, "Giant Fluctuations in Flow Through Fractured Media: A Stochastic, Self-Organized Dynamics Model," *International Conference on Chaos and Non-linear Dynamics: Dynamics Days University of Maryland, Baltimore, MD*.

Pringle, S. E., R. J. Glass, and M. J. Nicholl, "Unsaturated Flow Through a Fracture-Matrix-Network: Dynamic Behavior of Flow Pathways. Abstract accepted, *2001 Fall meeting of the American Geophysical Union, San Francisco, CA, December 10–14, 2001*.

Stoner, D. L., T. R. Wood, D. Peak, R. J. Glass, and R. A. LaViolette, "The Role of Complexity in the Prediction of Contaminant Transport in a Fractured Rock Vadose Zone Abstract," Abstract accepted, *2001 Fall meeting of the American Geophysical Union, San Francisco, CA, December 10–14, 2001*.

Wood , T. R., T. R. McJunkin, R. K. Podgorney, R. J. Glass, R. C. Starr, D. L. Stoner, K. S. Noah, R. A. LaViolette, and J. Fairley, 2001 "Assessment of Surrogate Fractured Rock Networks for Evidence of Complex Behavior" Abstract submitted, *2001 Fall meeting of the American Geophysical Union, San Francisco, CA, December 10–14, 2001*.

In Review

Fairley, J. P., "Conceptual Model Uncertainty for Flow in Unsaturated, Heterogeneous Media," *International High-Level Radioactive Waste Management Conference* (In Review for 2003).

LaBrecque, D. J., R. Sharpe, T. R. Wood, and G. Heath, "Small-Scale ERT Monitoring of Fluid Flow in Fractured Rocks," submitted to *Ground Water*, September 2002.

LaViolette, R. A., C. R. Tolle, T. R. McJunkin, D. L. Stoner, "Combining the ApEn statistic with Surrogate Data Analysis for the Detection of Nonlinear Dynamics in Time Series," submitted to *Applied Mathematical Modeling*, February 14, 2002.

Stoner, D. L., R. D. Stedtfeld, T. L. Tyler, F. J. White, and T. R. McJunkin, "The Effects of Microorganisms and Nutrient Amendments on the Dynamics of Unsaturated Flow within Fractures," Abstract submitted to *103rd Annual Meeting of the American Society for Microbiology, Washington, D.C.*, May 18–23, 2003.

In Preparation

Stoner, D. L., R. D. Stedtfeld, T. L. Tyler, F. J. White, and T. R. McJunkin, "Impact of Microorganisms on the Dynamics of Unsaturated Flow within Fractures," in preparation for *Geophysical Research Letters*.

Wood, T. R., T. McJunkin, R. K. Podgorney, R. J. Glass, R. C. Starr, D. L. Stoner, K. Noah, R. Laviolette, and J. Fairley, "Convergent Unsaturated Flow in a Small Fracture-Matrix Network," in preparation for *Vadose Zone Journal*, 2002.

REFERENCES

1. J. T. Fabryka-Martin, A. V. Wolfsberg, P. R. Dixon, S. Levy, J. Musgrave, and H. J. Turin, *Summary Report of Chlorine-36 Studies: Sampling, Analysis and Simulation of Chlorine-36 in the Exploratory Studies Facility Report*, LA-CST-TIP-96-002, Los Alamos National Laboratory, 1996.

2. S. O. Magnunson and A. J. Sondrup, *Development, Calibration, and Predictive Results of a Simulator for Subsurface Pathway Fate and Transport of Aqueous- and Gaseous-Phase Contaminants in the Subsurface Disposal Area at the Idaho National Engineering and Environmental Laboratory*, INEEL/EXT-97-00609, Idaho National Engineering and Environmental Laboratory, 1998.

3. E. R. Neher, D. B. Frederick, and G. S. Johnson, *Water Quality Trends in the Snake River Plain Aquifer at the Idaho National Engineering and Environmental Laboratory*, State of Idaho INEEL Oversight Program and Idaho Water Resources Research Institute, University of Idaho, 1998, http://www.oversight.state.id.us/ov_library/.

4. K. Pruess, B. Faybishenko, and G. S. Bodvarsson, "Alternative Concepts and Approaches for Modeling Flow and Transport in Thick Unsaturated Zones of Fractured Rocks," *Journal of Contaminant Hydrology*, Vol. 38, 1999, pp. 281–322.

5. O. Dahan, R. Nativ, E. Adar, B. Berkowitz, and Z. Ronen, "Field Observation of Flow in a Fracture Intersecting Unsaturated Chalk," *Water Resources Research*, Vol. 35, 1999, pp. 3315–3326.

6. B. Faybishenko, C. Doughty, M. Steiger, J. C. S. Long, T. R. Wood, J. Jacobsen, L. J., and P. Zawislanski, "Conceptual Model of the Geometry and Physics of Fluid Flow and Chemical Transport in Unsaturated Fractured Basalt: Box Canyon Site, Idaho," *Water Resources Research*, Vol. 37, 2000, pp. 3499–3522.

7. B. Faybishenko, C. Doughty, M. Steiger, J. C. S. Long, T. R. Wood, J. S. Jacobsen, J. Lore, and P. T. Zawislanski, "Conceptual Model of the Geometry and Physics of Water Flow a Fractured Basalt Vadose Zone," *Water Resources Research*, Vol. 36, 2000, pp. 3499–3520.

8. K. S. Noah, T. R. McJunkin, R. K. Podgorney, R. C. Starr, R. J. Glass, R. A. LaViolette, D. L. Stoner, F. J. White, and T. R. Wood, *Presented at the Spectrum 2002 Conference, 9th Biennial International Conference on Nuclear and Hazardous Waste Management,* August 4–8, 2002, Reno, NV.

9. T. R. Wood and G. T. Norrell, *Integrated large-scale aquifer pumping and infiltration tests: Ground water Pathways Operable Unit 7-06*, Idaho National Engineering Laboratory Summary Report INEL-96/0256, 1996.

10. R. J. Glass, M. J. Nicholl, S. E. Pringle, and T. R. Wood, "Unsaturated Flow through a Fracture-Matrix-Network: Dynamic Preferential Pathways in Mesoscale Laboratory Experiments," *Water Resources Research*, in review.

11. M. J. Nicholl, R. J. Glass, and H. A. Nguyen, "Small-Scale Behavior of Single Gravity-Driven Fingers in an Initially Dry Fracture," *Proc. of the 4th Ann. Int. Conf. on High Level Rad. Waste Mgmt, 2023–2032, Am. Nuclear Soc., Las Vegas, Nevada,* April 26–30,1993.

12. G. W. Su, J. T. Geller, K. Pruess, and F. Wen, "Experimental Studies of Water Seepage and Intermittent Flow in Unsaturated, Rough-Walled Fractures," *Water Resources Research*, Vol. 35, No. 4, 1999, pp. 1019–1037.

13. M. J. Nicholl, R. J. Glass, and S. W. Wheatcraft, "Gravity-Driven Infiltration Instability in Initially Dry Nonhorizontal Fractures," *Water Resources Research*, Vol. 30, No. 9, 1994, pp. 2533–2546.

14. J. K. Fredrickson, J. P. McKinley, S. A. Nierzwickibauer, D. C. White, D. B. Ringelberg, S. A. Rawson, S. M. Li, F. J. Brockman, and B. N. Bjornstand, "Microbial Community Structure and Biogeochemistry of Miocene Subsurface Sediments—Implications for Long-Term Microbial Survival, *Molecular Ecology*, Vol. 4, 1995, pp. 619–626.

15. M. G. Kalyuzhnaya, V. N. Khmelenina, S. Kotelnikova, L. Holmquist, K. Pedersen, and Y. A. Trotsenko, "*Methylomonas scandinavica* sp. nov., A New Methanotrophic Psychrotrophic Bacterium Isolated from Deep Igneous Rock Ground Water of Sweden," *Systematic and Applied Microbiology*, Vol. 22, 1999, pp. 565–572.

16. S. Kotelnikova, A. J. L. Macario, and K. Pedersen, "*Methanobacterium Subterraneum* sp. nov., A New Alkaliphilic, Eurythermic and Halotolerant Methanogen Isolated from Deep Granitic Ground water," *International Journal of Systematic Bacteriology*, Vol. 48, 1998, pp. 357–367.

17. S. Kotelnikova and K. Pedersen, "Distribution and Activity of Methanogens and Homoacetogens in Deep Granitic Aquifers at Aspo Hard Rock Laboratory, Sweden," *Fems Microbiology Ecology*, Vol. 26, 1998, pp. 121–134.

18. S. Kotelnikova and K. Pedersen, "Evidence for Methanogenic Archaea and Homoacetogenic Bacteria in Deep Granitic Rock Aquifers," *F.E.M.S. Microbiology Reviews*, Vol. 20, 1997, pp. 339–349.

19. L. R. Krumholz, "Microbial Communities in the Deep Subsurface," *Hydrogeology Journal*, Vol. 8, 2000, pp. 4–10.

20. L. R. Krumholz, J. P. McKinley, F. A. Ulrich, and J. M. Suflita, "Confined Subsurface Microbial Communities in Cretaceous Rock," *Nature*, Vol. 386, 1997, pp. 64–66.

21. W. D. Gould and R. G. L. McCready, "Biotechnological Treatment of Liquid and Solid Inorganic Wastes," *In* D. L. Stoner (ed.), Biotechnology for the Treatment of Hazardous Waste, Lewis Publishers, Boca Raton, FL, 1994, pp. 71–95,.

22. D. L. Stoner, "Hazardous Organic Waste Amenable to Biological Treatment," *In* D. L. Stoner (ed.), Biotechnology for the Treatment of Hazardous Waste, Lewis Publishers, Boca Raton, FL, 1994, pp. 1–25.

23. D. L. Stoner, *Organic Waste Forms and Treatment Strategies*, *In* D. L. Stoner (ed.), Biotechnology for the Treatment of Hazardous Waste, Lewis Publishers, Boca Raton, FL, 1994, p. 45–69.

24. R. A. LaViolette, R. J. Glass, T. R. Wood, T. R. Mcjunkin, K. S. Noah, R. K. Podgorney, R. C. Starr, and D. L. Stoner, "Convergent Flow Observed in a Laboratory Scale Unsaturated Fracture System," *Geophysical Research Letters*, in review, 2002.

25. D. L. Stoner, R. D. Stedtfeld , T. L. Tyler, F. J. White, and T. R. McJunkin, "Impact of Microorganisms on Unsaturated Flow Within Fractures," *Applied and Environmental Microbiology*, in preparation.

26. T. R. Wood, M. J. Nicholl, and R. J. Glass, 2002, "Fracture Intersections as Integrators for Unsaturated Flow," *Geophysical Research Letters*, in press.

27. R. J. Glass, M. J. Nicholl, and V. C. Tidwell, "Challenging Models for Flow in Unsaturated, Fractured Rock through Exploration of Small Scale Processes," *Geophys. Res. Lett.*, Vol. 22, 1995, p. 1457.

28. C. E. Russell, J. W. Hess, and S. W. Tyler, "Hydrogeologic Investigation of Flow in Fractured Tufts, Rainier Mesa, Nevada Test Site," in Flow and Transport through Unsaturated Rock, D. D. Evans and T. J. Nicholson, editors, Geophysical Monograph 42, Am. Geophys, Union, Washington D.C., Vol. 43, 1987.

29. J. T., Fabryka-Martin, P. R. Dixon, S. S. Levy, B. Liu, D. L. Brenner, L. E. Wolfsberg, H. J. Turin, and P. Sharma, "Implications of Environmental Isotopes for Flow and Transport in the Unsaturated Zone at Yucca Mountain, Nevada," *1996 Annual Meeting of the Geological Society of America, Ocober .28–31Denver CO, GSA Abstracts with Programs,* Vol. 28, No. A-416, 1996.

30. G. R. Davidson, R. L. Bassett, E. L. Hardin, and D. L. Thompson, "Geochemical Evidence of Preferential Flow of Water through Fractures in Unsaturated Tuft, Apache Leap, Arizona," *Applied Geochem*, Vol. 13, 1998, p. 185.

31. R. J. Glass, M. J. Nicholl, A. L. Ramirez, and W. D. Daily, "Liquid Phase Structure within an Unsaturated Fracture Network Beneath Surfacer Infiltration Event: Field Experiment," Water Resour. Res. (in press, 2002)

32. R. J. Glass, M. J. Nicholl, S. E. Pringle, and T. R. Wood, "Unsaturated Flow through a Fracture-Matrix-Network: Dynamic Pathways in Mesoscale Laboratory Experiments," *Water Resour. Res.*, (accepted for publication, 2002).

33. B. Efron and R. J. Tibshirani, *An Introduction to the Bootstrap*, New York: Chapman and Hall, 1993.

34. R. J. Glass and L. Yarrington, "Simulation of Gravity-Driven Fingering in Porous Media Using a Modified Invasion Percolation Model," *Geoderma*, Vol. 70, 1996, p. 231.

35. LaBrecque and Casale, "Experience with Anisotropic Inversion for Electrical Resistivity Tomography," submitted to *Proceedings of the Symposium on the Application of Geophysics to Engineering and Environmental Problems (SAGEEP),* 2002.

36. A. Dey and Morrison, "Resistivity Modeling for Arbitrarily Shaped Three-Dimensional Structures," *Geophysics*, Vol. 44, 1979, pp. 753–780.

37. S. C. Constable, R. L. Parker, and C. G. Constable, "Occam's Inversion: a Practical Algorithm for Generating Smooth Models from Electromagnetic Sounding Data," *Geophysics*, Vol. 52, 1987, pp. 289–300.

38. D. J. LaBrecque, G. Morelli, W. Daily A. Ramirez, and P. Lundegard, "Occam's Inversion of 3D ERT Data: in: Spies, B., (Ed.), *Three-Dimensional Electromagnetics,* SEG, Tulsa, 1999, pp. 575–590.

39. J. M. Lucas, "Combined Shewart- CUSUM Quality Control Schemes. *Journal of Quality Technology*, Vol. 14, 1982, pp. 51–59.

40. W. A. Shewart, *Economic Control of Quality of Manufacturing Products*, New York, NY: Van Nostrand, 1931.

41. E. S. Page, "Continuous Inspection Schemes, *Biometrika*, Vol. 41, No.1, 1954, pp. 100–114.

42. C. B. Davis and R. J. McNichols, "Ground Water Monitoring Statistics Update: Part I: Progress Since 1988, *Ground Water Monitoring Review*, Fall, 1994a, pp. 148–158.

43. R. O. Gilbert, *Statistical Methods for Environmental Pollution Monitoring*, New York, NY: Van Nostrand Reinhold, 1982.

44. R. H. Montgomery, J. C. Loftis, and J. Harris, "Statistical Characteristics of Ground-water Quality Variables, *Ground Water*. March–April, 1987, pp. 176–184.

45. T. H. Starks, *Evaluation of Control Chart Methodologies for RCRA Waste Sites*, EPA Technical Report CR 814342-01-3, 1989.

46. L. A. Currie, "Limits for Quanlitative Detection and Quantitative Determination," Application to Radiochemistry, *Analytical Chemistry*, 1998, pp. 586–593.

47. R. K. Podgorney, T. R. Wood, T. M. Stoops, B. Faybishenko, *Spatial and Temporal Instabilities in Water Flow Through Variably Saturated Fractured Basalt on a One-Meter Field Scale*, August 1999.

48. P. Bak, C. Tang, and K. Wiesnfeld, "Self Organized Criticality," *Physical Review A,* July 1988.

49. K. Pruess,, *TOUGH2—A General Purpose Numerical Simulator for Multiphase Fluid and Heat Flow,* Lawrence Berkeley Laboratory Report LBL-29400, Lawrence Berkley Laboratory, Berkley, CA, May 1991.

50. K. Preuess, C. Oldenburg, and G. Moridis, *TOUGH2—User's Guide, Version 2.0,* Lawrence Berkley National Laboratory Report LBNL-43134, Berkeley, CA, November 1999.

51. R. W. Zimmerman and G. S. Bodvarsson, "Effective Transmissivity of Two-Dimensional Fracture Networks," *International Journal of Rock Mechanics*, in press, 1996.

Spatial and Temporal Characterization of the Vadose Zone

Earl D. Mattson, Gail Heath, Joel Hubbell, Mitch Plummer, Annette Schafer, Clark Scott, and James Sisson (INEEL); Eric Miller and Mohamed Khames Miled (Northeastern University); and Robert Holt (University of Mississippi)

SUMMARY

An incomplete understanding of contaminant fate and transport mechanisms and an inadequate description of geologic heterogeneity have resulted in uncertain predictions of contaminant behavior in the vadose zone. This project focuses on the following three research areas identified to reduce this uncertainty:

- Developing innovative measurement tools
- Developing integrated approaches between temporal and spatial characterization
- Developing appropriate data interpretation techniques to provide a more holistic understanding of contaminant fate and transport.

Soil physical characterization tools have the advantage of providing continuous temporal data, but suffer from the fact that the measurement volume is small in comparison to the problem of interest. Alternatively, measurement techniques such as geophysics measure large volumes but do not provide direct measurements of state variables or parameters of interest, and are typically acquired at discrete points in time. The two measurement techniques are complementary and must be integrated and evaluated together to develop better conceptual and numerical models of contaminant fate and transport. The three focus areas will require innovative experiments at suitable spatial and time scales to develop data sets that can be integrated and evaluated to reduce uncertainty in predictions.

Understanding and predicting water movement and chemical transport at waste disposal sites requires measurement of four vadose zone variables: water content, water pressure, temperature, and chemical concentration. Richard's equation requires these variables as initial conditions in predictive models and to develop modeling transport parameters. Despite the apparent simplicity of the concept of four state variables, obtaining a complete data set that adequately describes the temporal and spatial distribution has not been achieved. Parameters required by the numerical models are nonlinear and require temporal evaluation. In addition, appropriate measurement techniques are not available to provide the spatial distribution of these variables in a heterogeneous subsurface. As a result, contaminant transport modeling with these nonlinear effects has resulted in an unacceptable degree of uncertainty. We need a methodology for the temporal and spatial measurement of state variables, and to develop appropriate techniques to interpret and integrate the data with flow and transport models.

PROJECT DESCRIPTION

The advective transport of water and gases is the primary mechanism controlling the distribution of contaminants, nutrients, and electron donors/acceptors in the vadose zone. Fluid pathways are determined by both the permeability distribution within the subsurface and the boundary conditions. Numerous controlled-boundary field-scale studies at various sites (Las Cruces Trench site, New Mexico Tech Golf Course site, Sisson and Lu's PNNL Borehole site, others) have indicated that the heterogeneity (distribution) of fluid transport properties is the controlling factor in the movement of subsurface fluids. Methodologies for determining fluid pathways, quantifying chemical transport fluxes, and describing subsurface heterogeneities are needed to ultimately describe spatial and temporal chemical transport in subsurface liquids and gases.

Three major tasks were developed to examine cross-cutting methodologies for integrating point

measurements of soil physics with spatial measurements of geophysics, and to integrate those into a quantitative description using numerical techniques (see Figure 1). Task 1 examines physical techniques for examining temporal changes in the vadose zone; Task 2 examines spatial distribution of geologic properties; and Task 3 develops methodologies to incorporate the first two tasks into a more holistic approach. The rest of this section describes each task in more detail.

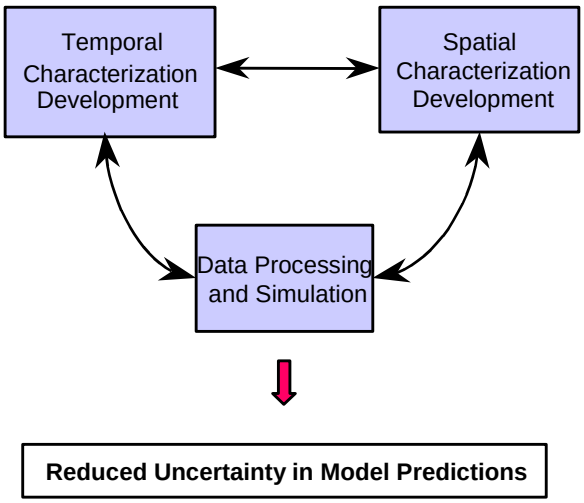

Figure 1. Relationship among temporal characterization, spatial characterization, and data processing to reduce numerical model uncertainties.

Task 1. Temporal Characterization

Our inability to adequately characterize the subsurface has been identified in numerous articles, books and workshops.[1,2,3] A draft copy of a DOE sponsored book describes the primary characterization needs (listed in order of importance) as techniques that (a) identify and describe heterogeneity, (b) describe the contaminant and controlling geology, and (c) improve sampling of the subsurface.[1] Not only is the subsurface environment spatially variable, but recent studies also suggest that temporal variability of infiltration has a profound effect on fluid transport within the vadose zone. Geophysical data collection techniques have evolved from sporadic manual sampling to automated continuous recording, and their application within the vadose zone is rapidly expanding. However, methodologies to interpret these data sets and incorporate the results into numerical transport models need to be developed. Subtasks of the temporal characterization task develop better methodologies to obtain temporal data from the vadose zone. These subtasks include the vadose zone monitoring system (VZMS), an in situ geochemical sensor, and development of a field site to test the integration of hydrological and geophysical methodologies.

Vadose Zone Monitoring System

The VZMS is a suite of instruments used to measure the state variables of water potential, water content, and temperature, and to allow for moisture extraction for chemical analysis. Data from the water potential, water content, and temperature sensors are collected on a daily basis and stored in a data logger. Moisture sampling for chemical analysis is performed periodically. Data can be retrieved remotely without having to access the sites. Instrument suites are placed at multiple depths within boreholes to determine the spatial and temporal characteristics of these sites. The sensor configuration and individual types may vary with individual site requirements. This monitoring system allows characterization of the moisture distribution and changes occurring over time indicative of flow and transport.

The VZMS has been installed at five sites this year: the B and SX tank farms at Hanford, the Vadose Zone Research Park and Radioactive Waste Management Complex (RWMC) at the INEEL, and the Gilt Edge EPA superfund site. The SX tank farm used only the tensiometer and water content sensors, all the remaining sites used the complete suite of sensors. The instrument design varied by location; the B Tank farm and Vadose Zone Research Park used the standard instrument suite described above, while the SX site used specially designed small diameter instruments installed using the drive point technology. The instruments placed at the RWMC were installed using a sonic/cone penetrometer technique. The RWMC site also included a unique imaging system for visual examination of the material penetrated. Data from these sites are

collected on a daily basis to evaluate of long-term trends in the soil moisture.

More information on the VZMS can be found in Hubbell et al..[4]

Chemical Sensor

A vadose zone geochemical sensor has been successfully incorporated into the INEEL VZMS. An electrical conductivity sensor was chosen as a "generic" sensor to verify the response of the Advanced Tensiometer's porous cup design. Field data collected during the demonstration agrees with independent measurements and analytical solutions.

DOE wants long-term measurements of in situ contaminant concentrations.[3] Potential users want a remote in situ geochemical sensor that requires little (or no) maintenance, exhibits long-term stability, has low detection limits, automatically transmits the data to a central location, is inexpensive, and is small and easy to install, understand, and calibrate. Due to these user-defined needs, DOE sponsored a workshop to discuss potential chemical sensors and field analytical methods that could be used to monitor subsurface contaminants in long-term monitoring programs. During the course of the workshop it became apparent that the participants (a mix of users and developers) felt that "surrogate measurements or alternative approaches to measuring contaminants directly are equally or more important for monitoring programs."[3] This revelation was due, in part, to the difficulty of directly measuring trace amounts of contaminants, even in the laboratory. By comparison, measurements of state variables such as moisture, pH, electrical conductivity, oxygen levels, etc., are generally simpler and can provide critical information needed to assess the potential for transport of a variety of contaminants in the subsurface.

Measuring geochemical concentrations in unsaturated soil pose a significant engineering challenge due to the difficulty in providing the appropriate contact between the soil water and the sensor. Previous research efforts have been directed towards developing long-term monitoring systems in saturated ground water environments, mainly due to current regulations of quarterly ground water monitoring at hazardous waste sites. Previous experience in developing long-term soil physics measurements gave the INEEL an ideal basis to begin developing instruments for the vadose zone, by incorporating geochemical measurements with routine soil physics measurements.

The choice of whether or not to incorporate the chemical sensor into the VZMS depends on the specific site conditions, the chemical to be measured, and the environmental decisions to be made with these measurements. Although a number of researchers in the DOE system are working to develop chemical sensors, much of the current research focuses on miniaturization, lowering detection limits, and evaluating the stability of chemical detectors. Little effort focuses on developing a suitable platform to measure chemical concentrations in soil water.

We chose to use the electrical conductivity sensor for our in situ geochemical sensor design because it offers the following advantages:

- The INEEL Advanced Tensiometer is a generic sensor platform capable of incorporating specific sensors that need a liquid medium connection. The electrical conductivity sensor is amenable to this task since it has good long-term stability and can be easily integrated into the current VZMS data-recording device.

- Electrical conductivity provides sufficient data resolution to compare the measurement results with analytical solutions.

- The measurement of in situ soil water electrical conductivity is practical for leak detection below subsurface storage tanks, performance evaluation of certain remediation processes, determination of evapotranspiration and plant stress, salt tracer studies, and salinity corrections of geophysical measurements used in this ESRA project.

We incorporated the geochemical sensor into the INEEL Advanced Tensiometer as part of the VZMS, because the water-filled tensiometer

provides the necessary liquid medium for geochemical measurements. The underlying principle is that the ion concentration of chemicals in the soil pore water will diffuse through the ceramic cup of the INEEL advanced tensiometer and come into equilibrium with water inside the INEEL Advanced Tensiometer (see Figure 2). The electrical conductivity of this water is then measured by the in situ geochemical sensor.

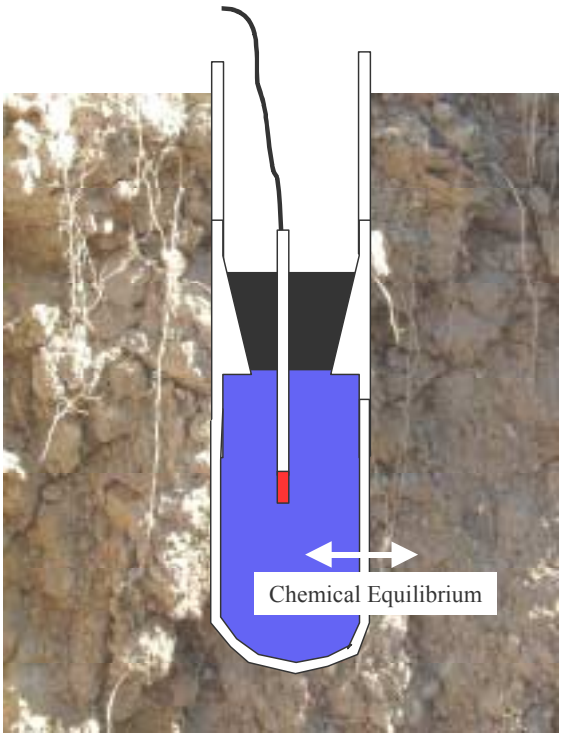

Figure 2. Schematic cross section of a tensiometer in soil.

Installing the geochemical sensor inside the porous cup of the INEEL Advanced Tensiometer is advantageous for several reasons. First, it allows easy connectivity between the sensor and the unsaturated soil through the water, and all of the equipment is basically available off-the-shelf. Second, the geochemical sensor is accessible from the soil surface and will allow the user to verify the sensor's calibration and allow for easy replacement. Third, efficient techniques have been established for installing tensiometers (standard vadose zone characterization equipment) in soil. Users and regulators should therefore feel comfortable with the operation and collection of data from the INEEL vadose zone chemical sensor. Finally, the chemical data can also be correlated with other monitoring data from the VZMS, such as temperature, moisture content, soil matric potential, and soil gas concentration, and can be verified with vacuum suction lysimeters.

A miniature electrical conductivity probe (MI-915, Microelectrodes, Inc) was incorporated into the INEEL Advanced Tensiometer and field-tested at the INEEL Vadose Zone Field Lab adjacent to the INEEL Research Center (IRC). The photographs in Figure 3 are of the actual electrical conductivity probe and the pressure transducer prior to and after assembly. The field site consists of a loamy soil vegetated predominantly with cheatgrass (*bromus tectorum*). The tensiometer porous cup was located approximately 120 cm below land surface.

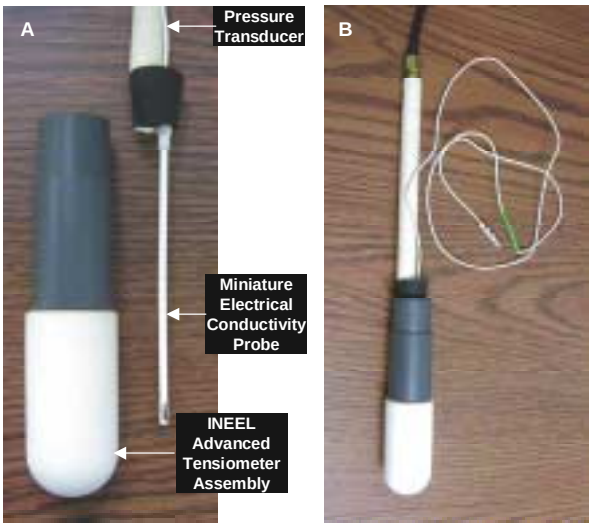

Figure 3. The INEEL vadose zone geochemical sensor.

Photograph A illustrates the geochemical sensor removed from the INEEL Advanced Tensiometer cup; photograph B illustrates the assembled vadose zone geochemical sensor as it is incorporated into the INEEL VZMS. To initiate the field demonstration, the porous cup was filled with deionized water and the rubber stopper containing the miniature electrical conductivity probe and the pressure transducer was seated in the INEEL Advanced Tensiometer. The rubber stopper seals the INEEL Advanced Tensiometer allowing only a small amount of water to leave the tensiometer through the porous ceramic until the

tension within the tensiometer equals the soil matric potential immediately surrounding the tensiometer. After that, there is little or no advective flow of the water between the tensiometer and the surrounding soil. Diffusion of ions, from the water contained in the soil pores into water in the tensiometer, is the primary mechanism by which the water in the tensiometer reaches chemical equilibrium with soil moisture.

Two diffusional analytic solutions were examined to estimate the geochemical sensor response time to a chemical change in the surrounding soil. The first solution follows that of Rita and Charpentier,[5] who examined the diffusion into a porous cup using a cylindrical coordinate system. For this solution, the underlying assumption is that the bottom of the cup and the soil beneath and above the cup do not contribute to the chemical mass transfer. Rita and Charpentier verified this solution in laboratory experiments in unsaturated soil, sand, and peat-perlite media. This solution can likely be used for a geochemical sensor incorporated into "tube" type porous material such as a drive cone tensiometer and filter candle tensiometer with little error. The second solution we evaluated is a spherical solution. The spherical solution is more appropriate for the "standard" porous cup tensiometer designs where the diameter of the porous cup is approximately that of its length. Both solutions indicate that under typical soil conditions chemical equilibrium between the soil water and the liquid contained in the tensiometer will be achieved in approximately 1–2 weeks.

Data from the in situ geochemical sensor demonstration is shown in Figure 4. The experiment was started on June 7, 2002. The electrical conductivity of the liquid inside the tensiometer starts at near zero (the electrical conductivity of deionized water) and asymptotically approaches ~2 mS/cm over a period of approximately 2 weeks. Concurrent soil water potential and temperature measurements were stable over this 2-week period (approximately 350 mbars and 12.5°C, respectively). The time to establish a near-stable electrical conductivity measurement is in the range of that seen by Moutonnet and others.[6] Moutonnet and others remotely sampled the tensiometer fluid for nitrogen and experimentally found an approximately 8 to 10 day response time in an irrigated field (~200 mbar).

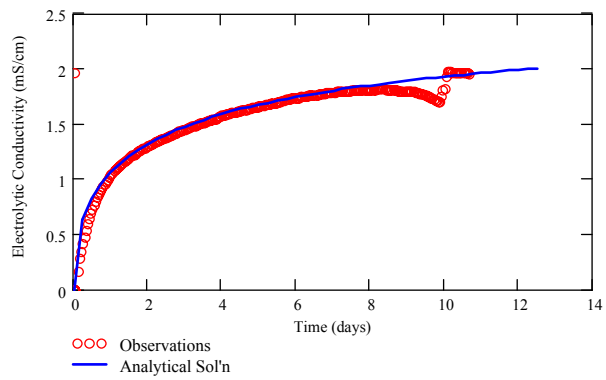

Figure 4. Field data of electrical conductivity measurements as a function of time. Actual field data is illustrated as the circles; the solid line is the analytical solution.

The final electrical conductivity measure in the vadose zone geochemical sensor is in general agreement with independent soil water electrical conductivity measurements. A soil sample was obtained adjacent to the vadose zone geochemical sensor and was analyzed with the SigmaProbe (EC1, Dynamax, Inc.). The SigmaProbe measurements indicated that the pore water conductivity was approximately 3 mS/cm. Although the SigmaProbe suggests that the soil water is more conductive than that which we have seen in the vadose zone geochemical sensor (3 mS/cm vs. 2 mS/cm), the SigmaProbe is fairly unreliable at this moisture content range and soil type.

A simple spherical diffusional analytical solution was used to evaluate the shape of the electrical conductivity response as a function of time. In this solution, we ignore the effects of the porous cup and assume that the diffusion rate is solely a function of soil porosity and tortuosity. Figure 4 illustrates fitted solution results and the field data. The spherical diffusion solution provides a good fit to the field data, suggesting that our conceptual understanding of the ionic transport processes is correct.

IRC Field Site

A number of vadose zone instruments were installed in 1996 on the IRC Campus for

evaluating sensor technologies being developed at the INEEL. Through the analysis of this vadose zone monitoring data, the formation and decay of perched water was observed at the basalt-sediment interface, which correlated with snowmelt events. The shallow geology found at the IRC field site is similar to that found at the Subsurface Disposal Area (SDA) located at the RWMC and at the Idaho Nuclear Technology and Engineering Center, (INTEC) site. We also identified the formation and decay of perched water bodies as an important mechanism for the transport of contamination buried at the SDA and subsurface contamination resulting from leaking transfer lines at INTEC. Identifying the specific mechanism whereby perched water enters the basalt, and being able to nonintrusively locate the infiltration pathways are needed to effectively manage buried waste at the INEEL.

The IRC field site is being developed into a useful study area for quantifying perched water behavior. This development is being accomplished in three distinct phases.

Phase 1 consisted of obtaining approval from the IRC landlord to use the site as a vadose zone research laboratory, which required describing use of the site for the near future and specifying requirements for personnel access, training, and safety. Permission was obtained in July 2002.

Phase 2 is initiated and includes several methods for determining the depth to basalt and defining the final boundaries of the area to be included in the field study. To begin with, we developed detailed contour maps of the site, obtained preliminary estimates of the basalt surface, and installed permanent benchmarks. We also developed a detailed topography map with contour lines at 0.1-ft intervals to identify local watershed conditions and provide input into the basalt surface mapping portion of this phase. We estimated the depth to basalt by drilling 16 boreholes at selected points in the study area and performed five transects of seismic soundings using ground penetrating radar and magnetic field surveys. The outcome of these studies is being integrated to map the basalt surface. Once the topographical map of the basalt surface is available, the final study area will be selected and marked with posts and identification signs.

Phase 3, which will be initiated in FY 2003, will consist of designing and executing a series of small-scale field experiments. Water and tracers will be infiltrated or injected into the subsurface to elucidate the mechanism and location of water perching on the basalt. This will be done through characterization with soil physical and geophysical techniques.

Task 2. Spatial Characterization

The advective transport of water and gases is the primary mechanism that controls the distribution of contaminants in the vadose zone. The fluid pathways are determined by the permeability distribution within the subsurface and the boundary conditions. Numerous controlled-boundary field-scale studies, such as those conducted at the Las Cruces Trench site, New Mexico Tech Golf Course site, and Sisson and Lu's PNNL Borehole site have indicated that the heterogeneity (distribution) of fluid transport properties is the controlling factor in determining the direction of fluid movement in the subsurface. Tools are needed to directly and indirectly describe and characterize subsurface processes. This task focuses on developing techniques to describe the spatial distribution of transport parameters in the vadose zone, and investigates both hydrological and geophysical data collection techniques to describe the subsurface.

Exfiltrometer

Accurate estimates of the unsaturated hydraulic properties of soils and geologic materials are essential in predicting the rate of contaminant transport away from buried wastes. Current methods used for estimating the required properties are time consuming and expensive. The exfiltrometer was designed and developed to quickly provide estimates of the unsaturated hydraulic conductivity and moisture release curves without the need for highly trained technicians. To determine if the exfiltrometer met these exceptions, a master level dissertation topic was developed to use the device under field conditions and evaluate its performance. The results of that

subtask suggest that the tensiometers used in the instrument need to be more robust and their physical mounting and must be redesigned to provide improved contact between the tensiometer and the soil. The results also indicated that the length of time the exfiltrometer is operated has a significant impact on the quality of the unsaturated hydraulic property estimates. Data collected over the first few minutes of operation were evaluated using the numerical inversion code HYDRUS 1-D to estimate unsaturated hydraulic parameters. These parameters were then compared to those determined from a longer period of operation. The comparison indicated that very little time is required to adequately predict the unsaturated hydraulic conductivity relationship; however, a significant difference was noted between the water potential-water content relationship between the short and long tests. The inversion process is currently being reevaluated to estimate how much actual field data is required to obtain reliable estimates of parameters describing the needed hydraulic properties. We are also evaluating the range of water contents and water potentials for optimal data collection, and techniques to better constrain the inversion of the exfiltrometer data. The ultimate goal is to develop a set of procedures that will provide quick/inexpensive reliable estimates of the unsaturated hydraulic properties to be incorporated with other spatial techniques.

Geophysical Spatial Analysis

Noninvasive characterization techniques are needed to cost-effectively characterize the vadose zone. Typically, soil physics measurements are costly, destructive, and mostly considered a point measurement. Geophysical techniques offer the advantage of interrogating a large section of the subsurface with minimal disturbance to the soil. The objective of this subtask was to develop suitable geophysical characterization techniques at the INEEL, and integrate this data collection with soil physical monitoring results (Task 1) and conventional and innovative numerical inversion models (Task 3).

We selected electrical resistivity tomography (ERT) as the geophysical technique to focus our efforts. Since the results from this technique are highly dependent on the moisture content of the soil, it can be integrated with soil physical measurements with a fair degree of resolution. The results are easily interpreted and the system can be operated remotely. As a general description, electrodes are placed along lines surrounding the area of interest. An electrical current is established between a pair of electrodes, and the resulting electric potential field is measured at the other electrodes. The process is repeated numerous times using different electrical pairs as the current electrodes. The resulting data are used in a numerical inversion model that adjusts the electrical resistivity (or electrical conductivity) of the domain until the model matches the electric potential field for all applied currents. Next the electrical resistivity field is correlated with the soil physical parameter of interest to evaluate potential distributions of this parameter. Temporal changes in this parameter can be examined if a time series of electrical resistivity measurements are made.

A Zonge electrical ERT system was purchased at the end of the first year of this project. Much of our effort this year (the second year) focused on developing appropriate data collection protocols and verifying that the data collection equipment was operating correctly. We built a series of physical models to evaluate the Zonge system and develop a protocol to collect the data. These physical models included a simple 2-D electrical resistor model, a 2-D homogeneous water model with single heterogeneity, and a 3-D homogeneous water background with single heterogeneity.

The 2-D water model was actually the first physical model built to test the newly purchased ERT equipment. However, the resulting conventional inversion results indicated large-scale heterogeneities in the homogeneous model. To resolve these discrepancies, the 2-D resistor network model was constructed as the most ideal physical model possible. Through a series of experiments, a wiring error in the Zonge data collection system was discovered and repaired. Further testing on the 2-D water model verified the inversion results, but problems were encountered when applying the 3-D inversion models to the 2-D system. The geophysicists hypothesize that the problem is due to using copper rod line electrodes rather than a point electrode.

The 3-D physical modeling improved the electrode problem. For this model, we used a small 4-acre, 25-ft-deep pond to field test the ERT system. The test was conducted during the winter, which allowed for easy access on the ice and fixed electrode positions. Four electrode arrays, each containing 13 copper electrodes, were designed, built, and installed at the pond site (see figure 5 for dimensions). A 2-ft-diameter hole was then drilled in the center of the electrode arrays, and a variety of targets were placed between the arrays.

Data were collected using variations of pole-to-pole and dipole-to-dipole arrays. Dipole-to-dipole data were collected using multiple dipole lengths (skip 1, skip 3, skip 5, and skip 13) and using full reciprocity. Pole-to-pole arrays were collected with the infinity electrodes 60 ft east and west of the target area. The goal of using different dipole lengths is to test sensitivities of the acquisition to sensing subsurface properties, and to evaluate the performance of different ERT inversion codes. Data were collected with and without a $3 \times 2 \times 1$-ft stainless-steel box present in the center of the arrays. For each model the data collection was repeated multiple times using the same geometry over a 1-week period in February 2002.

The data from the pond were extremely repeatable as well as consistent with the electrode geometry. The datasets collected with the same acquisition configuration and modeled at different times during the measurement cycle matched within 1%. The processed data from the background data set are the least noisy and most reproducible data collected by the project to date.

However, the data with the steel target provided an unexpected result. Specifically, the steel target shows up as a slight resistor. Examination of the raw data (both the dipole-dipole and pole-pole data) also shows the target as a resistor. The geophysicists hypothesized that the problem does not reside in the inversion codes. A literature search revealed some previous work (Guptasarma 1983), which shows instances where a metal target in electrolytes within certain ranges of temperature, pH, and water conductivities can behave as a resistor due to the electrochemical boundary between water and metal. Unfortunately, the spring melt prevented additional data collection and confirmation of this hypothesis.

As part of the ERT data collection protocol, Clark Scott of the INEEL performed a sensitivity analysis to determine an optimal acquisition geometry for the pond data set. The results from this analysis showed that electrode skip values above skip 3–4 did not increase sensitivity in the central regions (see Figure 6). These results are fairly counterintuitive. We originally believed that large skip patterns (greater than 10) would pass the greatest amount of current through the heterogeneity and therefore would result in the greatest sensitivity between the electrodes. Analysis of this data is continuing.

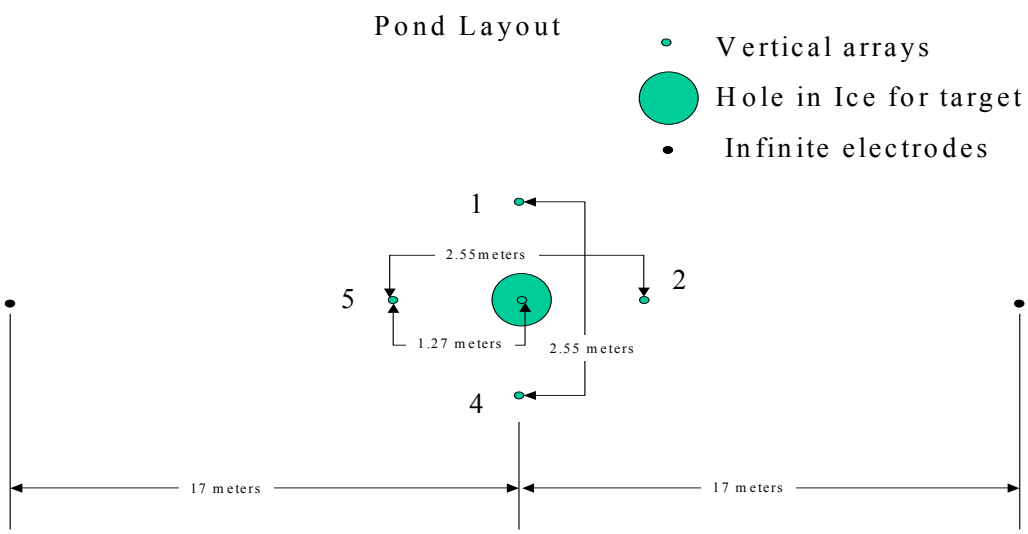

Figure 5. Electrode layout for the pond ERT 3-D study.

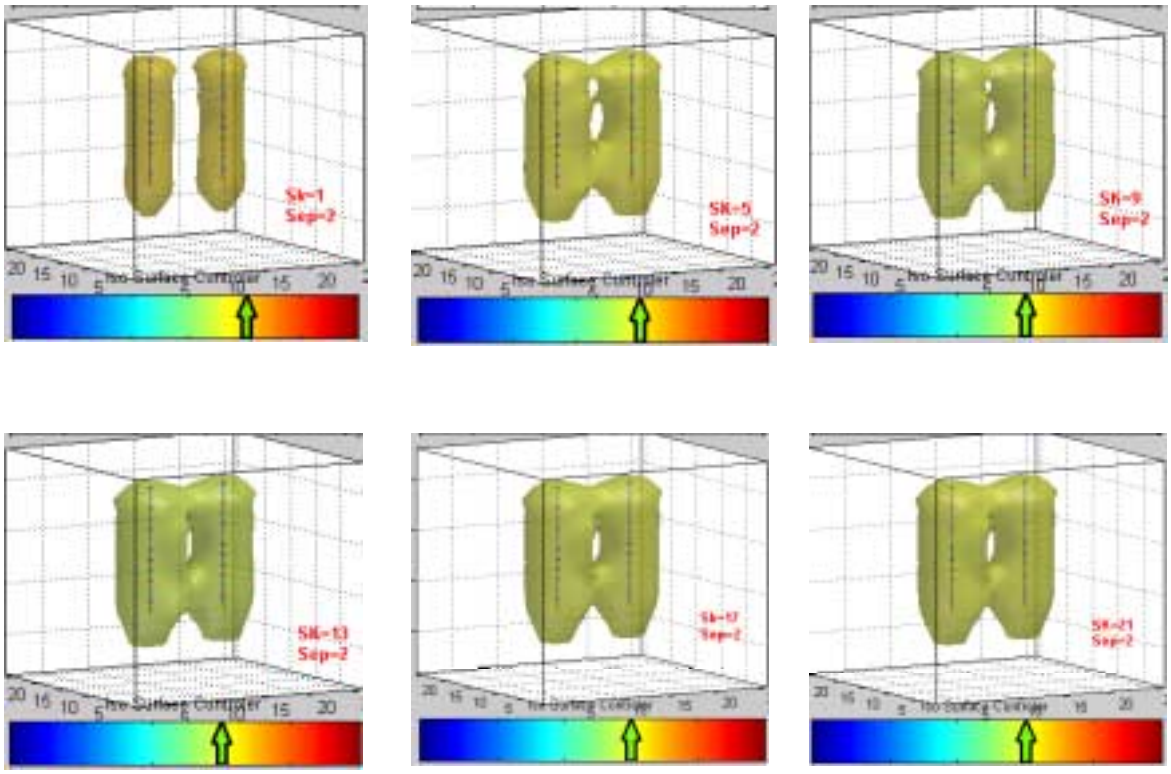

Conductive body central 18 inch square

Figure 6. An example of the sensitivity analysis for a two-boreholeERT system. Different skip values are used and the surface is constructed around the top four decades of sensitivity. Note the 'hole' never goes away and the sensitivity remains essentially unchanged beyond skip 5.

Task 3. Data Integration and Simulation

New interpretation methodologies are needed to analyze temporal and spatial data sets (Tasks 1 and 2) and to incorporate these data sets into numerical flow and transport models. We presently have the ability to collect nearly continuous temporal vadose zone monitoring data, multiple soil physical data points, and spatial geophysical images. However, we have few techniques to integrate these data or effectively incorporate these data sets into numerical transport models. Results of these research efforts is leading to better understanding of the functional interrelatedness between specific geophysical and hydrogeophysical parameters, and ultimately contribute to more accurate subsurface modeling. The subtasks in this section examine temporal and spatial analysis of the data and methodologies to combine the two characterization techniques.

Statistical and Time Series Analysis of Data

Quantitative methodologies are needed to interpret long-term monitoring data sets so that they can be used to monitor the effectiveness of remedial strategies at DOE waste sites. Considerable time and effort are expended in hydrology studies to identify, justify, and remove "false positives" from hydrologic data. For tensiometric data, barometric and earth tides are the major sources of the noise in the "raw" tensiometer signal. These mask the desired soil matrix measurement and indicate false infiltration events. While the eventual removal of these and other noise sources is a goal of most studies, isolating the noise and correlating it with the barometric and

tidal signals can be equally valuable. For example, extracting the barometric and tidal signal from measured water level data has lead to improved estimates of aquifer physical properties such as the transmissivity and the storage coefficient. Unfortunately, currently available methods are tedious to apply and the final product has been questionable. While the application of Fourier methods is an obvious choice for extracting fixed frequency sources from noisy data, Fourier methods do not work that well when the frequency varies in a random manner. The barometric signal is an excellent example of a signal with random components in its frequency and amplitude. The tidal signal has components of several frequencies and its low amplitude makes its identification difficult. While the variable frequency and amplitudes make Fourier series methods difficult, the presence of long term trends and very-low-frequency components make using the Fourier methods an impossible task because detrending the data is subjective and operator dependent.

In an attempt to overcome these problems, wavelet methodology was applied to the long-term tensiometric data sets in an attempt to remove noise and extemporaneous signals. The wavelet method separates a signal into a slowly changing smooth signal and a rapidly changing signal. In our case, we assume that the longer wavelength portion of the signal is due to water infiltration events where as the nonsmooth portion of the wavelet contains the barometric, tidal, and random noise. The wavelet method was applied repeatedly to data sets until the desired level of "smoothness" was obtained. With the assistance of M.E. Velasquez (INEEL physics department), we were able to separate the smooth underlying signal relating to the annual hydrologic cycle from the nonsmooth signal. The nonsmooth portion of the signal can be discarded if only the matrix potential data is required; however, in theory, this portion of the signal contains the barometric and tidal signals. Additional signal processing would be required to fully identify these signals.

Development of a 3-D Level Set Code

Through a subcontract with Dr. Eric Miller of the National Science Foundation's Center for Subsurface Imaging Systems (CenSSIS), we are examining numerical inversion alternatives to electrical resistivity tomography. Based on a sensitivity analysis of ERT data, we have developed a new level set approach in which the speed function is equalized to guarantee coherent evolution of the level sets with fast convergence. We are also working on imaging systems that have a greater than binary (two distinct electrical conductivity) distribution. Both of these advancements are being verified using data supplied by the INEEL from laboratory controlled 3-D field experiments and "real" vadose zone soils. The following paragraphs describe some of the advancements made this year.

Level Set Implementation: A level-set based algorithm was implemented for ERT inversion that extended the velocity and the narrow band implementations. In the former case, the update in the level set function is almost negligible; in the latter case, the evolution of the level sets is much faster in the neighborhood of the sensors compared to far away regions. This phenomenon leads to inaccurate solutions and very slow convergence.

Sensitivity Analysis and Speed Equalization: In order to improve the level set algorithm performance, different regularization methods were applied. These methods include the incorporation of different curvature or constant terms in the speed function to speed up the interface evolution. None of these methods provided a satisfactory result. Our next step consisted in performing a set of simulations and observing and analyzing the sensitivity function. The theoretical analysis and simulation results show that the adjoint field takes very large values around the sensors and decays rapidly as the distance from the sources and receivers increases. This fact explains the behavior of the level sets since the speed function is equal to the adjoint field. To overcome the sensitivity problem, the speed function was scaled in different ways, that is, by the distance to the closest sources or by the resistivity of the algorithm. Finally, we tried an equalization technique that provided very good results for 2-D and 3-D models of binary media.

Greater than Binary Medium: An improved speed function in the algorithm for Nary media was implemented and simulated. In the obtained

results, convergence is achieved only when starting with a good initial guess.

Sensitivity and other Equalization Methods: At the end of this year, we started to develop a new speed equalization method based more explicitly on the physics of the problem (behavior of sensitivity). Through some theoretical derivations, we show that in the ERT problem, inhomogeneities behave as reflectors that can be modeled with a set of sources on the boundaries of the anomalies.

Zonal Approach to Simulation

Cost effective and timely remediation of DOE facilities requires making good remedial decisions in the presence of uncertainty. A variety of risk-based tools have been developed by the scientific community to assist in the decision-making process, but many of these tools have limited ability to address sources of uncertainty. In principle, uncertainty due to site-specific geologic variability can be incorporated into these tools through use of stochastic flow and transport models. Since 1985 a variety of stochastic (probabilistic) modeling approaches have been developed to quantify transport behavior through heterogeneous unsaturated materials. All of these models are parameterized with spatial statistics that characterize the subsurface variability of measured hydraulic properties. In contrast with most site-specific geologic descriptions, nearly all of these approaches assume that hydraulic properties are continuously and smoothly varying within the subsurface. Recent work by Holt et al.[7,8,.9] has illuminated a more serious flaw affecting current stochastic flow and transport modeling approaches. Small simple errors in hydraulic property measurements can lead to a significant distortion (bias) in the spatial statistics required for stochastic models. This bias can lead to order-of-magnitude errors in stochastic model predictions. The effects of these errors are insidious, as hydraulic property estimates may appear reasonable and generate realistic looking spatial statistics that are, however, inaccurate and misleading. In the context of risk-based decision making, a new approach for characterizing spatial variability of hydraulic properties is needed.

It has been observed that unless errors completely dominate measurements, measured hydraulic properties retain some information about the spatial structure and the shape of the distribution. But, the problem remains one of "extracting the information necessary to characterize the spatial distribution of hydraulic properties for stochastic flow and transport predictions."

A nonparametric "indicator approach" can be used to define the spatial pattern of hydraulic properties. Indicator approaches are subject to fewer restrictions and are more robust than traditional spatial statistical approaches. Errors introduced using indicator approaches are due to misclassification or from the deformation of the original distribution shape. The use of indicator geostatistics allows the spatial pattern of hydraulic properties to be defined in terms of zones, without specific knowledge of the actual property values for each zone.

Once the spatial pattern is known, the values of each zone can be determined through a constrained optimization procedure with constraints supplied by other sources of information such as moisture content, pressure head, or concentration data. This procedure could also help refine the spatial pattern. If constraints are collected at the scale of the prediction problem, the resulting spatial distribution of properties may overcome "up-scaling" issues. The resulting "parameterized" pattern can then be used for flow and transport prediction.

In order to develop and validate a new "zoned" approach for stochastically modeling flow and transport, five research questions have been identified:

- How robust is the indicator approach for determining the spatial pattern of biased hydraulic properties?
- How many zones are required to preserve transport behavior?
- What and how much additional information is required to estimate property values within indicator-defined zones?

- Can general flow and transport behavior be accurately predicted using this approach?

- What is the prediction uncertainty using this approach (compared to traditional stochastic methods)?

The work described in this report addresses the first two of these research questions and shows that:

- The indicator approach for determining a zoned spatial pattern for biased hydraulic properties is robust for even highly biased hydraulic property estimates

- Flow and transport behavior is adequately preserved with as few as 10 zones.

Our overall approach is summarized below; a detailed discussion is in preparation as a journal manuscript.

An error analyses approach was used to evaluate the impact of hydraulic property measurement errors on the indicator variogram. A series of idealized simulated realities (spatially correlated random fields) were constructed with completely known spatial statistics. Properties were then reestimated by simulating field measurements of hydraulic properties in the presence of small, simple, and completely known errors. Hydraulic property data (original and re-estimated) were transformed to indicator functions based on quantiles and variograms, which were determined from the indicator data. Indicator variograms for both the true and estimated fields were compared, and the extent of bias was then assessed. The mean hydraulic property values were varied between 221 different realities to reveal the connection between true property values and bias affecting indicator variograms.

Although the mean, variance, and variogram for the nontransformed data are significantly biased, the correlation lengths determined from indicator variograms are more accurate than those determined from the continuous data because spatial errors simply reflect misclassification. Correlation lengths of rescaled indicator variograms tend to be as accurate or overestimated rather than underestimated. In a well sampled field, overestimation leads to more accurate stochastic realizations of hydraulic property variability, while underestimating correlation lengths introduces more random behavior at the short scale. These indicator functions reveal the spatial structure of even highly biased hydraulic properties, even when the empirical distribution remains unknown. Therefore, we conclude that the indicator approach allows delineation of the spatial pattern of hydraulic properties.

This zoned approach of characterizing the hydraulic parameter fields through application of nonparametric descriptions of the porous medium structure appears to produce representations capturing the primary hydrogeologic features. The next step in the analysis was to determine the number of quantile-based zones required to preserve simulated transport behavior. The question was addressed by comparing simulated transport of a conservative tracer through a series of indicator-derived hydraulic fields as a function of the number of zones used in creating the indicator variograms. Results of simulated tracer transport were analyzed through the use of moments. We computed the first temporal moment of concentration, number of pore volumes required for 5% of tracer recovery, and number of pore volumes required to retrieve 95% of the tracer were computed. These computations indicate that the statistical measures of transport were well preserved for quantiles less than 0.1 ($Q<0.1$) (see Figure 7). This analysis effectively addresses the first two reseach questions by suggesting that the indicator approach provides a robust means of removing bias from field data, and that as few as 10 zones are required to preserve transport.

This work also has implications from a practical perspective in that the results obtained using fewer zones produce conservative transport predictions. As the corresponding number of zones falls below 10 ($Q>0.1$), the statistical measures deviate from those obtained for the full field case. This deviation results in over-predicting the first temporal moment of concentration, under-predicting the time required to recover 5% of the tracer, and over-predicting the time required to recover 95% of the tracer. In terms of contaminant management, the direction of deviation is

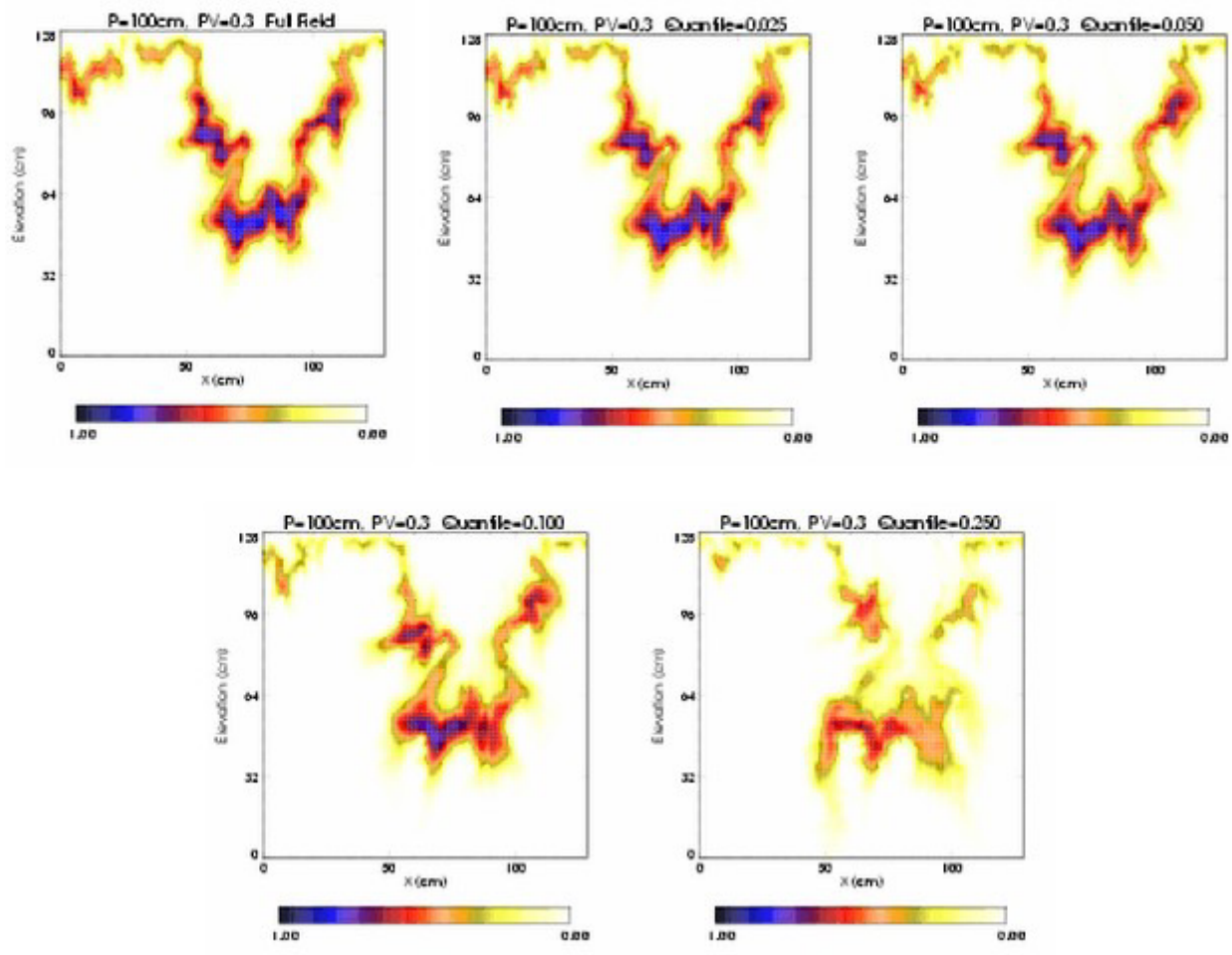

Figure 7. Results of simulated tracer transport analyzed through the use of moments.

conservative because the tracer will arrive later than predicted and take less time to clean-up than predicted using the zonal approach. The general ability to reproduce the statistical structure of the hydrogeologic properties with relatively few zones has profound implications in terms of characterization requirements. Because the indicator approach is based on delineating zones, rather than delineating the continuously varying distribution of parameters, data requirements are less onerous and should result in lower site characterization costs.

Anisotropic Effects on ERT Measurements

Knowledge of the relationship between the soil bulk electrical conductivity (EC) and moisture content is required to quantify subsurface moisture variations using ERT. Typically, repacked field samples are used to establish the EC-moisture content relationship because of difficulty removing and analyzing intact samples. However, internal sample structure can influence EC measurements, as complicated wetted-phase structures can evolve during drainage, and repacking errors can lead to increased uncertainty in subsurface moisture contents estimated with ERT. In this subtask we are developing a percolation code to predict the internal soil-phase structure, and will then use this structure to determine the apparent electrical conductivity both parallel and perpendicular to microscale layering. In addition, a set of laboratory experiments has been initiated to verify these predictions.

We use a numerical approach to investigate the impact of wetted-phase structure on EC-moisture content relationships in layered and homogenized sandy materials. We simulate

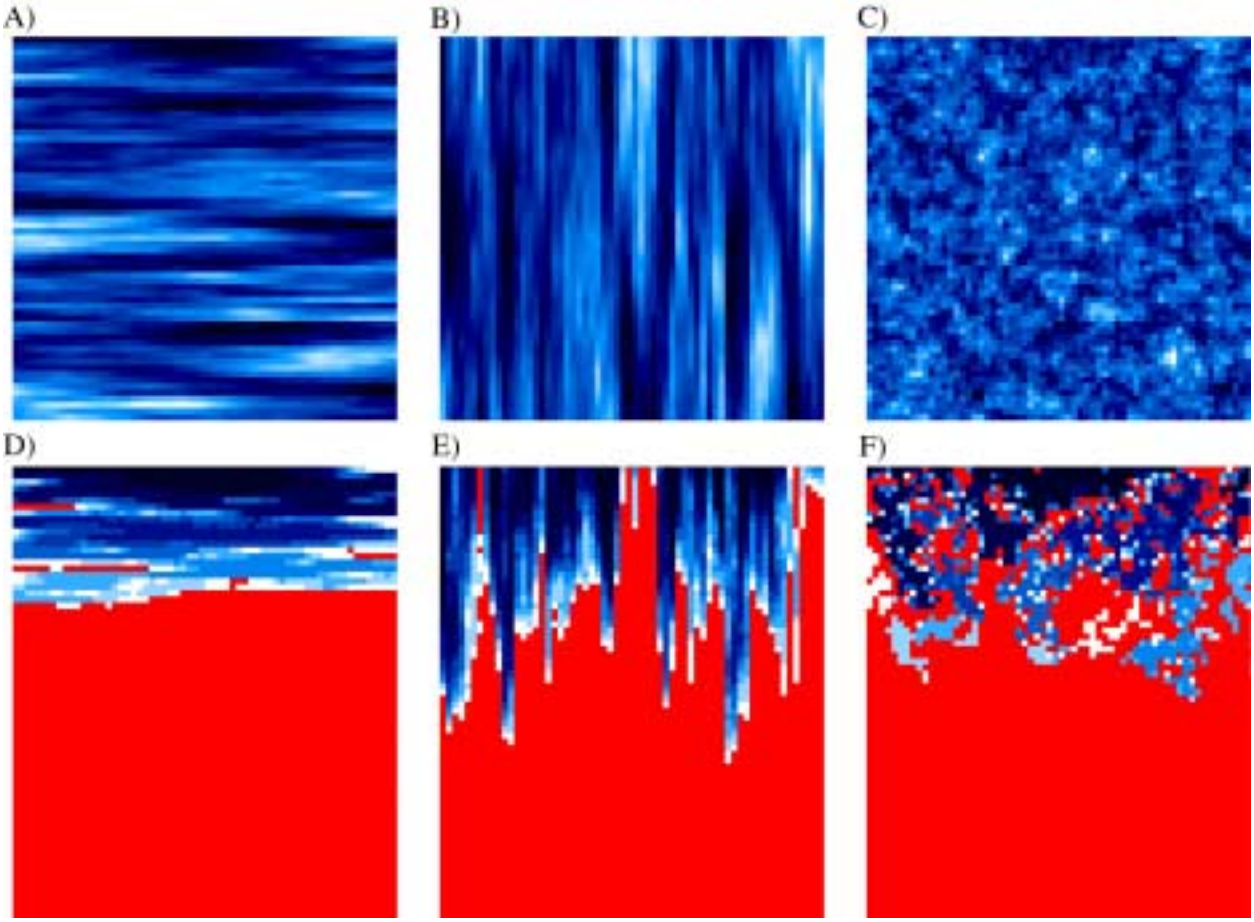

Figure 8. Figures 8A, B, and C show the air-entry pressure distribution within the cells of each sample (horizontal packing, vertical packing, and random packing). The mean ψ_{ae} = 80 cm and the standard deviation of ψ_{ae} = 30 cm. For all cells, the porosity and the Brooks and Corey λ are constant and equal to 0.33 and 6.0 respectively. ψ_{ae} is largest for dark colors and smallest for light colors. Figures 8D, E, and F show the equilibrium wetted phase structure at a tension of 102 cm. Color gradations from dark to light reflect the invasion order. Red regions are noninvaded cells.

laboratory drainage in samples using a macroscopic invasion percolation model that includes capillary and gravity forces. Cell moisture contents are then mapped to cell-specific EC values using the constitutive model of Mualem and Friedman.[10] Resulting heterogeneous EC fields are then used in a finite-difference model to simulate sample-scale EC measurements. We consider EC measurements on heterogeneous layered samples oriented both perpendicular and parallel to layering and samples with no internal spatial correlation. Examples of the numerical results are illustrated in Figures 8 A to F.

Although the equilibrium moisture retention relationships for the three sample structures are nearly identical (see Figure 9a), Calculated EC values tend to be highest in samples oriented parallel to layering and lowest in samples oriented perpendicular to layering, while statistically homogeneous samples have moderate EC values (see Figure 9b). Although these results are not surprising, EC differences are greatest at intermediate saturation where they can exceed an order of magnitude. These preliminary results suggest that electrical anisotrophic behavior must be incorporated into the geophysical inversion models.

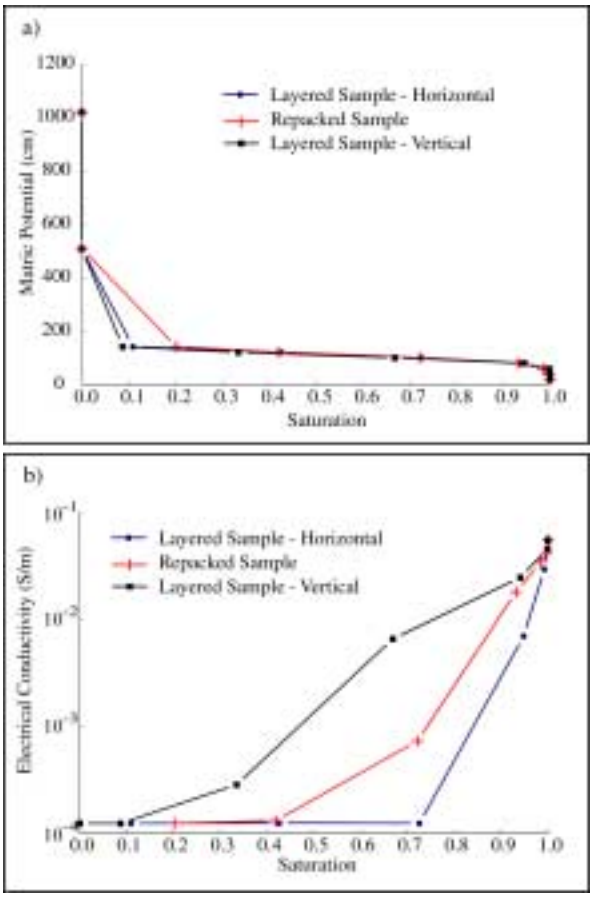

Figure 9. Chart (a) gives the pressure-saturation curves; Chart (b) gives the electrical conductivity-saturation relationships for the three different sample configurations.

ACCOMPLISHMENTS

This research project has developed improved soil physics monitoring systems and incorporated these instruments sets into contaminated field sites belonging to DOE and other federal agencies. An in situ chemical sensor was developed and tested in response to identified DOE needs of long-term chemical monitoring in unsaturated soil. The wavelet methodology approach was applied to tensiometric data to separate the desired signal from the noise.

We have continued to develop our expertise in ERT data collection and analysis. Equipment purchased in previous years was used to evaluate well-controlled laboratory and 2-D and 3-D field structures. Data from these tests were evaluated using the standard Occam's inversion techniques as well as the CenSSIS alternative Level Set 3-D model, which has been transferred to the INEEL. Laboratory testing of the anisotropic effects of electrical ion mobility through soil is being investigated through laboratory experiments.

We are integrating these techniques through the use of a zonal technique in hydrologic transport models. It is becoming more apparent that the stochastic continuum approach may not be the best approach to characterize heterogeneous subsurface vadose zones. Our recent results in the zonal approach indicates that if we can characterize the subsurface into a small number of zones, our transport predictions do not suffer to any great extent. This alternative modeling approach couples well with our efforts with CenSSIS Level Set inversion technique and our temporal characterization advancements. These tasks are being integrated at the IRC field site as a stepping stone to application at DOE and other contaminated facilities. The following specific deliverables were described in the FY 2002 work plan:

1. Hire unsaturated zone contaminant transport modeler (11/01)

2. Chair AGU session (1/02) on Chemical Heterogenieties in the Vadose Zone

3. Present three posters at AGU fall session (1/02)

4. Complete instrumentation of a vadose zone research site (7/02)

5. Prepare a report describing chemical sensor integration into VZMS (9/02)

6. Prepare report for the ESR annual report describing progress made in all tasks (9/02)

We have met all the deliverables except for completion of the IRC field site (deliverable 4). Unexpected delays in obtaining the Environmental Safety and Health documentation were encountered, however, we expect this deliverable to be completed before the end of the calendar year.

In addition, we have:

- Installed the INEEL VZMS at the Hanford B and SX tank farms, INEEL RWMC, and EPA Gilt Edge Superfund site.
- Developed an in situ vadose zone chemical sensor platform to measure chemical concentration in unsaturated soils.
- Established a field test site adjacent to the INEEL IRC facility to evaluate soil physical and geophysical equipment.
- Continued development of a rapid instantaneous profile method to characterize surface soils.
- Investigated the use of wavelet theory to analyze long-term monitoring data sets.
- Developed 3-D ERT field collection capabilities at the INEEL.
- Developed a 3-D Level Set ERT inversion code to define boundaries between electrically contrasting layers.
- Developed alternative methodology to characterize vadose zone materials through a zonal approach rather than a continuum approach.
- Incorporated percolation theory with a geophysical model to examine the effects of layering on the electrical resistivity tomography.
- Increased INEEL hydrologic capabilities through hiring of Mitch Plummer, a Ph.D. graduate from New Mexico Institute of Mining and Technology. Mitch has expertise in isotope chemistry and climate change and will be examining the inclusion of these techniques upon vadose zone chemical transport.
- A session entitled "Chemical Heterogeneities and Contaminant Transport in the Vadose Zone" was co-chaired by Drs. Earl Mattson (INEEL) and Pat Brady (SNL) at the Fall American Geophysical Union meeting.

Publications

Accepted or Published

Environmental Protection Agency, 2002, "Advanced Tensiometers for Vadose Zone Monitoring," *EPA Technology Innovation Office's Tech Trends*, November, pp1-5. This site can be accessed at http://www.clu-in.org, go to What's New, then November 2001 Tech Trends.

Hubbell, J. M., and J. B. Sisson, "Measuring Water Potential Using Tensiometers," *Encyclopedia of Water Science*, Agropedia, Marcel Deeker, Inc.

Hubbell, J. M., E. D. Mattson, J. B. Sisson, and D. L. McElroy, "Water Potential in Fractured Basalt from Infiltration Events," in review for *Evaluation and Remediation for Low permeability and Dual Porosity Environments,* ASTM Special Technical Publication, 1415.

Hubbell, J. M., E. D. Mattson, J. B. Sisson, and S. O. Magnuson, 2002, "Understanding Fluid and Contaminant Movement In the Unsaturated Zone using the INEEL VZMS," *Waste Management 2002* conference proceedings.

Innovative Technology Summary Report (ITSR), "Advanced Tensiometer for Vadose Zone Monitoring," (TechID 2122), submitted to DOE headquarters for approval. Provides sections on the technology description, instrument performance, technology applicability and alternatives, costs, regulatory and policy issues and lessons learned.

Sisson, J. B., G. W. Gee, J. M. Hubbell, W. L. Bratton, A. L. Ward, and T. G. Caldwell, 2002, "Advances in Tensiometery for Long-Term Monitoring of Capillary Pressures," *Vadose Zone Journal*. (accepted for publication)

In Preparation or Submitted

The Innovative Technology Summary Report (ITSR), "Advanced Tensiometer for Vadose Zone Monitoring" (TechID 2122) was submitted to DOE headquarters for approval. This document has sections on the technology description, instrument

performance, technology applicability and alternatives, costs, regulatory and policy issues, and lessons learned.

Presentations

Hubbell, J. M., "Geology and Hydrology of the Subsurface Disposal Area of the RWMC," Idaho Falls, ID, Utah State University faculty and students April 22, 2002.

Hubbell, J. M., E. D. Mattson, and J. B. Sisson, 2002, "Estimating Annual Infiltration Using Tensiometers," *American Geophysical Union, San Francisco, December 12, 2001*.

Hubbell, J. M., E. D. Mattson, J. B. Sisson and S. O. Magnuson, "Understanding Fluid and Contaminant Movement in the Unsaturated Zone Using the INEEL VZMS," *Waste Management 2002 conference proceedings*,2002.

Miled, M. K. and Eric L. Miller, "Level Set Methods for Cross-Borehole ERT," *Proceedings of the Progress in Electromagnetics Symposium, Boston, MA, July 2002.*

Miled, M. K., and Eric L. Miller, "Extension of Level-Set Curve Evolution Methods for Low-Sensitivity Imaging Problems," *IEEE International Conference on Image Processing, Rochester, NY, October, 2002.*

Miled, M. K., B. H., Eric L. Miller, "Geometric Inversion Methods for 3-D Resistance Tomography," *First SIAM Conference on Imaging Science, Boston MA., March 2002*.

Miller, Eric L., Gregory Boverman, and Mohamed Khames Miled, "Geometric Methods for Diffuse Wave Inverse Problems," *Review of Scientific Instrumentation*, under review.

A R&D 110 award entry form with an accompanying 8-minute video was completed and submitted to Cahners Scientific publishing for the "INEEL Direct-Push Instrumented Visual, Tensiometer and Lysimeter Probe System." The initial concept of installing vadose zone instruments using direct push/sonic drilling methods and early designs of these probes originated from the vadose zone instrument development in the ESRA and LDRD programs within the Geosciences Research Department (J. Hubbell and B. Sisson). These tools and techniques were developed for Environmental Restoration and installed in the Radioactive Waste Management Complex in FY 2001.

Patents

Hubbell, J. M., and James B. Sisson, U.S. Patent Number 6,308,563, for "Vadose Zone Isobaric Wells," granted October 30, 2001. This patent describes improved tensiometers designs to improve the precision of the water potential measurements for use in deep vadose zones for detection of wetting fronts and for estimation of flux. The patent contains 13 claims and six drawings.

Hubbell, J. M., and J. B. Sisson, U.S. Patent number 6,405,588 B1 for "Automated Deairing System to Allow Tensiometers to Operate Unattended for Extended Time Periods in the Field," June 18, 2002. This patent describes tensiometer designs to obtain unattended soil water potential measurements for extended time periods. These measurements are less affected by environmental conditions at the point of measurement. These designs improve the precision of the water potential measurements for use in deep vadose zones for detection of wetting fronts and for estimation of flux. The patent contains 27 claims and five drawings. This patent presents a technological advancement in vadose zone instrumentation developed at the INEEL

Patent Applications

A patent application for "A method for retrieving a liquid sample, a suction lysimeter, a portable suctions lysimeter, a lysimeter system, and a deep lysimeter" was submitted to the U.S. Patent and Trademark Office. This invention describes instruments used for water sampling in either the vadose zone or from ground water. This device is unique in that it can sample from unsaturated sediments, from very thin layers of standing water, or it allows passive sampling in the vadose zone when temporary saturation forms (intermittent perched water). These instruments have been constructed, tested, and are being used at the Subsurface Disposal Area of the Radioactive Waste

Management Complex on the INEEL for the Environmental Restorations Department (WAG 7) for sampling perched water wells.

A patent application for a "Horizontal Tensiometer" was prepared by the DOE Chicago Intellectual Property law Division for submittal to the U.S. Patent and Trademark Office. This invention disclosure describes designs for installation of horizontally installed advanced tensiometers for measurement of soil water potential of soil and rock beneath objects or overlying material. These instruments are designed for use at sites like the RWMC, where they could be installed prior to disposal of the waste.

A patent application for a "Surface, Borehole, and Laboratory Exfiltrometer" is being prepared. This invention describes the designs and concepts of devices to measure in situ soil hydrologic properties rapidly and with low cost. This application will be submitted to the U.S. Patent and Trademark Office in the next 3 months.

A patent application was submitted to the U.S. Patent and Trademark Office for a "Lysimeter Methods and apparatus and Tensiometer Methods and Apparatus." This patent describes several sonically installed tensiometers and lysimeters that were deployed at the RWMC.

New Intellectual Properties (Invention Disclosure Reports)

Three invention disclosures were prepared and submitted to the Technology Transfer and Commercialization Officer of Bechtel BWXT Idaho, LLC and the Chicago Intellectual Property Law Division (DOE). These intellectual properties include:

Single-Shot Tensiometer. This device is used for measurement of soil water potential at sites where field instrument maintenance is not desired or allowed. It is used for monitoring continuous, long-term water potential in the subsurface at depths greater than about one meter below land surface. This instrument has been incorporated into the VZMS, developed at the INEEL. These devices will have application at numerous commercial and government sites for characterization, performance assessment, validation of remediation activities, and long term stewardship. Instruments were deployed at the 200 West Area, Hanford, WA. This task is part of a Work For Others project with Dr. Gee at PNNL.

Direct Push Vadose Monitoring System. This device is a direct push VZMS that combines tensiometry, lysimetery, water content, and gas sampling into a single direct push penetration. This versatile system has a simple design (no moving parts), provides state-of-the-art data, is installed using standard direct push technology (no cuttings generated), and has low construction, installation, and operational costs.

Installation of vadose zone instruments in contaminated materials (Sealed Drive Point). This declosure describes a simple but versatile design and technique for installing tensiometers, lysimeters, gas sampling ports (optional), temperature, geophysical instruments or other instruments in contaminated or noncontaminated materials using the drive point or sonic drilling methods. This design has low cost materials and is versatile, allowing a multitude of instruments to be placed in the well and the option to add new instruments at a later time.

Collaborations

New Collaborations

University of Idaho. A masters level hydrology student (Mitch Poulson) was funded under this project to evaluate the versatility and to develop an acceptable methodology to analyze exfiltrometer data. Drs. Allan Wylie and Gary Johnson are the student advisors.

Beltsville, MD. Dr James Starr of the ARS deployed advanced tensiometers (supplied by the INEEL) for a Nuclear Regulatory Commission investigation for an engineered barrier study located at Beltsville, MD.

Ruby Gilt Waste Rock Dump. The Geosciences Research Department designed and deployed a

perched/ground water and VZMS at the 65-acre Ruby Gilt Waste Rock Dump of the Gilt Edge Mine in Lawrence County, South Dakota. This site is on the U.S. EPA National Priorities List. The waste rock dump generates acid mine drainage. Four vadose zone wells were drilled and instrumented with a combination of advanced tensiometers, single shot tensiometers, solution samplers, and gas sampling ports to characterize and monitor the temporal and spatial soil water potential, perched water depth, temperature, and allow solution and gas sampling. The information from the 24 monitoring depths will provide information on the effectiveness of the remedial action (placement of a liner over the waste rock with recontouring) and indicate if the site has the potential to impact ground water resources. While on assignment at the mine site an improved design of the single shot tensiometer was identified. The improvement allows for easy installation and further improvement of tensiometer reliability.

Continuing Collaborations

University of Mississippi. In collaboration with Dr. Robert Holt of the University of Mississippi, we are developing an alternative method for characterizing the spatial variability of hydraulic properties. This approach assumes that the classical geostatistical approach is not feasible due to measurement errors in obtaining the data sets. In our alternative method, a nonparametric "indicator approach" is used to define the spatial patterns of the hydraulic properties. In this case, we propose not to interpolate for the value of the parameter of interest but to use the data to define zonal spatial patterns for the parameters. After the zones are determined, parameterization of these zones can be made. Both the classical and the indicator methods of geostatistical approaches will be evaluated and compared in numerical models and field experiments.

National Science Foundation (NSF) Center for Subsurface Imaging Systems (CenSSIS). The National Science Foundation (NSF) Center for Subsurface Imaging Systems (CenSSIS) was tasked to evaluate an alternative inverse methodology called Level Sets. Occam's inversion calculates an acceptable electrical conductivity distribution that satisfies the response to a set of measurements. The level set inversion method defines boundaries between contrasting electrical conductive materials. In this case, ERT measurement will be used at the Vadose Zone Research Park to establish the boundaries between the basalt and sedimentary materials. As in the indicator geostatistical approach, once the zones are established, they will be parameterized in predictive models.

Hanford Site B Tank Farm. VZMS was designed, constructed, and installed at the B Tank Farm in the 200 E Area of the Hanford Site using instruments and techniques developed for this project and adapted for use at the Hanford Site. Eight depths were instrumented with a combination of water content, temperature, water potential, shallow flux meter, and solution samplers to characterize the soil moisture movement between the tanks at depths of 3 to over 200 ft. These instruments will provide a comprehensive data set of deep vadose zone properties to assist in understanding the dynamics of unsaturated flow at this site. This will be the first vadose zone monitoring installation measuring these parameters ever installed near the single walled tanks. These instruments are connected to a data logger for the unattended collection, storage, and transmittal of data using a cell phone system. Work is being conducted in conjunction with Glendon Gee of PNNL as part of the Subsurface Contaminants Focus Area (Subcon) EM-50 Project (RL31SS31), and in collaboration with the RPP Vadose Zone Characterization Project.

Vadose Zone Research Park. Vadose zone instruments, borehole instrumentation techniques, and information obtained from monitoring the deep vadose were combined to support vadose zone instrumentation at the Vadose Zone Research Park being established at the location of the new INTEC percolation ponds. The research park will serve as a place to test hypotheses about water movement through the vadose zone and to compare new instrumentation to established methods of vadose zone characterization. Instrumented boreholes are being installed to depths of over 400 ft. Laboratory techniques were developed to calibrate the borehole water content sensor to allow measurement of

moisture content within basalt. This will provide the first ever measurements of water content in situ within the basalt matrix. The calibration indicated a linear fit for moisture content versus output from the sensor.

Environmental Restoration Operations at the RWMC. A network of advanced tensiometers are monitored at the RWMC to characterize soil water potential in the deep vadose zone beneath the buried waste. Instruments are located from depths of 20 to over 220 ft below land surface. Data from this site was used in the ASTM paper and is being used to understand the flow and transport in this heterogeneous geologic media. The Geosciences research department is assisting Environmental Restoration Operations in improving in improving collection efficiencies from soil solution samplers and interpreting data from the advanced tensiometers used for characterization and monitoring at the Radioactive Waste Management Complex. The soil water potential data from the tensiometers and chemical analyses from solution samplers will improve the understanding of the flow and transport of water and contaminants at this site. This information can be used to improve risk assessments. This work is funded by Environmental Restorations.

Instruments under this funding (drive cone tensiometer, imaged drive tube and drive cone lysimeter) were installed below, within and above the waste in pits 4, 5, 6 and 10 at the RWMC to characterize the distribution and movement of moisture and contaminants in these waste pits. The Geosciences research department is assisting Environmental Restoration Operations in improving collection efficiencies from soil solution samplers and interpreting data from these drive point instruments. This work is funded by Environmental Restorations.

REFERENCES

1. B. B. Looney and R. W. Falta, *Vadose Zone Science and Technology Solutions*, Battelle Press, Columbus, OH, ISBN 1-57477-085–3, 2000.

2. National Research Council, *Research Need in Subsurface Science*, National Academy Press, Washington, D.C., ISBN 0-309-06646-8, 2000.

3. DOE, 2001, "Workshop Report: Long-Term Monitoring Sensor and Analytical Methods Workshop (Draft)," Orlando FL, June 13–15, 2001.

4. J. H. Hubbell, E. D. Mattson, J. B. Sisson, and S. O. Magnuson, 2002, *Understanding Fluid and Contaminant Movement in the Unsaturated Zone Using the INEEL Vadose Zone Monitoring System*, Waste Management, Tucson, AZ, 2002.

5. P. Rita and S. Charpentier, "Ionic-Equilibrium Time Inside Ceramic Cups In Unsaturated Porous Media," *Soil Sci. Soc. Am. J.* Vol. 62, 1998, pp. 574–579.

6. P. Moutonnet, J. F. Pagenel, and J. C. Fardeau, "Simultaneous Field Measurement of Nitrate-Nitrogen and Matric Pressure Head," *Soil Sci. Soc. Am. J.*, Vol. 57, 1993, pp. 1458–1462.

7. R. M. Holt, J. L. Wilson, and R. J. Glass, "Spatial Bias In Field-Estimated Unsaturated Hydraulic Properties," in press *Water Resour. Res.*, 2002a.

8. R. M. Holt, J. L. Wilson, and R. J. Glass, "Error In Unsaturated Stochastic-Models Parameterized with Field Data," in press *Water Resour. Res.*, 2002b.

9. R. M. Holt, R. J. Glass, and J. L. Wilson, "Spatial Bias In Laboratory-Estimated Unsaturated Hydraulic Properties, submitted to *Water Resour. Res.*, in review.

10. Y. Mualem and S. P. Friedman, "Theoretical Predictions of Electrical Conductivity In Saturated and Unsaturated Soil, *Water Resour. Res.*, Vol. 27, 1991, pp. 2771–2777.

Mesoscale Investigations of Vadose Zone Carbon Cycles

Larry Hull, Kristine Baker, Craig Cooper, Don Fox,
Mitch Plummer, and Dave Thompson

SUMMARY

The objective of this project is to provide more defensible predictions of radionuclide migration in the vadose zone where multiphase transport and variable gas-phase composition may impact radionuclide mobility. Inorganic carbon is selected as the integrating variable for multiphase and multicomponent vadose zone processes because it serves as a coupling component among microbial productivity, solution pH, control of mineral-solute interactions, gas-phase transport, and dissolved phase transport. Radionuclides being investigated are carbon-14 and uranium. Results of the investigation will apply to DOE waste disposal sites in the arid west, and are directly applicable to the Subsurface Disposal Area (SDA) at the INEEL. The experimental conditions have been selected to represent important components of the subsurface environment at the SDA including material composition, variable gas-phase composition, and unsaturated moisture conditions. Carbon-14 and uranium are two significant components of the buried waste inventory with estimated high mobility.

A mesoscale column (3 m high and 1 m in diameter) was packed with sediment representative of the SDA and instrumented to monitor moisture potential, solution chemistry, gas-phase chemistry, and temperature. Gas-phase tracer tests were conducted with sulfur hexafluoride to quantify appropriate transport parameters for pore gas. Dissolved-phase tracer tests were conducted with lithium bromide to quantify appropriate transport parameters for solutes. Constitutive relations for microbial activity as a function of moisture content were derived from measured microbial productivity. Sediment samples were collected to determine microbial and mineralogy composition. Using these parameters, computer models were used to predict the migration of carbon-14 and uranium in the column. In August 2002, three liters of tracer solution containing tritium, carbon-14, and uranium were injected into the column ~60 cm below the sediment surface. Sampling showed that carbon-14 migrated rapidly in the gas phase. Uranium has not been detected in the solution samplers, but predictive models indicate that it will take several months for uranium migration to be detected. Results of this experiment allow the phase-transfer parameters for carbon-14 to be determined, which can be applied to predictive models of carbon-14 migration at the SDA. The results support the position that a significant fraction of the carbon-14 in buried waste will be transported to the surface in the gas phase and will not be transported to the aquifer.

PROJECT DESCRIPTION

Background

The long-term fate of contaminants will depend on the subsurface geochemical environment. Significant system variables include redox potential, pH, mineral surfaces, and water chemistry. The vadose zone microbial community plays a significant role in defining the geochemical environment, particularly with respect to redox potential and pH. Microbes depend on the physical properties of the vadose zone such as gas-filled pore space. Thus physical, geochemical, and biological components of the system are interrelated. In this project, we employ inorganic carbon as the integrating variable for multiphase and multicomponent vadose zone processes. Inorganic carbon serves as a coupling component among microbial productivity, solution pH, control of mineral-solute interactions, gas-phase transport, and dissolved phase transport.

Description of the Problem

Past industrial practices at DOE facilities included discharge of liquid wastes to infiltration

ponds and cribs, burial of solid wastes in landfills, and inadvertent spills and leaks of contaminants. These planned and unplanned disposal activities have resulted in contamination of the vadose zone. Over the past 12 years, DOE has worked to remediate these contaminated areas so that they do not pose a risk to future generations. The only apparent options available for much of the radionuclide and metal contamination are to leave it in place or excavate and move it to a subsurface repository. Either way, the contamination remains buried in the vadose zone where long-term stewardship is required. We currently lack understanding of the movement and transformation of contaminants and the physical, chemical, and microbial processes in the vadose zone. This leads to inaccurate predictions and overly conservative assumptions regarding long-term remediation decisions, which results in increased spending on remediation and limited remedial action options. A lack of understanding of vadose zone processes also increases uncertainty in monitoring of remedial actions to detect failures in selected remedies quickly enough for actions to be taken before contaminant migration becomes significant.[1]

Project Objectives

The technical objective of this project is to understand the coupled process taking place in the vadose zone among water movement, microbial activity, gas transport, and the migration of solutes, so we can develop constitutive and thermodynamic relations among the system variables. Once these improved relations are incorporated into computer models, more reliable predictions can be made to support remedial action programs at DOE sites.

The results of this project will apply directly to immediate DOE needs. Two key radionuclide contaminants buried in the SDA at the INEEL are carbon-14 and uranium. Both are identified as potentially impacting the performance assessment for the burial grounds.[2,3] Experiments being conducted in the mesoscale column and supporting laboratory experiments are designed to better understand the migration of these two contaminants under conditions similar to those expected at the burial ground. Results will be constitutive relations and thermodynamic parameters applicable to contaminant transport in the vadose zone. They will be validated using INEEL soil materials. Environmental restoration and waste operations use predictive computer models to assess risk posed by inactive waste sites and active radioactive burial grounds. Once demonstrated as a viable technology, these organizations can begin to use this approach to make decisions.

Conceptual Model

The long-term fate of contaminants in the vadose zone will depend on the geochemical environment. Significant system variables include redox potential, pH, microbial community, mineral surfaces, and water chemistry. Both advection of water and diffusion/advection of gases in the vadose zone can transport volatile reactive species. This project focuses on the role inorganic carbon plays in transporting contaminants through the vadose zone. A significant component of this effect will be in the control of pH of advecting vadose zone waters. Inorganic carbon often controls pH in natural waters through reaction with calcite to produce soluble calcium, CO_2, and water. Atmospheric levels of CO_2 are on the order of 350 to 400 ppmv ($\sim 10^{-3.4}$ atm). Shallow desert soils can have a partial pressure of CO_2 of 1,000 to 3,000 ppmv (10^{-3} to $10^{-2.5}$ atm), while soil gas around waste disposal trenches at the SDA, where organic debris has been disposed, can be as high as 10% by volume (100,000 ppmv or 10^{-1} atm) or higher. This can change the hydrogen ion concentration in soil water 1 order of magnitude.

We have developed a simplified conceptual model of the vadose zone to illustrate our focus on the inorganic carbon cycle (see Figure 1). Plant roots and microorganisms in the vadose zone produce CO_2 gas by respiration, which enters the unsaturated pores in the vadose zone. CO_2 is very soluble in water, and so the gas-phase CO_2 will dissolve in the pore water. Calcium carbonate (the mineral calcite) is a common accessory mineral in soils, and the excess hydrogen ion generated by the dissolution of CO_2 gas reacts with the calcite to be removed from the pore water solution. Thus, the distribution of CO_2 among the three phases (solid calcite, gas-phase CO_2, and aqueous phase dissolved carbonate) buffers the pH of the pore water.

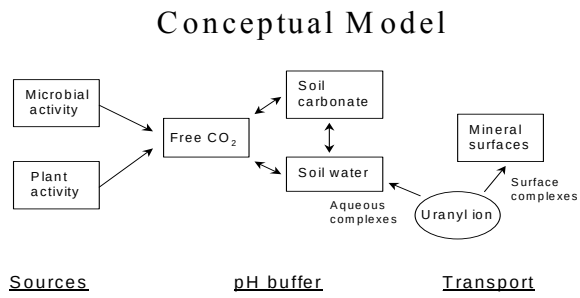

Figure 1. Conceptual model of vadose zone geochemical environment.

The mobility of a contaminant in the vadose zone will depend on the pH and aqueous chemistry of the pore water as well as the presence of surface sites on mineral grains for adsorption. A uranium (VI) ion (uranyl), in the vadose zone will be distributed between surface adsorption sites on minerals and held in the pore water as aqueous complexes (mainly of carbonate ions). The mobility of uranium will depend directly on the inorganic carbon cycle.

Approach

Our general project approach is to start with a hypothesis of a constitutive or thermodynamic relation that defines how an important process within the conceptual model such as CO_2 production or contaminant retardation depends on material properties such as moisture content. Controlled experiments are conducted on laboratory microcosms, small laboratory columns, and a flow-through centrifuge to gather data from which parameters of the constitutive relations can be determined. While the lab work proceeds, computer algorithms are developed expressing the constitutive relations. The algorithms are used to modify or amend existing computer models such as PHREEQC, UNSATCHEM, or STOMP (Subsurface Transport Over Multiple Phases), which currently incorporate many of the important processes. Mesoscale experiments are used to gather coupled data from systems where multiple processes occur at scales that approach the field scale, yet maintain controlled boundary conditions. Finally, field data are analyzed, so that conditions under which laboratory and mesoscale experiments are conducted represent field conditions. Two activities were conducted in FY 2002: microbial activity as a function of moisture potential and multiphase transport of contaminants. In addition, surface geochemistry and microbial characterization of solid phases is underway to define the biogeochemical environment.

Key environmental variables that control the activity of microorganisms in the subsurface are the availability of water and water borne nutrients. In addition to water stored in the gross interstitial voids between particles, significant volume may be accounted for in pores within the particles. We hypothesize that: (1) At very low water contents, water in unsaturated soil becomes unavailable for microbial use because the bulk of the remaining water is held in pores too small to be reached by microorganisms; and (2) At very high water contents, microbial activity is limited by the diffusion of oxygen through pores mostly filled with water. We are developing a constitutive relationship between microbial activity and matric potential. This will be derived from the measured relationship between microbial activity and available water, which depends on the pore size distribution, and from the measured matric potential at each water content. This is a significant improvement over the current approach to modeling microbial activity in soil, which assumes that all soil water is available to the microbes.

A mesoscale experiment is being conducted in a 3-m high, 1-m diameter column (Figure 2) packed with sediment. A vacuum applied at the bottom of the column induces water movement under unsaturated conditions. The column is instrumented with measurement devices and sampling ports to measure matric potential, water content, water chemistry, gas composition, and temperature (Figure 3). Additional instrumentation can be installed as needed or developed: RH probes to monitor vapor density, thermocouples to monitor temperature, tensiometers to monitor matric potential, and reflectometers to monitor water content. Gas and water samples are extracted via gas sampling tubes and lysimeters, and effluent lysimeters remove water from the lower portion of the column to maintain a steady-state flow condition.

Figure 2. August 2002 photograph of the mesoscale unsaturated flow column apparatus.

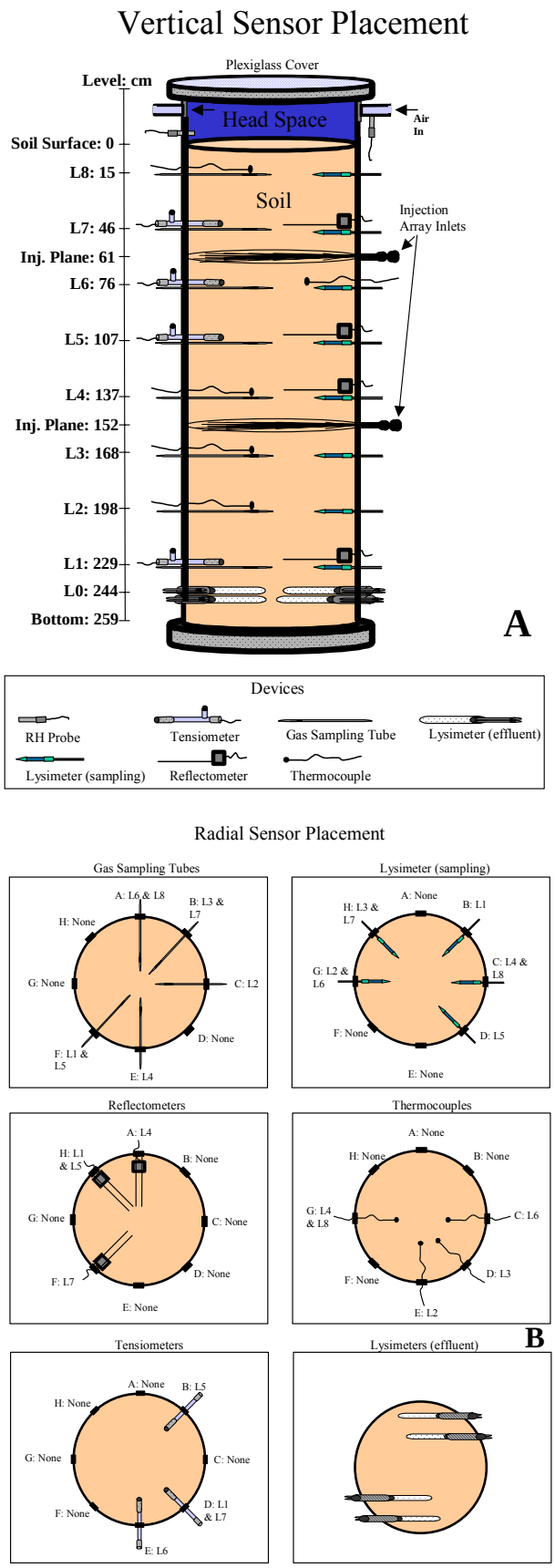

Figure 3. *(to the right)* (A) Schematic illustrating locations of sampling devices and monitoring instruments in the mesoscale column. Cross sections (B) illustrating the vertical ("L" notation refers to height of port, in feet, above bottom of the column) and horizontal distribution of the various monitoring devices within the column are only approximately to scale.

Relationships Between Moisture Content, Tension, and Biogeochemical Activity in the Vadose Zone

Traditional methods for adding substrate solution to soil for microbial activity investigations of vadose zone soils include drop-wise application followed by soil mixing to distribute the substrate throughout the soil. Although this method distributes the substrate, it alters the in situ pore volume distribution, increases initial microbial activity, and, when constant amounts of substrate are added to soils of varying moisture content, varies the initial substrate concentration among the samples. In addition, past investigations of microbial activity in unsaturated soils report activity as a function of total soil water content.[4–6] However, a large percentage of the isolated water-filled pores may be smaller than the diameter of soil microorganisms and therefore inaccessible for microbial degradation of substrates present in the soil water solution. For this reason, a complete knowledge of the pore volume distribution of a soil is necessary for examining the available water content for microbial activity.

Background

The objectives of this investigation are to (1) determine the pore volume distribution of pores ranging from the diameter of a water molecule to the diameter of the largest pores present in the sandy loam soil being investigated in this study, and (2) examine the impact of considering inaccessible soil water on the effect of moisture on predictions of microbial activity in unsaturated soils.

To obtain a complete pore volume distribution of a sandy loam soil used in this study, we examined alternative methods for measuring a wide range of pore volumes. These methods include geocentrifuge moisture extraction methods,[7] mercury intrusion porosimetry,[8] nitrogen adsorption BET method,[9] and solute exclusion methods.[10]

To examine the microbial activity at various degrees of soil saturation, intact soil cores were first saturated at 5°C with a carbon-14-labeled glucose solution, and then drained to the desired moisture content in 8 hours or less in a geocentrifuge at 4°C. Intact aliquots of the cores were then incubated, sacrificing samples at 30, 60, and 90 days. Respired CO_2 was quantitatively recovered and measured via liquid scintillation. The volume of soil water available to microbes, ranging in size from 0.2–1 μm, was estimated from the pore volume distribution (accounting for compaction in the geocentrifuge) and correlated with the measured microbial activity at each degree of saturation.

Materials and Methods

The sandy loam soil used in this study along with sampling, subcoring techniques, nitrogen adsorption, solute exclusion, and traditional and geocentrifuge measurement of moisture retention properties were previously described.[11] Six additional intact subcored soil samples were sent to Daniel B. Stephens and Associates (Albuquerque, NM) for mercury intrusion porosimetry analysis. Using the capillary rise relationship between pore diameter and matric potential,[12] moisture retention data measured in the geocentrifuge were converted to pore volume distribution (PVD) data and combined with the PVD data measured using the various methods. The combined PVD data were then converted to moisture retention data and fitted to the van Genuchten equation[13] to obtain fitting parameters describing the shape of the moisture retention curve. Finally, the predicted curve was converted back to a PVD curve to obtain the fit to the PVD data. This coupled PVD was used to estimate the percent inaccessible water content as a function of soil saturation to correlate with microbial activity measurements.

Subcores prepared as described above (Reference 11) were vacuum-saturated with a sterile aqueous solution containing 0.225 g/L D-glucose comprised of 99.07% unlabeled glucose and 0.93% D-^{14}C(U)-glucose. The cores were drained using geocentrifuge techniques directly to desired saturation levels of 100, 80, 50, 40, 20, 17, 13, and 10%, assuming no compaction. However, compaction did occur during drainage and altered the sample volume, porosity, and PVD. This resulted

in final saturation values of 100, 75, 63, 52, 47, 37, 31, and 26%. The changes in the PVD were accounted for in the PVD measurements by using the geocentrifuge moisture retention data to obtain the upper portion of the distribution. For each moisture content, three replicate control "blanks" were prepared by saturating replicate cores with nanopure water and draining the cores to the desired equilibrium saturation levels.

After draining, the cores were sliced into five sections of equal length. The top and bottom sections were used to determine average moisture content within the core while the remaining three replicate sections were inserted into serum bottles and sealed for monitoring soil respiration. Because moisture content between replicate samples varied by as much as 10%, the moisture content of the inner three sections were interpolated from moisture content measurements of the top and bottom sections, assuming a linear distribution of moisture along the length of the core. The three replicate bottles were sacrificed at 30, 60, and 90 days each and the respired CO_2 was quantitatively recovered as previously described (Reference 11). Liquid scintillation techniques were used to measure CO_2 concentrations recovered from each bottle.[14] The scintillation counter, model LS 6000, (Beckman-Coulter, Boston, MA) was calibrated prior to each run using manufacturer-supplied calibration standards. The three replicate control blanks and a separate carbon-14 standard were analyzed during each run to determine the carbon-14 background concentrations and instrument accuracy.

CO_2 respiration rates (µmoles/g soil/day) were estimated for each serum bottle at each recovery time point. This was done by calculating the percentage of total glucose mineralized from the percentage of label released to CO_2. Since a relatively low initial glucose concentration was used and very little activity was observed in the cores, it was assumed that the microbes were maintained in maintenance metabolism. The µmoles of CO_2 produced were then calculated assuming quantitative mineralization of glucose. These values were then normalized to the dry weight of soil for each sample and plotted versus both the total moisture content the available moisture content for each sample.

Results and Discussion

Figure 4 shows the cumulative pore volume distribution obtained from the coupled moisture retention curve data. Accessible water as a function of soil saturation (Figure 5) was estimated by subtracting the volume percent estimated from Figure 4 at 0.5 µm cell diameter from the total volume of soil water at moisture equilibrium.[15]

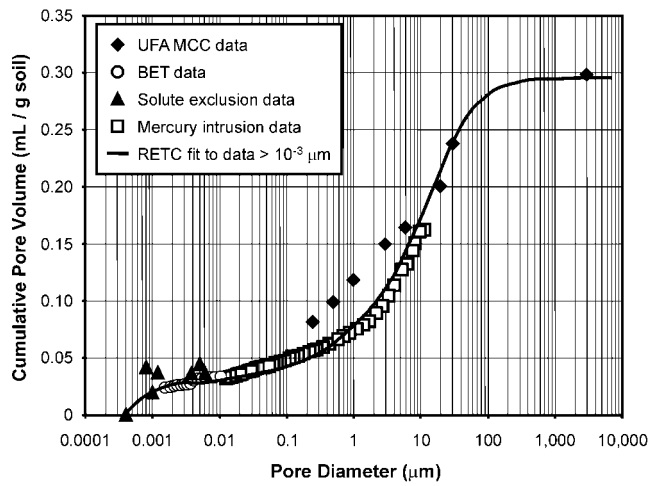

Figure 4. Cumulative pore volume distribution curve obtained from coupled moisture retention curve data.

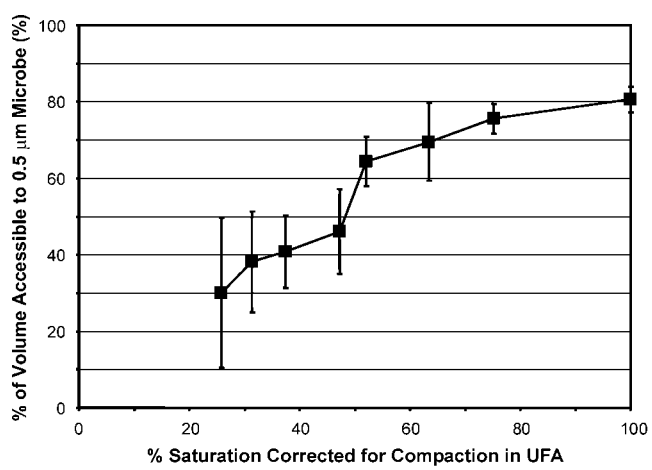

Figure 5. Accessible water as a function of soil saturation estimated by excluding the volume fraction of soil water obtained from the cumulative pore volume distribution curve at 0.5 µm cell diameter.

Figure 6 shows glucose degradation and label respiration rates for samples drained to 63% saturation (after compaction). Figures 7 and 8 show the respired CO_2 (µmole/g soil/day) versus percent saturation and percent saturation accessible to a 0.5 µm diameter microbe for each sample analyzed and recovered after 30 days incubation.

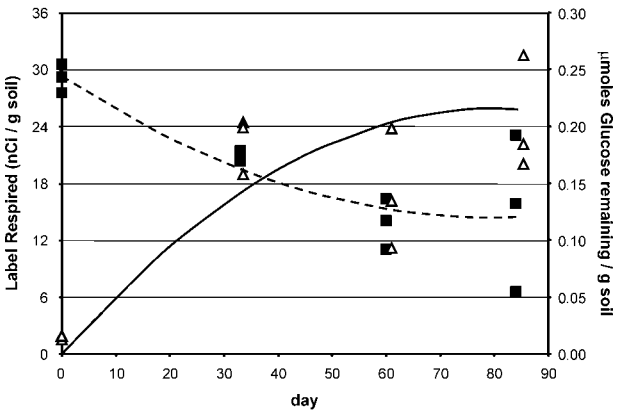

Figure 6. Glucose degradation and label respiration rates for samples drained to 63% saturation.

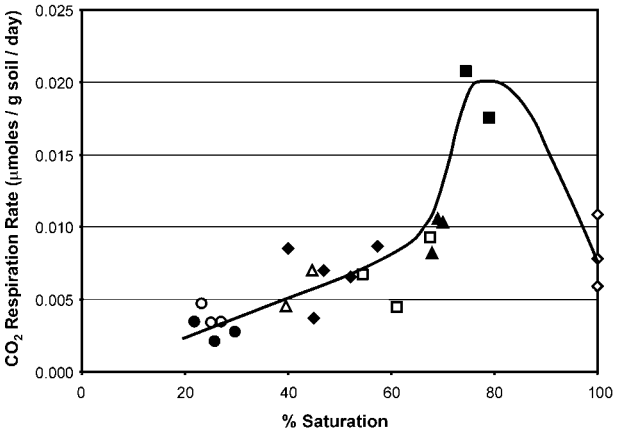

Figure 7. Respired CO_2 (µmole/g soil/day) versus total percent saturation.

Coupled cumulative pore volume distributions show high volume fractions (0.07 mL/g soil) of soil water in pores inaccessible to 0.5 µm diameter soil microbes. There is significant compaction of soil drained in the geocentrifuge, which affects both the final equilibrium moisture content and available soil volume for microbial activity. For the soil

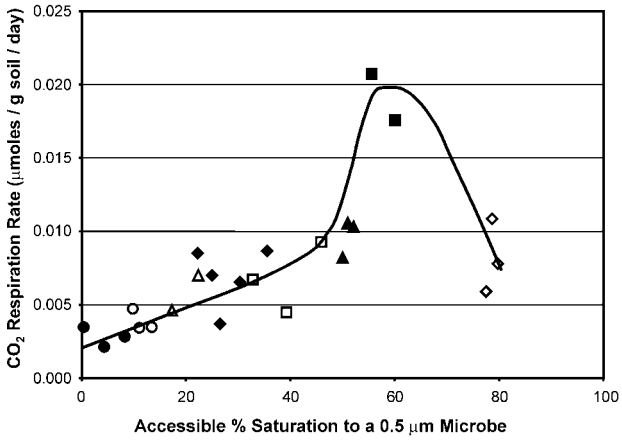

Figure 8. Respired CO_2 (µmole/g soil/day) versus accessible percent saturation to a 0.5 µm microbe.

examined in this study, microbial activity peaks sharply near 75% total saturation compared to 55% accessible saturation. Considerations for determining if only accessible water limits microbial activity depends on whether the substrate in the inaccessible volume is connected to pores that are large enough to contain microbes. Empirical models for predicting soil microbial activity should also consider changes in pore volume distributions within similar soil types to accurately determine accessible pore water.

Characterization of Sediment Biogeochemistry and Surface Geochemistry

Results from experiments to characterize the microbiology and surface geochemistry of RWMC sediments are discussed in the following sections. Sediment samples for microbiological and surface-geochemical characterization were withdrawn from the mesoscale column (MSC) upon establishment of hydrologic and geochemical steady state (as determined by moisture content, pore gas CO_2, and pore gas O_2). Replicate samples were withdrawn from the column surface, 0.5-ft below ground surface (bgs) in the column, 5.5-ft bgs, 6.5-ft bgs, and reserves of the original packing material (SDA sediment from Spreading Area B). One sample of interbed material collected from a well drilled at the SDA was also included in the analysis (see Table 1). All MSC samples and the Spreading Area B sediment were analyzed for microbial cell number and community structure. Samples from the column surface and

from a depth of 5.5-ft bgs were also analyzed for surface geochemistry. A sample collected from an INEEL interbed sediment was analyzed for surface chemistry, but not for microbiological parameters. These results provide the type of rigorous scientific foundation necessary to develop predictive models of contaminant transport based on proven scientific theory, rather than condition-specific observations.

Table 1. Samples analysed for geochemical surface and mineralogic properties.

Sample	Description
SAB-Sed	Spreading Area B sediment. Sediment from a dry playa lake west of the SDA. This is the fill material used in the column.
MSC-0	Sediment on the surface of the column
MSC-0.5	Sediment collected from 0.5 ft below the surface of the column.
MSC-5.5	Sediment collected from 5.5 ft below the surface of the column. Collected through a port in the side of the column.
MSC-6.5	Sediment collected from 6.5 ft below the surface of the column. Collected through a port in the side of the column.
4702	Sedimentary interbed sample from the C-D interbed collected at a depth of 230 ft bgs of the SDA.

Characterization of INEEL Sediment Surface Geochemistry

Although the bulk mineralogical composition and physical properties of RWMC surficial and basalt-interbed sediments were thoroughly characterized by previous researchers,[16] virtually nothing was known about the surface-geochemical properties of these sediments. This section presents the results of surface-geochemical characterization of RWMC sediments conducted to address this knowledge gap.

Samples of RWMC sediment were analyzed by Mössbauer spectroscopy, x-ray fluorescence (XRF), electron microscopy, scanning laser-ionization surface mass spectroscopy (LOCI), and ICP-MS. Additional analyses via quantitative XRD, ion-microprobe, and scanning high-energy XRF (Advanced Photon Source) were conducted during research associated with the Interfacial Processes task of the ESR program, and will be referenced herein.

Mössbauer, SEM/EDS, and LOCI data are available for three samples (MSC-0, MSC-5.5, and 4702). The MSC-0 sample has low moisture content and is always in equilibrium with atmospheric O_2, while sample MSC-5.5 has a relatively high moisture content and has been periodically exposed to hypoxic/anoxic conditions within the column. The interbed sediment was collected from the C-D interbed located 230 ft bgs at the RWMC. SEM/EDS/Elemental map data representative of samples MSC-0 and MSC-5.5 (see Figure 9) indicate that Fe, Al, and Si are all evenly distributed on sediment particles, and that these elements co-exist within the same area. Sediment mineralogical data and quantitative-XRD data collected by other researchers (see section on Interfacial Processes; ESR task) indicate that RWMC sediments are composed primarily of quartz and smectite/illite clays. Thus, the best interpretation of these results is that Fe, Al, and Si are present as clay minerals that are either discrete particles or present as surface coatings on quartz particles. Analyses of RWMC basalt-interbed sediments yield similar results. SEM/EDS/Elemental map data representative of most particles within these interbed sediments (see Figure 10) indicate that Ca, Fe, Al, and Si are all evenly distributed on sediment particles and that these elements co-exist within the same area. As with sediment samples from the MSC-0 and MSC-5.5, the best interpretation of these results is that Ca, Fe, Al, and Si are present as clay minerals that are either discrete particles or present as surface coatings on quartz particles.

Sediments from all samples contained small amounts of hematite, though the percentage of hematite is much greater in the interbed sediments (sample 4702) than in the sediments collected from the mesoscale column. SEM/EDS analyses from a representative particle are also provided in Figure 11.

These analyses indicated that the particle surfaces mostly consist of Fe and O, with small amounts of Si and trace amounts of Ca and Na.

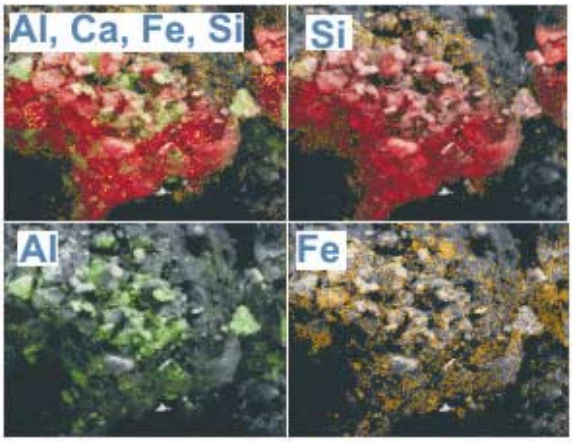

Figure 9. SEM/EDS/Element map image of element distribution on SDA sediment.

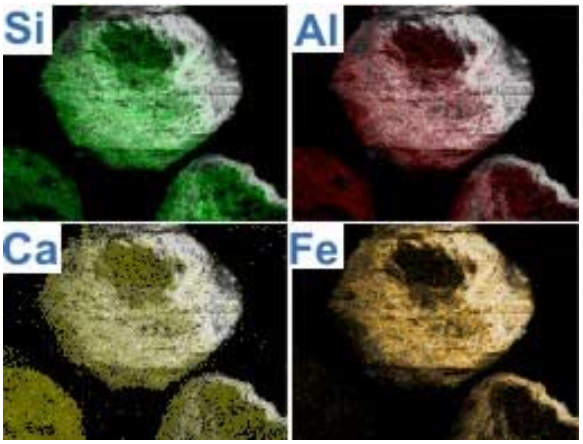

Figure 10. SEM/EDS/Elemental map image of element distribution on INEEL interbed sediment.

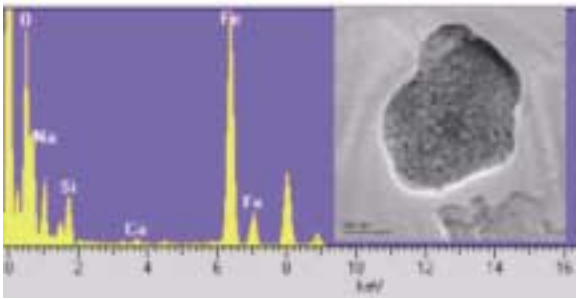

Figure 11. SEM/EDS of hematite particle from INEEL interbed sediment.

Although these data do not provide a definitive answer, it is likely that the hematite exists as a coating on a quartz particle. SEM/EDS analyses did not reveal any indication of Fe-oxyhydroxide minerals (e.g. goethite, ferrihydrite) on any of the particle surfaces, though small regions of discrete Fe-oxyhydroxide surfaces may still be present.

Mössbauer spectroscopy is a surface analytical technique that is much more sensitive towards iron bonding environments than SEM/EDS or LOCI techniques. Thus, this technique will specifically measure the iron chemistry of sediment surfaces and identify iron oxide and oxyhydroxide minerals at much lower abundance. Mössbauer analyses of bulk sediments from each of these samples (Figure 12) support the SEM/EDS findings, and indicate that iron within RWMC sediments is predominantly found within illite-clay and small amounts of hematite. Fitting of theoretical iron bonding models with observed data indicates that minor amounts of poorly crystalline iron oxyhydroxide minerals are present in sample MSC-0. Comparison of spectra from untreated sediments with those obtained from sediments that had been extracted to remove iron oxyhydroxide minerals indicates that these iron moieties are probably either goethite or ferrihydrite, though they were not abundant enough to allow for specific identification. Interestingly, these minerals are not present within MSCR-5.5 sediments (exposed to low-O_2 conditions), nor are they found within basalt-interbed sediments.

Scanning laser-ionization surface mass spectroscopy analyses (LOCI) have reinforced these observations. The greater mass resolution of these analyses provides a map of surface mineralogy, and can distinguish between small sections of quartz, clay minerals, calcite, and iron oxide minerals. Although this technique is in its infancy, it has the capability to provide data analogous to the scanning micro-XRD analyses that are currently possible only with high-energy synchrotron radiation sources. Results from these analyses have indicated that a significant portion of the clay minerals present in the RWMC sediments are present as a surface coating on quartz particles, and that there are few exposed quartz surfaces. Most calcite is present as hetero-genously dispersed micro-crystallites (<50 μm dia.) attached to clay and quartz surfaces, and there is some evidence for discrete regions of dispersed microcrystalline iron oxide particles, though this data is inconclusive. The primary advances

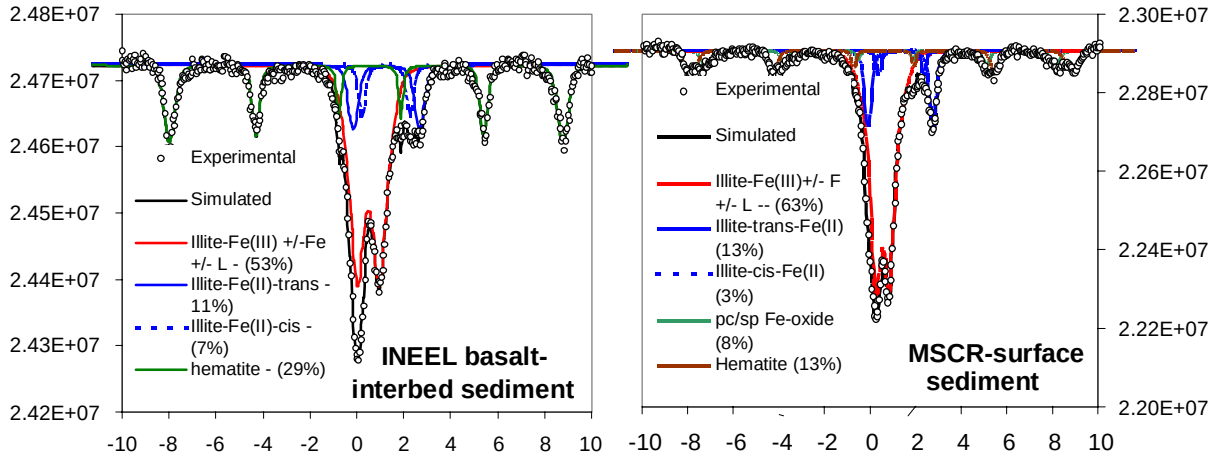

Figure 12. Mössbauer spectra reveal the bonding environment and mineralogy of surficial iron in SDA and basalt-interbed sediments.

achieved through this work are the (a) establishment of the maximum size of "typical" calcite and iron oxide particles within SDA sediments, and (b) the initial calibration of the LOCI technique to INEEL sediments (via comparison of data from other surface analytical techniques).

The most important result of this work is the identification of the primary phase(s) that react to form surface complexes, nucleate mineral precipitates, or undergo ion exchange reactions within RWMC sediments. When combined with quantitative XRD, ion-microprobe analyses, chemical extraction data, and synchrotron-XAS/XRF data collected as part of the Interfacial Processes ESR project, these data provide as complete a characterization of SDA sediment surfaces as is possible with current technology. This advance provides a foundation for interpreting results from contaminant sorption studies and developing accurate transport models that are based on scientific theory rather than environment-specific observations. Such models can account for change in future environmental conditions and thereby provide forecasts of contaminant transport under various remediation scenarios. These predictions cannot be made with the current generation of reactive transport models.

Characterization of INEEL Subsurface Microbial Communities

This section presents the results from microbiological characterization of RWMC sediments. Biomass was analyzed by total-DNA, direct cell counts, and cell culture techniques, and DNA extracted from sediments was amplified and separated via polymerase chain reaction (PCR) and denaturing gradient gel electrophoresis (DGGE) techniques. Ongoing experimental work will sequence the purified DNA-separates and thereby describe the composition of the RWMC microbial community. These data will (a) provide a basis for estimating the effect of microbial processes in RWMC-sediment geochemistry, and (b) guide future experiments that seek to quantify the effect of these processes on contaminant transport through these sediments.

Biomass data (see Figure 13) indicate that the total cell number does not change appreciably with depth in the mesoscale column, and the dry, carbon-poor sediments at the RWMC contain ~ 1 x 10^7 cells/g. Of this number, only ~1% of the biomass are culturable heterotrophs. This proportion of culturable microorganisms is fairly typical for shallow sediment systems, and is thought to result from a combination of inactive sedimentary cells and well known difficulties in emulating natural environmental conditions in the lab.[17–19] Though number of culturable heterotrophs (a subset of the total population) seems to decrease with increasing there is considerable scatter within the data, the depth (surface >0.5 ft bgs, >5–7 ft bgs). This observation is reinforced by the DGGE data (DNA-based identification) presented in Figure 14, which provides an initial estimate of the distribution of microbial genera present within

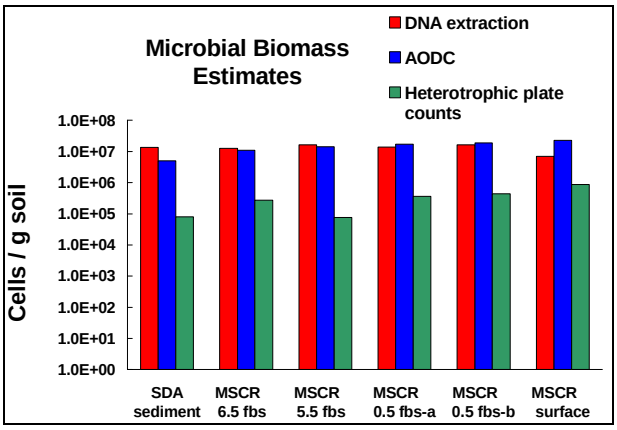

Figure 13. Microbial cell number in SDA sediment and sediment samples withdrawn from the mesoscale column.

the total population of each sediment depth intervals. With current data, we can only isolate species that comprise more than 2–5% of the total population. More detailed data will be available once genetic sequencing analyses have been completed. These results indicate that species diversity is much greater in hydrated column sediments (10–20 species) than in the dry "sediment stock" (<5 species). The greatest diversity is seen at the sediment-air interface (MSC-0), and then decreases steadily with depth and decreasing O_2 (0.5 ft bgs, >5.5 ft bgs, >6.5 ft bgs). This decrease in diversity is accompanied by a disappearance of surficial genera and the appearance of new genera at depth. Even though some of the high diversity at the surface can be attributed to contamination by airborne microorganisms, the general trend of decreasing diversity and shifts in microbial community structure with increasing depth reflect real changes in sediment biogeochemistry.

The primary accomplishment of this work is the compilation of evidence that the structure of the RWMC sediment's native microbial community changes in response to shifts in sediment O_2 and CO_2 concentrations, thereby providing a potential for the occurrence of anaerobic microbial metabolism in bulk aerobic sediments. Although the nature and effect of these changes has yet to be quantified, these initial data provide a foundation for developing a mechanistic description of the effect of microbial processes on uranium and carbon-14 transport in RWMC sediments.

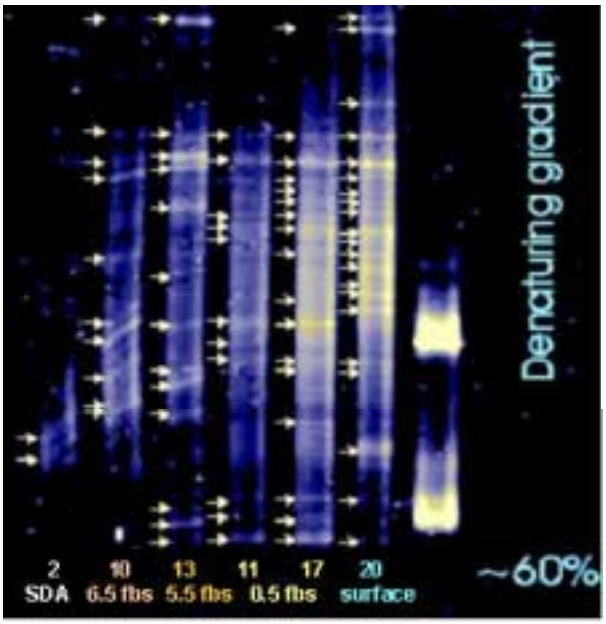

Figure 14. Number of bacterial DNA signatures extracted from SDA sediment and MSCR sediment samples.

Another significant result of this work is the compilation of evidence that microbially driven dissimilatory iron reduction may occur within RWMC sediments, and subsequently alter contaminant sorption and transport properties. This evidence is provided by the presence of small amounts of poorly-crystalline iron-oxide minerals (pc/sp) in Spreading Area B sediments, coupled with the absence of these iron moieties within interbed sediments and surficial sediments exposed to hypoxic conditions. Although dissimilatory iron reduction is not expected to occur in bulk aerobic sediments, a number of studies of natural systems have indicated that this process can occur within hypoxic systems that may contain anaerobic microzones or be subjected to a periodic onset of anoxic conditions.[20–22] Seasonal fluctuations in temperature have caused the column to reach extremely hypoxic conditions despite the maintenance of unsaturated flow conditions. Thus, it is not unreasonable to expect that RWMC sediments may become hypoxic or anoxic during periodic flooding events. Given that RWMC sediments can become extremely hypoxic under controlled unsaturated conditions, and *Cellulomonas* spp. capable of Fe^{3+}, Cr^{6+}, U^{6+}, and NO_3^- reduction with a variety of terminal electron

acceptors have been isolated from INEEL surficial sediments by INEEL researchers[23]; it is reasonable to suspect that microbial iron reduction may be occurring periodically within the unsatu-rated RWMC sediments. Although the Mössbauer data provide support for this potentiality, these data do not provide sufficient evidence to prove that dissimilatory iron reduction has occurred within these sediments. Identifying facultative anaerobic microorganisms capable of dissimilatory iron reduction living with mesoscale column sediments may provide further insight into this issue.

Multiphase Transport of Radionuclides

Primary controls on multiphase contaminant transport in the vadose zone include the gas and hydraulic flow regimes. Even where the gas phase is primarily stagnant air, gas-phase contaminants may be transported through the unsaturated zone by diffusion.[24] Predictive modeling of transport behavior thus requires a reasonably accurate model of the liquid and gaseous flow regimes and of the diffusive characteristics of the medium for aqueous and gaseous transport. We conducted a number of laboratory and numerical modeling studies to collect the necessary data for construction and refinement of our transport models. These included direct laboratory measurements of soil hydraulic properties; in situ measurements of column response to the initiation of flow; gas diffusion tests using sulfur hexafluoride; and liquid tracer experiments using dissolved lithium bromide. The test objectives and the information obtained from each are summarized below.

Derivation and Measurement of Transport Parameters

To limit the number of variables in our analysis of transport behavior, we attempt to maintain a steady-state unsaturated flow regime in the column during transport experiments. Characterization of the flow regime, including volumetric water content, soil moisture tension, temperature, and average seepage velocity is thus a critical step in the development and calibration of a flow model of the column. We quantify these hydraulic properties in several ways. By carefully monitoring the column water balance, we know the volume of water stored in the soil at any time as well as the average flux. Water content reflectometers and tensiometers (see Figure 3) distributed throughout the column monitor the forces and conditions that control liquid flow; measurements on soil samples removed from the column supplement those data. Nonetheless, the hydraulic properties of the large volume of soil in the column are not always as well known as is desirable for careful transport experiments. During calibration of the flow model for the column, for example, we observed a large discrepancy between the measured infiltration rate and simulated infiltration rate based on laboratory measurements of soil hydraulic properties. After noting that the latter were obtained at a bulk density approximately 15% greater than that of the soil in the column, we used the INEEL's unsaturated flow apparatus (UFA) centrifuge to estimate the effect of compaction on soil hydraulic conductivity. This allowed us to better estimate the proper bulk density. Compaction is often described as a power law stress/strain relationship,[25] and is therefore roughly linearly proportional to the rotation rate in the centrifuge (see Figure 15). Assuming an essentially linear relationship between compaction and hydraulic conductivity, our centrifuge measurements suggested that the added compaction reduced conductivity by approximately an order of magnitude. Using the revised hydraulic conductivity relationship, the modeled wetting front progress agrees well with the experimental data (see Figure 16).

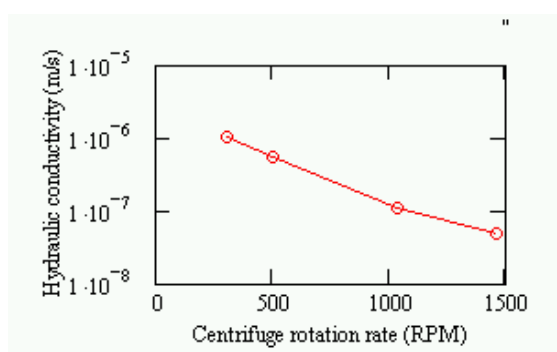

Figure 15. Saturated hydraulic conductivity of the column soil as measured in the UFA geocentrifuge device at different rotation rates. The decrease in hydraulic conductivity with increasing rotation rate results from sample compaction; the sample is subject to approximately 100•g at 1,000 rpm.

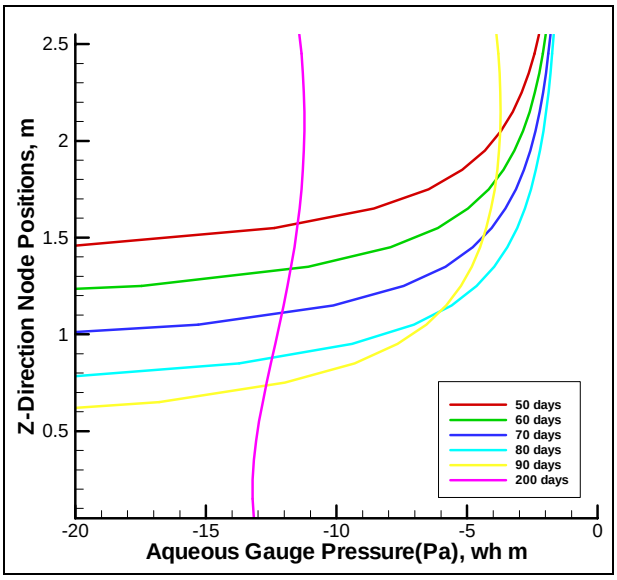

Figure 16. Simulated propagation of the wetting front (soil moisture potential versus height above bottom of column at times indicated in legend) in the column during initiation of unsaturated flow.

Carbon-14 is transported in the vadose zone by gaseous diffusion as well as aqueous advection and diffusion. Gaseous diffusivity depends on the volume of pore space available in the soil and on the tortuosity of the paths connecting separate pores (Reference 24). To estimate the gas-phase diffusion characteristics of the column soil at different water contents, we conducted several tests in which we injected concentrated sulfur hexafluoride (SF_6) gas into the lower injection port of the column (see Figure 3), monitored the movement of the gas until concentrations in the column were close to background levels, and used the results to refine our estimates of the gas-phase diffusivity parameters. Immediately after the injection, SF_6 is transported both upward and downward by diffusion. Because the bottom of the column is a barrier to gas transport, while the top is open to the atmosphere, gas escapes only from the top of the column, and the initial peak rapidly evolves into a nearly uniform upward gradient in the concentration of SF_6. In the initial tests, water content was essentially uniform throughout the column and we modeled the diffusion process using an analytical solution.[26] Comparisons between observed and simulated data for the sulfur hexafluoride tests were very good (Figure 17), and generally demonstrated that the commonly used Millington-Quirk equations (Reference 24) adequately describe the relationship between tortuosity and saturation in the SDA sediment. Later tests, which were analyzed with a numerical model because water saturation varied with depth, yielded similar results.

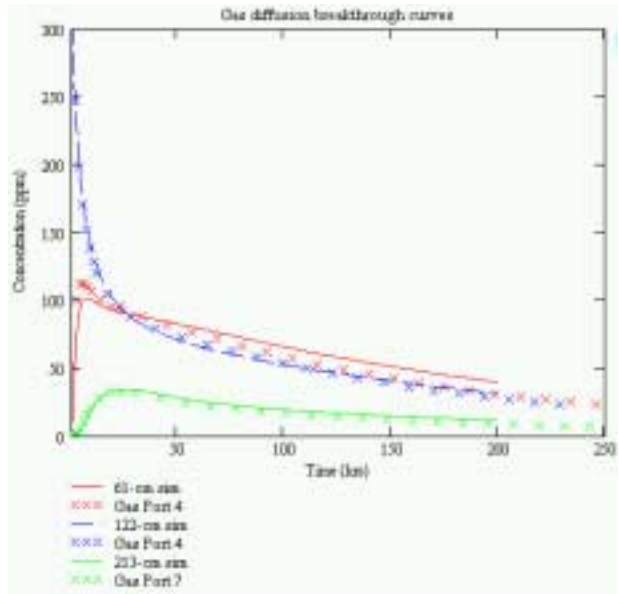

Figure 17. Comparison of simulated and observed gas concentration breakthrough curves during the initial sulfur hexafluoride gas injection test conducted in March 2001, prior to initiation of unsaturated flow experiments.

Average seepage velocity is a critical parameter in transport experiments. To better constrain that parameter, we estimated it using both measurements of flux and water content and conservative tracer tests. Though flux at the top of the column is controlled and therefore relatively well constrained, different means of measuring water content give significantly different results. Volumetric water content in two samples obtained from the column after establishing steady-state flow were both 23%. Mass balance on the fluxes into and out of the column, on the other hand, suggest an average water content of ~40%. Water content reflectometers (Figure 18A) generally indicate water content of ~30–40%, but higher uncertainties are associated with the higher values as they are also associated with higher salinities. Comparisons with tensiometer data (Figure 18B) suggest that the water content is relatively

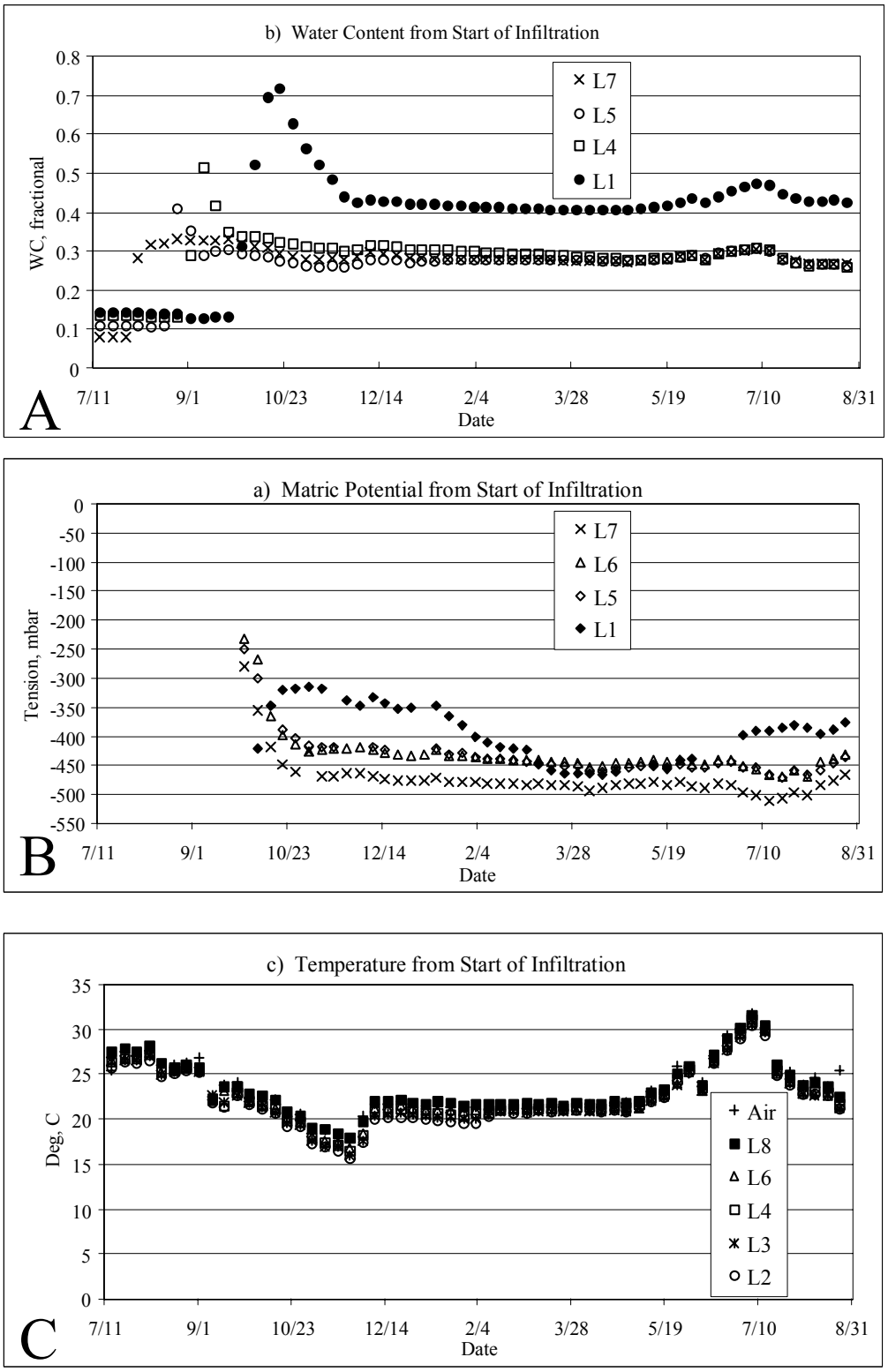

Figure 18. Weekly averages of (A) soil water content, (B) soil moisture potential, and (C) temperature, as indicated by water content reflectometers, tensiometers, and thermocouples, at the indicated levels in the column.

uniform, probably between 30 and 35%. Assuming an average water content of ~30%, the seepage velocity in the column, under an infiltration flux of ~1.52 mm day^{-1}, should be on the order of 5 mm day^{-1}, with an uncertainty of approximately 1 mm day^{-1}. We plan to improve our ability to accurately measure water content during the next fiscal year by installing time-domain reflectometers at several locations in the column.

Aqueous-phase transport in the mesoscale column occurs by advection and diffusion. The advective transport introduces a second diffusive term in the flow equations that, in saturated flow systems, often dominates the overall hydro-dynamic dispersion of solutes. At the moderate saturation and low water velocity (~5 mm/day) in the column, however, molecular diffusion should dominate the transport process and dispersivity may be relatively insignificant. Conservative tracer tests provide a means of assessing the relative importance of molecular diffusion and mechanical dispersion, and the only reliable means of measuring the latter. They also provide an independent means of measuring average seepage velocity and are therefore a critical step in developing reliable transport models. To examine these transport parameters in the column, we injected a slug of concentrated lithium-bromide solution into the upper injection port and monitored the movement of bromide by liquid sampling from the eight liquid extraction ports (Figure 3). Using analytical models of the flow and transport of conservative solutes in a steady-state 1-D flow field, we constrain the dispersivity by fitting the model to the tracer data.

The lithium bromide solution was injected on March 22, 2002, and the concentration at the first downstream port (~15 cm below the injection) peaked approximately 1 month later. Bromide breakthrough curves obtained thus far (Figure 19) confirm that diffusion dominates the dispersive processes in the column and also support our estimate that the average linear seepage velocity is about 5 mm day^{-1}, consistent with an average moisture content of ~30%. The bromide tracer tests also indicate that, while transport is generally consistent with a 1-D model to a depth of ~45 cm below the injection point, 3-D effects become increasingly important below that depth.

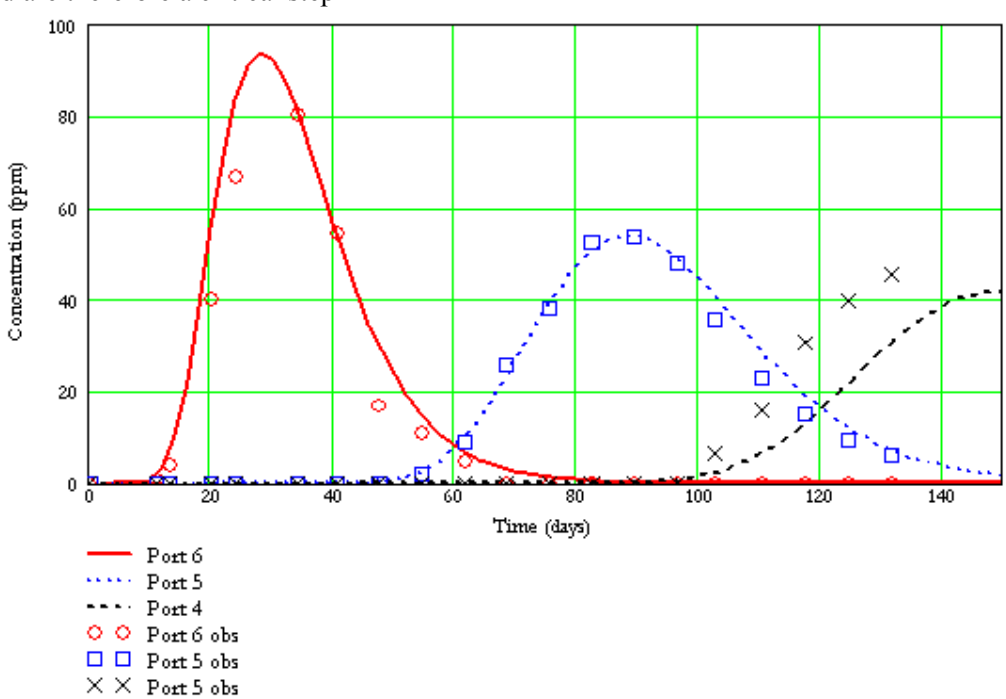

Figure 19. Comparison of simulated bromide tracer transport (lines) with observed data from the March 2002 bromide tracer injection experiment (symbols). Simulation assumes 1-D flow and conservative transport with a seepage velocity of ~5 mm day^{-1}, a molecular diffusion coefficient of 2 x 10^{-5} cm^2 sec^{-1}, and a volumetric water content of 30%.

As a preliminary attempt at examining the spatial variability of hydraulic properties in the column, we conducted two constant-head liquid injection tests through the injection ports of the column. The injection ports consist of 24 individual stainless-steel tubes with ends laid out on a horizontal grid within the soil column. We connected small graduated cylinders filled with water to each of the steel tubes to provide a head of ~24 cm on each, and measured the rate of inflow as the water entered the column. The inflow rate depends on both the soil moisture potential gradient and unsaturated hydraulic conductivity of the soil, which are both functions of antecedent water content. Infiltration rates were relatively constant during our tests, however, suggesting that the measured fluxes should be roughly proportional to unsaturated hydraulic conductivity. The observed infiltration rates (see Figure 20) demonstrated significant variability in their spatial distribution across each plane and between the two injection levels. Although much of the observed differences are likely attributable to obstructions within the small-diameter injection tubes themselves, the test emphasizes the need for better in situ characterization of soil hydraulic properties. This need can be addressed with additional instrumentation, but not without some risk of interrupting the existing flow regime. The risks and benefits of installing additional instrumentation will be assessed during the next fiscal year.

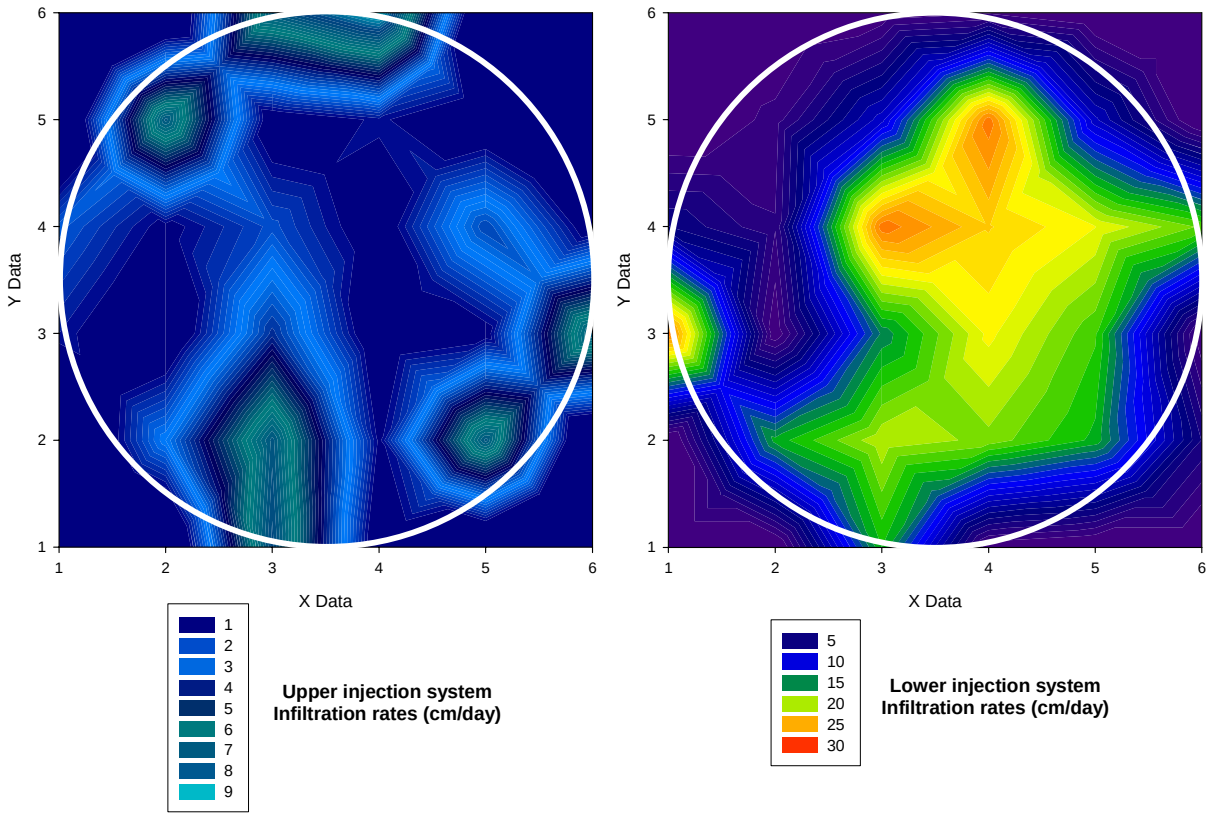

Figure 20. Contour plots of infiltration rates measured during constant head flow tests conducted in the mesoscale column gas injection systems.

Modeling Reactive Multiphase Transport

Reliable models describing the transport of radioactive species such as carbon-14 and uranium require consideration of both mechanical transport properties and reactions that occur along a flow path. Using data from the mesoscale column transport experiments, we are developing models that can more reliably predict the fate and transport of these species in the subsurface, with specific attention to contaminants and subsurface conditions of concern at the RWMC.

Transport of carbon-14 occurs in both the aqueous and gas phase, and sorption to the solid phase retards transport. To simulate these processes, we are developing a multiphase flow and contaminant transport model using the STOMP[27] code developed at Pacific Northwest National Laboratory. The model will incorporate both advective and diffusive movement of water and air and gaseous and aqueous transport of carbon-14. This will allow us to examine the affect of fluctuations in surface boundary conditions, such as daily to seasonal barometric pressure variations, changes in infiltration rates, and different distributions of source material. To validate the model, we predict the transport behavior of carbon-14 in the mesoscale column (see Figure 21) and compare the results to those observed following an injection of carbon-14. Preliminary modeling of carbon-14 transport in the column indicates that gas transport, which is commonly neglected in carbon-14 transport studies, is significant both as a source of contamination to the vadose zone above the buried radiocarbon source and as a moderating influence on downwardly advected contamination.

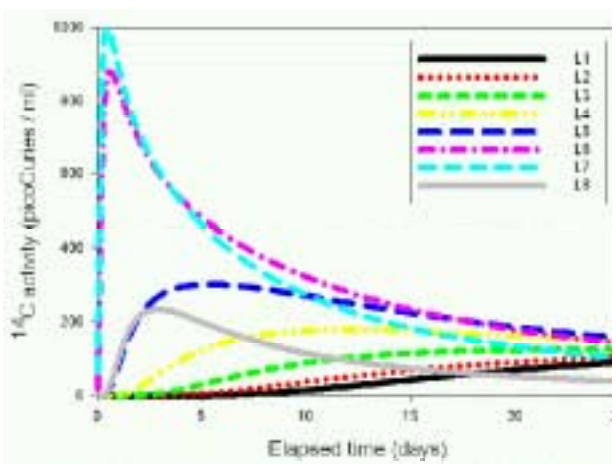

Figure 21. Simulated breakthrough curves of carbon-14 at the eight sampling locations in the mesoscale column following introduction of 1.6 mCi of carbon-14 at the upper injection port.

While uranium transport is limited to the aqueous phase, its solubility is a strong function of geochemical conditions, with particular sensitivity to pH, alkalinity, and oxidation/reduction state. We are pursuing two modeling approaches to use in predicting the fate and transport of uranium in the vadose zone. The first of these includes a detailed treatment of the geochemical reactions controlling uranium sorption. We model these processes using the geochemical speciation, batch-reaction, and steady-state aqueous-phase transport code (PHREEQC) developed by the USGS.[28] The Freundlich sorption isotherm model will be incorporated using parameters developed specifically for this study last fiscal year (Reference 11). PHREEQC also provides a means of analyzing changes in column geochemistry as a function of time and depth that may or may not play an important role in the transport of uranium. Preliminary inverse modeling conducted using PHREEQC, for example, demonstrates that exchange reactions can play a dominant role in the water chemistry of infiltration as it migrates through the SDA soil. Based on the results of verification simulations conducted with PHREEQC, and subsequent experiments to examine sensitivity to various parameters, we will develop a simpler model that handles the primary geochemical reactions in a more ad hoc manner. UNSATCHEM, developed at the USDA-ARS U.S. Salinity Laboratory,[29] should provide a relatively straightforward path to implementing the simpler model. UNSATCHEM also contains modules describing the production and transport of carbon dioxide as a primary component of the gas phase, and both the detailed geochemical modeling approach and ad hoc approach to incorporating the principle geochemical reactions will be coupled to CO_2 production and the redistribution model of UNSATCHEM.

Radionuclide Transport Experiments

We are conducting a multispecies radionuclide transport experiment in the mesoscale column to provide the data for developing and testing predictive models. This experiment consists of injecting a solution containing ~0.6-mCi tritium (as tritiated water), ~1.6-mCi carbon-14 (as radio-labeled carbonate), and 5.07 mg natural uranium in 2,850 mL pore water approximately 60 cm below the soil surface, and monitoring those species in the gas and liquid phases as they migrate upward and downward along the column. To minimize hydraulic and chemical perturbations, water for the injection solution was drawn from the lysimeters located at Levels 6 and 7. We began

withdrawing pore water for the solution on August 7. We prepared and injected the solution on August 12, 2002, over a period of 4 hours.

Experimental Apparatus. The experimental apparatus is a 3-m-high, 1-m-diameter, stainless-steel cylinder packed with a 2.6-m-high column of soil that represents the cover material at the SDA. Syringe pumps periodically deliver water to the column's surface at approximately 1 L/day. Unsaturated flow is maintained by applying vacuum to suction lysimeters in the bottom of the column. The column has four data and sample collection systems. Three of them monitor and determine the hydrologic state (pore-water chemistry and gas composition) (Figure 3). The fourth monitors gas and vapor fluxes in the headspace above the soil surface, and captures CO_2 diffusing from the soil into the headspace with a sodium hydroxide (NaOH) solution (see Figure 22). The upward flux of radio-labeled CO_2 from the soil can be quantified by radiological analysis on aliquots of the NaOH solution.

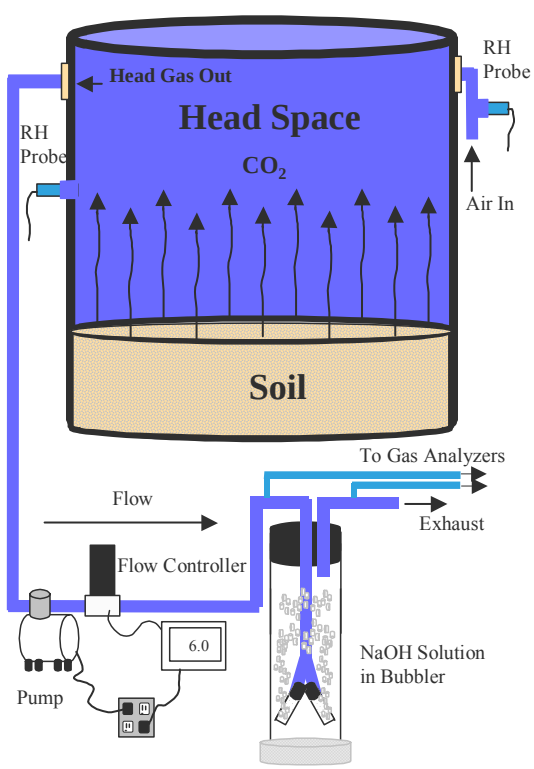

Figure 22. Gas monitoring and CO_2 collection devices attached to the headspace above the column.

Hydrologic Measurements and Water Sampling. The column is instrumented to monitor matric potential, temperature profiles, and water content (Figure 18 gives the raw parameter measurements). The column temperature increased, then decreased over a 3-month period (May–July, 2002). System response to the thermal change is observed in measurements of both CO_2 concentration and water content, though the latter likely represents inaccuracies in the reflectometer calibration equations. Before injecting the isotopes we took weekly measurements of pore water pH and alkalinity. Figure 23 shows the average alkalinity and pH profiles for the 6 months prior to the isotope injection. We will resume these measurements as the isotopic activity of water samples decline. The column is fitted with three separate fluid injection arrays (Figure 3) composed of 24 individual tubes that deliver fluid to 24 evenly spaced locations in a single horizontal plane. One array supplies influent water to the soil's surface, the other two are located below the soil's surface.

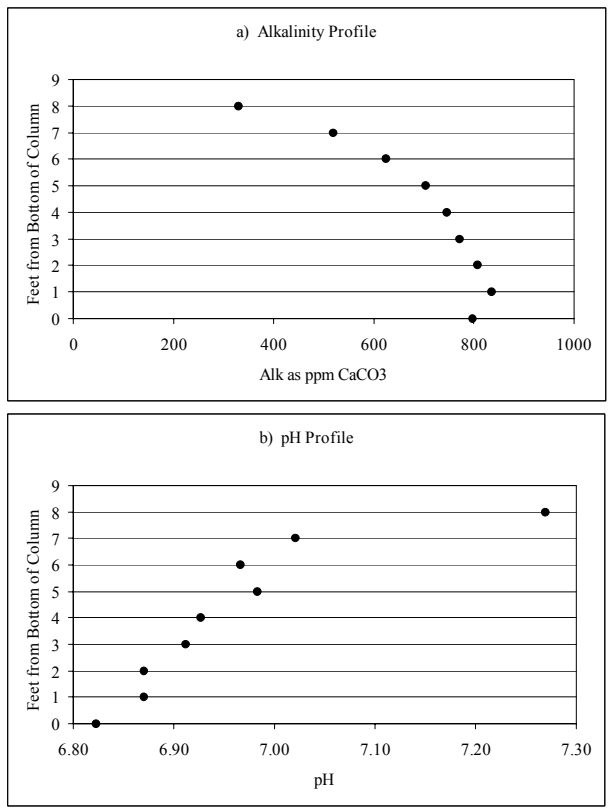

Figure 23. Profiles of Alkalinity and pH in the mesoscale column after steady-state flow was established.

Gas Measurement and CO_2 Capture Systems. An automated system takes weekly measures of ambient, head-space, and pore-gas concentrations. Gas concentrations in the system vary in response to temperature fluctuations and to perturbations caused by adjustments to the gas pressures in the lysimeters. Gas concentration time series for CO_2 and O_2 are shown as Figure 24, profiles from selected times are included as Figure 25. Increases in suction in the lysimeters causes an increase in O_2 and a decrease in CO_2, as O_2-enriched air is drawn downward. The disproportionately lower decrease in CO_2 concentrations results from the release of gas from the CO_2-charged pore water. Following calibration of the gas measurements, the system response to these perturbations will be analyzed with our CO_2 production and redistribution model to better estimate CO_2 production rates as a function of soil moisture content, temperature, and other parameters.

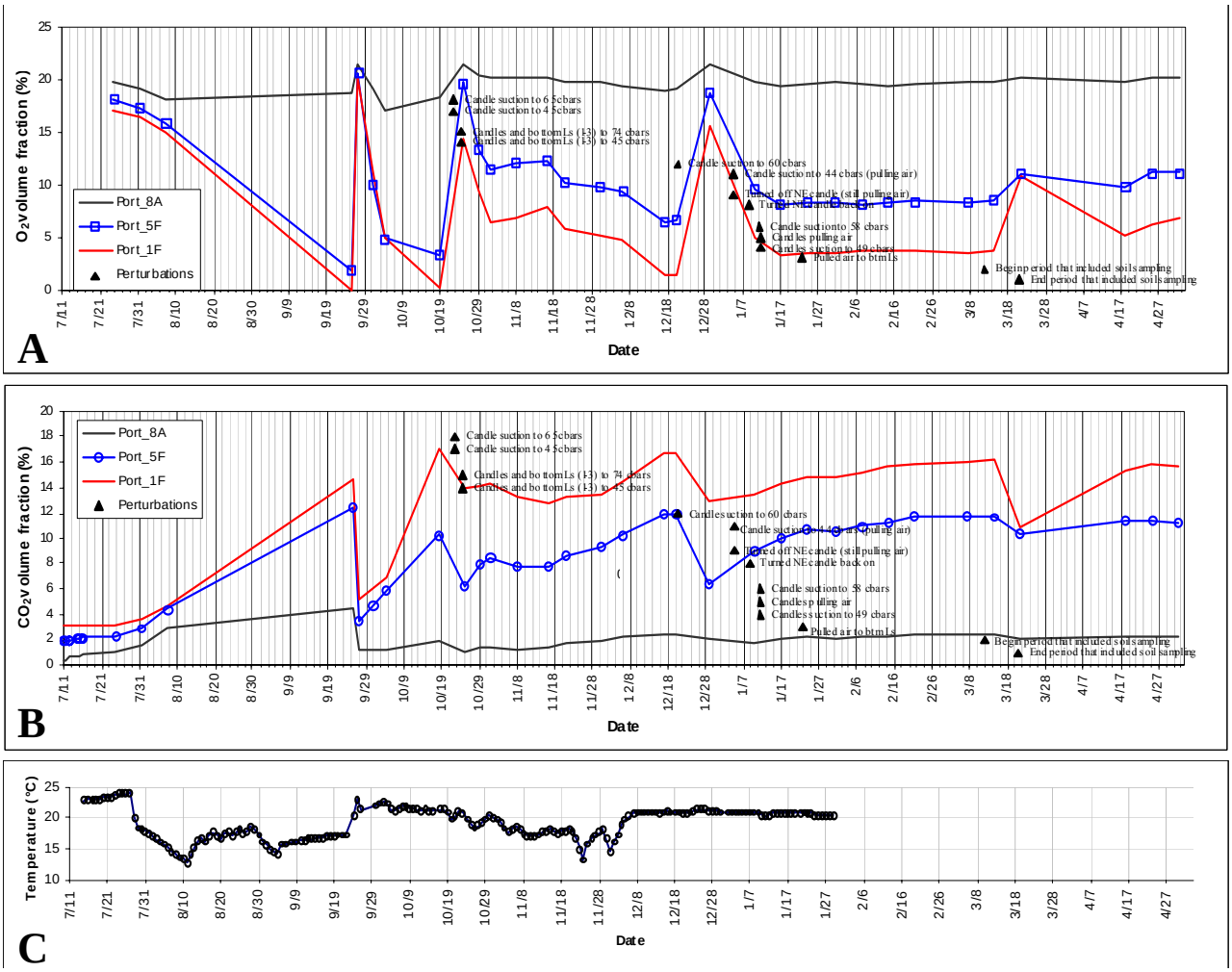

Figure 24. Carbon dioxide and oxygen concentration (uncalibrated measurements) histories by date. Perturbations in gas concentrations caused by adjustments to the lysimeters are indicated with symbols (diamonds).

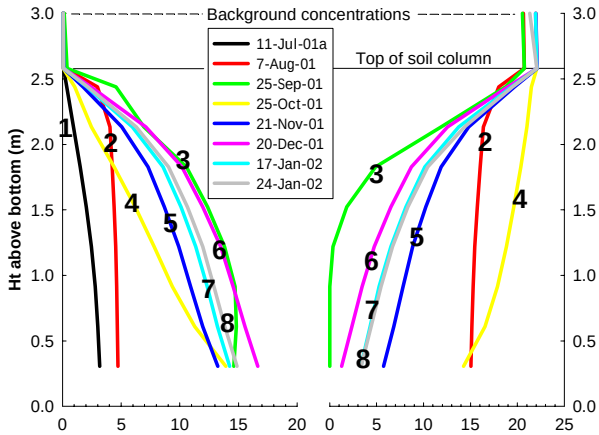

Figure 25. Vertical profiles of CO_2 and O_2 (uncalibrated measurements) in the column at selected times in 2001 and early 2002.

Radionuclide Transport Tests–Preliminary Results. Transport behavior of the three radionuclides is dramatically different because of their radically different partitioning behavior in the subsurface. Preliminary data from the carbon-14 transport experiment are compared with our model predictions in Figure 26. The simulated breakthrough curves match the observations quite well, suggesting that our model adequately captures the principal physical processes controlling transport. These results generally confirm that gas-phase movement to the land surface will play a significant role in carbon-14 transport at the SDA, mediating to a significant extent the downward movement of carbon-14 to the water table. They also demonstrate the importance of accurately estimating sorption behavior in determining the significance of gas release from the surface, as stronger sorption tends to decrease the flux of carbon-14 escaping the surface.

Consistent with preliminary modeling predictions, assuming a high sorption coefficient under the geochemical conditions at the injection point, uranium has not been detected in samples from the lysimeters. Tritium movement occurs by advection and diffusion in both the gas and vapor phases. However, because water-vapor partitioning heavily favors the liquid phase, vapor phase migration tends to be significant only over long time-scales or in cases where secondary porosity creates fast paths for vapor transport. Although both

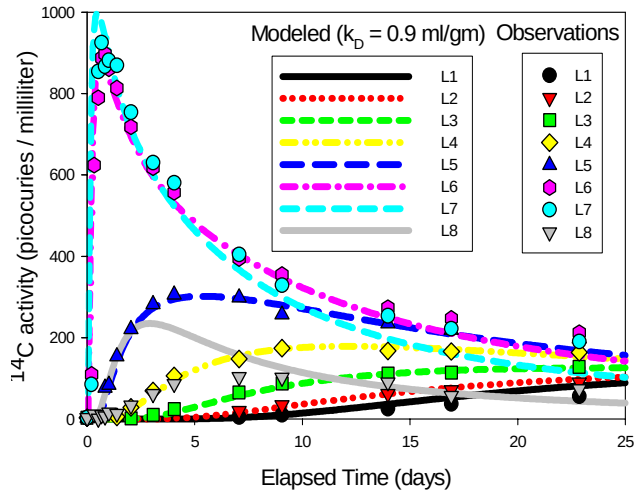

Figure 26. Simulated breakthrough curves (lines) for the eight gas sampling ports following a 1.6 mCi injection of carbon-14 at the upper injection port (between levels 6 and 7) compared to preliminary carbon-14 measurements (symbols) of gas samples from the same ports.

of these factors should be negligible in the relatively homogeneous sediment contained in the column, unexplained tritium transport has been observed in unconsolidated sediments in the vadose zone.[30] Thus, the mesoscale tritium transport experiment provides a means of testing standard conceptual models, or, assuming tritium behaves as predicted, a nearly ideal conservative tracer for improving our estimates of aqueous-phase transport parameters. Simulations of the movement of tritiated water (HTO) through the column indicate that it should be virtually undetectable in the upstream end of the column, while concentrations 1 meter below the injection point should peak at approximately 190 days after the injection (see Figure 27).

Effect of INEEL Subsurface Microbial Communities on Uranium Transport

Determining the effect of natural microbial communities on uranium transport within RWMC sediments presents a difficult problem. A simple analysis would predict that microbial CO_2 production would increase carbonate concentration leading to the formation of aqueous uranyl-CO_3^{2-} complexes and subsequently enhanced uranium transport.[31] However, other processes may interact

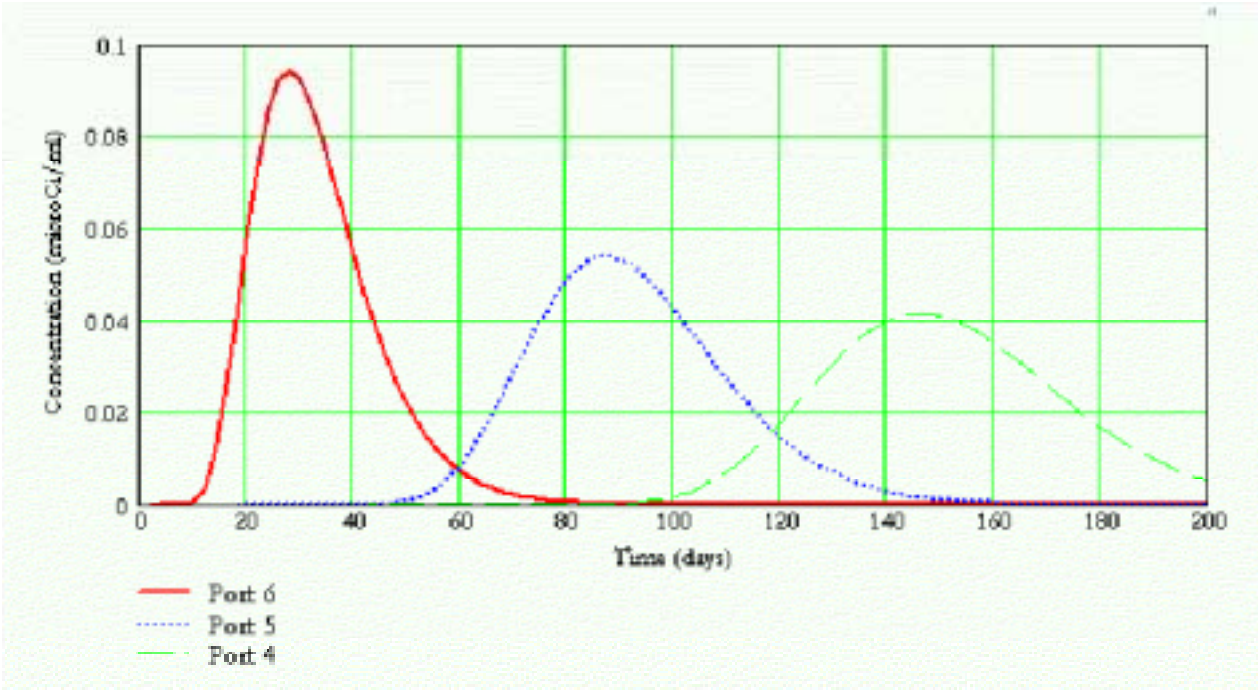

Figure 27. Simulated tritium breakthrough curves following introduction of 0.8 mCi of tritiated water at the upper injection port.

to create a more complicated system.[32–34] For example, *Geochemist's Workbench*© calculations indicate that pH decreases resulting from CO_2 production may also dissolve calcite, leading to increased [Ca^{2+}-aq] and decreased solubility of $CaUO_4$. This precipitation process, coupled with the ability of U(VI) to form a variety of $>SiOH_2$-UO_2-CO_3 surface complexes with >SiOH sites on quartz or clay minerals can potentially offset the effect of UO_2-carbonate complexation and lead to decreased uranium transport under strongly oxidizing conditions (data not shown). Alternatively, reduced Eh can lead to the formation of mixed-valence uranium minerals, which can then control U-solubility and transport (Reference 34). Depending on the uranium sorption coefficients used, estimates of U-K_D in the system can range from 100 to >10,000 (*Geochemist's Workbench*© calculations, data not shown). This estimate does not include more direct microbial influences such as the potential for microorganisms to degrade sediment organic matter that alters U-solubility,[35–40] nor does it include the potential for microorganisms to bind uranium onto cellular structures and thereby alter the particle-assisted transport of uranium.[41–43] Consequently, there is a great deal of uncertainty about the effect of natural microbial communities on uranium transport within RWMC sediments, and how this effect might change over longer time scales that cannot be emulated under typical laboratory conditions.

In order to support the project's efforts to describe this effect, a series of bench-scale column experiments were conducted under conditions of varying biomass. Microbial activity was controlled by adding sterile simulated ground water (no exogenous carbon) to sediment columns packed with either sterile RWMC sediment, unaltered RWMC sediment, or mixtures of sterile and unaltered RWMC sediment. These columns were allowed to operate under saturated, uranium-free conditions until pH, O_2, and CO_2 levels in the columns' effluent reached steady state. At that point, a spike UO_2^{2+}-containing ground water was added and column effluent was monitored for total uranium. Representative initial data from these experiments are presented in Figure 28. Data indicate that all columns have comparable pore volumes (overlapping Br^- breakthrough), and that uranium breakthrough has not occurred within the uranium data reveals that (a) there may be a small

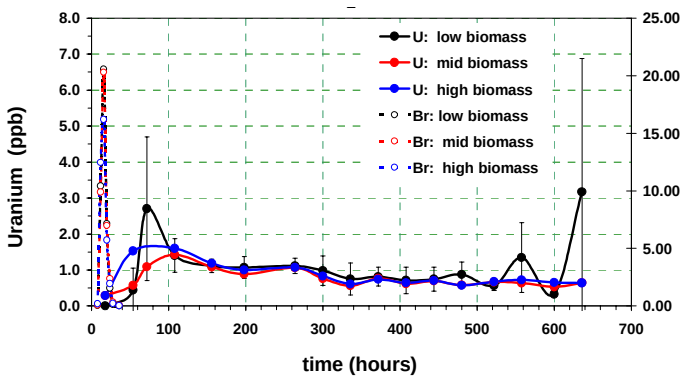

Figure 28. Br^- and U as a function of time in bench-scale columns containing SDA sediment with varying microbial biomass.

first 50 pore volumes. Careful examination of the "fast fraction" of uranium that breaks through at 4–12 pore volumes (50–150 hours), and (b) the presence of microorganisms may maintain depressed concentrations of mobile uranium after ~44 pore volumes (~520 hours). Furthermore, although the large scatter in the low-biomass data confuses interpretation, comparison of the mid and high-biomass data indicates that the mobility of the potential uranium fast-fraction may increase with increasing microbial biomass. Ongoing experiments being performed here and at McMaster University seek to examine this possibility in greater detail under both saturated and unsaturated hydrologic conditions. If these results persist throughout this experiment and can be duplicated in subsequent experiments, then they provide evidence for a significant microbial impact on uranium transport processes in RWMC sediments.

ACCOMPLISHMENTS

Determined the dominant reactive moieties present on RWMC sediment surfaces, which:

- Provides a foundation for interpreting results from contaminant sorption studies and develops accurate transport models that are based on scientific theory rather than environment-specific observations that have extremely limited predictive capability.

- Provides for the development models that can account for change in future environmental conditions and thereby predict contaminant transport under various remediation scenarios.

- Indicates potential for occurrence of Fe(III) and U(VI) reduction in RWMC sediments.

- Provides a roadmap for conducting studies that will enhance our ability to develop and refine these improved models of contaminant transport in the RWMC.

- Provides a basis for interpreting results from other research tasks that seek to determine the effect of environmental variability on contaminant sorption mechanisms (e.g., ESR program, Interfacial Processes task).

Demonstrated potential for INEEL sediment microbial processes to alter uranium mobility, which:

- Provided indication that microbial processes may enhance the amount of uranium associated with the "fast-fraction," possibly via colloid generation or formation of aqueous complexes.

- Provided indication that microbial processes may suppress the long-term transport of uranium, possibly via inducement of conditions that favor U-mineral formation.

Developed a preliminary description of microbial community structure within RWMC sediments and how that structure changes with decreasing oxygen content, which:

- Provides support for the surface-geochemistry data that indicate Fe(III) reduction may be occurring within bulk-aerobic SDA sediments exposed to hypoxic conditions.

- Indicates that the effect of sediment microorganisms on contaminant geochemistry may change significantly with increasing depth in an unsaturated, oligotrophic sediment system.

Demonstrated that carbon-14 rapidly partitions between aqueous and gas phases in the unsaturated sediments with transport in both phases, which:

- Supports vapor phase diffusion of carbon-14 to the land surface at the SDA significantly reducing the carbon-14 activity that will be transported to the Snake River Plain Aquifer.

- Provides modeling parameters for carbon-14 developed for materials and conditions very similar to those at the SDA.

Determined that ion exchange plays a very significant role in controlling water chemistry in the mesoscale column. Inverse modeling of pore water in the column using PHREEQC suggests that exchange of calcium for ammonia on clays, with subsequent oxidation of the ammonia to nitrate, results in significant levels of dissolved nitrate in pore water. Elevated nitrate levels have been observed in pore water at the SDA and at INTEC. These levels have been attributed to contaminant sources. Results from this investigation suggest that this may be a natural process.

Determined that microbial activity in unsaturated sediments is a function of matric potential, which:

- Developed a functional relation that can be used in predictive computer models to link hydrologic properties (water content) to geochemical properties (carbon dioxide production).

- By combining several methods for measuring pore volumes of soil samples, we were able to obtain a complete pore volume distribution of pores ranging from the diameter of water to macropores present in soils.

- We showed that the inclusion of micropores in these distributions highly impact moisture retention of soils and predictions of moisture dependent microbial activity and hydraulic conductivity.

- We identified compaction during drainage of soils in a geocentrifuge as a critical outcome for measuring hydraulic and biogeochemical processes and properties of compactable soils.

- We developed a model for correcting hydraulic property measurements or compacted soils in a geocentrifuge to represent uncompacted soils.

- We developed a new method for uniformly distributing labeled substrate within a soil column to obtain similar, evenly distributed, initial concentrations within replicate soil samples.

- We demonstrated that a relatively innovative technique for obtaining moisture equilibrium at various matric potentials (geocentrifuge methods) can be used to obtain steady state unsaturated conditions for measuring hydraulic and biogeochemical properties of soils.

- We developed a new method for recovering large volumes of CO_2 from alkaline soils at a high recovery rate (99%).

- We were able to demonstrate that a complete pore volume distribution of a soil type is necessary to accurately predict microbial activity as a function of soil moisture.

Publications

Baker, K. E., and D. N. Thompson, "Available Soil Water and its Effect on Microbial Activity, I. Determination of Cumulative Pore Volume Distribution and the Water Available to Soil Microbes, *Vadose Zone Journal*, September 2002. (Submitted)

Thompson, D. N., and K. E. Baker, "Available Soil Water and its Effect on Microbial Activity, II. Measurement of Microbial Activity and Correlation with Total and Available Soil Water," *Soil Biology and Biochemistry*, September 2002. (Submitted)

Presentations

Baker, K. E., A. P. Poloski, A. T. Owen, C. W. Lindenmeier, and D. N. Thompson, "The Effect of Compaction on Moisture Characteristic Curves of Compactible Soils Measured in a UFA," Poster H31C-0264, *2001 Fall Meeting of the American Geophysical Union, San Francisco, CA, December 10–14, 2001*.

Baker, K. E., and D. N. Thompson, "Improved Methods for Estimating Microbial Activity and Moisture Characteristic Curves in Intact Unsaturated Soil Cores," Poster H42B-0356, *2001 Fall Meeting of the American Geophysical Union, San Francisco, CA, December 10–14, 2001*.

Hull, L. C., C. Grossman, R. Fjeld, J. Coates, and A. Elzerman, "Estimating Uranium Partition Coefficients From Laboratory Adsorption Isotherms," *American Nuclear Society, Spectrum 2002, Reno, NV, August 2002*.

Plummer, M. A., L. C. Hull, D. T. Fox, D. C. Cooper, C. W. Bishop, "Examining the Dependence of Radionuclide Transport on Microbial Activity through Experiments with a Mesoscale Unsaturated Flow Column," (Abstract accepted for presentation at *GSA Fall Meeting*, 2002),

REFERENCES

1. DOE, A National Roadmap for Vadose Zone Science and Technology, Understanding, Monitoring, and Predicting Contaminant Fate and Transport in the Vadose Zone, DOE/ID-10871, U.S. Department of Energy, Idaho Falls, Idaho, August 2001.

2. J. M. McCarthy, B. H. Becker, S. O. Magnuson, K. N. Keck, T. K. Honeycutt, *Radioactive Waste Management Complex Low-Level Waste Radiological Composite Analysis*, INEEL/EXT-97-01113, Bechtel BWXT Idaho, LLC, September 2000.

3. M. J. Case, A. S. Rood, J. M. McCarthy, S. O. Magnuson, and B. H. Becker, *Technical Revision of the Radioactive Waste Management Complex Low-Level Waste Radiological Performance Assessment for Calendar Year 2000*, INEEL/EXT-2000-01089, Bechtel BWXT Idaho, LLC, 2000.

4. F. J. Brockman, C. J. Murphy, B. Bjornstad, D. Balkwill, D. B. Ringelberg, S. Pfiffner, and R. Griffiths, "Microbial Life in the Unsaturated Subsurface Under Conditions of Extremely Low Recharge: An Extreme Environment. In Instruments, Methods, and Missions for the Investigation of Extraterrestrial Microorganisms," R. B. Hoover (Ed.), *SPIE*, Vol. 3111, 1997, pp. 388–394.

5. T. L. Kieft, E. M. Murphy, D. L. Haldeman, P. S. Any, B. N. Bjornstad, E. V. McDonald, D. B. Ringelberg, D. C. White, J. Stair, R. P. Griffiths, T. C. Gsell, W. E. Holben, and D. R. Boone, "Microbial Transport, Survival, and Succession In A Sequence of Buried Sediments," *Microbial Ecology*, Vol. 36, 1998, pp. 336–348.

6. F. J. Brockman, T. L. Kieft, J. K. Frederickson, B. N. Bjornstad, S. W. Li, W. Spangenburg, and P. E. Long, "Microbiology of Vadose Zone Paleosols in South-Central Washington State," Microbial Ecology, Vol. 23, 1992, pp. 279–301.

7. UFA Ventures, Inc., "Matric Potential Technical Brief," *http://www.UFAVENTURES.COM/ufa_ventures/tech_briefs/matric_potential.html*, 1996.

8. ASTM, Standard Test Method for Determination of Pore Volume and Pore Volume Distribution of Soil and Rock by Mercury Intrusion Porosimetry," Subcommittee D-18 on Soil and Rock, Annual Book of ASTM Standards, ASTM Standard D4404-84, ASTM, Philadelphia, PA, 1984.

9. A. Klute (ed.), "Methods of Soil Analysis," Agronomy, Part 1, Number 9, 2nd edition. ASG, Inc. and Soil Science Society of America (SSSA), Inc., Madison, WI, 1986, pp. 414–420.

10. J. E. Stone and A. M. Scallan, "The Effect of Component Removal Upon the Porous Structure of the Cell Walls of Wood," *Pulp and Paper Mag. Can.*, Vol. 69, 1968, p. 288.

11. L. C. Hull and D. N. Thompson, *Reactive Transport in Variably Saturated Heterogeneous Media, In: Environmental Systems Research, FY-01 Annual Report,* Idaho National Engineering and Environmental Laboratory, Idaho Falls, ID. INEEL/EXT-01-01402, pp. 18–28, 2002.

12. D. B. Stephens, *Vadose Zone Hydrology*, Lewis Publishers, Inc., Boca Raton, FL, 1996, page 4.

13. M. Th. van Genuchten, F. J. Leij, and S. R. Yates, 1991, *The RETC Code for Quantifying the Hydraulic Functions of Unsaturated Soils*, United States Salinity Laboratories, United States Department of Agriculture, EPA/600/2-91/065.

14. Beckman Instruments, Inc., *LS 6000 Series Liquid Scintillation System Operating Manual*, Beckman Instruments 015-247971, Fullerton, CA, June 1991.

15. C. T. Rightmire and B. D. Lewis, "Hydrogeology and Geochemistry of the Unsaturated Zone, Radioactive Waste Management Complex, Idaho National Engineering Laboratory, Idaho," U.S. Geological Survey, 1987.

16. P. Holbrook, 2001, "Pore Pressure through Earth Mechanical Systems: The Force-Balanced Physics of the Earth's Sedimentary Crust," Force Balanced Publications, ISBN: 0-9708083-0-5, Vol. 136, p. 37 fig.

17. T. L. Bone and D. L. Balkwill, "Morphological and Cultural Comparison of Microorganisms in Surface Soil and Subsurface Sediments at a Pristine Study Site in Oklahoma," *Microb. Ecol.* Vol. 16, 1988, pp. 49–64.

18. D. L. Balkwill, F. R. Leach, J. T. Wilson, J. F. McNabb, D. C. White, "Equivalence of Microbial Biomass Measures Based on Membrane Lipid and Cell-Wall Components, Adenosine-Triphosphate, and Direct Counts in Subsurface Aquifer Sediments," *Microb. Ecol.*, Vol. 16, 1988, pp. 73.

19. D. L. Balkwill and W. C. Ghiorse, "Characterization of Subsurface Bacteria Associated with 2 Shallow Aquifers in Oklahoma," *Applied and Environmental Microbiology*, Vol. 50, 1985, pp. 580–588.

20. W. K. Dodds, C. A. Randel, C. C. Edler, "Microcosms for Aquifer Research: Application to Colonization of Various Sized Particles by Ground-Water Microorganisms," *Ground Water*, Vol. 34, 1996, pp. 756–759.

21. K. Kusel, C. Wagner, T. Trinkwalter, A. S. Gossner, R. Baumler, H. L. Drake, "Microbial Reduction of Fe(III) and Turnover of Acetate in Hawaiian Soils," *FEMS Microbiol. Ecol.*, 2002, Vol. 40, pp. 73–81.

22. A. L. Shanks and M. L. Reeder, "Reducing Microzones and Sulfide Production in Marine Snow," *Mar. Ecol.-Prog. Ser.*, Vol. 96, 1993, pp. 43–47.

23. W. A. Smith, W. A. Apel, B. M. Peyton, J. N. Petersen, R. K. Sani, "Hexavalent Chromium Reduction by *Cellulomonas* Spp. Isolated from Subsurface Soils," *Applied and Environmental Microbiology*, Vol. in review 2002.

24. W. A. Jury, W. R. Gardner, and W. H. Gardner, "Soil Physics: New York," John Wiley and Sons, Inc., 1991, p. 328.

25. P. Holbrook, "Pore Pressure through Earth Mechanical Systems: The Force-Balanced Physics of the Earth's Sedimentary Crust," Force Balanced Publications, ISBN: 0-9708083-0-5, 2001, p. 136, Figure 37.

26. A.V. Luikov, "Analytical Heat Diffusion Theory, *Hartnett, J. P., ed.*, New York, Academic Press, 1968, p. 685.

27. M. D. White, M. Oostrom, and R. J. Lenhard, "Modeling Fluid Flow and Transport in Variably Saturated Porous Media with the STOMP Simulator. 1. Nonvolatile Three-Phase Model Description," *Advances in Water Resources*, Vol. 18, No. 6, 1995, pp. 353–364.

28. D. L. Parkhurst and C. A. J. Appelo, 1999, *User's Guide to PHREEQC (Version 2)—A Computer Program for Speciation*, Batch-Reaction, One-Dimensional Transport, and Inverse Geochemical Calculations: U.S. Geological Survey Water-Resources Investigations Report 99-4259, p. 312.

29. J. Simunek, D. L. Suarez, and M. Sejna, 1996, *The UNSATCHEM Software Package for Simulating One-Dimensional Variably Saturated Water Flow, Heat Transport, Carbon Dioxide Production and Transport, and Solute Transport with Major Ion Equilibrium and Kinetic Chemistry, Version 2.0*, Research Report No. 141, USDA-ARS U. S. Salinity Laboratory, Riverside, California.

30. D. E. Prudic and R. G. Striegl, 1995, *Tritium and Radioactive Carbon (^{14}C) Analyses of Gas Collected from Unsaturated Sediments Next to a Low-Level Radioactive-Waste Burial Site South of Beatty, Nevada*, April 1994 and July 1995, Open-File Report 95-0741, U. S. Geological Survey, Reston, VA.

31. M. C. Duff and C. Amrhein, *Soil Sci. Soc. Am. J.*, Vol. 60, 1996, pp. 1393–1400.

32. M. C. Duff, C. Amrhein, G. Bradford, "Nature of Uranium Contamination in the Agricultural Drainage Water Evaporation Ponds of the San Joaquin Valley, California, USA," *Can. J. Soil Sci.*, Vol. 77, 1997, pp. 459–467.

33. M. C. Duff, D. B. Hunter, P. M. Bertsch, C. Amrhein, "Factors Influencing Uranium Reduction and Solubility in Evaporation Pond Sediments," *Biogeochemistry*, *Biogeochemistry*, Vol. 45, 1999, pp. 95–114.

34. M. P. Elless and S. Y. Lee, "Uranium Solubility of Carbonate-Rich Uranium-Contaminated Soils," *Water Air Soil Pollut.*, Vol. 107, 1998, pp. 147–162.

35. J. J. Lenhart, S. E. Cabaniss, P. MacCarthy, B. D. Honeyman, "Uranium(VI) Complexation with Citric, Humic and Fulvic Acids," *Radiochim. Acta*, Vol. 88, 2000, pp. 345–353.

36. K. Schmeide, S. Pompe, M. Bubner, K. H. Heise, G. Bernhard, H. Nitsche, "Uranium(VI) Sorption onto Phyllite and Selected Minerals in the Presence of Humic Acid," *Radiochim. Acta*, Vol. 88, 2000, pp. 723–728.

37. J. J. Lenhart, B. D. Honeyman, "Uranium(VI) Sorption to Hematite in the Presence of Humic Acid," *Geochim. Cosmochim. Acta*, Vol. 63, 1999, pp. 2891–2901.

38. P. Benes, K. Kratzer, S. Vlckova, E. Sebestova, "Adsorption of Uranium on Clay and the Effect of Humic Substances," *Radiochim. Acta*, Vol. 82, 1998, pp. 367–373.

39. G. Redden, J. Bargar, R. J. Bencheikh-Latmar, "Citrate Enhanced Uranyl Adsorption on Goethite: An EXAFS Analysis," *Colloid Interface Sci.*, Vol. 244, 2001, pp. 211–219.

40. T. Saito, S. Nagasaki, S. Tanaka, "Evaluation of the Complexation Behavior between Humic Acid and Uo22+ with Fluorescence Spectroscopy and Its Mixture Analysis," *Radiochimica Acta*, Vol. 90, 2002, pp. 27–33.

41. D. R. Lovely, E. J. P. Phillips, Y. A. Gorby, E. R. Landa, "Microbial Reduction of Uranium," *Nature*, Vol. 350, 1991, pp. 413–416.

42. J. K. Fredrickson, J. M. Zachara, D. W. Kennedy, M. C. Duff, Y. A. Gorby, S.-M. W. Li, K. M. Krupka, "Reduction of U(VI) in Goethite (α–Feooh) Suspensions by a Dissimilatory Metal-Reducing Bacterium," *Geochim Cosmochim Acta*, Vol. 64, 2000, pp. 3085–3098.

43. A. Abdelouas, Y. Lu, W. Lutze, H. E. J. Nuttall, "Reduction of U(VI) to U(IV) by Indigenous Bacteria in Contaminated Ground water," *Contam. Hydrol.*, Vol. 35, 1998, pp. 217–233

Geomicrobiology of Subsurface Environments

F. Colwell, R. M. Lehman, G. Bala, and D. Cummings and research contributors M. Delwiche, M. Downing, R. Fox, S. Fox, Y. Fujita, G. Geesey, K. Gering, J. Ingram, M. Kauffman, J. Lord, T. McLing, B. Mincher, D. Newby, L. Petzke, D. Reed, D. Siemer (INEEL); A. Igoe (Albertson College), T. Magnuson, J. Taylor, and A. Ray (Idaho State Univ.), S. O'Connell (Western Carolina Univ.), B. Peyton (Washington State Univ.), K. Reardon (Montana State Univ.), F. Rosenzweig (Univ. of Montana), and M. Whiticar (Univ. of Victoria)

SUMMARY

The overall objective of this project is to enhance the understanding of biological properties in the subsurface to develop predictive knowledge of contaminant fate and transport. The research targets two knowledge gaps that have been identified with respect to DOE's subsurface contamination problems.[1] These gaps relate to our current inability to (1) characterize physical, chemical, and biological properties of the subsurface, including approaches to understanding the properties of the geologic system and relating them to contaminant fate and transport; and (2) characterize highly heterogeneous systems. The basic research conducted within this project seeks to address needs arising from these knowledge gaps. Specifically, to improve the capabilities for characterizing the biological properties of the subsurface, including biological heterogeneity, at the scales that control contaminant fate and transport.

Microorganisms are the primary agents of geochemical change in the subsurface, and these changes mediate transport and degradation phenomena. The following research tasks are driven by critical deficiencies in the existing microbiological knowledge base that limit in situ remedial applications:

- Quantifying the impact of microbial partitioning between geological media and ground water on biogeochemical transformations
- Quantifying the biological effects on wettability and imbibition because these physical parameters impact contaminant partitioning as well as the access and bioavailability of contaminants to transformation
- Establishing the connection between the structure and function of subsurface microbial communities and specific environmental conditions of the habitat
- Determining how co-contaminants impact biotransformation of metals and radionuclides.

These tasks are consistent with those of the INEEL's Subsurface Science Initiative, which has identified "biogeochemical transformations" as a key research focus. Furthermore, the tasks target real site problems within the DOE complex. End point applications of the work include remediation of contaminated geologic media at DOE sites and facilities nationwide and industrial sites throughout the world as well as agriculture, mining, resource recovery (energy), aquifer contamination, and waste disposal.

PROJECT DESCRIPTION

Four tasks were undertaken in FY 2002: (1) microbial partitioning in geological media, (2) biological effects on wettability/imbibition and contaminant partitioning, (3) the link between structure and function of subsurface microbial communities and environmental conditions, and (4) determining how co-contaminants impact biotransformation of metals and radionuclides. These tasks are described individually.

Molecular Assessment of Partitioning of Microorganisms and Their Activities In Saturated Geologic Media

This task, which continues from FY 2001, consists of experimental work that effectively describes the distribution and spatial scales of biogeochemical processes in the subsurface.

Microorganisms are known to inhabit the subsurface and influence fate and transport of subsurface contaminants. However, little emphasis has been placed on distinguishing organisms (and their functions) in the saturated subsurface that are associated with the geologic media from those suspended in the ground water. Emerging evidence demonstrates that both microbial functional traits and the rates of biogeochemical transformation are unevenly distributed between these two habitats.[2,3] There is extensive literature that documents radical changes in the physiology (enzyme expression) when single organisms become attached to or detached from substrata during laboratory experimentation.[4] The dichotomy between attached and unattached microbe-mediated transformations in aquifers represents an additional facet of heterogeneity in the subsurface.

A long-term goal of subsurface microbiological investigations is to develop a predictive knowledge base concerning the distribution of microorganisms and their activities in subsurface environments so that activities such as remediation can be accomplished efficiently with a minimum of costly site characterization studies at each location (see Reference 1). Many of these locations that are amenable to remediation are saturated. To achieve degradation (or other desirable interaction), it is necessary to place the substrate, transforming population, and stimulus at the same location simultaneously. Predictive knowledge relative to microbe distribution and activities drives the design of relevant laboratory biodegradation and numerical models, allowing site characterization efforts to focus on either core or ground water, and which should be subsequently monitored.

Specific task objectives involve quantifying the impact of microbial partitioning between the geologic media and ground water on biogeochemical transformations—both metabolic capabilities and rates of biotransformations. Compositional and functional attributes of attached and unattached communities have been examined in controlled laboratory experiments using both porous- and fracture-flow columns, and in paired field samples of the core and ground water. Strategies for appropriate sampling and analysis of attached and unattached aquifer microorganisms are being considered. Several experimental subtasks have been developed to empirically address these questions and progress during FY 2002 as reported below.

Subtask 1

This subtask involves the use of laboratory columns constructed with geologic media and perfused with ground water to simulate an aquifer and provide materials that were subjected to microbiological analyses. In FY 2002, a paper describing experiments that tested the effect of trichloroethylene (TCE) on microbial partitioning was submitted and accepted and published[5] (the results of the experiments were reported in last year's report.) In FY 2002, pilot studies and a replicated experiment were performed to examine the effect of biostimulation conditions on the partitioning of aquifer microorganisms between attached and free-living states. Columns were constructed with sediments collected using a Powerprobe rig from a shallow (ca. 5 m BLS) aquifer located 20 km north of Idaho Falls near the town of Roberts. Feed for the columns was ground water collected with the Powerprobe from the same site, at the same depth as the sediments. For the replicated study, 10 columns were perfused with ground water for 4 weeks under a recirculating regime to create similar conditions in each column. The feed ground water was aerated to prevent low oxygen concentrations from limiting microbial activity in the columns. At the conclusion of the 4-week conditioning period, the flow regime was changed from a recirculating system to a flow-through system, and five columns were designated to receive a treatment that would simulate the nutrient addition typical of a biostimulation remedial strategy. These five columns received the addition of 25 mg/L (projected concentration in the column) of potassium phosphate, glucose, yeast extract, and peptone delivered in filtered ground water that augmented the primary column feed. The five remaining columns were designated as controls and received the augmentation of filtered ground water with no added nutrients. The columns were operated for an additional 3 weeks to achieve a steady-state of operation so that cell attachment and detachment processes would be constant. At this point, ground water effluent was collected

from all 10 columns and the sediments in the columns were destructively sampled. Samples of column effluent and sediments were subjected to the following analyses: total cell counts, frequency of dividing cells, percentage of cells with visible exopolymer accumulations, respiration of C-14 labeled glucose and mixed amino acids, extracellular enzyme activity using analogue substrates for beta-glucosidase and aminopeptidase, community structural profiles by separation of eubacterial 16S rDNA fragments amplified by PCR on denaturing gradient gels, and identification of populations by sequencing of 16S rDNA fragments. Physical and chemical analyses of the ground water and sediments were also performed: sediment textural analysis and classification, mineralogy, bulk density and porosity as packed in the columns, sediment moisture content, sediment organic content; and pH, conductivity, cation, anion and dissolved organic carbon concentrations of the ground water. Many of these analyses are in progress. Figure 1 shows the relative respiration of C-14 labeled glucose and mixed amino acids for attached and free-living bacterial communities from the treatment and control columns.

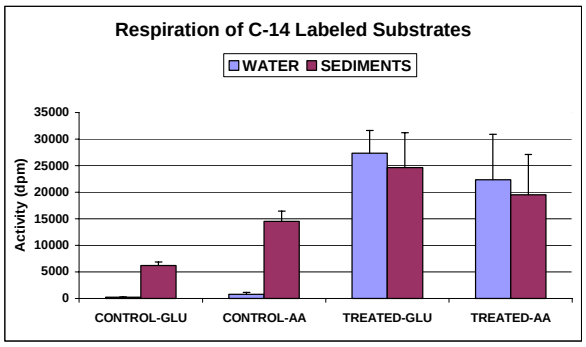

Figure 1. Relative respiration of C-14 labeled glucose and mixed amino acids for attached and free-living bacterial communities from the treatment and control columns.

Subtask 2

This subtask, which was initiated in FY 2002, involves investigating the feasibility of ground-water sampling for attached organisms. The representation of subsurface communities by ground water samples has been discussed in the literature and the factors affecting ground water sampling (well construction, pumping duration) examined.[6–8] In these studies and studies performed in our laboratory (O'Connell, unpublished data), it is clear that both well construction and pumping duration affect the microbiology observed in a ground water sample. With respect to aquifer properties, it was shown that hydraulic conductivity had negligible effects on the ground water community sampled from a single borehole.[9] Despite the presence of organisms in ground water, it has been suggested by some researchers that organisms associated with the solid phase (majority in many environments) are the ones to study, and that core is the true representative sample of subsurface environments[10,11] (Colwell, unpublished presentation). However, other reports have shown distinctive and sometimes dominant micro-organisms appearing exclusively in the ground water (see Reference 3 and references therein). It now appears that there are two communities of subsurface microorganisms—attached and unattached—and that they are probably compositionally and functionally different and may be performing fundamentally different roles in subsurface biogeochemical cycles. One community must be sampled by the expensive process of aseptic core sampling of the geologic media; the other by simply pumping ground water from drilled wells. Direct observation of cells in ground water from TAN-37 during the lactate injection field trial demonstrated large amounts of cell-associated exopolymer (Lehman, unpublished observations). It may be possible that sufficient shear is developed from the pumping force so that cells may be released from the geologic media and entrained in the ground water that is delivered to the surface. To investigate the feasibility of sampling both unattached and attached organisms via only ground water collections, the following sequence of studies was proposed:

1. Estimate (by calculation) the amount of shear force exerted in representative formations under a range of pump discharge rates that are commonly available.

2. Examine the literature to produce a range of shear forces expected to remove both loosely attached cells and tightly attached cells.

3. If the results from Steps 1 and 2 indicate that pumping can achieve the shear force necessary to remove loosely, and perhaps tightly bound organisms, replicate (3-5×) a laboratory column experiment under a single model formation type, single organism type (that is pre-adhered to geologic substrata) to examine the relationship between shear force (by pump rate) and produced cells (total cell counts).

4. If the results from Step 3 indicate the feasibility of this approach in the field, take the following steps:

    a. Identify the site and well where: ground water sampling can be performed with minimal logistical issues (esp. regulatory), we can deploy the necessary equipment (pump and packer), and we can isolate pumping rate as the only test variable

    b. Collect replicated (five times) ground-water samples under three or four flow rates calculated to produce the shear forces necessary to remove cells from the geologic media

    c. Examine the samples to determine the community from both compositional and functional aspects (measures total cells, PCR-DGGE or FISH for composition, C-14 labeled substrates for function, and quantify exopolymer content).

5. Analyze the data to determine if the pumping rate affects the measured variables. Offer conclusions as to whether attached organisms can be sampled in this manner, and seek opportunity to test against field collected core samples.

Preliminary calculations show that the force exerted by the pumping of a well may be sufficient to remove some bacteria from the porous media surfaces. In a literature review, quite a range of forces are associated with removal of cells from surfaces (working range would be 10^{-8} to 10^{-12} N/cell, although a conceivable range would be approaching zero up to forces substantially higher than possible by pumping). A first estimate of shear forces associated with pumping indicated the development of 2.14×10^{-11} N/cell. More refined calculations resulted in a matrix of shear forces that can be developed in a representative basalt aquifer under different pumping regimes. Figure 2 shows the theoretical distribution of shear forces that develop in a basalt aquifer under assumed conditions of porosity, mean pore throat diameter, radial distance from the well, and pump discharge rate. The range in forces predicted overlaps the forces reported to remove detached cells in carefully controlled laboratory studies. The results of these theoretical analyses indicate the theoretical potential for removing various proportions of cells attached to geologic media by controlling pump discharge rates.

We then conducted two unreplicated column studies to test the effect of hydrodynamic shear forces on the removal of indigenous aquifer sediment-associated bacteria. The aquifer sediments (with associated microbes) were collected from the site near Roberts using a Powerprobe push corer. The sediments (sieved and that which passed a 150 mesh sieve was discarded) were packed into the column and flow was initiated using filter-sterilized artificial ground water. Initial flooding of the columns was performed over several days during which the production of fine sediment particles gradually declined. Aliquots were collected from the column effluent and cells were enumerated in these samples by direct observation of acridine-orange stained cells under epifluorescent illumination at 100× magnification. The feedstock was monitored by the same approach to ensure continuing sterility. The pump discharge rate was then stepped up several times. After each step increase, samples were taken in logarithmic fashion and the number of cells enumerated to document changes in the number of cells associated with step increases in flow velocity. Figure 3 is an example of a plot of cells in the effluent over time during one of these experiments.

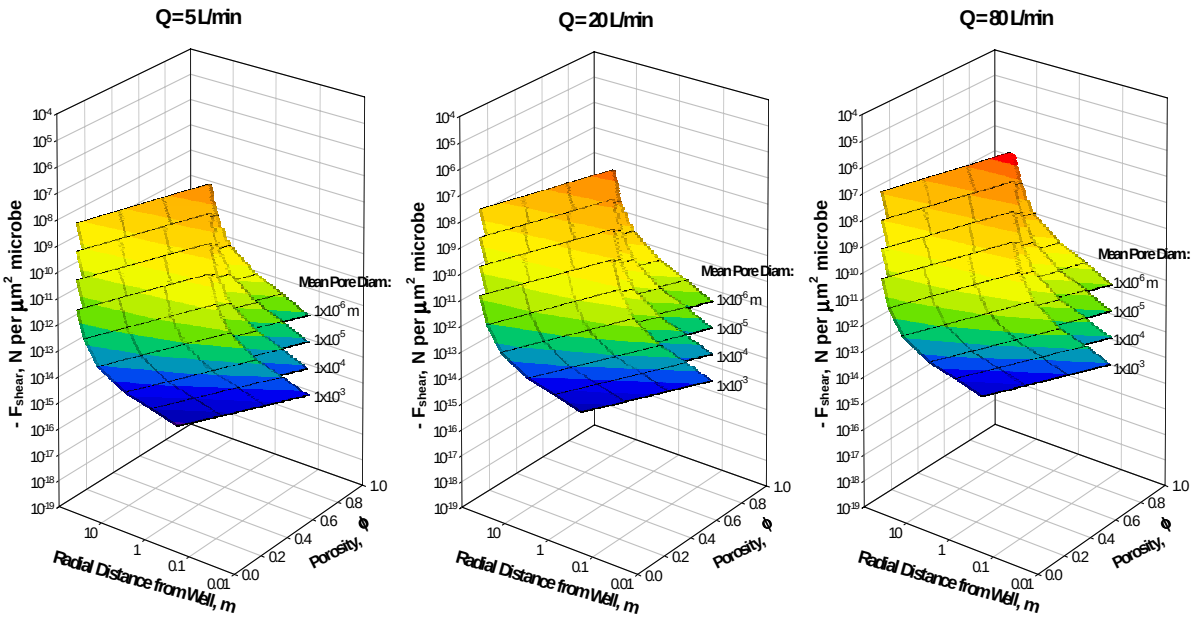

Figure 2. Predicted shear force on inter-pore subsurface microbes (basis of 1 μm^2 microbe surface area). Note: Some of the shown conditions would produce impractical pumping scenarios.

At present we are considering the appropriate range of flow velocities with which to conduct these step tests on column studies. The appropriate range will cover velocities that are subthreshold for the removal of cells to velocities that remove all detachable cells. This range has an empirical basis, our observations in these pilot experiments, and theoretical basis. These unreplicated column runs will use 2-in.-inside-diameter columns, porosity = 0.31, and flow rate = 0.5–20 mL/min, and assuming the average pore diameter is between 10 and 100 µ, the calculated shear force ranges from -1.6e-12 (at 0.5 mL/min) to -6.5e-11 (at 20 mL/min) N/μm^2 of microbe surface area. The experimental design includes the ability to increase the velocity over this range without adjusting the plumbing or changing the pump. For extrapolation to the field, it is also important that the range of shear forces induced in laboratory columns are within the range that may be generated by traditional well pumps. After these logistical constraints are eliminated and the experimental design is repeatable for a single column, we will commence replicated experiments (in FY 2003).

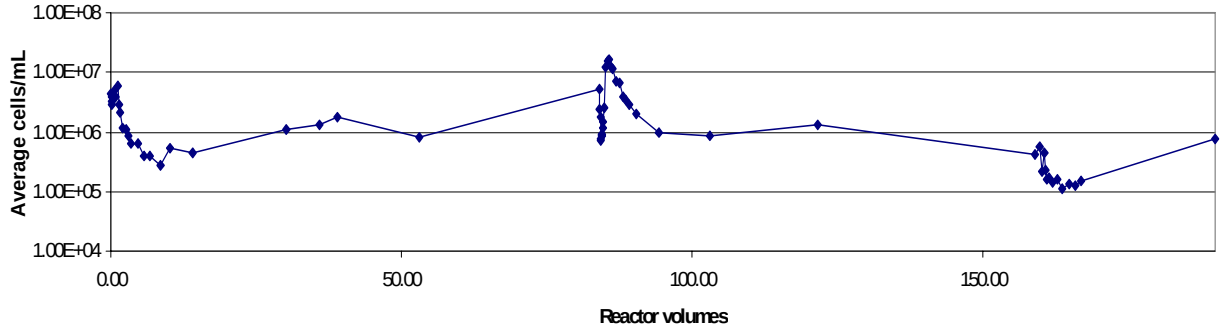

Figure 3. Effect of hydrodynamic shear forces on the removal of indigenous aquifer sediment-associated bacteria. This figure depicts cell numbers released from sediments during continuous flow of liquids through the sediments.

A conceptual model has been developed of shear force-induced detachment of aquifer micro-organisms from porous media surrounding a well (data not shown). A similar conceptual model has been developed for the laboratory column experiments (data not shown). Parallel consideration of these two models involves contrasting the effects of 3-D radial flow in the field and 1-D pipe flow in the columns. In addition to the practical objective of sampling attached cells by ground water pumping, we are interested in the relative attachment strengths of different populations of sediment-associated aquifer bacteria. In contrast to the experimental approach of using a highly engineered system and a single population, we will attempt to examine this phenomenon by analyzing the indigenous populations that are removed during step increases in flow velocity by compositional analyses such as 16S rDNA sequence analysis.

Subtask 3

This subtask involves noninvasive assessment of in situ microbial activities using low-energy infrared radiation. It includes a study of the surface associations of organisms, degradative substrate, and mineral type on basalt by applying synchrotron radiation-based Fourier transform spectromicroscopy (SR-FTIR) using the 1.4.3 Beamline experimental end station of a particle accelerator, the advanced light source (ALS) at LBNL. Advantages of this nondestructive method are the resolution conferred by a 10-µm spot size and the high intensity infrared radiation source. This technique is being used to study the degradation kinetics of aromatic and chlorinated hydrocarbons by attached and unattached organisms. Burkholderia cepacia G4 is being used as a test organism, basalt as the mixed-mineral substratum, and TCE as the organic substrate. The induction of the enzymes (toluene mono-oxygen-ase,[TMO]) which co-metabolically degrade TCE, are being studied with toluene and phenol as an inducer, and 3-hydroxyphenyl-acetylene as an analogue substrate and activity indicator. In FY 2002, progress on this subtask was devoted to the preparation of three manuscripts (see below). In addition, several experiments were performed to strengthen these papers. One experiment involved the FTIR analysis of pure biochemicals (phospholipids, PHB, proteins, etc.) on different mineral substrata to determine if the changes in biochemical signatures noted with SR-FTIR when whole cells were attached to different mineral substrata were actually due to physiological changes. This work demonstrated that the FTIR spectra of the pure chemicals was not dependent on the mineral substrata, and therefore, the changes noted in pure cells may be attributed to physiological changes. A second experiment involved realignment of the experimental conditions so the differences in TMO activities between attached and free-living cells can be attributed to their attachment to the mineral substrata and not to other experimental conditions.

Evaluation of Imbibition and Wettability Parameters Mediated by Microbial Perturbations

This work describes imbibition studies to assess the incipient interaction between select hydrocarbons and pertinent mineral surfaces as a function of aqueous chemistry and microbiological perturbation. These studies were aimed at quantifying the areal extent of altered wetting and the nature of the surfaces produced. This information is needed to understand how contaminant distribution and recovery may be influenced. This research supports the Subsurface Science Initiative by promoting more effective fate and transport modeling for risk analysis and remediation. An understanding of wetting in the systems of interest will lead to better strategies for remediation. The technology has broad application to the INEEL and other DOE sites. The rate of fluid imbibition can be scaled, and this scaled rate can be used in simulators to correctly predict contaminant movement from fractures to matrix as the contaminant percolates through the vadose and saturated zones. Similar scaled rates can be determined for contaminant recovery.

Fate and transport of organic contaminants (nonaqueous phase liquids [NAPLs]) in the subsurface depend on very complex interactions between several system components such as fluid chemistries, geochemistry, microbiology, geology, and physical (gravitational and capillary force) parameters. Past literature suggests that flow of

NAPLs in saturated media is ostensibly predicated on the spatial arrangement of contrasting textures.[12–15] However, the cited literature wholly assumes that all of the solid surfaces are preferentially water-wet (but not organics, will spread across the surface).

A more detailed investigation of NAPL flow acknowledges several effects that range from macro to micro scale phenomena. Examples of these phenomena include the effect of pore scale processes such as "snap off" (the physical release of contaminants from a solid surface) on NAPL entrapment[16] as well as larger-scale processes such as "fingering" (see Reference 15). Microscale processes such as wettability (the tendency of a fluid to spread along a solid surface in the presence of another immiscible fluid) have profound impacts on capillary pressure[17] and relative permeability[18] relationships. Changes in wettability have been documented to effect the fate and transport of organic materials.[19] Numerous factors have been described that mediate wettability changes such as contaminant aging,[20] contaminant adsorption,[21] addition of surface active constituents,[22] mineralogy,[23] distribution of organic complexes,[24] and pore surface topology.[25] Wettability effects with respect to the relations of hydraulic properties are a matter of debate and have been reported to be both dependent[26–28] and independent[29,30] of saturation.

Allowing for interaction of all recognized components, the flow and transport of NAPLs in high permeability (fracture) subsurface environments is dominated by viscosity and gravity, while low permeability (matrix) systems are dominated by capillary forces. In fracture-matrix systems, fluid distribution in the matrix is dictated by capillarity—which is in turn influenced by wettability. Wettability is one of the system properties that influences capillary processes during multiphase flow. In general terms, imbibition describes how fast capillarity takes place—the rate kinetic of capillarity is imbibition. Hence, wettability of subsurface rocks and soils and the effect of wetting on imbibition processes significantly influence contaminant distribution and the rate at which bulk contaminant saturations can be reduced by displacement processes. The imbibition or mass transfer of contaminant liquids between fractures and matrix blocks is an important phenomena in establishing the distribution and flow of contaminants in the subsurface. It is equally important in determining the rate and degree to which contaminants can be recovered from matrix blocks in a fractured porous medium.

In heterogeneous subsurface systems, highly irregular distribution and flow patterns of NAPLs have been observed (see References 12 and 14), and it is logical to extrapolate that discrepancies are driven by a combination of physical and chemical heterogeneities in the environment. With the advent of aggressive remediation technologies, it is important to understand the effect of technology strategy on the ultimate fate and transport of the contaminant. Although this will be very complex, changes in wettability will be a key factor. With respect to biologically mediated remediation strategies, the potential effect of biologically mediated changes to wettability have been largely unreported in the past. Recent investigations (personal communications) support the viability of the hypothesis focused on biologically driven change. Although complex, the biological component can be viewed simplistically as the discrete presence of cells or biofilms, nutrient packages that may be introduced to support or suppress these organisms, and the end products resulting from metabolism and growth. Microbial activities capable of affecting surface or aqueous chemistries that mediate change in the wettability index include the introduction of nutrients; attachment, detachment, and film formation; transformation of contaminants; production of metabolites; and cell death.

The effect of wettability alterations driven by microbiological perturbations may be both positive and negative. If the system is driven to a less water-wet condition, the organic contaminants will have a tendency to spread across the surface of the solid media resulting in a larger bulk volume of contaminated solids. Conversely, this could be a positive outcome if the intention of the remediation technology is to improve the bioavailability of the contaminant and the appropriate organisms are present to transform or degrade the contamination.

Measurement techniques (dynamic imbibition measurements reduced to dimensionless time[31]),

rationale for use, and core preparation have all been reported[32] and are largely unchanged.

Selected system components (Berea Sandstone, synthetic SRPA water, microbiological growth media R_2A, Berea sandstone cores [1 × 3 in.] and dodecane) have been previously described (see Reference 32). Sections of Berea Sandstone were prepared using previously reported methodologies (see Reference 32). The physical characterization of the cores is presented in Table 1.

Table 1. Characterization of Berea Sandstone cores used for wettability/imbibition experiments.

Core	Length (cm)	Diameter (cm)	Porosity	Permeability Water (mD)	Organic Sat. Initial (mL)	Water Sat. Initial (mL)
S39	7.382	2.512	0.213	605	4.78	0.388
S41	6.709	2.534	0.208	507	4.58	0.348
S42	6.188	2.554	0.211	572	4.25	0.365
S43	7.131	2.513	0.216	640	4.70	0.387
S49	7.164	2.565	0.216	668	4.85	0.393
S50	6.770	2.539	0.214	525	4.91	0.330
S55	7.140	2.545	0.208	1799	4.92	0.350
S56	7.327	2.542	0.211	1123	5.69	0.276
S57	6.872	2.525	0.211	1522	5.00	0.311
S58	7.558	2.527	0.208	2073	3.58	0.455
S59	7.591	2.554	0.212	2177	5.67	0.313
S60	7.439	2.539	0.207	926	3.03	0.526
S61	7.115	2.538	0.209	852	4.62	0.386
S62	7.322	2.539	0.219	1070	5.43	0.330
S63	7.533	2.532	0.224	1038	5.70	0.329
S66	7.340	2.531	0.211	1089	4.02	0.485
S67	7.513	2.533	0.214	1357	5.28	0.349
S68	7.193	2.528	0.206	691	4.62	0.379
S69	7.300	2.543	0.220	903	6.00	0.265
S70	7.587	2.533	0.221	1203	5.77	0.317
S71	7.124	2.510	0.215	1251	5.00	0.339
S72	7.476	2.250	0.250	1364	3.48	0.531
S73	7.603	2.532	0.209	1283	5.05	0.369
S74	7.447	2.545	0.208	939	5.13	0.348
S75	7.561	2.549	0.214	1651	5.01	0.393
S76	7.433	2.543	0.214	1214	5.04	0.377
S77	7.337	2.522	0.216	1286	4.86	0.388
S78	7.378	2.536	0.212	1130	4.80	0.391
S79	7.234	2.525	0.218	1189	4.80	0.392
S80	6.768	2.517	0.216	839	4.35	0.396
S81	7.357	2.559	0.212	409	4.58	0.427
S82	7.360	2.536	0.213	749	4.82	0.391
S83	7.335	2.533	0.206	441	4.73	0.379
S88	7.419	2.533	0.223	791	5.28	0.368

Microorganisms selected for study were five microbial isolates from Well no. 33 (Table 2) at Test Area North (TAN). One freezer stock of each organism was used to prepare an overnight seed culture. A 1% inoculum was transferred from the overnight seed culture to 500 mL fresh R_2A medium in a 2 L flask. Triplicate flasks were used. The cultures were incubated at 30°C and 150 rpm for 72 hours. The culture fluids were centrifuged at 8,000 rpm and 10°C for 20 minutes. The supernatant was collected and used for imbibition experiments. The cells were resuspended in 20 mL of each supernatant and saved for sonication. The harvested cells from the culture fluids were lysed using sonication. The 20 mL volume of suspended cells was added to a glass 40 mL test tube and sonicated for five cycles using a Branson Model 450 Sonifier. One full sonication cycle is equal to 30 seconds with the probe immersed two-thirds into the test tube and 30 seconds with the probe not immersed in the test tube while cooling on ice. After sonication, the debris was removed by centrifugation at 10,000 rpm and 10°C for 10 minutes. The supernatant from the sonicated cells was designated sonicant. The sonicant was added to 500 mL of fresh R_2A medium and used for imbibition experiments.

A Bradford Protein assay was completed to determine the amount of protein released during sonication in the pre- and post-sonication supernatant. Increased protein was observed in all supernatants following sonication indicating that cells were lysed.

One-liter glass beakers containing 500 mL of fresh R_2A medium, SRPA, supernatant, or sonicant were used for imbibition experiments. A 254 nm germicidal light was placed 5–6 in. above the beaker to reduce unwanted microbial growth in the core system. Cores were hung from an analytical balance and weights were recorded automatically in 5-minute intervals using Balance Talk software. The imbibition experiments were completed in triplicate.

Past data sets from Berea Sandstone cores (ostensibly a very strongly water-wet system) and synthetic SRPA water were compared to literature data for accuracy and system performance. Data were compared to strongly water-wet systems originally using alundum and sandstone cores,[33] aluminum silicate systems,[34] and Berea sandstone systems.[35] All literature systems evaluated resulted in a mass transfer function (α) of –0.03 to –0.07 for strongly water-wet systems. Although original data sets fell well within this bracket irrespective of the configuration (one end open vs. two ends open or vertical or horizontal position), it was later determined that for experiments using fluids of lower viscosities, specifically dodecane vs. "heavier organics" utilized in literature studies (1.38 cp vs. 37.82 cp) the data sets were shifted right to a position bounded by $\alpha = -0.02$ and -0.005. Any deviation from this range was considered to be less water-wet than control. However, this did not impact the relationship between measured modulation of the system; very strongly water-wet systems were easily distinguished from those that were less water-wet. Bacterial supernatants from *Arthrobacter globiformis* and *Rhodococcus luteus* were less water-wet than the control systems. Bacterial supernatants form *Hydrogenoflava pseudoflava* and *Acintobacter genospecies* and *Bacillus atrophaeus* showed mixed wettability results. Sonicants from *Arthrobacter globiformis*, *Hydrogenoflava pseudoflava*, *Acintobacter genospecies*, and *Bacillus atrophaeus* were less water-wet than the supernatants. On the contrary, supernatants from *R. luteus* were less water-wet than the sonicants from *R. luteus*.

Table 2. Microbial isolates selected for wettability/imbibition experiments.

Isolate	Gram Reaction	Spore Formation	Growth Temp
Acintobacter genospecies	–	No	20–30°C
Rhodococcus luteus	+	No	26–30°C
Hydrogenophaga pseudoflava	–	Yes	20–45°C
Arthrobacter globiformis	+	No	25–30°C
Bacillus atrophaeus	+	Yes	20–30°C

These data do not include effects mediated by whole cell systems, although it is reasonable to expect that differences will be evident. This is supported by not only the data at hand (ostensibly both supernatants and sonicants could contain fractions of cell detritus) but by personal communication with other researchers using electron microscopy to investigate the effects of whole cell systems with respect to wettability.

Although the most plausible mechanistic explanation for these observations is a discrete change in the interfacial tension mediated by the organisms, this is clearly not the case since the measured tensions (video image analysis of inverted pendant drops) of the microbial systems are greater than the media control (Table 3).

Careful examination of the data results in a slight discrepancy with respect to those data points collected during the early time frame and the mass transfer function. Although this discrepancy does not influence the overall interpretation, it is important to understand the origin of the difference. During early time points, a very slight retardation in the release of organic from the face of the core can drive very large apparent delays in dimensionless time.

Linking Microbial Community Structure and In Situ Function to Aquifer Conditions

Subtask 1

Trichloroethylene (TCE) contamination is a widespread problem in both ground water and soil environments. The Snake River Plain Aquifer (SRPA) near the TAN facility at the INEEL is of particular interest due to an apparent natural attenuation of the TCE plume at this site.[36] Ubiquitous aerobic gram-negative methanotrophic bacteria (methanotrophs) are believed to be one of the microbial populations responsible for attenuation of the TCE plume Independent studies of uncontaminated areas throughout the SRPA have found dissolved organic carbon concentrations of 0.3 to 0.9 mg/L [37] and low levels of methane in ground water samples (J. McKinley and F. Colwell, unpublished data), suggesting a potential niche for co-metabolic activities of methanotrophic populations. Microorganisms from the pristine basalt aquifer surrounding TAN were studied in order to gain insight into the observed natural attenuation of TCE. Samples were screened for the presence of Type I and II methanotrophs, since both types have co-metabolic capabilities and diverse populations have been detected in freshwater environments.[38–41]

By definition, methanotrophs obtain all of their carbon and energy from the oxidation of methane. Methane mono-oxygenase (MMO), the first enzyme involved in this oxidation converts methane to methanol, and is also capable of co-metabolic oxidation of chlorinated compounds, including TCE. This enzyme exists in one of two structures: a soluble cytoplamsmic form (sMMO) or a membrane associated particulate form (pMMO).[42] Although both forms of the enzyme are capable of degradative process, presumably the soluble form of this enzyme is environmentally important since it demonstrates substantially higher rates of co-metabolism of halogenated solvents than does pMMO.[43,44] Methanotrophs are classified taxonomically into two groups: Type I methanorophs belong to the γ-proteobacteria and

Table 3. Measurement of interfacial tensions (as mN/m) for biological materials.

Measurement	*Acintobacter genospecies*	*Arthrobacter globiformis*	*Bacillus atrophaeus*	*Hydrogenoflava pseudoflava*	*Rhodococcus luteus*
Interfacial tension of cell supernatants against dodecane[a,b]	51.93	47.26	42.80	51.29	47.51
Interfacial tension of culture sonicants against dodecane	43.14	43.40	44.70	42.44	41.21

a. Medium (R_2A)/dodecane IFT control = 40.66 mN/m.

b. Dodecane/water IFT control =53.30 mN/m.

assimilate carbon via the RuMP pathway; Type II methanotrophs are members of the α-proteobacteria and use the serine carbon assimilation pathway (see Reference 42). Both types have been shown to be capable of degradation of chlorinated compounds, including TCE (see Reference 42). Type I methanotrophs generally have only the pMMO, while Type II methanotrophs typically have both the soluble and particulate forms of MMO (see Reference 42), although there are exceptions. The goals of this study were to assess the phylogenetic diversity of methanotrophs in pristine ground water in the SRPA and to examine the genetic diversity of the MMO genes, and thus, the potential role of this group of bacteria in the observed attenuation of the TCE plume at TAN.

To determine the types of methanotrophs present in the SRPA, samples were acquired from four wells (ANP9, USGS 8, USGS 17, and USGS 112) in a pristine location. Three well volumes (calculated based on well depth, diameter, and pump rate) were purged prior to collection of water samples for molecular and culture based diversity analyses of methanotroph populations and for geochemical analysis. The total number of cells in the ground water was determined by acridine orange direct counts. Biomass for molecular analyses was collected via filtration of 100 L of ground water. Filters were immediately frozen in dry ice, transported to the laboratory, and stored at -80°C. DNA from the filters was extracted using a bead beating kit and then characterized using polymerase chain reaction (PCR), cloning, restriction fragment length polymorphism (RFLP), and sequencing. To determine if methanotrophs could be isolated from the ground water and to facilitate detection of genes otherwise undetectable in the environment, culture based enrichments were prepared from ground water using nitrate minimal salts (NMS) broth.[45] Cultures were incubated in the dark at 28°C using various gas mixtures in the headspace.

DNA primers (obtained from the literature and Reference 46) that specifically target 16S rRNA gene(s) in methanotrophs or genes, which code for subunits of soluble (*mmoX*) or particulate (*pmoA*) methane mono-oxygenase, were used to characterize the diversity of microbial populations. To identify unique amplified 16S rDNA or pMMO gene clones, approximately 50 clones from each well were screened by RFLP analysis. Clones possessing unique restriction patterns were identified and selected for sequencing. Sequencing was carried out at the INEEL or by Amplicon Express (Pullman, WA). Sequences were checked with Chimera Check from the Ribosomal Database Project II (RDP) (http://www.cme.msu.edu/RDP/html/index.html). 16S rDNA sequences were aligned against known sequences in the GenBank database using the gapped BLAST tool (http://www.ncbi.nlm.nih.gov/BLAST/) and percent relatedness to the closest relative was determined.

Water from each well was near neutral pH and oxic (see Table 4). In addition to these standard measures of water chemistry, water from the four wells was analyzed to determine the stable carbon isotope ratios in the methane and dissolved inorganic carbon. The methane from three of the wells yielded $\partial^{13}C$ values of about –61/mL, indicating that this methane is of biogenic origin (data not shown). While the stable carbon isotope ratios for the methane in the fourth well (ANP9) was heavier, that well also yielded somewhat lighter ratios for the stable carbon isotopes in the dissolved inorganic carbon suggesting that the methane had been oxidized by methanotroph communities. Total counts of microbial cells were between 10^3 and 10^4 cells/mL. Dissolved methane in the wells varied from near local atmospheric methane levels (3 nM) to significantly greater.

Table 4. Geochemical and microbial properties from sampled ground water at each well.

Condition	Well			
	ANP9	USGS 8	USGS 17	USGS 112
pH	7.86	7.7	7.89	7.62
Temp (C)	14.10	11.37	12.78	13.06
Dissolved Oxygen (mg/L)	8.43	8.18	9.65	8.63
Cell Mass (cells/ml)	3.9×10^3	1.7×10^3	3.3×10^3	3.7×10^3
Methane (nM)[a]	40	70–1050	50–90	1–6

a. ATM methane in water is about 3 nM.

RFLP and sequence analyses suggest that methanotroph populations vary between wells, and potentially, according to methane concentration. For example, USGS 8 had the highest dissolved methane concentration of the wells and the lowest RFLP 16S rDNA Type II diversity from enrichments, whereas USGS 112 had the lowest methane concentration and the highest RFLP 16S rDNA Type II diversity from enrichments. Although AODC indicated a very low biomass within the ground-water, bacterial 16S rDNA from the filtered ground water was detected from each well. However, only DNA from USGS 8 unenriched ground water could be used to directly detect Type I and Type II methanotroph specific 16S rDNA using PCR. This suggests that a more abundant methanotroph population (particularly Type I) may exist in ground water with higher dissolved methane levels.

A phylogenetic tree composed of 16S rRNA gene sequences from ground water enrichments and filters indicates the presence of multiple methanotrophs in the SRPA (see Figure 4). Both Type I and Type II methanotrophs were enriched from all wells, although enrichment tended to favor growth of Type II methanotrophs. Generally, differential enrichment, depending on NMS concentration, was consistent with an earlier report.[47] 1X NMS enriched for microorganisms that could be amplified using Type I methanotroph specific primers and the 0.2X NMS preferentially enriched for microorganisms that could be amplified using Type II primers. Analysis of sequence data indicate that Type I specific primers amplified 16S rDNA from enrichments for Type I methanotrophs related *to Methylomonas methanica* (97–99% identity) and *Methylobacter psychrophilus* (98% identity). Most of the 16s rDNA amplified from enrichments using Type II specific primers was most closely related to the Type II *Methylocystaceae* group (96–99% identity). In fact, RFLP pattern A (*Methylocystaceae*) was the predominant Type II 16S rDNA in all the wells. pMMO genes amplified from filtered ground water were closely related to the Type I *Methylobacter* (91% identity) and *Methylococcus* (87% identity) genus, and the Type II *Methylocystaceae* group (97–98% identity) (see Figure 5). One isolate (5) enriched from USGS 112, had genes for both sMMO and pMMO and thus is presumably Type II, although neither Type I nor Type II methanotroph 16S rDNA specific primers amplified the DNA from this isolate, suggesting a methanotroph population not yet detected with currently designed primers. Isolates 8 and 9 from ANP 9 displayed the pink pigmentation characteristic of methantrophs, and had a pMMO gene most closely related to the Type I *Methylomonas* genus. Microorganisms are significant components in the natural remediation of contaminants in the subsurface. Adequate understanding of the factors associated with microbial communities is an integral component to productive environmental management. The parameters involved in natural attenuation of a complex environment are not easily obtained. We developed and used molecular capabilities to help determine the ability of microorganisms to carry out natural attenuation of chlorinated solvents. Our investigation of the diversity of methanotrophs in the SRPA relates to the genetic capability of these TCE co-metabolizing microorganisms. We have identified several methanotrophs that may be participatory in the coabolic degradation of TCE at TAN. This work suggests that variations do exist between methanotrophic communities in wells with different methane concentrations.

Subtask 2

Radionuclide and metal contaminants are present in the vadose zone and ground water throughout the DOE weapons complex. Demonstrating in situ immobilization of these contaminants in vadose zones or ground water plumes is a cost-effective remediation strategy. However, the implementation of in situ remediation requires definition of the mechanism that controls sequestration of the contaminants. One such mechanism for metals and radio-nuclides is co-precipitation of these elements in authigenic calcite and calcite overgrowths. Calcite is a common mineral in aquifers and vadose zones in the arid western U.S. and can incorporate divalent metals such as strontium, cadmium, lead, and cobalt into its crystal structure by the formation of solid solutions. While calcite precipitation in aquifers in arid climates tends to be slow, encouraging certain microbial activities that are inherent to the aquifer can increase the rate of precipitation.

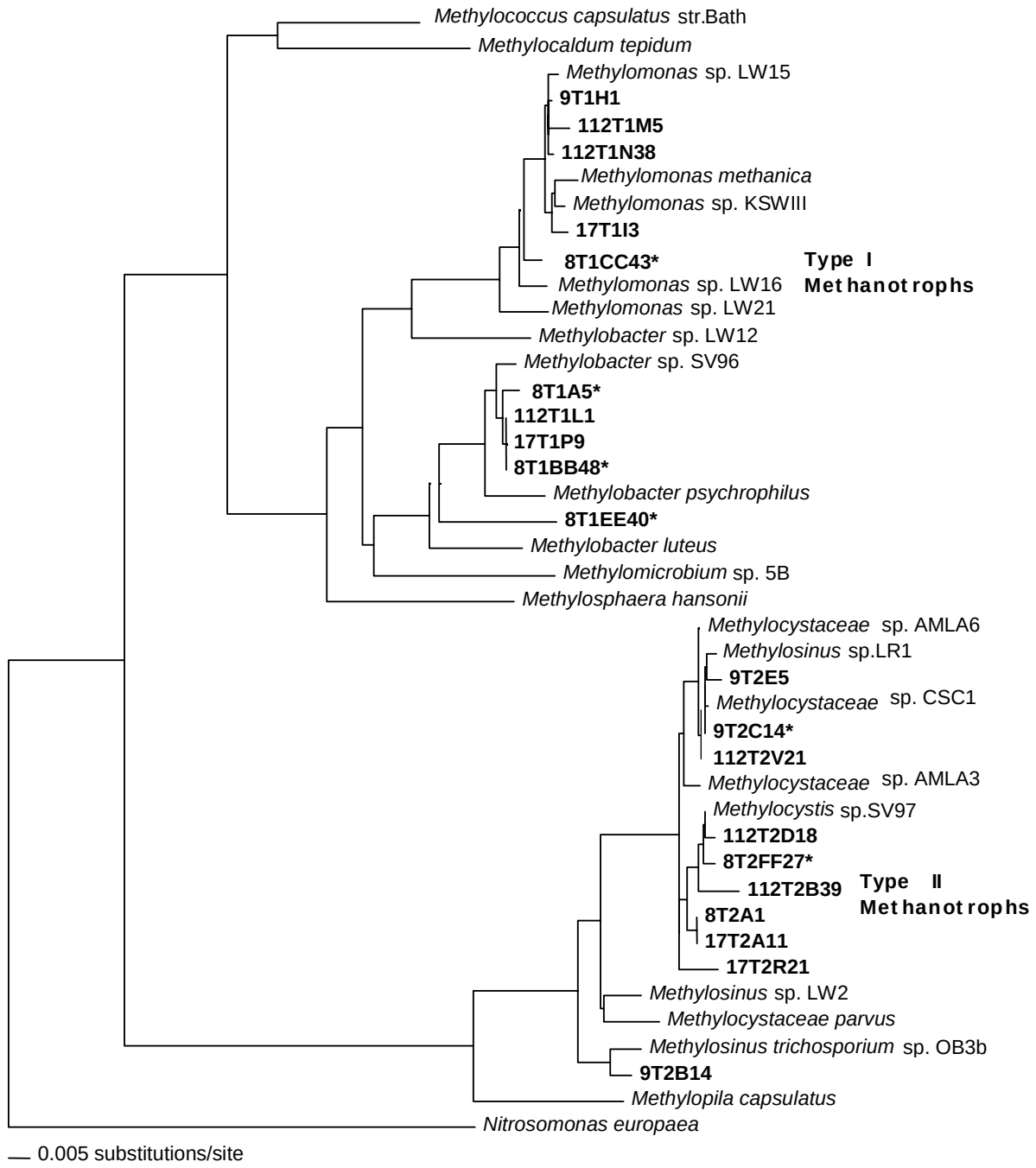

Figure 4. Phylogenetic relationships of 16S rRNA sequences from Type I and Type II methanotrophs. The phylogenetic tree was constructed as determined by the distance Jukes-Cantor analysis. The scale bar indicates 0.005 nucleotides per site. Unique clones obtained from wells ANP 9, USGS 8, USGS 17, and USGS 112 in the SRPA are indicated by boldface type. Type I (884 base pairs) and Type II (914 base pairs) sequences were obtained from enrichments or directly from ground water (specified by asterisk). The remaining sequences were obtained from the RDP or were obtained from GenBank and aligned with sequences from the RDP.

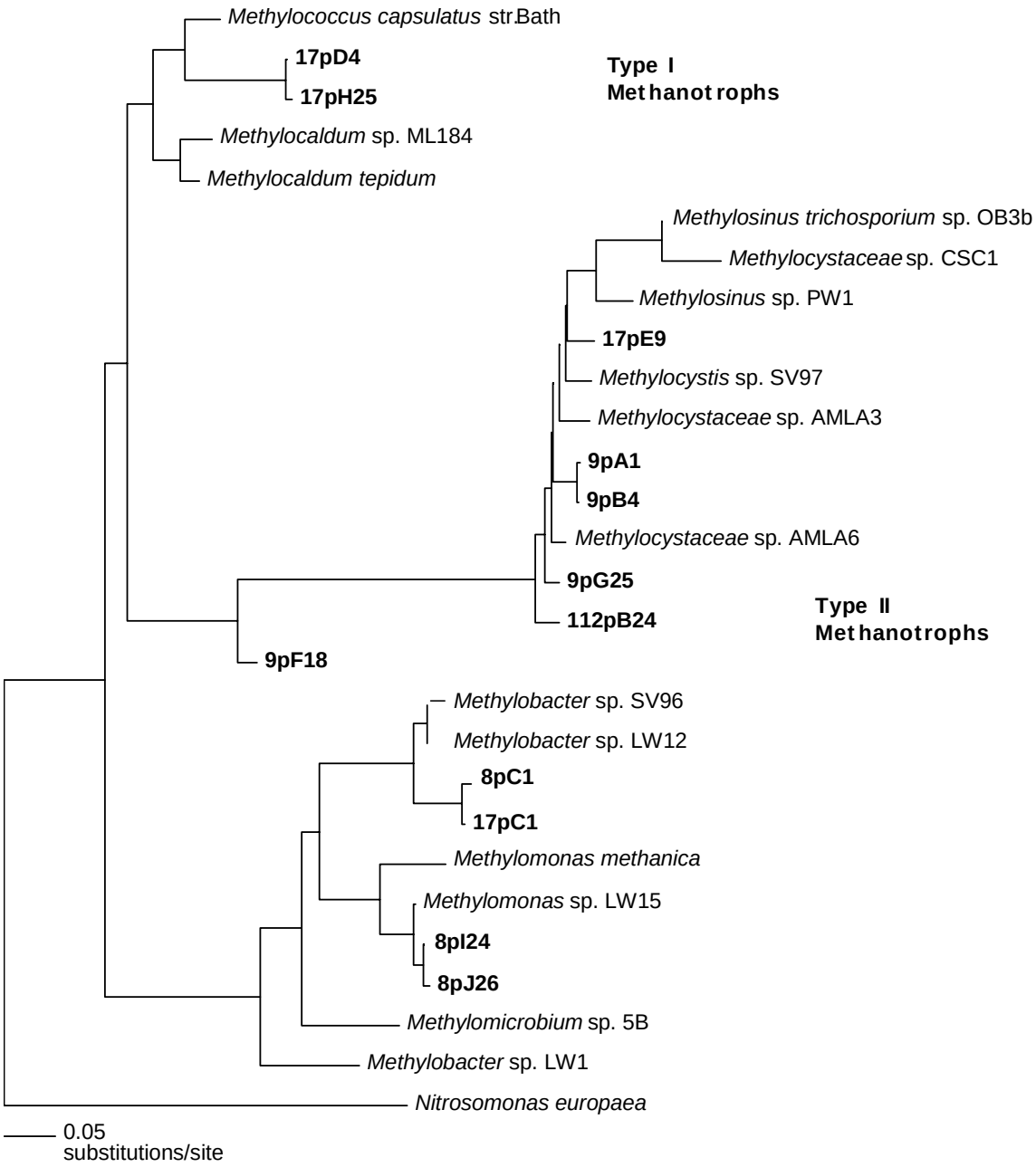

Figure 5. Phylogenetic relationship of *pmoA* gene sequences obtained from wells in the SRPA. The tree was constructed based on distance Jukes-Cantor analysis with a scale bar of 0.05 nucleotides per site. All sequences were extracted directly from ground water. Sequences analyzed were 283 base pairs according to *pmoA* specific primers. Unique clones from wells ANP 9, USGS 8, USGS 17, and USGS 112 are indicated by boldface type. The remaining sequences were obtained from GenBank.

Ureolytic microorganisms common in soils and waters can hydrolyze urea causing a gradual increase in the pH of the solution through the production of ammonia. The calcite precipitation reaction is sensitive to pH and occurs more rapidly at high pH. The research described herein used a single-well push-pull test to determine whether ureolytic aquifer microbial communities can be stimulated in situ through the introduction of urea.

The push-pull research was conducted in the Owsley-2 well near TAN, selected for its

availability and similarity to the ground water in that area. The total depth of the well is 310 ft and depth to standing water is 223 ft (Figure 6). The ground water has a pH of 8.0, a temperature of 14.5°C, and a conductivity of 328 µS/cm^3. Potentiometric surface determinations in the wells near Owsley-2 indicate that the ground water in this location has a gradient that is typical of the INEEL, varying between 4.1 and 15.2 ft per mile. Flow direction is generally to the south. Three draw-down tests conducted in Owsley-2 indicated the presence of multiple recharge sources within the well. Recovery of the well after the draw-down test was slow with the last foot of recovery taking several days. The shape of the recovery curve also suggests multiple recharge zones in the well. A bromide tracer study in the well indicated that while the tracer was displaced by ground water flow during the test, ground water flows in the well appear to be low relative to other places in the SRPA. The low ground water flow in this well was fortuitous, as it suggested that an effective push-pull test could be conducted with urea while minimizing the chance that the urea and the microbial product (ammonia) would be lost down-gradient. The low ground water flow rates allowed a longer "resting" phase and a longer period for urea hydrolysis to occur.

Lab studies indicated that microorganisms from the SRPA are unable to degrade urea unless a carbon source is added to the samples. When 0.1% molasses was used as a supplementary source of carbon and energy, significant urea hydrolysis and an accompanying increase in pH were detectable over a 35 day incubation period. Among the carbon sources that were tested, molasses was judged to be the best based on the amount of urea that was hydrolyzed and the degree of pH increase. Molasses additions caused an increase in cell numbers, as determined by turbidity; however, it was not believed to be high enough to cause plugging of the borehole by microbial biomass during the field test.

To begin the push-pull experiment, a solution containing potassium bromide as a tracer (~0.8 mM final concentration in the aquifer), urea (~30 mM final concentration in the aquifer), and

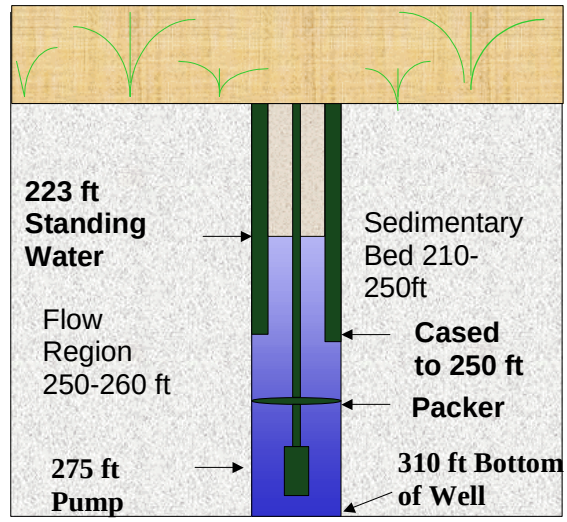

Figure 6. Cross-section view of Owsley-2 well used for push-pull research.

molasses (~0.1% final concentration in the aquifer) was injected into the SRPA at a specific depth interval below the casing using a packer pump. Prior to injecting the Br-urea-molasses solution water, samples were collected and analyzed for cations (calcium, magnesium, sodium, potassium, strontium), anions (bromide, chloride, sulfate, nitrate), urea, ammonia, temperature, conductivity, dissolved oxygen, redox, alkalinity, and pH. Total microbial cells, bacteria capable of hydrolyzing urea (urease-positive cells), and the kinetics of microbial urea hydrolysis were also analyzed in water before starting the experiment. After a 10-day rest period with no pumping, ground water was extracted from the same depth with the packer and analyzed for the same properties as described above. During the extraction phase, samples were collected daily and analyzed for all of the properties described above except microbial parameters that were determined over longer intervals.

Prior to the push-pull experiment, acridine orange direct microscopic counts (AODC) of bacterial cells in the ground water from the Owsley-2 well indicated the presence of 1.88×10^5 cells per mL ($\pm 1.77 \times 10^5$ S.D.) (see Figure 7). This number of cells is consistent with past determinations of cell numbers in the SRPA at other locations. The addition of urea and molasses caused the total cell numbers to increase by one

order of magnitude. Samples from the well were also used to determine the number of urease positive cells by most probable number (MPN) analysis. This culture-based method depends on the number of urease positive cells that can be grown in specific media and yielded a value of 12 ureolytic cells per mL (±2.83 S.D.) before starting the field experiment. This value is much lower than that typically derived from soil. Following the injection of urea the number of ureolytic cells increased 4-fold (Figure 7).

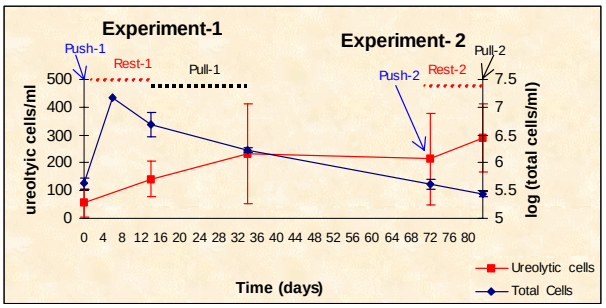

Figure 7. Values for total microbial cells and urease positive cells in ground water obtained from Owlsey-2 before, during, and after the push pull experiment. Total cells were determined by microscopic enumeration of acridine orange stained cells and urease positive cells were determined by most probable number enumeration in Urea R broth. Data represent the mean of samples taken in triplicate

Kinetic parameters of microbial ureolytic activity were investigated in ground water microbial cells obtained before, during, and after the push-pull test. The ground water samples were collected at the respective time points during the study, and returned to the laboratory. These samples were amended with different concentrations of urea and monitored for urea concentration changes over a 21-day period. Experiments were conducted aerobically with shaking at 22°C and 15°C. The addition of urea and molasses to the aquifer caused a decrease in the Km (Michaelis constant) which infers an increase in the affinity of the urease enzyme for urea (Table 5). At 4.6 mM (measured in the 15°C incubations), the Km of urease positive cells in the aquifer following the introduction of urea and molasses is much higher than most comparable values obtained in other environmental studies. This indicates that the cellular urease in the aquifer has a relatively low affinity for the substrate compared to soil systems.

Prior to the start of the field experiment, ground-water communities exhibited a Vmax of 0.69 µmol of urea hydrolyzed per mL per day (Table 5). When compared to published Vmax values for environmental ureases (largely from soils) this number is low indicating that in the SRPA prior to the push-pull test, the microorganisms within a given volume of ground water do not exhibit a high rate of urea turnover. These kinetic data were acquired over long lab incubation periods due to the low levels of activity in the samples. For this reason, the kinetic data need to be confirmed in short-term experiments in which urease positive populations are unlikely to fluctuate markedly. The addition of urea and molasses to the aquifer resulted in a lower Vmax for urea (0.19 µmol of urea hydrolyzed per mL/day), indicating that the experiment caused lower urease activity at high urea concentrations.

Table 5. Kinetic parameters for community urease activity in samples acquired from the Owsley-2 well before, during, and after the urea-molasses push-pull test.

Sample Name	Kmapp (mM urea)	Vmax (µmol urea hydrolyzed/mL/day)	Slope = Km/Vmax (/day)
Pre-injection 22C	62.45	1.27	49.32
Pre-injection 15C	24.23	0.69	61.23
Rest Phase 22C	3.58	0.295	12.16
Post-Extraction 22C	15.8	0.481	32.78
Post-Extraction 15C	4.58	0.194	23.63

The specificity constant (Vmax/Km) is used to determine the efficiency of the enzyme system. The more efficient the enzyme the higher the specificity constant. The most efficient urease activity was observed during the rest phase immediately after urea and molasses had been introduced to the aquifer (Table 5). The primary reason for this high specificity constant during the rest phase is the low Km (high affinity) for urea that occurred at this time. Based on data from the Lineweaver-Burke plots, the addition of urea and a carbon source to the aquifer appeared to stimulate urease activity at low urea concentrations.

The pH initially dropped and then rebounded to background concentrations (Figure 8). This was not the intended effect of the experiment as hydrolysis of urea is anticipated to yield higher pH values that would encourage calcite precipitation. Despite the fact that we observed an increase in the number of urease positive cells in the ground-water, we did not detect either a decrease in ground water urea concentrations or an increase in ground water ammonia concentrations (data not shown). The microbial fermentation of the molasses and the resulting production of organic acids can explain the drop in pH in this well. Unlike most wells in the SRPA, Owlsey-2 appears to be anaerobic and may be maintained in that condition by limited exchange with the vadose zone. Thus, calcite precipitation may have been inhibited by the unexpected decrease in pH.

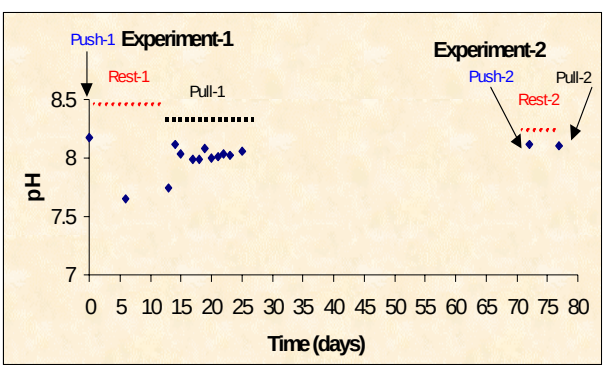

Figure 8. pH values obtained from Owsley-2 before, during, and after the push-pull test using a field portable Hydrolab minisonde water quality multiprobe.

Through this research, we have tested a push-pull approach to biostimulation in a fractured bedrock aquifer. We successfully caused a short-term increase in both the total numbers of microorganisms and numbers of urease positive microorganisms in the aquifer. Preliminary laboratory-derived values have been obtained for the urease kinetics of SRPA microbes prior to and after the addition of urea and molasses to the aquifer. The kinetics for community urea hydrolysis were altered during the field experiment and the values derived indicate a lower Vmax (lower maximal velocity of substrate turnover) and a higher Km (lower substrate affinity) than published research on samples collected from surface soils and waters. Although we did not note the desired increase in pH during the study, we believe that there is an explanation for this. The fermentation of the molasses that was added with the urea may have resulted in the production of organic acids, which caused the temporary decrease in pH in this portion of the SRPA. The local confinement of the SRPA at the Owsley-2 well would enhance anaerobic conditions that would encourage molasses fermentation.

Future investigations will be conducted in a section of the SRPA where molasses fermentation is less likely due to higher dissolved oxygen levels at the beginning of the experiment. This should encourage the increase in pH that the laboratory studies predict when urea is hydrolyzed by SRPA microorganisms. In this next field project we will conduct kinetic experiments using 14-C-labelled urea in laboratory studies so that Km and Vmax can be determined over a matter of hours rather than days. This will allow a more rapid and accurate assessment of the community kinetics for this compound. Eventually, this research will seek an opportunity to test the technology in an aquifer or vadose zone perched water that contains strontium-90 (Sr-90). Strontium is a primary target for this remedial technology because it is readily incorporated into calcite and Sr-90 has a relatively short radioactive half-life (30 yr) and so can decay away to safe levels within a short period. Furthermore, this work will aid in the development of estimates of in situ subsurface microbial activities (enhanced and background) based on the rate of substrate consumption or product formation. Such information will be important for the design of low

cost engineered solutions to subsurface contamination that are stable over long time periods. Our experience acquired through these field studies will help with the conceptualization of new applications of the push-pull technology for remediation or interrogation of the subsurface and of the calcite precipitation process.

Abiotic Constraints on Microbial Metal Reduction

The primary goal of Task 4 is to understand the qualitative and quantitative limits imposed on the function of anaerobic metal-reducing bacteria by abiotic, inorganic environmental components. Three specific questions evolved and were addressed in FY 2002:

1. How do pH and adsorbed trace metals affect attachment to, reduction of, and reduction products of Fe(III)-(hydr)oxides by *Shewanella* and *Geobacter* spp.?

2. What are the chemical characteristics of Fe and Mn oxides at the NABIR Field Research Center and how do the indigenous populations interact with them?

3. Are metal-reducing *Geobacteraceae* spp. capable of inhabiting metal-polluted sediments?

Subtask 1: Effects of surface molecules on cell attachment.

Shewanella oneidensis and *Geobacter sulfur-reducens* are two model dissimilatory metal-reducing bacteria that have received a good deal of attention of late. The entire genomes of both organisms have been completely sequenced and are being annotated currently. *Shewanella* spp. are frequently encountered in freshwater and estuarine sediments while *Geobacter* spp. are found commonly in freshwater surface and subsurface environments. Both of these organisms are capable of the anaerobic reduction of a wide variety of metal species such as Fe(III), Mn(IV), Cr(IV), U(VI), and Tc(VII). While reduction of Fe and Mn oxides leads to dissolution of the mineral and any adsorbates, reduction of soluble Cr, U, and Tc leads to their precipitation and immobilization. The metal-reducing bacteria, in particular *Shewanella* and *Geobacter* spp., may be useful for the bioremediation and/or natural attenuation of metal- and radionuclide-contaminated environments, such as are often encountered within the DOE Complex, including the INEEL.

Trace elements such as Ni, As, and P adsorb strongly to the surface of Fe and Mn oxides. Preliminary studies in late FY 2001 and early FY 2002 indicated that both arsenite and arsenate, of which arsenite is far more toxic to living cells, adsorbed to the surface of amorphous Fe(III)-oxyhydroxide (a.k.a. ferrihydrite) impeded the attachment of *Shewanella* cells to the mineral by approximately 20% at pH 7.0. Attachment of an iron reducer to the solid iron mineral is thought to be a critical step in the bioreduction process. To examine the effects of adsorbed trace elements on the attachment to, reduction of, and reduction products of Fe oxide reduction by *Shewanella* and *Geobacter* we have been using electrophoretic mobility (DELSA). It is anticipated that adsorbed arsenic reverses the surface charge of the ferrihydrite from net positive to net negative, thus causing electrostatic repulsion between the mineral and the negatively charged bacterial cell. Preliminary results support this hypothesis. We have also found that altering the pH of the buffer in which the cells and/or mineral are suspended can significantly change surface charge properties and may affect cell attachment.

Subtask 2: Molecular and microscopic effects of surface molecules on cell attachment.

In situ molecular methods offer a promising way to analyze surface colonization patterns in metal reducers. Currently, techniques exist that allow for this analysis, but further refinement is necessary. To this end, we continued work in the refinement of these techniques along several lines. First, better methods were needed that would detect presence of transcripts in whole-cell in situ PCR analysis. Second, solid-phase biochemical methods had to be developed that would actually show the expression of putative metal-reductase proteins. Third, methods for characterization of surface attachment and colonization by metal reducers needed to be used to ascertain the effects

of contaminant metals on surface colonization patterns.

Using the metal reducers *Geobacter sulfurreducens* and *Geobacter pelophilus*, new primers were developed that would recognize the presence of and expression of *ferA* (outer membrane cytochrome c). Out of five sets evaluated, one set (FERA1F/FERA1R) proved to be the most effective in RT-PCR experiments. This set targets the N-terminal coding region of *ferA*, which has a sequence unique from other membrane-associated cytochrome c genes in *G. sulfurreducens*. This allows for higher gene specificity, since it is now known that there are homologous c-type cytochromes present in the *Geobacter* genome.

Current in situ labeling technologies rely on hydrophobic fluorescent-labeled nucleotides, which cause problems in situ PCR because of strong nonspecific binding to minerals and cells. Although much of this background can be eliminated after extensive washing, the availability of alternative fluorphores needed to be addressed. A new generation of hydrophilic fluorophore-nucleotides was evaluated, and it was found that they were effectively incorporated into amplicons generated by RT-PCR reactions using *G. sulfur-reducens* 16S rRNA- and *ferA*-specific primers.

As an adjunct method, direct biochemical analysis of proteins produced by DMRB will be useful in confirming data obtained by molecular analysis. *G. sulfurreducens* was grown on minimal medium containing ferrihydrite as electron acceptor, and after sufficient colonization had developed, the ferrihydrite was harvested by centrifugation. The solids were suspended in a Tris buffer and lysozyme was added to disrupt cell walls. Finally, SDS was added to 1%, and the suspension extracted for 1 hour at room temper-ature. Solids were removed by centrifugation, and the resulting supernatant was concentrated by ultrafiltration. The extracts were then resolved on SDS-PAGE gels, and stained for hemoprotein (cytochrome c) content. The results of these experiments conclude that *ferA* is expressed in large quantity by *G. sulfurreducens* grown on ferrihydrite. Similar results were observed for analogous high-mass cytochrome c expression in *G. pelophilus*. This approach will be useful in 'profiling' cytochrome c metal reductase expression under different conditions, is amenable to solid-phase cultures, and will complement data obtained by other methods.

Wet-bench analysis of ferrihydrite colonized by *S. oniedensis* MR-1 in the presence of As (as AsO_4^{3-}) revealed an inhibition of surface colonization. To confirm these findings, microscopy was performed to look at surface colonization patterns in As+ and As- cultures. Ferrihydrite suspensions (with cells attached) were removed by centrifugation at low speed (200×g), and then stained with acridine orange. Fluorescence microscopy was performed, and colonization patterns were determined for the As+ and As- cultures. These observations show a distinctly different pattern of colonization, in that single-cell and small colony attachment were significantly inhibited in cultures containing As. Large colonies were observed in As+ cultures, but the frequency was lower than that found in As- controls. These results suggest that overall attachment is inhibited by As, but in areas where cell density becomes high, attachment is maintained.

Previous studies have not investigated the attachment of *G. sulfurreducens* to ferrihydrite in the presence of other metals and metalloids. Experiments were performed to compare attachment and colonization patterns of *G. sulfur-reducens* in response to presence of As. Staining and fluorescence microscopy were performed as described for *S. oniedensis*. Results were very similar in that presence of As inhibited attachment and colonization to ferrihydrite, although some limited attachment was still observed. The results from experiments with both *G. sulfurreducens* and *S. oniedensis* would suggest that As (as AsO_4^{3-}) inhibits microbial attachment, perhaps because of surface charge reversal, or limitation of attachment sites due to adsorbed arsenate.

Subtask 3: Microbe-metal interactions at the NABIR Field Research Center.

The DOE-NABIR Program has established a Field Research Center (FRC) at ORNL to focus investigators on a single site with complex

problems, hoping to attain sufficient understanding to implement a bioremediation program within the next decade. We examined the nature of the Fe and Mn oxides in the contami-nated and pristine subsurface sites at the FRC, and began microbiological analyses to determine community diversity and structure. Wet chemistry sequential extractions were performed on the subsurface sediments in order to operationally define the phase partitioning of Fe, Mn, and associated trace metals and radionuclides. These data are available on the NABIR FRC web page at http://public.ornl.gov/nabirfrc/pi.cfm. The most significant findings were (1) that the majority of Fe is poorly bioavailable and likely bound in mineralogical form, (2) that the majority of the Mn is in potentially bioavailable oxide forms, and (3) that Ni is co-distributed with potentially bioavailable Fe and Mn phases. The Fe- and Mn-bound Ni may influence the interactions between cells and the mineral, and thus deserves further attention.

Initial microbiological characterization of the sediments included aerobic heterotrophic plate counts, followed by isolation and identification of unique colony types. This method suggested that between 10^5 and 10^6 cells per g of background area sediments, which were predominated by *Pseudomonas* spp. Only one colony type could be found by this method in the contaminated sediments at a density of 10^2 cells per g; this isolate was identified as a species of *Brevibacillus*. DNA was extracted from sediments at both locations, but only DNA from the background area could be amplified by PCR. A clone library was constructed from amplified 16S rRNA genes and 100 clones screened. Twelve unique RFLP types were identified, and like the plate counts, the gene library also appears to be predominated by *Pseudomonas* spp.

Hematite biofilm coupons were deployed in the NABIR FRC wells from which we received sediment materials during their construction. The sterile hematite particles were allowed to incubate for eight weeks before being recovered and transported to the INEEL for molecular analyses of resultant biofilms. Intact biofilm PCR was developed and applied to the hematite particles to describe the biofilms. Briefly, whole hematite chips were used directly in PCR reactions without any sample preparation or DNA extraction. Full-length 16S rRNA genes were amplified and clone libraries constructed. The biofilm from the background area was more than twice as complex as that from the contaminated site, and only one or two taxa are held in common between them. The background area biofilm was predominated by *Acidovorax* spp. and *Dechlorimonas* spp., while the contaminated area was predominated by *Alcaligenes* spp. and *Frateuria* spp. *Alcaligenes* spp. are notoriously tolerant of metals such as Cr, Co, and Ni, all of which are abundant in the contaminated ground water, and many strains can denitrify nitrate to N_2O. *Frateuria* spp. are acidophiles, preferring pH 3.5–4.0. The pH in the contaminated area sediments is 3–4. Both taxa appear to be adapted to the harsh FRC conditions.

Subtask 4: Colonization of metal-polluted sediments by *Geobacteraceae* spp.

We examined the ability of Fe-, Mn-, and radionuclide-reducing *Geobacteraceae* spp. to inhabit the metal-polluted sediments of Lake Coeur d'Alene, Idaho. Clone libraries were constructed from sediments at three sites along a well-defined gradient of metal contaminants in the lake using PCR primers specific for the family *Geobacteraceae*. Of 148 clones, 16 unique phylotypes were identified spanning the entire phylogenetic breadth of the family. The most abundant clone, clone B14, was most similar to *Geobacter metallireducens*, and was distributed evenly at all three sites along the metals gradient. All other clones were restricted to one or two sites, and both the most contaminated and pristine sites shared no other clones. The next most abundant clone, clone Q2, predominated the most contaminated site and was most similar to two isolates from the same area, strains CdA-2 and CdA-3, suggesting a predominance of this type in the contaminated sediments. Real-time PCR was used to enumerate *Geobacter* genomes in the DNA extracts and found that very little difference existed among the three sites; MPN-PCR confirmed these results. The primary conclusion of the work is that *Geobacteraceae* spp. appear to have colonized the contaminated sediments in Lake Coeur d'Alene with equal success as the

pristine sediments, although the composition of the community is quite different.

ACCOMPLISHMENTS

Our FY 2002 accomplishments were as follows:

- We found evidence that attached and free-living aquifer microbial communities reacted differently when subjected to nutrient enrichment (biostimulation) conditions.

- We developed conceptual models for cell detachment from aquifer materials under field and laboratory column conditions and began testing the validity of these conceptual models.

- We found that theoretical shear forces that may be developed in representative basalt aquifers overlap the range of shear forces reported to remove attached bacteria.

- We found in laboratory column experiments that step increases in flow velocity resulted in an increased number of cells in the column effluent suggesting shear-related cell detachment.

- We demonstrated that the FTIR spectra from pure chemicals was not dependent on the mineral substrata and therefore, the changes noted in pure cells may be attributed to physiological changes.

- We demonstrated that differences in the TMO activities between attached and free-living cells can be attributed to their attachment to the mineral substrata and not to other experimental conditions.

- We determined that strongly water-wet systems comprised of two liquid components of similar densities such as water and dodecane are bounded by a fit coefficient that is different from those measured for systems of greater density difference.

- Wetting mediated by microbiological perturbations was observed for culture supernatants as well as culture sonicants. Supernatants from *Hydrogenoflava pseudoflava* and *Acintobacter genospecies* were slightly less water-wet than control systems and sonicants from the same organisms were less water-wet than the supernatants. In contrast, supernatants from *Rhodococcus luteus* were less water-wet than the sonicants of the same culture. *Arthrobacter globiformis* and *Bacillus atrophaeus* showed mixed wettability results. Although the most plausible mechanistic explanation for these observations is a discrete change in the surface tension mediated by the organisms, this is not the case because the measured tensions (video image analysis of inverted pendant drops) of the microbial systems are greater than the media control (Table 3).

- Sequencing results indicate that the *Methylocystaceae* is the predominant Type II methanotroph group in the SRPA. Results suggest that methanotroph populations vary with methane concentration, and that Type I and Type II methanotrophs can be enriched and detected from ground water containing very low methane concentrations (1-6 nM). Methanotrophs appropriate for the co-metabolic degradation of TCE are present in the SRPA, thus providing one plausible explanation for the natural attentuation of this chlorinated compound in the aquifer.

- Stable carbon isotope ratios for dissolved methane in the SRPA suggest a microbial source for the methane (del 13C values of about -61 per mil in three wells). The combination of 13C enriched methane and 13C depleted-dissolved inorganic carbon in one well suggests that microbial oxidation of methane occurs. These data help in the development of an intriguing story of microbial metabolism of C1 compounds that appears be occurring in the SRPA. This cycling of the simplest organic molecule (methane) by indigenous microbial communities in the deep basalt aquifer may benefit DOE's cleanup needs.

- We conducted the first push-pull experiment in the SRPA aimed at encouraging urea hydrolysis by indigenous microorganisms as a

means to enhance calcite precipitation and the co-precipitation of divalent cations. As a result of this study we observed a 10-fold increase in the total microbial biomass in the aquifer and a four-fold increase in the number of ureolytic cells. Also, the kinetics for community urea hydrolysis were altered during the field experiment and the values derived indicate a lower Vmax (lower maximal velocity of substrate turnover) and a higher Km (lower substrate affinity) than published research on samples collected from surface soils and waters. Our preliminary data indicate that the push-pull experiment induced a low Km (high affinity) for urea in the indigenous microbial community. The most efficient urease activity (as determined by a high specificity constant [Vmax/Km]) was observed during the rest phase immediately after urea and molasses had been introduced to the aquifer.

- We made the first observations that surface molecules can alter the ability of metal-reducing bacteria to adhere to metal oxides. This finding will provide the basis for future research including work to be supported by the INRA Program to examine mechanisms underlying selective attachment of *Shewanella* and *Geobacter* to various solid surfaces and the effects on activities and bioreduction products (funded with T. Magnuson, Idaho State University).

- We successfully obtained field samples from the NABIR FRC, normally reserved for NABIR-funded investigators. From these samples we determined that bioavailable forms of Fe and Mn control Ni distribution at the NABIR FRC. The impact of this association is unknown, but is certain to influence efforts to biostimulate metal-reducing bacteria at the site.

- The combination of hematite biofilm coupons for the recovery of uncultured microbes with the newly developed intact biofilm PCR dramatically improved our understanding of the diversity of microbes at the FRC. This combination of techniques needs to be adapted to other field sites, including those at the INEEL.

- We documented for the first time that metal-reducing *Geobacteraceae* spp. successfully colonize metal-polluted sediments. This finding has implications for the management of metal-contaminated sites worldwide.

Publications

Accepted or Published

Lehman, R. M., and S. P. O'Connell, "Comparison of Extracellular Enzyme Activities and Community Composition of Attached and Free-Living Bacteria in Porous Media Columns," *Appl. Environ. Microbiol.*, Vol. 68, No. 4, 2002, pp. 1569–1575.

O'Connell, S. P., and J. L. Garland, 2001, "Dissimilar Response of Microbial Communities in Biolog GN and GN2 Plates," *Soil Biol. Biochem.*, Vol. 34, pp. 413–416.

Submitted or in Preparation

Cummings, D. E., O. Snoeyenbos-West, D. T. Newby, A. M. Niggemyer, C. W. Passavant, D. R. Lovely, L. A. Achenbach, and R. F. Rosenzweig, "Colonization of Metal-Polluted Freshwater Lake Sediments by *Geobacteraceae* Species as Assessed by 16S rDNA Analyses," 2002. (in preparation)

Ingram, J. C., W. F. Bauer, R. M. Lehman, S. P. O'Connell, and A. D. Shaw, "Detection of Fatty Acids from Intact Microorganisms by Molecular Bean Static Secondary Ion Mass Spectrometry," *J. Microbiol. Meth*. (resubmitted)

Kauffman, M. E., and R. M. Lehman, "Fluorescent Probe for the Direct Visualization of Toluene-Oxidizing Bacteria on Mineral Surfaces," *Appl. Environ. Microbiol.*(in preparation)

Kauffman, M. E., W. Keener, M. E. Watwood, S. Clingenpeel, R. M. Lehman, "Activity-Dependent Enzyme Probe for Detection of Toluene-Oxidizing Bacteria Capable of Co-abolic Trichloroethylene Degradation," *Appl. Environ. Microbiol.*(in preparation)

Kauffman, M. E.,H-Y. Holman, M. Martin, W. F. Bauer, R. M. Lehman, "Biochemistry of Bacterial Attachment to Minerals using SR-FTIR," *Environ. Sci. Technol.*, (in preparation)

Lehman, R. M., . P. O'Connell, A. Banta, J. K. Fredrickson, F. J. Brockman, A-L. Reysenbach, T. L. Kieft, and F. S. Colwell. "Microbiological Analysis of a Fractured Basalt Aquifer by Sampling Attached and Free-Living Populations," *Geomicrobiol. J.* (in revision).

Newby, D. T., D. W. Reed, L. M. Petzke, A. L. Igoe, M. E. Delwiche, J. P. McKinley, F. F. Roberto, and F. S. Colwell, "Diversity of Methanotrophic Communities from a Pristine Basalt Aquifer," *Appl. Environ. Microbiol.* (in preparation).

O'Connell, S. P., D. E. Cummings, R. M. Lehman, O. Snoeyenbos-West, M. E. Watwood, and F. S. Colwell, "Detection of Archaeal DNA Sequences in an Oxic, Fractured Rock Aquifer," *FEMS Microbiol. Ecol.* (in revision).

Reardon, K., D. E. Cummings, B. Peyton, and G. G. Geesey, "Bacterial Diversity of U- and Tc-Contaminated Subsurface Sediments using Intact Biofilm PCR of Colonized Hematite Coupons." (in preparation)

Wilson, M. S., R. M. Lehman, S. E. Gilk, J. P. McKinley, M. E. Delwiche, and F. S. Colwell, "Enumeration of Methanotrophic Bacteria in a Deep Basalt Aquifer using Molecular and Culture-Based Approaches," *FEMS Microbiol. Ecol.* (in revision).

Presentations

Cummings, D., and J. Ingram, "Constraints on Microbial Metal Reduction in the Contaminated Subsurface," *General Meeting of the American Chemical Society, Orlando, FL*, 2002.

Cummings, D., J. Ingram, and M. Downing, "Effects of Arsenic on the Dissimilatory Metal-Reducing Bacterium Shewanella Putrefaciens," *General Meeting of the American Society for Microbiology, Salt Lake City, UT,* 2002.

Cummings, D., K. Reardon, B. Peyton, and G. Geesey, "Bacterial Diversity of U- and Tc-Contaminated Subsurface Sediments using In-tact Biofilm PCR of Colonized Hematite Coupons," *NABIR FRC Workshop, Oak Ridge, TN,* 2002.

Cummings, D., R. Fox, S. Fendorf, and J. Ingram, "Investigation of Metal Oxides in Subsurface Sediments at the NABIR Field Research Center using Wet and Spectroscopic Chemical Analyses," *NABIR Workshop, Warrenton, VA,* 2002.

Kauffman, M. E., and R. M. Lehman, "Nondestructive Imaging of Bacteria and Their Biochemical Alterations upon Attachment to Specific Mineral Phases of Basalt using Synchrotron Radiation-Based Fourier Transform Microspectroscopy," *General Meeting of the American Society for Microbiology, Salt Lake City, UT, May 2002*.

Kauffman, M. E., W. K. Keener, M. E. Watwood, R. M. Lehman, 2001, "Fluorescent Probe for the Detection of Toluene-Oxidizing Bacteria in Ground water and On Mineral Surfaces," *Annual Fall Meeting of the American Geophysical Union, San Francisco, CA, December 2001*.

O'Connell, S. P., R. M. Lehman, M. E. Watwood, and F. S. Colwell, "Impacts of Chemical Disturbance on the Diversity of Subsurface Microbial Communities," *Annual Meeting of the Ecological Society of America, Tucson, AZ, August 2002*.

Taylor, J. L., M. Delwiche, Y. Fujita, F. S. Colwell, M. Watwood, "Evaluation of Aquifer Urease Activities Using a Single Well Push-Pull Test," 2002, *General Meeting of the American Society for Microbiology, Salt Lake City, UT, May 2002*.

Taylor, J. L., M. E. Delwiche, Y. Fujita, T. Tyler, F. S. Colwell, M. Watwood, "Field Test of a Method to Co-precipitate Strontium with Calcite in a Fractured Basalt Aquifer," *Spectrum 2002, Reno, NV, August 2002*.

Taylor, J. L., Y. Fujita, M. Delwiche, F. S. Colwell, M. Watwood, "Evaluation of

Various Nutrient Additions for Enhancement of Urea Hydrolysis by Snake River Plain Aquifer Microorganisms," *Intermountain Conference on the Environment*, *Pocatello, ID, April 2002*.

Taylor, J. T., Y. Fujita, M. Delwiche, F. S. Colwell, and M. Watwood, "Urease Activity in Organisms Collected from the SRPA," *INRA/INEEL Subsurface Science Symposium*, *Idaho Falls, ID, 2001*.

REFERENCES

1. National Research Council, *Research Needs in Subsurface Science*, National Academy Press, Washington, D.C., 2000.

2. R. M. Lehman, F. S. Colwell, and G. A. Bala, "Attached and Unattached Microbial Communities in a Simulated Basalt Aquifer Under Fracture- and Porous-Flow Conditions," *Appl. Environ. Microbiol.*, Vol. 67, 2001, pp. 2799–2809.

3. R. M. Lehman, F. F. Roberto, D. Earley, D. F. Bruhn, S. E. Brink, S. P. O'Connell, M. E. Delwiche, and F. S. Colwell, "Attached and Unattached Bacterial Communities in a 120-Meter Corehole in an Acidic, Crystalline Rock Aquifer," *Appl. Environ. Microbiol.*, Vol. 67, 2001, pp. 2095–2106.

4. M. C. M. Van Loosdrecht, J. Lyklema, W. Norde, and A. J. B. Zehnder, "Influence of Interfaces on Microbial Activity," *Microbiol. Rev.*, Vol. 54, 1990, pp. 75–87.

5. R. M. Lehman and S. P. O'Connell, "Comparison of Extracellular Enzyme Activities and Community Composition of Attached and Free-Living Bacteria in Porous Media Columns," *Appl. Environ. Microbiol.*, Vol. 68, 2002, pp. 1569–1575.

6. A. Alfreider, M. Krossbacher, and R. Psenner, "Ground water Samples Do Not Reflect Bacterial Densities and Activity in Subsurface Systems," *Wat. Res.*, Vol. 31, 1997, pp. 832–840.

7. P. Hirsch and E. Rades-Rohkohl, "Some Special Problems in the Determination of Viable Counts of Ground water Microorganisms," Microb. Ecol., Vol. 16, 1988, pp. 99–113.

8. J. M. Thomas, M. D. Lee, and C. H. Ward, "Use of Ground Water in Assessment of Biodegradation Potential in the Subsurface," *Environ. Toxicol. Chem.*, Vol. 6, 1987, pp. 607–614.

9. F. S. Colwell and R. M. Lehman, "Carbon Source Utilization Profiles for Microbial Communities from Hydrologically Distinct Zones in a Basalt Aquifer," *Microb. Ecol.*, Vol. 33, 1997, pp. 240–251.

10. A. M. Gounot, "Microbial Ecology of Ground waters," in *J. Gibert, D. L. Danielopol, and J. A. Stanford (ed.), Ground water Ecology*, Academic Press, San Diego, CA, 1994, pp. 189–207.

11. T. C. Hazen, L. Jimenez, G. L. de Victoria, and C. B. Fliermans, 1991, "Comparison of Bacteria from Deep Subsurface Sediment and Adjacent Ground water," *Microb. Ecol.*, Vol. 22, pp. 293–304.

12. H. I. Essaid, W. N. Herkelrath, and K. M. Hess, "Simulation of Fluid Distributions Observed at a Crude Oil Spill Site Incorporating Hysteresis, Oil Entrapment, and Spatial Variability of Hydraulic Properties," *Water Resour. Res.*, Vol. 29, 1993, pp. 1753–1770.

13. B. H. Kueper and E. O. Frind, "Two-Phase Flow in Heterogeneous Porous Media 2, Model Application," *Water Resour. Res.*, Vol. 27, 1991, pp. 1059–1070.

14. M. Poulsen and B. H. Kueper, "A Field Experiment to Study the Behavior of Tetrachloroethylene in Unsaturated Porous Media," *Environ. Sci. Technol.*, Vol. 26, 1992, pp. 889–895.

15. J. L. Wilson, S. H. Conrad, W. R. Mason, W. Peplinski, and E. Hagan, *Laboratory*

Investigation of Residual Liquid Organics from Spills, Leaks and the Disposal of Hazardous Wastes in Ground water, EPA/600/6-90/004, 1990.

16. I. Chatzis, N. R. Morrow, and H. T. Lim, "Magnitude and Detailed Structure of Residual Oil Saturation," *Soc. Petrol. Eng. J.*, Vol. 23, 1983, pp. 311–326.

17. W. G. Anderson, "Wettability Literature Survey—Part 4: Effects of Wettability on Capillary Pressure," *J. Petrol. Technol.*, Vol. 39, 1987, pp. 1283–1300.

18. E. C. Donaldson and R. D. Thomas, "Microscopic Observations of Soil Displacement in Water-Wet and Oil-Wet Systems," *SPE 3555 SPE Annual Technical Meeting*, 1971.

19. N. R. Morrow, "Wettability and its Effect on Oil Recovery," *J. Petrol. Technol.*, Vol. 42, 1990, pp. 1476–1484.

20. S. E. Powers and M. E. Tamblin, "Wettability of Porous Media after Exposure to Synthetic Gasolines," *J. Contam. Hyudrol.*, Vol. 19, 1995, pp. 105–125.

21. J. Jan, H. Plancher, and N. R. Morrow, "Wettability Changes Induced by Adsorption of Asphaltenes," *SPE Prod. & Facil.*, November 1997, pp. 259–266.

22. A. H. Demond and P. V. Roberts, "Effect of Interfacial Forces on Two-Phase Capilary Pressure-Saturation Relationships," *Water Resour. Res.*, Vol. 27, 1991, pp. 423–437.

23. W. G. Anderson, "Wettability Literature Survey—Part 1: Rock/Oil/Brine Interactions and the Effects of Core Handling on Wettability," *J. Petrol. Technol.*, Vol. 38, 1986, pp. 1125–1144.

24. L. W. Dekker and C. J. Ritsema, "How Water Moves in a Water Repellent Sandy Soil, 1, Potential and Actual Water Repellency," *Water Res. Res.*, Vol. 30, 1994, pp. 2507–2519.

25. N. R. Morrow, "The Effects of Surface Roughness on Contact Angle with Special Reference to Petroleum Recovery," *J. Can. Petrol. Technol.*, Vol. 14, 1975, pp. 42–53.

26. S. A. Bradford and F. J. Leij, "Fractional Wettability Effects on Two- and Three-Fluid Capillary Pressure-Saturation Relations, *J. Contam. Hydrol.*, Vol. 20, 1995, pp. 89–109.

27. R. J. S. Brown and I. Fatt, "Measurements of Fractional Wettability of Oilfield Rocks by the Nuclear Magnetic Relaxation Method," *Trans. Am. Inst. Min. Metall. Pet. Eng.*, Vol. 207, 1956, pp. 262–264.

28. R. A. Salatheil, "Oil Recovery by Surface Film Drainage in Mixed-Wettability Rocks," *J. Petrol. Technol.*, Vol. 255, 1973, pp. 1212–1224.

29. A. H. Demond, F. N. Desai, and K. F. Hayes, "Effect of Cationic Surfactants on Organic Liquid-Water Capillary Pressure-Saturation Relationships," *Water Resour. Res.*, Vol. 30, 1994, pp. 333–342.

30. N. R. Morrow, "Capillary Pressure Correlations for Uniformly Wetted Porous Media," *J. Can. Petrol. Technol.*, Vol. 15, 1976, pp. 49–69.

31. S. Ma, N. R. Morrow, and X. Zhang, "Generalized Scaling of Spontaneous Imbibition Data for Strongly Water-Wet Systems," *J. Pet. Sci. & Eng.*, Vol. 18, 1997, pp. 165–178.

32. J. Jan, H. Plancher, and N. R. Morrow, "Wettability Changes Induced by Adsorption of Asphaltenes," *SPE Prod. & Facil.*, November 1997, pp. 259–266.

33. C. C. Mattax and J. R. Kyte, "Imbibition of Oil Recovery from Fractured, Water Drive Reservoir," *Soc. Pet. Eng. J.*, June 1962, pp. 177–184.

34. G. Hamon and L. V. Vidal, "Scaling-Up the Capillary Imbibition Process from Laboratory

Experiments on Homogeneous and Heterogeneous Samples," SPE 15852, *Euro. Pet. Conf.*, London, 1986.

35. X. Zhang, N. R. Morrow, S. and Ma, "Experimental Verification of a Modified Scaling Group for Spontateous Imbibition," SPE 30762, *Annual Technical Conference,* November 1996.

36. K. S. Sorenson, L. N. Peterson, R. E. Hinchee, and R. L. Ely, "An Evaluation of Aerobic Trichloroethene Attenuation using First-Order Rate Estimation," *Bioremed. J.*, Vol. 4, 2000, pp. 337–357.

37. J. Schramke, E. Murphy, B. Wood, "The Use of Geochemical Mass-Balance and Mixing Models to Determine Ground water Sources," *Appl. Geochem.*, Vol. 11, 1996, pp. 523–539.

38. A. J. Auman, S. Stolyar, A. M. Costello, and M. E. Lidstrom, 2000, "Molecular Characterization of Methanotrophic Isolates from Freshwater Lake Sediment," *Appl. Environ. Microbiol.*, Vol. 66, pp. 5259–5266.

39. M. Bender and R. Conrad, "Methane Oxidation Activity in Various Soils and Freshwater Sediments: Occurrence, Characteristics, Vertical Profiles and Distribution on Grain Size Fractions," *J. Geophys, Res.*, Vol. 99, 1994, pp. 16531–16540.

40. L. A. Buchholz, J. Valklump, M. L. P. Collins, C. A. Brantner, and C. C. Remsen, "Activity of Methanotrophic Bacteria in Green-Bay Sediments," *FEMS Microbiol. Ecol.*, Vol. 16, 1995, pp. 1–8.

41. A. M. Costello and M. E. Lidstrom, "Molecular Characterization of Functional and Phylogenetic Genes from Natural Populations of Methanotrophs in Lake Sediments," *FEMS Microbiol. Ecol.*, Vol. 65, 1999, pp. 5066–5074.

42. R. S. Hanson and T. E. Hanson, "Methanotrophic Bacteria," *Microbiol.*, Rev. 60, 1996, pp. 439–471.

43. A. A. Dispirito, J. Gulledge, J. C. Murrell, A. K. Shiemke, M. E. Lidstrom, and C. L. Krema, "Trichloroethylene Oxidation by the Membrane Associated Methane Mono-oxygenase in Type I, Type II and Type X Methanotrophs, *Biodegradation*, Vol. 2, 1992, pp. 151–164.

44. R. Oldenhuis, J. Y. Oedzes, J. J. Van der Waarde, and D. B. Janssen, "Kinetics of Chlorinated Hydrocarbon Degradation by Methylosinus Trichosporium OB3b and Toxicity of Trichlorethylene," *Appl. Enivron. Microbiol.*, Vol. 57, 1991, pp. 7–14.

45. R. S. Hanson, "Ecology of Methylotrophic Bacteria," in R. S. Burlage, R. Atlas, D. Stahl, G. Geesey, and G. S. Sayler (eds), *Techniques in Microbial Ecology*, Oxford University Press, New York, 1998, pp. 137–162.

46. D. W. Reed, D. T. Newby, M. E. Delwiche, A. Igoe, J. P. McKinley, F. F. Roberto, Colwell, F. S., "Diversity of Methanotrophic Communities in a Pristine Basalt Aquifer: Implications for Natural Attenuation of TCE," *Eos Trans. AGU. 82 (47) Fall Meeting Suppl.*, Abstract B42B-0138, 2001.

47. M. G. Wise, J. V. McArthur, and L. J. Shimkets, "Methanotroph Diversity in Landfill Soil: Isolation of Novel Type I and Type II Methanotrophs Whose Presence was Suggested by Culture-Independent 16S Ribosomal DNA Analysis," *Appl. Environ. Microbiol.*, Vol. 65, 1999, pp. 4887–4897.

Interfacial Processes Controlling Fate and Mobility of Actinides, Fission Products, and Other Contaminants

Gary S. Groenewold and George D. Redden

SUMMARY

Radionuclide contamination in mixed waste burial grounds poses a long-term threat to the underlying ground water because the contamination is susceptible to hydrological, chemical, and biological perturbations that could significantly alter its stability and enhance its transport within the subsurface. However, the majority of the interred contamination is stable over the near-term with respect to subsurface transport. Specific factors with a higher probability for perturbing radionuclide transport behavior are (a) extended radionuclide-mineral contact time, (b) periodic wetting and drying cycles, (c) colloids, and (d) microbial ligands.

We initiated this task in 2001 with the goals of evaluating these transport-perturbing factors and understanding their behavior in terms of radionuclide speciation on relevant mineral surfaces. This report describes the progress made by the project at the conclusion of FY 2002, which was originally scoped for 3 years. When complete, this project will provide a defendable assessment of whether these perturbations could significantly augment radionuclide transport in the subsurface. In some cases, radionuclide solubilization may be inhibited, which may suggest approaches for manipulation of contaminated zones such that risk from mobilization is decreased. We also pursued characterization approaches for identifying radionuclide surface speciation.

PROJECT DESCRIPTION

Actinide contamination in the geological subsurface is a widely recognized problem across the DOE complex.[1] It exists in contaminated zones together with radioactive fission products and organic compounds, which in aggregate, comprise source terms that have the potential for substantial environmental damage. In particular, mobile forms of the actinides and fission products could threaten underlying aquifers if they were transported through the vadose zone, but at the present time, the threat to the aquifer is probably not acute, since radionuclide contamination by and large does not appear to be moving rapidly through the subsurface. For example, actinides have been buried at the Radioactive Waste Management Complex (RWMC), but only trace amounts have been detected in the perched water zones.[1,2] Nevertheless, these detections may indicate radionuclide movement, which would imply that some processes mobilize radionuclides, and that interment sites may be susceptible to events that enhance transport.

The contamination history, hydrology, geology, and geography of the INEEL (and other arid western DOE sites) point to several factors that have the potential to perturb radionuclide mobility and extend radionuclide-mineral contact time,[3] periodic wetting and drying cycles, colloidal transport,[4] and microbial ligand production.[3]

Extended Radionuclide-Mineral Contact Time. Radionuclide waste has been interred at the INEEL for over 40 years. The effect of contaminant-matrix contact time has not been widely studied, and processes that act over long time scales could serve to either increase or decrease radionuclide mobility. In the case of Cs, kinetically slow occupation of thermodynamically favorable clay-sorption sites would serve to decrease lability and hence mobility, provided the clay minerals themselves are fixed in the subsurface. On the other hand, if the clay minerals are slowly suspended (colloidal), then the sorbed radionuclides could be transported with the clay functioning as a transport vector through the subsurface. Another possibility is that infiltration of native cations over time would slowly displace radionuclides from strongly-binding surface sites to more weakly-binding sites, thus increasing lability and mobility. These considerations, and the fact that radionuclide waste will require long-term stewardship, have motivated the initiation of

research to evaluate changes in the sorption and lability of radionuclides over periods of extended contact with the mineral matrix. This research is conducted within Subtask 1, "Reversibility, Equilibrium, Forward and Reverse Reaction Kinetics, and Reversibility of Surface Reactions Over Extended Contact Periods."

Periodic Wetting and Drying Cycles. In addition to extended contact time, periodic wetting and drying could also alter radionuclide lability and transport within INEEL sediments. This condition arises when the spring snowmelt saturates the soil and enables downward permeation of soil water into the underlying fractured basalt. Subsequently, the prevailing arid conditions are reestablished, and the soil is dried via evapotranspiration. Radionuclide speciation and solubilization behavior may be subject to alteration as a consequence of these periodic wetting and drying cycles. Subtask 2, "Periodic Wetting and Drying Cycles and Their Potential for Altering Radionuclide Transport," was initiated to determine whether modified radionuclide speciation and mobility was occurring as a consequence of these cycles.

Colloidal Transport. A third factor that could alter radionuclide mobility is the behavior of the colloidal fraction of the geosphere. Colloids are variably defined, but all definitions place them in the 10 nm to 10 μm size range. Colloids can be highly adsorptive toward radionuclides and other metals, and are different from other mineral matter in that they can be suspended in water without truly being dissolved. These two attributes make colloids a potential vector for the fast transport of radionuclides, which would otherwise be immobile due to insolubility. The role that colloids might play in transporting radionuclides from mixed waste burial grounds to underlying zones of fractured flow has not been established; consequently, we initiated Subtask 3, "Colloid-Facilitated Radionuclide Transport." The behavior of the native colloids was the starting focus of the task, acknowledging that bioorganic and or actinide-rich (actinide-core) colloids may also play a role in the radionuclide transport, and must also be investigated.

Microbial Ligand Production. Finally, microbially generated ligands could alter radionuclide speciation and significantly impact contaminant transport within the subsurface. Because the nature of ligands produced depends on the type of microbial consortium employed, as well as the redox state and nutritional composition of the soil system, it is possible that microorganisms could either mobilize or sequester radionuclides depending on how these factors interact within INEEL sediments. Consequently, Subtask 4, "Microbial Ligand-Modified Transport," was initiated. This task is extremely complex and poses tremendous experimental challenges. Initially, we sought to determine whether a native microbial population could produce ligands capable of binding UO_2^{+2}, and determine the effect of ligation on UO_2^{2+} speciation and transport within a ground water mineral matrix. These experiments were intended to enable formation of more specific hypothesis focused on determining the identity of the active ligands, their mode of action, and their ability to alter radionuclide transport under field or simulated field conditions.

The approach chosen for investigation of factors having a high potential for altering radionuclide mobility was to establish phenomenological behavior specific to INEEL soils and conditions, and to utilize surrogate isotopes that exactly mimic the sorption and transport behavior of the target radionuclides. Soil samples collected at, or near RWMC on the INEEL were used for sorption and spectroscopic studies. These soils were chosen for study from the in situ vitrification pit (ISV soil) and from settling area B (SAB soil), a flood water infiltration zone. These soils are similar to each other in terms of particle size distribution, chemical composition, and mineralogy, but RWMC soils are highly heterogeneous, consist of a mixture of quartz and clay particulates, and tend to be coated with iron oxides that have the potential for strongly influence sorption behavior. Sediment heterogeneity results in experimental complexity that cannot be avoided. However, as this is the material with which the radionuclides interact, interactions with this specific material must be understood as a first step in evaluating possible transport.

Contaminant elements of interest have long-lived radionuclides that pose a risk to ground water. In general, use of the actual radioactive isotopes was minimized to avoid difficulty in dealing with radioactive waste. Instead ^{88}Sr, ^{133}Cs, and natural abundance U (low ^{235}U) were used in the present sorption and transport experiments. In our opinion, there are no suitable surrogates for Pu, Am, and Np, and sorption experiments were performed that used these radioelements.

Determining whether sorption and transport were perturbed by extended contact times, periodic wet-dry cycles, colloid behavior, or microbial ligands initially required a thorough understanding of sorption under 'normal' conditions. For this reason, solid/solution partitioning, cation exchange capacities, sorption hysteresis phenomena, and sequential extractions were investigated. These studies established benchmark sorption behavior against which contact time, wet-dry cycle, colloidal, and bioligand studies will be compared. All sorption studies were complemented with surface analyses in order to provide a molecular surface understanding of the interfacial processes responsible for sorption. The surface spectroscopic examinations focused on secondary ion mass spectrometry (SIMS), a historical strength at the INEEL.[5] Prior research demonstrated that unique SIMS instrumentation was capable of highly specific detection of surface absorbed organics, and more recent research suggests that cation surface speciation could also be achieved. Ultimately, it is hoped that SIMS can be used to generate surface speciation and concentration information in a facile manner, which will enable fast and accurate assessments of contamination history and the likelihood of radionuclide desorption.

Synchrotron radiation techniques,[6] specifically extended x-ray atomic fine structure (EXAFS) are acknowledged to be the technique of choice for explicit determinations of surface speciation, and are capable of generating a level of detail that is superior to a SIMS approach in many respects. SIMS is nevertheless being pursued because it is more surface specific (using a polyatomic projectile), more sensitive, and easily accommodates natural mineral samples. It is further attractive because the data is easily interpreted, is fast enough to support sorption studies, and does not require a synchrotron radiation source. Several characterization challenges exist, however, in using SIMS for biogeochemical surface characterizations, which served to focus the analytical research over the course of the project. The research addressing these challenges is described in Subtask 5, "Surface Speciation." We conducted benchmark analyses of radionuclide salt forms to improve recognition of surface precipitates and adsorptive mineral moieties, with an emphasis (ongoing) on carbonate and clay. Speciation recognition research was extended to analysis of exposed soils subjected to adsorption isotherm experiments. These experiments provided a sample set having variable surface speciation and cation concentrations, which provided an ideal training set for surface speciation and quantitation using SIMS.

One long-term objective of surface characterization research is not only to understand composition and speciation, but to ultimately be able to forecast reactivity. The ability to directly observe reactions as they proceed, identifying pathways and measuring kinetics, would greatly aid understanding of biogeochemical interfacial processes. A unique attribute of the ion trap SIMS instrumentation is that it is capable of generating and mass-isolating reactive surface moieties in the gas phase, where their reactions can be readily studied from a temporal perspective, and hydration conditions can be explicitly controlled.[7] Fundamental studies of hydration reactions of silicate and aluminate were completed in 2001, and reactions of chromium oxyanions were initiated. In the past year, the Cr oxyanion reactivity studies were largely completed.

Radionuclide solution speciation is equally important in dictating solubilization or sequestration events. In those instances where one or two metals are in solution, or where there is a single ligand, solution-phase speciation is well understood. However, the situation becomes much more complex in those instances where multiple metals and ligands are present in heterogeneous systems. Identification of the speciation in solution is particularly difficult when the radionuclides are complexed by bioorganic ligands, most of which have not been rigorously characterized. It was felt

that despite this complexity, solution speciation could be understood by using electrospray ionization-mass spectrometry (ESI-MS), which has been successfully applied to a vast range of bioorganic and organometallic analyses over the past two decades.[8,9] The INEEL does not currently possess ESI-MS instrumentation equipped with multiple stage MS capability that could support radionuclide-partitioning research, therefore analytical support in this area was solicited from Wichita State University, where prior collaborative arrangements had been made. Initial speciation results of uranyl with solvent and saccharide ligands were completed.

Subtask 1: Reversibility, Equilibrium, Forward and Reverse Reaction Kinetics, and Reversibility of Surface Reactions Over Extended Contact Periods

This multiyear task has five objectives:

- Determine the rate and extent of adsorption and desorption of selected radionuclides and fission products on INEEL RWMC surficial sediments. This activity is critical for providing the benchmark adsorption behavior needed to quantify the influence of perturbing factors, including extended contact time.
- Identify the metal adsorbing mineral surfaces present on and in INEEL RWMC surficial sediments.
- Identify the physical and chemical properties that most influence metal adsorption and desorption on those mineral surfaces.
- Determine the extent to which those physical and chemical properties influence forward and reverse metal sorption behavior.
- Evaluate the consequences of long-term contact times on metal partitioning into and onto various adsorbing surfaces.

Sorption of Cs^+ to RWMC Sediments

Long-term sorption studies for Cs and Sr on ISV and SAB soils were initiated in FY 2000. Samples were prepared using nanopure water, synthetic ground water (SGW), and SGW having 2, 5, 10, and 20 times the initial ionic strength. In addition, each metal, soil, and SGW concentration was prepared at pH 3, 6, 6.5, 7, 7.5, 8, and 8.5 to determine the influence of pH changes on metal sorption/partitioning. The influence of ionic strength and pH on adsorption and desorption was also deduced from these experiments. The influence of long contaminant-matrix contact time will be assessed in FY 2003.

Short-term (18–24 hour) adsorption studies were completed. These provided a detailed understanding of pH and ionic strength perturbations on Cs and Sr sorption on ISV and SAB soils. Decreasing pH caused increased mobility for both Cs and Sr on both soils at all ionic strengths. Similarly, increased ionic strength also resulted in increased mobility. This detailed information enabled the development of a more versatile multiparameter model for Sr^{2+} adsorption that had far greater predictive power than simple solution/solution partitioning constants (K_d) values, which are applicable only to the specific contaminant/matrix system for which they were generated. In FY 2002, a multiparameter model was completed for Sr. The model was based on the experimental data that corresponded well with literature reports of metal sorption to similar sediment matrixes. This enabled development of a theoretical foundation for interpretation of these data in terms of fundamental geochemical mechanisms—thereby providing an improved predictive modeling capability.

Sorption of Cs^+ to RWMC sediments was empirically modeled using two Freundlich isotherms, which was consistent with the involvement of multiple adsorption sites. This conclusion was consistent with the complexity of the RWMC sediments (a quartz/illite/smectite mixture). The data in Figure 1 were generated from this study, and include values published in the literature: the more steeply sloped line ($y = 85.8x^{0.71}$) generated using low Cs^+ exposures had a power coefficient (0.71) consistent with the

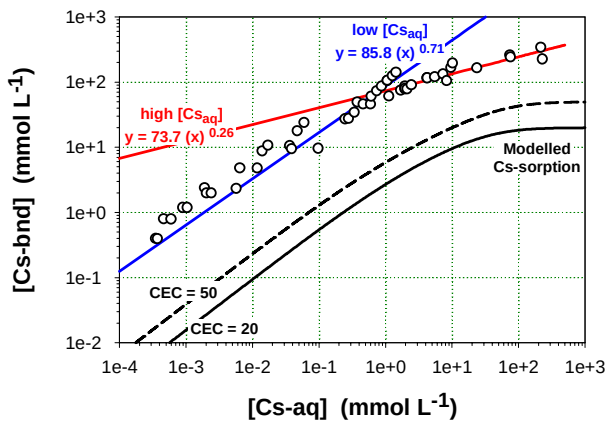

Figure 1. Adsorption data and models for Cs^+ adsorption on RWMC sediments. The black circles are data from this study and from published data. The blue and red lines are Freundlich isotherms that empirically describe data on either end of the concentration ranges. The black lines are geochemical adsorption models generated using two CEC values.

literature, but the 'effective K_d' of 85.8 was ~4 times greater than what was previously reported. This discrepancy is most readily explained by the existence of highly selective adsorption sites on the clay edges. We hypothesize that the clay mineral assemblages present in INEEL sediment (mixture of illite, smectite, and kaolinite) are 10–50 times more selective for Cs^+ than "typical" natural clays. Zachara et al. have reported that muscovite fragments in Hanford sediments have Na-Cs selectivity coefficients of ~100 times greater than "typical" at a small number of "frayed edge sites.[10] Thus, it is not unreasonable that INEEL sediments display greater Cs^+ selectivity compared with "typical" sediments.

Higher than anticipated Cs^+ selectivity is probably also responsible for the significant under calculation of sorbed Cs^+. Using *Geochemist's Workbench*© geochemical modeling package, Cs sorption on INEEL-RWMC sediment was modeled by employing generalized ion selectivity coefficients for natural clay minerals. This showed that the adsorption isotherm shape can be reproduced using a clay adsorption conceptual model, but that there is an offset between one and two orders of magnitude depending on the cation exchange capacity (CEC) used (see black lines in Figure 1). The difference between the adsorption models and data again points to the involvement of highly selective adsorption sites in the soil samples. Experiments to quantify Cs^+ selectivity on INEEL sediments are currently underway, and results will be incorporated into an updated Cs^+ sorption model.

The more modestly sloped line ($y = 73.7x^{0.26}$) in Figure 1 agreed reasonably well with literature reports of Cs sorption to natural clay minerals,[11] which underscored the fact that Cs^+ sorption on INEEL sediments was influenced by multiple mineral forms and processes.

Sorption of Sr^{2+} to RWMC Sediments

Sr^{2+} sorption can be accurately described using a 2-site Langmuir isotherm (see Figure 2), but such an empirical description does not provide any interpretive value and cannot predict Sr^{2+} sorption under perturbed conditions. A more robust theoretical framework was needed before a chemically meaningful explanation of the effects of contact time and wet-dry cycling on Sr^{2+} sorption to INEEL sediments could be developed, and hence more rigorous geochemical modeling was undertaken. Literature reports indicated that Sr^{2+} geochemistry was predominantly controlled by formation of solid solutions with $CaCO_3$ minerals in most natural systems.[12–17] The geochemical equilibrium code *PHREEQC*© was used to model the effect of competition among Sr^{2+} ion exchange, Sr^{2+} complexation with surface iron oxides, and [Sr, Ca]CO_3 mineral formation on overall Sr^{2+} sorption to INEEL-RWMC sediments. The possible involvement of these processes constituted the initial assumptions for the modeling, and were supported by the composition of the soil matrix and the processes Sr^{2+} is likely to participate in.

Comparison of model predictions with observed results (see Figure 2) showed that Sr^{2+} sorption is controlled by the formation of [Sr, Ca]CO_3 solid solutions, and that the initial precipitate is can be loosely described as an ideal solid solution of aragonite, calcite, and strontianite. Even though the ideal solution model gives a reasonable fit to the data, a closer inspection

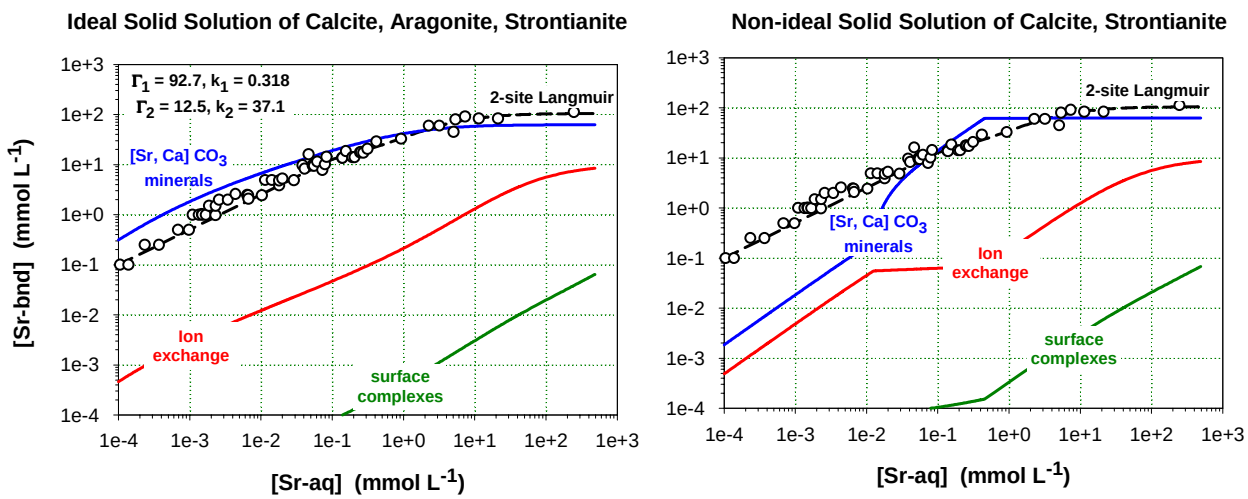

Figure 2. Left, Sr^{2+} adsorption, modeled using an ideal solution of $[Sr,Ca]CO_3$. Black circles represent data from this study. Black dashed line represents a two-site Langmuir model. Blue line represents Sr adsorption dominated by formation of an ideal solid solution of [Sr,Ca] carbonates. Red and green lines represent Sr adsorption controlled by ion exchange and surface complexation, respectively. Right, Sr^{2+} adsorption, modeled using a nonideal solution of $[Sr,Ca]CO_3$. Line identification is the same as for the left plot.

shows that the Sr^{2+} adsorption is slightly over represented, which is motivating continued research focused on improved modeling that incorporates nonideal [Sr,Ca] carbonate solutions. A nonideal solid solution model is favored because:

- It is unlikely that an ideal solid solution of aragonite, calcite, and strontianite represents a true equilibrium end point for the adsorption process.
- Aragonite is typically metastable in the presence of calcite.
- Sr^{2+} is poorly miscible in calcite. The assumption of an ideal solid solution requires complete miscibility of Sr^{2+} in $CaCO_3$ minerals, which is unlikely.

When Sr^{2+} adsorption forming a nonideal solid solution of calcite and strontianite was modeled, the degree of Sr^{2+} adsorption was under represented. Nevertheless, we feel that this likely represents a more realistic equilibrium end-point. If so, then the observed Sr^{2+} sorption data should approach the nonideal prediction as contact time increases and the metastable "ideal solid solution" (aragonite, calcite, strontianite) dissolves and slowly recrystallizes into the more stable nonideal solid solution of calcite and strontianite.

SIMS data supported model predictions, and provided some additional insight (see Figure 3). When Sr^{2+} was initially added, Ca^{2+} and Na^{+} increased, which was predicted by modeling as a consequence of increased ionic strength. As $[Sr^{2+}]_{aq}$ increased past 1.e-3 mM, $[Na^{+}]_{aq}$ was driven to zero, but Ca^{2+} remained in competition with Sr^{2+} until the highest exposure concentrations. This result suggested that the spectral data could be used in conjunction with the model to predict desorption behavior without having to perform desorption experiments.

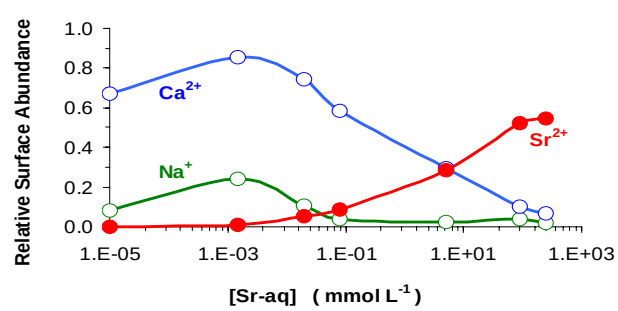

Figure 3. Sr^{2+} isotherm generated using SIMS.

Together, these experiments and models indicated that carbonate mineral formation controlled Sr^{2+} sorption and mobility in INEEL sediments. Model predictions were consistent with many observations to date, and provide a strong foundation for interpretation of results from ongoing experiments. These results will lead to a theoretical understanding of Cs^{+} and Sr^{2+} sorption phenomena in INEEL sediments and a significantly enhanced ability to provide predictive models of Sr^{2+} transport under a variety of future perturbation scenarios.

Sorption of Actinide-Series Elements to RWMC Sediments

Adsorption partitioning for Eu, Pa, U, Np, Pu and Am to RWMC sediments was measured at short contact times (15 minutes to 3 hours) over a broad range of concentrations in dilute solution (very low ionic strength except for the metal, see Figure 4). A comparison of the data for the different actinides shows widely varying behavior. Scatter for Eu, Pa Am and 3 h contact Pu data was too severe to justify calculation of isotherms.

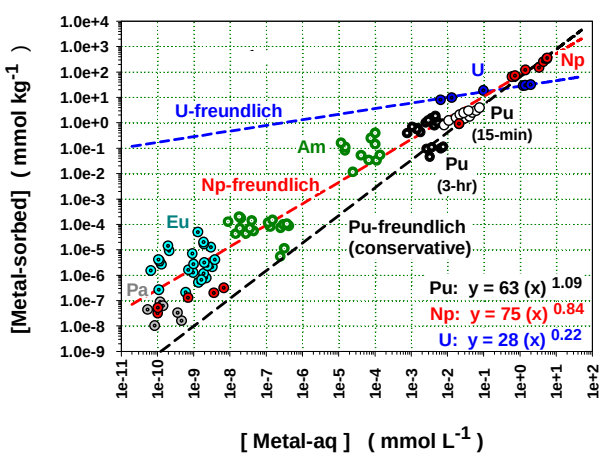

Figure 4. Adsorption data for Eu, Pa, U, Np, Pu and Am from dilute solution. U, Np and 15 min contact Pu data were modeled using Freundlich isotherms (blue, red and black lines, respectively).

Np adsorption followed a well-behaved isotherm over three orders of magnitude, that was readily modeled using a Freundlich isotherm in which the 'effective K_d' was 75 mL g^{-1}. The Freundlich isotherm enabled good estimates of sorption at exposure concentrations that were nine orders of magnitude lower. This result motivated initial attempts to develop geochemical models for Np adsorption (*vide infra*). U adsorption also described a well defined isotherm, however, in the case of U the 'effective K_d' was substantially less than that for Np, 28 mL g^{-1}. This suggested that solution phase species were competing effectively with surface moieties for uranyl coordination sites. Carbonate was suspected, resulting in formation of soluble $UO_2(CO_3)_n^{-m}$ species, but this speculation requires experimental verification. Geochemical adsorption modeling for U has not yet been initiated. Pu adsorption behavior was variable depending on the Pu-matrix contact time; after 15 minutes, a linear isotherm was described, but when contact time was extended to 3 hours, the adsorption profile shifted toward the surface and developed substantial scatter. Because Pu transport is the subject of widespread speculation, several modeling experiments were performed (*vide infra*). Adsorption profiles for Am, Eu, and Pa displayed a large degree of scatter, which prevented the development of meaningful isotherms for these elements (*vide infra*) and pointed to the need to identify sorption processes operative in these cases. Alternatively phrased, the inventory of processes is incomplete, even for a controlled experimental system, which means that meaningful transport modeling is not currently within reach.

Further Pu Adsorption and Modeling Experiments. Geochemical modeling was performed for Pu assuming that Pu would adsorb to FeOOH, and as hydroxide complex $Pu(OH)_{4(aq)}$.

The combined model (represented as the red line in Figure 5) fit the 15 minute adsorption data well, which supported the supposition that both FeOOH and Pu oxyhydroxide complexes were involved in the adsorption process. This was also supported by sequential chemical extraction results for Pu on INEEL soils which show that Pu was largely associated with the "reducible" (amorphous iron oxides) and "residual" (insoluble and recalcitrant Pu oxyhydroxide) fractions. The large degree of scatter that developed in the 3-hour Pu data suggested that Pu hydrolyses was occurring: in fact Pu (and Am and Eu) will undergo rapid hydrolysis to form oxide and oxyhydroxide metal

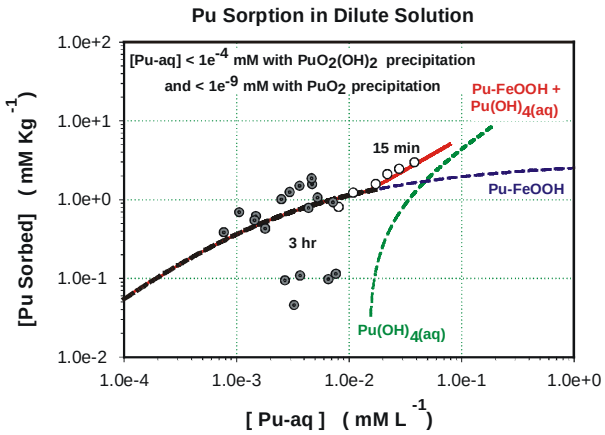

Figure 5. Pu adsorption on RWMC sediments from low ionic strength solutions. Both data and modeling exercises are plotted. Open circles are data from 15 minute Pu adsorption experiments and dark circles are 3-hour Pu adsorption experiments. The green line is a modeled adsorption of a Pu hydroxide complex denoted $Pu(OH)_{4(aq)}$, the blue dashed line is modeling of Pu adsorption to FeOOH sites, and the red line is a combined model of Pu hydroxide adsorption and Pu adsorption to FeOOH.

precipitates, which may represent ultimate (stable) mineral forms in subsurface systems.[18–20]

The final modeling exercise conducted for Pu was to assume that as time progresses, the initially formed $Pu(OH)_{4(aq)}$ and FeOOH-complexed Pu will be completely converted to more stable oxide and oxyhydroxide surface complexes $PuO_2(OH)_2$ and PuO_2 precipitates and correspondingly higher sorbed proportions. These results generally agree with previous findings,[21–23] and indicate that Pu sorption should be controlled by the rate of Pu transformation into more stable solid species from the metastable hydroxide precipitates. To evaluate this possibility, the 15-minute Pu adsorption data was "corrected" using this assumption, and replotted. The corrected data could be fitted using a Freundlich isotherm having an apparent K_d of 63 mL g^{-1}, which is consistent with the Np Freundlich, and suggests similar adsorption phenomena operating for both elements.

Summarizing the Pu adsorption and modeling studies results indicate that short-term Pu-sorption is governed by a competition between site-specific surface complexation and precipitation of the metastable Pu-hydroxide minerals such as $Pu(OH)_{4(aq)}$. The scatter in the 3-hour adsorption data was interpreted in terms of competition between the short-term factors and emergence of multiple Pu hydrolysis products (oxide/oxyhydroxide species) which display variable adsorption behavior that is very sensitive to subtle changes in the solution chemistry that at present are not well understood. At very long times, this system would be expected to display normal adsorption behavior defined by a limited number of species, and could be represented using a Freundlich isotherm. However, time to reach this state is unknown at present, as is an explicit understanding of the intermediate species and their adsorption behavior.

Further Np Adsorption Experiments and Modeling Exercises. Np adsorption experiments performed in low ionic strength water and in SGW resulted in sorption plots that were nearly linear in both cases (see Figure 6). Empirical Freundlich isotherms were calculated that had exponential factors near unity (0.95), which suggested that most of the $[Np]_{aq}$ was available for surface complexation, in other words, there was nothing in solution effectively competing for the $[Np]_{aq}$. However, the slope of the isotherm in the low ionic strength experiments was ~30% greater than in the SGW experiment. This observation suggests that constituents in the SGW are competing with Np_{aq} species for available surface sites, which is expected behavior for metal sorption in high ionic strength aqueous environments.

Adsorption modeling that involved precipitation of hydroxide/oxide Np species, and adsorption to FeOOH sites produced isotherms that were shifted toward the solution phase by two orders of magnitude in the case of the low ionic strength experiment, and even more than that for the SGW experiment. This failure clearly indicates that Np is not associating with FeOOH sites. Knowledge of the suite of Np adsorption processes is incomplete, and points to the need for further adsorption and speciation research.

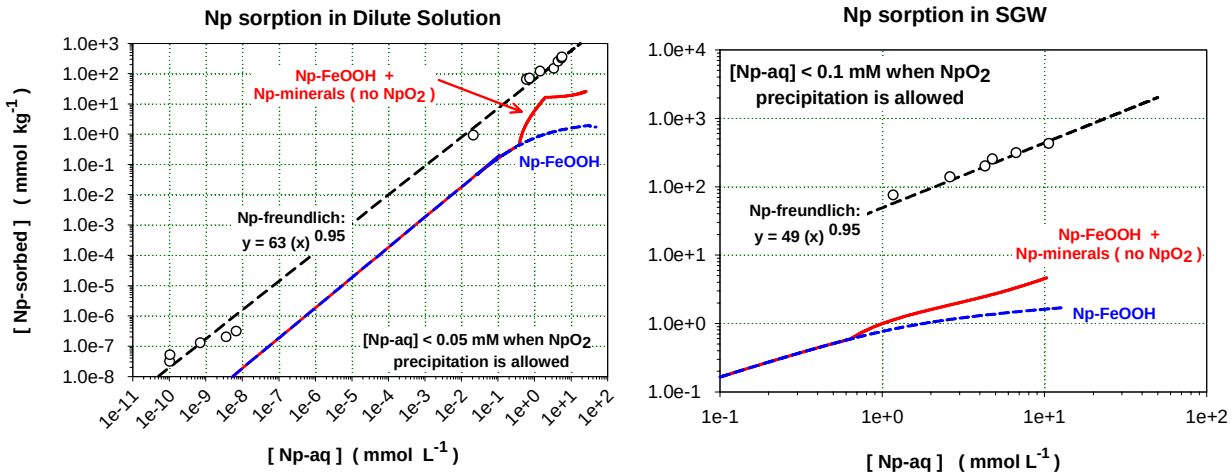

Figure 6. Np adsorption plots. Left, adsorption experiments performed in dilute solution (only Np in solution, low I experiment). Circles represent adsorption data from this study. The dashed black line is Freundlich adsorption isotherm; the blue dashed line is adsorption to FeOOH surface minerals, predicted using *Geochemists' Workbench*©; and the red line is adsorption to FeOOH and formation of Np minerals. Right, Np adsorption experiments performed in SGW. Line and data point identification is the same.

Path Forward

The first priority for FY 2003 tasking will be to harvest the long-term contact experiments and compare sorption behavior with the short-term speciation and sorption behavior for Sr and Cs to INEEL soils. Long-term sorption experiments will also be completed for the actinides currently under study. The sorption experiments have been initiated and will need to be harvested to complete understanding of actinide adsorption. Pu, U and Np adsorption processes will be emphasized. Finally, surface spectroscopic examinations and model development will need to catch up with phenomenological adsorption studies in order to generate a scientific (as opposed to empirical) understanding of the factors responsible for adsorption behavior.

Subtask 2. Periodic Wetting and Drying Cycles, and Their Potential for Altering Radionuclide Transport

The INEEL, located along the Snake River Plain in eastern Idaho, is the site of surface and subsurface metal contamination due to decades of nuclear waste handling, storage, and disposal. Infiltration in this arid region occurs primarily in the spring with snow melt and stream flooding. Because long periods of dry weather are punctuated by short, intense periods of recharge, we hypothesize that as contaminants become immobile due to lack of a transport medium, it will become increasingly difficult to remobilize these metals upon seasonal inundation. We devised a series of experiments to determine the effect of repeated episodes of wetting and drying on the mobility of metals in INEEL soil and a subset of soil constituents. These experiments were based on those described by Lee and others,[24] who found fewer metals were released from soils that had been wet and dried repeatedly.

Methods

INEEL soil, quartz, Fe-quartz (goethite-coated quartz), andesine (a plagioclase), and sediment-free control samples were exposed to 200 µM of Cs, Sr, Cd, Cr, and U, and allowed to equilibrate for 2 weeks. Samples of the aqueous phase were collected and analyzed for metals using ICP-MS. Replicate samples were allowed to dry and then rewetted with deionized water equilibrated with atmospheric CO_2. After the 2-week equilibration, aqueous samples were collected and analyzed for metals. As an additional experimental control, all sediments and the sediment free control samples were exposed to continuously wet conditions.

Since the effect of a brine-like solution on sorption, precipitation, and ion exchange was also significant, pore water from slurries was sampled and analyzed for metals. Other types of aqueous phase analyses included determination of anions and organic and inorganic carbon. Electron probe microanalysis (EPMA) and XANES were used to analyze the solid phases.

Batch Drying-Wetting Adsorption Experiments

Preliminary results from sequential wet-dry experiments conducted with no-sediment, INEEL sediment, quartz, goethite-coated quartz, and andesine exposed to 200 µM of Cs, Sr, Cd, Cr, and U indicated that wet-dry cycling does impact contaminant sorption under simulated environmental conditions. All sediments were also exposed to these metals under a "continuously-wet" control condition. No evidence for Cs^+ sorption was seen during the initial equilibration period for quartz, Fe-quartz (goethite-coated quartz), and the no-sediment control. During this period, the percentage of Cs^+ remaining in the aqueous phase decreased to 42.5% and 1.45% for andesine and soil, respectively. Wet-dry cycling reduced the $[Cs^+]_{aq}$ in the INEEL sediment to 0.8%, but did not notably affect the $[Cs^+]_{aq}$ in the other treatments with the possible exception of the andesine (see Figure 7). The behavior of Sr^{2+} was similar to Cs^+, except in the INEEL sediment, where the $[Sr^{2+}]_{aq}$ increased from 14.5 to 19.5% during the wet-dry cycling period.

At initial equilibration, $[U^{6+}]_{aq}$ had decreased notably in all samples including the controls, but especially in soil, Fe-quartz, and quartz treatments, which decreased by a factor of 10. During the wet-dry cycling period, the $[U^{6+}]_{aq}$ decreased by an additional factor of 10 in all treatments (see Figure 8), which indicated that drying resulted in formation of uranyl species that were (at least initially) insoluble during subsequent rewetting.

The concentrations of pore waters from the dried (brine) samples, sampled at 28 days, generally indicate that an additional quantity of the contaminants are either precipitated onto or otherwise "sorbed" to the mineral phases. The majority, of this portion of the contaminants is resolulibized upon rewetting, followed by a 2 week equilibration time.

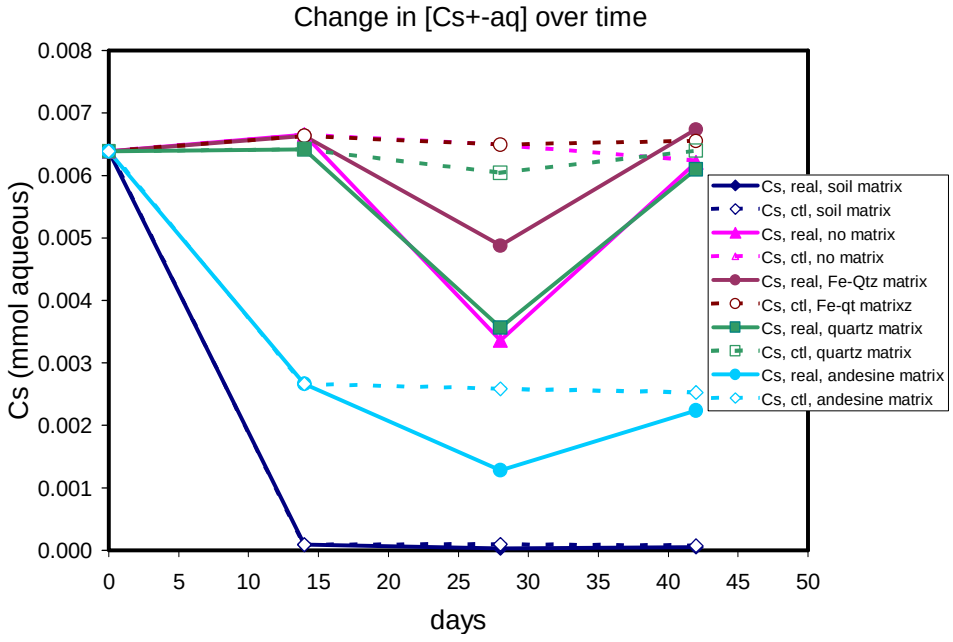

Figure 7. $[Cs^+]_{aq}$ plotted versus contact time, normalized to the amount of solution in the slurry. Initial solution concentration for all treatments is 200 µM at 0 days. Initial equilibrium sampling occurs at 14 days. Pore water for brine samples (dried) is sampled at 28 days. The first wet-dry sample period ends with sampling at 42 days.

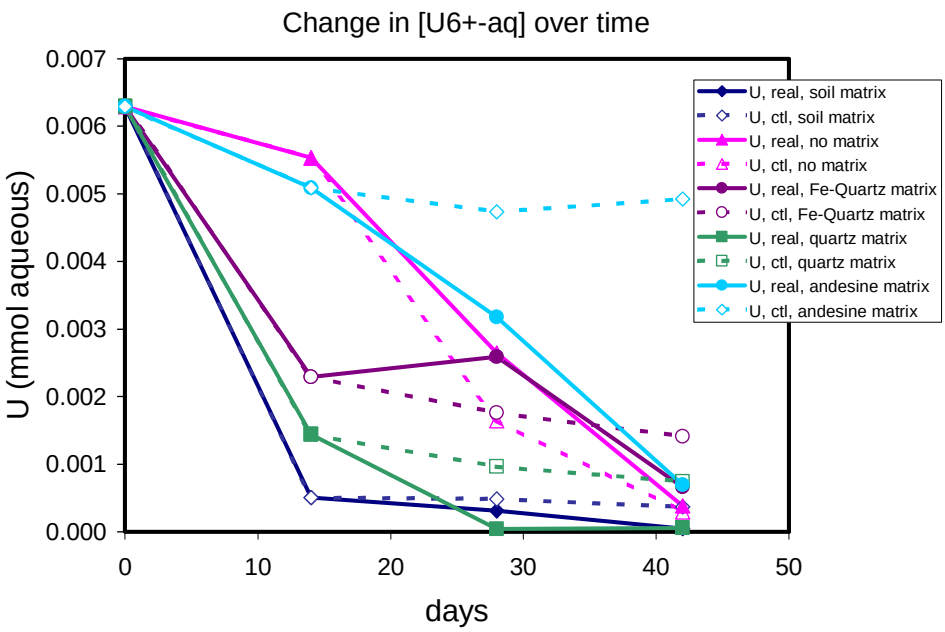

Figure 8. Plot of $[U^{6+}]_{aq}$ versus time, normalized to the amount of solution in the slurry. Initial solution concentration for all treatments is 200uM at 0 days. Initial equilibrium sampling occurs at 14 days. Pore water for brine samples (dried) is sampled at 28 days. The first wet-dry sample period ends with sampling at 42 days.

The sediments were analyzed at each time point using EPMA. Images of soil were acquired after it reached initial equilibrium with metals (see Figure 9). Most of the sediment consisted of mixed smectite-illite clay, quartz, and minor feldspar. Cs, Cr, Cd, and U clearly associated with the mineral phases, while Sr was less strongly correlated with the mineral phases. Heterogeneity in the Cr image, and similarity with the Fe image, suggested the formation of an unanticipated surface precipitate.

Next, EPMA was used to analyze soil samples that were nearly dry—the soil still contained pore water (see Figure 10). Consistent with the initial analyses, most of the sediment consisted of mixed smectite-illite clay, quartz, and minor feldspar. The analyses showed strong correlation between the U and Sr images, which suggested adsorption of uranyl to high silicate regions. The Sr and Cd were markedly depleted compared with the initial analysis. These preliminary EPMA results indicated that the technique will allow the determination of those phases responsible for enhanced contaminant metal sequestration over the course of periodic wetting and drying cycles.

Ion chromatographic analyses of Cl^-, SO_4^{2-}, NO_3^- showed no change in concentration between initial equilibrium and the concentration after one cycle for any of the treatments. After one cycle, inorganic C (aq) increased by a factor of 10 in all real samples but was unchanged in control (continually wet) samples. Organic C was unchanged from equilibrium values in all samples, real and control.

Conclusions: Initial Wetting/Drying Experiments. The batch wetting/drying adsorption experiments, and the EPMA analyses were consistent with Cs^+ sorption behavior largely controlled by ion exchange mechanisms prevalent in clay, which is present primarily as a mixed smectite-illite phase in INEEL soil. A decrease in $[Sr^{2+}]_{aq}$ followed by an increase, as noted in the soil sample, may be due to initial precipitation and subsequent dissolution of a phase such as aragonite, or may be due to leaching of Sr^{2+} from the soil. Decreased $[U^{6+}]_{aq}$ is due to precipitation of a U-bearing phase (possibly schoepite or $CaUO_4$) as well as adsorption to various solid phases.

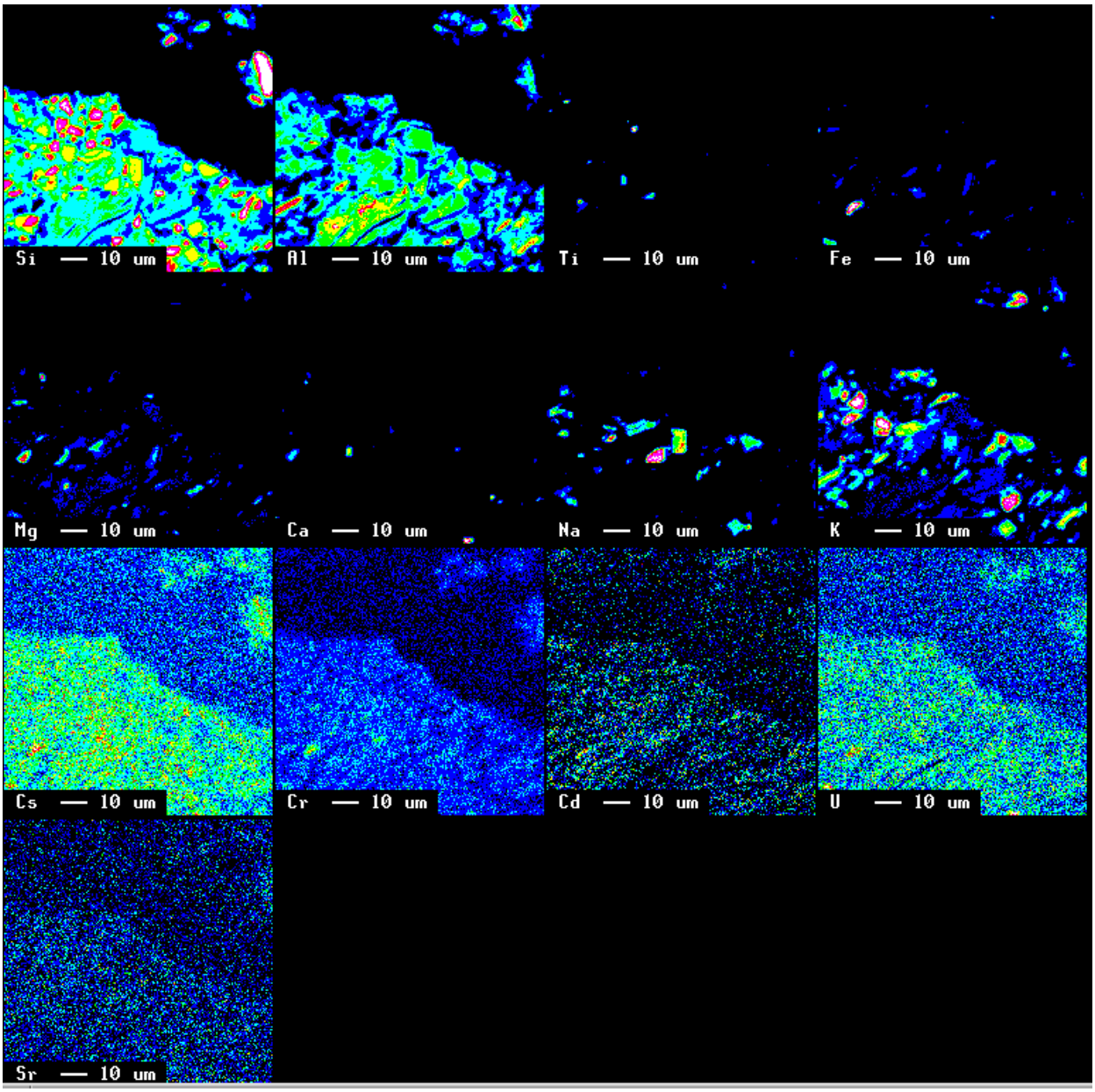

Figure 9. EPMA image of soil contaminated by 200 µM of Cs, Cd, Cr, Sr, and U after a 2-week equilibration period with the metals.

Path Forward

Additional wetting and drying cycles are ongoing as well as Cr and Cd analyses. Duplicate experiments using kaolinite, calcite, orthoclase, smectite, and mixed smectite-illite will be conducted in FY 2003, because knowledge of which phases were responsible for augmented contaminant adsorption as a function of periodic wetting/drying cycles would enable prediction of contaminant behavior. The U-bearing precipitate will be analyzed by x-ray diffraction to determine what phase or phases comprise it. EMPA techniques will be examined more closely to determine whether contaminants are being detected or not. If necessary, sample preparation techniques can be modified to facilitate detection of contaminants.

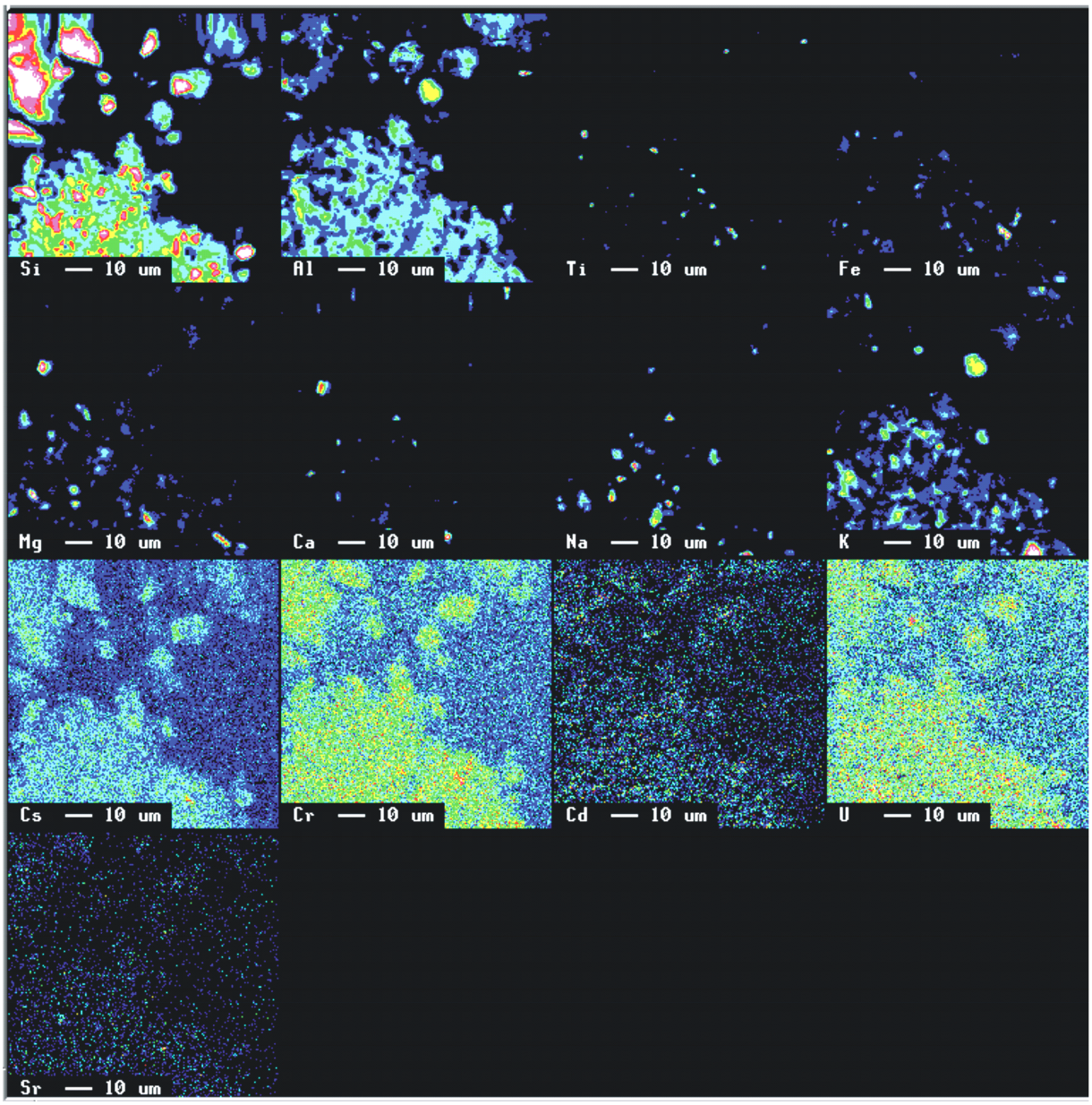

Figure 10. EPMA image of soil contaminated by 200 µM of Cs, Cd, Cr, Sr, and U after metals have equilibrated 2 weeks and most of the aqueous phase has been evaporated.

Subtask 3. Colloid-Facilitated Radionuclide Transport

An evaluation of the role colloids may play in radionuclide transport was motivated by the fact that colloids have been implicated in actinide migration at the Nevada Test Site,[25] Los Alamos,[26] and other locations. Since actinide contamination exists in the vadose zone at the INEEL, an evaluation of colloid transport in surficial soils is needed. In FY 2001, the indigenous colloid population resident in soils from the RWMC was separated and characterized. The colloids were predominantly clay in nature, and very sensitive to changes in the ionic strength of the pore water such that an infiltration of very dilute water would result in suspension of the colloids. When the ionic strength approached that of the natural ground water, precipitation would result.

A possible consequence of this behavior would be colloid suspension upon infiltration of low ionic strength water, which could arise from snow melt or a rain shower. Suspended colloids would then be advectively transported until they encountered pore constrictions or until the ionic strength of the infiltrating water increased to that of the pore water. The result of these actions would be colloid precipitation, which would serve as a barrier to further downward flow, and may cause lateral flow to occur. Such an event could compromise man-made caps over contaminated sites. The primary objective in FY 2002 was to evaluate this possibility.

The problem with evaluation of flow alterations derived from colloid barrier formation is that there are no validated methods for determining flow pathways in a noninvasive manner. One potentially attractive approach is to utilize x-ray computer assisted tomography, referred to as digital radiography and computed tomography (DRCT).

Baseline studies to visualize fluid pathways created by extreme pH gradients using DRCT were initiated. Metal tubes having different diameters were inserted into a column filled with quartz sand to simulate flow channels. Preliminary results demonstrated that the INEEL in-house DRCT scanner was capable of detecting a capillary tube as small as 375 μ in diameter.

During these experiments, a 3 × 12 in. Plexiglas container was filled with a column of dried sand mixed with carbonate particles (see Figure 11). Subsequently, three stainless-steel tubes (1/8 × 1/16 in., and 1/64 in. diameter) were pushed through the matrix at random positions. 2-D and 3-D spatial images were then generated, which demonstrated that metal inclusions could be located and imaged (see Figure 12A). Subsequently, a small volume of nitric acid was added to the top of the column, and then imaged. The black and white image of a horizontal slice reconstructed from near the top of the column (Figure 12B) showed some contrast corresponding to the HNO_3 intrusion. Subtraction of the non-infiltrated spectrum clearly showed the HNO_3 intrusion (Figure 12C).

A second test was initiated in which 20 mL of concentrated nitric acid was poured into a Plexiglas cylinder filled with dried sand and

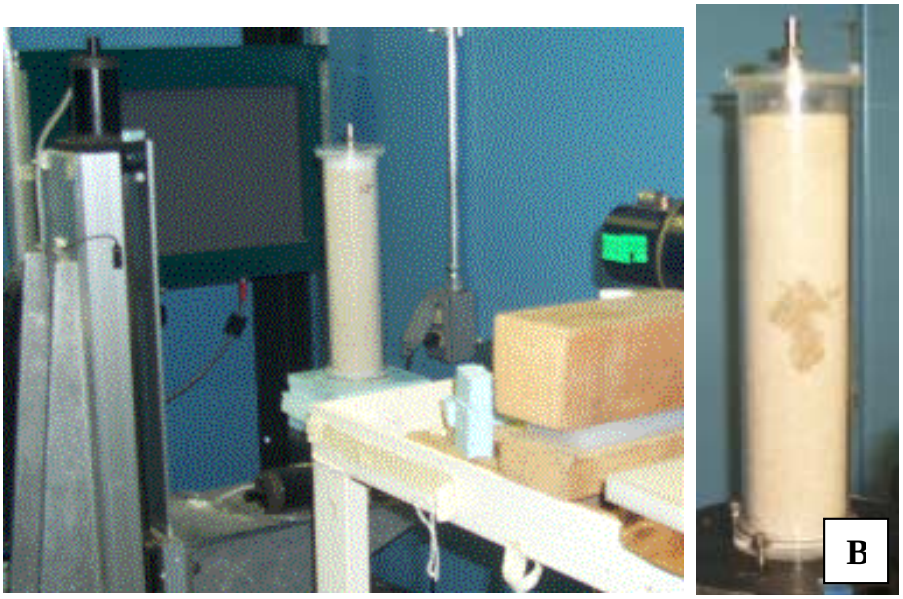

Figure 11. Soil column in 3-D x-ray imaging system (DRCT). The cylinder resides on a rotating stage. The x-ray generator is on the right (black cylinder), the 2-D x-ray area detector is on the left (gray panel). Image data is collected in cone-beam geometry. A single projection provides a radiograph. To create tomographic data, multiple projections are collected for different angular positions of the soil column and the data is processed to produce a 3-D image file.

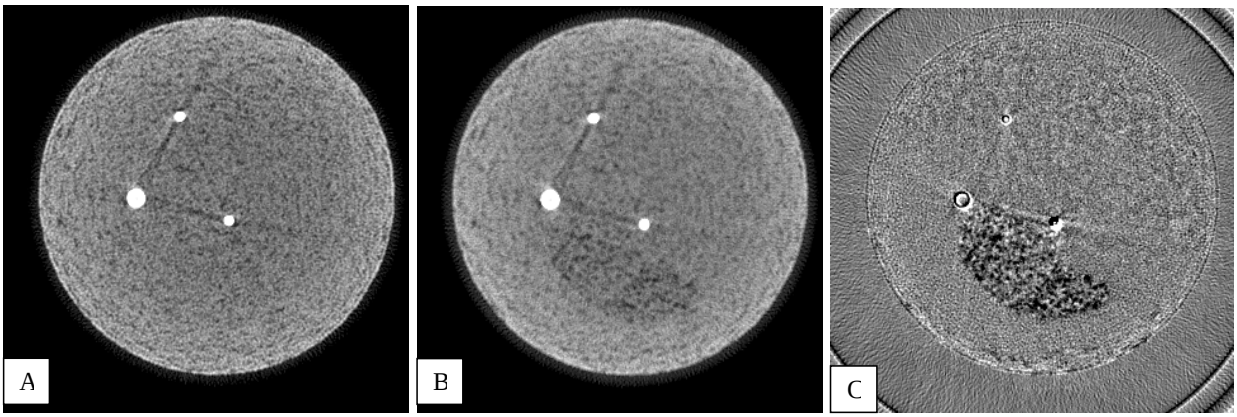

Figure 12. 2-D horizontal slices derived from the 3-D tomographic reconstruction of the soil column. (A) Shows a slice of the soil column prior to insertion of the nitric acid, with the three steel tubes clearly visible. (B) Shows the same slice more than 45 minutes after the introduction of nitric acid to the soil column. A region of varying contrast is seen in the lower half of the figure that corresponds to the HNO_3 infiltration. (C) Shows a scaled difference image created by subtracting A from B. The difference image clearly shows the location of the HNO_3 infiltration, and arises from a local variation in density.

carbonate (Figure 13). After a 45-minute wait, DRCT imaging was used to generate a complete 3-D cone beam tomography data set, which required approximately 90 minutes using a micro-focal x-ray generator and an amorphous-silicon flat-panel area detector array (refer to Figure 11). Image reconstruction was performed on the cone beam data and a 3-D image file of the soil column was generated. Only the upper portion of the soil column was imaged and reconstructed. The slice in Figure 13 is taken from near the center of the soil column. Image A shows the slice before HNO_3 infiltration; B shows it approximately 45 minutes after infiltration; and C is a scaled difference image created by subtracting A from B, showing both the displacement of the soil due to the initial pour and the density change created by the nitric acid interacting with the soil. It is clear from these images that tomographic imaging has the potential for tracking the development of channels in soil columns, which in turn would guide interrogation of 3D experiments in terms of matrix and colloid sampling.

Path Forward

To date, it has been concluded that indigenous colloids are likely not responsible for actinide or fission product transport, unless highly perturbed conditions develop. From a chemical perspective, actinide transport could still occur via Pu-intrinsic colloids, and this possibility will be pursued in the inorganic speciation task. DRCT has been demonstrated as a potentially powerful technique for evaluation fluid pathways, and research should be continued. However because it is hydrologically oriented, it should be managed under a hydrological project.

Subtask 4. Microbial Ligand-Modified Transport

Metal radionuclides and organic contaminants have been found in the vadose zone beneath the Subsurface Disposal Area (SDA) at the RWMC near the southern boundary of the INEEL. Actinides including U and Pu, along with organics such as Texaco Regal Oil and carbon tetrachloride, were disposed of in pits and trenches within the SDA.[27] Due to container corrosion, these waste constituents have become environmental contaminants. Decomposition of the Regal Oil as well as packaging such as cardboard and wood crates used to containerize waste may lead to the formation of various organic ligands that could increase the mobility of radionuclides in the vadose zone. Ligand precursors formed during the biodegradation of these organic contaminants include (but are not limited to) carbon dioxide, organic carboxylates, and polysaccharides.

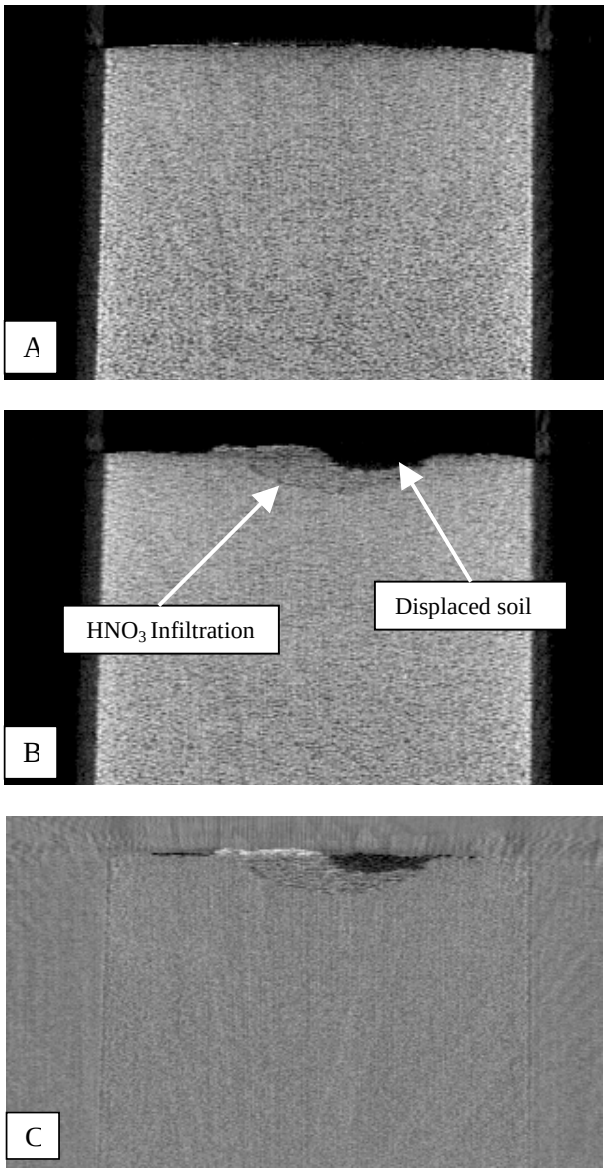

Figure 13. A single 2-D vertical slice derived from the 3-D tomographic reconstruction of the soil column.

The purpose of this task is to determine the effect of microbial communities on metal fate and transport and the influence of organic ligands produced by these communities in regions down stream of the microbes. The primary hypothesis driving the research is that ligands produced during the biodegradation of organic contaminants in the vadose zone will alter the formation of solution and surface complexes resulting in significantly faster or slower migration of radionuclides in the geologic subsurface. Research objectives for the first year of research included:

- Identifying metal complexing compounds produced by microbial populations indigenous to the RWMC during the biodegradation of Regal Oil and sawdust.
- Identifying changes in the microbial community during biodegradation of Regal Oil and sawdust.
- Determining the effect of metal complexing compounds on the adsorption of metal radionuclides to soil.
- Developing an understanding of how microbially-produced compounds influence metal partitioning between solution and mineral surfaces.

During FY 2002, 12 microcosm experiments were performed to determine the ability of microbes indigenous to Spreading Area B soil to produce organic ligands by the biodegradation, such as Regal Oil and sawdust, which are waste constituents. Experiments ran for 6 months and samples were taken to determine shifts in the microbial population using molecular techniques as well as ligand speciation using electrospray ionization mass spectrometry (ESI-MS). Ligand speciation will be performed as part of Subtask 8, “Solution Speciation by ESI-MS.”

Approach

Twelve 500 mL microcosms were set up to monitor the production of organic ligands during the biodegradation of Regal Oil and sawdust under optimum conditions for microbial activity. Experiments were designed to compare results from four controls without soil, four controls containing autoclaved soil, and four test microcosms containing unaltered soil. Microcosm studies were performed using aerobic growth conditions. Periodic oxygen addition occurred when the microcosms were opened for sampling. Each microcosm contained M9 growth medium (pH 8.0) which provided nitrogen and phosphorus for microbial growth. Microcosms were shaken at a temperature of 22°C. No exogenous microbes

were added to the microcosms for this set of experiments.

Microcosms were initially sampled weekly, followed by less frequent sampling after the first month of incubation. Liquid samples were taken to monitor solution organic compounds using high pressure liquid chromatography (HPLC), and speciation using ESI-MS. Soil samples were taken and analyzed for surface speciation by SIMS and microbial speciation using denaturing gradient gel electrophoresis (DGGE) to monitor changes in the microbial population.

Results

During the first month the microcosm bottles were sampled weekly in the event that organic ligand production was rapid. Following the first month sampling was done biweekly.

During the first 3 weeks of incubation there was no evidence of ligand production from the HPLC analysis performed on the liquid samples. Preliminary results from weeks 5–11 indicated the appearance of peaks on the chromatograms, which coincided with standards containing organic acids such as acetate and propionate.

Samples from the experiment were archived by freeze drying, and an initial set of 11 samples were sent to Wichita State for ESI-MS analysis. Results from both gas chromatographic and ESI-MS analysis were inconclusive due to interfering compounds in the growth medium. However, alternative approaches using uranyl as a derivatizing agent are being pursued.

A number of molecular techniques were applied to soil samples taken from the microcosm during the course of the experiment. Shifts in the microbial population were initially determined by separating amplification products from the 16S rRNA gene using DGGE. Genomic DNA extracted from the soil was amplified using oligo-nucleotide primers specific for the 16S rDNA gene of *Eubacteria*. Due to different melting properties of DNA products from different microbes, each band theoretically represents a single unique bacterial strain. Results from the test microcosm indicated significant diversity in the soil following incubation for several weeks, as well as shifts in the microbial population over the time course of the experiment. Analysis of the microbial population using DGGE indicated only subtle changes during the first 3 weeks of incubation. Soil samples analyzed at time zero indicated only a few distinct microbial populations. DNA samples processed after this time indicated an increase in the number of bands in each lane of the gel indicating the growth of bacteria that may have been dormant in the soil. The number of bands in the microcosms containing sawdust and Regal Oil was greater than in the microcosm containing only soil. suggesting a greater probability of producing complexing ligands in the experiments containing the organic carbon sources.

In an attempt to separate functionally unique DNA from that of the entire population, clone libraries are being made for each time point for the microcosms containing soil plus media, soil plus media and sawdust, and soil plus media and Regal Oil. The clone library is being screened using restriction fragment length polymorphism (RFLP) analysis. Once unique clones have been identified, comparisons will be made to the genomic DNA from the population using DGGE. Clones that are classified with bands representing significant changes by DGGE will be sequenced to make some determination of the functional significance of the strain sequenced.

Path Forward

RFLP analysis of the clone library will be performed in FY 2003. This task depends on preliminary comparison to the genomic DNA from the population. and sequencing and identification of dominant species.

Methods will be developed to separate or selectively identify analytes of interest from interfering ions in the growth medium. Two methods we may attempt in FY 2003 will be solid phase microextraction (SPME) followed by GC analysis, and the addition of uranium to the samples followed by ESI-MS analysis. We have already developed methods to identify uranyl complexes, which may represent a way to identify compounds of interest in the samples.

Once the compounds are identified, adsorption experiments will be run to determine their effect on uranium sorption to Spreading Area B soil.

Subtask 5. Surface Speciation

The factors that underlay those events having the potential to perturb radionuclide mobility are chemical structure and reactivity on the mineral surface. The range of oxidation states and complexes in which a given radionuclide can exist is referred to as the speciation of that element. It is this speciation which largely dictates the propensity of a given radionuclide to solubilize.

Analytical chemists are adept at distinguishing between oxides, ionic salts, and organometallic complexes for a bulk metal-bearing sample; however, the analytical problem as it exists on a mineral surface is far more difficult, particularly when the surface in question is of natural origin with inherent chemical inhomogeneity and irregular morphology. Consequently, improved surface analytical approaches were pursued to generate a molecular understanding of the microscopic phenomena established in Subtasks 1–4.

SIMS was the instrumentation emphasis of this research, capitalizing on over 10 years of INEEL state-of-the-art expertise. SIMS is based on a simple phenomena. A high energy atomic or polyatomic projectile impacts the mineral surface from which atoms and molecules are ejected. Some of the ejected particles are charged, and their masses can be measured using time-of-flight (TOF), quadripole (Q), or ion trap (IT) mass analyzers. Finally, the masses of the ejected atoms and molecules are used to identify and correlate original surface species.

Even though SIMS is not typically used for biogeochemical surface characterization, we used it for this subtask because of its apparent superior sensitivity and surface specificity to the irregular and chemically heterogeneous samples of the natural world. Specific research conducted in FY 2002 focused on gaining improved understanding in the following areas:

- *Characterization of Metal Adsorption on Soil Particles.* We are seeking approaches that will enable easy determination of the level of contaminant exposure, history, and likely desorption behavior. Current approaches rely on wet chemical investigations that are time consuming. Adsorption isotherms and cation substitution selectivity's were generated and compared with parallel information generated using conventional wet chemical approaches.

- *Clay Interlayer Metal Characterization.* Surface measurements are by definition unable to detect contaminants held within a given mineral matrix. Laser assisted SIMS was developed and evaluated together with a cooperative INRA project that demonstrated facile analysis of metals adsorbed to interlayer sites in 2:1 swellable clays.

- *Characterization of Carbonate-bearing Surfaces.* Carbonates are critical in control of Sr adsorption, and are also difficult to characterize in low concentrations on surfaces. Analytical research resulted in the ability to recognize carbonate on basic, alkali-bearing surfaces. Patterns on alkaline earth carbonates were also established, together with a possible approach for improved analysis of these materials.

- *Actinide Surface Speciation.* Direct, sensitive analyses of actinide species will be critical for characterizing samples from contaminated zones. SIMS and laser desorption mass spectrometry (LDMS) were used to establish speciation signatures for a variety of uranium-bearing surfaces.

- *Metal Oxide Ion-Molecule Reactivity.* Many of the projected speciation analyses will use ion trap mass-spectral approaches. Because of the presence of reactive gases such as H_2O and O_2 in the ion trap atmosphere, ion-molecule reactions will occur, and must be understood if mass spectral signatures are to be correlated with surface species. Furthermore, the ion molecule reactions provide unique insight into the intrinsic reactivity of the metal oxide species.

- *Characterization of Surface and Gas-Phase Oxide Structure using Isotopic Oxygen*

Exchange. Identification of metal oxide structure, particularly for naturally occurring materials, is challenging because NMR and vibrational approaches struggle with these materials. Yet the topic is important because the surface structure dictates reactivity (adsorption and desorption). One promising approach is to combine metal characterization with oxygen speciation, which may be deducible from isotopic oxygen exchange reactions.

These research areas are addressed in sequence below, and demonstrate that facile characterization of Cs^+ contaminated soils is within reach using a SIMS approach.

Characterization of Metal Adsorption on Soil Particles

Approaches were sought that would enable easy determination of the level of contaminant exposure, history, and likely desorption behavior. Current approaches rely on wet chemical adsorption investigations that require time consuming laboratory procedures. This study employed SIMS for characterization of clay materials that contained contaminant metals. Adsorption isotherms and cation substitution selecitivities were generated and compared with companion information that was generated using a conventional wet chemical approach.

In FY 2001, research was initiated that investigated the use of surface analysis for characterizing contaminated INEEL sediments. This research showed that adsorption behavior actually consisted of a summation of contributions from soil aggregates that had variable adsorption and desorption behavior. It is well known, for example, that swellable clays like montmorillonite, or smectites had substantial ability to adsorb Cs^+ in interlayer sites that exist between 2:1 alumino-silicate sheets. In contrast, illites, also a 2:1 clay, did not display pronounced tendency for interlayer adsorption of Cs^+. In this mineral, only surface adsorption was thought to occur. Similarly, kaolinite, a 1:1 aluminosilicate clay, was capable only of surface adsorption. Since the INEEL soils were composed of a mixture of these types of materials, it was deemed necessary to investigate their individual behavior when subjected to $[Cs^+]_{aq}$ exposure and subsequent SIMS analysis. This research was conducted in collaboration with Prof. W. L. Manner of BYU-Idaho, and also with Prof. L. Van Vaeck and Dr. R. Van Ham, Universitaire Instelling Antwerpen, Belgium.

Standard kaolinite, illite, and montmorillonite clay samples were acquired and exposed to a suite of $CsNO_3$ solutions that varied in concentration from 0.05 to 50 mM. After a 24-hour exposure time, the samples were decanted; the supernatant was analyzed for residual Cs^+, and the solid clay samples were washed with distilled water and dried for SIMS analysis. SIMS analysis was performed using the triple quadripole SIMS instrument at the INEEL that is equipped with the polyatomic projectile ReO_4^-. This projectile is more surface selective compared with other conventional projectiles, and hence offers analytical information with enhanced surface selectivity.

Analysis of kaolinite exposed to the lowest $[Cs^+]_{aq}$ showed that the spectrum was dominated by Al^+, with a significant Si^+ (see Figure 14). These ions were expected since kaolinite is a 1:1 silicate/aluminate clay; further, since they are always observed in the mass spectra, they comprised a mass spectral internal standard against which the abundances of the counter cations could be normalized. The counter cations observed were NH_4^+, low abundance Mg^+, with much lower abundance K^+ and Ca^+. Cs^+ was also clearly observed above the background at *m/z* 133.

As $[Cs^+]_{aq}$ increased, the abundance of Cs^+ in the SIMS spectrum increased; however, the abundance of the other cations did not change substantially, other than NH_4^+, which did decrease with increasing Cs^+. This was interpreted in terms of Cs^+ adsorption to the kaolinite surface without necessarily exchanging cations. The Cs^+ SIMS abundance, $I(Cs^+)$, was normalized to the sum of Al^++Si^+, and plotted versus the equilibrium concentration $[Cs^+]_{aq}$. Cs^+ adsorption isotherms were also generated by difference—the difference between the initial $[Cs^+]_{aq}$ and equilibrium $[Cs^+]_{aq}$ was assumed to be adsorbed. SIMS and difference isotherms were plotted together by normalizing the SIMS ion abundances to the $[Cs^+]_{sorbed}$ corresponding to the adsorption capacity (marked

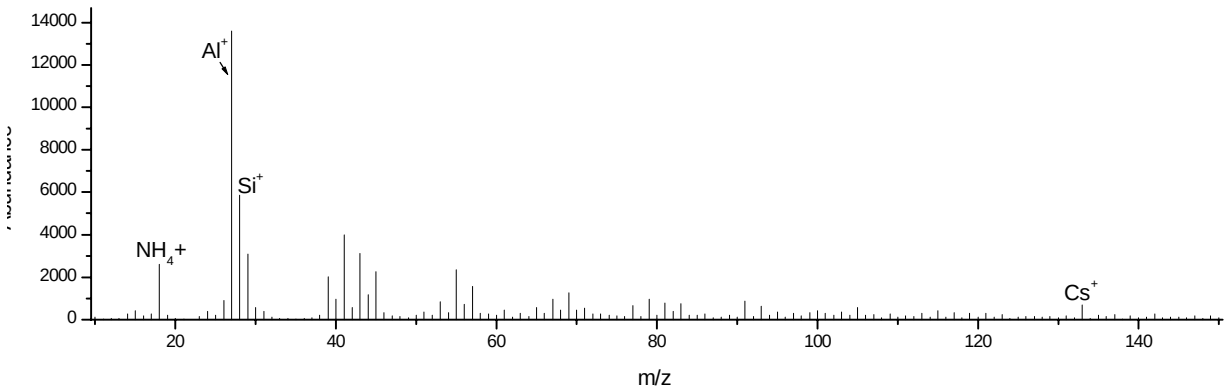

Figure 14. Cation SIMS analysis of kaolinite exposed to 0.05 mM $[Cs^+]_{aq}$, showing the matrix cations Al^+ and Si^+, and the counter cations NH_4^+, Mg^+, K^+, Ca^+ and Cs^+.

by an arrow in Figure 15). Good agreement was observed when comparing the shape of the two isotherms at equilibrium $[Cs^+]_{aq}$ < ~ 8 mmol L^{-1}.

$I(Cs^+)$ increased sharply with increasing $[Cs^+]_{aq}$ at the lowest values, which indicated that Cs^+ was taken up initially at surface sites. As these are occupied, less is partitioned onto the surface. At $[Cs^+]_{aq}$ > ~ 6 mmol L^{-1}, the slope of the curve decreased dramatically. A slow increase in $[Cs^+]_{sorbed}$ was observed in the difference isotherm, which is indicative of formation of a second Cs^+ surface mineral. Cs cluster ions were not observed in the SIMS spectrum, other than *m/z* 177, which may be due to $CsSiO^+$ or $CsAlOH^+$. These results indicated that, for kaolinite, the exposure history could be deduced with reasonable accuracy from the cation SIMS spectrum.

Attention was next focused on a swellable 2:1 silicate/aluminate clay, montmorillonite. This is the adsorption antithesis of kaolinite, because it can strongly adsorb Cs^+ into interlayer sites, which results in more aggressive binding behavior in terms of distribution coefficients and cation exchange capacities. The behavior was manifest in the SIMS spectrum (see Figure 16); Cs^+ was observed only when the initial $[Cs^+]_{aq}$ reached 3 mM. This value was nearly 60 times that observed for Cs^+ on kaolinite, which implies that when Cs^+ adsorbs to montmorillonite, it initially occupies sites that are not accessible to the SIMS primary ion (not on the surface of the particle).

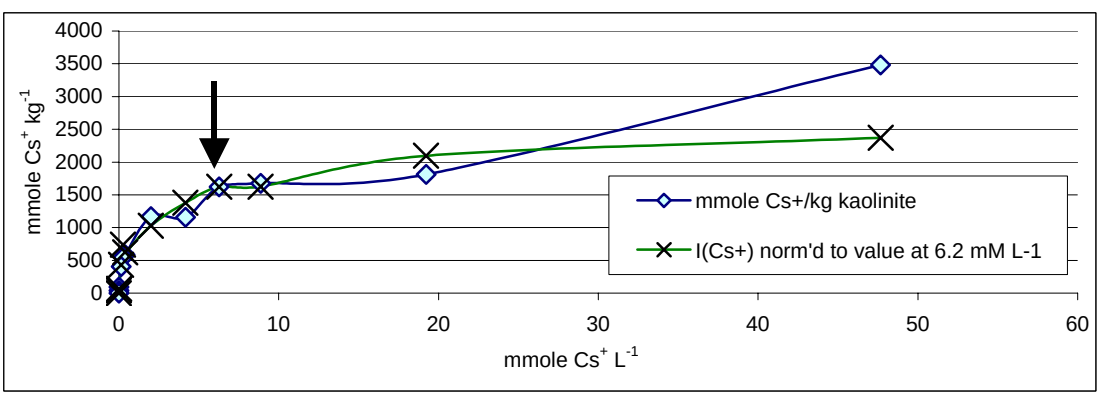

Figure 15. Cs^+ adsorption isotherms plotted for standard kaolinite. Diamond data markers represent sorbed data generated by difference from what was measured in solution using ICP-AES. X data markers represent Cs^+ abundance measured using SIMS, normalized to the apparent cation exchange capacity (marked with arrow).

A comparison of the difference and SIMS isotherms revealed reasonably good agreement when all data were considered (see Figure 17a). However, a close examination of the data at the lowest concentrations (see Figure 17b) showed that Cs^+ was being taken up by the 2:1 montmorillonite clay, but was not observable on the surface using SIMS. This phenomenon again points to adsorption by the interlayer sites, and pointed to the need to address analysis of cations occupying these areas.

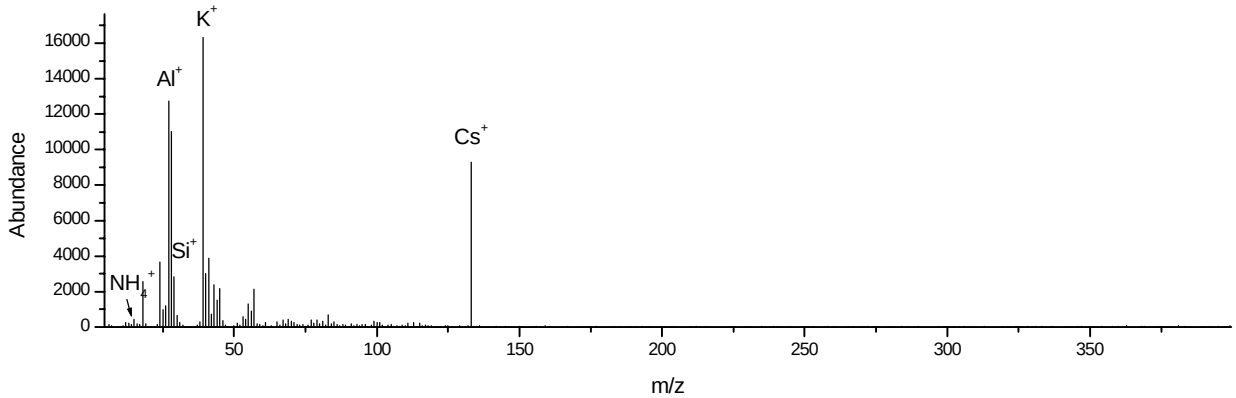

Figure 16. Cation SIMS spectrum of montmorillonite exposed to 3.0 mM Cs^+. This was the lowest initial $[Cs^+]_{aq}$ at which Cs^+ could be observed.

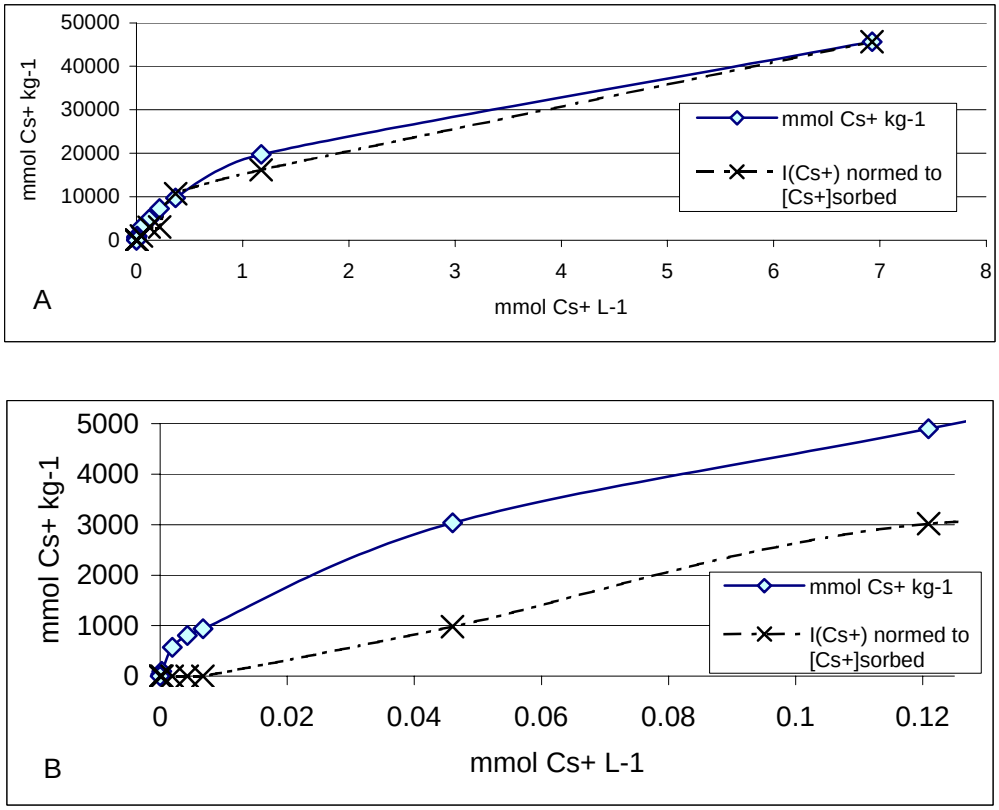

Figure 17. Cs^+ adsorption isotherms for montmorillonite. (A) Entire isotherm. Cs^+ sorption data generated by difference, and by normalized SIMS data. (B) Expansion of low concentration regime. Here, the SIMS isotherm significantly lags the adsorption isotherm.

Clay Interlayer Metal Characterization

The experience in analyzing montmorillonite clays showed the surface measurements were unable to detect contaminants held within a given mineral matrix. Laser assisted SIMS, or LA-SIMS, was developed and evaluated specifically to address this problem. The research hypothesis was that rapid heating of the contaminated mineral would redistribute the contaminant from interlayer sites to surface sites, where a surface analysis technique such as SIMS would be able to detect the once-matrix-bound metal. This task was conducted in collaboration with Professor R. Avci, of the Image and Chemical Analysis Laboratory, located within the Montana State Physics Department, with the support of the Inland Northwest Research Alliance (INRA) and ESR.

Cs^+-contaminated samples of INEEL soil were prepared for analysis by pressing particle aggregates into indium foil. The mounted samples were analyzed using a Charles Evans and Associates triple energy focusing, imaging ToF-SIMS instrument, which was operated in a combined microscope-microprobe mode. 25 keV Ga^+ was used to scatter-raster across the target region. The instrument was modified with a nitrogen UV laser that was spatially co-located with the area sampled by the Ga^+ gun. Co-location was achieved by the repeated laser pulsing of a Si wafer that had been previously etched using the Ga^+ gun. Experiments were conducted by initially imaging a 100×100 μm area, then irradiated with five laser pulses, and finally reimaging the same area.

Analysis of the soil particles exposed to Cs^+ solutions having the lowest concentrations did not contain significant Cs^+ (*m/z* 133). The spectra were dominated by abundant ions arising from the prevalent exchangeable and mineralized cations in the samples, which were Na^+ (*m/z* 23), Mg^+ (24), K^+ (39), Ca^+ (40), and Fe^+ (56) (see Figure 18). Other abundant cations were Al^+ (27) and Si^+ (28) derived from the aluminosilicate clay matrix. The spectra were very consistent from all areas of the region studied. The secondary ion distribution was very homogeneous from all regions.

Subsequently, the area was irradiated using one to five 337 nm laser pulses. A reanalysis of the area showed that the Cs^+ and K^+ abundances were significantly enhanced in the irradiated area (see Figure 19). Significantly, the regions of enhanced Cs^+ abundance did not explicitly coincide with regions of enhanced K^+. This was interpreted principally in terms of matrix heterogeneity. Mass spectra retrospectively produced from the high-Cs^+ regions contained *m/z* 133 peaks that were >100 times more intense than the unirradiated spectra when normalized to Si^+ (see Figure 20).

When samples exposed to high concentrations of [Cs^+] were examined, laser irradiation had no significant enhancing effect. In these cases, the surface was already highly contaminated with Cs^+, and the surface concentration was not significantly influenced by cation redistribution using the laser.

Significantly, other metals were not enhanced by laser irradiation. Since Cs and K have the highest vapor pressures and lowest melting points of the metals present, this observation suggests a thermal effect that results in redistribution of the metals from the interlayer sites on the clays to the surface, where they can be detected using SIMS. This explanation draws support from a comparison of two adsorption isotherms, one where the adsorbed quantity is proportional to the SIMS analysis, the other in which the adsorbed quantity is calculated by difference from the residual amount measured in solution. The comparison showed that the SIMS values at lowest concentrations were significantly less than the difference values. The difference can be reconciled if initial Cs^+ adsorption occupies interlayer sites.

The LA-SIMS research demonstrated that this approach works well for facile characterization of minerals in which the contaminant metal is sequestered within interlayer sites, as is the case for 2:1 clays. Implementation of this approach using a less sophisticated mass spectrometer, such as an ion trap or a quadripole mass analyzer, can be readily envisioned.

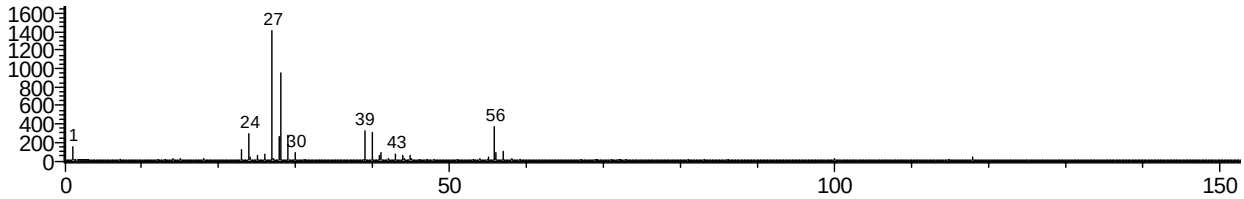

Figure 18. SIMS spectrum of soil sample exposed to 0.1 mM [Cs^+], prior *to* irradiation. Spectrum was derived from the area that was high in Cs^+ *after* laser irradiation.

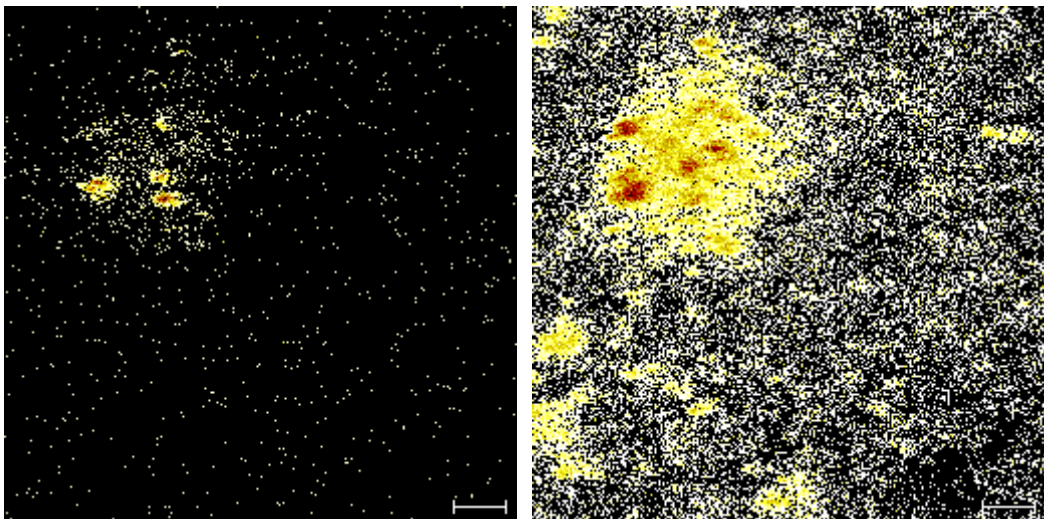

Figure 19. Ion images 100 µm on a side, of soil aggregates exposed to 0.1 mM $[Cs^+]_{aq}$, and then irradiated with the 337 nm laser. Left, Cs^+ image; right, K^+ image.

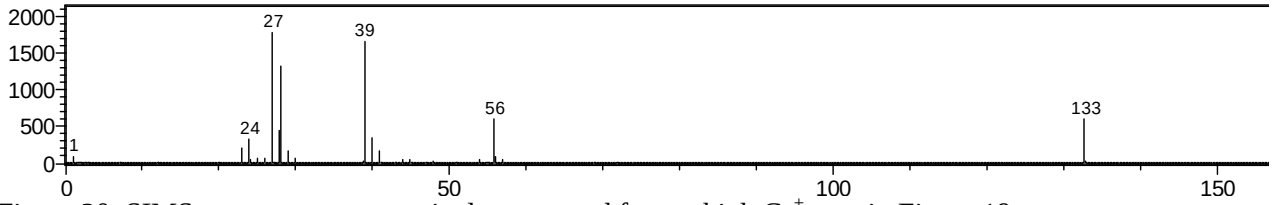

Figure 20. SIMS spectrum retrospectively generated from a high Cs^+ spot in Figure 19.

Characterization of Carbonate-bearing Surfaces

Research described previously in this report has shown explicitly that carbonate minerals are critical in controlling adsorption processes of alkaline earth metals like Sr^{2+}. In addition, they are known to play a crucial role in UO_2^{2+} adsorption/ transport, because of their pronounced tendency to complex to equatorial coordination sites. For this reason, approaches for characterization of sub-monolayer concentrations of carbonate minerals are sought, specifically for providing metal speciation. This research was conducted in collaboration with Mr. Andrew Shaw of Westminster Christian Academy, St. Louis, MO, and Prof. R. Avci of Montana State University.

Initial SIMS analyses of calcite and strontianite showed that cluster ions derived from the intact carbonate species were not produced using SIMS. However, alkali carbonate cluster ions were observed in the SIMS analyses of carbonate and bicarbonate salts, and in the analyses of basic

surfaces. The primary ion signature of carbonate on basic surfaces corresponded to $M_3CO_3^+$ where M = an alkali cation. This phenomenon is illustrated in the comparative analysis of six different sodium salts (see Figure 21), each of which displays a prominent $Na_3CO_3^+$. As expected, the ion is very abundant in the spectra of sodium carbonate and sodium bicarbonate (see graphs 21b and c). But it is also abundant in the spectrum of NaOH (see graph 21d), which is interpreted in terms of CO_2 fixation by the basic surface. This phenomenon is well known—NaOH primary standards are not reliable for long-term storage because of the carbonate equilibria that will be established with the atmosphere. However, facile means for observing carbonate fixation have been lacking.

Abundant $Na_3CO_3^+$ was also observed on the surfaces of sodium nitrite and sodium oxalate (21a, e). In both of these salts, the conjugate base is fairly strong, and they serve to again fix CO_2, to the extent that the carbonate bearing ions are more abundant than are the nitrite or oxalate-bearing ions. In contrast, $Na_3CO_3^+$ is less abundant in the spectrum of sodium nitrate, probably because nitrate is a much weaker base. These results show how the natural atmosphere is modifying any basic surface, thereby changing the intrinsic reactivity of that surface, and the finding is relevant to any site where high pH contamination has occurred, such as underneath the Hanford storage tanks.

Sodium oxalate was also examined to investigate another phenomenon that appeared in the carbonate spectra, specifically lower abundance ions at *m/z* 157, 135, and 113. Analysis of sodium oxalate showed that these ions could correspond to $Na_{3-x}H_xC_2O_4^+$, where $0 \leq x \leq 2$. If so, then this indicates that reductive coupling is occurring on the basic alkaline surfaces, either before, or during SIMS bombardment.

These results may also have some atmospheric significance, which relates to the fact that $NaNO_2$ will fix carbon dioxide. The byproduct of this surface reaction is nitrous acid HONO, which once formed might evaporate, thus forming gaseous HONO, which is known to be a precursor of atmospheric NO_2.

Actinide Surface Speciation

Comparisons of the SIMS spectra of a suite of uranyl salts and uranium oxides showed that mass spectral differences could be identified that enabled speciation. However, in several cases the spectral differences were not dramatic, which could lead to inaccurate identifications. We then initiated collaborative research with Dr. J. R. Scott (INEEL) for the purpose of evaluating whether a combined surface fluorescence/mass spectral approach would serve to enhance distinction of uranium species on surfaces.

The approach was to employ a laser optical chemical imager (LOCI) consisting of a laser fluorescence/laser desorption ion source with a high resolution Fourier transform mass spectrometer (FTMS). Initial demonstration analyses showed that regions, which contained adsorbed uranyl (U(VI) as UO_2^{2+}), had optical spectra that were quite distinct from those containing UO_2 and nonstoichiometric uranium oxides (see Figure 22). This distinction could be substantiated by then acquiring the laser desorption FTMS spectra (see Figure 23), which showed more subtle, but measurable differences. Particularly intriguing were the observation of abundant multiply charged uranium ions. These ions may be highly diagnostic for speciation, and this instrumental approach has potential for optimizing their detection.

Metal Oxide Ion-Molecule Reactivity

The adsorption and desorption behavior of metal ions in the geosphere is largely controlled by their reactivity with mineral oxide surfaces. These ionic reactions are influenced by the intrinsic chemistry of the metal ion with the surface adsorptive moiety, and solvent effects. Prediction and eventually, manipulation of these processes will require explicit knowledge of the relative contributions of these factors. When studied in the condensed phase, these factors are practically impossible to untangle; however, in the gas-phase, the intrinsic reactivity of the metal ion species can be determined, and the influence of the solvent can be assessed in a stepwise fashion.

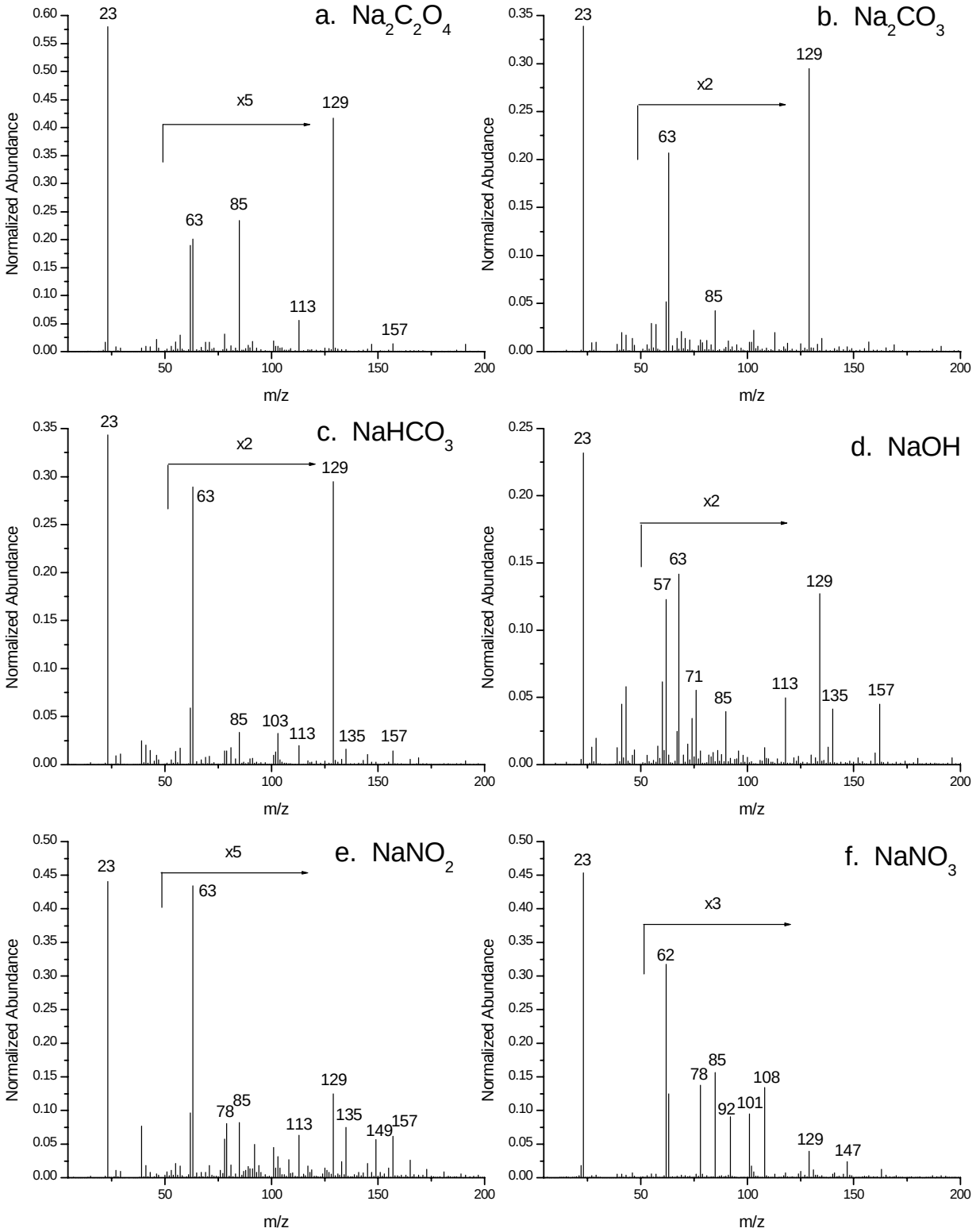

Figure 21. Cation SIMS spectra acquired using a polyatomic projectile; (a) Sodium oxalate, $Na_2C_2O_4$; (b) Sodium carbonate, Na_3CO_3; (c) Sodium bicarbonate, $NaHCO_3$; (d) Sodium hydroxide, NaOH. (e) Sodium nitrite, $NaNO_2$; (f) Sodium nitrate, $NaNO_3$.

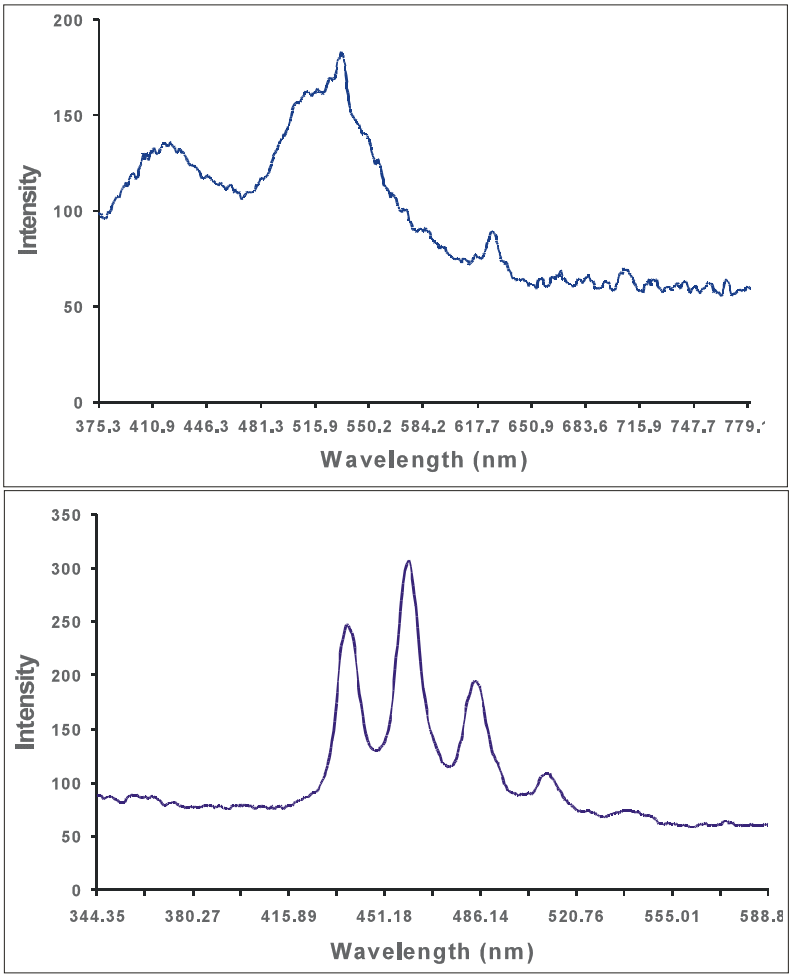

Figure 22. Surface fluorescence spectra of substoichiometric uranium oxide (top) and UO_2^{2+} (bottom).

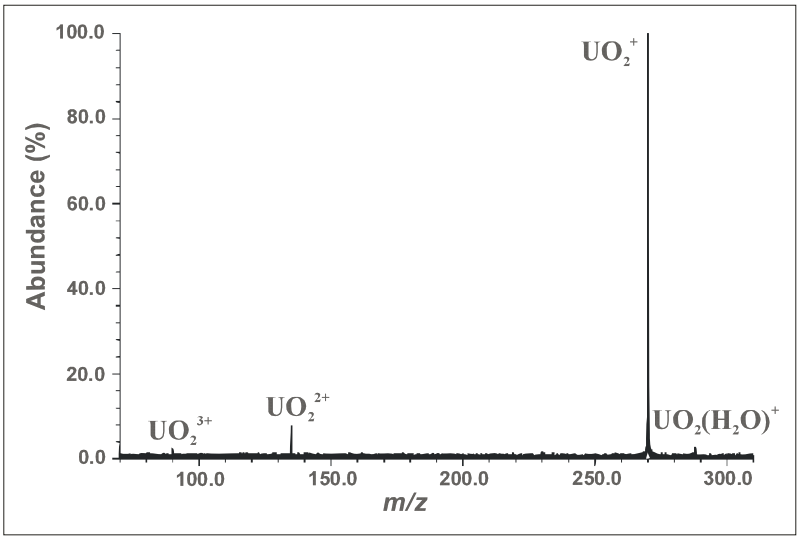

Figure 23. Laser desorption mass spectrum of a substoichiometric mixed oxidation state uranium oxide surface, acquired using the LOCI instrument.

A second motivation for studying the ion molecule reactivity is that many of the characterization approaches are mass spectrometry-based. In desorption ionization, and trapped ion mass detection, ion-molecule reactions are occurring, and hence influence the mass spectral signature that is finally recorded. Thus an understanding of the ion-molecule reactions occurring for the metal ion species is needed to correlate the mass spectral, gas-phase signature with the metal species originally present on the sample surface.

In prior years, great strides were made in studying alumina, silicate, and chromium oxide systems. Substantial research was directed at completing studies of hydration and oxidation of chromium oxide anion systems, and detailed descriptions of this research were described in the FY 2001 ESR report, and submitted for publication at the end of FY 2002. Attention was then directed toward understanding uranium cation hydration reactions. Studies previously reported in the literature had noted both water and O_2 oxidation of U^{2+}, U^{+}, UO^{+}, and UO_2^{+}, but there have been no reports of gas-phase complexes formed in which the equatorial coordination sites of uranium oxides have been occupied.

SIMS analysis of uranium-bearing surfaces showed a predominant UO_2^{+} ion, which was accompanied by several peaks that corresponded to the addition of H_2O. If the analysis is performed in an ion trap, then the water addition peaks grow in intensity (see Figure 24) as time between ion formation and mass measurement and detection is increased. This experiment showed that up to four, *but not five*, ligands would add, presumably around the equatorial coordination sites of UO_2^{+} (see Figure 25). This conclusion assumes that UO_2^{+} holds the same leitmotif as UO_2^{2+}, that is, two axial O atoms, with equatorial coordination sites. The finding was surprising because it is known in solution that UO_2^{2+} will accommodate five equatorial ligands. One explanation might be that the reduced uranyl UO_2^{+} cannot bind a fifth equatorial ligand as a consequence of the extra electron that it possesses (compared with UO_2^{2+}).

In addition to establishing reaction pathways for UO_2^{+}, the ion trap SIMS was used to establish the kinetics of the water addition processes.

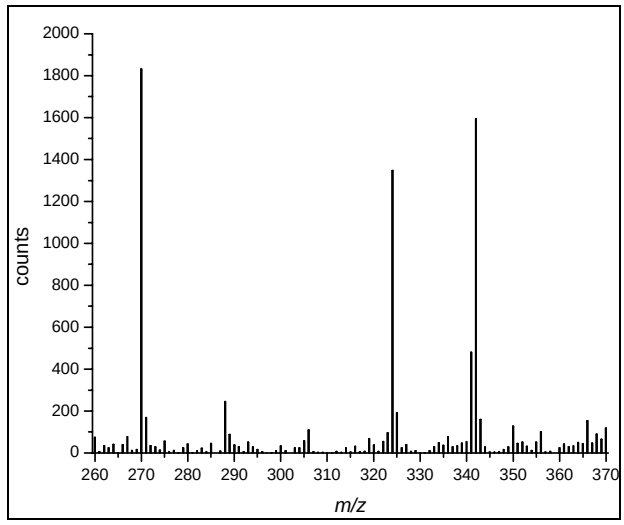

Figure 24. Ions arising from hydration reactions of UO_2^{+} are observed at *m/z* 288, 306, 324, and 342. UO_2^{+} was formed, trapped, and isolated using an ion trap secondary ion mass spectrometer. The surface analyzed was U(IV, VI) oxide.

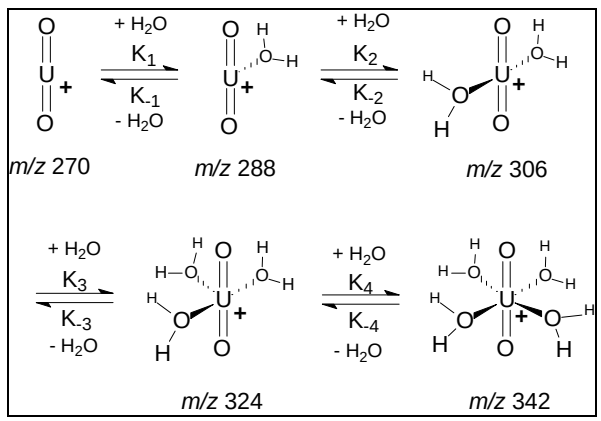

Figure 25. Four sequential equilibrium reactions of UO_2^{+} with H_2O occurring in the gas-phase environment of the ion trap secondary ion mass spectrometer.

Using a stochastic kinetic modeling approach, it was observed that the disappearance of UO_2^{+} could not be represented using a single exponential decay. However, the kinetic behavior could be accurately modeled by incorporating a series of forward and reverse hydration reactions (see Figure 26). This exercise enabled the relative reactivities and the stabilities of the different hydrated $UO_2(H_2O)_n^{+}$ species to be compared ($0 \leq n \leq 4$), based on a comparison of their rate constants (see Table 1).

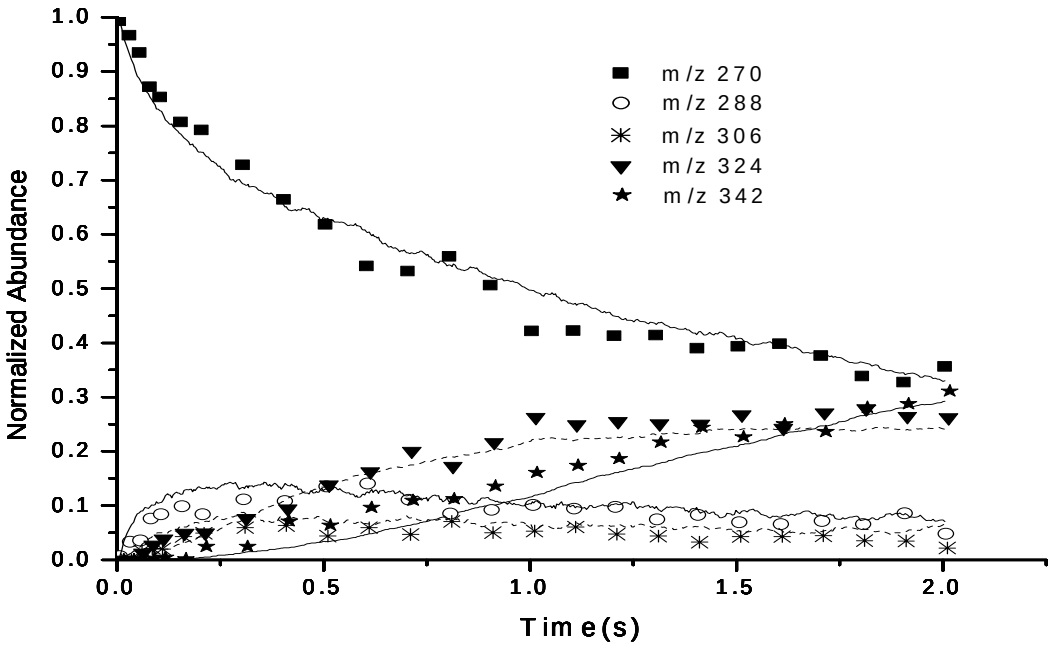

Figure 26. Kinetic plot for the reactions of UO_2^+ with H_2O. Lines that were generated using rate constants presented in table 5.1, and using the H_2O number density actually present in the ion trap SIMS, represent the stochastic kinetic model.

Table 1. Summary of modeled rate constants generated by stochastic kinetic modeling.

Rxn. #	Reaction	$k_{forward}$, $cm^3mLc^{-1}s^{-1}$	Forward Reaction Efficiency	$k_{reverse}$, s^{-1}
1	$UO_2^+ + H_2O \rightleftharpoons UO_2(H_2O)_1^+$	5×10^{-11}	2%	8.
2	$UO_2(H_2O)_1^+ + H_2O \rightleftharpoons UO_2(H_2O)_2^+$	18×10^{-11}	8%	13.
3	$UO_2(H_2O)_2^+ + H_2O \rightleftharpoons UO_2(H_2O)_3^+$	10×10^{-11}	5%	0.4
4	$UO_2(H_2O)_3^+ + H_2O \rightleftharpoons UO_2(H_2O)_4^+$	1.6×10^{-11}	0.8%	0.2

An ordering of the forward rate constants constitutes a qualitative comparison of the relative reactivity of the five $UO_2(H_2O)_n^+$ species:

$UO_2(H_2O)_1^+ > UO_2(H_2O)_2^+ > UO_2^+ > UO_2(H_2O)_3 > UO_2(H_2O)_4^+$

The general trend is that as the degree of H_2O complexation increases, reactivity slows down, which is what would be expected on the basis of fewer equatorial coordination sites available for reaction. This finding is in accord with the general observation that undercoordinated metal oxides are generally more reactive. The exception to this trend is UO_2^+, which reacts quite a bit slower than the monoaquo or diaquo complexes. Thus, formation of the initial complex increases reactivity with respect to further ligand addition. The explanation for this behavior may lie in the fact that addition of the initial H_2O ligand perturbs the symmetry of the UO_2^+ molecule, inducing a permanent dipole in the ion that would serve to orient incoming H_2O molecules. We have offered this explanation for the rates observed for reactions of H_2O with SiO_2^-, AlO_2^-, and CrO_2^-,

which are very slow compared with corresponding dimeric ions $M_2O_4^-$ (M = Al, Cr) and $Si_2O_5H^-$.

Ordering the reverse rate constants provides a relative ranking of complex stability with respect to elimination of H_2O:

$UO_2(H_2O)_4^+ > UO_2(H_2O)_3^+ > UO_2(H_2O)_1^+ > UO_2(H_2O)_2^+$

Regarding the reverse reactions, it must be stated that it is not known whether they are unimolecular or collision induced in the present case. In Table 1, $k_{reverse}$ values are presented as unimolecular constants, although corresponding bimolecular constants are easily calculated by dividing the unimolecular constants by the number density of H_2O. This treatment assumes that H_2O is the dissociation-inducing collision gas. He may also serve in this function, but in the near-thermal environment of the ion trap, He tends to collisionally stabilize adducts. Irregardless of the treatment, the relative order remains unchanged, and shows that stability increases markedly for n = 3 and 4. This suggests that the H_2O ligands stabilize each other around the equatorial coordination sites of UO_2^+, which may occur through hydrogen bonding. Conversely, hydrogen bonding between the equatorial ligands may not occur for n = 2, and cannot occur for n = 1, which may account for the lack of stability of these complexes.

The results of the ion-molecule investigations revealed that strong bonding can only be expected for the first four equatorial ligands—certainly there was opportunity for addition of a fifth ligand. Hence this suggests that the fifth ligand that is observed in solution is weakly bound, and likely is rapidly exchanging with other ligands present in solution. This in turn will influence uranium speciation, sorption, and transport behavior.

Characterization of Surface and Gas-Phase Oxide Structure using Isotopic Oxygen Exchange

Under nearly all circumstances, metal reactivity is described in the context of metal speciation, and, for those cases where the metal acts as a strong electrophile, this is appropriate. However, in the majority of systems, metals exist as oxides, and an alternative way to consider reactivity is to look at the various types of reactive O atoms (oxygen speciation). The problem with this approach is that there are few good ways to probe oxygen speciation on amorphous, inhomogeneous mineral oxides. One approach pioneered by W. H. Casey at UC-Davis has been successfully used for oxygen characterization in solution-phase alumina Keggin complexes is $H_2{}^{17}O$ substitution followed by ^{17}O NMR spectroscopy.[28] These results suggested that surfaces might be similarly probed using SIMS with $H_2{}^{18}O$ exchange.

In initial experiments, alumina was exposed to 95% $H_2{}^{18}O$, and then analyzed using SIMS. This revealed that some of the $^{16}O^-$ signal was partitioned to *m/z* 18, corresponding to $^{18}O^-$ (see Table 2 and Figure 27). After 5 minutes, 15% of the O had exchanged; at longer times, the amount of exchange slowly increased to about 25%. Thus, about 75% of the O atoms that contribute to

Table 2. Oxygen isotopic exchange measured via $^{16}O/^{18}O$ partitioning observed in secondary ions from alumina and silica analyses conducted using a SIMS instrument with a ReO_4^- primary ion.

Substrate	Ion	Percentage Exchanged after 7d.
Alumina	O^-	25.
	OH^-	38.
	AlO_2^-	32.
	$Al_2O_4H^-$	59.
Silica	O^-	19.
	OH^-	34.
	SiO_2^-	36.
	SiO_3^-	42.
	SiO_3H^-	49.

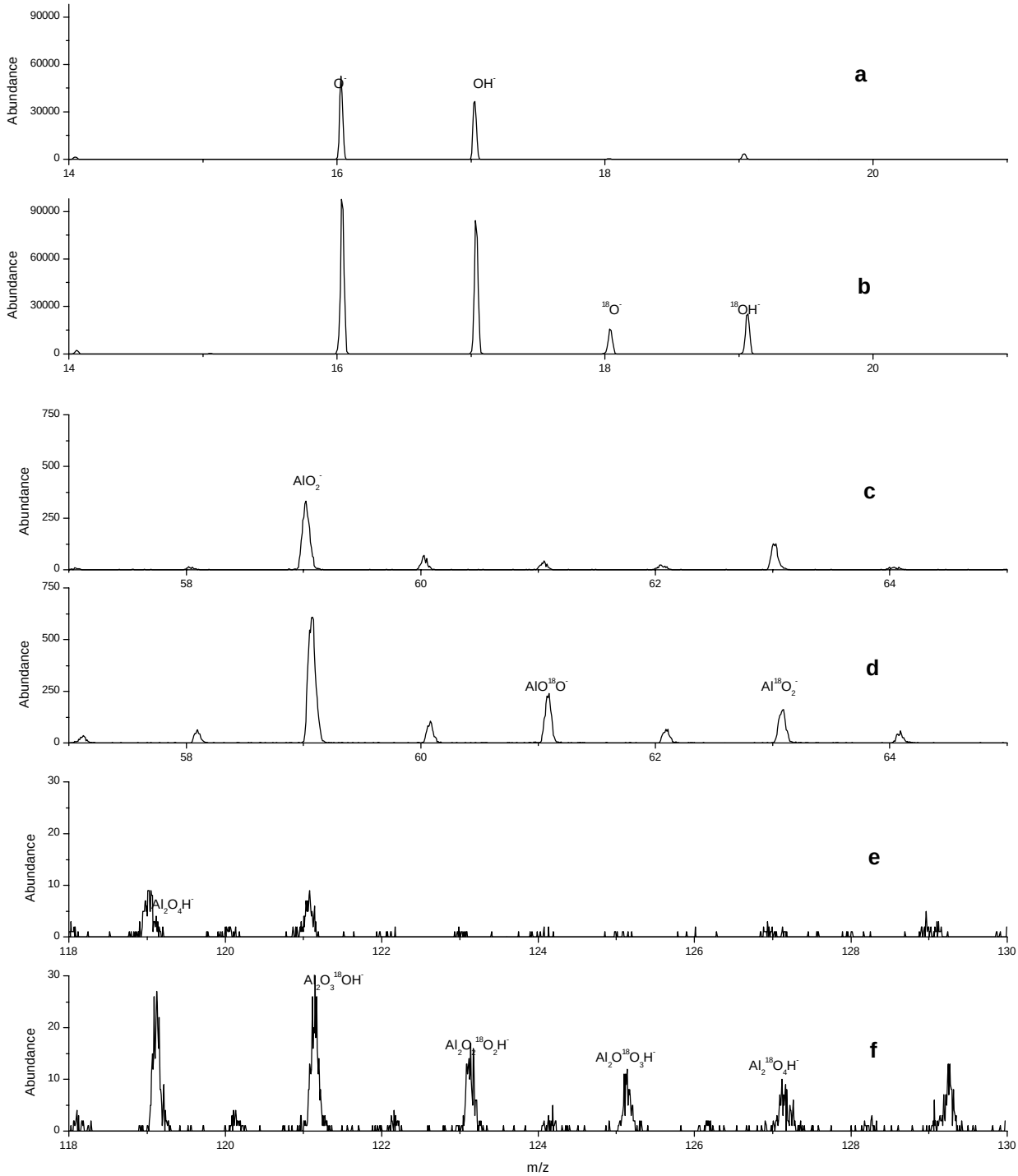

Figure 27. Partial anion SIMS spectra of nonexchanged, and ^{18}O isotopically exchanged alumina: (a) Nonexchanged alumina, O^- and OH^- region; (b) ^{18}O exchanged alumina, O^- and OH^- region; (c) Nonexchanged alumina, AlO_2^- region; (d) ^{18}O exchanged alumina, AlO_2^-region; (e) Nonexchanged alumina, $Al_2O_4H^-$ region; and (f) ^{18}O exchanged alumina, $Al_2O_4H^-$ region. Data was acquired using a Ga^+ primary projectile.

the formation of O^- were nonexchangeable. These measurements were also made for other alumina-derived secondary ions OH^-, AlO_2^-, and $Al_2O_4H^-$. The molecular secondary ions all underwent a larger fraction of exchange than did the atomic O^-. This observation suggests the following two self-consistent conclusions: (a) on average, the O^- ions are derived from deeper within the target matrix than are the molecular secondary ions; and (b) O atoms deep within the matrix are exchanged to a much less extent than are those on the surface.

The similarity in the degree of exchange observed when comparing OH^- and AlO_2^- suggests that these ions are formed from similar depth regimes. The largest degree of exchange was observed for $Al_2O_4H^-$, where more than half of the O atoms were observed to be exchanged. This indicates that $Al_2O_4H^-$ is formed from atoms originating from very near the surface, where a large degree of exchange would be anticipated.

Oxygen isotopic exchange patterns occurring in secondary ions originating from silica behaved in a similar fashion, i.e., the more complex the secondary ion, the higher the degree of isotopic oxygen exchange. The degree of exchange for O^- was less than in the case of alumina, which may suggest a more condensed structure for silica that is less susceptible to exchange. Extent of exchange for OH^- and SiO_2^- were comparable to each other and to their counterparts in the alumina experiment, OH^- and AlO_2^-. SiO_3^- and SiO_3H^- experienced even higher degrees of isotopic exchange, but not to the degree of the dimeric $Al_2O_4H^-$.

The structural implications of these varying degrees of exchange reactions have not been established. However, by examining the rates of exchange and drawing parallels with Casey's ^{17}O NMR experiments, some reasonable conjecture may be offered. The NMR experiments revealed the presence of four types of O atoms that displayed different rates of isotopic O exchange. The rate of exchange decreased in the following order: molecularly bound H_2O > pendant OH > bridging OH > M-O-M. In the kinetic experiments performed using ^{18}O exchange and SIMS, the extent of exchange as a function of time showed evidence for two components, a fast exchange, and a second process that was ~1,000 times slower. Based on the values of the rate constants measured, it is likely that molecularly-bound H_2O exchanges immediately, followed by rapid exchange of the pendant OH groups. The bridging OH moieties exchange at a much slower rate, which accounts for the slow component in the SIMS experiment. The Al-O-Al moieties do not exchange at all, and represent the nonexchangeable fraction.

These experiments indicate that insights into surface speciation can be derived from isotopic O exchange reactions. One particularly intriguing suggestion is that rate of exchange might be correlated to long-term oxide form stability, since oxygen exchange necessarily occurs during the dissolution process. This might provide a new approach for facile experimental validation of dissolution rates for oxide forms under varying conditions.

Path Forward

Vast opportunities exist for characterizing actinide speciation on natural and industrial surfaces using SIMS and LDMS. Initial experiments characterizing U-bearing surfaces using these techniques revealed the ability to determine speciation; intrinsic reactivity information emerged as well. FY 2003 studies will focus on determining variable speciation on specific surfaces encountered on INEEL surficial soils, basalts, and or interbed materials, with a particular emphasis on transuranic speciation. The utilization of the LA-SIMS, LOCI (LDMS) and isotopic oxygen exchange must also move forward because these techniques have the potential for great improvements in actinide (and fission product) speciation measurements. Close contact with the extended contact time, periodic wet-dry, colloid-facilitated transport, and microbial ligand tasks must be maintained.

Subtask 6. Sputtered Neutrals

Bombarding surfaces with either energetic charged particles or lasers produce a gas phase mixture of neutral and charged particles that have varying degrees of representation of the surface. Neutral species predominate, and are thought to be

more representative of the true nature of the surface, although the ions that are produced are much easier to detect, since mass spectrometers are very sensitive for the detection of ions. In contrast, the neutral species sputtered into the gas-phase must be ionized prior to being measured by a mass spectrometer. Certain species can be detected directly as ions with excellent sensitivity due to their propensity to form ions. Other species such as the iron oxides are difficult to ionize, and hence are difficult to measure by SIMS. However, ion beam bombardment sputters abundant neutral molecules from these surfaces.[29] Recent research at the INEEL funded by a completed Environmental Management Science Program project demonstrated excellent sensitivity for detection of neutral Ag and Bi oxide molecules, which was achieved by bombarding target surfaces with high energy ions.[30] The resulting sputtered neutral molecules are ionized when they drift through an electron beam, with subsequent mass spectrometric detection. It was believed that difficult-to-detect, environmentally relevant matrix (e.g., Fe, Mn oxides) and contaminant (actinide oxide) species might also be measurable using this approach. If so, this would result in a substantial improvement for the molecular inorganic characterization of mineral surfaces.

Consequently, the technique of sputtered neutral mass spectrometry (SNMS) was researched to determine whether improved radionuclide identification, speciation, and quantitation across the range of mineral and organometallic forms could be achieved. Specifically, improved determination of the surface atomic composition, and speciation of refractory oxide forms were emphasized.

Experiments were conducted into the investigation of Fe_xO_y-bearing surfaces. The iron oxides were the subject of this study because they are notorious for being difficult to characterize, particularly in terms of distinguishing between the Fe(II) and Fe(III) oxidation states. Further motivation was derived from the fact that the iron oxides play a critical role in adsorption of several contaminant metal species, and that areas proximate to rusting steel containers (barrels) will be high in iron oxides. Analysis of SIMS and SNMS spectra from FeO and Fe_2O_3 resulted in observation of predominantly Fe^+, using a high flux ReO_4^- primary ion gun. Few molecular species were produced, which demonstrated that SNMS will probably not work for speciation measurements of Fe_xO_y residues on surfaces.

An alternative approach was pursued that was based on the observation that iron oxides will form chloride complexes, and that these complexes appeared to be sensitively detected using SIMS. Iron oxide-bearing surfaces were treated with dilute HCl_{aq}, dried, and analyzed. Envelopes of $FeCl_x^-$ isotopic ions were readily detected, and the relative abundances suggested that oxidation state determination was achievable using this simple derivatization technique in concert with SIMS detection. Analysis of Fe(II)-bearing surfaces resulted in a higher relative abundance of $FeCl_3^-$, whereas analysis of Fe(III) resulted in a higher abundance of $FeCl_4^-$, indicating that oxidation state determination was possible. The one issue that needs further study is that the sample has to be analyzed very soon after being derivatized, since allowing it to sit for 24 hours with a large excess of HCl in the presence of air prior to analysis caused all of the Fe to oxidize to ferric chloride.

Path Forward

The Fe oxide oxidation state results clearly demonstrate that a sample that has only ferric oxide can be speciated unambiguously by treatment with HCl and observing the SIMS spectra of the ferric chloride species. Funding ran out prior to completing the studies with ferrous iron. Further studies need to be conducted to determine if it is feasible to conduct the same analysis for ferrous iron. Use with too large of an excess of HCl and allowing the sample to sit for a long period of time was shown to not work—ferrous was oxidized to ferric. Further experiments need to be conducted with lower concentrations of HCl, with alternate methods of introducing Cl to the sample (NaCl), and under inert atmospheres. There is an inert gas glove box adjacent to the instrument where these samples are analyzed, and the next series of experiments will be conducted in this facility. Alternate complexing agents such as fluoride, bromide and iodide can also be explored. Once a suitable complexing process has been proven, we need to determine sensitivity limits and

whether the technique would be applicable for characterization of actual sample materials. The study should then be extended to natural and industrial surfaces, such as corroded steel, basalt-related minerals, and Fe-containing soil materials. This approach, if successful, would make a significant contribution to the suite of analytical approaches for understanding Fe speciation on mineral surfaces.

Subtask 7. Bioanalytical Surface Studies: Characterization of Microbial Interfacial Chemistries using Surface Analytical Techniques

The capability of naturally occurring microbes to modify man-made contamination is important to the EM mission as it offers significant potential to reduce overall remediation costs. In order to take advantage of this capability the development of improved, direct methods for in situ characterization of the microorganisms and their chemistry is needed. Microbial alteration of contaminant metals and adsorptive surfaces has the potential to effect large changes in sorption, reversibility, and consequently mobility. Since microbial populations can be easily influenced by small changes in their geochemical environment, the possibility for altered radionuclide transport is substantial. Altered transport may be a consequence of a number of microbial-induced chemistries. For example, biotic electron transfer processes can affect the redox chemistry of metal contaminants; microbially-derived biopolymers such as oligosaccharides can act as chelating agents for metal contaminants; and biotically-induced geochemical changes can alter conditions such as pH, precipitation, and rock porosity. Characterization of microbes and their processes on mineral surfaces represents a challenge, which is addressed by this subtask. Recent developments in the area of microbial identification and the characterization of biopolymers have hinged on techniques such as matrix-assisted laser desorption ionization mass spectrometry (MALDI-MS), electrospray ionization mass spectrometry (ESI-MS), and fluorescent-tagging microscopic techniques. For example, a variety of groups have reported the use of MALDI-MS for the analysis of intact microbial cells.[31] In the work of Si, et al., a family of amino-oligosaccharides from *Streptomyces* spp. was identified using ESI-MS.[32]

The bioanalytical surface studies of this subtask provides an essential bioorganic complement to the inorganic geochemical speciation research performed in Subtask 5, Inorganic Surface Speciation: Development and Application of Techniques to Characterize Geochemical Mineral Surface Speciation." The objective of this subtask is to provide the breadth of research required to understand the primary environmental controls on surface speciation in INEEL sediments needed to underpin sorption and reversibility issues addressed in Subtasks 1–4.

Project Plan

The objective of this subtask is to improve the understanding of interfacial chemical interactions of microorganisms with radionuclide-contaminated soils, and how radionuclide transport is affected. Direct interrogation of these interactions by surface analytical techniques provides insights into mechanisms associated with biotically-induced transformations of radionuclides in the environment.

The planned activities for FY 2002 were as follows:

- Complete the minimum detection limit (MDL) of microorganisms using SIMS that was initiated in FY 2001 as part of the ESRA project "Investigation of Interfacial Chemistry of Microorganisms."

- Complete the toxicological study (Arsenic with *Shewanella putrefaciens*) initiated in FY 2001 as part of the ESRA project listed above.

- Initiate surface investigations to characterize interfacial, microbe-related chemistries that likely function to sequester radionuclides. An element of this activity is to be conducted in collaboration with Subtask 4, "Ligand Modified Partitioning: Heavy metal Partitioning and Modification of Mineral Surface Properties in

Systems with Natural and Synthetic Ligands." In addition to the surface analysis approaches, ESI-MS (Subtask 8) will be used to determine solubilized species.

Minimum Detection Limit

The biomass detection limit of a single bacterial type was determined. In order to use SIMS to analyze intact microorganisms directly on environmental surfaces, MDL was determined to establish how many microbial cells must be present on the sample for detection by SIMS. *Arthrobacter globiformis* was selected for this MDL measurement, as it is a well-characterized soil bacterium. The anion *m/z* 241^-, which is the $[M-H]^-$ from $C_{15}H_{30}O_2$ fatty acid, was used to indicate detection because it is the dominant fatty acid present in *A. gobliformis* (see Figure 28).

In these experiments, *A. globiformis* was grown aerobically on tryptic soy agar, then suspended into filtered, distilled water. The suspended cells were pipetted directly onto a planchet, allowed to dry for approximately 30 minutes, then analyzed by SIMS. The background was determined by pipetting 4 μL of filtered, distilled water onto the planchet, allowing it to dry (ca. 20 minutes), then analyzing by SIMS. For total cell counts, an identical aliquot of the aforementioned cell suspensions were fixed in 2% formalin solution (final concentration) and maintained on ice for direct enumeration.[33] Aliquots of the fixed samples were filtered under vacuum onto 0.2 μm pore-size, black, polycarbonate membrane filters with cellulose-acetate support filters. The total number of cells were enumerated by direct counts of acridine orange-stained (0.01%, 2 min.) cells[34] using epifluorescent illumination on a Nikon E-600 light microscope equipped with a xenon lamp and a Nikon EF-4 B-2E/C filter cube (Nikon Inc., Melville, NY). A minimum of 10 fields containing a minimum total of 200 cells were counted on each filter.

For the detection limit determination, five background samples were analyzed by SIMS. The MDL was determined by comparing the *m/z* 241^- peak abundance of *A. globiformis* to the abundance of this same peak from the background samples. The S/N was determined by dividing the ion abundance of the *m/z* 241^- peak by the average background value for the *m/z* range 270 to 280. The S/N values for the five background samples were averaged, and standard deviations (σ) were calculated for the *m/z* 241 anion. The detection limit was established at an abundance for the *m/z* 241 anion of greater than the background plus 3σ. The results indicated that SIMS was capable of detecting ca. 10^6 cells of *A. globiformis* present on a stainless steel sample holder (see Figure 29).

This result suggests that SIMS can be used to directly investigate microorganisms on environmental samples, as common cell concentrations in soils and sediments are 10^9 to 10^{10} cells/g. Assuming a soil surface area of 1 m^2/g and even distribution of cells, the surface coverage of microbial cells on soil can be estimated at 10^5 to 10^6 cells/cm^2. This estimate is conservative since distributions are not uniform, and some of the surface area will be inaccessible to microorganisms. Environmental densities at the scale of 0.06 cm^2 (the area of SIMS analysis) will most likely be higher than the estimated values. The results from this study indicate that SIMS is capable of detecting 10^6 cells on a 0.06 cm^2 sample holder, or ca. 10^7 cells/cm^2. Improved detection limits may be possible with ion trap SIMS instrumentation that has been demonstrated to be as much as two orders of magnitude more sensitive than the quadripole-based SIMS instruments.[35]

Toxicological Study

The objective of this work was to investigate biomolecular changes of dissimilatory metal-reducing bacteria (DMRB) due to interactions with contaminant metals, which may function to alter the surface chemistry of the bacterial cell. This alteration can affect adhesion and electron transfer behavior of the bacteria that may result in variations in the sorption, reversibility, and consequently mobility of contaminant metals in the environment.

In these experiments, *Shewanella putrefaciens* (ATCC 8051) was grown in a defined medium (M1)[36] under batch aerobic conditions. All experiments were performed with *S. putrefaciens* grown under aerobic conditions as these initial experiments were used to establish protocols as

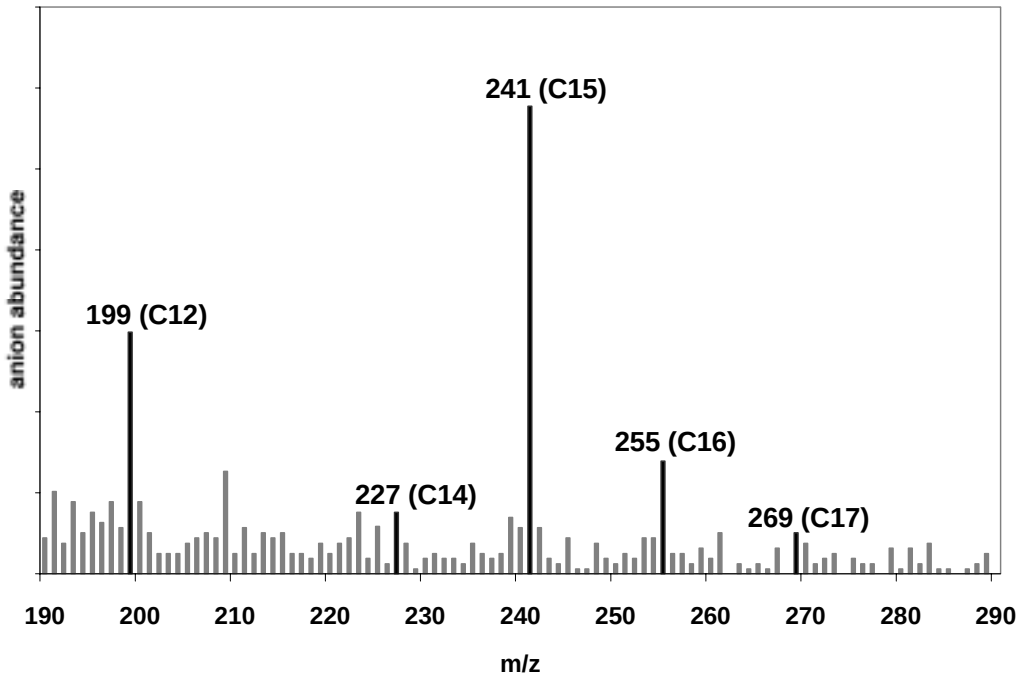

Figure 28. Anion SIMS spectrum of *Arthrobacter globiformis*. The anions highlighted in black originate from fatty acids.

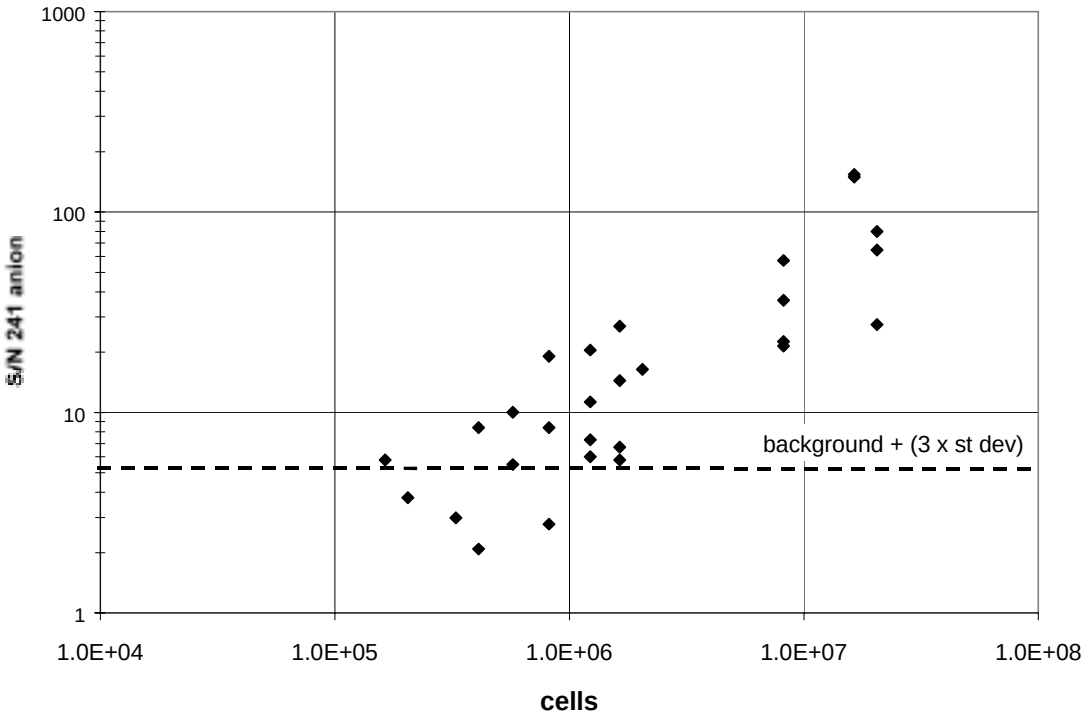

Figure 29. Results from SIMS analysis of various concentrations of *A. globiformis* on stainless steel in order to determine the limits of biomass detection. The dashed line indicates S/N value necessary to detect *A. globiformis.*

well as investigate the physiological and biochemical effects of metal exposure. Culture growth was monitored by the absorbance of light at a wavelength of 600 nm, or by total protein in the culture flask using the Lowry method.[37]

All chemicals were reagent grade or higher. Stock sodium arsenite ($NaHAsO_2$) was prepared in anoxic (N_2-purged) nanopure water and sterilized by autoclaving. Various concentrations of arsenite were added to sterile growth medium from stock solutions to test the effects of arsenic on the growth kinetics of *S. putrefaciens*. Figure 30 showed that *S. putrefaciens* growth in 1 mM As(III) was biphasic, in contrast to growth in the absence of As(III). This concentration caused not only an extended lag, diminished growth rate, and lower final density, but also a second lag at 48 h, suggesting a secondary physiological response of the cells to accumulating insult.

SIMS was used to monitor the cell surface chemistry of the *S. putrefaciens* exposed to 1 mM As (III) and no As (control). In these experiments, we were interested in changes in the fatty acid profiles of the lipid composition of *S. putrefaciens* during various stages of its growth. The anion SIMS spectrum of *S. putrefaciens* collected of the inoculum is shown in Figure 31. At various points along the growth curve, triplicate samples of *S. putrefaciens* exposed to and in the absence of As(III) were collected and analyzed by SIMS. Samples were prepared by washing cells in nanopure water and concentrating them 20 times. 10 uL of this washed 20-times suspension was then applied to a planchet and allowed to dry for 24 hours. The abundances of the fatty acid-related anions from the triplicate samples were normalized to the total ion current, then averaged. The average anion abundances of the various fatty acid anions (m/z 227 (C14), 241 (C15), 255 (C16), and 277 (C18:3)) were plotted versus the growth time. The trends of these results were similar to that of m/z 255 (C16 fatty acid; see Figure 32). Comparing the SIMS results of the C16 fatty acid production for the *S. putrefaciens* exposed to and in the absence of As (III), the fatty acid production is high for the *S. putrefaciens* control (no As(III)) at the 7-hour mark. The growth curves show that the cell numbers for *S. putrefaciens* in the control are also beginning to increase at this mark; however, the *S. putrefaciens* in the As(III) are relatively low at this point in the growth curve. At the 23-hour mark, the C16 production increased dramatically for the *S. putrefaciens* in As(III) compared to that in the control sample. Likewise, the growth curve of the *S. putrefaciens* in As(III) shows the cell numbers begin to increase at this time. Production of the C16 fatty acid remain similar at growth times of 31, 48, 55, 74 hours, with the *S. putrefaciens* in As(III) slightly higher than the control. At the 78-hour growth time, there is a substantial increase in the C16 fatty acid production for the *S. putrefaciens* in As(III) that corresponds to the second growth phase. These results suggest that there is some correlation in the secondary physiological response of the *S. putrefaciens* cells exposed to As(III) the cells and increased production of fatty acids. We concluded that SIMS has the potential to track differential regulation of fatty acid biosynthesis under varying environmental conditions.

Interfacial Microbe-Related Chemistries

As part of this subtask, collaborative work with Subtask 4, “Ligand Modified Partitioning,” was performed to assist in the characterization of ligand detection and bacterial characterization. Experiments in Subtask 4 were aimed at determining the ability of microbes indigenous to Spreading Area B soil to produce organic ligands from their food source (Regal Oil or Sawdust). Samples were collected from the microcosms, and a variety of analyses were performed, including SIMS.

Initially, the SIMS results showed the presence of fatty acids on RWMC soils containing indigenous microbes suggesting microbial activity. However, after performing control experiments to validate these results, we found that the sample vials used to store the sample had a surfactant present that was dissolved by water present in the samples. We believe that the surfactant was the source of the fatty acids observed in the SIMS data. We will use improved storage procedures for future work.

In addition to the collaborative work with Subtask 4, we also performed some preliminary experiments to assess the capability of SIMS for

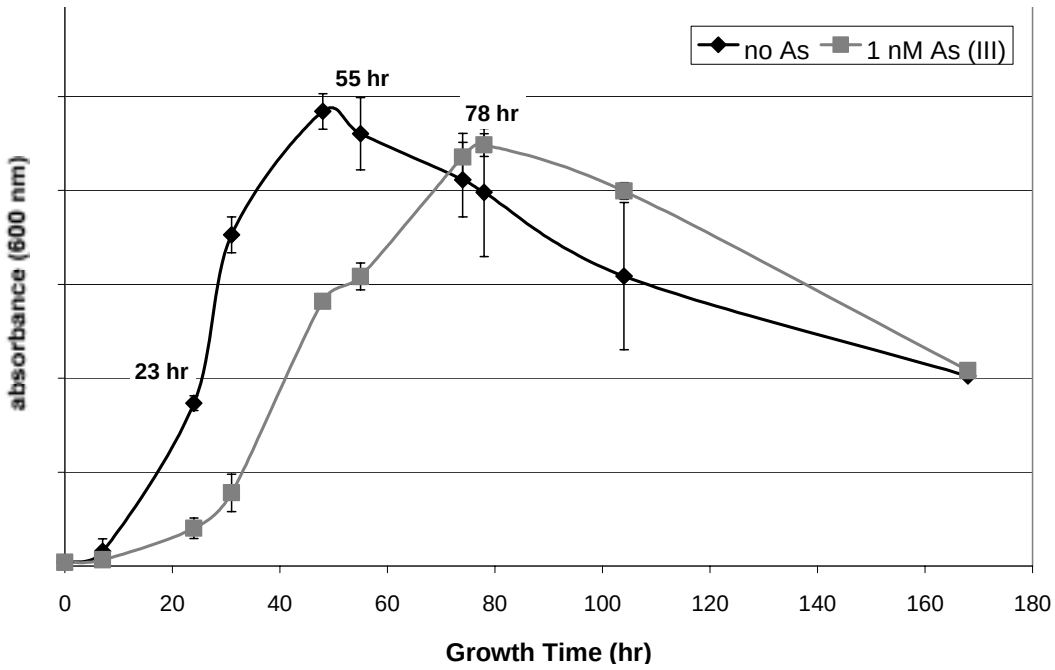

Figure 30. Growth curve for *Shewanella putrefaciens* grown in the presence (gray) and absence (black) of 1 mM As (III). Absorbance is directly proportional to cell number.

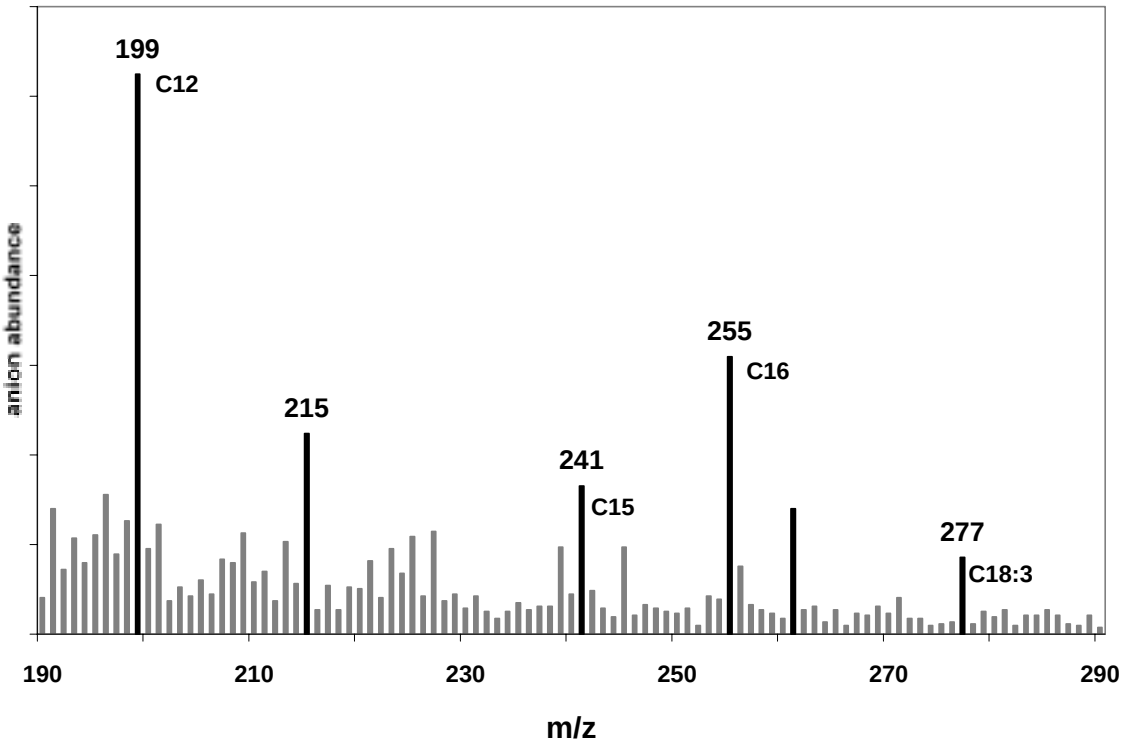

Figure 31. Anion SIMS spectrum of *Shewanella putrefaciens* collected at the start of the experiment (inoculation). The anions highlighted in black are anions originating from fatty acids.

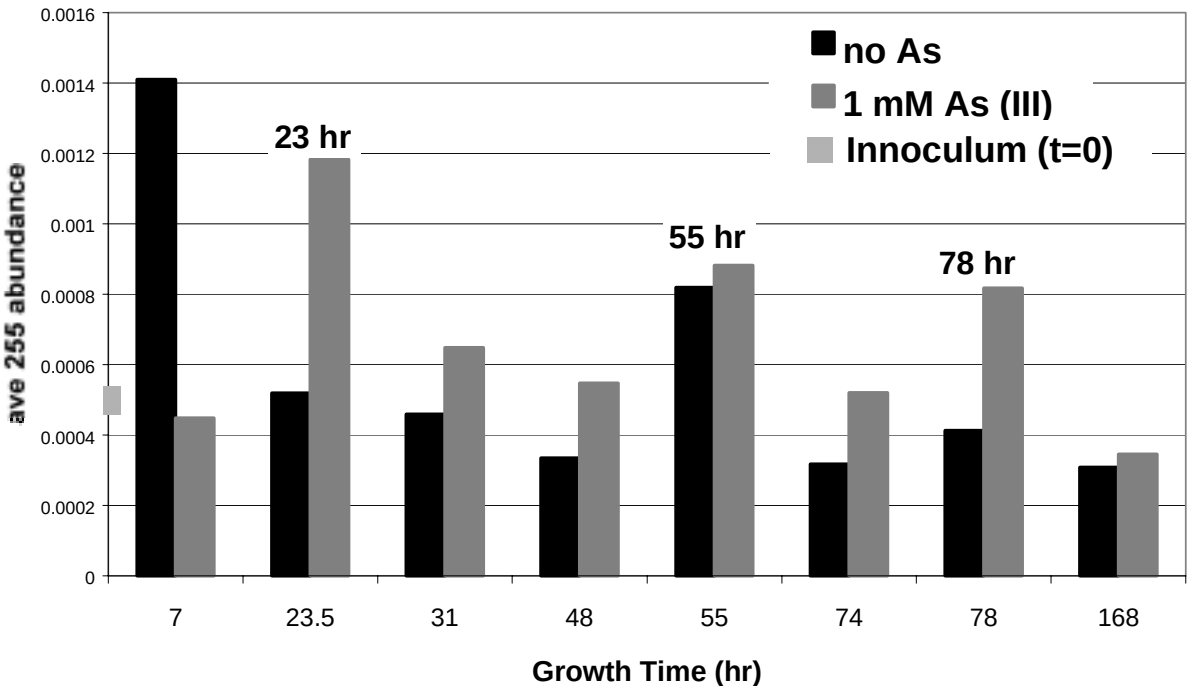

Figure 32. C16 fatty acid of Shewanella putrefactiens grown in the presence (gray) and absence (black) of 1 mM As(III). Average of SIMS ion abundance of m/z 255^- plotted versus growth time.

providing microbial characterization without having to remove them from their local micro-environment. An example of this type of analysis is demonstrated with the detection of *Shewanella oneidensis*, a dissimilatory iron reducing bacteria grown in the presence of crushed hematite. In these experiments, *Shewanella oneidensis* (ATCC 700550) was grown under anaerobic conditions in minimal salts medium (M-1) containing lactate as a carbon and energy source and crushed hematite (Wards Natural Science Establishment, Inc.) as a terminal electron acceptor.[38] The surface area of the crushed hematite was determined by N_2 adsorption at 35 m^2/g. Bacterial growth was monitored by tracking cell numbers. Cell numbers were determined by staining the bacteria with acridine orange and performing direct counts using an epifluorescent microscope. Prior to staining, samples were treated with 0.005% Tween and sonicated in an ice bath for 15 minutes to dislodge cells from the hematite particles. At the time samples were taken for analysis, the culture had reached a density of 5.1×10^8 cells/mL. For SIMS analysis, an aliquot of the microbe/hematite was removed from the culture, placed on aluminum foil to dry, and attached to a sample planchet using double-stick tape. Although a direct determination was not made, our conservative estimate is a maximum of 10^7 cells were present on the hematite surface analyzed by SIMS, assuming 0.1 mL of the culture exposed to 10 mg hematite in the sample.

The anion SIMS spectrum of the *S. oneidensis* attached to the hematite contains fatty acid peaks at m/z 227^- ($C_{14}H_{28}O_2$), m/z 241^- ($C_{15}H_{30}O_2$), m/z 255^- ($C_{16}H_{32}O_2$) (Figure 33). The anions at m/z 223^-, 237^-, and 265^-, as well as a small contribution to the peak m/z 255^-, are present in both the background and the *S. oneidensis* spectra. The m/z 223^- and 265^- anions have not been identified, but are presumed to be associated with the growth medium as they are not present in the anion spectrum of the blank hematite. The m/z 237 anion increased in abundance during the duration of the growth of the *S. oneidensis*. Since this anion was not easily identified by comparing to our SIMS library of biomolecules, we used the MS/MS capability of an ion trap SIMS instrument (see Reference 35) to gain further structural information concerning this molecule. The MS/MS results of the m/z 237 anion showed that it

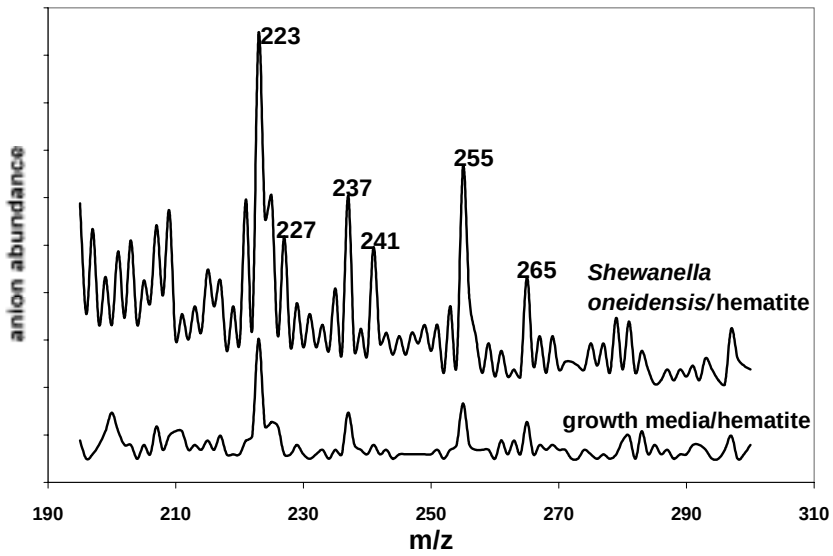

Figure 33. Anion SIMS spectrum of *Shewanella oneidensis* grown on crushed hematite (top) compared to the anion SIMS spectrum of the growth medium on crushed hematite.

fragmented to m/z 207 and 193, which are losses of 30 and 44 d respectively (see Figure 34). This fragmentation pattern is interpreted as being a loss of formaldehyde (CH_2O) and carbon dioxide (CO_2). These losses suggest that the m/z 237 anion may be associated with a saccharide. This preliminary result demonstrates both the potential for using SIMS to directly detect microbes present on solid surfaces and to investigate chemical alterations that may occur as a result of the interactions of microbe with the mineral surface.

Summary and Path Forward

Results of this project demonstrated the capability of SIMS for probing the interfacial chemistry of microorganisms and their chemistries in environmental settings. SIMS was found to be capable of detecting cell concentrations consistent with many environmental samples. The SIMS analysis of a pure culture of untreated, nontagged, intact bacterial cells (*S. oneidensis* on hematite) provides an example of how SIMS may be used for direct identification/detection of microorganisms in environmental samples or microcosms without the complications of cell extraction. Current efforts involve parallel work for continued development of SIMS along with the application of this technique to assist in the characterization of microbes and their processes on mineral surfaces to probe microbial alteration of contaminant metals and adsorptive surfaces.

Subtask 8. Solution Speciation using Electrospray Ionization Mass Spectrometry (ESI-MS)

In the geologic subsurface, metal transport is strongly influenced by partitioning that occurs between the solution phase and the surfaces of the mineral matrix. The partitioning behavior depends on the specific chemical species that exist on the mineral surface (both contaminants and adsorptive sites), and also in solution. Solution-phase species can range from the very simple, to the very complex, particularly in systems that contain actinides, and or biomolecules. The objective of subtask 8 was to begin to evaluate uranyl speciation in solution using electrospray ionization mass spectrometry (ESI-MS). The research would serve the dual purpose of evaluating the utility of this technique for characterization of complex organometallic species. Studies were conducted in collaboration with Professor Michael Van Stipdonk, Department of Chemistry, Wichita State University, under a subcontract arrangement.

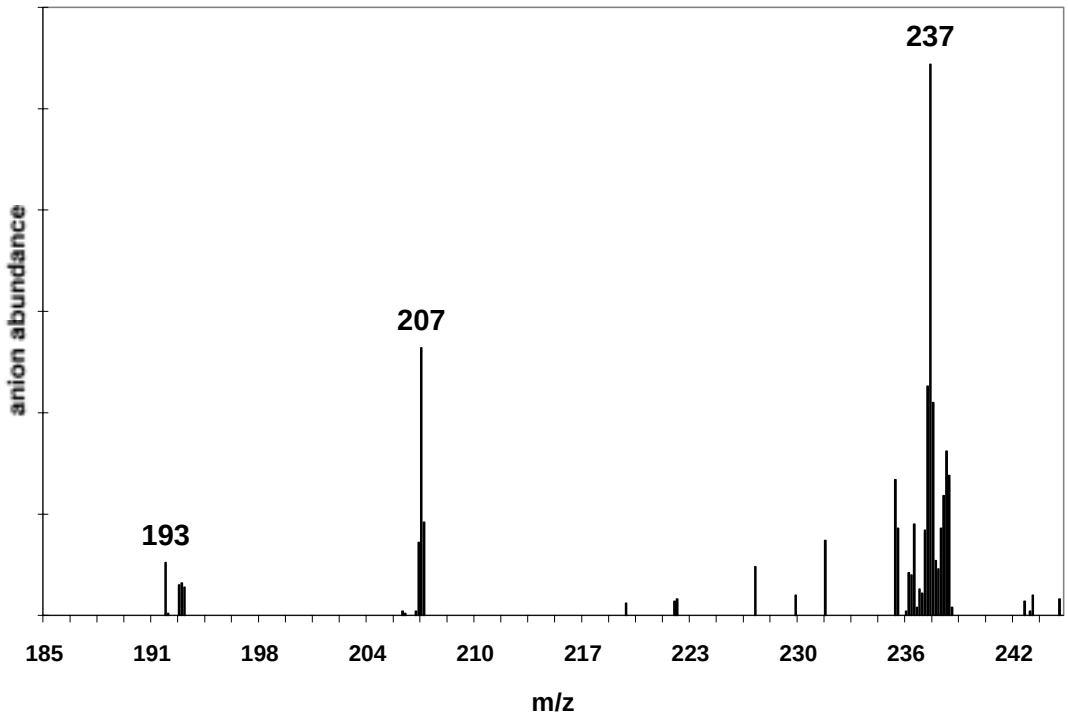

Figure 34. Anion MS/MS spectrum the m/z 237 parent anion from a sample of *Shewanella oneidensis* grown on crushed hematite.

To perform the experiments, 1 mM uranyl nitrate solution was electrosprayed using a Finnigan LCQ Deca ESI instrument. This instrument consists of an ESI source and an ion trap mass spectrometer. The ion trap is controlled by a data system capable of executing multiple stage mass spectrometry experiments, both collision induced dissociation and ion-molecule condensation reactions.

The positive ion mass spectrum contained cluster ions that contained up to five uranyl moieties, with a combination of nitrate, methanol, and methoxy ligands attached (see Figure 35 and Table 3). The base peak at *m/z* 428 is easily interpreted in terms of $UO_2NO_3^+$ solvated with three methanol molecules arranged with the nitrate around the equatorial coordination sites. Water does not effectively compete with methanol for the uranyl coordination sites.

Cluster ions containing two UO_2 units were observed at *m/z* 822 and 762. The *m/z* 822 ion is interpreted in terms of two uranyl moieties with three nitrate and three methanol ligands, where the uranyl moieties share two of the ligands (see Figure 36). This explanation satisfies charge balance requirements in a straightforward fashion, with uranyl contributing 2x(+2), nitrate 3×(-1), and methanol 3×(0) for a net charge of +1 (observed). The situation becomes more complicated for *m/z* 762, whose composition would appear to leave the molecule with a +3 charge. This observation is explained in terms of CH_3OH adding across the uranyl double bonds, which satisfies mass and charge requirements by reducing the uranium (see Figure 36). This explanation is supported by the observation of CH_3O^- ligands present on other cluster ions (results not presented in this report).

Higher mass molecules containing >2 UO_2 units were also observed. These ions contain substantial information describing intrinsic uranyl reactivity, and suggests that polymerization reactions of other actinides would be readily attackable using this strategy. Explicit discussion of these more complex molecules is not included in this report.

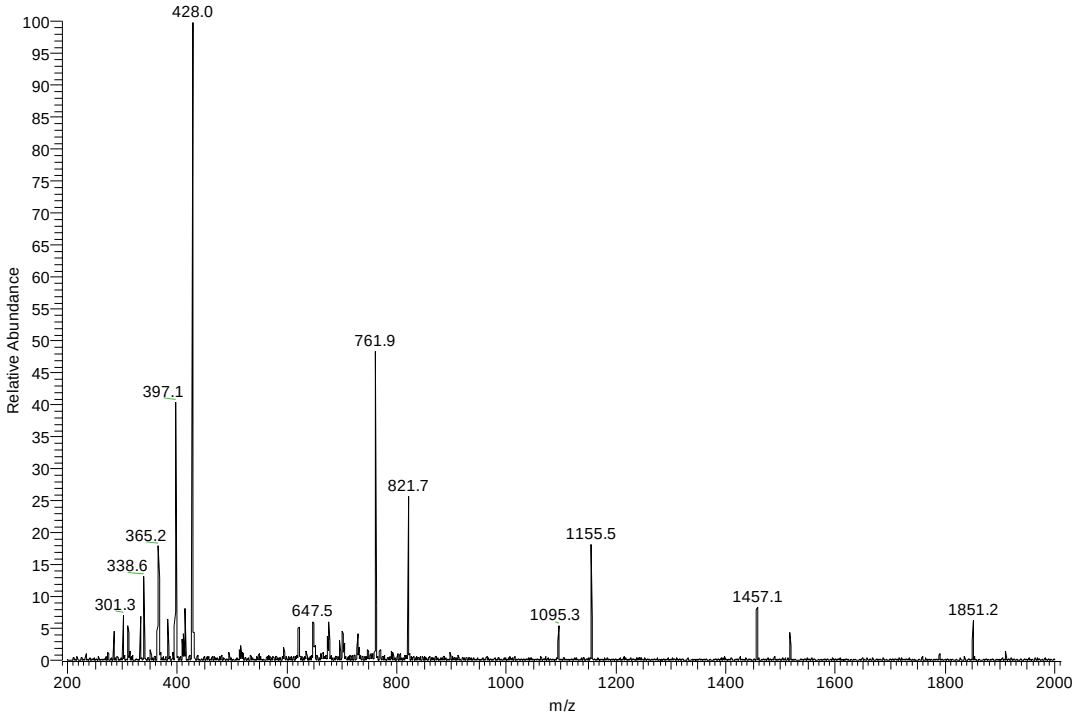

Figure 35. Positive ion ESI-MS analysis of uranyl nitrate electrosprayed as a 1 mM solution in a 1:1 methanol/water solvent.

Table 3. Compositions of ions observed in the positive ion ESI-MS analysis of uranyl nitrate sprayed as a 1 mM solution in 1:1 methanol/water.

m/z	Composition
428	$UO_2NO_3(CH_3OH)_3^+$
762	$(UO_2)_2NO_3(CH_3OH)_5^+$
822	$(UO_2)_2(NO_3)_3(CH_3OH)_3^+$
1095	$(UO_2)_3NO_3(CH_3OH)_6(CH_3O)^+$
1156	$(UO_2)_3(NO_3)_3(CH_3OH)_3^+$
1457	$(UO_2)_4(NO_3)_3(CH_3OH)_5(CH_3O)^+$
1851	$(UO_2)_5(NO_3)_5(CH_3OH)_5(CH_3O)^+$

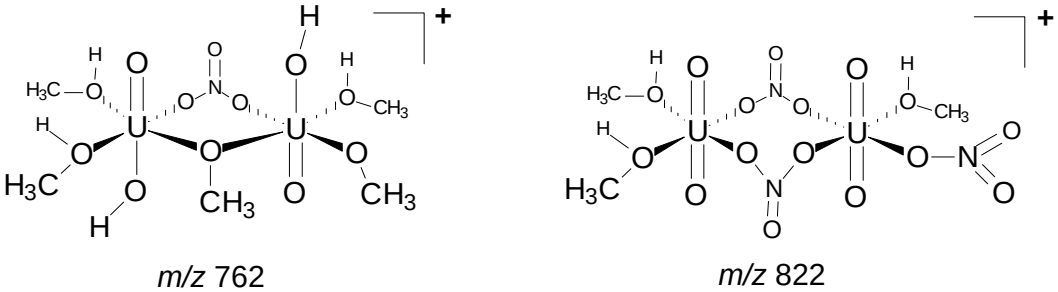

Figure 36. Proposed structures for abundant $(UO_2)_2$ species observed in the cation ESI-MS spectra of uranyl nitrate. In these structures, nitrate is assumed to be the bridging ligand, although there is currently no explicit evidence for this.

One final experiment is included in this report, because it portends great significance for solving complex bioorganic actinide speciation problems. We electrosprayed 1 mM Uranyl nitrate with an excess of sucrose to see whether uranyl-sucrose complexes would form in solution and whether these complexes could be observed intact in the mass spectrum. An analysis of the solution showed that the majority of the high abundance ions corresponded to $[\text{sucrose}]_n H^+$, but that a uranyl-sucrose adduct was clearly observed (see Figure 37). The ion at *m/z* 1295 corresponds to $[UO_2(\text{sucrose})_3\text{-}H]^+$, which suggests that two sucrose molecules are bound in a monodentate fashion around the uranyl equator, while a third sucrose is monodeprotonated, and binds in a bidentate fashion. The identity of this ion was identified using collision induced dissociation (CID) experiments, which showed that two sucrose molecules could be removed intact, but that the third could not be removed under the collision energies used. Curiously, the two CID product ions $[UO_2(\text{sucrose})_2\text{-}H]^+$ and $[UO_2(\text{sucrose})_1\text{-}H]^+$ showed no tendency to add solvent after the sucrose ligands had been knocked off. This indicates that the large sucrose ligand is capable of wrapping itself around the equatorial coordination sites of UO_2^{2+}, thereby excluding inner sphere solvent interactions.

More generally, this experiment showed that ESI-MS was capable of characterizing actinyl-carbohydrate complexes, thought to play a role in controlling adsorption in heterogeneous systems. This capability will eventually reveal the intrinsic reactivity behavior of actinide ionic species and provide an analysis approach that will unravel complexities encountered in actinide-contaminated systems having a strong geochemical component.

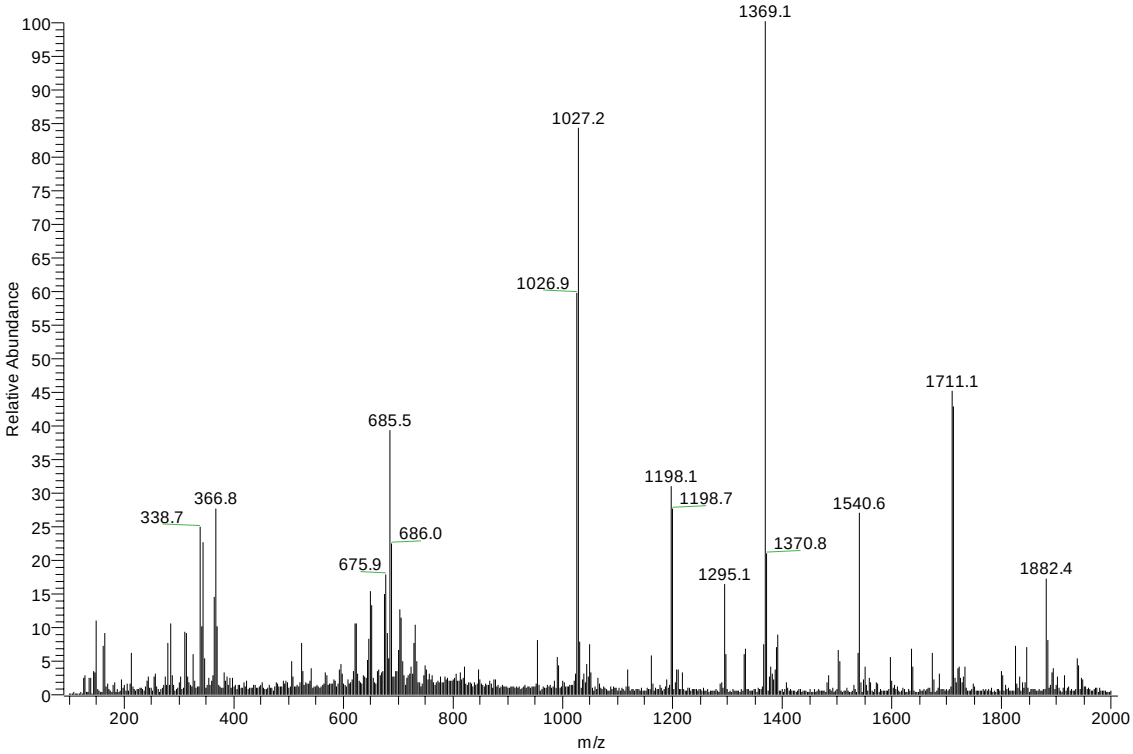

Figure 37. ESI-MS positive ion spectrum of 1 mM uranyl nitrate in 1:1 methanol/water, together with an excess of sucrose. Sucrose cluster ions are observed at 685, 1027, 1369, and 1711. The lower abundance ion at *m/z* 1295 corresponds to $[UO_2(\text{Sucrose})_3\text{-}H]^+$.

ACCOMPLISHMENTS

Subtask 1: Reversibility, Equilibrium, Forward and Reverse Reaction Kinetics, and Reversibility of Surface Reactions Over Extended Contact Periods

- A multiparameter model for Sr^{2+} adsorption was completed which enables prediction of K_d values over broad ranges of pH, ionic strength and other factors.
- Thirty-month contaminant-matrix studies were continued.
- Actinide distribution behavior was established.

Subtask 2. Periodic Wetting and Drying Cycles, and Their Potential for Altering Radionuclide Transport

- Initial experiments demonstrated altered partitioning behavior after only one dry/wet cycle.
- Multiple wet/dry cycle experiments were continued.

Subtask 3. Colloid-Facilitated Radionuclide Transport

- Digital radiography—computer tomography experiments demonstrated that aqueous intrusions into a column containing particulate material could be imaged.

Subtask 4. Microbial Ligand-Modified Transport

- Microbial diversity increased with the addition of organic carbon to mesocosm experiments containing RWMC soils and organic carbon.

Subtask 5. Surface Speciation

- Reactivity studies were completed for U and Cr ionic species.
- Isotherm development based on surface analysis data (SIMS) was demonstrated.
- Laser irradiation and oxygen isotopic exchange techniques were conceived and demonstrated.

Subtask 6. Sputtered Neutrals

- An approach for determination of Fe oxidation state on surfaces, that utilizes a simple derivatization together with SIMS, was developed.

Subtask 7. Bioanalytical Surface Studies: Characterization of Microbial Interfacial Chemistries using Surface Analytical Techniques

- Sensitive bacterial detection approaches were developed based on fatty acid conjugate detection.

Subtask 8. Solution Speciation using Electrospray Ionization Mass Spectrometry (ESI-MS)

- Direct detection of uranyl complexes demonstrated, including carbohydrate complexes.

Publications

Published

LaViolette R. A. and G. D. Redden, 2002, "Comment on Modeling the Mass-Action Expression for Bidentate Adsorption," *Environmental Science & Technology*, Vol. 36, No. 10, pp. 2279–2280.

Lee, B. D., M. R. Walton, and J. L. Meigio, 2001, "Interaction of Microbes and Uranium during Enrichment for TCE Reductive Dechlorination," *In* Anaerobic Degradation of Chlorinated Solvents, V. Magar, D. Fennell, J. Morse, A. Leeson and B. Alleman (eds.), pp. 77–85.

Submitted

Gianotto, A .K., B. D M. Hodges, M. T. Benson, P. B. Harrington, A. D. Appelhans, J. E. Olson, and G. S. Groenewold, "Ion-Molecule Reactions

of Gas-Phase Chromium Oxyanions: $Cr_xO_yH_z^-$ + H_2O," *J. Phys. Chem. A, submitted*.

Gresham, G. L., J. R. Scott, J. E. Olson, A. D. Appelhans, and G. S. Groenewold, "Gas-Phase Reactions of UO_2^+ with H_2O," *J. Phys. Chem. A, submitted.*

Ingram, Jani C., William F. Bauer, R. Michael Lehman, Sean P. O'Connell, A. D. Shaw, "Detection of Fatty Acids from Intact Microorganisms by Molecular Beam Static Secondary Ion Mass Spectrometry", *Journal of Microbiological Methods, submitted*.

Shaw, A. D., M. M. Cortez, A. K. Gianotto, A. D. Appelhans, J. E. Olsen, C. Karahan, R. Avci, and G. S. Groenewold, "Static SIMS Analysis of Carbonate on Basic Alkali-bearing Surfaces," *Surface and Interface Analysis, submitted*.

Presentations

Gianotto, Anita K., Brittany D. M. Hodges, Anthony D. Appelhans, Michael T. Benson, Peter B. Harrington, and Gary S. Groenewold, "Oxidation of $Cr_xO_y^-$ in an Ion Trap Secondary Ion Mass Spectrometer," *50th ASMS Conference on Mass Spectrometry and Allied Topics, June 2–6, 2002, Orlando, FL.*

Gianotto, Anita K., Brittany D. M. Hodges, Anthony D. Appelhans, John E. Olson, Michael T. Benson and Gary S. Groenewold, "Condensation Reactions of $Cr_xO_y^-$ in an Ion Trap Secondary Ion Mass Spectrometer," *Meeting of the Federation of Analytical Chemistry and Spectroscopy Societies, October 13–17, Providence, RI.*

Gresham, Garold L., Jill R. Scott, Paul Tremblay, Bruce Mincher, John Olson, Gary S. Groenewold, "Uranium Speciation Using SIMS And LD-MS," *50th ASMS Conference on Mass Spectrometry and Allied Topics, June 2–6, 2002, Orlando, FL.*

Groenewold, G. S., "Analytical and Intrinsic Reactivity Investigations using an Ion Trap SIMS," *Departmental Seminar, University of Antwerp, Antwerp, Belgium, May 30, 2001.*

Groenewold, G. S., "Challenges in Analysis of Real World Particles," *Conference on Real World Challenges and New Developments in Environmental Mass Spectrometric Measurements, Asilomar, CA, October 2001.*

Groenewold, Gary, Recep Avci, Lee Richards, Jan Sunner, Bob Fox, and Jani Ingram, "Laser-Assisted SIMS of Metal-Contaminated Minerals," *50th ASMS Conference on Mass Spectrometry and Allied Topics, June 2–6, 2002, Orlando, FL.*

Hodges, Brittany D. M., Anita K. Gianotto, Gary S. Groenewold, "Isotopic Oxygen Exchange Of Si And Al Oxyanions," 50*th ASMS Conference on Mass Spectrometry and Allied Topics, June 2–6, 2002, Orlando, FL.*

Ingram, J. C., "Application of Static SIMS to Investigate Environmental Geomicrobiology," *Conference on Real World Challenges and New Developments in Environmental Mass Spectrometric Measurements, Asilomar, CA, October 2001 (invited talk).*

Ingram, J. C., "Interfacial Chemistry Investigations of Microbial Processes," *Pittsburgh Conference Symposium Celebrating Diversity in Analytical Chemistry, New Orleans, LA, March 2002 (invited talk).*

Wright, Karen E., D. Craig Cooper, William F. Bauer, George D. Redden, "Effects of Wet-Dry Cycling on the Mobility of Cs, Sr, Cr, Cd, and U in Idaho National Environmental and Engineering Laboratory (INEEL) Soil and Soil Constituents," *AGU 2002 Fall Meeting, San Francisco, December 6–10, 2002.*

REFERENCES

1. *Research Needs in Subsurface Science*. J. C. S. Long, Ed., National Academy Press: Washington, D.C., 2000, p. 159.

2. J. Langston, *Idaho Falls Post Register*, 2001, A1–A3.

3. J. Brown (G.E.), V. E. Henrich, W. H. Casey, D. L. Clark, C. Eggleston, A. Felmy,

D. W. Goodman, M. Gratzel, G. Maciel, M. I. McCarthy, K. H. Nealson, D. A. Sverjensky, M. F. Toney, J. M. Zachara, *Chem. Rev.*, 1999, Vol. 99, pp. 77–174.

4. K. B. Krauskopf and D. K. Bird, *Introduction to Geochemistry*, 3rd ed., WCB McGraw-Hill: Boston, MA, 1995.

5. G. S. G. Groenewold (A.K.); J. C. Ingram, A. D. Appelhans, *Current Topics in Analytical Chemistry*, Vol. 1, 1998, pp. 73–91.

6. S. D. Conradson, *Applied Spectroscopy*, 1998, Vol. 52, pp. 252A–279A.

7. J. R. G. Scott G. S., A. K. Gianotto, M. T. Benson, J. B. Wright, *Journal of Physical Chemistry A*, 2000, Vol. 104, pp. 7079–90.

8. W. J. Griffiths, A. P. Jonsson, S. Y. Liu, D. K. Rai, Y. Q. Wang, *Biochemical Journal*, 2001, Vol. 355, pp. 545–561.

9. Stewart, II. *Spectrochimica Acta Part B—Atomic Spectroscopy*, 1999, Vol. 54, pp. 1649–1695.

10. J. M. Zachara, S. C. Smith, C. X. Liu, J. P. McKinley, R. J. Serne, P. L. Gassman, *Geochimica Et Cosmochimica Acta*, 2002, Vol. 66, pp. 193–211.

11. T. Shahwan and H. N. Erten, *Journal of Radioanalytical and Nuclear Chemistry*, 2002, Vol. 253, pp. 115–120.

12. A. J. Tesoriero and J. F. Pankow, *Geochimica Et Cosmochimica Acta*, 1996, Vol. 60, pp. 1053–1063.

13. N. E. Pingitore, F. W. Lytle, B. M. Davies, M. P. Eastman, P. G. Eller, E. M. Larson, *Geochimica Et Cosmochimica Acta*, 1992, Vol. 56, pp. 1531–1538.

14. R. H. Parkman, J. M. Charnock, F. R. Livens, D. J. Vaughan, *Geochimica Et Cosmochimica Acta*, 1998, Vol. 62, pp. 1481–1492.

15. A. Katz, A. Starinsk, E. Sass, H. D. Holland, *Geochimica Et Cosmochimica Acta*, 1972, Vol. 36, pp. 481–488.

16. E. Curti, *Applied Geochemistry*, 1999, Vol. 14, pp. 433–445.

17. W. H. Casey, P. A. Rock, J. B. Chung, E. M. Walling, M. K. McBeath, *American Journal of Science*, 1996, Vol. 296, pp. 1–22.

18. G. R. Choppin, *Journal of Radioanalytical and Nuclear Chemistry-Articles*, 1991, Vol. 147, pp. 109–116.

19. G. R. Choppin, A. H. Bond, and P. M. Hromadka, *Journal of Radioanalytical and Nuclear Chemistry*, 1997, Vol. 219, pp. 203–210.

20. J. W. Morse and G. R. Choppin, *Reviews in Aquatic Sciences*, 1991, Vol. 4, pp. 1–22.

21. R. A. Fjeld, T. A. DeVol, R. W. Goff, M. D. Blevins, D. D. Brown, S. M. Ince, A. W. Elzerman, *Nuclear Technology*, 2001, Vol. 135, pp. 92–108.

22. C. Degueldre, A. Bilewicz, W. Hummel, J. L. Loizeau, *Journal of Environmental Radioactivity*, 2001, Vol. 55, pp. 241–253.

23. E. N. Rizkalla, L. F. Rao, G. R. Choppin, J. C. Sullivan, *Radiochimica Acta*, 1994, Vol. 65, pp. 23–27.

24. S.-Z. Lee, L. Chang, C.-M. Chen, H.-H. Yang, P.-Y. Hu, *Journal of Environmental Science and Health*, 2001, Vol. A36, pp. 63–74.

25. A. B. Kersting, D. W. Efurd, D. L. Finnegan, D. J. Rokop, D. K. Smith, J. L. Thompson, *Nature*, 1999, Vol. 397, pp. 56–59.

26. R. C. Marty, D. Bennett, P. Thullen, *Environmental Science and Technology*, 1997, Vol. 31, pp. 2020–2027.

27. U.S. Department of Energy, *Report number DOE/ID-10622*, 1998, August 1998.

28. W. H. Casey, B. L. Phillips, M. Karlsson, S. Nordin, J. P. Nordin, D. J. Sullivan, S. Neugebauer-Crawford, *Geochimica et Cosmochimica Acta*, 2000, Vol. 64, pp. 2951–2964.

29. S. J. Pachuta and R. G. Cooks, *Chemical Reviews*, 1987, Vol. 87, pp. 647–669.

30. J. E. Delmore, *EMSP Project number 60424*, 2000.

31. B. L. M. van Baar, *FEMS Microbiol. Rev.*, 2000, Vol. 24, pp. 193–219.

32. D. Si, D. Zhong, X. Chen, *Analytical Chemistry*, 2001, Vol. 73, pp. 3808–3815.

33. R. L. Kepner and J. R. Pratt, *Microbiology*, 1994, Vol. 58, pp. 603–615.

34. J. E. Hobbie, R. J. Daley, S. Jasper, *AEM*, 1977, Vol. 33, pp. 1225–1228.

35. J. C. Ingram, A. D. Appelhans, and G. S. Groenewold, *Int. J. Mass Spectrom. Ion Proc*,. 1998, Vol. 175, pp. 253–262.

36. C. Myers and K. H. Nealson, *Geochim. Cosmochim. Acta*, 1988, Vol. 52, pp. 751–756.

37. O. H. Lowry, N. J. Rosebrough, A. L. Farr, R. J. Randall, *J. Biol. Chem.*, 1951, Vol. 193, pp. 265–275.

38. J. Kostka and K. H. Nealson, "Isolation, Cultivation and Characterization of Iron and Manganese-Reducing Bacteria," In *Techniques in Microbial Ecology*, R. S. Burlage, R. Atlas, D. Stahl, G. Geesey, G. Sayler, Eds., Oxford University Press: New York, 1998, pp. 58–78.

Biogeochemical Controls on the Migration of Cesium in the Rhizosphere

Carl D. Palmer, Melinda A. Hamilton, and Richard Hess (INEEL);
Bruce Bugbee (Utah State University); and Lori Siegel (Northeastern University)

SUMMARY

Successfully designing environmental remediation strategies for soil contaminated with metals, radionuclides, and mixed waste requires fundamental understanding of key processes that affect the transport and transformation of contaminants. For example, the nature of radiocesium sources is such that they often result in the contamination of shallow (<1 m) vegetated soils. This surface and near-surface soil contamination on vegetated sites can be susceptible to migration by plant-facilitated ^{137}Cs translocation. Once inside the plant, ^{137}Cs is not only repositioned within the soil profile, but can move through the food chain via grazing and predation, or be further dispersed throughout the environment by range fires. Therefore, the bioavailability of metals and radionuclides is a key concern in developing successful biological remediation technologies, assessing long-term performance of barriers, and maintaining long-term stewardship of DOE lands.

This research project addresses these important issues by investigating specific biogeochemical processes occurring in plant/soil systems of the sagebrush steppe ecosystem at the INEEL. Our objective is to obtain the necessary knowledge to manipulate contaminant mobilization, transport, transformation, and ultimate fate in near-surface and subsurface soils. This knowledge will enable development of technologies and methods for manipulating the rhizosphere (root zone and associated ecology) to control contaminant migration and transformation; either to promote upward migration for remediation or to prohibit upward migration to improve barrier performance.

Our research focuses on investigating the binding and solubilization of cesium (Cs) in soils and the rhizosphere, and plant uptake of Cs from rhizosphere systems, Cs being the most commonly encountered contaminant by number of DOE sites. The biomolecules in root exudates are being identified and quantified. The interactions of biomolecules (microbial or plant produced) with clays that bind Cs are being investigated. Complex interactions between soil, plants, and microbes are simulated using a “systems approach” model. We are investigating the feasibility of using mesoscale physical models of plant/soil systems to test our conceptual and computational models.

In support of alternative cleanup strategies and long-term stewardship obligations at the INEEL, extensions of this work to WAG-3 and WAG-7 contaminants would resolve concerns that any vegetated cap will eventually bring contaminants to the surface. This work also offers the potential for bioinduced decontamination of contaminated near-surface soils. The breadth of users that will benefit from low capital and low operating cost ecosystem-based technologies include the DOE, the Department of Defense, the mining industry, oil and gas industry, and the U.S. Department of Agriculture. This effort will advance ecological engineering technologies that are unique and competitive and address pressing environmental problems and demands.

PROJECT DESCRIPTION

A legacy of previous activities at DOE sites is contamination of soil and ground water. The cleanup of these sites is expected to be a long-term mission and the total estimated costs are relatively high.[1] Containment and remediation designs depend on an accurate understanding of the zone of contamination and the extent to which these contaminants migrate. Unexpected translocation of contaminants due to biological activity greatly increases the risks associated with these decisions. In contrast, knowledge of translocation processes can be used to design more effective and less expensive approaches to remediation. Understanding the biogeochemical processes affecting contaminant mobility and availability will allow DOE to improve its ability to (a) assess

bioavailability of contaminants in soil systems; (b) determine the rate of contaminant migration in soil systems either upward, downward, or laterally from the point of origin; (c) determine the long-term risk to human health and the environment; and (d) make informed decisions regarding the management of wastes.

This project specifically seeks to understand and quantify the role of plants and their associated rhizosphere systems in translocation of radionuclides through the soil. The proposed project directly supports Subsurface Science Initiative objectives by developing the fundamental understanding needed to predict and control the fate and transport of contaminants, and to design better remediation strategies. The three key outcomes that we are anticipating are:

- Validation that plants can actively translocate contaminants by upward or downward migration of Cs through the soil profile
- Elucidation of the mechanisms by which plants and their associated rhizosphere achieve this translocation
- Quantitative measures of the magnitude and rate of the upward translocation of Cs.

To achieve this outcome, the *Biological Studies* are designed to provide information about the exudates that can enhance the solubility of Cs, the uptake of Cs to soil microbes, and the transfer coefficients between Cs-loaded clays and crested wheatgrass. *Geochemical Studies* will provide information on the bioavailability of Cs as plant exudates and cations are added to the soil. The quantitative data obtained from this work will be input to the comprehensive model for comparison with the results of the mesoscale experiment. This comparison can be used in the validation the mathematical model. The database from mesoscale experiments can be used to verify mathematical models developed by other researchers. In summary, the expected outcomes include:

- Quantitative measurement of the magnitude and rate of translocation of Cs in desert soils dominated by crested wheatgrass
- Model of Cs bioavailability and translocation in soils
- Database for validation of models for the transport and fate of Cs in soil
- Parametric studies illustrating the range of expected behavior of Cs in soil under a range of reasonable conditions.

Characterization of Root Exudates from Crested Wheatgrass

Overview

The objective of this work is to identify root exudates from crested wheatgrass by quantifying the effect of environmental factors on the production of exudates. Root exudates are typically comprised of low-molecular-weight compounds, including organic acids, sugars, phenols, and amino acids. The quantity and quality of these compounds have a significant effect on microbial activity in the rhizosphere and are important in the function of the plant/soil system. Some of these compounds can increase the mobility and bioavailability of metals such as Cs from contaminated soils.

Under a subcontract with the INEEL, the Utah State University (USU) Crop Physiology Laboratory is performing experiments on crested wheatgrass using sterile root-zone environments. Solutions collected from these model systems are being analyzed to characterize root exudates. The amount and composition of these exudates is expected to vary with the type and amount of plant stress. Therefore, USU is examining the effects of K^+, NH_4^+, drought, and flooding stresses. These conditions in hydroponic/sterile media model systems will be manipulated to determine conditions that promote production of exudates. The information obtained in this study is crucial to INEEL operations and DOE for their estimation of contaminant migration from the shallow soil systems, the quantification of the bioavailability of metal contaminants, and their evaluation of potential remedial strategies of metals-contaminated soil. The specific studies include:

- Improved design of experimental hydroponic systems to maintain sterile conditions for extended periods of time.

- Experiments to recover and measure the quantity and quality of root exudates of select genotypes of crested wheatgrass in sterile hydroponic systems.

- Experiments to measure the quantity and quality of root exudates as a function of plant stress, including nutrient availability (particularly K+), nitrogen form, root-zone water potential, root-zone oxygen availability, and plant age.

Materials and Methods

The root-zone container is a 22-cm-long glass tube (38-mm outside diameter, 35-mm inside diameter) containing Ottawa sand (Figure 1). Five layers of sand grain sizes were used to maintain uniform water content throughout the growth container. Grain size and layer thickness were determined using the van Genuchten (1980) water retention model.[2] The sand depths were, from top to bottom: 4.5 cm fine (40–50 grit); 3.5 cm fine/medium mix (30–50 grit); 2.5 cm medium (30–40 grit); 2.5 cm medium/coarse mix (20–40 grit); 3 cm coarse (20–30 grit). The top of the container was made from a second 22-cm-long glass column connected by a ground glass joint. The column was sealed with an open-cell foam plug to prevent contamination. The tube was closed on the bottom with a one-holed silicone stopper with a 9.5-cm-long glass tube lined with a silanized glass wool wick to aid water flow out of the growth container. The glass wool wick and glass tube were attached to a leachate collection vial via a two-holed silicone stopper (one hole filled with glass wool to allow air displacement while preventing contamination). The sand in the columns was preloaded with iron to improve iron nutrition during the trial.

Figure 1. Plants from Trial 6 growing in containers in a laminar flow hood.

All columns were maintained for 70 days in a laminar flow hood (Contamination Control Inc). The hood was modified for plant growth by fitting with two high-pressure sodium lamps to supply a PPF of 550 µmol m^{-2} s^{-1} (16-hr photo period). The air temperature was maintained at 25°C. Plants were watered to excess every 1–4 days with filtered nutrient solution to obtain at least 25 mL of leachate and maintain healthy plants. Airflow through the upper columns was supplied during the light period and maintained at 65 mL/min to 1 L/min based on plant size and air flow necessary to eliminate condensation inside the columns.

Nutrient solutions and watering volumes were manipulated to induce treatments of low K^+, increased NH_4^+, drought, and flooding. Two plants were assigned to each treatment beginning on day 35, with 6 control plants watered with the same frequency and nutrient solution as previous, with the exception of reducing the strength of the nutrient solution to reduce the buildup of salts. Low K^+ was induced by decreasing the concentration of K^+ in the nutrient solution from 5.5 to 0.5 mM. For the NH_4^+ treatment, the NH_4^+: NO_3^- ratio was changed from 0:7 to 2:6. This ratio was increased again to 4:3 on day 57. Drought was induced by watering with 75% less volume than the controls, with intermittent watering of an adequate volume of nutrient solution to obtain leachates. A stopper was placed in the drain tube of the flood treatment to inhibit water from dripping out of the column and induce flooding.

The precautions taken to maintain sterile conditions in the hydroponic systems as long as possible included (a) surface sterilization of the seeds, (b) cleaning and sterilization of the sand, (c) cleaning and sterilization of the column components, (d) sterile transfer of germinated seed from petri dishes to glass columns, (e) filtration of the column air, (f) sterilization of the nutrient solution, (g) using sterile syringe injection of nutrient solutions, and (h) using a laminar flow hood with HEPA filters. Column contamination was tested by visual examination of plates using aliquots of leachate (20 mL per column) on 1/10 strength nutrient broth with 1.5% agar.

We also performed a direct total microbial count using the epifluorescent Microscopic Method[3] wherein 5 mL of leachate was stained with acridine orange, filtered through a 0.2 µm nonfluorescent membrane, and observed at 100× under a UV light. Microbes could be seen in samples from columns identified as contaminated on the plates.

Results

Contamination was reduced compared to previous trials by growing the plants in a laminar flow hood and enclosing the shoot in a glass column (Figure 2). We made the following improvements in sterile technique in Trial 6:

- Exposure time of the growth columns and germinated seeds to the surrounding air during planting was minimized by preassembling components before sterilizing.
- Sterile gloves were used for all manipulations.
- Extra sand was autoclaved separately to pour on top of seedlings during planting. This procedure eliminated the need for burying the seedling with a spatula, thereby reducing the number of manipulations and the exposure time of the column to the surrounding air.
- Airflow manifolds were mounted directly to the racks holding the columns, which improved laminar flow of sterile air through the workspace.

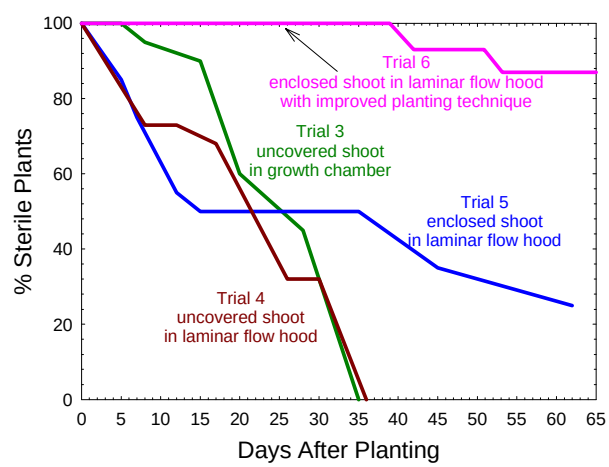

Figure 2. Percent sterile plants under various trials of column construction and manipulation.

Ammonium was effective in acidifying the rhizosphere. On day 65, the pH of the leachates ranged from 4.2 in the NH_4^+ treatment to 8 in the control and water stress treatments (Figure 3).

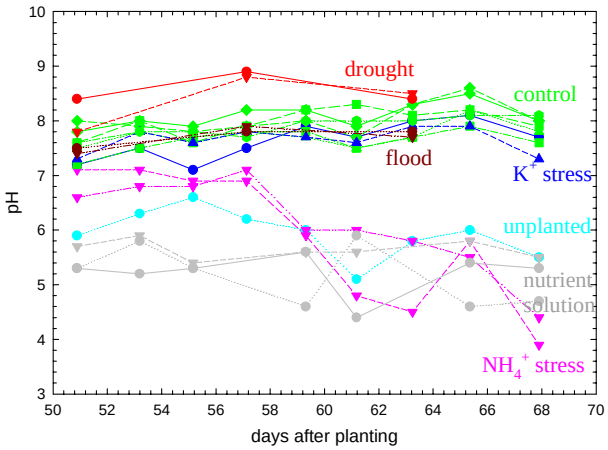

Figure 3. pH of nutrient solutions used for watering and leachates from all plants. Treatments were started on day 35.

The total organic carbon (TOC) in leachate samples was monitored throughout the trial (Figure 4). The cumulative amounts of carbon collected were compared to the control (Table 1). The amounts of carbon released were increased compared to the control in the K^+ stress, drought, and flooding treatments, but the NH_4^+ treatment decreased compared to the control. Only the amount of carbon per gram of dry plant released due to the drought treatment was significantly higher than the other treatments ($p > 0.05$).

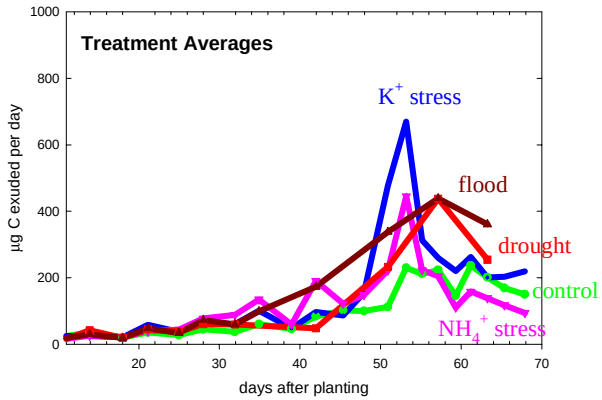

Figure 4. Organic carbon per day in leachate samples as a function of time for different treatments.

Table 1. Cumulative carbon (since 11 days after planting) collected as exudate on a per gram dry shoot basis.

	mg C exuded per gram of dry plant		
	Average	Std. dev.	% of control
Control	2.58	0.43	
K+	3.72	0.57	144
NH4+	2.33	0.10	90
Drought	4.40	0.52	171
Flood	3.75	0.94	145

Ion chromatography analysis was performed on plant shoots to determine nutrient content. The potassium content of the plants in the K^+ stress treatment was about 50% of the controls. All other nutrients were present in normal amounts. Organic acids in roots obtained by derivativization demonstrate that fumarate, malate, and succinate are three of the most common acids (Figure 5). The highest concentrations were obtained under drought conditions.

Overview

The uptake of Cs by plants will be greatly affected by its bioavailability on the clay materials commonly found in the soil. This uptake can be affected by competing ions in the soil, the specific type of sorption site (labile, strongly bound), and the rate at which interlayer cations can be released to the soil solution as a result of ligand-promoted dissolution of the clay minerals. Most of our experimental work focused on Cs binding to illite clay because Cs is known to bind strongly to illite and illite is a common constituent in soils at the INEEL. We have conducted experiments on illite to assess

- The effect of pH and time on Cs adsorption to illite
- Effect of NaCl concentrations on Cs sorption
- Effect of pH and time on the rates of sorption
- Cs sorption in the presence of organic acid anions

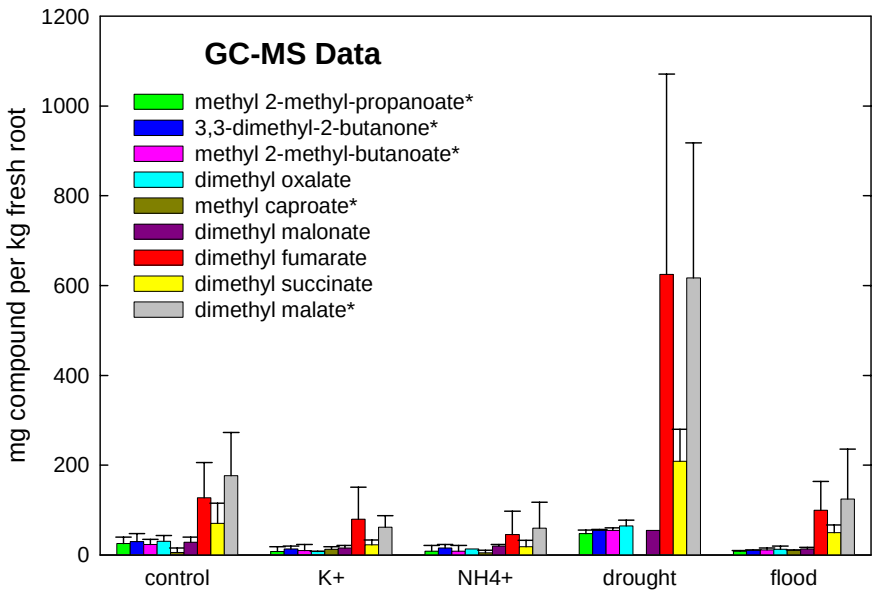

Figure 5. Derivatized organic acids obtained by gas chromatography on plant roots. Binding of Cs to Clays.

- Cs desorption from illite.

Ms. Laura Hanson, a Ph.D. candidate in the Department of Crop and Soil Science at Washington State University (WSU), conducted this work at the INEEL. Ms. Hanson's Ph.D. supervisor at WSU, Dr. James Harsh, has an INRA grant to study Cs binding to soils. A series of adsorption experiments were conducted at the INEEL using a reference clay and stable Cs. An IMt-1 illite was obtained from The Source Clays Repository and the 0.2–2.0 µm size fraction was isolated by sedimentation. Clays were treated with sodium acetate ($NaC_2H_3O_2$) at pH ~5 to remove carbonates, then washed with 18.0 MΩ•cm deionized water. Illite was subsequently treated with KCl to saturate exchange sites with K^+, then washed again with 18.0 MΩ•cm deionized water. The K^+-saturated IMt-1 was oven-dried to a constant mass at 60°C and stored in an airtight container prior to use.

Results

Solution pH had a significant effect on the extent of Cs^+ sorption to IMt-1 illite, however the rate of Cs^+ sorption to IMt-1 did not appear to depend on solution pH. The most rapid sorption occurred within the first 48 hours, followed by slower Cs^+ uptake that reached a maximum at approximately 96 hours. Further examination of the effect of solution pH on Cs^+ sorption to IMt-1 illite showed that after 96 hours, there was an increase in Cs^+ sorption to IMt-1 with initial CsCl concentration as solution pH increased from 6.0 to 10.0. A range of NaCl solution concentration (0.015 to 0.075 M) was selected to examine the effect [NaCl] on Cs^+ sorption to IMt-1 illite. An initial Cs^+ concentration of 0.04 mM and solution pH of 8.0 were used throughout this experiment. As the concentration of NaCl increased there was a corresponding decrease in Cs^+ sorption to IMt-1 (Figure 6). As NaCl concentration increased to 0.075 M, Cs^+ sorption to illite approached zero. This indicates that the majority of Cs^+ sorbed to IMt-1 illite is not selectively sorbed and is exchangeable by Na^+.

Dilute sodium oxalate was added to the system to assess the effect of plant root exudates on Cs^+ sorption to IMt-1 illite at pH 8. A large increase in Cs^+ sorption to illite was observed in the presence of 0.04 mM $Na_2C_2O_4$ (Figure 7). Oxalate is not a strong complexant of Cs^+; therefore, we assume that the cause of the increase is due to $Na_2C_2O_4$ reaction with illite.

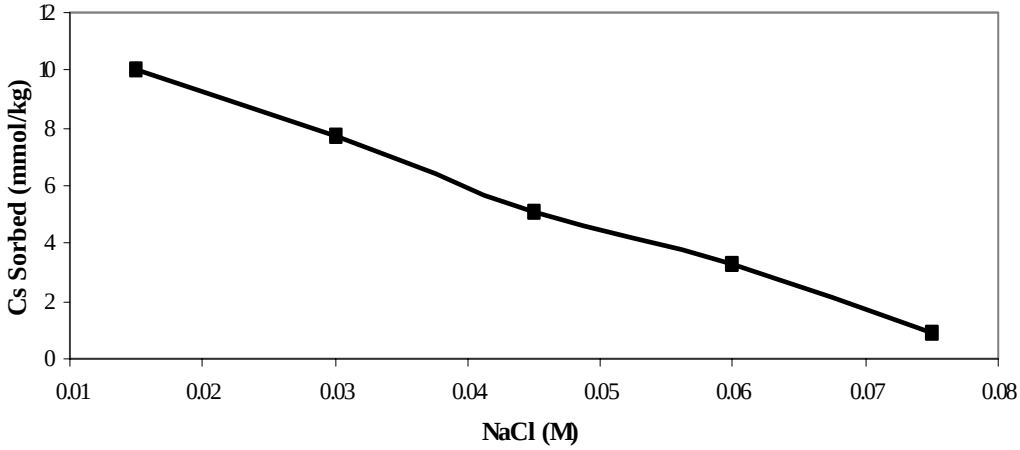

Figure 6. Cs sorption to IMt-1 illite (mmol kg^{-1}) at NaCl solution concentrations between 0.015 and 0.075 M. Initial Cs^+ concentration of 0.04 mM and solution pH of 8.0 were the same in all cases.

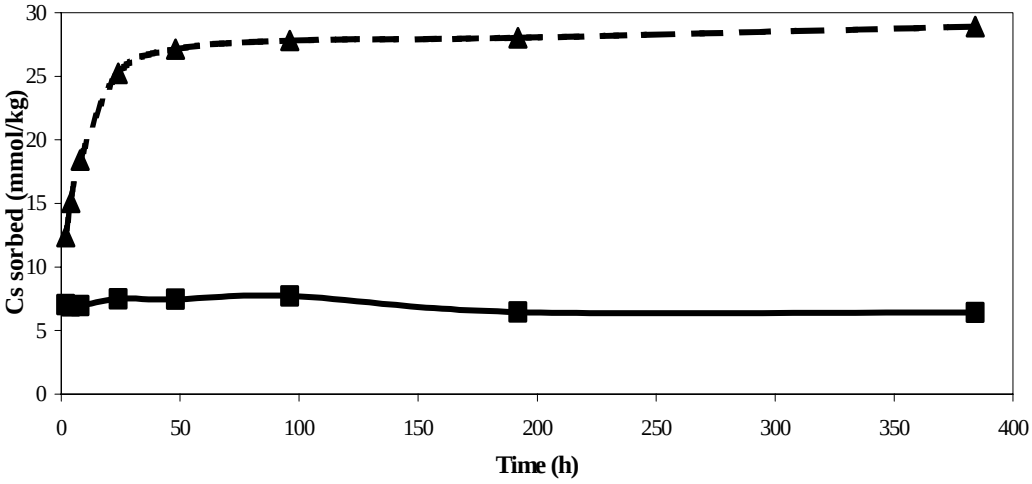

Figure 7. Cs sorption to IMt-1 illite at pH 8 in the presence ( ) and absence ( ) of 0.04 mM $Na_2C_2O_4$. Initial Cs^+ concentration of 0.007 mM and background NaCl concentration of 0.015 M were the same in both cases. Initial concentration of Cs^+ on IMt-1 was ~229 mmol kg^{-1}.

Cs desorption from IMt-1 illite was significantly enhanced (α=0.05) in the presence of 0.04 mM $Na_2C_2O_4$ as compared to deionized water (Figure 8). However, the increase in Cs^+ desorption observed here may not indicate accelerated mineral weathering. There were no cations present in the deionized water sample to compete with Cs^+ for binding sites on the illite, whereas 235 mmol Na^+ kg^{-1} illite were present in the oxalate-amended sample. The initial concentration of Cs^+ on IMt-1 illite is 229 mmol kg^{-1}. Therefore, the difference in the observed Cs^+ desorption may be solely due to Na^+ in the oxalate-amended sample.

Cs desorption from IMt-1 illite was measured in the presence of each Na^+, K^+, Ca^{2+}, and Mg^{2+} to examine the effect of competition from the major cations in the INEEL system on Cs^+ desorption from IMt-1. Desorption of Cs^+ from IMt-1 illite in the presence of 0.4 mM $MgCl_2$ was significantly enhanced (α=0.05) by the addition of 0.04 mM $Na_2C_2O_4$. However, the charge concentration in the sample amended with $Na_2C_2O_4$ is10% higher than the nonamended sample, and the difference in Cs^+ desorption was only 2–3% higher in the illite sample amended with $Na_2C_2O_2$. Thus, the increase in Cs^+ desorption in the Mg^{2+} system observed in

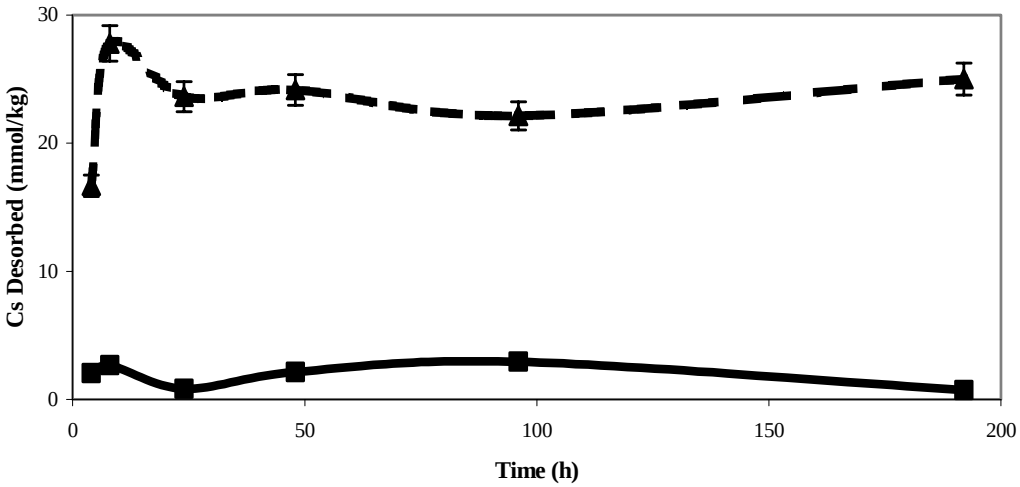

Figure 8. Cs desorption from IMt-1 illite in deionized water (—■—) and in 0.04 mM $Na_2C_2O_4$ (—▲—). Initial concentration of Cs^+ on IMt-1 was ~229 mmol kg^{-1}. The solution pH was maintained at approximately 8.0 throughout the course of the experiment. Error bars indicate 5% error.

the presence of $Na_2C_2O_4$ is likely primarily due to the increase in cation concentration.

Desorption of Cs^+ from IMt-1 illite in the presence of 1.0 mM $CaCl_2$ was also significantly (α=0.05) enhanced by the addition of 0.04 mM $Na_2C_2O_4$. The IMt-1 illite sample amended with $Na_2C_2O_4$ desorbed 5–10% more Cs^+ than the non-amended sample, while the cation concentration was only 4% higher in the oxalate-amended illite sample. In this case, the difference in Cs^+ desorption cannot be explained by the increase in cation charge concentration alone. In the IMt-1 sample amended with $Na_2C_2O_4$, Cs^+ desorption increases rapidly for the first 24 hours before reaching a plateau, supporting the hypothesis that oxalate is reacting with the illite mineral.

Significantly greater desorption (α=0.05) of Cs^+ from IMt-1 illite was observed in the presence of 10 mM NaCl and 0.04 mM $Na_2C_2O_4$ as compared to 10 mM NaCl alone (Figure 9). Desorption of Cs^+ from IMt-1 illite amended with $Na_2C_2O_4$ was 14–22% higher than in the non-amended illite sample. The difference in cation concentration between the two samples could not account for the increase in Cs^+ desorption, as the difference was only 0.4%. As observed in the Ca^{2+} system, Cs^+ desorption from IMt-1 in the sample amended with $Na_2C_2O_4$ increases with time, reaching a plateau at approximately 96 hours.

Only the K^+ system exhibited decreased Cs^+ desorption when treated with $Na_2C_2O_4$ (Figure 10). Approximately 8% less Cs^+ was desorbed from the illite sample amended with $Na_2C_2O_4$ as compared to the nonamended illite sample. For the first 8 hours of the experiment, Cs^+ desorption from IMt-1 in 0.1 mM KCl alone was not significantly different (α=0.05) from desorption in KCl amended with $Na_2C_2O_4$. However, while Cs^+ desorption in the oxalate-amended sample reached a maximum at 8 hours, Cs^+ desorption from illite in the absence of $Na_2C_2O_4$ continued to increase until it reached a plateau at approximately 48 hours.

We initially hypothesized that plant root exudates would enhance Cs^+ desorption from micaceous minerals in the rhizosphere by accelerating weathering of frayed-edge sites (FES). Measurement of FES on IMt-1 illite prior to and following treatment with $Na_2C_2O_4$ indicated that the simulated root exudates significantly (α=0.05) increased the quantity of Cs^+-selective sites on IMt-1 (Table 2).

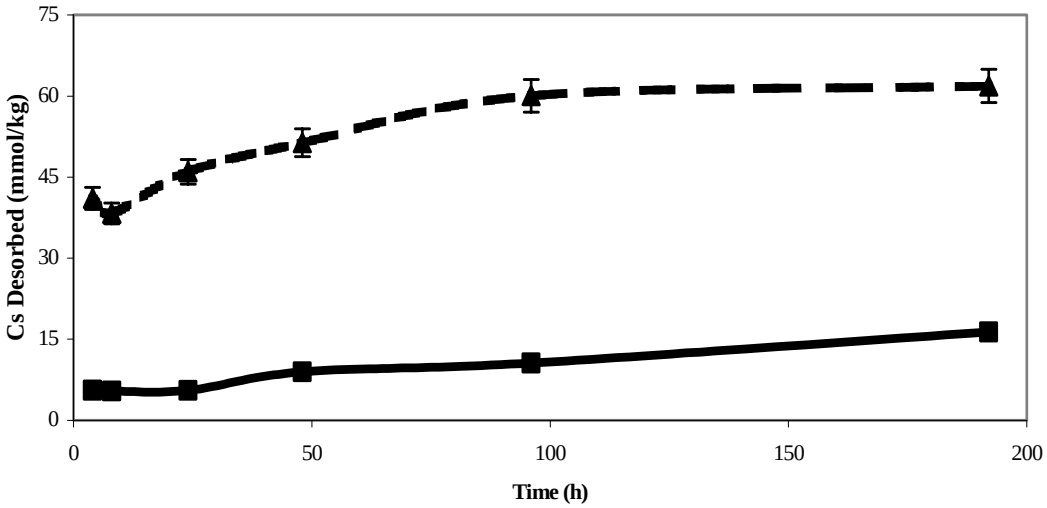

Figure 9. Cs desorption from IMt-1 illite in the presence of 10 mM NaCl (—■—) and 10 mM NaCl + 0.04 mM $Na_2C_2O_4$ (— ▲—). Initial concentration of Cs^+ on IMt-1 was ~229 mmol kg^{-1}. The solution pH was maintained at ~8.0 throughout the experiment. Error bars indicate 5% error.

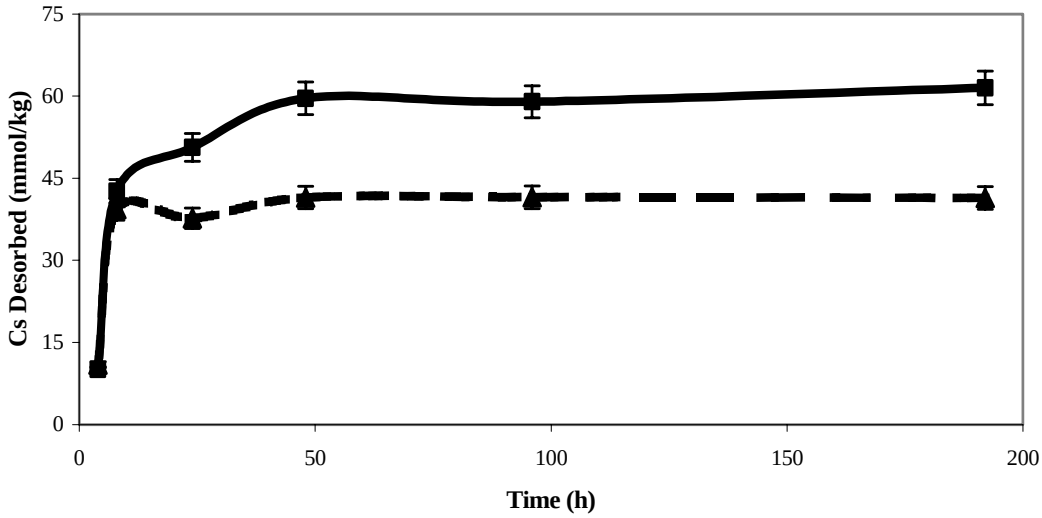

Figure 10. Cs desorption from IMt-1 illite in the presence of 0.1 mM KCl (—■—) and 0.1 mM KCl + 0.04 mM $Na_2C_2O_4$ (— ▲—). Initial concentration of Cs^+ on IMt-1 was ~229 mmol kg^{-1}. The solution pH was maintained at ~8.0 throughout the experiment. Error bars indicate 5% error.

Table 2. Measurement of FES concentration on IMt-1 illite prior to and following treatment with 0.04 mM $Na_2C_2O_4$.

Sample	FES ($mmol_c$/kg)
IMt-1	2.91
IMt-1 + 0.04 mM $Na_2C_2O_4$	4.11

Microbiology

Overview

Microorganisms may be involved in the weathering of aluminosilicate clay particles and the release of Cs trapped therein. Therefore, our overall goal of this task is to isolate and study microorganisms from INEEL soil that can enhance the release of bound Cs from clays minerals. Specific task objectives are to:

- Identify potentially important groups of bacteria involved in aluminosilicate weathering
- Develop a screening assay for bacteria capable of chelating aluminum (Al) and develop laboratory methods to identify bacterially produced compounds involved in aluminosilicate weathering
- Screen INEEL soils for relevant bacteria and design experiments to determine the effects of these bacteria and their secreted compounds on Cs release.

The subtasks to accomplish these objectives are as follows:

1. Determine from the literature those bacteria (microorganisms) that should affect the composition of exudates present either through degradation of the exudates or through stimulation of production by the plants.
2. Verify using enrichment culture techniques and physiological characterization that the relevant bacteria are present at the INEEL site in noncontaminated (newly acquired) rhizosphere soil. These bacteria will then be proposed for use in Dr. Bugbee's exudate microcosm studies.
3. From a search of the literature, formulate a plan for an assay to isolate bacteria with Al or Cs binding capabilities. Make go/no go decision based on feasibility of plan.
4. Develop one or more assays and screen bacteria from noncontaminated INEEL soil for the ability to bind Al. Obtain bacteria known to secrete chelating compounds from ATCC for use as positive control organisms in the assay. Develop a quantitative laboratory assay method for analyzing secreted Al chelating compounds.
5. After metal binding bacteria are isolated, kinetic geochemistry laboratory experiments will be designed to evaluate the effect of the bacteria on Cs release.

Results

A literature review indicates that degradation of exudates is predicted for bacteria in the genera *Pseudomonas* and *Burkholdaria*, which are known to degrade a wide variety of organic compounds. Stimulation of production would be predicted for pathogenic bacteria (*Xanthomonas*, *Erwinia*, some species of *Pseudomonas*) and also potentially for symbiotic bacteria such as *Rhizobium*. Al also stimulates production of chelating organic acids.

A literature search suggests that the Chrome Azurol S (CAS) assay, which is well developed for identifying bacteria that secrete iron-chelating compounds, could be adapted to identify bacteria that secrete Al chelating compounds. Al binds to CAS to produce a colored complex. This is a common method for quantifying Al in ground water. Citrate is able to remove Al from its CAS complex, and was shown to bind Al much more tightly than oxalate in this work. Based on this review, we decided to continue work to develop an assay for the Al-chelating capability in bacteria.

Development of an assay for identifying bacteria capable of chelating Al was initiated by adapting a classical indicator medium developed for analyzing the secretion of iron binding molecules (siderophores) by bacteria. The assay involves the dye chrome azurol S (CAS) that binds iron to form a colored complex. Iron-chelating molecules remove the iron from the CAS complex that drastically decreases the color intensity. When the iron-CAS complex was incorporated into solid microbiological medium, bacterial colonies secreting iron-binding molecules formed orange halos around themselves against the dark blue of the surrounding medium. CAS also binds Al to form a colored complex, which is the basis of a spectrophotometric assay for aluminum in water.

However the Al-CAS complex was not as tight as the iron-CAS complex, and components of the medium destroyed the complex. Several components were involved, but phosphate in the medium destroyed the complex most severely. After investigating a variety of approaches to solve this problem, we switched to a different dye, pyrocatechol violet (PCV), which has also been used for spectrophotometric determination of Al in water. The PCV-Al complex was not destroyed by phosphate under our medium conditions, but the complex was destroyed by citric acid, our positive control. The PCV-Al complex was incorporated into solid growth medium.

Several bacteria that secrete citrate were identified in the ATCC culture collection. These include *Arthrobacter paraffineus* (ATCC 15590, 15591), *Rhodococcus rhodochrous* (ATCC 21198), *Raoultella planticola* (ATCC 21609), *Bacillus licheniformis* (ATCC 21610, 21667), *Acinetobacter* species (ATCC 21683), and several *Corynebacterium* species. These bacteria were obtained for assay verification.

Soil samples were collected from the rhizosphere of crested wheatgrass plants from an uncontaminated site at the INEEL. These soils were inoculated onto the Al chelating assay plates, and colonies producing a halo of lighter color were observed. To better understand the mechanism of Al chelation by these bacteria, it is necessary to determine if the Al chelation is occurring due to a secretion of a chelating compound by the bacteria. To do this, the cells in these colonies were isolated and grown up in liquid medium, without the PCV-Al complex, the cells were centrifuged, and the supernatant was filtered to give a cell free solution. These supernatants were concentrated approximately 10-fold by lyophilization and then assayed by combining them with a known quantity of the PCV-Al complex and measuring the optical density at the absorbance maximum of the complex. Several of the concentrated extracts produced significant decreases in the optical density of the complex, presumably due to removal of the Al from the complex.

To develop a quantitative assay to identify the Al-chelating compounds present in the supernatant, it is necessary to first optimize the growth of the bacteria to produce sufficient quantities of the chelating compounds for laboratory analysis. To do this we tested the effects of various modifications of the growth medium on the production of the complex destroying compound. Modifications were made to growth pH, carbon source, and the presence or absence of the amendments iron and case amino acids. The medium producing the highest levels of complex destroying activity varied for each parameter except pH. Differences in chelating activity were also observed when the supernatants were harvested at different times. We are therefore currently performing experiments to assess production of the complex-destroying activity through the growth cycle of the bacteria. Based on these experiments, we anticipate being able to produce large amounts of the complex-destroying compounds from the bacteria to be used both in qualitative analysis and in vitro experiments with Cs containing clays.

Compounds and bacterial cultures identified in the preceding tasks will be incubated with reference clays that are loaded with Cs to determine the effects of this incubation on rate of Cs release and changes in extractability of Cs. Cs extractability will be determined using various extractants, changes in number of frayed-edge sites, etc. This work will closely model the FY 2002 experiments conducted under the “Binding Cs to Clay” task.

Cs Uptake by Crested Wheatgrass

Overview

To quantify the translocation of Cs in soil profiles, it is necessary to understand the uptake of Cs by plants. We obtained some preliminary estimates of Cs uptake by plants by analyzing data from two contaminated sites at the INEEL, the Central Facilities Area (CFA) drain field, and the area around the former SL-1 reactor facility.

The CFA drain field is a $200 \times 1{,}000$ ft area comprised of five distribution areas that are contaminated with radionuclides. Each area had 20 distribution lines that carried discharge water evenly across the drain field from the old Central Facility Sewage Treatment Plant that operated from 1953 until 1995. The radioactive sewage was deposited in the drain field 90 cm below the surface. In 1999 a Comprehensive Remedial

Investigation/Feasibility Study (DOE/ID-10680) identified ^{137}Cs as the contaminant of primary concern. Data from CFA was obtained by a collaborative effort between researchers at the INEEL Research Center and scientists in Environmental Restoration responsible for cleaning up Waste Area Group 4 (WAG 4). Fieldwork for this study was completed in August of 2001, and analyses were conducted during the ensuing fall and winter.

Interpretation of data from samples collected at the site of the former Stationary Low-Power Reactor Number One (SL-1) at the INEEL in southeastern Idaho is providing information on the variation in Cs uptake with the stage of plant growth. On January 3, 1961, while the SL-1 reactor was undergoing annual maintenance, it went critical resulting in an explosion that caused the death of three crewmembers working at the facility and contaminated the surrounding soil with ^{137}Cs.[4] Fieldwork at the SL-1 site consisted of four sample collections in April, May, and June of 2001 and April of 2002. Sample analyses were conducted following each sampling date and all analyses were complete by the end of FY 2002. Sample locations were established using a radiation survey map provided by WAG 5 personnel. Eight locations were established within a relatively high radiation zone on the contaminated site and eight sites were established outside of the contaminated area to serve as controls. Samples of bulk and rhizosphere (root-associated) soil, aboveground plant tissues, and roots were taken at each location and transferred to INTEC for analysis. All plant tissue samples were digested and analyzed for total potassium and Cs as well as radiocesium. Soil samples were subjected to four extraction methods: water, ammonium acetate, sodium tetraphenyl boron, and nitric acid and hydrogen peroxide per EPA Method 3050. These four methods extract progressively more Cs from the soil and provide insight into the fraction of Cs that is readily available to the plant.

Results

The sagebrush steppe ecosystem at the INEEL is dominated by crested wheatgrass, rabbitbrush, and sagebrush. Average total Cs concentration in soils ranged from 2.8–3.6 mg kg^{-1} soil. These values fall within the range of soil Cs values reported in the literature. The mass of soil radiocesium on the contaminated site was determined to be, on average, five orders of magnitude less than the mass of total Cs (stable plus radiocesium) in the soil. Crested wheatgrass of the only plant species that had significantly higher activity for shoots collected from the contaminated site (0.93 pCi g^{-1}) than for the control site (0.22 pCi g^{-1}) (Figure 11).

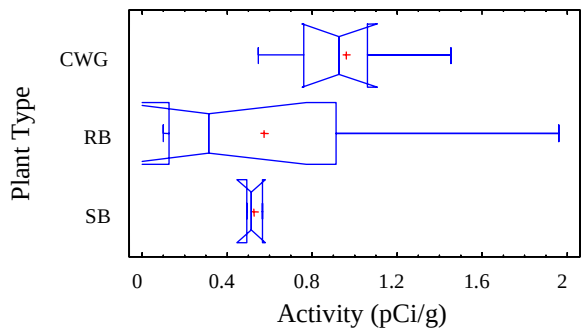

Figure 11. Radiocesium activities in shoot samples collected within the drain field site.

Median radiocesium activity in the root mass of crested wheatgrass plants (100 pCi g^{-1}) is significantly greater than that in the brush plants (0.34 and 0.63 pCi g^{-1} for rabbitbrush and sagebrush, respectively) within the contaminated site (Figure 12).

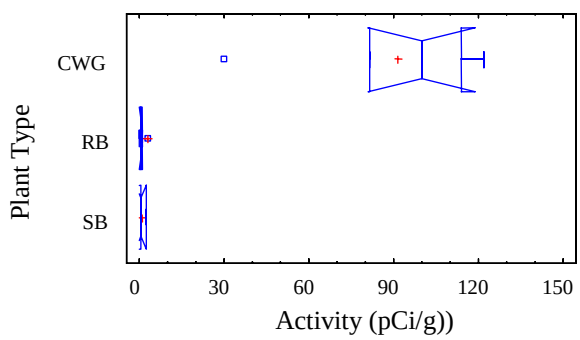

Figure 12. Radiocesium activities in root samples collected within the drain field site at CFA.

Total aboveground biomass production by crested wheatgrass is estimated to be 4–6 tons, and constitutes 89% of the aboveground biomass on the contaminated site. This biomass estimate combined with the ^{137}Cs activity measurements in the shoots indicates that an estimated 94% of the ^{137}Cs accumulation in aboveground biomass is associated with crested wheatgrass.

Under conditions of senescence, the crested wheatgrass root-to-soil and shoot-to-root ratios (transfer factors) are different for ^{137}Cs and stable Cs (^{133}Cs). These differences are partially attributed to the differences in the binding mechanisms of ^{137}Cs and ^{133}Cs in the soil. Results and findings from this study are described in a manuscript submitted to the *Journal of Environmental Quality* for publication. A conceptual model for the uptake of both stable Cs and radiocesium is proposed. The manuscript is currently under peer review.

Data from the former SL-1 site provide information about Cs uptake by crested wheatgrass over several growth stages. The ranges of total Cs in rhizosphere and bulk soils are similar, (1.7–5.2 mg kg^{-1}), and do not appear to vary seasonally. In contrast, radiocesium activities in rhizosphere and bulk soils are significantly different from one another, vary over an order of magnitude (10–180 pCi g^{-1}) and show seasonal differences. Shoot and root ^{137}Cs activities decrease between April and May. Total Cs shoot-to-root ratios are greater than the corresponding ratios for radiocesium. Total Cs root-to-rhizosphere soil ratios are lower than the corresponding ratios for ^{137}Cs. The ratio of rhizosphere- to bulk-soil ^{137}Cs activities are much higher in April than they are in May and June (Figure 13). These results will enhance our understanding of phytoremediation scenarios and issues associated with long-term stewardship of ^{137}Cs-contaminated lands.

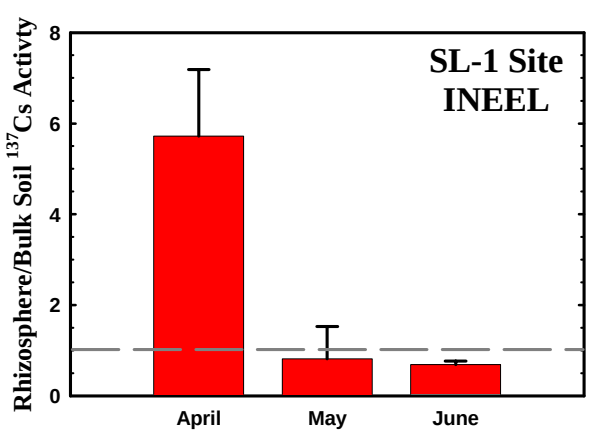

Figure 13. Ratio of ^{137}Cs activity in rhizosphere soil to ^{137}Cs activity in bulk soil for April, May, and June, 2001.

Modeling

Overview

An essential part of this project is to develop a computational model of Cs solubilization in the rhizosphere that includes key geochemical, biological, and physical processes. Lori Siegel at Northeastern University is doing this modeling. The objectives to accomplish this goal are to:

1. Develop a conceptual comprehensive model of Cs partitioning in the rhizosphere using a "Systems Approach" to integrate the complex physical and biochemical processes.

2. Develop a quantitative submodel describing the production and fate of root exudates within the context of the comprehensive model.

3. Quantitatively relate the exudate submodel to Cs solubilization and incorporate the relationship into the comprehensive model. The conceptual and quantitative models will be implemented iteratively for validation and refinement.

To achieve these objectives, the factors and relationships affecting Cs solubilization must first be identified. Subsequently, it is necessary to select those assumed to warrant inclusion in the comprehensive conceptual model. A model rhizosphere system must also be chosen such that the parameters of the model plant/soil system to be studied can be investigated with sufficient control. A preliminary conceptual model will establish basic associations using software that allows these relationships to be set up in sectors, with each sector representing a submodel. Available data will be used to determine functional relationships within and between submodels. Parametric values will be evaluated only for functional relationships that are well understood and for which data are properly presented within the model framework. The model code will be evaluated and refined as needed. To develop the exudate model, field and experimental data will be used to characterize exudate production and fate in the rhizosphere system. To relate the root exudate submodel to Cs solubilization, the rate of binding and release of Cs^+ from phyllosilicates, commonly found at INEEL and DOE sites and known to bind Cs, will be quantified for varying conditions affected by

the exudates. Using additional experimental data, the equation will be solved and the results used to evaluate and update the specific model. Finally the mathematical exudate model will be incorporated into the comprehensive conceptual model, which will then be evaluated and refined.

Model Description

After identifying the key variables affecting Cs solubilization in the rhizosphere, we categorized the factors. We then selected the relationships within and between these categories assumed to warrant inclusion in the comprehensive conceptual model. This selection was based on hypotheses developed from the initial literature review.

The solution procedure is implemented using Systems Thinking, integrating the relationships between the factors affecting Cs fate. Submodels are defined as geochemistry, physical factors, root system density, microorganisms, nutrients, and root exudates. A seventh submodel relates the three specific forms of Cs (bound, aqueous, and phytoextracted). This approach allows for expertise in defining each sector, while simultaneously promoting the ecological packet. Finite difference methods are used in the Stella® Research 6.0 software package (High Performance Systems, Inc., Hanover, NH) to numerically solve the system of differential equations that comprise the model. The software performs numerical integration according to Euler's method, the second-order Runge-Kutta method, or the fourth-order Runge-Kutta method. Each method provides similar output, but Euler's method requires the least computing time and therefore is applied to this model. The basic relationships within each submodel and interactions between submodels have been established. The model is ready for entry of the field characterization and experimental data.

Conceptual Comprehensive Model

The conceptual comprehensive model has been implemented using the Stella 6.0 software. User interface files have been created in Microsoft Excel, facilitating the model's practicality in modifying parametric values. Figure 14 presents the overview of the model. Functional relationships within and between the submodels drive the comprehensive model. These relationships define the required inputs of the model.

Currently, hypothetical data consistent with those presented in the literature are used to define the relationships. However, statistical analyses have been performed on available field characterization data that have been used to replace hypothetical data, as well as guide future field characterization tasks. The Cs fate submodel (Figure 15) includes the two critical functional relationships for the flows between the bound phase and the aqueous phase and between the aqueous phase and the phytoextracted phase ($Flow_{sol}$ and $Flow_{phy}$, respectively). The codes for these relationships have been derived and incorporated into the model.

Numerical Root Exudates Submodel

The modeling effort currently focuses on the effects that the root exudates have on Cs solubilization. Literature has been used to formulate the functional relationships and estimate parametric values within the root exudate submodel and between the root exudate submodel and the geochemistry and Cs fate submodels. Sensitivity analyses have been performed to assess the effects that the exudates have on Cs partitioning, as well as the effects that certain parameters outside these submodels have on the root exudates and accordingly Cs partitioning.

Mesoscale Experiment at the Engineered Barrier Testing Facility

Overview

Cs translocation in soil may be better quantified using mesoscale experiments where the initial contaminant distribution can be made to approximate a simple ideal geometry. Changes in concentration over time from this initial condition would be clear indication of translocation. Mesoscale experiments will allow us to obtain data over several years on Cs translocation and factors that affect this translocation. These data serve as a database against which our modeling efforts can be validated. These mesoscale physical models will provide reasonable estimates of the time and spatial scales of the translocation of Cs by plants.

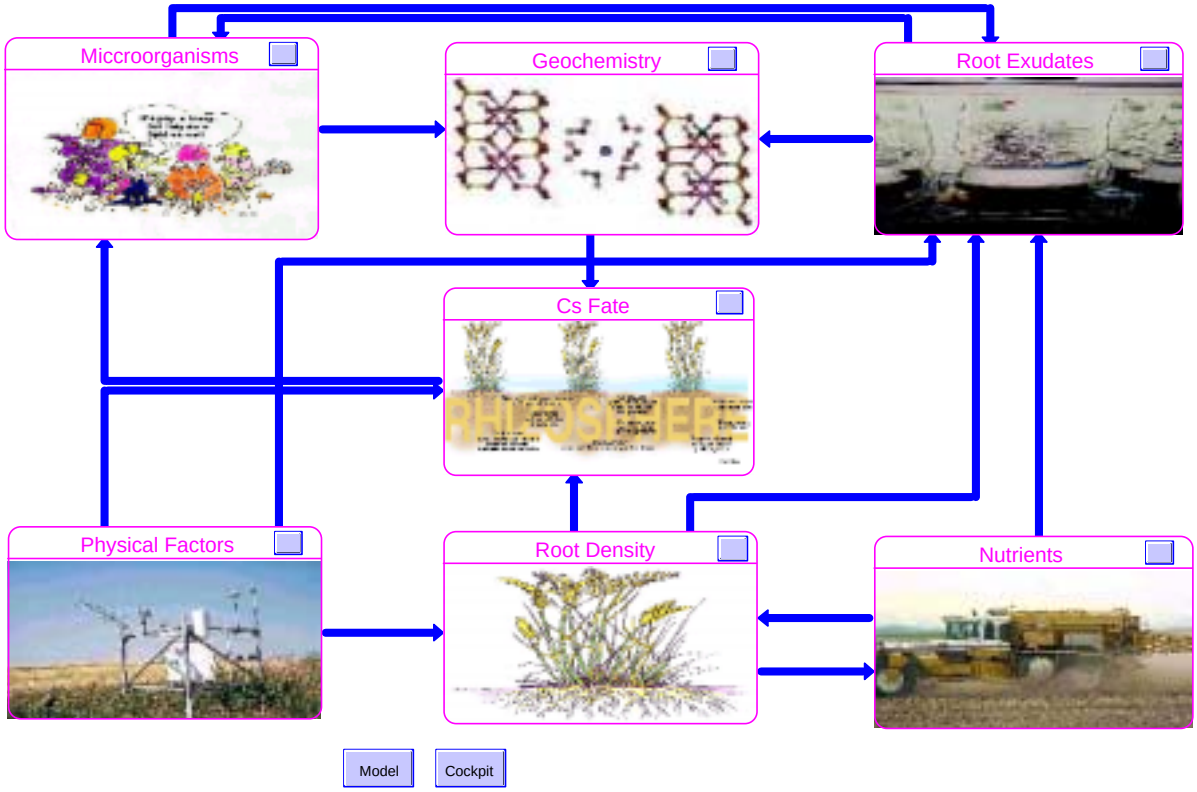

Figure 14. Interface level of Stella software indicating the Cs Fate sector and the six sectors affecting it.

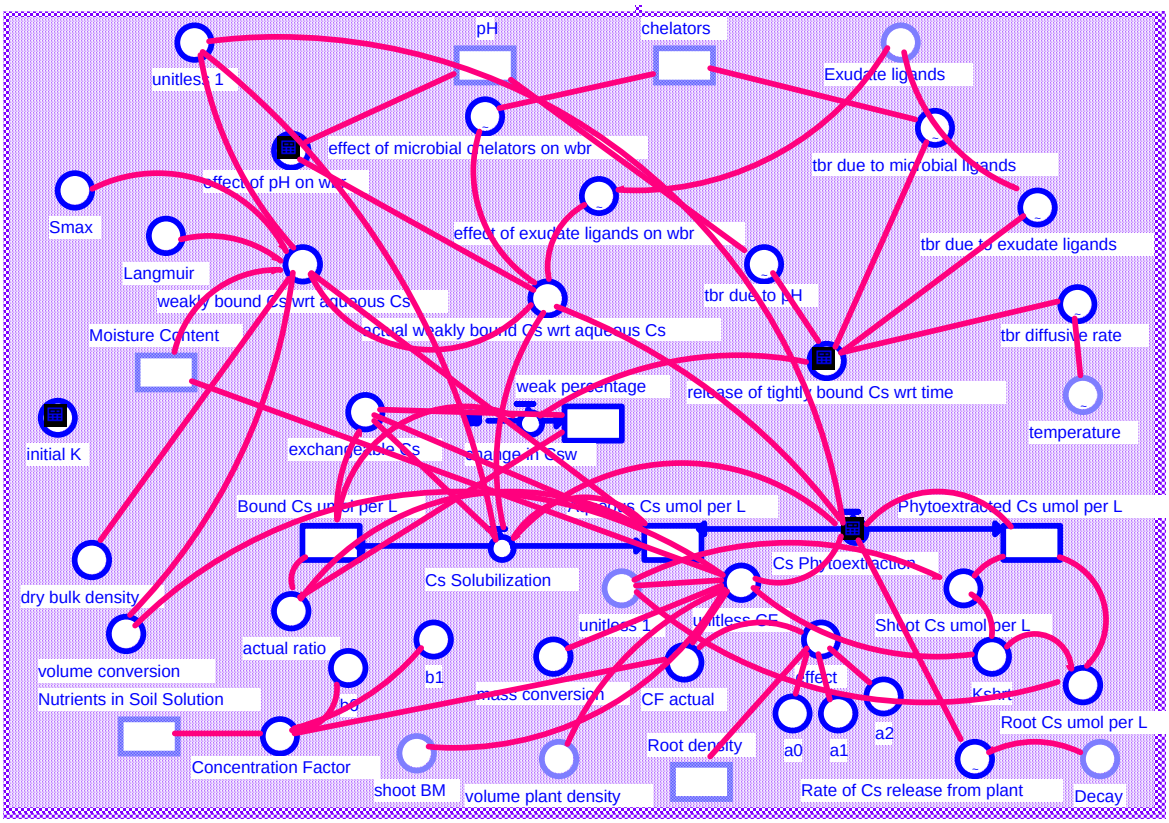

Figure 15. Cs fate submodel.

We investigated the feasibility of using the existing Engineered Barrier Testing Facility (EBTF) located near the Radioactive Waste Management Complex (RWMC) on the INEEL. In FY 2002 our goals were to:

- Design the mesoscale experiment
- Remove the existing soil from the existing cells
- Prepare the cells for installation of the soil
- Acquire and calibrate the necessary monitoring equipment
- Construct instrument towers for installation in the cells
- Obtain the necessary permissions to remove contaminated soil and install it in the EBTF
- Install the soil and associated monitoring systems in the cells at the EBTF.

Our expectations were that the actual data on the translocation of ^{137}Cs would be obtained beginning in FY 2003 and continue through succeeding years.

The EBTF was designed and built for multi-year mesoscale testing of engineered barriers under several different operating conditions. Monitoring and control design features of the EBTF are ideally suited for conducting mesoscale experiments on Cs translocation and factors that affect this translocation.

The EBTF is a concrete structure consisting of five cells (plots) on each side of an enclosed access trench (Figure 16). Each cell has four walls and a floor measuring 3.05 m wide by 3.05 m long by 3.05 m deep. The top of the cells is open to the atmosphere, but can be covered thereby allowing better control of all environmental inputs (water, light, heat, etc.). The cell floor is an impermeable barrier that allows quantitative collection of all leachates. The environmentally controlled access trench is designed to accommodate a diverse array of automated soil, moisture, gas, and other monitoring systems necessary to conduct long-term mesoscale biological studies.

Figure 16. EBTF access trench showing instrumentation in each of the 10 cells and collection pumps of the cell leachate.

Mesoscale Experimental Design

The four cells at the North end of the EBTF were dedicated to the mesoscale Cs migration experiments, thus giving us two cells on each side of the access trench. The facility and our instrumentation design allow each of the four cells to be controlled and monitored as independent experimental units. In the first phase of the EBTF mesoscale Cs migration experiment construction, the key design considerations were:

- Construct an appropriate soil profile that supports the crested wheatgrass plants and provides opportunity to monitor distinctive changes in Cs concentrations throughout the profile.
- Select and install the configuration of an array of sensors systems that allow autonomous and nonintrusive monitoring of the biological and geochemical systems as they affect Cs migration.

Soil Profile Construction

There are substantial differences in physical and chemical properties of our local soils with depth, many of which can dramatically influence water movement and plant growth. A number of these parameters are described for local (INEEL) soils in Nimmo et al.[5] These parameters will be influenced to some degree when the soil is

disturbed, such as in the case of a waste cap or with the refilling of the experimental cells as we are planning. The key point is that these properties dictate how water moves through the system, and also directly or indirectly determine root growth and distribution. Recognizing that we cannot replicate an undisturbed soil profile, we determined that a simple system of four distinct layers of three different soils should be constructed. From bottom to top, these layers are (1) uncontaminated subsurface soil, (2) uncontaminated surface soil, (3) contaminated surface soil, and (4) uncontaminated surface soil (see Figure 17).

12 in. of uncontaminated surface soil
6 in. of contaminated soil
6 in. of uncontaminated surface soil
6–8 ft of uncontaminated subsurface soil (below root zone)

Figure 17. Uncontaminated subsurface soil collected locally from beneath the root zone (>18 inches) of an undisturbed, uncontaminated area. Uncontaminated surface soil (<18 inches) collected locally from an undisturbed, uncontaminated area. Contaminated surface soil (<12 inches) collected from the SL-1 windblown contamination area.

Sensor Systems

We selected seven separate types of sensors to use in monitoring the soil. These sensors included tensiometers, time-domain reflectometry devices(TDRs), heat dissipaters, thermocouples (TCs) or thermisters, soils gas monitors (CO_2 and O_2), radiation detectors, and a rhizotron camera system. The Tensiometers, TDR probes, heat dissipaters, and TC were selected to monitor soil moisture. Gas monitors were selected to measure biological respiration, and both CO_2 and O_2 measurements are required to distinguish biological and geochemical contributions to the gas flux in the soil. A gamma radiation detector with a specially designed shield was selected for nonintrusive monitoring of the radiocesium migration through the rhizotron tubes. The rhizotron camera system is a commercial tool designed to quantitatively monitor root growth.

For each cell, the tensiometers, TDR probes, heat dissipaters, and TC will be placed at depths of 4, 8, 12, 15, 18, 24, 36, 54, and 84 inches as measured from the cell soil surface. At each depth, the sensors will be placed at two locations in the cell. A PVC pipe (instrumentation tower) was designed to house the electrical wiring for the TDRs, heat dissipaters, and the TCs. This pipe will be sealed to the cell floor with sensor wiring running from the instrumentation tower to the EBTF control room. Soil will be compacted around the instrumentation.

The tensiometers and gas sampling ports will be placed at depths of 8, 12, 15, 24, and 54 inches measured from the surface. The tensionmeters and the gas sampling ports will only be installed in one location at each of the specified depths.

The radiation detector and the camera system will be deployed using 3-in-diameter tubes that penetrate the soil from the surface. Six tubes will be placed in each of the four concrete cells. These 6-ft long 3-in inner-diameter tubes will be placed at an angle such that the bottom end of the tube rests on the compacted soil at a 24 in depth and the top of the 6-ft tube rests on the concrete side of the cell (Figure 18).

EBTF Cell Preparation

Upon acquiring the four EBTF cells, the previous experiments needed to be excavated and the cells prepared to accept the new Cs migration experiment, which included preparing the facility to receive ^{137}Cs-contaminated soil. Excavation of the previous experiments took from July to September 2002. The engineering design was completed for preparing the cells to receive radiological contaminated soil. This design included:

- Sealing drains, cracks, and all other exits in the cells
- Preparing and coating the cells with an epoxy paint

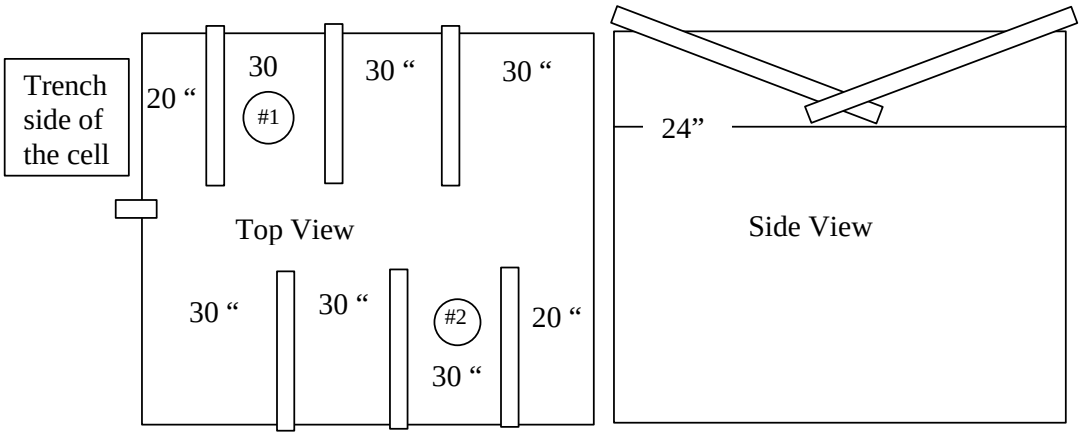

Figure 18. Diagram showing the placement of the 3-in access tubes for the rhizotron and radiation sensor.

- Perform a base line survey of the cells before introducing contaminated soil
- Baseline analyses of the all soil to be placed in the facility
- Installing a plastic apron on the walls of each cell down to a depth of 3 ft (just below the contaminated soil level).

Excavation of the previous experiment was completed, and the EBTF cells are now ready to be painted and the soil/instrumentation installed.

Permissions and Forms

We have completed several health and safety documents. No major issues that would prevent such an experiment from being conducted at the EBTF were identified.

ACCOMPLISHMENTS

Characterization of Root Exudates from Crested Wheatgrass

During FY 2002 we:

- Completed a new design for a sterile hydroponics system.
- Tested the sterility of the system using a epifluoresent microscope method. The results indicate that 85% of the plants were still sterile after 65 days.
- Grew plants with nutrient solutions containing less potassium than the controls. This potassium stress resulted in 1.4 times greater carbon in the exudate compared with the control.
- Grew plants with nutrient solutions containing more NH_4^+ than the controls. Plants grown under this ammonium stress had roughly the same amount carbon in the exudate as compared with the control.
- Induced drought by watering plants with 75% less water than the controls. Plants grown under this drought stress had 1.7 times more carbon in the exudate as compared with the control.
- Induced flooding by stoppering the drain tubes to prevent the water from draining from the root zone. Plants grown under this flood stress had 1.5 times more carbon in the exudate as compared with the control.
- Obtained organic acids from roots by derivatization to demonstrate that fumarate, malate, and succinate are three of the most common acids. The highest concentrations were obtained under drought conditions.

Binding Cs to Clays

During FY 2002 we:

- Measured the sorption of Cs^+ to IMt-1 illite over time and at solution pH ranging from 6.0 to 10.0. The most rapid sorption occurred within the first 48 hours, followed by slower Cs^+ uptake that reached a maximum at approximately 96 hours. Further examination of the effect of solution pH on Cs^+ sorption to IMt-1 illite showed that after 96 hours, there was an increase in Cs^+ sorption to IMt-1 with initial CsCl concentration as solution pH increased from 6.0 to 10.0

- Conducted Cs sorption experiments in solutions with a range in NaCl concentrations. As NaCl concentrations increased to 0.075 M, Cs^+ sorption to IMt-1 illite clay decreased to zero. This result indicates that the majority of Cs^+ sorption to IMt-1 illite is not selective and occurs on exchange sites accessible to Na^+.

- Conducted a series of Cs sorption and desorption studies in IMt-1 illite clay in the presence of 0.04 mM sodium oxalate. A large increase in Cs^+ sorption to illite was observed in the presence $Na_2C_2O_4$. Cs desorption from IMt-1 illite was significantly enhanced (α=0.05) in the presence of 0.04 mM $Na_2C_2O_4$ as compared to deionized water.

- Conducted Cs desorption studies in IMt-1 illite clay in the presence of $Ca^{2+}$and Mg^{2+}. A large increase in Cs^+ desorption from illite was observed for both ions.

- Conducted Cs desorption experiments in the presence of KCl. Of the cations examined, only the K^+ system exhibited decreased Cs^+ desorption when in combination with $Na_2C_2O_4$.

- Measured the concentration of frayed edge sites (FES) prior to and after treatment with 0.04 mM $Na_2C_2O_4$. FES concentration is 1.4 times greater after treatment.

- Calculated selectivity coefficients for Cs exchange from the experimental data. The selectivity coefficients for oxalate-treated illite are greater for K^+ but lower for Ca^{2+}, Mg^{2+}, and Na^+. These results indicate that oxalate treatment increases the number of sites accessible to ion exchange, but not the concentration of FES.

- Prepared and submitted a manuscript to the *Journal of Clays and Clay Minerals*.

Microbiology

During FY 2002 we:

- Completed a literature review. Results indicate that degradation of exudates is predicted for bacteria in the genera *Pseudomonas* and *Burkholdaria*, which are known to degrade a wide variety of organic compounds. Stimulation of production would be predicted for pathogenic bacteria (*Xanthomonas*, *Erwinia*, some species of *Pseudomonas*) and also potentially for symbiotic bacteria such as *Rhizobium*. Al also stimulates production of chelating organic acids.

- Reviewed literature on assay methods that suggests that the Chrome Azurol S (CAS) assay could be adapted to identify bacteria that secrete Al chelating compounds. Al binds to CAS to produce a colored complex. Citrate is able to remove Al from its CAS complex. Citrate was shown to bind Al much more tightly than oxalate in this work. Based on this review, the decision was made to continue work to develop an assay for Al-chelating capability in bacteria.

- Initiated development of an assay for identifying bacteria capable of chelating Al by adapting a classical indicator medium developed for analyzing the secretion of iron binding molecules (siderophores) by bacteria. We encountered some difficulty because components of the medium, primarily phosphate, destroyed the complex. We therefore switched to a different dye, pyrocatechol violet (PCV). The PCV-Al complex was not destroyed by phosphate under our medium conditions, but the complex was destroyed by citric acid, our positive control. The PCV-Al complex was incorporated into solid growth medium.

- Identified several bacteria that secrete citrate in the ATCC culture collection. These include

Arthrobacter paraffineus (ATCC 15590, 15591), *Rhodococcus rhodochrous* (ATCC 21198), *Raoultella planticola* (ATCC 21609), *Bacillus licheniformis* (ATCC 21610, 21667), *Acinetobacter* species (ATCC 21683), and several *Corynebacterium* species. These bacteria were obtained for assay verification.

- Collected soil samples from the rhizosphere of crested wheatgrass plants from an uncontaminated site at the INEEL. These soils were inoculated onto the Al chelating assay plates, and colonies producing a halo of lighter color were observed. The cells in these colonies were isolated and grown in liquid medium, without the PCV-Al complex, the cells were centrifuged, and the supernatant was filtered to give a cell free solution. These supernatants were concentrated approximately 10 fold by lyophilization and then assayed by combining them with a known quantity of the PCV-Al complex and measuring the optical density at the absorbance maximum of the complex. Several of the concentrated extracts produced significant decreases in the optical density of the complex, presumably due to removal of the Al from the complex.

- Tested the effects of growth pH, carbon source, and the presence or absence of the amendments iron and case amino acids the production of the complex destroying compound. The medium producing the highest levels of complex destroying activity varied for each parameter except pH. Differences in chelating activity were also observed when the supernatants were harvested at different times. We initiated experiments to assess production of the complex destroying activity through the growth cycle of the bacteria. Based on these experiments, we anticipate being able to produce large amounts of the complex destroying compounds from the bacteria to be used both in qualitative analysis and in vitro experiments with Cs containing clays.

Cs Uptake by Crested Wheatgrass

During FY 2002 we:

- Analyzed data from the CFA drain field and adjacent noncontaminated area. The analysis provided shoot-to-soil, root-to-soil, and shoot-to-root ratios for crested wheatgrass, rabbitbrush, and sagebrush for a one-time sampling in August, 2000. The results demonstrate that 94% of the ^{137}Cs accumulation in aboveground biomass is associated with the crested wheatgrass.

- We prepared a manuscript (Hamilton et al., 2002) describing the sampling and results from CFA drain field area and submitted it to the *Journal of Environmental Quality*. The model for the uptake of radiocesium and stable Cs by crested wheatgrass was developed and presented in the manuscript.

- Performed additional sampling in the uncontaminated area near the SL-1 site.

- Analyzed soil and plant samples collected last year. Procedures for a water extraction and a tetraphenylboron extraction were developed.

- Performed a preliminary review of the data from the SL-1 site that shows that total Cs concentrations vary over a very narrow range and they are similar in the bulk and rhizophere soils. In contrast, ^{137}Cs activities in rhizosphere and bulk soils are significantly different, vary over orders of magnitude (10-180 pCi g^{-1}), and show seasonal differences. Shoot and root ^{137}Cs activities decrease between April and May. Total Cs shoot-to-root ratios are greater than the corresponding ratios for radiocesium. Total Cs root-to-rhizosphere soil ratios are lower than the corresponding ratios for ^{137}Cs.

- Received acceptance for an abstract on the SL-1 results from the *American Society of Agronomy* for the meeting in November 2003 (Hess et al., 2002).

- Submitted an abstract on the general results of our field sampling to the *Fall 2002 American Geophysical Union* meeting (Palmer et al., 2002).

Modeling

During FY 2002 we:

- Defined many functional relationships more accurately and enhanced the derivation of the model code. In particular, the solution code for $Flow_{sol}$ now accounts for a Langmuir type sorption isotherm between the weakly bound and aqueous phases and the change in the sorption parameters with time.

- Received laboratory data on the production and fate of root exudates under nonstress and various stress conditions. In addition, we now have new data regarding the sorption properties and release of interlayer Cs in response to the presence of exudates, and have calibrated model parameters accordingly.

- Conducted sensitivity analyses to evaluate the effects of root exudates on Cs partitioning. The model was also used to test the sensitivity of root density, microbial population, potassium requirement and concentration, and moisture content on the concentration of root exudates and consequently on Cs partitioning. An increase in the concentration of root exudates results in a greater decrease in the bound concentration and greater increase in the aqueous and phytoextracted concentrations. In general, the other parameters affect Cs partitioning according to how they affect the fate of root exudates. However, the comprehensive nature of the system renders a complex overall effect on Cs partitioning.

- A paper (Siegel et al., 2001a) was presented at the Wetlands and Remediation II Conference in Burlington, VT, October 22–25, 2001. A peer-reviewed paper (Siegel et al., 2001b) appeared in the proceedings from that meeting.

- A manuscript (Siegel et al., 2002) on the modeling of Cs partitioning in the rhizosphere with a focus on the role of root exudates was submitted to the *Journal of Soil and Sediment Contamination*.

Mesoscale Experiment at the Engineered Barrier Testing Facility

During FY 2002 we:

- Identified the four cells on the north end of the EBTF as those that will be used in the experiment.

- Developed a general design of the cells, made a plan for a soil profile, and determined the layout of instrumentation. Instrumentation will consist of tensiometers, TDRs, heat dissipaters, thermocouples, soil gas monitors, gamma detectors, and a rhizotron camera system.

- Acquired all of the instrumentation.

- Calibrated TDRs and heat dissipation devices (calibrations done by D. B. Stevens, Inc.).

- Removed the sediment from the four cells we plan to use.

- Developed and obtained approval for the plan to clean the cells, prepare the walls, and seal the surfaces with epoxy paint.

Collaborations

During FY 2002 we maintained collaborations with scientists at other institutions as follows:

- We worked with Dr. Bruce Bugbee at the Department of Plants, Soils, and Biometeorology, Utah State University, who has been characterizing root exudates from crested wheatgrass.

- We supported Lori Siegel at Northeastern University, who is developing the computational model for the biogeochemistry of Cs in the rhizosphere.

- Laura Hanson, a Ph.D. candidate in the Soils Department at Washington State University worked in our laboratory on the binding of Cs to clay minerals. Her work in our laboratory was the result of an INRA grant shared by her advisor, Dr. James Harsh.

- We communicated with Dr. Matthias C. Rillig, Assistant Professor of Microbial Ecology, Division of Biological Sciences, The University of Montana, Missoula, MT about the role of fungi on the bioavailability of Cs in the rhizosphere. Dr. Rillig has only recently received his funding so we are looking forward to further collaborations with him.

Publications

We presented the results of our research at several professional meetings and have submitted peer-reviewed manuscripts. This section lists the publications and presentations resulting from our research.

Submitted

Hamilton, M. A., L. S. Siegel, C. D. Palmer, N. E. Yancey, and L. L. Cook, "Cesium Uptake by Vegetation on a Contaminated Site in Southeastern Idaho," *Journal of Environmental Quality*, 2002. (submitted)

Hanson, L. A., J. B. Harsh, C. D. Palmer, and M. A. Hamilton, "Cesium Interactions with Illite in the Presence of Sodium Oxalate," 2002. (In preparation)

Siegel, L., A. N. Alshawabkeh, C. D. Palmer, and M. A. Hamilton, "Modeling Cesium Partitioning in the Rhizosphere: Focus on the Role of Root Exudates," *Journal of Soil and Sediment Contamination: An International Journal*, 2002. (Accepted pending minor revisions)

Presentations

Bertsch, P., "Mineral Weathering Effects on Cesium Sorption: Implications on Contaminant Cycling," *The Clay Minerals Society 39th Annual Meeting, Boulder, CO, June 8–13, 2002.*

Chard, J., A. Henry, B. Doucette, S. Jones, J. Norton, B. Bugbee, and C. Palmer, R. Hess, "Sterile Culture Techniques for Characterization of Root Exudates," *Soil Science Society of America Annual Meeting, October 21–25, 2001, Charlotte, NC.*

Hamilton, M. A. J. R. Hess, L. L. Cook, G. J. White, C. D. Palmer, and N. A. Yancey, "The Effect of Environmental and Ecological Factors on Cesium Bioavailability," *Soil Science Society of America Annual Meeting, Charlotte, NC, October 21–25, 2001*.

Hanson, L. A., J. B. Harsh, C. D. Palmer, and M. A. Hamilton, "Potential for Phytoextraction of Cesium from Contaminated Soils," *American Chemical Society Annual Meeting, Boston, MA, August 18–22, 2001*.

Henry, A., J. Chard, B. Doucette, B. Bugbee, J. Norton, R. Hess, and C. Palmer, "Characterization of Root Exudates from Crested Wheatgrass," *Exudates Soil Science Society of America Annual Meeting, Charlotte, NC, October 21–25, 2001*.

Siegel, L. S., A. N. Alshawabkeh, and M. A. Hamilton, "Modeling the Fate of Root Exudates and Their Effects on Cesium Partitioning in the Rhizosphere," *The 17th Annual International Conference on Contaminated Soils, Sediments & Water, Amherst, Massachusetts, October 22–25, 2001.*

Yancey, N., M. Hamilton, C. D. Palmer, and J. R. Hess, "Uptake of Cs-137 by Vegetation at the Idaho National Engineering and Environmental Laboratory," *Intermountain Conference on the Environment, Idaho State University, Pocatello, ID, April 2–3, 2002.*

Peer-Reviewed Proceedings

Seigel, L. S., A. N. Alshawabkeh, and M. A. Hamilton, "Modeling Cesium Partitioning in the Rhizosphere," IN: K. Nehring and S.A. Brauning (Eds.), *Wetlands & Remediation II*, Battelle Press, Columbus, OH, pp. 73–81. Poster presented at *Wetlands & Remediation: The Second International Conference, Burlington, Vermont, September 5–6, 2001*. (Paper published in Conference Proceedings)

Abstracts Submitted

Hanson, L., J. B. Harsh, C. D. Palmer, and M. A. Hamilton, "Potential for Phytoextraction of Cesium from Contaminated Soils," *Inland*

Northwest Research Alliance (INRA) Subsurface Science Symposium, Boise, ID, October 13–16, 2002.

Hanson, L.A., J.B. Harsh, C.D. Palmer, M.A. Hamilton, 2002. Geochemical effects on Cesium bioavailabilty and mobility in the rhizosphere. Soil Science Society of America. October 2002.

Henry, A., J. Chard, M. Peterson, J. Norton, M. Hamilton, C.D. Palmer, J.R. Hess, B. Bugbee, 2002. Do water and nutrient stresses increase root exudation? Soil Science Society of America, October 2002.

Hess, J. R., C. D. Palmer, M. A. Hamilton, L. L. Cook, L. S. Siegel, N. A. Yancey, and G. J. White, 2002. Growth stage dependent Cesium uptake by crested wheatgrass in a sagebrush-steppe ecosystem. American Society of Agronomy, October 2002.

Palmer, C. D., J. Richard Hess, M. A. Hamilton, L. L. Cook, L. S. Siegel, and N. A. Yancey, Biogeochemistry of Cesium in a Sagebrush Steppe Ecosystem," *American Geophysical Union, Fall 2002 meeting, San Francisco, CA, December 6–10, 2002*.

Palmer, C. D., J. Richard Hess, T. G. Kaser, and M. A. Hamilton, "Plant Facilitated Translocation of Cesium in a Sagebrush Steppe Ecosystem: Moving Toward Mesoscale Testing," *Inland Northwest Research Alliance (INRA) Subsurface Science Symposium*, Boise, ID, October 13–16, 2002.

REFERENCES

1. National Research Council (NRC), *Research Needs in Subsurface Science*, National Academy Press, 2000.

2. M.T. van Genuchten, "A Closed-Form Equation for Predicting the Hydraulic Conductivity of Unsaturated Soils." *Soil Sci. Soc. Am. J.*, Vol. 44: 1980, pp. 892–898.

3. L. Clesceri, A. Greenberg, and A. Eaton (Eds.), *Standard Methods for the Examination of Water and Wastewater, 20th Ed.*, Baltimore MD, United Book Press Inc., 1998.

4. S. M. Stacey, *Proving the Principle, A History of the Idaho National Engineering and Environmental Laboratory 1949–1999*, Idaho Operations Office of the Department of Energy, Idaho Falls, ID, DOE/ID-10799, 1999, p. 325.

5. J. R Nimmo, S. M. Shakofsky, J. F. Kaminsky, and G. S. Lords, *Laboratory and field hydrologic characterization of the shallow subsurface at the Idaho National Engineering and Environmental Laboratory waste-disposal site*, U.S. Geological Survey Water-Resources Investigations Report, 99-4263, 1999, p. 31

Borehole Probe Development

C. A. McGrath, R. P. Keegan, J. D. Baker, C. L. Riddle, J. E. Lee, R. Hertzog, and W. Yoon

SUMMARY

In situ subsurface characterization data that describes the location and concentration of radionuclides and RCRA contaminants is difficult to obtain. The main goal of this project is the construction and characterization of two prototype neutron-generator based borehole-logging instruments that will generate these types of data. To date, this has involved building the probes, the construction of calibration facilities, and a full program of instrument modeling.

Two probe designs have been chosen to fill needs present at the INEEL. The pulsed fission neutron (PFN) probe is designed to detect fissile material in the subsurface. The neutron gamma (NG) probe is designed to detect many different elements in the environment surrounding the tool.

Alone, these probes are technologically interesting, but provide little useful information. It is only when combined with a comprehensive calibration and characterization program that these tools begin to provide useful data. This calibration program requires both a calibration facility and a comprehensive modeling program.

The calibration facility constructed for this program was once the critical facility for the Engineering Test Reactor at the INEEL. Surrogates, which are described in more detail later, have been prepared for use in the facility. Filled with carefully chosen materials, these surrogates can be used to mimic the subsurface environment. With ports that allow the insertion of sources or other target materials, the surrogates will allow for mockups of many different environments.

Computer modeling is the final important component of the borehole probe program. Still in the early stages, the modeling will bridge the gap between the actual measurements and the calibrated results. It would be impossible to exactly simulate all the environments that may be encountered. For this reason, computer models will be used to allow extrapolation to what may be found in the field.

The probes, facility, and modeling have been the focus of the work for the past year. The prototypes are basically completed and need only be characterized and calibrated, which will be the focus of future work on the project.

PROJECT DESCRIPTION

We recently concluded the second year of a 3-year project established to develop two prototype neutron-generator based borehole-logging instruments. This project also includes the construction of calibration facilities and instrument modeling. Our ultimate goal is to transfer this technology to the Environmental Restoration operations units.

We chose two probe designs that complement the skills available at the INEEL and solve very specific problems inherent to the waste buried in the Subsurface Disposal Area (SDA). The PFN probe is designed to detect fissile material in the subsurface. The NG probe uses prompt gamma neutron activation analysis (PGNAA) to detect many different elements in the surrounding environment.

The PFN probe uses a “Zetatron” design neutron generator and a detector unit that can contain either neutron detectors or gamma-ray detectors. A “Zetatron” neutron generator is designed to pulse both the target and the source. This prevents the production of “dark current” neutrons and allows for the use of the differential die-away detection technique. This technique will be described in more detail in a later section.

The neutron detectors on the PFN probe are ^{3}He detectors surrounded by moderating polyethylene and wrapped in cadmium shielding (see Figure 1). The neutron detector package will also be described in more detail in succeeding sections.

Figure 1. Assembled PFN probe without the pressure housing.

In addition to the neutron detectors, gamma-ray detectors have also been designed and built. These sodium iodide detectors have been designed to be used to measure macroscopic cross sections, and will complement the neutron detectors.

The NG probe uses a more traditional neutron generator design (see Figure 2) and a high-purity germanium (HPGe) gamma-ray detector to perform subsurface PGNAA measurements. Properly calibrated, this instrument will perform many different elemental analyses. In studying the waste buried in a shallow burial ground, chlorine is perhaps the most significant element to determine. With the large amount of chlorinated organic solvents in the waste, safety considerations require some analysis of the volatile organic solvents. Measurement of the chlorine and the carbon content of the waste, mixed with some process knowledge should allow for as complete an analysis of the organic solvents as possible, under the circumstances.

The high-purity germanium detector used in the NG probe has resolution far superior to the sodium iodide detectors often used in well-logging spectroscopy tools. This resolution would be greatly degraded by the 800 ft of logging cable necessary to make measurements in the aquifer. For this reason, a spectroscopy unit has been designed that will allow the spectra to be digitized and stored within the probe. The spectra are then transmitted up the logging cable as digital signals. This will preserve the normally fine resolution of the HPGe detector.

Alone, these probes are technologically interesting, but provide little useful information. It is only when combined with a comprehensive calibration and characterization task that these tools begin to provide useful data. This calibration task requires both a calibration facility and a comprehensive modeling task.

The calibration facility constructed for this task was once the critical facility for the Engineering Test Reactor at the INEEL. The pit that contained the critical experiments has been converted for use in borehole calibration measurements. An assembly of large (29 and 60 in.) tubes was mounted in the pit and filled with gravel. In addition to a diagonally-placed 5-in. tube, these tubes were intended to provide maximum flexibility for future use of the facility.

Figure 2. Electronics and neutron generator for the NG probe.

Surrogates prepared for use in the 29-in. tube were filled with carefully chosen materials. These surrogates, which can be used to mimic the

subsurface environment, have ports that allow the insertion of sources or other target materials. They will allow for mockups of different environments.

Computer modeling is the final important component of the borehole probe project. Still in the early stages, the modeling will bridge the gap between the actual measurements and the calibrated results. It would be impossible to exactly simulate all the environments that may be encountered. For this reason, computer models will be used to allow extrapolation to what may be found in the field.

The probes, the facility, and the modeling tasks have been the focus of the work in FY 2002. More specific details are presented in the project description section.

Electronics Upgrades

Initial work with the probes in FY 2001 revealed certain deficiencies in some of the probe electronics. One of the tasks for the last year was to identify these shortcomings and correct them.

Neutron Detector Design

In some of the first tests of the PFN neutron detectors we observed that the thermal neutron background was unacceptably high. Eighty percent of the neutron detectors are covered with cadmium shielding. This shielding is designed to prevent thermal neutrons from reaching the detectors. As a result, the signal from the cadmium-wrapped neutron detectors is predominantly from epithermal neutrons.

Epithermal neutrons are the key to the differential die-away analysis technique that will be used with the PFN probe. Basically, the technique works in the following manner. Neutrons are created using the neutron generator. Depending on the environment surrounding the generator and the detectors, the epithermal neutron flux takes a certain amount of time to die off. If fissile material is present in the surrounding environment, neutrons emitted during fission lengthen the time required for the epithermal flux to die off. It is this effect that is measured in the differential die-away technique.

The sensitivity of this technique is determined by many factors, including the thermal neutron background. If the thermal neutron background is high, the sensitivity is greatly decreased. This is exactly what was observed in FY 2001. The thermal neutron background was quite significant and the sensitivity of the instrument was not near the design specification of 100 nCi/g Pu in soil.

The thermal neutron background is largely defined by the quality of the cadmium shielding. It can be inferred from the high background that the original shielding design was inadequate. It was, in fact, quite difficult to shield the detectors fully in the original design. This likely lead to the leakage of thermal neutrons, which was observed as the high background rates.

It was decided that the neutron detector package would be completely redesigned to be both easier to shield and easier to mount on the probe. The only requirements would be that it fit in the same space and contain the same number of detectors. Great care would need to be taken to ensure that no path is available for thermal neutrons to reach the detectors. Only if this is achieved can the current sensitivity goal of 100 nCi/g of Pu be reached.

A review of the initial shielding design indicated that the largest neutron “leaks” were present in places where cables were forced to pass through the cadmium shielding. It was necessary to remedy this problem in order to properly shield the detectors. A simple feed-through was designed that allowed the signals to pass through the cadmium without the necessity of piercing the shielding in any way.

The feed-through that was designed consists of individual cadmium discs and two circuit boards that act as “dog-legs.” These boards are built so that a signal can enter on one side and exit on the other, a significant distance away. By using two separate boards, it is possible to layer cadmium in such a manner as to make the minimum cadmium thickness of any path the same as that on the rest of the detectors. It is now possible to fully shield the neutron detectors with no apparent penetrations.

As long as the neutron detector package was being redesigned, it seemed appropriate to consider changing the configuration of the moderator within the shielding. As has been previously stated, the cadmium shielding filters out the thermal neutrons. Unfortunately, it is the thermal neutrons to which the ^{3}He tubes are sensitive. In practice, this means that the epithermal neutrons must be further moderated to be efficiently detected by the neutron tubes. We accomplished this by placing the detectors in a polyethylene cylinder. We did a rudimentary sensitivity analysis to determine the exact size and shape of that tube.

In the original design, polyethylene was placed inside an aluminum tube and the detectors were evenly spaced around the perimeter of the interior cylinder of polyethylene. The new design completely eliminates the aluminum and allows for more polyethylene (see Figure 3). In the end, sensitivity calculations showed that the exact position of the detectors was not very important given the increased polyethylene. Thus, they were placed in a circle with a radius perhaps two-thirds that of the polyethylene cylinder.

The resulting neutron detector package is better shielded and easier to assemble and mount. Hopefully, this will allow the tool to reach the sensitivity goal of 100 nCi/g of Pu in soil.

Amplifiers and Power Supplies

One feature of the old detector design that made it difficult to shield was the mounting of the amplifiers and power supplies onto the package itself. This approach was no longer feasible in the new neutron detector design. Unfortunately, the size of the amplifiers and power supply (shared by all detectors) made it impossible to mount them in the remaining space below the neutron detector package. The amplifiers in the original detector package were approx. 4 in. long and 1-1/2 in. wide. Our solution was to make them smaller.

The amplifiers were built using antiquated components that were expensive and hard to acquire. The approximately 1-1/2 in. diameter by 4 in. long power supply was shared between the three sets of detectors. Using only one power supply was found to create a significant amount of noise and it was decided that individual power supplies for each set of detectors would be better.

The new amplifiers are half the size of the old and built with modern, cheap, easy to obtain components. Tests showed that they performed at least as well as the old design. The reengineered power supplies produced a version that is small enough to allow for the use of three separate supplies. Tests showed them to be slightly unstable, but not fatally so.

The new amplifier and power supply designs have proven to perform quite well. They are also flexible enough to be used for both the neutron detectors and for sodium-iodide gamma-ray detectors. A piece was built to install the amplifier/discriminators and the power supplies on and they are now mounted below the neutron detectors at the bottom of the probe (see Figure 4).

Figure 3. The redesigned PFN neutron detectors. Note the orange color is Kapton tape that serves to isolate the detectors electronically and prevent access to the cadmium shielding.

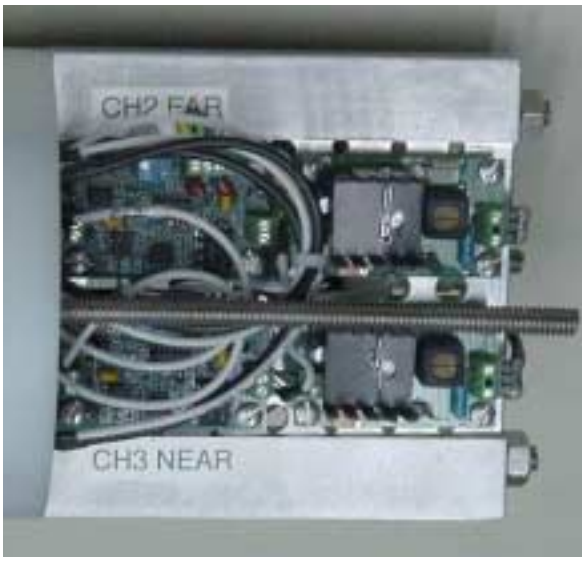

Figure 4. Close-up of the PFN neutron detector electronics showing two of the three detector channels. The amplifier and discriminators are on the right and the power supplies on the left.

Digital Spectrometer and Communications Bus

Transmission of the preamplifier signal from an HPGe detector over 800 ft of logging cable results in severe signal degradation. Since the best resolution possible is generally required for environmental PGNAA measurements, some solution to this problem was required. It was decided that the best solution was to digitize the preamplifier signals on the probe and transmit digital signals over the logging cable. To do this, we purchased a customized digital signal processor (DSP) from XIA.

When used as a digital spectrometer, a DSP performs the functions of an amplifier, an ADC, and a histogramming memory. This program had previously purchased a customized DSP from XIA that, while not designed to fit on the probe, was modified to meet the rigorous requirements of neutron-generator-based environmental PGNAA. Specifically, the DSP was modified to allow the simultaneous collection of 16 different gamma-ray spectra. These spectra would be differentiated by the time in which the gamma ray was collected following the neutron generator pulse. This makes it possible to know which neutron reaction predominates which spectra.

Two additional modifications were made to the design of the original spectrometer that was purchased for use with the NG probe. The circuit board was reengineered to fit probe dimensions, and the circuitry was modified to allow the use of an external communications unit. This unit was designed by and acquired from the University of Idaho. This new communications system is based on an industrial Ethernet-like protocol called ARCNET, a robust protocol with 2.5 megabit transmission rates and a maximum cable length of 2,000 ft. This system will relay digital data from the “downhole” DSP to a computer at the surface. Various error-correcting techniques will be used to ensure the integrity of the spectra that are digitally passed through the logging cable. Computer software will be provided that will allow this communications system to be easily incorporated into virtually any data acquisition system.

All the electronics upgrades were performed in the past year shared the same goal, making the collection of data more accurate and more efficient. Without exception, these upgrades went well and have done much to improve the quality of the borehole probe data.

Surrogate Construction

Calibration and characterization of borehole probe prototypes will require laboratory-based mock-ups of the subsurface environment. In fact, many different surrogates will need to be constructed. The subsurface environment is, of course, much different in the shallow burial grounds than it is in a monitor well. Even within a single monitor well, the environment changes significantly with depth.

Traditionally, oil-well-logging companies that wish to calibrate borehole instruments have constructed large tanks (approx. 1,000–2,000 gal) that are carefully filled with sand or some other well-characterized material. Often, an elaborate pumping system is installed to allow the fluid in the tank to be completely changed. In this manner, the salinity of the system can be rapidly changed. By using a liquid other than water, it is even possible to change the hydrogen content of the tank. As chlorine is a very effective neutron absorber and hydrogen is the best neutron moderator, it is

possible to radically alter the neutron distribution in the subsurface environment.

This would be the ideal type of system to install at INEEL for a calibration facility. Unfortunately, this system would require far more space than is currently available. What we have chosen to do is convert a decommissioned critical facility into our borehole probe calibration facility. As we have described previously, the pit that comprised the critical facility was decommissioned and modified to accommodate calibration surrogates. A system of tubes was installed, and the pit was then filled with gravel (see Figure 5).

Figure 5. The modified pit in ETRC. Note the diagonal tube in the lower right corner of the picture.

The modified pit was approximately 17 by 10 by 17 ft deep. Vertical pipes were installed that are 29 and 60 in. in diameter. An additional smaller pipe (approx. 5 in. diameter) was installed diagonally for use by other programs. The pit was then filled with pea-sized gravel. At this time the 60-in. tube contains a water tank that was installed in order to provide a simplified environment for testing the modeling (see Figure 6).

Figure 6. The water tank installed to provide a simplified environment to test the modeling.

Surrogate Shell Construction

Although our goal is to build surrogates that fill a 60-in. hole, we started by building surrogates that occupy the 29-in. pipe. The diameter of an 83-gal barrel is just less than 29 in. and the decision was made to modify them to produce the surrogates. These surrogates would then be stacked inside the 29-in. pipe and used for the calibration measurements.

There are several requirements that the surrogates must meet. They must fit within the 29-in. tube, they should stack well, they should withstand a full load of concrete, and they should be relatively thin-walled to prevent the surrogate material from overwhelming the signature of the contents. The 83-gal drums easily meet these requirements. The surrogates must generally be doughnut-shaped to allow the probes to pass through them. This is the only way to “simulate” a subsurface borehole environment. This problem is solved for the 83-gal drums by welding sections of penetrometer pipe in the center of each drum (See

Figure 7). This is the same penetrometer casing used in the subsurface disposal areas. It is 4.5 in. on the inside diameter, with a one-half-in. wall thickness. Finally, within the planned calibration and characterization program it will be necessary to place different materials within the surrogates, in such a way as to prevent contamination of the bulk medium. With the 83-gal drum, this is facilitated by welding 2-in. pipe into a radial 4-spoke arrangement in the center of the drum (see Figure 8). With these sample ports, materials, radioactive or not, can be easily placed within and removed from the surrogates.

Figure 7. The top of a surrogate shell with center penetrometer pipe and four holes for even filling.

Figure 8. Side view of a surrogate shell with capped sample port in the center.

Approximately 10 surrogates were constructed in the last year. About half have sample ports, but the others were constructed without sample ports to increase the homogeneity of the bulk material. Two of those with ports were filled with concrete for use as the bottom plug and top shield in a stack with five surrogates. The welded ports in these concrete-filled surrogates serve no purpose other than supporting the outer wall of the drum. Without them, it was feared that the drums would bow significantly under the load of concrete (~700 kg). This might prevent the surrogates from being lowered into the 29-in. tube, or worse, cause them to become irretrievably jammed in the tube.

Surrogate Filling

Once the surrogate shells were completed, we began to plan the surrogate filling process. There were two main questions regarding this process: what do we fill the surrogates with, and what is the best way to fill the surrogates? What we fill the surrogates with is one of the most important questions to be answered by this project. The question of the mechanics of surrogate filling is much more mundane. We considered many factors in choosing the bulk fill materials. Some of the most important were ease of use, repeatability of filling, similarity to the subsurface environment, and ease of acquisition. Silica was chosen because it is readily available, easy to pack, well understood, the largest part of standard soil, and fairly easy to use. Silica had only one significant drawback, it is a serious respiratory hazard, which forced anyone participating in surrogate-filling activities to become respirator trained.

Once the bulk material was chosen, it was necessary to choose the method by which the “saturation” of the subsurface with water would be duplicated. Subsurface soil, or even rock for that matter, is relatively porous. The pores are often filled with water. The largest effect of the water is to increase the amount of hydrogen in the environment. In turn, this hydrogen increases the thermalization of the neutrons, and thus, decreases the average neutron path length.

It turns out that the use of water to simulate water is less than ideal. It is very difficult to control or even to measure the uniform water content of the surrogate. It is especially hard to see

how one would make a surrogate in which the "pores" are only partially saturated. Since it is the hydrogen content that is truly important, one solution to this problem is to use a more easily controlled substance that provides hydrogen. Hydrated alumina, $Al(OH)^3$ was chosen in this instance. Used in the right ratios, it provides sufficient hydrogen and is relatively easy to use.

Finally, the decision was made to build some surrogates with a significant amount of sodium chloride (NaCl) contained within. This serves two purposes. Since one of the primary purposes of the NG probe is to detect chlorine in the subsurface, adding NaCl to the surrogates will provide a direct calibration of chlorine. In addition, chlorine is a good neutron absorber and its addition will allow for the characterization of the performance both tools in the presence of significant neutron absorbers.

Having chosen the bulk materials, it was then necessary to determine the mechanics of the surrogate filling operation. A consultant, John Spallone, was hired for this particular part of the project. He has a large amount of experience constructing surrogates for Schlumberger, one of the oil-field services companies. He was able to provide valuable insight into all portions of the surrogate-filling process.

In short, the process is really quite straight forward. Care must be taken in order to produce verifiable results, but it is not difficult. Basically, the first step is to determine the volume of the surrogate to be filled. This volume is then separated into layers and the correct amount of material for each layer is calculated. The materials for each layer are exhaustively mixed and carefully layered within the surrogate. The layers are then packed using a vibrating platform (see Figure 9), upon which the surrogate is placed. When the filling is completed, the bulk density can be calculated using the mass of material added and the volume of the surrogate. Using the bulk density of the surrogate and the grain density of the material, it is possible to calculate the remaining porosity of the surrogate.

Figure 9. Surrogate shell on the vibrating platform prior to filling.

In FY 2002, one surrogate was completed. This surrogate has the radial sample ports and is filled with sand and enough hydrated alumina to reproduce 10% moisture in soil (see Figure 10).

Figure 10. Filled surrogate being lowered onto the scale for weighing.

The surrogate is currently stacked in the 29-in. tube and will be used for the initial calibrations (see Figures 11 and 12). Additional surrogates will be constructed, as they are required. Construction of each surrogate requires approximately 4 man-days and should proceed much more smoothly in the winter months. In the summer, it is difficult to spend more than one or two hours in a respirator without perspiring excessively. This requires the construction to be spread out over several days. In any other season, this should not be a problem.

Theoretical Modeling

Constructing surrogates is an important part of the calibration and characterization of the borehole probes. Because the surrogates are fairly small (<30 in. diameter), they do not represent what might be called an infinite medium. That is to say, the surrogates cover only a fraction, albeit a large fraction, of the interesting interaction area. This problem will be reduced significantly if the 60-in. tube is used for surrogates, but this is currently not the case. Therefore, it is necessary to "fill in the gaps" using modeling.

Figure 11. Completed surrogate being lowered into the 29-in. tube for use.

Figure 12. PFN probe lowered into the 29-in. tube and through a short stack of surrogates for use.

For the purposes of this work, an infinite medium is defined as one for which a statistically significant increase in the radius does not lead to a corresponding increase in the measured signal. Depending on the hydrogen and chlorine content of the 83-gal surrogates, they are generally between 40 and 85% of infinite, meaning that the signal measured from these surrogates is between 40 and 85% of the maximum achievable signal. Modeling is responsible for the missing 15–60%.

These types of instruments are normally calibrated by operating them in a simulated environment similar to that expected to be seen in the field. One variable is modified over a chosen range from which a calibration "curve" is generated. This approach is unlikely to be effective with these new tools. Most importantly, the subsurface environment is unlikely to be homogeneous. It will be difficult, if not impossible, to simulate every heterogeneity. In addition, the possibly large amount of signal missing from the noninfinite surrogates will make calibration difficult. For this reason, a path was chosen with an unusual reliance on the modeling.

We chose to perform calibration measurements to prove the validity of a model. If the modeling can be shown to fit the limited subset of surrogates constructed, we can reasonably assume that it will work with a more heterogeneous situation. Proceeding with the PFN probe in this manner will prevent contaminating thousands of pounds of sand with plutonium. Calibration facilities are available at Grand Junction that have concrete homogeneously contaminated with uranium. Individual sources of plutonium will also be placed in the sample ports of the surrogates measured. Combining this data with that from Grand Junction should provide sufficient confidence in the models to allow for extrapolation to other, irreproducible situations.

The PFN probe is relatively simple to model because it requires only neutron transport and fission reactions from neutron interactions to be modeled. Basically, the fission process is generally comparable across those few isotopes that are of interest in this work. The probe can be calibrated with one source and the data adjusted depending on the fissioning isotope. The NG probe is much more difficult to model and calibrate.

The NG probe is designed to detect many different elements; thus, the calibration and modeling requires far more work. In addition to neutron transport and neutron interactions, the complication of gamma-ray transport is added to the mess. It is perhaps easiest to view the situation in different steps. Neutrons are emitted from the generator and travel generally radially outward from the source. This leads to some spatial distribution of neutrons of different energies. This is the neutron transport part of the problem. This distribution of neutrons interacts with the various elements present in the environment to produce gamma rays through various types of reactions. Some of these gamma rays are transported back to the gamma-ray detector where there is some small chance of detecting them.

Problems are inherent in every step of this process. The neutron transport is very sensitive to the hydrogen content of the surrounding medium. It is important to model this correctly because it has a large impact on the depth of investigation and the measurement point for the particular probe. However, it is not always easy to do so with the information that is generally available. The gamma-ray producing neutron interactions are dependent on the energy distribution of the neutrons. Even with the correct neutron distributions, modeling these interactions is often dependent on reaction cross sections that are not well known. Finally, the gamma-ray transport is dependent on the energy of the gamma rays and on the absorbing properties of the environment surrounding the borehole.

In conclusion, the modeling effort is necessary but extremely complicated. We will likely be forced to separate the modeling of the NG probe into successive steps. For instance, modeling the neutron transport, neutron interactions, and gamma-ray transport separately will allow for quick changes, and will prevent the process from becoming overly obtuse. However, it will be vital to keeps these sections connected because of their inherent interconnectedness.

Miscellaneous Concerns and Activities

Throughout its brief history, this project has proven to be quite compliance-intensive. Significant effort has been required to gain approval for the various activities involved in the probe development. The past year was no exception. We secured official approval to operate in our laboratory at TRA, which was no small task. A lack of familiarity with D-T neutron generators caused some consternation in our relationship with the E&SH organizations. After a period of

acclimatization, we appear to have reached a steady-state where significant work is possible.

We also had to, once again, secure permission to operate on the Subsurface Disposal Area at RWMC. Having been through an exhaustive process in the last fiscal year, we were well prepared and this proceeded smoothly. Finally, we attempted to secure permission to operate in the field, at a test well, under the R&D IHR safety guidelines. Unexpectedly, it was this that created the largest problem. In this process, which generally went very well, a problem was identified with the lack of load testing on the hoisting equipment in the logging van. This forced our scheduled field test beyond FY 2002 into the uncertainty of FY 2003.

In the future we expect these issues to become less and less intrusive. We now have a safety envelope in place that allows for any work that needs to be done. Changes to the program should be made with little delay, from this point on.

Looking Ahead

With one year left in this project, significant works remains to be accomplished. Calibration and characterization work will be completed, which will include the construction of many more surrogate containers. The modeling effort will be started and proven to be extendible to the many situations that might be encountered. Finally, some work will be done to ease the transition to an operations funding base. Issues such as operator training, quality certification, and ease-of-use must be considered. A series of estimates will need to be prepared for presentation to those who may have need of these probes. This should keep us occupied for all of FY 2003.

ACCOMPLISHMENTS

In FY 2002 we accomplished the following:

- Completed an upgrade of the neutron generator assembly and the associated electronics.
- Acquired a digital spectrometer and communications system to use on the NG probe.
- Completed the construction of approximately 10 surrogate shells.
- Filled and put into use the first of the surrogates.
- Installed a water tank for use in simplified testing of the various models.
- Built the handling tool required to transport the surrogates on a crane.
- Secured all the necessary approvals to operate nearly sitewide.

Publications

Keegan, R. P., J. C. Lopez, C. A. McGrath, “Development of a field well head safety system for use with radiation generating devices,” Accepted for Publication in Safety Science.

Presentations

Keegan, R. P., C. A. McGrath, J. C. Lopez, “Development of Neutron Probes for Characterization of Hazardous Materials in the Subsurface Medium,” presented at the Spectrum 2002 International Conference on Nuclear and Hazardous Waste Management, Reno Nevada, August 2002.

Geocentrifuge Research Laboratory Development

Alan T. Stadler

SUMMARY

The INEEL is developing a 287 m^2 centrifuge facility for geoenvironmental and geotechnical applications. The centerpiece of the facility is a 2-meter-radius Actidyn Systemes Model C61-3 civil engineering centrifuge with a payload capacity of 500 kg at 100 g's. Data acquisition is accomplished through an on-board computer linked via a fiber optic rotary joint to a user computer located in the centrifuge control room. The initial focus of this geocentrifuge research facility will be on subsurface transport studies and the performance of engineered caps and barriers. It will be available for use by national laboratory, university, and private sector investigators. The centrifuge is an exciting research capability that will allow hydrologic and biogeochemical investigations using intact blocks and cores of vadose zone materials and reconstructed models with idealized 2- and 3-dimensional (2-D and 3-D) physical and chemical heterogeneities. The geocentrifuge will allow researchers to study in a few hours or days the effects of decades of gravity-induced fluid movement.

This ESRA project initiates the development of this geocentrifuge research capability at the INEEL. Activities have included the commissioning of the 2-m-radius centrifuge and the establishment of the supporting laboratory areas. These areas include soil storage, sample preparation, the centrifuge control room, and office/meeting space for the geocentrifuge research staff and investigators. Commissioning has included centrifuge performance verification and the development of procedures for use of the device. The project activities were divided into three tasks: laboratory capability, research programs, and outreach.

For FY 2002, the major products and deliverables include an operational 2-m-radius geocentrifuge with associated procedures for its use, functional supporting laboratory capabilities, initiation of geocentrifuge research activities, and establishment of both internal and external outreach programs.

This ESRA project was administered in parallel with a Corporate Funded Research and Development (CFRD) project that provided the funds to purchase and install the geocentrifuge.

PROJECT DESCRIPTION

Introduction

The INEEL is developing a geocentrifuge research capability focused on subsurface contaminant transport studies. The INEEL is a multipurpose DOE national laboratory operated by Bechtel BWXT Idaho, LLC. Historically, the INEEL had focused on nuclear reactor research, it being the site of construction and operation of 52 test reactors, including the first to generate commercial electricity. Currently, the INEEL is focusing on subsurface science research to understand and model the complex geological, geochemical, biological, and hydrological processes influencing the subsurface behavior of contaminants at DOE sites.

DOE has conducted energy research and weapons development and production at facilities across the United States. Toxic or contaminated wastes generated at these sites have been introduced into underlying soils and aquifers from past disposal practices. Subsurface contamination issues common to DOE sites (including the INEEL) include mixed waste landfills, contaminated vadose zones, mixed contaminant ground water plumes, and contaminated soils. Development and implementation of enhanced innovative clean up technologies and long-term stewardship strategies are limited by lack of understanding fluid movement and biogeochemical processes occurring in the subsurface, especially the vadose zone. Historically, controlled field experiments and laboratory column tests have provided the bulk of the experimental data on subsurface contaminant fate and transport. Although controlled field experiments have the

advantage of being representative of the field-scale problem, these experiments are costly, difficult to perform, limit the use of relevant contaminants, and offer little direct control over boundary conditions. Conversely, laboratory column experiments, which are generally inexpensive and relatively easy to conduct, are of limited value because they do not mimic field conditions. These problems are compounded in vadose zone studies because of the length of time required for water to move through partially saturated media.

A geotechnical centrifuge offers a method for overcoming the limitations of traditional field- and column-based approaches, and is useful for investigating the behavior of subsurface materials and systems at decreased size and time scales. In centrifuge studies, a scale model with all linear dimensions reduced by a factor of n, and which captures the essential features of the field system being investigated is subjected to a centrifugal acceleration of n gravities (ng). Well-developed scaling theory for centrifuge studies suggests static-testing size scales as a function $1/n$ and time scales as a function of n^2. For example, a 50 x 75-cm model evaluated at 100 g can represent a 50 x 100-m field problem. In addition, each hour of centrifuge operation can simulate over 400 days of the field-scale problem. This scaling is for physical processes influenced by gravity such as fluid flow. Biogeochemical processes are not expected to scale the same as physical processes. However, similarity of behavior such as adsorption in equilibrium at both field-scale and model-scale will result in data sets collected under well-defined conditions for processes similar to those occurring at field-scales. These data sets can be used to test numerical models that can then be applied to field-scale problems.

To support the application of centrifuge testing to DOE environmental issues as well as more traditional geotechnical testing, the INEEL has procured a geocentrifuge and is developing the supporting facilities with funds provided by the CFRD and ESRA programs. The geocentrifuge laboratory will be available to address pressing INEEL and DOE research needs in areas such as fluid and colloid movement in the vadose zone and the long-term stability of engineered caps and barriers.

Centrifuge Laboratory

The INEEL centrifuge facility is located in north Idaho Falls, Idaho adjacent to the INEEL Research Center (IRC). The leased space for the facility is located in the Bonneville Country Technology Center. Because this space is leased, the landlord has requested that all building modifications be completed such that the space can be readily reconfigured (including removing the centrifuge) at the end of the lease. Conference rooms and a receptionist are shared by all building tenants and are included in the lease.

The 287-m^2 centrifuge laboratory (see Figure 1) consists of a 21.5 x 9.1-m high-bay engineering space (9.1-m ceiling height), a 10.2 x 8.8-m dry laboratory space for data storage and analysis, a control room, and office space. Approximately 40% of the high-bay space will be used to house the centrifuge in a 5.6 m removable steel-walled (provided by the manufacturer), concrete chamber (see Figure 2). The centrifuge has a removable chamber to allow for the possibility of future relocation to another facility where transport studies may be conducted using radionuclides. Access to the centrifuge and its supporting systems are gained through an electronically interlocked enclosure. The enclosure provides an unmanned area outside the centrifuge door with access control into the centrifuge during operations, and minimizes modifications to the building ventilation and fire protection systems. The remaining high-bay space (120 m^2) will be used to prepare models and store soils.

The laboratory space is configured into the centrifuge control room, office space for three people, and electronics/instrumentation support for configuring and testing sensors for use in centrifuge models. Extensive chemistry, physics, microbiology, and instrument laboratories are available in the IRC.

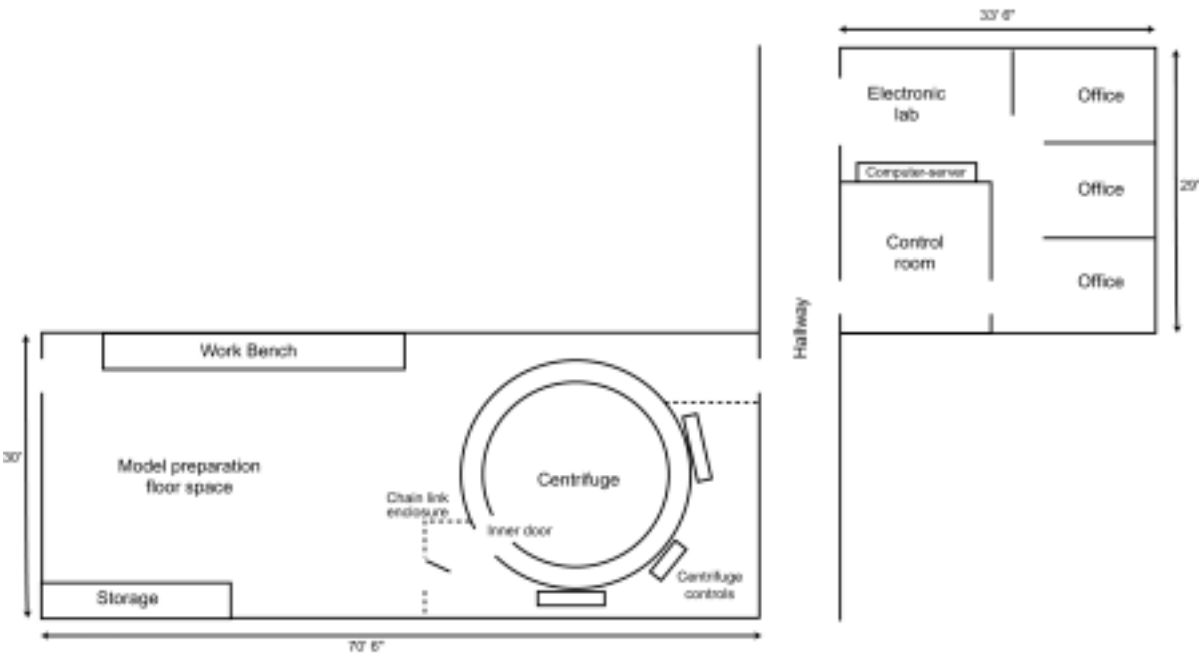

Figure 1: Geocentrifuge research laboratory floor plan

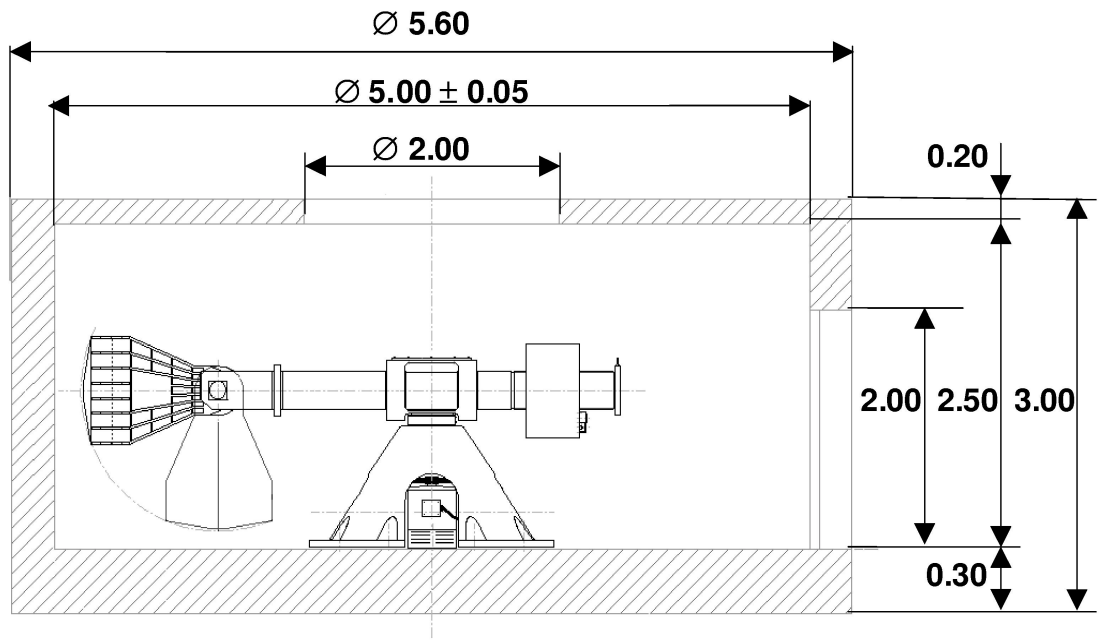

Figure 2. Schematic of the 2-m centrifuge and aerodynamic chamber (units in meters).

Courtesy of Actidyn Systemes

Figure 3 shows the computer-controlled INEEL 2-meter radius, 50 g-tonne Actidyn Systemes model C61-3 centrifuge. The centrifuge has an asymmetric beam equipped with a pendulum swinging basket that rotates in a cylindrical steel and concrete enclosure, which offers both centrifuge safety and aerodynamic efficiency during operation. An automatic balancing system compensates for shifts in the center of mass during operation. Table 1 gives the specifications for the centrifuge.

Figure 3. Actidyn Systemes model C61-3 geotechnical centrifuge.

Table 1. Centrifuge Specifications

Radius	Nominal	1.7 m
	Platform	2.0 m
Acceleration	Nominal radius	10 to 130 g
	Platform radius	11 to 145 g
	RPM	51 to 262
Useable Payload	Depth	0.7 m
	Width	0.5 m
	Height	0.6 m
	Mass at 100 g	500 kg
	Mass at 130 g	230 kg
Electrical Slip Rings	Signal	30
	Power	4
	Video	2
Rotary Joints	Oil	2
	Water or Air	2
	Fiber Optic	2

Control and data acquisition system

A stand-alone operator's computer, located in the control room, provides fully automated operation of the centrifuge. Because many environmental centrifuge applications may require hundreds of hours of centrifuge time, the centrifuge is configured to operate continuously without the operator being physically present. When development is complete, all important centrifuge functions will be able to be monitored from remote locations via the Internet. The data acquisition system employs a fiber optic rotary joint with a 100-MHz transmission rate, which links the computer at the center of the centrifuge arm with the user's computer in the control room.

Using the fiber optic rotary joint and the on-board computer avoids transmitting analog data signals through slip rings and eliminates the noise associated with electrical slip rings. The expandable on-board computer allows for the installation of controls for in-flight experimental manipulations. In addition, the system's flexibility will allow incorporation and signal processing of miniaturized geophysical instruments for real-time tomographic imagining of fluid flow and other processes occurring in centrifuge models. As with the operator's computer, the user's computer will be configured to allow remote Internet monitoring and control of experimental and data collection functions.

Research Plans

Concurrent with geotechnical centrifuge facility development, the INEEL is developing expertise in environmental centrifuge applications by recruiting staff and collaborating with other centrifuge users. The INEEL has staffed the centrifuge facility with a centrifuge principal investigator who will supervise centrifuge activities, one or more centrifuge operators, and technicians to support model preparation, sensor system testing, and data acquisitions. Initial activities include training, developing specific procedures, and procuring/constructing equipment needed for centrifuge research. Training activities include workshops involving engineers from other

centrifuge facilities and extended working visits at operating centrifuge laboratories.

Initial research activities will address both physical and chemical processes in the vadose zone. A partial list of centrifuge projects include:

- Investigation of the physics of multiphase fluid flow, which addresses the development and spreading of light nonaqueous phase liquid lenses at the vadose zone-water table interface.

- Assessment of facilitated vadose zone transport, which focuses on the mobility of colloids in the vadose zone.

- Determination of vadose zone reactive transport, which will assess reactive chemical transport in vadose zone materials at varying water contents.

The INEEL geotechnical centrifuge facility will operate as a research resource with centrifuge time being available to investigators at other national laboratories, universities, and industries interested in environmental or geotechnical studies. An example of this type of collaboration is described as follows:

> "Accelerated transport of actinide contaminants in the subsurface is thought to be facilitated, in part, by association with colloids or pseudocolloids. This project, a collaboration with the Massachusetts Institute of Technology, uses a geocentrifuge to conduct accelerated colloid transport studies in order to determine which principles govern migration of colloidal particles in porous media. In the geocentrifuge experiments, transport of model colloids will be measured in a porous media system that replicates soil moisture conditions in the field. The experimental technique uses a two-dimensional "transparent soil" profile made of crushed, prewetted Pyrex glass. Below the model water table, the material is saturated with an optical fluid of matching refractive and dispersive indices. Colloid movement is monitored using fluorescent tags and particle tracking software. These experiments will be performed initially on MIT's 1m geocentrifuge. When the INEEL 2m geocentrifuge comes on line, the experiments will be replicated in higher gravity environments. This work will provide fundamental insight into how colloids move in porous media and what surface chemical parameters affect migration. It will also serve as one of a number of basis studies at the INEEL directed toward the engineered movement and targeting of synthetic colloids in subsurface environments."[1]

Outreach

News Releases/Media Activity

There has been a substantial amount of public relations activity related to this project and includes the following:

- A brief article appeared in the May 9 *iNotes*.

- A second, longer article appeared in the June issue of the *Subsurface Topics* newsletter.

- A ribbon cutting ceremony was performed on Monday, August 19, 2002. Tom Hash, president of BNI performed the honor. Bill Shipp was also in attendance. The local media was invited and a press release was made. As a result of this event, the geocentrifuge facility was the lead story on the late local news for the Idaho Falls ABC network affiliate, and mentioned on the NBC network affiliate. It was the front page article in the August 20, 2002, edition of the Idaho Falls Post Register newspaper, and radio interviews were broadcast on two local radio stations on Wednesday, August 21, 2002.

Web Site

The geocentrifuge web site is now up and running and available to the public on the Web at: http://www.inel.gov/env-energyscience/centrifuge/.

Future Facilities Development

INEEL is currently in the conceptual design phase of its proposed Subsurface Geosciences

Laboratory to be located in Idaho Falls. An important feature of the laboratory, scheduled for completion in 2007, will be a 5.5-meter, 250 g-tonne centrifuge, which will allow investigations using larger highly instrumented models. The 2-meter centrifuge facility will be instrumental in developing hypotheses, approaches, and techniques that will be used for environmental centrifuge studies to be conducted in the larger centrifuge to be located in the Subsurface Geosciences Laboratory.

Conclusions

The INEEL is developing a geotechnical centrifuge capability to address geoenvironmental and geotechnical issues. This capability includes two centrifuges. The first is a computer-controlled 2-meter 50 g-tonne centrifuge, the second is a 5.5-meter, 250 g-tonne centrifuge to be housed in the proposed Subsurface Geosciences Laboratory scheduled for completion in 2007.

ACCOMPLISHMENTS

We constructed the 2-meter geocentrifuge and associated facilities.

Publications

Smith, R.W., S. J. Payne, and D. L. Miller, "INEEL environmental geocentrifuge facility developments", Physical Modeling in Geotechnics: ICPMG '02, Philips, Guo & Popescu (eds), pp 55-58, July 2002.

Presentations

Bechtel Fellows Workshop, April 2002, Idaho Falls, ID.

One poster and two presentations in conference sessions at the 1st International Conference on Physical Modeling in Geotechnics (ICPMG '02), St. John's, Newfoundland, Canada, July 2002.

BCTC Board of Directors, July 2002, Idaho Falls, ID.

Bechtel Discipline Workshop, September 2002, Frederick, MD.

Stadler, A. T. (Dr.), was invited by Bechtel Corporate personnel to make a presentation on the INEEL geocentrifuge at their annual Discipline Workshop. Dr. Stadler made presentations to the Geotechnical and Hydraulic Engineering Services and the Environmental Services Groups.

Notable Visitors/Tours

Ms. Linda Trocki of Bechtel Corporate toured the facilities on June 5, 2002. Several DOE-ID representatives (Neil Burrell, George Schneider, Don Shadley, and Joanne Malmo) toured the facilities on June 12, 2002.

Ms. Nancy Williams of Yucca Mountain toured the facilities on July 8, 2002.

Mr. John Anderson of Senator Crapo's staff visited on August 15, 2002.

Dr. Dick Pratt, Dean of the College of Arts and Sciences at Idaho State University toured the facilities on August 21, 2002.

Ms. Bev Cook, DOE Assistant Secretary for Environment, Safety, and Health toured the facilities on August 26, 2002.

REFERENCES

1. Patricia J. Culligan, "Colloid Migration in Saturated and Unsaturated Media: Influence of Surface Chemistry and Accelerated Testing Using a Geocentrifuge." Massachusetts Institute of Technology, and Ralph M. Parsons, Laboratory for Water Resources and Hydrodynamics, INEEL Collaborator: George Redden, "Colloids," *reddgd@inel.gov*.

Waste Management

Advanced Concepts of Nuclear Physics Applied to DOE's Mission

R. Aryaeinejad, R. J. Gehrke, J. D. Cole, M. W. Drigert, J. K. Hartwell, C. A. McGrath, E. L. Reber, R. P. Keegan, and D. F. Spencer (INEEL); R. G. Helmer (Idaho State University); H. C. Griffin (University of Michigan); and D. Ramsden (University of Southampton, England)

SUMMARY

This is a multidisciplinary research effort to pursue advanced concepts in nuclear physics using theory, modeling, experimentation, and applications. This project supports DOE and INEEL missions in both site closure and alternative development by dedicating its resources to both the short- and long-term challenging needs of DOE Environmental Management (DOE-EM) in the advanced characterization of radioactive waste. This research involves the development of more definitive, accurate, faster, and safer methods of characterization, which will be critical in attaining the 2012 cleanup vision at the INEEL.

During FY 2002, our research focus was on identifying and quantitatively characterizing TRU waste, mixed waste, low-level waste, spent fuel for radionuclides (activation, fission product, and actinide), fissile content, and elemental content. Information was gathered using sophisticated detection instruments, which involved singles as well as coincidence measurements using single or multi-detector arrays. This project involved four main tasks: fission studies, decay and reaction studies, high performance radiation detection systems, and advanced methods and modeling.

PROJECT DESCRIPTION

Fission Studies

The goal of fission studies is to produce data for use by the DOE-EM programs to identify, and to some extent, characterize the presence and types of fissile material in the various waste and materials collected from remediation sites. The studies provide signatures of gamma rays for this identification process. In general, fissile isotopes do not emit energetic or intense gamma rays, which precludes the identification or even detection of fissile material present in waste. This is because the gamma rays following alpha decay are either low in energy (<500 keV) or intensity due to the long half-lives of most fissile materials.

Fission Yields and the Structure of Fission Fragments

Since the early 1990s, significant new fission studies have been completed or are still ongoing that use arrays of detectors to look directly at the prompt fission process. As a result, we now have specific information available that correlates various radiation emissions with fragment emission before beta-decay, and new information on the excitation modes of the fragments. These data are specific to this prompt-time region following fission and before the first beta-decay occurs.

Prior to the 1990s, most fission studies measured average quantities or totals of parameters such as total energy release or mass yields. Models of fission were based on a liquid drop model of the nucleus with some parametric correction for shell model effects in both the isotopes undergoing fission and the fission fragments produced. Experimental low-energy nuclear structure physicists were focused on nuclear models that involved both collective and single particle motions of the nucleons in a meson-type potential. The study of nuclear deformation and rotational motion, as observed in bands or cascades of gamma rays, required the study of a series of nuclei over as large a region of mass, neutron number, or proton number as possible to establish trends or changes in the nuclear states. The nuclei produced in fission comprise a rich set of isotopes for such studies, but producing these isotopes for study by traditional methods or using them for reaction studies are impossible at this time. Our primary goal in beginning the fission studies was to study the structure of the prompt fission products.

The new models, advanced to describe nuclei and nuclear structure physics, primarily looked at level schemes. The liquid-drop model was generally abandoned in these studies, but it was not abandoned in describing fission. This was because most fission studies either measured average values or studied the fragments by beta-decay. Experiments with fission chambers and various gamma-ray calorimetric methods did not reveal specifics on the prompt states occurring immediately following the fragment separation. This situation changed however, with the development of arrays of detectors optimized for measuring coincident radiation signatures, with extremely fast timing electronics that use list-mode data storage and post-acquisition sorting-based analysis. What was once considered a dead subject for experimental measurement and theoretical interest has been revived to provide new information for the many-bodied nuclear problem.

Figure 1 illustrates the prompt-time region revealed by the new studies. Considerable energy is available from isotopes in spontaneous fission, or that are fissile (fission induced by neutrons). Most of this energy appears as kinetic energy of the two fragments, but 10s of MeV are available for particle or gamma ray emission. Exactly what occurs depends on the conservation of angular momentum, spin, and parity. These three parameters are such that the liquid-drop model does not correctly explain or predict some of the basic average values assigned to fission, nor does it explain the experimental results reported in these studies.

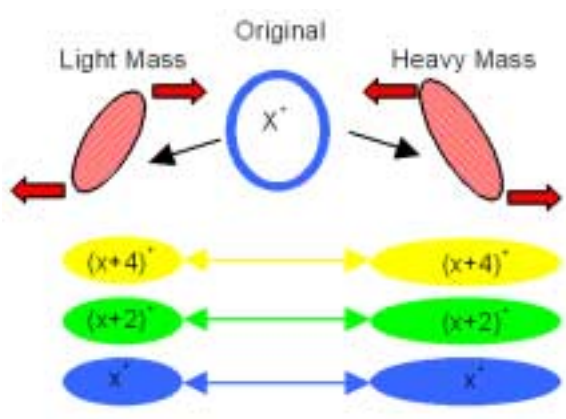

Figure 1. Graphical represation of high spin, parity selection, and rotational excitation in fission.

Our first important observation was that the rotational motions of the fragments carry significantly more energy than allowed by traditional views. Level energies of states depopulated by gamma-ray emission exist well above the energy needed to evaporate a neutron. The fragments display the typical rotational bands seen in in-beam studies. This should not have been a surprise because high-spin bands allow the nucleus to have high-excitation energy that cannot be dissipated by the emission of a particle. The rotational state is blocked from the emission of particles, and gamma-ray emission occurs only when a state is reached where particle emission is allowed. In general, the first such states where particle emission is possible for the fragments is energetically too low for particle emission. Figure 1 represents the situation when the two fragments will have very similar angular momentum states. The angular momentum of the two fragments must conserve the initial angular momentum of the fissile isotope; therefore, if one fragment has high angular momentum, so must the other. The spin and parity of the fragments must also conserve the initial numbers of the fissile isotope. However, the initial states of the two fragments will be that allowed by the parent. This becomes a considerably more complex problem for ternary or higher fragmentation, but is not important for this discussion.

We are able to observe these experimental results and explain them because of a theoretical basis developed in the past few years. In our studies, the high-energy part of the gamma-ray energy spectra show a rich population of transitions that the coincidence methods enhance, just as these methods suppress the backgrounds from the fission source. For the case of ^{252}Cf, these results have been presented in various papers that cover the new high-energy gamma rays observed, and the new yield data from approximately 120 fragment pairs. There is no reason to think that the structure information developed for the fragments from the ^{252}Cf data will not be the same for uranium and plutonium. It may well be that even more fragments would be produced in high-spin states for the uranium and plutonium fission because the competing neutron emission (average neutron multiplicity) is lower in these isotopes than in the case of ^{252}Cf.

Experimental Program of FY 2002

FY 2002 was a year of moves and new equipment. FY 2001 saw the installation of the array of new Compton-suppressed, high-purity germanium (CSHPGe) detectors at the Oak Ridge Electron Linear Accelerator (ORELA). This installation was followed by our first efforts of studying induced fission on ^{235}U over a wider range of neutron energies than are available at Argonne National Laboratory's Intense Pulsed Neutron Source (ANL/IPNS). Unfortunately, ORELA was unable to produce sufficient beam intensity to induce adequate fission rates for the studies. As a result, the setup was moved to ANL/IPNS.

Moving the equipment to ANL benefited the experiments being conducted at IPNS. First, we have 11 new HPGe detectors and 11 new Compton shields. The detectors that were being used at IPNS were borrowed from the ANL Physics Division. Although their support enabled these induced-fission studies to begin, replacing ANL's detectors with new ones improved experimental energy resolution significantly. It should be noted that the nuclear physicists at ANL showed their support of the fission work by loaning us about $600K of equipment. Secondly, we were able to use the new detector array stand that holds 12 HPGe detectors and Compton shields. To make full use of the stand we are still using one HPGe and Compton shield from the ANL Physics Division. Figure 2 shows the new Compton shields being readied for installation at ANL.

Figure 2. Installation of new detectors at ANL.

The move took the first quarter of FY 2002 with the system actually installed and operational in January 2002. The fissile target that has been used during this year is the ^{237}Np that was bought from Russia. Figure 3 shows the encapsulated neptunium target with the two halves of the target holder. The neptunium target provided us with our first experiment where fission was not the dominant reaction of the neutron irradiation. The ^{237}Np has a large prompt n-γ reaction. This will provide important information for DOE-EM programs because knowledge of the gamma rays from this reaction are important in identifying ^{237}Np in waste with a high α-n reaction rate to produce neutrons. The knowledge of gamma rays from n-γ reactions in the actinides is very limited and an effort is underway to identify these gamma rays. The *n*-γ data from the fission studies is simply a bonus.

Figure 3. Neptunium target in welded SS container with target holder.

The data acquisition system was upgraded with a second dual-ported memory module to decrease the system dead time at higher event trigger rates. Some additional monitoring software was installed in order to identify equipment or detector problems during the course of the long runs. The data acquisition system operated uninterrupted for several months without user interaction. With the use of the online monitoring capabilities, we were able to identify problems with the Ge detectors so that we could ask our on-site collaborators to intervene. A total of three Web-cameras have now been installed, which allow us to remotely monitor the physical condition of the experiment. In particular, we are now able to

determine the state of the LN2 fill system and pressure in the large LN2 tank, which is critical for a successful fill of the Ge detectors. The Web-cameras also allow us to check the status of the Ge high voltage power supplies, which are the only critical pieces of equipment in the setup that have no computer interface and control capability.

FY 2002 saw our first use of the time tagging of the fission events to determine neutron energy. This will enable the excitation function measurement and the additional correlation of fission events to neutron energy.

Decay and Reaction Studies

The purpose of this task is to use gamma rays emitted from nuclear decay and nuclear reactions to provide quantitative information that heretofore has not been obtained or processed for radioanalysis or nuclear data. We have carried out the methodical study of actinide and other radionuclides with calibrated Ge spectrometers to improve our understanding of the nuclear decay chains and schemes of individual actinides, and how this information can be used to enhance radioanalyses, especially of TRU waste and spent fuel. This past year a major effort was placed on developing alternate methods of radioanalysis of TRU with one or more Ge spectrometers operated in the singles mode.

First, the use of gamma rays from the spontaneous fission of actinides ^{252}Cf and ^{244}Cm were studied. While our first priority was to measure the gamma-ray production yields for ^{240}Pu, this isotope in the gram quantity needed could not be shipped to TRA because it would put us over the limit of the amount of radioactive material we are allowed to have there. Instead, we studied the (α, n) and (α, p) reactions with the 8.7 mg of ^{244}Cm obtained on-loan from Oak Ridge National Laboratory. For this reason the gamma-ray production yields from the spontaneous fission of ^{252}Cf was studied first. Comparisons of the measured gamma-ray yields with the calculated cumulative and independent yields were made for a number of the fission product gamma rays, including from decay and direct prompt feeding of excited states. These values are given in Table 1. The results were reported at the International Conference, "Industrial Radiation and Radioisotope Applications -V (IRRMA-V)," held June 9–14, 2002 at the University of Bologna in Bologna, Italy. The full paper was submitted at the conference for publication as the proceedings of the conference in Nuclear Instruments and Methods in Physics Research.[2]

Second, the use of α-induced reactions was studied to measure the neutron-to-gamma emission rate ratio (n/γ) for ^{244}Cm for the reactions ^{19}F(α, n) ^{22*}Na, ^{25}Mg(α, n) ^{28*}Si, and ^{27}Al(α, n)^{30*}P in three matrixes of CaF_2, MgO, and Al_2O_3. These materials and reactions were studied as a possible method for the radioassay of TRU material when the dominant source of neutrons appears to be from (α, n) reactions on materials of low atomic number comprising the waste matrix. The emission rate of the prompt reaction gamma rays is measured, and the neutron emission rate due to (α, n) reactions is calculated by multiplying the gamma ray emission rate by the n/γ ratio. Figure 4 is an example of the types of Doppler and non-Doppler broadened peaks from a gamma-ray spectrum from the CaF_2 matrix. Nickel oxide and nickel powder matrixes were also studied. These were initially included to serve as a background, but it was quickly learned that the stock curium used to prepare the matrixes contained a trace amount of fluorine as a fluoride. This meant that the neutrons resulting from the α-induced reactions due to the trace fluoride had to be subtracted from the total neutron emission rate in addition to the spontaneous fission neutron rate.

This unanticipated contamination had the effect of increasing the uncertainties for n/γ ratios for the MgO and Al_2O_3 matrixes. The preliminary n/γ values were reported at the mid-year review. In addition to the measurement of n/γ ratios, the relative intensities of the ^{19}F(α, n) ^{22*}Na prompt reaction gamma rays is reported in Table 2 and compared to other results. The final values are given in Table 3. A paper describing this method of analysis with a singles Ge spectrometer has been written and will be submitted to the journal Nuclear Instruments and Methods in Physics Research.[6] Just before presentation of this paper, a similar paper was presented at the INMN meeting on ^{244}Cf .[7]

Table 1. Measured fission product gamma rays per spontaneous fission for several gamma-ray peaks that are relatively free of serious interference from other fission product gamma rays.

Energy (keV)	Fission Product[a] ^{A}Z	$P_{\gamma}(E_{\gamma})$	γ ray Emission Rate (3/19/02)[b]	γ rays/spf[c] (%)	Decays/spf[d] (%)	Yield Values[a] in %	
						Cumulative (^{A}Z)	Independent $^{A}(Z+1)$
240.7	110Tc	0.824	$(1.86 \pm 0.10) \times 10^{2}$	5.9±0.4	5.9±0.5[e]	0.88	3.62
242.3	108Tc	0.816 ± 0.07	$(2.01 \pm 0.11) \times 10^{2}$	5.20±0.3	6.4±0.7	4.01	1.98
249.8	9h 135Xe	0.90 ± 0.03	$(1.80 \pm 0.11) \times 10^{2}$	5.7±0.4	6.3±0.5	4.19	0.002
293.3	143Ce	0.428 ± 0.005	$(1.10 \pm 0.06) \times 10^{2}$	3.5±0.2	8.2±0.6	6.25	2.27×10^{-5}
306.8	101Tc	0.89 ± 0.05	$(1.56 \pm 0.08) \times 10^{2}$	5.0±0.3	5.6±0.5	3.93	1.90×10^{-7}
358.0	104Tc	0.89 ± 0.03	$(2.58 \pm 0.14) \times 10^{2}$	8.2±0.5	9.2±0.6	5.65	3.14×10^{-3}
376.7	140I	0.905 ± 0.011	$(8.86 \pm 0.50) \times 10^{1}$	2.8±0.2	3.1±0.2	0.12	2.55
381.4	46s 136I	1.00 ± 0.06	$(7.75 \pm 0.42) \times 10^{1}$	2.47±0.16	2.5±0.2	0.939	
447.0	102Nb	0.196 ± 0.020	$(3.81 \pm 0.23) \times 10^{1}$	1.22±0.08	6.2±0.8	3.57	0.464
453.9	146Pr	0.48 ± 0.03	$(9.60 \pm 0.52) \times 10^{1}$	3.1±0.2	6.5±0.6	4.43	9.21×10^{-5}
465.6	108Tc	0.143 ± 0.013	$(7.60 \pm 0.41) \times 10^{1}$	2.43±0.15	17±2	4.01	1.98
475.2	4m 102Tc	0.87 ± 0.01	$(1.02 \pm 0.05) \times 10^{2}$	3.3±0.2	3.8±0.2	4.04	7.61×10^{-6}
497.1	103Ru	0.910 ± 0.013	$(2.08 \pm 0.11) \times 10^{2}$	6.6±0.4	7.3±0.5	5.45	9.5×10^{-4}
541.2	144La	0.392 ± 0.010	$(1.22 \pm 0.07) \times 10^{2}$	3.9±0.3	9.9±0.8	5.80	0.10
588.8	6s 138I	0.56 ± 0.06	$(1.61 \pm 0.09) \times 10^{2}$	5.1±0.3	9.2±1.1	1.06	3.63
602.4	140Cs	0.53 ± 0.03	$(1.04 \pm 0.06) \times 10^{2}$	3.3±0.2	6.2±0.5	5.44	0.52
667.7	^{132}I	0.987	$(9.73 \pm 0.55) \times 10^{1}$	3.1±0.2	3.1±0.3	2.15	2.44×10^{-5}
756.8	95Zr	0.54 ± 0.05	$(2.87 \pm 0.17) \times 10^{1}$	0.92±0.06	1.7±0.2	1.24	9.12×10^{-6}
798.7	143Ba	0.156 ± 0.019	$(3.95 \pm 0.23) \times 10^{1}$	1.26±0.08	8.1±1.1	5.18	1.05
815.8	140La	0.2328 ± 0.0020	$(6.79 \pm 0.37) \times 10^{1}$	2.17±0.14	9.5±0.6	5.96	
912.7	133Te	0.55 ± 0.03	$(4.61 \pm 0.26) \times 10^{1}$	1.47±0.10	2.7±0.2	1.40	0.22
1009.8	33m ^{138}Cs	0.298 ± 0.007	$(6.75 \pm 0.37) \times 10^{1}$	2.16±0.14	7.4±0.5	5.47	
1072.7	52m ^{134}I	0.149 ± 0.005	$(2.54 \pm 0.15) \times 10^{1}$	0.81±0.06	5.4±0.5	3.85	0.026
1131.5	135I	0.226 ± 0.008	$(2.80 \pm 0.16) \times 10^{1}$	0.89±0.06	3.9±0.3	3.78	0.186
1133.9	135Te	0.00	$(2.80 \pm 0.16) \times 10^{1}$	0.89±0.11		1.91	1.85
1180.9	^{151}Nd	0.133 ± 0.009	$(2.20 \pm 0.13) \times 10^{1}$	0.70±0.05	5.3±0.5	1.93	0.022
1260.4	^{135}I	0.287 ± 0.010	$(4.35 \pm 0.25) \times 10^{1}$	1.39±0.09	4.9±0.4	3.78	0.186
1279.1	0.8s ^{134}Sb	0.0	$(7.55 \pm 0.41) \times 10^{1}$	2.41±0.15[f]		0.571	2.35
1313.0	46s 136I	1.00 ± 0.006	$(1.08 \pm 0.06) \times 10^{2}$	3.4±0.2	3.4±0.3	0.939	
1427.7	94Sr	0.942 ± 0.009	$(2.74 \pm 0.25) \times 10^{1}$	0.87±0.08	0.93±0.09	1.02	0.060
1435.8	33m ^{138}Cs	0.763 ± 0.016	$(1.39 \pm 0.11) \times 10^{2}$	4.4±0.4	5.8±0.5	5.47	
1524.7	146Pr	0.156 ± 0.009	$(2.85 \pm 0.26) \times 10^{1}$	0.91±0.09	5.8±0.7	4.43	9.25×10^{-5}
1596.2	^{140}La	0.954 ± 0.015	$(1.77 \pm 0.14) \times 10^{2}$	5.7±0.5	6.0±0.5	5.96	

a. The following peaks may contain interferences by the fission products listed in parenthesis behind the energy: 240.7 (131Te), 243.3 (138Xe), 249.7 (105Mo & 152Nd), 293.3 (144Ba), 306.8 (101Tc), 453.9 (145Cs), 465.6 (143Ba), 497.1 (102Tc & 108Rh), 541.2 (144Ba), 588.8 141Cs), 602.4 (99Y), 667.7 (112Rh).

b. The gamma-ray emission rate is corrected for absorption in the stainless steel source backing, beryllium absorber and for pulse pileup.

c. The uncertainty in the γ-rays/spf is from propagating the uncertainties in the gamma-ray emission rate with the uncertainty in the spontaneous fission rate of 3.4% (all uncertainties at one estimated standard deviation).

d. No attempt was made to correct for peak interferences.

e. An uncertainty of 5% was assigned to the 240-keV emission probability.

f. The 1279-keV γ ray is not observed in the decay of 0.8s ^{134}Sb.

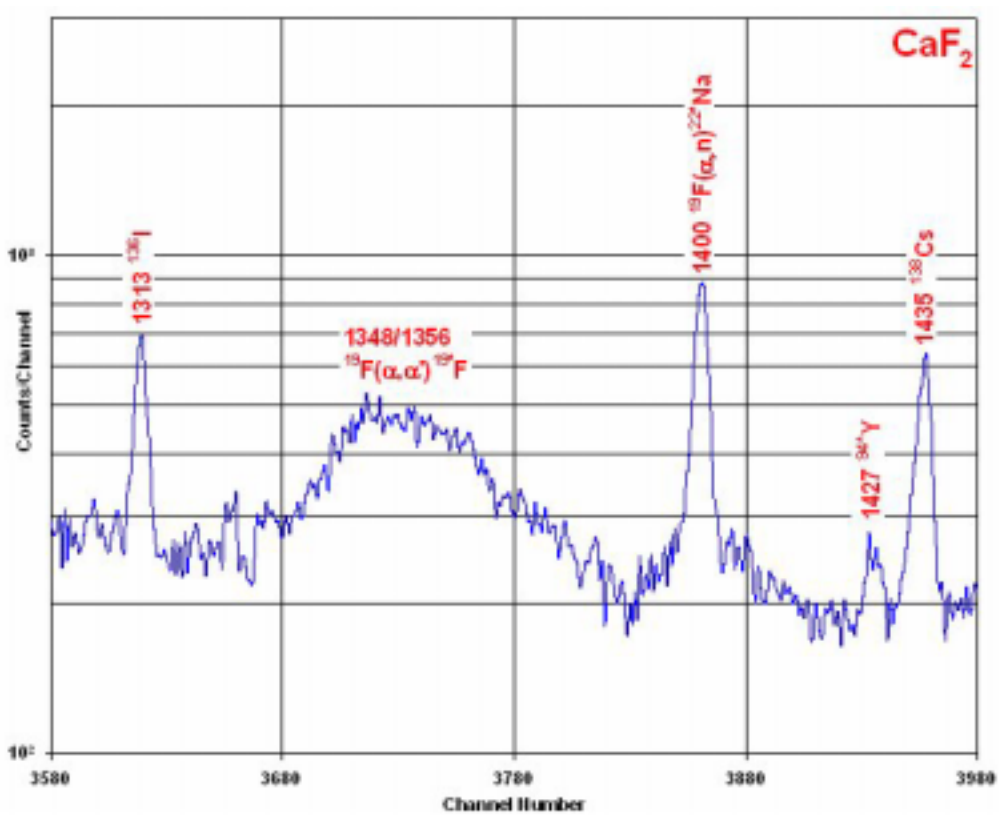

Figure 4. A partial spectrum from the CaF_2 matrix showing several gamma-ray peaks consisting of sharp non-Doppler broadened, and Doppler broadened.

Table 2. Reported relative gamma-ray intensities produced by the $^{19}F(\alpha, n)\,^{22*}Na$ reaction in CaF_2. The relative intensities without parenthesis are the narrow peak component. The total (narrow + broad component) relative intensity values from the present measurements are given in parenthesis. The uncertainties (one standard deviation) include the components stated in the text combined in quadrature.

α Source, α Energy	$I_{\gamma r}(582)$	$I_{\gamma r}(890)$	$I_{\gamma r}(1235)^a$	$I_{\gamma r}(1400)$	$I_{\gamma r}(1528)$	Reference
^{244}Cm (5.8 MeV)	≡ 100.0 (≡ 100.0)	37.1±2.2 (37.1±2.2)	19.8±0.8 (19.8±0.8)	7.94±0.50 (13.4±0.60)	13.0±1.2 (16.4±1.5)	Present measurements
^{241}Am (5.5 MeV)	≡ 100.0	41.24	19.18	5.59	14.02	C. Moss[3]
^{238}Pu (5.5 MeV)	≡ 100.0	35.62	17.85	5.66	18.19	Table 4 of A. V. Shumakov et al.[4]
^{241}Am (5.5 MeV)	≡ 100.0	35.74	17.83	5.60	18.14	Table 5 of A.V. Shumakov, et al.[4]
$^{241}Am^b$ (5.5 MeV)	≡ 100.0	40.0		6.4	15.6	Lees and Lindley[4]

a. This γ ray results from the $^{19}F(\alpha, \alpha')\,^{19*}F$ reaction.

b. Renormalized to 582-keV γ ray from the 890-keV γ ray.

Table 3. Measured n/γ ratio from (α, *n*) reactions for ^{244}Cm alphas in specified matrix.

Nuclear Reaction	γ-ray Energy (keV)	Capsule Matrix	*n*/γ Ratio[a] (not corrected for trace F)	*n*/γ Ratio[b] (corrected for trace F)
^{19}F(α, *n*)^{22}Na	582.	CaF_2	2.85 ± 0.37	
^{19}F(α, *n*)^{22}Na	582.	Ni	3.1 ± 2.1	
^{25}Mg(α, *n*)^{28}Si	1778[3]	MgO	5.3 ± 2.9	5.1 ± 2.9
^{27}Al(α, *n*)^{30}P	709	Al_2O_3	7.0 ± 5.7	6.3 ± 5.1

a. This is the calculated ratio for the case where the neutrons from (α, *n*) reactions on the traceCaF_2 present are not subtracted out.

b. This is the calculated ratio for the case where the neutrons from (α, *n*) reactions on CaF_2 are subtracted out.

c. The 1778-keV peak is comprised of two components. One, the broad component, is from the (α, *n*) reaction and the other, the peak component, is from the decay of 2.25 min ^{28}Al produced from the (α, *p*) reaction.

Third, the ability to characterize TRU waste for ^{237}Np or to measure the age of the TRU waste with no additional information has been extended from a previous study for waste primarily containing ^{241}Am to waste containing weapons-grade plutonium. This method is based on full use of the Bateman equations and the decay chain ^{241}Pu → ^{237}U and ^{241}Am → ^{237}Np → ^{233}Pa. The method allows initial amounts of activity for each daughter, and makes no assumption about the relative abundance between ^{241}Pu and ^{239}Pu. The technique works when the source is a point or extended in space, and is somewhat independent of attenuation between the source and detector. The latter property is because the gamma energy lines are close together and have approximately the same linear attenuation coefficient. The technique has been demonstrated to work well when determining the age of a weapons grade plutonium source at the INEEL. This study is close to completion, and a paper is being written for submission to a refereed nuclear science journal such as the Nuclear Instruments and Methods in Physics Research, Journal of Radioanalytical and Nuclear Chemistry.[8]

Fourth, a program developed at the INEEL for the Radiation Measurements Laboratory (RML) for the analysis of Ge gamma-ray spectra has been modified to be of greater use to the gamma-ray spectrometrist performing the research. The changes to the program now allow examination of each automatically analyzed peak with the option for the user to refit the peak interactively. This change reduces the time by a factor of two to manually fit individual peaks into a spectrum. Further changes to this program for enabling it to operate under the Windows 2000 operating system is progressing. When successfully implemented, this will allow the program to operate under the same operating system used by almost all INEEL employees, and thereby eliminate, in many cases, the need for a Windows NT operating system for this program. Also, a study has been conducted regarding the collection of quality Ge gamma-ray spectra for routine spectral radioanalysis. A draft paper on this work has been prepared.[9]

Fifth, the analysis of specific radionuclides to develop a database on the web to allow for the examination of the gamma-ray spectra was continued. This year, due to other pressing priorities, only a few radionuclides were added to the Gamma-ray Spectrometry Center Web Site and they include: ^{126}Sn → ^{126}Sb, ^{252}Cf, and a more pure ^{239}Pu spectrum. Prof. Henry Griffin, Chemistry Department, University of Michigan, has collected spectra of ^{234m}Pa, ^{234}Pa, ^{229}Th and other Ge gamma-ray spectra under a subcontract. This was done to identify gamma-ray peaks that are present from daughter activities of ^{238}U. When most all of the peaks can be identified, the Ge gamma-ray spectrum of ^{238}U will be annotated and placed on the Gamma-ray Spectrometry Center Web Site.

Sixth, the collection of neutron cross-sections of use in environmental remediation continued during FY 2002. Much of a large backlog of data acquired from Ron Nelson at LANL was analyzed and new data was acquired at the Los Alamos Neutron Science Center (LANSCE). In addition, separated germanium isotopes were acquired and will be pressed into targets for another experiment at LANSCE in October 2002. This experiment would be the first of these experiments to be performed on the GEANIE array. This is an array of approximately 20 HPGe detectors that will provide significantly improved statistics in a short time. At this point, most of the backlog has been analyzed to a convenient stopping state. A series of corrections must be applied to the data to reach the final state. These corrections are very similar among the various data sets, and these last steps are quite efficient. Several of the data sets remain to be analyzed, including the newly acquired LANL data, but this should not take much time. When all the data has been fully analyzed, it will be combined into a single database for distribution. It will also be submitted for publication to a refereed nuclear science journal.

High Performance Radiation Detection Systems

The goal of this task is the development of advanced room-temperature radiation detection systems, sophisticated systems comprised of multiple detector arrays, and digital signal processing instrumentation. This will be done for lower cost and higher sensitivity than present characterization detection systems.

Room-Temperature Si PIN Diodes Detection System

In some nuclear physics applications, there is a need to use Si PIN diodes to detect electrons, x-rays, and low-energy gamma rays with very good energy resolution.[10-13] The advantage of these detectors in such particular applications when compared with others is the ease of the operation at room temperature and at much lower bias voltages. We are currently investigating the feasibility of using silicon PIN photodiodes to detect the L-x-rays of U, Th, Am, and Pu for monitoring and characterizing top soil contamination. Because detection efficiency is a function of the thickness of the silicon, one of the advantages of this system is that for a thickness of 300 μ, the detection efficiency is close to 100% at 10 keV, falling to approximately 1% at 150 keV. For energies above approximately 100 keV, photons interact almost entirely through Compton scattering.

In this work we report on the performance of the Si PIN diode and its associated electronics at room temperature for two different detector-pre-amplifier combinations. Spectroscopy applications require the best in low-noise performance from the detector and its amplifying system, therefore, the circuit components and active devices must be selected specifically to match the application at hand. In particular, the amplifying stage at the input of the charge-integrating preamplifier must be chosen to match the capacitance of the detector diode so that the lowest possible noise and best pulse-height resolution can be achieved. In addition, the time constant in the shaping amplifier must be optimized to minimize the line broadening effects that result from the noise and non-uniform charge-collection time in the detector. We selected the Hamamatsu 9×9 mm^2 (V_{bias} = 100VDC) detector, which has very low capacitance (C_j = 25 pF), low dark current (8 nA), and a low cost (~$120). This detector can be operated at a low bias voltage of 24 Vdc (partially depleted) to the maximum voltage of 100 Vdc (fully depleted). Low cost, compactness, low power consumption, and high performance were our primary considerations in designing the circuit board which is to be used for preamplification and analog charge processing of the charges delivered by the Si detector.

We have tested the performance of two pre-amplifiers, one from REL-LABS and the other from EV product, in terms of the gain, rise time, and energy resolution. Figure 5 shows gamma-ray and x-ray spectra of the ^{241}Am source taken at room temperature with the amplifier shaping time of 0.25 μsec. The prominent peaks for this source are 13.9, 17.8, 20.8, and 59.5 keV. The black spectrum is taken with the REL-LAB preamplifier, which does not have a good signal-to-noise ratio and therefore is not capable of resolving 17.8 keV L x-ray from the 20.8 keV gamma ray. The pulse-height resolution is 5.4 keV at 59.5 keV. Also, it can only measure x-ray energies down to 20 keV.

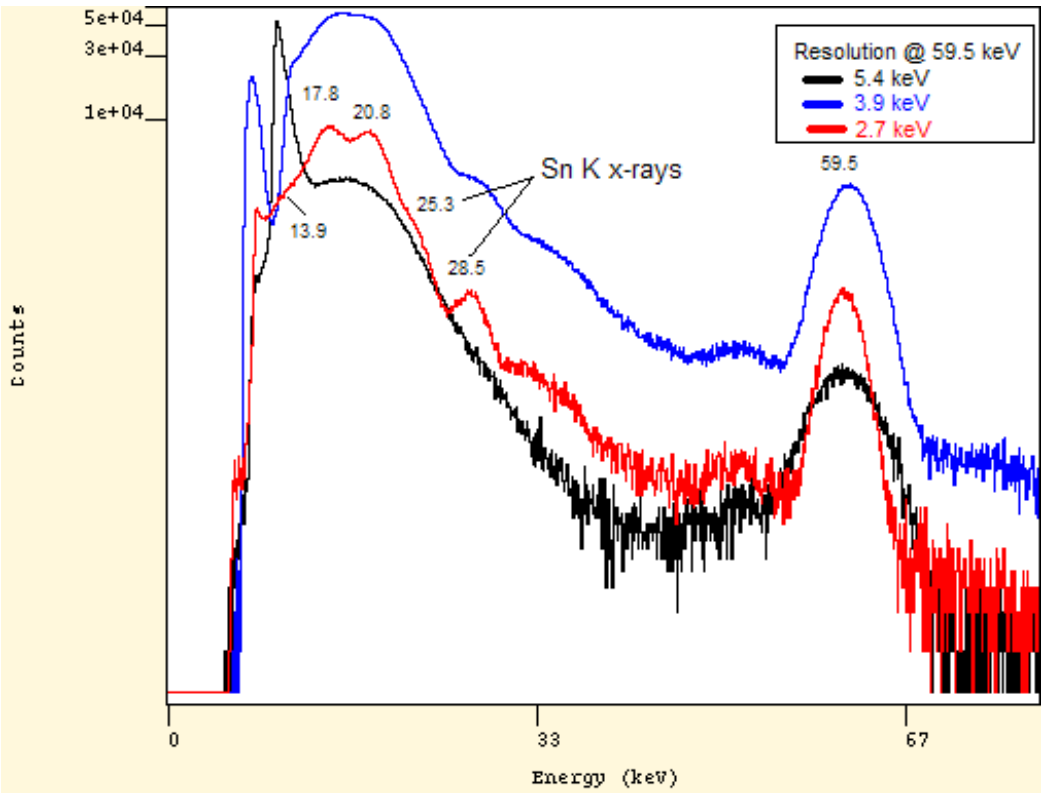

Figure 5. Gamma-ray and x-ray spectra of the ^{241}Am source.

The blue spectrum is taken with the EV Product preamplifier, which has a higher gain and much better signal-to-noise ratio. The 17.8 and 20.8 keV peaks are starting separate, although it is not very distinct.

This improved the energy resolution to 3.9 keV for 59.5 keV gamma ray and now it is possible to be able to measure the x-ray energies down to 14 keV. The red spectrum was taken after some improvements were made to the electronic circuit board to reduce the electronic noise to about 1 mV. These improvements resulted in a better signal-to-noise ratio that enabled us to measure energies down to 8 keV and achieve the energy resolution of 2.7 keV at 59.5 keV. Now, two peaks at 17.8 and 20.8 keV are separated. The peaks at 25.3 keV and 28.5 keV are due to x-ray fluorescence from Sn soldering on the circuit board. Figure 6 shows the spectrum taken with the ^{152}Eu source. The L x-rays of Sm daughter are at 40.1 and 45.4 keV, respectively. Again, peaks at 25.3 keV and 28.5 keV from K x-rays of the Sn can be clearly seen.

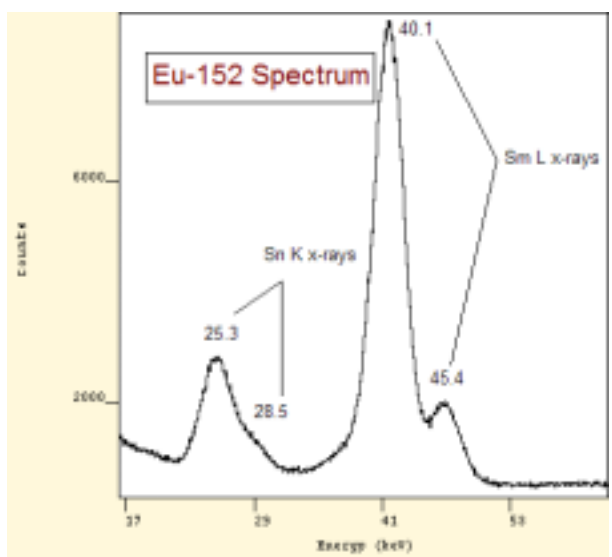

Figure 6. Eu-152 spectrum showing the L x-rays of Sm daughter.

We also repeated the above measurements using the Si PIN diode and digital signal processor of the Canberra Inspector 2000 to see whether this would lead to a better signal-to-noise ratio in

eliminating the electronic noises. No improvements were observed over the previous analog measurements.

The ultimate goal of this work is to build an array of 10 × 10 Silicon PIN diodes with integrated signal processing and a fast digital data acquisition and analysis system for monitoring and characterizing topsoil contamination.

High Rate Electronics

The excellent performance that we measured on two commercial digital gamma-ray spectrometers motivated an investigation of two additional units new to the market. Unlike the laboratory-size ac line powered units, whose performance was documented in Reference 14, the new units are small (nominally 20 × 10 × 2 cm), can be battery powered, and incorporate all of the features of the large laboratory units. The portable digital spectrometers available were the Inspector 2000 (Canberra Industries) and the DigiDart (ORTEC). Testing of the high-input rate performance of these two units was conducted using the same detector, sources, and procedures used to evaluate their much larger laboratory counter parts.

These tests were disappointing. The ORTEC DigiDart exhibited very poor photopeak resolution (about 6 keV FWHM at 1,332 keV, approximately three times the expected value) even at low input rates. After several attempts to clear this problem with a variety of setup changes, the unit was returned to the manufacturer and replaced with an entirely new unit. The new unit gave exactly the same results. Testing that we conducted, and tests conducted here by a manufacturer's technical expert, determined that there is a definite incompatibility between the DigiDart and all of the high-rate transistor reset preamplifier-equipped (TRP) detectors that we have available. The unit works well with other non-TRP-equipped detectors. The nature of that incompatibility remains a mystery, and awaits the results of testing at ORTEC using one of our detectors.

Some rate-effects data was acquired on the Canberra Inspector 2000 digital gamma-ray spectrometer. This unit acquired acceptable spectra at input rates approaching 600 kc/s, a rate capability better than the best commercial analog equipment. However, the early test data indicated that while the throughput of the Inspector 2000 may be slightly better than its larger counter part, the Canberra DSA2000, the overall performance of this small unit was not as good. Desirable features in a high-rate spectrometry system include photopeak centroid stability and limited peak width broadening over a wide range of input rates. Figures 7 and 8 present the measured comparison of the portable Inspector 2000 and the laboratory-sized DSA2000 for these two important parameters. The graph lines are provided as eye guides only.

CZT Pulse Shape Classification:

An extreme delay in return of our digital pulse shape acquisition system following an upgrade, and an incompatibility between the upgraded unit and the old software resulted in no measurement progress on this subtask. These problems should now be resolved.

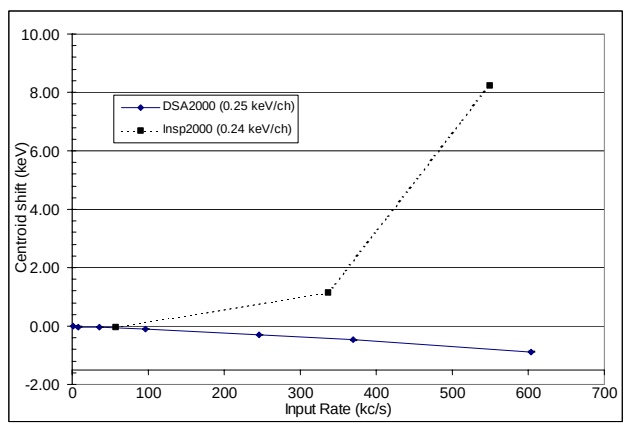

Figure 7. Centroid shift of the 1,408 keV peak of ^{152}Eu as a function of input rate measured using the Inspector 2000 and the DSA2000.

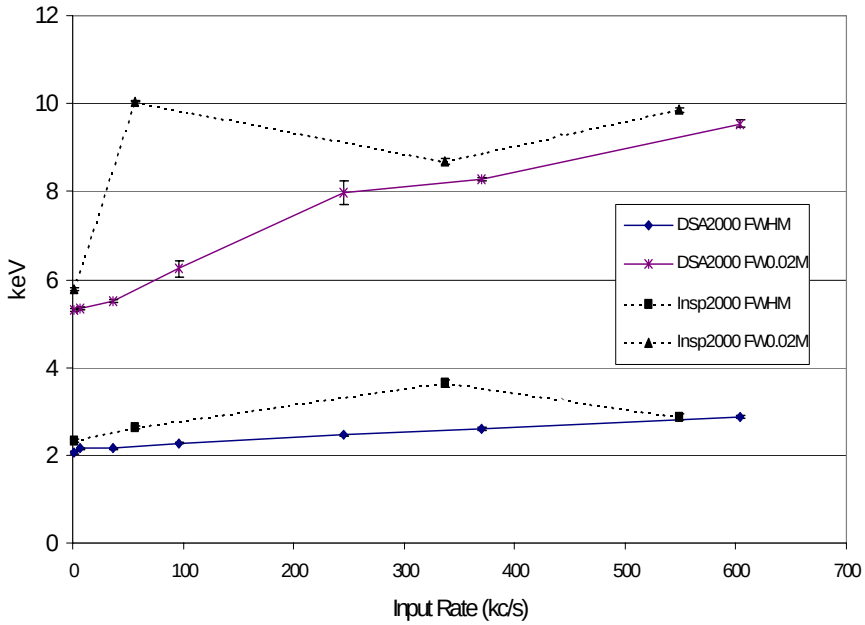

Figure 8. A comparison of the width of the 1,408 keV peak measured using the Inspector 2000 and the DSA2000 as a function of input rate. Data are presented for the full width of the peak at half of its maximum height (FWHM) and at 1/50th max (FW0.02M).

Advanced Methods and Modeling

Spectrum Enhancement Technique for NaI and CsI Scintillators

This work was carried out in collaboration with professor David Ramsden from the University of Southampton in England. Spectra-deconvolution algorithm methods such as Maximum Likelihood Expectation Maximization (ML-EM)[15,16] were used to enhance the quality of the spectrum provided by a NaI or CsI scintillation counter, and thereby eliminate the need for using an expensive and bulky cooled HPGe detector. This method could play an important role in a simple, accurate, and rapid characterization of spent nuclear fuels and TRU waste.

We used a spectral-deconvolution algorithm on NaI spectra taken with enriched uranium samples ranging from 10 to 90%, and compared the results to high-resolution spectra taken with the Ge detector. Figures 9 and 10 show one example of the deconvolved data for the low- and high-energy regions compared with the original NaI and Germanium spectra. The raw NaI and Ge data have been rebinned to 6 keV to match the bin width of the deconvoluted data.

The preliminary results show that the deconvoluted NaI spectra and the relative line intensities are in very good agreement with those derived from the germanium spectra within the limits of the detector calibration. It was discovered that the original NaI spectral calibration was not very good, and that created some problems during the deconvolution process. This is because this method requires a precise and reliable energy calibration to deliver the best results. Also, there is a noticeable offset between the Ge and deconvolved data at higher energies. This is due to nonlinearity in the NaI detector. In addition, the feature above the 2.6 MeV line is an artifact introduced by the deconvolution process due to the abrupt cutoff in counts at the end of the file. The effect of this artifact can be minimized by extending the dynamic range of the detector by 500 keV above the highest energy line of interest in the spectra.

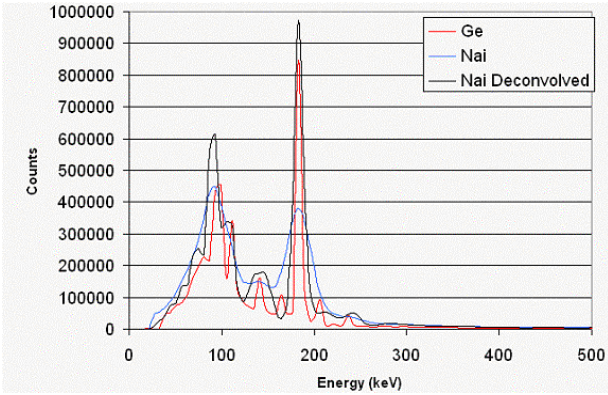

Figure 9. Spectra of the 90% enriched sample from 0 to 500 keV.

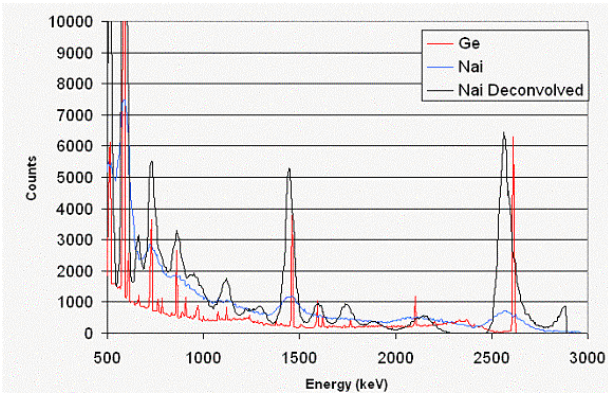

Figure 10. Spectra of the 90% enriched sample from 500 to 3000 keV.

The raw germanium spectra and the deconvolved NaI spectra for different enriched uranium samples were analyzed by applying three regions of interest (ROI) corresponding to the 186 keV, 1001 keV and 2615 keV lines, respectively. In analyzing the ROIs, the gross count value was used for the deconvolved spectra, since the spectra has, in effect, had the Compton background component from higher energy sources already removed. In the case of the germanium detector, this background was very much present, and therefore the net value was used. The results of the ROI analysis are shown in the Figures 11 and 12. The integrated counts in the deconvolved data was normalized to the 37% enriched data point of 1001 keV gamma ray emitted from the ^{238}U radioisotope. With the exception of 20% and 90% enriched samples, both the enhanced NaI data and

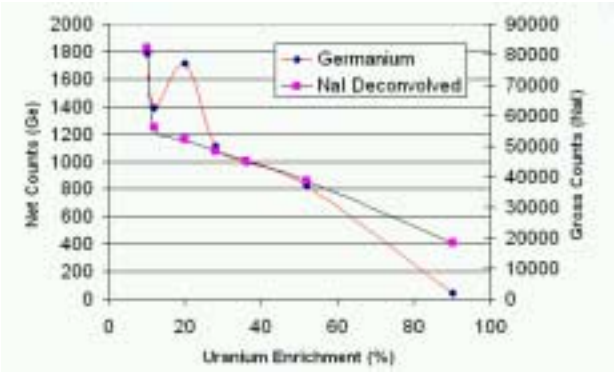

Figure 11. The number of counts in the 1001 keV region of interest as function of sample enrichment for both the NaI and Ge detector.

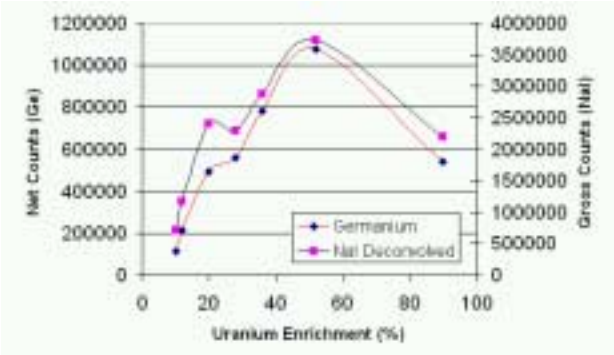

Figure 12. The number of counts in the 186 keV region of interest as function of sample enrichment for both the NaI and Ge detector.

the Ge data follow the same trend. We are still investigating why the 20% and 90% enriched data do not agree with each other.

The increase in the number of counts in the NaI detector for 186 keV gamma ray, shown in Figure 12, is a factor of ~3 greater than those in the germanium spectra. Here again, the deconvoluted NaI data follows the same profile as the germanium data. The ROI analysis so far has demonstrated that the deconvoluted NaI detector represents an improvement in sensitivity by up to a factor of 45.

Application of Monte Carlo Techniques in High-Accuracy HPGe Full-Energy Efficiencies Determination

The measurement of gamma-ray spectra with Ge semiconductor detectors is a widely used tool in

basic research of many fields and in numerous applications. In order to make quantitative measurements of the amount of radioactive material present, one needs to determine the efficiency of the detector as a function of the gamma-ray energy for the source geometries of interest. In the past, even in the laboratory where the measurement parameters can be controlled, the most precise efficiency calibrations had uncertainties of about 0.5% over the commonly used energy range of 100–1500 keV.

Past efforts by R. G. Helmer[17] have shown that it should be possible to use Monte Carlo electron and photon transport codes to enhance the precision of the efficiency curves obtained from the common method of measurements with calibrated sources. Since the Monte Carlo code provides a good approximation to the physics of the interactions in the detector, the change in the efficiency over a limited energy range that it calculates will be very accurate, and therefore, provides an excellent interpolation tool once it is shown to agree with the measured efficiency at some energy or energies.

Study with Professor John Hardy, Texas A&M University

The goal of this work over the past 2 years has been to demonstrate the advantage of combining measured and calculated efficiencies and to determine the precision that is currently possible. (The resulting efficiency curve is being used to support some measurements for basic properties of β decay, as well as other experiments.) The measurements were made at Texas A&M University of the ratios of efficiencies for gamma rays of precisely known relative intensities for several radionuclides on a 280-cm^3 Ge detector. Generally these ratios had uncertainties of less than 0.1%. A source of ^{60}Co used in these measurements has an activity that is known to 0.06%,[18] so it was used to provide absolute efficiency values at 1173 and 1332 keV.

The Monte Carlo calculations of the detector efficiency at various gamma-ray energies require the physical dimensions of the sensitive volume of the Ge crystal. The initial Monte Carlo calculations, with the CYLTRAN code[19] run at the INEEL used the nominal detector dimensions provided by the manufacturer. These calculations produced efficiencies that differed from the measured values by 3–9% from 50–1800 keV. X-rays of the detector and scans with collimated gamma-ray beams provided a better length and position for the sensitive volume, and initial adjustments of the thicknesses of the Ge dead-layers were made. With these dimensions, another set of Monte Carlo results were obtained and compared with measured data from seven radionuclides. These results provided an efficiency curve with an estimated uncertainty of 0.2–0.4% from 50–1400 keV and have been published.[20] In these comparisons, the activity of each radio-nuclide must be normalized to put the measured values on the same curve (except for the value for the ^{60}Co source). This is done by doing a least-squares fit to minimize the differences between the measured values and those from Monte Carlo calculations.

A second round of adjustments of the detector dimensions for another set of Monte Carlo calculations, done both at the INEEL and Texas A&M University, and measurements for three additional nuclides, which were especially useful below 100 keV, have been made. The detector parameters specified by the manufacturer and our final value are given in Table 4. The final results of this effort are contained in a manuscript, which will be submitted for publication[21] and are shown in Figures 13 and 14.

Table 4. Detector parameters used in the Monte Carlo calculations from the manufacturer and our final set. Dimensions are in cm, except external dead layer, which is in microns.

Parameter	Manufacturer	Our Final
Length—active	7.76997	7.5395
Length—total	7.77	7.73975
Radius—active	3.495	3.4485
Radius—total	3.495	3.44875
Cap-crystal distance	0.56	0.72
Internal dead layer	0.10	0.134
Hole radius	0.58	0.58
Hole depth	6.97	6.92
External dead layers	0.3	2.5

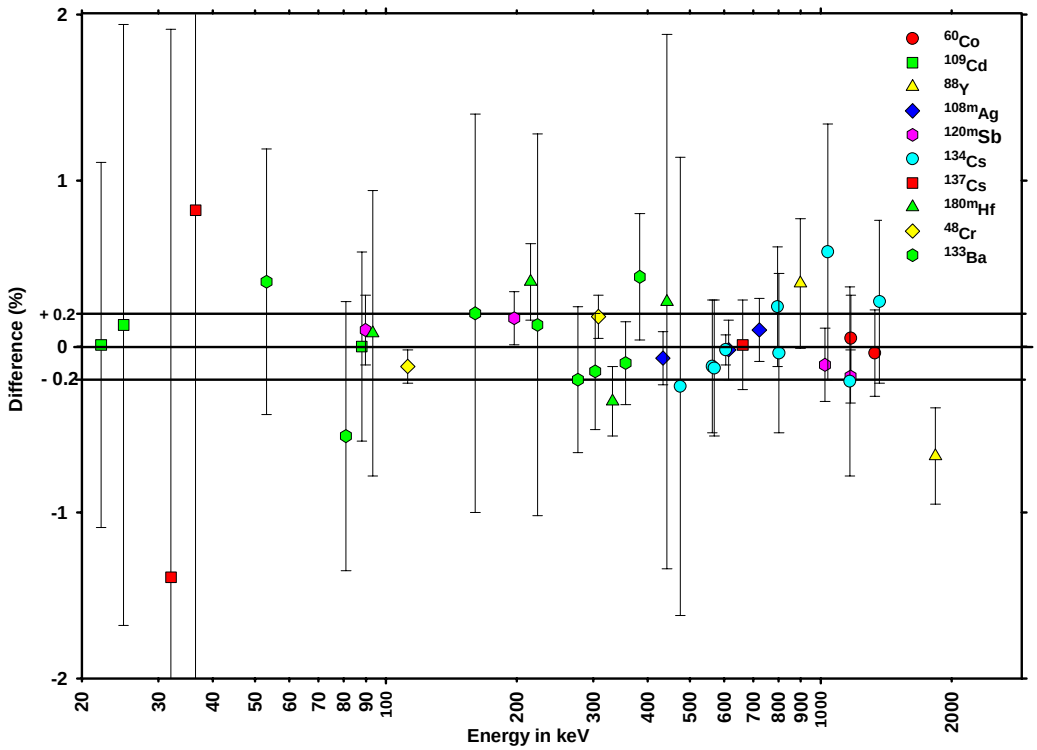

Figure 13. Comparison of measured efficiencies (points) with Monte Carlo calculated efficiencies (line at 0) with the final detector parameters.

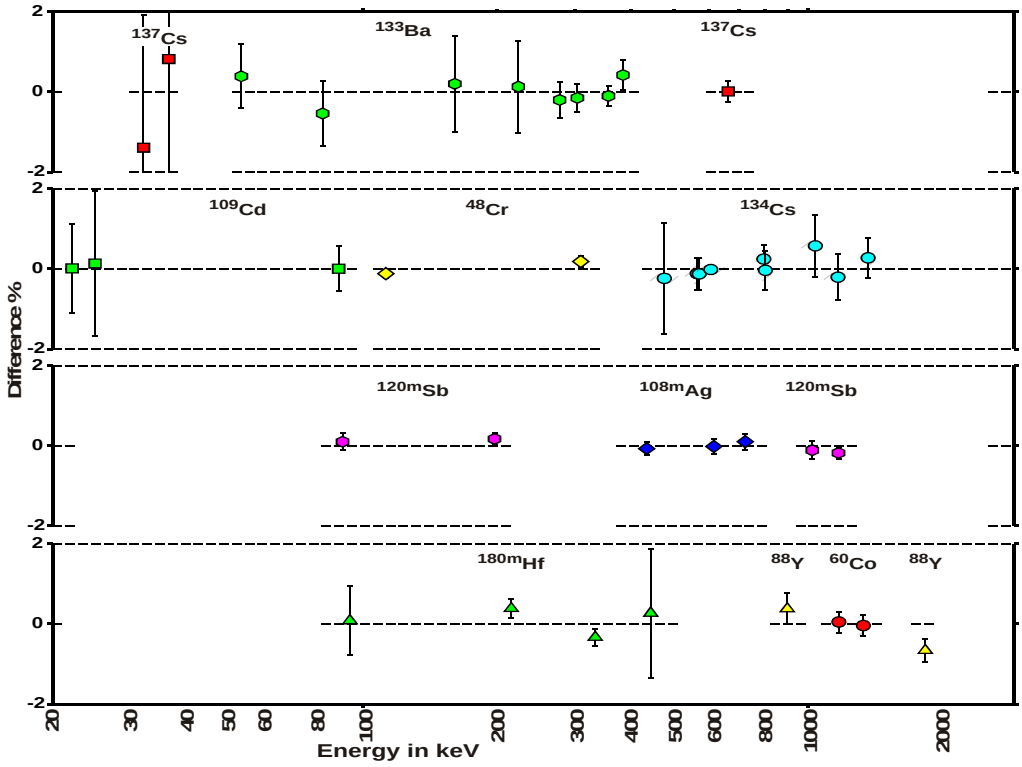

Figure 14. Comparison of measured efficiencies (points) by nuclide with Monte Carlo calculated efficiencies (line at 0) with the final detector parameters.

We consider this detector efficiency curve to be a significant improvement over what has been possible in the past. In the future, we will extend this work to higher energies where the photon interactions in the detector produce three strong peaks: one at the photon energy, one at 511 keV (the electron mass) below the photon energy, and one at 1,022 keV below that.

Study with Dr. Gabor Molnár, Chemical Research Center, Budapest, Hungary

During this study, a series of relative detector efficiency measurements ranging from 100 keV to 11 MeV were made on a 100 cm^3 Ge detector in Budapest, and a series of Monte Carlo calculations were made at the INEEL. In contrast to the above work, these Monte Carlo calculations were done with the original detector dimensions. Also, this detector has a collimator in front of it that must be included in the CYLTRAN input.

In the comparison of the measured and Monte Carlo calculated efficiencies, the Monte Carlo values were simply scaled to partially compensate for the incorrectness of the representation of the sensitive volume of the detector and of the collimator. With this scaling, only one difference is larger than 2.5% between 100 keV and 8.5 MeV.

These figures show the difference between the measured efficiencies and the Monte Carlo results, and indicate that the detector efficiency can be interpolated with an estimated uncertainty of 0.2% from 50–1,400 keV.

Another preliminary comparison compared the ratio of the escape peaks, at 511 (single-escape peak [SE]) and 1,022 (double-escape peak [DE]) keV below the full-energy (FE) peak as measured and computed by Monte Carlo calculations. The calculated SE/FE ratios are about 5% smaller than the measured ratios and calculated DE/FE ratios are about 10% smaller. A manuscript describing this work is being prepared for publication.

ANSI Performance Standards for Radiation Measurement Instruments

A draft of the American National Standard Calibration of Germanium Detectors for In Situ Gamma-ray Measurements has been balloted and submitted to the American National Standards Institute for public review and publication. This standard has been in development for 4–5 years. The PI of this task served on the Writing Group of ANSI as one of the project co-leaders.

ACCOMPLISHMENTS

Our project accomplishments during FY 2002 are as follows:

- The new equipment for fission studies was installed and made into an operational system by January 2002. The ^{237}Np target was run for the entire year as only about 600 events per second are produced using the low-energy neutron beam at IPNS. The data collected through June has been sent to the Russians for yield analysis. This data includes the neutron energy for the first time.

- New, highly enriched uranium targets of 97% ^{235}U were obtained from Oak Ridge for further measurements in FY 2003. These targets total 87 grams of uranium that cannot be obtained in the U.S. at this time. A neutron flux monitor was designed for installation at IPNS. This will allow the intensity of the IPNS neutron beam to be monitored continuously and recorded in the data stream.

- The new mount for the neutron detectors was designed and fabricated. The neutron detectors were previously down stream of the HPGe array, but with the new and more numerous HPGe detectors, they had to be moved, as very few neutrons were observed in the down stream location. These eight neutron detectors are now mounted above the target location and shielded from the gamma rays by bismuth cups. Bismuth was chosen for its high density (approximately twice that of lead) and because the cost had become competitive with lead, now a costly material due to it hazardous properties. There are also no contamination or disposal issues with the bismuth.

- The analysis of the ^{235}U and ^{239}Pu data to extract fission fragment yields were started. The preliminary results will be reported at the

Third International Conference on Fission and Properties of Neutron-Rich Nuclei to be held November 3–9, 2002, on Sanibel Island, Florida. This conference is patterned after the previous two conferences held in 1997 and 1999. A paper outlining the experimental capabilities of the IPNS experimental apparatus, the new correlations in the data, and applied uses of these experiments will also be presented.

- A data acquisition system that is robust and capable of performing detailed error checking of the incoming data stream was developed and refined because of the need to operate the fission studies experiment remotely over long periods of time with little or no operator intervention.

- The relative intensities of the reaction gamma rays from the $^{19}F(\alpha, n)^{22*}Na$ reaction were measured along with the neutron-to-gamma ray intensity ratios for the $^{19}F(\alpha, n)^{22*}Na$, $^{25}Mg(\alpha, n)^{28*}Si$, and the $^{27}Al(\alpha, n)^{30}*P$ reactions. These measurements were completed to meet the PEMP commitment.

- The gamma ray production yields from the spontaneous fission of ^{252}Cf were measured. During this study a method was developed to determine the activity and age of the ^{252}Cf source since it was last chemically prepared or produced (when the chemical equilibrium caused the fission product ^{137}Cs to become separated from the parent ^{252}Cf).

- A method for measuring the amount of ^{241}Pu and ^{237}Np activity in plutonium-contaminated waste and its age was developed using key gamma-ray peaks from ^{241}Pu, ^{241}Am, and ^{233}Pa.

- Spectral information was gathered and processed for several nuclides. This information has been or will be placed on the INEEL Gamma-ray Spectrometry Center Web site. The radionuclides include $^{126}Sn \rightarrow {}^{126}Sb$, $^{178}Hf/^{182}Hf \rightarrow {}^{182}Ta$, ^{234}Pa, ^{234}mPa and ^{229}Th, and ^{252}Cf.

- Most of the archived data for the neutron cross-section measurements were analyzed. An experiment was performed at LANSCE to acquire neutron cross-section data with a chlorine target, and time was secured on the GEANIE array to perform a measurement on the separated germanium targets that were acquired.

- Measurements of x-rays and low-energy gamma rays emitted from ^{241}Am, ^{152}Eu, ^{133}Ba, ^{207}Bi, and other radioactive sources were performed using 9×9 mm^2 Si-PIN diodes with several different low-noise preamplifiers. We were able to improve the electronics to reduce the electronic noise to about 1 mV. This resulted in a better signal to noise ratio to achieve an energy resolution of 2.7 keV at 59.5 keV, and to measure x-ray energies down to 8 keV at room temperature.

- The high-rate performance of a portable, battery-powered digital gamma-ray spectrometer was studied. Although the unit showed better performance than most analog systems, it did not perform as well as its larger AC-powered counterpart. Updated hardware, firmware, and operational software for the digital pulse shape classification system have been received, but have not yet been tested.

- We used spectral-deconvolution algorithm methods like Maximum Likelihood Expectation Maximization (ML-EM) to enhance the quality of the information provided by a scintillation counter. So far, the preliminary results of enhancing the quality of the NaI spectra taken with enriched uranium samples ranging from 10–90% enrichment are very encouraging.

- We demonstrated the advantage of combining measured and calculated efficiencies to determine the precise efficiency calibration for a Ge detector with an uncertainty of about 0.2% or less from 50–1400 keV.

Publications

Accepted or Published

Aryaeinejad, R., Edward Reber, and Dave Spencer "Development of a Handheld Device for Simultaneous Monitoring of Fast Neutrons and Gamma Rays," *IEEE Transactions on Nuclear Science,* accepted to be published in the August 2002 issue.

Gehrke, R. J., R. Aryaeinejad, J. K. Hartwell, W. Y. Yoon, E. Reber, and J. R. Davidson, "The Gamma-Ray Spectrum of ^{252}cf and the Information Contained Within It," presented at the *5th International Topical Meeting on Industrial Radiation and Radioisotope Measurement Applications held June 9–14, 2002 in Bologna, Italy*. Full paper submitted for publication in a special issue of *Nuclear Instruments and Methods in Physics Research*.

Hamilton, J. H., A. V. Ramayya, J. K. Hwang, G. M. Ter-Akopian, A. V. Daniel, J. O. Rasmussen, S. C. Wu, R. Donangelo, C. J. Beyer, J. Kormicki, X. Q. Zhang, A. M. Rodin, A. S. Fomichev, G. S. Popeko, J. Kliman, L. Krupa, M. Jandel, Yu. Ts. Oganessian, G. Chubarian, D. Seweryniak, R. V. F. Janssens, W. C. Ma, R. B. Piercey, W. Greiner, and J. D. Cole, "Cold and Hot Binary and Ternary Fission Yields in the Spontaneous Fission of Cf-252," *Physics of Atomic Nuclei*, Vol. 65, No. 4, April 2002, p. 645–652.

Hamilton, J. H., A. V. Ramayya, J. K. Hwang, G. M. Ter-Akopian, A. V. Daniel, T. N Ginter, C. J. Beyer, J. Kormicki, X. Q. Zhang, A. M. Rodin, A. S. Fomichev, J. Kliman, L. Krupa, J. Jandel, Yu. Ts. Oganession, W. Greiner, D. N. Poenaru, G. Chubaryan, D. Seweryniak, R. V. F. Janssens, J. O. Rasmussen, S. C. Wu, R. Donangelo, W. C. Ma, R. B. Piercey, and J. D. Cole, "Behavior of Nuclear Matter Under Extreme Conditions in Fission," *Acta Physica Hungarica NEW SERIES-HEAVY ION PHYSICS*, Vol. 14, No. 1-4, 2001, pp. 161–168.

Hardy, J. C., V. E. Iacob, M. Sanchez-Vega, R. T. Effinger, P. Lipnik, V. E. Mayes, D. K. Willis, and R. G. Helmer, "Precise Efficiency Calibration of an HPGe Detector: Source Measurements and Monte Carlo Calculations with Subpercent Precision," *Appl. Radiat. Isot.* Vol. 56, 2002, p. 65.

Luo, Y. X., J. O. Rasmussen, J. H. Hamilton, A. V. Ramayya, J. K. Hwang, C. J. Beyer, S. J. Zhu, J. Kormicki, X. Q. Zhang, E. F. Jones, P. M. Gore, T. N. Ginter, K. E. Gregorich, I-Yang Lee, A. O. Macchiavelli, P. Zielinski, C. M. Folden III, O. Fallon, G. M. Ter-Akopian, Yu. Ts. Oganessian, A. V. Daniel, M. A. Stoyer, J. D. Cole, R. Donangelo, S. C. Wu, and S. J. Asztalos, "Level Structure of ^{141}Ba and ^{139}Xe and the Level Systematics of N = 85 Even-Odd Isotones," *Physical Review C*, Vol. 66, 2002, 014305.

Spencer, D. F., R. Aryaeinejad, and E.L. Reber, "Using the Cockroft-Walton Voltage Multiplier With Small Photomultipliers, " *IEEE Transactions on Nuclear Science*, Vol. 49, No. 3, June 2002, pp. 1150–1153.

Xu, R. Q., S. J. Zhu, J. H. Hamilton, A. W. Ramayya, J. K. Hwang, X. Q. Zhang, K. Li, L. M. Yang, L. Y. Zhu, C. Y. Gan, Z. Zhang, Z. Jiang, S. D. Xiao, W. C. Ma, J. Kormicki, E. F. Jones, J. D. Cole, R. Aryaeinejad, M. W. Drigert, I. Y. Lee, J. O. Rasmussen, M. A. Stoyer, G. M. Ter-Akopian, and A. V. Daniel, "Observation of Rotational Bands in Neutron-Rich Mo-106 Nucleus," *Chinese Physics Letters*, Vol. 19, No. 2, February 2002, pp. 180–183.

Zhu, J., J. H. Hamilton, A. V. Ramayya, J. K. Hwang, C. Y. Gan, X. Q. Zhang, C. J. Beyer, J. Kormicki, M. Sakhaee, L. M. Yang, L. Y. Zhu, R. Q. Xu, Z. Zhang, Z, Jiang, W. C. Ma, E. F. Jones, P. M. Gore, J. D. Cole, M. W. Drigert, I. Y. Lee, J. O. Rasmussen, T. N. Ginter, Y. X. Luo, S. C. Wu, C. Folden, P. Fallon, P. Zielinski, K. E. Gregorich, A. O. Macchiavelli, S. J. Asztalos, G. M. Ter-Akopian, Yu. Ts. Oganession, M. A. Stoyer, J. P. Greene, R. V. F. Janssens, and I. Ahmad, "Observation of Rotational Bands in the Neutron-Rich 107Ru Nucleus," *Physical Review C*, Vol. 65, 2002, 014307 (6 pages).

Manuscripts Being Prepared

Helmer, R. G., J. C. Hardy, V. E. Iacob, M. Sanchez-Vega, R. G. Neilson, J. Nelson, "The Use of Monte Carlo Calculations in the Determination of a Ge Detector Efficiency Curve," to be submitted to *Nucl. Instr. Meth. A*.

Molnár, G. L., R. G. Helmer, T. Belgya, tentatively entitled "Monte Carlo Calculations of Full-Energy and Escape Peak Efficiencies of a HPGe Detector from 100 keV to 11 MeV."

Presentations

Aryaeinejad, R., "Instrumentation for the Measurements of Mixed Gamma and Neutron Fields" invited talk to the *Health Physics John Horan Symposium, on April 20, 2002 at ISU*.

Aryaeinejad, R., E. L. Reber, and D. F. Spencer, "Handheld Device for Simultaneous Monitoring of Fast Neutrons and Gamma Rays," presentation at the *IEEE Nuclear Science Symposium and Medical Imaging Conference held on November 4–10, 2001 in San Diego, California*.

Aryaeinejad, R., E. L. Reber, J. K. Jewell, J. D. Cole, M. W. Drigert, "Excited States in Light Mass Nuclei via Induced Fission," *Joint Meeting of the Nuclear Physics Divisions of American Physical Society (APS) and Japanese Physical Society (JPS) held on October 17–20, 2001, in Maui, Hawaii*.

Gehrke, R. J., "Participation in Radiation Metrology Measurements: ^{252}Cf ν bar, ^{56}Mn Half-life, ^{93m}Nb P_{KX} and ^{226}Ra P_{γ}(186)," presented at the *2001 Winter Meeting of the American Nuclear Society held November 11–15, 2001, in Reno Nevada, ANS Transactions* 85 *(2001) 233.*

Gehrke, R. J., R. Aryaeinejad, J. K. Hartwell, W. Y. Yoon, E. Reber and J. R. Davidson, "The Gamma-Ray Spectrum of ^{252}cf and the Information Contained within It," *5th International Topical Meeting on Industrial Radiation and Radioisotope Measurement Applications held June 9–14, 2002, in Bologna, Italy*. Full paper submitted for publication in a special issue of *Nuclear Instruments and Methods in Physics Research*.

Helmer, R. G., "Modern Tools for Precise γ-ray Spectrometry with Ge Detectors," invited presentation at the *Symposium on Radiation Measurements and Applications, May 21–23, 2002, Ann Arbor, Michigan*.

Helmer, R. G., "The Joys of Doing Precise Spectrometry and Data Evaluation," presented at the *2001 Winter Meeting of the American Nuclear Society held November 11–15, 2001, in Reno Nevada, ANS Transactions* 85 *(2001) 230*.

Reber, E. L., R. Aryaeinejad, J. K. Jewell, J. D. Cole, M. W. Drigert, "Experimental Setup for Neutron Induced Fission Studies," *Joint Meeting of the Nuclear Physics Divisions of American Physical Society (APS) and Japanese Physical Society (JPS) held on October 17–20, 2001, in Maui, Hawaii*.

Reich, C. W., "Nuclear Light: What is It? Has It Been seen?," *2001 Winter Meeting of the American Nuclear Society held November 11–15, 2001, Reno Nevada, ANS Transactions* 85 *(2001) 231*.

Spencer, D. F., R. Aryaeinejad, and E. L. Reber, "Using the Cockroft-Walton Voltage Multiplier Design in Handheld Device," *IEEE Nuclear Science Symposium and Medical Imaging Conference held on November 4-10, 2001, San Diego, California*.

Professional Activities related to ESRA

R. J. Gehrke, Session organizer of "Radiation Metrology, Nuclear Data, and Reminscences: A Special Session Honoring Dr. Richard Helmer (recipient of the American Nuclear Society's 2001 Radiation Science and Technology Award) for ANS winter Meeting of the American Nuclear Society held November 11–15, 2001, in Reno, Nevada.

R. J. Gehrke, Session organizer of "Prompt Gamma Applications I and II" for the 5th International Topical Meeting on Industrial Radiation and Radioisotope Measurement Applications (IRRMA-V) held June 9–14, 2002, in Bologna, Italy.

J. Gehrke, Session organizer of "Radiation Metrology, Nuclear Data, and Reminscences," A Special Session Honoring Dr. Richard Helmer (recipient of the American Nuclear Society's 2001 Radiation Science and Technology Award) for ANS winter Meeting of the American Nuclear Society held November 11–15, 2001, in Reno, Nevada.

R. J. Gehrke, Session organizer of "Prompt Gamma Applications I and II," for the 5th International Topical Meeting on Industrial Radiation and Radioisotope Measurement Applications (IRRMA-V) held June 9–14, 2002, in Bologna, Italy.

REFERENCES

1. T. R. England and B. F. Rider, "Fission Product Yields per 100 Fissions for ^{244}Cm Spontaneous Fission and Decay," LA-OR-94-3106, ENDF-349, ^{244}Cm independent and cumulative yields from http://ie.lbl.gov/fossion/244cm.txt.

2. R. J. Gehrke, R. Aryaeinejad, J. K. Hartwell, W. Y. Yoon, E. Reber, and J. R. Davidson, "The Gamma-Ray Spectrum of ^{252}cf and the Information Contained Within It," submitted for publication in a special issue of *Nucl. Instr. and Meth*.

3. C. E. Moss and T. J. Caldwell, "Assay of TRU Wastes containing (α, *n*) Sources," *Journal of the Institute Nuclear Materials Management,* Vol. XV, 27th Annual Meeting, 1986, p. 427.

4. A. V. Shumakoo, G. N. Vlaskin, V. F. Kositsyn, and Naumov, "Estimated Detection Limits of B, C, N. O, and F in α-Emitters by Using γ-Radiation From (α, xγ) Reactions," *Radiochemistry*, Vol. 36, 1994, p. 62.

5. E. W. Lees and D. Lindley, "Neutron Production from (α, *n*) Reactions in 241AmO2," *Annual of Nuclear Energy*, Vol. 5, 1978, p. 133.

6. R. J. Gehrke, J. D. Baker, J. K. Hartwell, C. Riddle, and C. A. McGrath, "Measurement of Neutron-to-γ-ray Production Ratios, n/γ, from (α, n) Reactions for their Application to Assay TRU Waste," in draft form and to be submitted for publication in the journal of Nuclear Instruments and Methods in Physics Research.

7. I. Ahmad, E. F. Moore, J. P. Greene, C. E. Porte and L. K. Felker, "Quantitative Determination of ^{252}Cf," presented at the Annual Meeting of the Institute for Nuclear Materials Management, 2002.

8. R. Keegan and R. J. Gehrke, "A Method to Determine the Age of Weapons Grade Plutonium," draft paper is being written. R. J. Gehrke, R. G. Helmer, and J. R. Davidson, "Acquisition of Quality Ge γ-ray Spectra, " in draft form and to be submitted for publication in the journal Nuclear Instruments and Methods in Physics Research

9. W. D. Schmidt, U. Bosch, and Th. Mahlenkamp, "PIN Diodes for Electron Detection," *Nucl. Instr. Meth*., Vol. A285, 1989, p. 459.

10. D. Sueva, V. Spassov, N. Chikov, and E. I. Vapirev, Manufacturing Avalanche Diodes for Detection of Low-Energy Gamma- and X-rays," *Nucl. Instr. Meth*., Vol. A288, 1990, p. 460.

11. I. Ahmad, R. R. Betts, T. Happ, D. J. Henderson, F. L. H. Wofs, and A. H. Wuosmaa, "Nuclear Spectroscopy With Si PIN diode detectors at Room Temperature," *Nucl. Instr. Meth*. Vol. A299, 1990, p. 201.

12. R. Aryaeinejad, J. D. Cole, and R. C. Greenwood, "Performance of High Resolution Silicon Pad Detector and Associated Preamplifier Circuit Board," *Nucl. Instr. Meth*., Vol. A316, 1992, p. 354.

1. J. K. Hartwell and G. D. McLaughlin, "A Comparison of the High Count-Rate Performance of Two Commercially Available Digital Gamma-Ray Spectrometers," *Radioactivity & Radiochemistry*, Vol. 11, No. 4, December 2000.

2. L. J. Meng and D. Ramsden, "An Inter-comparison of Three Spectral-Deconvolution Algorithms for Gamma-Ray Spectroscopy," 1999 IEEE Nuclear Science Symposium and medical Imaging Conference record CD-RO, October 24–30, 1999, in Seattle, Washington.

3. L. A. Shepp and Y. Vardi, "Maximum Likelihood Reconstruction for Emission Tomography," IEEE MI1, No. 2, 1982.

4. M. A. Ludington, R. G. Helmer, "High Accuracy Measurements and Monte Carlo Calculations of the Relative Efficiency Curve of an HPGe Detector From 433 to 2754 keV," *Nucl. Instr. Meth*., Vol. A446, 2000, p. 506.

5. E. Schönfeld, H. Janßen, R. Klein, J. C. Hardy, V. E. Iacob, M. Sanchez-Vega, H. C. Griffin, M. A. Ludington, *Appl. Radiat. Isot.* Vol. 56 (220), p. 215.

6. J. Law and A. Suzuki, "Orbital K-electron Shakeoff in β Decay," *Phys. Rev. C*, Vol. 25, No. 1, 1982, p. 514.

7. J. A. Halbleib, T. A. Mehlhorn, *Nucl. Sci. Eng.* Vol. 92, 1986, p. 338I.

8. J. C. Hardy, V. E. Iacob, M. Sanchez-Vega, R. T. Effinger, P. Lipnik, V. E. Mayes, D. K. Willis, R. G. Helmer, *Appl. Radiat. Isot*. Vol. 56, 2002, p.65.

9. R. G. Helmer, J. C. Hardy, V. E. Iacob, M. Sanchez-Vega, R. G. Neilson, J. Nelson, entitled "The Use of Monte Carlo Calculations in the Determination of a Ge Detector Efficiency Curve" to be submitted to *Nucl. Instr. Meth. A*.

Biocorrosion

Patrick J. Pinhero, Ph.D. and Richard N. Wright, Ph.D.

SUMMARY

Microbially-influenced corrosion (MIC) as it relates to the storage of spent nuclear fuel (SNF) is a potential problem at the INEEL, and other sites across the DOE complex. Detection and mitigation of MIC in SNF storage, both wet and dry, is the ultimate goal of this task. Supporting goals are to (a) verify that MIC is active and indeed a problem in SNF storage facilities, (b) identify and understand the fundamental corrosion mechanisms inherent to MIC, and (c) design and construct a deployable device that can be used to measure MIC activity in SNF storage environments. These goals are congruent with those of the DOE Office of Environmental Management (DOE-EM) to invest in research and development that can provide long-term, cost-effective solutions for dealing with an increasing inventory of nuclear waste.

This report constitutes a closeout summary of accomplishments for both FY 2002 and the past 4 years of the biocorrosion task of the Environmental Systems Research (ESR) Program at the INEEL. In FY 2002 this task developed a novel fundamental science capability for pinpointing localized corrosion at its inception using conductive atomic force microscopy (C-AFM). Additional accomplishments include development of a database of Tafel-determined corrosion rates for a library of microbiological systems, development of electrochemical noise (EN) systems for real-time monitoring of INEEL service environments, and development of a corrosion inhibitor for aluminum alloys. Prior years saw vast accomplishment in determining the radiation-tolerance of microbes, establishing new protocols with respect to microbiologically sterile system controls, and development of many new capabilities for studying localized corrosion. Significant effort has been devoted to establishing links between new capabilities developed through ESR funding and the National Spent Nuclear Fuel Program (NSNFP), the former Tanks Focus Area (TFA), and DOE-Basic Energy Sciences (BES).

PROJECT DESCRIPTION

Introduction

DOE is the custodian of several thousand metric tons of SNF, primarily as a result of experimental nuclear reactor development and Naval Reactor activities during the Cold War. This stockpile also includes fuel from energy research and naval reactors. The long-term containment performance of the fuel under storage and disposal conditions is uncertain. These uncertainties have a direct bearing on DOE's ability to license disposal methods. The DOE-EM emphasizes the fundamental need to identify mechanisms that may adversely affect the performance of the fuel package during storage. Deleterious effects recognized as being incompletely characterized include corrosion and degradation rates for the fuel matrices, mechanisms that may lead to accelerated degradation of containers, and the effects of microbes on fuel packages.

MIC is a known problem in various industries; for example, severe biofouling occurs in transport piping used in the petroleum industry. Sulfate-reducing bacteria (SRB) are particularly important because they are responsible for souring of oil and for MIC. Water content of just 1% is adequate to support substantial development of SRBs within a few weeks. The INEEL uses large "swimming pools" of water to temporarily store and cool SNF before it is processed and transported to final storage. Before being transported to a repository for final disposition, the SNF is dried and placed in appropriate transport containers. Prior research examined the viability of bacteria and their ability to form biofilms in radiation-rich environments. As described in the following sections, our FY 2002 research focused on developing real-time monitoring systems for implementation in SNF pool service environments.

This task has produced many innovations for INEEL research and development (R&D) both in the development of new capabilities and in

successful integration of R&D solutions with Operations needs. During FY 2002, research accomplishments include the first use of conductive atomic force microscopy (C-AFM) to characterize the initial events leading to localized corrosion in commercial alloys, the first use of Mott-Schottky Electrochemical Impedance Spectroscopy (EIS) to examine the semiconductive character of biopassivity at alloy surfaces, the first use of Scanning Electrochemical Microscopy (SECM) to characterize localized corrosion in welded alloys, and the first silanyl-bonded perfluorinated corrosion inhibitor for aluminum alloys. In addition to the many accomplishments in fundamental science, the biocorrosion task has made a significant impact on problems of practical importance to INEEL Operations. Recent discussions with managers at the Idaho Nuclear Technology and Engineering Center (INTEC) located at the INEEL have examined the implementation of the EN surveillance systems as a real-time monitor of corrosion activity in the INTEC-666 spent nuclear fuel (SNF) pool. Additionally, the expertise developed as part of this task has been sought or implemented by the following activities and programs: the DOE-Basic Energy Sciences (BES) Center for Synthesis and Processing (CSP) on Localized Corrosion, National Spent Nuclear Fuel Program (NSNFP), the DOE Tanks Focus Area (TFA), the DOE Nuclear Materials Focus Area (NMFA), the Yucca Mountain Project (YMP), and potentially new programs as part of the INEEL transition from the Office of Environmental Management (EM) to the Office of Nuclear Energy (NE).

This report summarizes the accomplishments of the ESR Biocorrosion task for FY 2002, and, because 2002 is a closeout year for this task, lists all accomplishments for the three previous years. The first section of this report provides a complete list of all accomplishments for 1999–2002; sections two and three detail both fundamental science accomplishments and practical applications for FY 2002; and the last section presents conclusions based on all of the studies undertaken over the course of the task.

Fundamental Studies of Localized Corrosion

Localized corrosion (pitting, crevice, and cracking) is a problem that has perplexed corrosion scientists for over a century. Addressing the issue of localized corrosion is critical, because its corrosion rates are often several orders of magnitude higher than those observed in general dissolution (uniform corrosion). Investigations of local corrosion mechanisms are now of great interest to the scientific community because there are numerous tools that are now at their disposal that were not available 5–10 years ago. Two powerful techniques used during this task to examine localized corrosion were SECM and C-AFM. This section will review each of the techniques used in the biocorrosion project to characterize local corrosion processes, particularly focusing on experimental advances for FY 2002.

SECM

Once the SECM was constructed (February 2001) we chose to evaluate our system using a recently published study by Paik et al.[1] This seemed a good place to start since the study focused on the dissolution of manganese sulfide (MnS) inclusions in Type 304 stainless steel. From the perspective of biocorrosion, it is even more relevant due to the connection between sulfate reducing bacteria (SRB) and MIC processes. Using SECM, the detection of localized dissolved sulfide could be correlated with SRB activity, thus providing a tool for the study of what is considered the most common type of steel biocorrosion. Two probes considered for the detection of sulfide are an iodide/tri-iodide (I^-/I_3^-) mediated detection scheme developed by Paik et al. (see Reference 1) and commercially available hydrogen sulfide (H_2S) amperometric microelectrode sensors. In FY 2002, we extended this study to include both the 304L and 316L stainless alloys, an addition to the previously studied 304 stainless steel.

In brief, SECM was used to study the corrosion behavior of 300 series austenitic steels. Using the substrate generation/tip collection (SG/TC) mode, the I^- ion was used as both the

aggressive species and the method of detecting oxide breakdown. With the microelectrode tuned to detection of oxidized product (I_3^-), it was brought to within 10 µm of the sample surface. Mapping of the surface showed that current was isolated to discrete locations where pitting corrosion was observed. The maps of the surface followed the expected trend of stability: 316L >> 304L > 304. The 316L sample did not pit in I^- solution unless Cl^- was also added. As a test of the technique, the corrosion of a cross-sectioned 316 weld was imaged. The expected behavior was to observe pitting surrounding the weld due to heat sensitization. The results showed that the base 316 material was contaminated with nonmetallic inclusions and showed high activity compared to the filler material which showed no activity. The potential of SECM in studying corrosion was discussed.

Cyclic voltammograms of 304, 304L, and 316L in 10 mM KI are shown in Figure 1. In the forward sweep, current begins to rise near approximately 500 mV and results in a peak near 650 mV. This feature is attributed to the localized oxidation of I^- as the E^o for the I^-/I_3^- couple is approximately 400 mV. After going through the peak, the current increases further due to oxidation of I^- across the entire surface due to tunneling across the oxide film. Poising the potential at 1,000 mV resulted in yellow color across the entire surface due to I_3^- production. For 304 and 304L samples, a hysteresis current is observed in the negative sweep that suggests activation of the surface via pitting. Following passivation, all samples exhibit a peak near -50 mV, which is attributed to I_3^- reduction. Note that more overpotential is required for reduction of I_3^- than for oxidation of I^-, due to reformation of the passive film over pits at negative potentials. The behavior of 316L is somewhat different from that of the 304 and 304L samples. Figure 2 shows the results of continuous cycling of a 316L sample. The amount of oxidation current in the 500–800 mV region diminishes significantly with each sweep, indicating an increased passivation of the surface. This passivation is not observed for either 304 or 304L samples.

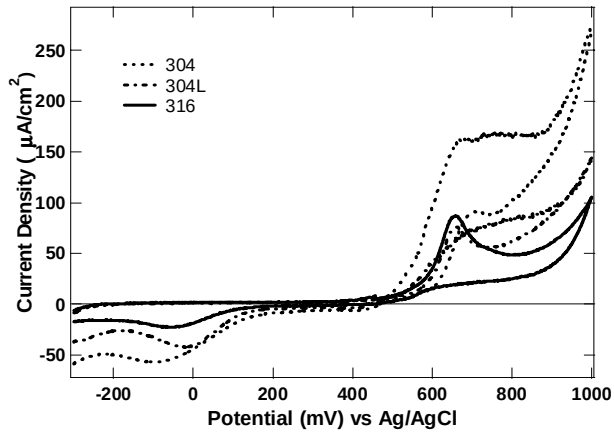

Figure 1. Cyclic voltammograms of 300 series stainless steels in 10 mM KI.

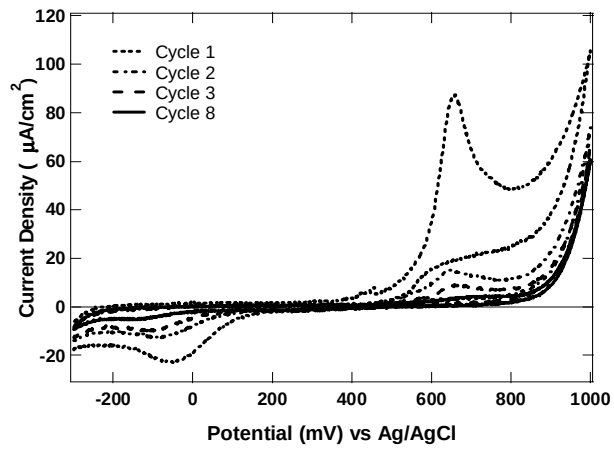

Figure 2. Multiple cycles showing gradual passivation of 316L in 10 mM KI.

Several conclusions can be drawn from the above results. First, the expected order of stability was observed as 304<304L<316L. Second, in the positive sweep, two zones of activity are observed: 500–900 mV where localized activity is observed with reaction likely at metal-like sites created by pitting, and above 900 mV where general reactivity across the oxide surface is observed. Third, the current in the 500–900 mV region diminishes with repeated sweeping, particularly for 316L, suggesting the formation of a thicker passive film.

The SECM was used to detect the presence of I_3^- species across the surface while holding the potential in the localized regime (500–900 mV). Using the same solution and fresh coupons, the

sample was jumped from OCP (approx. -100 mV) to the imaging potential. The microelectrode was poised at -200 mV while being rastered across the surface to detect I_3^-. Figure 3 shows the first image collected for each sample type at 600 mV. As expected from the cyclic voltammograms the number of active sites in the SECM images is greatest for 304 and virtually absent for 316L. The active sites are symmetric in nature due to radial diffusion of I_3^- from the active site. Although the exact nature of the electron transfer between the I^- species and the surface is not known, it appears through microscopic observation of the surface during reaction, that pits form at the most large active sites in the SECM image. More in question are smaller sites that could be smaller pits that passivate prior to maturation. Further studies are planned to understand this relationship. In any event, it is expected that the oxide film must be weakened to allow electron transfer to I^- as oxidation of the entire surface is not observed until ~900 mV. Previous work for 304 has shown that under these conditions the reactivity is dynamic when collecting consecutive images.[2] This too would suggest that the active sites are due to pitting corrosion.

The measurements above were performed in relatively mild conditions and thus, did not show any detectable corrosion in 316L samples. Even at 1,000 mV, pitting corrosion is not observed (see Figure 4A). The image shows a uniform response across the entire surface of ~10 mA, likely due to homogeneous tunneling (relative to the tip size) across the oxide film, as mentioned above. In order to induce pitting corrosion in 316L, 10 mM NaCl was added to the solution. The cyclic voltammograms for that solution indicate hysteresis on the return sweep, suggesting pitting corrosion. The SECM image in Figure 4B was taken at 500 mV after first initiating pits at 800 mV, then dropping the potential back to near the repassivation potential (500 mV) during measurement. Upon bringing the potential back to OCP conditions then switching back to 500 mV the activity was extinguished, thus showing that breakdown was needed to induce activity. Imaging at 800 mV was possible, however excessive corrosion resulted.

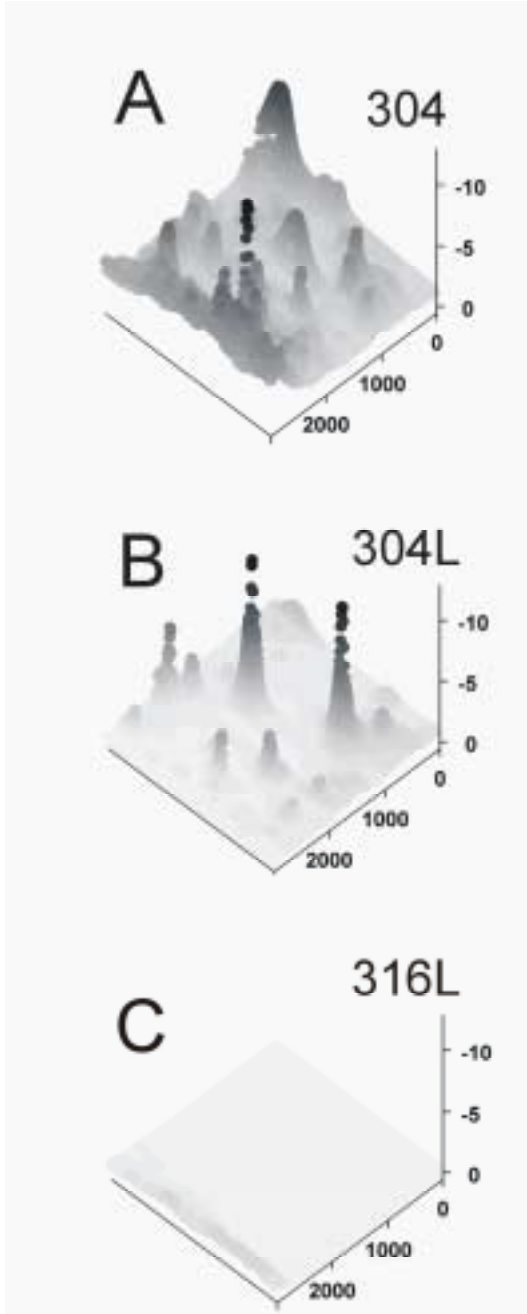

Figure 3. SECM images of (A) 304, (B) 304L, and (C) 316L in 10 mM KI taken at a sample potential of 600 mV and a microelectrode potential of -200 mV.

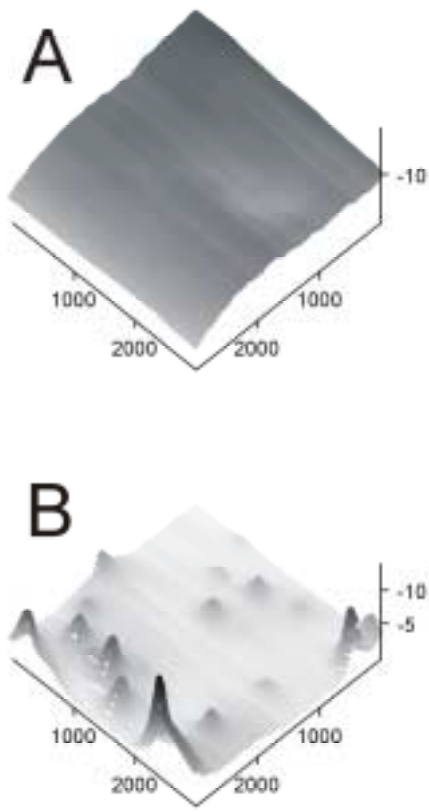

Figure 4. SECM image of 316L in a solution of 10 mM KI at (A) 1,000 mV, and (B) with 10 mM NaCl added. In (B) sample, potential was stepped into breakdown region around 900 mV, then dropped to 600 mV for measurement.

In addition to imaging homogenous alloys, the corrosion behavior of welds has been investigated. Initial interest in determining intergranular corrosion susceptibility due to heat sensitization was the initial focus in these experiments. Heat sensitization of stainless steels occurs due to formation of chromium carbides at the grain boundaries.[3,4] The SECM image in Figure 5 is the cross-section of a weld with both 316 base and fill material, where the weld fills a u-shaped groove machined in a 316L plate (as roughly sketched on Figure 5). The image shows the corrosion behavior in the entire base material, not isolated to a thin heat affected zone surrounding the weld. The weld material was not attacked, as evidenced by the wedge of inactivity and the absence of pitting inside the weld when observed following the experiment. Optical microscopy showed the pits in the base material only, in agreement with the SECM image. Our previous experience with 316L was that corrosion was not observed in 10 mM KI. Subsequent analysis of the cross-sectioned base material indicated a high concentration of inclusions when electrochemically etched in oxalic acid. The inclusions did not extend to the edges of the cross-section (the plate surface). Corrosion behavior of the plate surfaces indicated normal 316L corrosion resistance. Thus it appears that the inclusions were isolated to the center of the plate during processing. Previous work has shown the common inclusions in 300 series stainless steels are Al_2O_3, MnS, and silicates.[5,6]

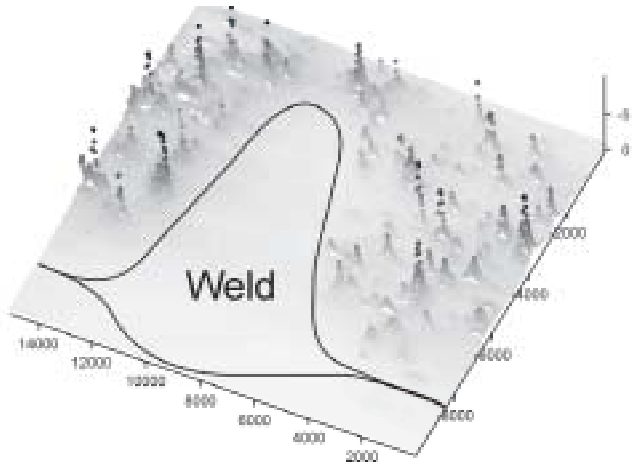

Figure 5. SECM of 316L weld region imaged in 10 mM KI at 700 mV.

C-AFM

C-AFM is a powerful current sensing technique for the electrical characterization of conductivity variations in medium resistive samples. C-AFM allows the user to measure currents in the range of 1 pA to 1 µA at a lateral resolution better than 10 nm. By simultaneously mapping the topography and current distribution, the direct correlation of a sample location with its electrical properties is easily possible. Applications include identification of leakage paths, mapping of contaminants and different components in composite materials, and differentiating regions of higher and lower conductivity. The circuitry for the C-AFM technique was constructed in-house and is

integrated into both the digital instruments Multimode Nanoscope and the molecular imaging PicoSPM is integrated in small modules.

C-AFM modules can be operated in either imaging or spectroscopy mode. In the imaging mode, images of the electrical current are obtained, while in the spectroscopy mode one can collect current-voltage (I-V) or current-force (I-Z) spectra. For local corrosion studies, the conductivity is a measure of thinning passivity, where electron transfer can occur across the passive film. Localized regions of high conductivity are the defect points where localized corrosion (pitting, crevice, stress corrosion cracking) will most probably occur.

In the imaging mode, an electrically conductive probe is scanned over the sample surface in contact mode while a feedback loop keeps the deflection of the cantilever constant and the local height of the sample is measured. While scanning, the user can apply a dc (direct current) bias between the tip and the sample. A low-noise linear current amplifier senses the resulting current passing through the sample as the topography image is simultaneously obtained (see Figure 6). The observed current can be used as a measure for the local conductivity or electrical integrity of the sample under study. For C-AFM, the noise level (typ. 1 pA RMS) and current range (from 1 pA to 1 mA) allowing performance of accurate current measurements on samples with medium conductivity values.

In addition to the imaging mode, C-AFM also allows one to measure local current-voltage (I-V) or current-force (I-Z) spectra using the spectroscopy mode. In order to obtain I-V spectra, the imaging scan is stopped and the tip is held in a fixed location while the sample bias is ramped up or down. The resulting current through the sample is plotted versus the applied bias. Parameters include start and end voltage of the ramp, ramp direction, ramp rate, and delay times between individual ramps. Software can either record a single spectrum or average over multiple spectra. In order to obtain I-Z spectra, the sample bias is kept constant, while the scanner is moved in the Z-direction, similar to the measurement of force-displacement curves. The resulting current through the sample is plotted versus the Z-position of the scanner.

To date, preliminary C-AFM studies have focused on Al 6061-T6 and 304 stainless alloys. The included particles in these two alloys helped prove that there is higher local conductivity in the proximity of inclusions, a hypothesis supported by recent microcell studies performed by Alkire.[7] Figure 7 displays a ca. $(20\ \mu m)^2$ conductivity map acquired for Al 6061-T6 after a 1 hour open circuit reaction in 100 mM HCl. One can observe the enhanced conductivity at the edges of the inclusion. This higher conductivity is not observed immediately after polishing. More than likely, the higher conductivity is due to preferential etching by HCl of the interface separating the inclusion from the base material. This preferential etching thins the passive (more than likely oxide) layer so that electron tunneling can occur between the specimen surface and the tip, resulting in the observed high conductivity. It is believed that these local sites of high conductivity will be the

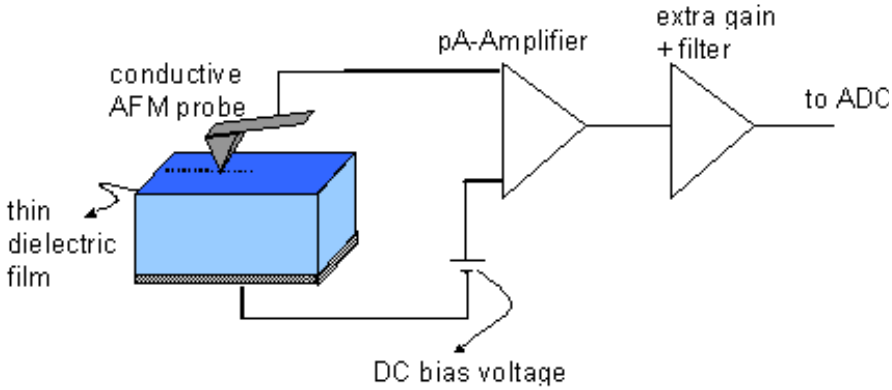

Figure 6. Schematic representation of the C-AFM.

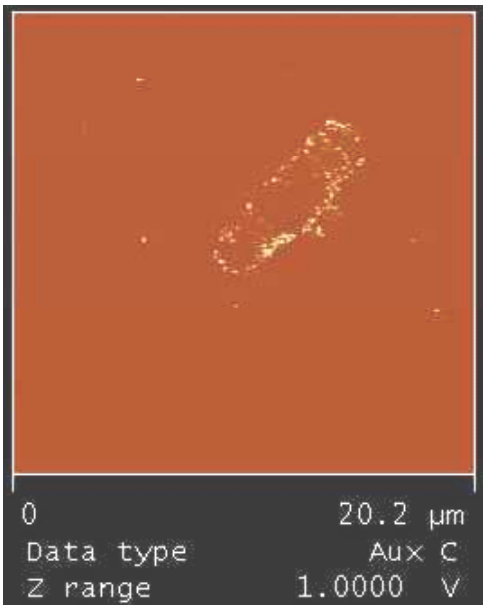

Figure 7. C-AFM data showing conductivity maps of AI 6061-T6 specimen after 1 hour immersion in 100 mM HCl at open circuit.

points where local corrosion initiates. Energy Dispersive Spectroscopy (EDS) mapping has identified this inclusion as an aluminum-iron-silicate.

The acquisition of C-AFM is nontrivial. Very few groups attempt such measurements, and the INEEL biocorrosion team is the first to apply C-AFM to corrosion problems. The trick to successful C-AFM is possession of a very good AFM tip. Collaboration with Dr. Julie MacPherson and Professor Patrick Unwin (University of Warwick, United Kingdom) have allowed the INEEL Team to acquire images like those in Figure 8. The INEEL tips outperform all of the sensors available commercially.

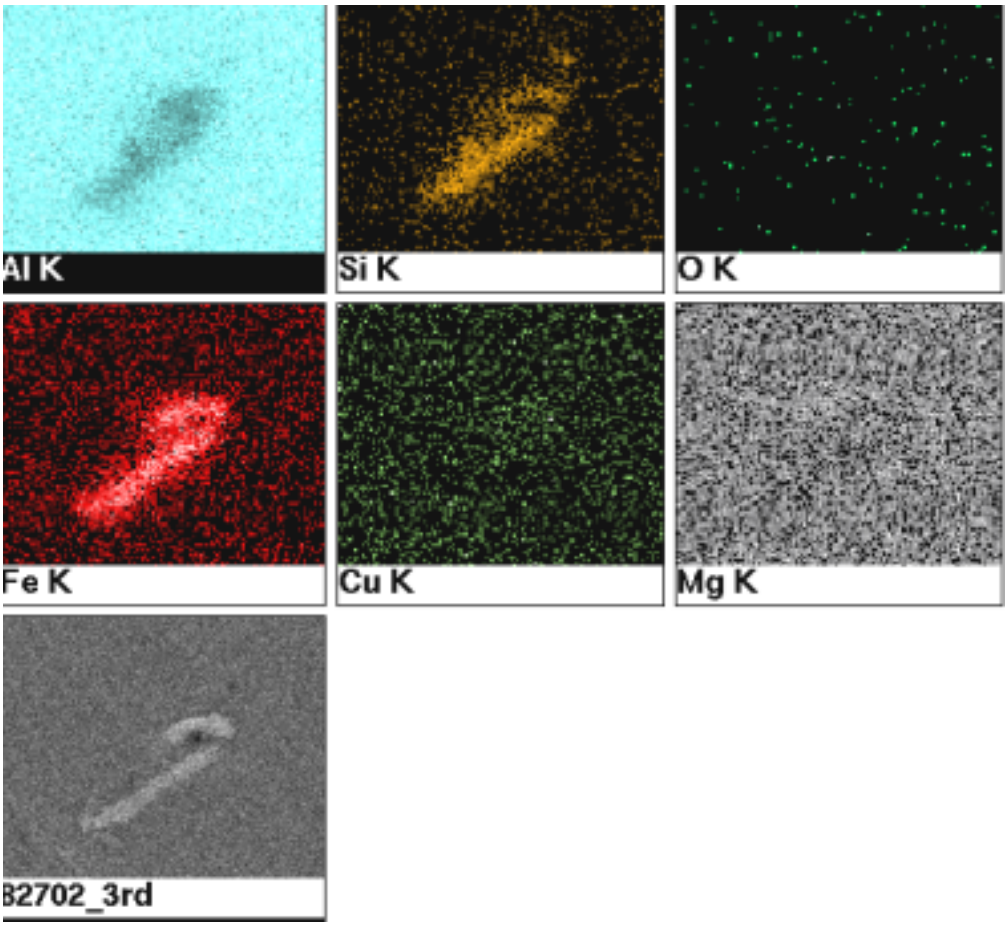

Figure 8. EDS map of inclusion of AI 6061-T6.

Application of INEEL Biocorrosion Capabilities to INEEL Operations

One of the obvious goals of the INEEL ESR Program is to use R&D to help reduce the costs of Operations, especially with respect to EM cleanup. This section demonstrates one such application, the application of EN to monitoring corrosion in high-level waste (HLW) storage tanks located at INTEC. In addition, recent discussions with INTEC managers may lead to the implementation of EN surveillance systems in the INTEC-666 SNF pool, and potentially a role in monitoring the corrosion stability of SNF in dry storage.

EN of HLW Tanks–Study of Simulant Systems

These tests have involved collecting and analyzing data taken in a simulant solution with chemistry similar to waste tank WM-189. The purpose of these experiments was to collect EN data in solutions representing the tank for future implementation. This chemistry, outlined in Table 1, is comprised of the most prevalent anions from the chemical analysis.[8] Welded bullet electrodes obtained from Hi-line Engineering were used in this testing. The electrodes were used as-received (machine finish) or lathe sanded to 200-grit finish (reconditioned electrodes). Degreasing in acetone, ethanol, and ultra-pure water preceded immersion of the probes. During testing, a cell containing ultra-pure (18 Mohm) water was also observed on a separate channel. This was used as a control to discriminate between real signals and electrical interference, which does not appear to be an issue in this work.

The three experiments outlined here were performed using welded 304L bullet electrodes in WM-189 simulant at 30°C. The tests lasted various times from 5 to 12 days. The raw voltage and current data from the tests, taken with 1-second resolution are shown in Figure 9. Three items should be noted on the tests: (a) the water bath was not turned on for the initial 4 days of test 1 (temp approx 22°C); (b) test 3 was spiked with NaCl dissolved in a small volume of water to double the concentration (0.040 M) of Cl^-; and (c) test three used reconditioned electrodes. With exception of the first test, the current noise data is composed of regular amplitude oscillations between 5 and 15 nA. The voltage data likewise showed very uniform amplitude noise of less than 1 mV superimposed on a drifting background. These observations would suggest that localized behavior is not occurring in the second two tests. Additionally, the first test shows more localized events (higher amplitude sporadic signals) before turning on the bath. Thus, for a majority of the test conditions at 30°C, the general corrosion signal was observed. The single test of 304L nonwelded electrodes indicated localized corrosion in the simulant solution. This was corroborated with microscopy data. It should also be noted that the simulant solution for this test was also used subsequently for Test 1. Likewise, a new solution was made for Test 2 and used subsequently for Test 3. It suggests that an error was made making one of these solutions.

Table 1: WM-189 simulant solution.

Ion	Conc. (Mol/L)	Chemical	FW (g/mol)	Weight (grams)	
Cl^-	0.021	NaCl	58.44	1.2272	
NO_3^-	6.62	$NaNO_3$	84.99	562.6338	
SO_4^{-2}	0.182	Na_2SO_4	142.04	25.8513	
H^+	0.223	HNO_3	63.01	14.0512	20.07319

Note: $NaNO_3$ is reduced due to addition of HNO_3 to reduce pH.

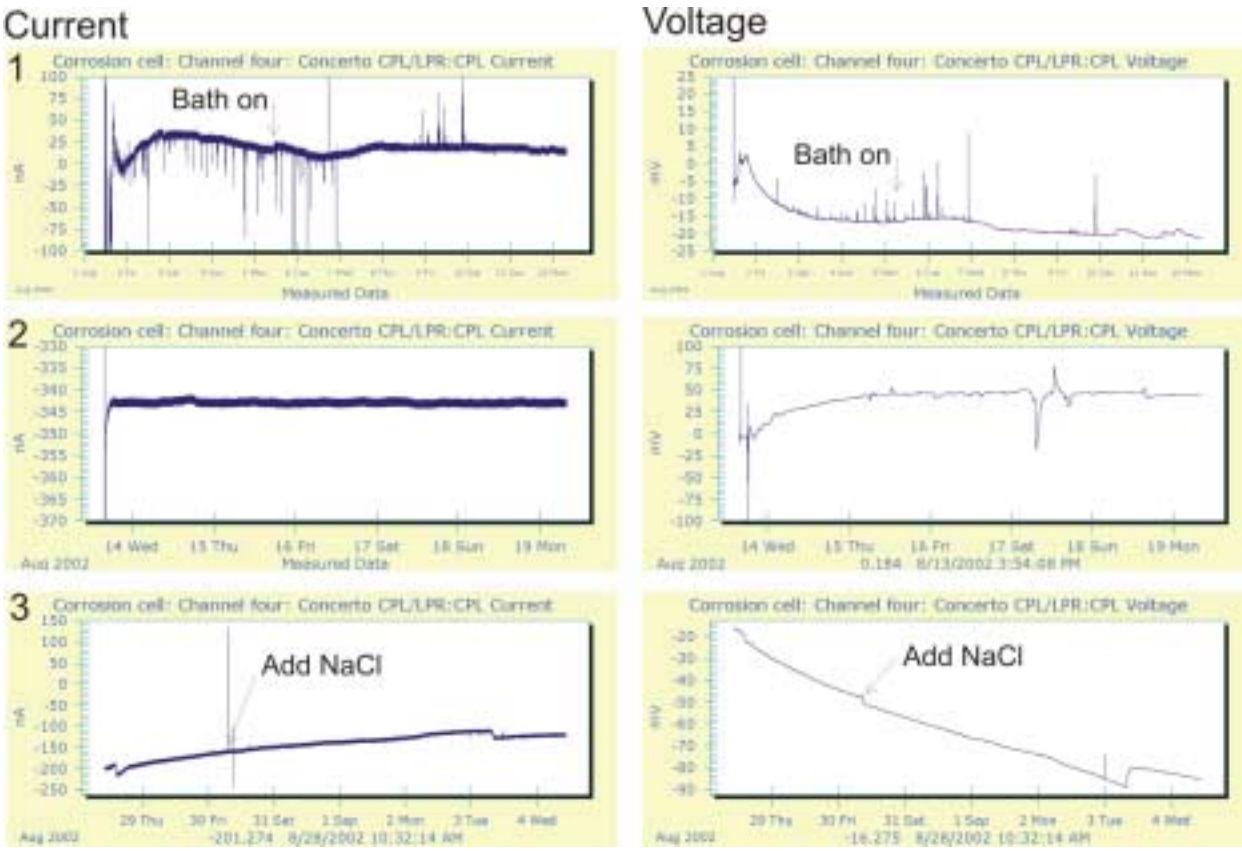

Figure 9. ECN data for welded 340L electrodes obtained in WM-189 simulant solution at 30ºC except where noted.

Images of the bullet electrodes were taken following the tests to determine the extent of surface damage for correlation purposes. Visually, the electrodes appear very clean after removal with a matt finish. It appears that a slow etching process is occurring to create this surface finish. Figure 10 shows optical microscopy images (tip and weld area) of the samples following the tests. These images generally corroborate the noise data—less pitting is observed than in the nonwelded sample mentioned earlier. The exception is Test 3 where the electrodes were left in the simulant for 2 weeks following the end of the test. The electrodes showed significantly more pitting in that case. Also note that those electrodes were exposed to twice the Cl^- concentration (0.04 M) and the bath was turned off during the 2 weeks prior to analysis. Pitting in all cases appears to be less than for the nonwelded sample, thus creating a contradiction in the test results. In any case, it appears that the noise data is generally in agreement with the observed microscopy.

In the ECN data collected to date there appears to be two signal types that can be treated in separate manners. The first most common signal is the constant amplitude oscillations present throughout all these measurements. This signal is attributed to uniform or general corrosion in the literature and is quantifiable by calculating the noise resistance (R_n), the standard deviation of the voltage divided by the standard deviation of the current. This can then be used to calculate a corrosion rate by assuming R_n is equivalent to R_p (polarization resistance). The second type of noise is the higher amplitude stochastic noise that is indicative of pitting corrosion. To our knowledge, this type of noise cannot be treated mathematically to obtain a corrosion rate. Thus our use of such data will be qualitative in nature and more "experience" based.

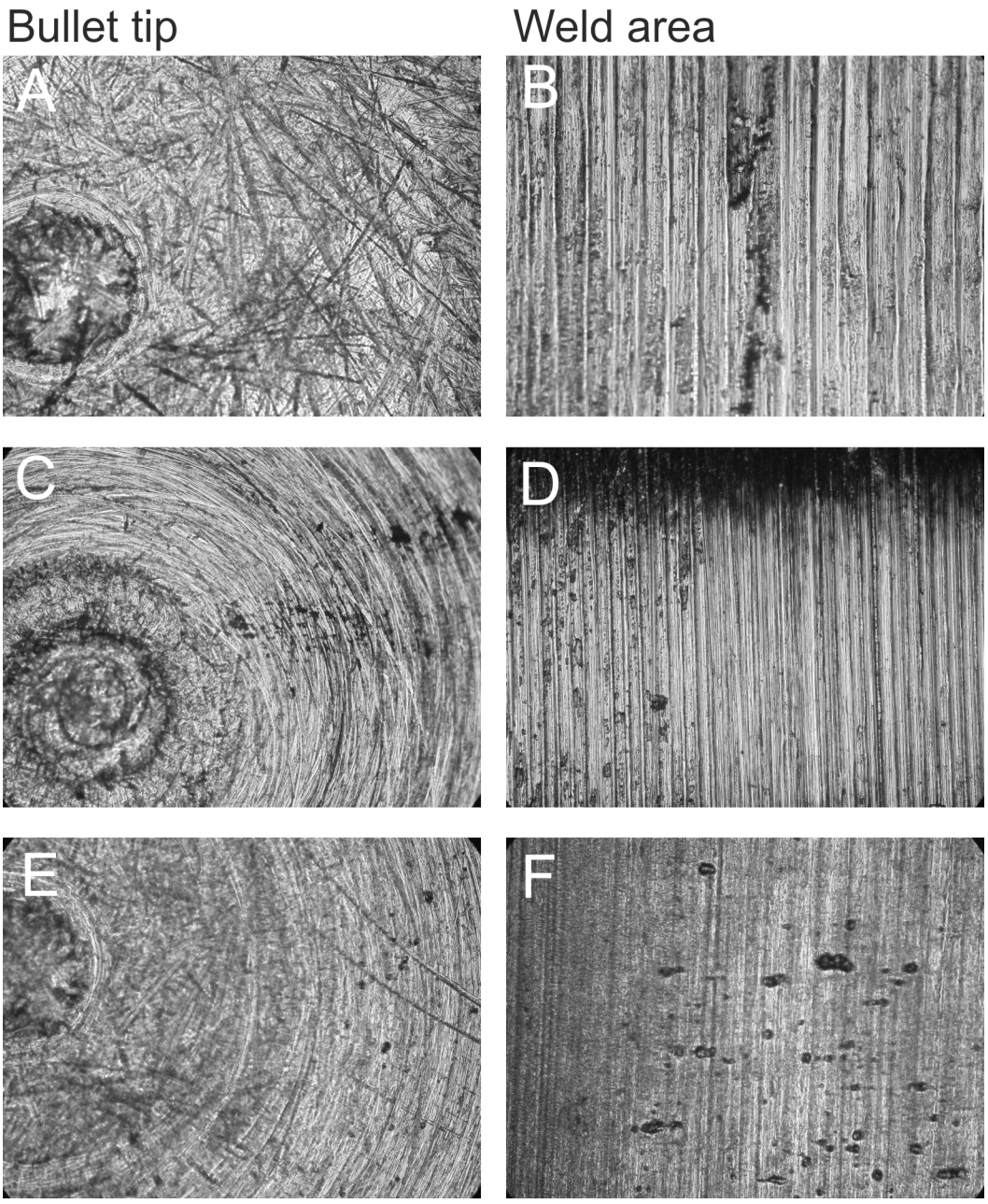

Figure 10. Optical microscopy images of coupons from A-B Test 1, C-D Test 2, and E–F Test 3. The bullet tip images are left and the weld area is right.

Figure 11 shows the corrosion rates calculated for each 5-minute group of data (300 points) for all three tests. These rates vary over a wide range during any test, and there is a variation between each test. The calculated average corrosion rate for the tests are (in order): 2.11×10^{-2}, 3.52×10^{-4}, and 1.75×10^{-2} mm/year, respectively. At this point, it is not known why the Test 2 values show a two orders of magnitude lower corrosion rate. More testing is needed to figure this out.

The results of testing to this point show that more laboratory work should be done to answer some of the reproducibility issues. The chemistry that was chosen for these tests might be close to the stability point for 304L. While it is possible that some error was made in making up solutions, these errors should be a couple percent at most.

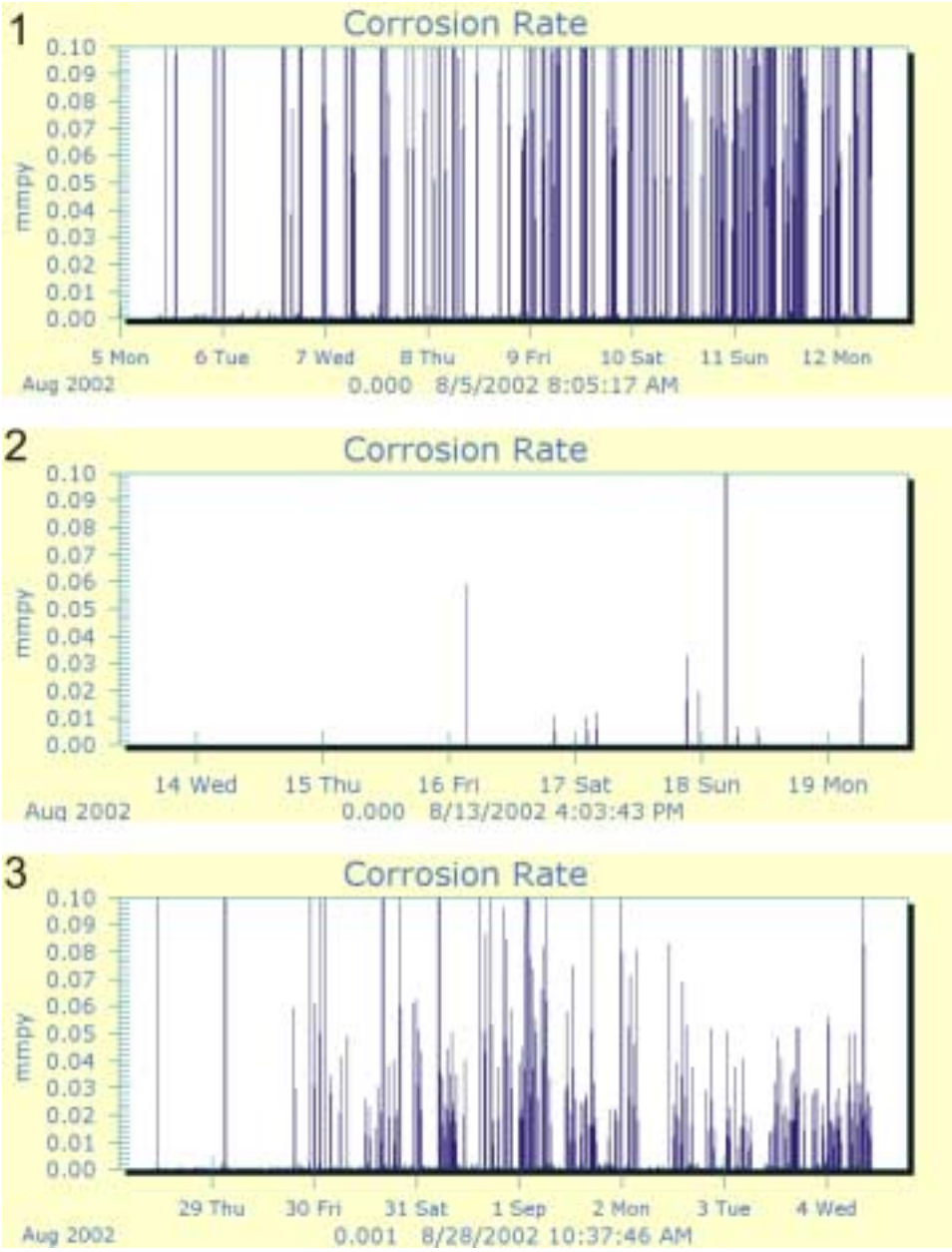

Figure 11. Calculated corrosion rates for the three tests. Each corrosion rate data point is calculated from 300 pairs of voltage/current data points. The current data range is clipped to decompress lower corrosion rate data.

Further work will detail a solution make-up procedure and solutions made in bulk to achieve identical compositions between tests. It is also suggested that the tests themselves be standardized in the length of time such that microscopy of damage can be directly correlated. After this work is done, a better handle on the reproducibility of the noise measurement itself can be made.

The correlation of noise to the actual surface damage on the coupons is an important issue. The use of the bullet electrodes, while likely a good field design, is not ideal for performing post-mortem microscopy studies due to the lack of flat surfaces. The size of the electrodes also make a statistical study (pit density) quite difficult.

ACCOMPLISHMENTS (1999–2002)

During the course of the Biocorrosion project, there have been many accomplishments. In the past 2 years several results have been acquired that are seminally significant from a fundamental science perspective. This section lists all major accomplishments in a reverse chronological order, and furnish a statement that highlights its significance.

FY 2002 accomplishments were as follows:

- Development of C-AFM for characterizing local corrosion sites on surfaces. This accomplishment is significant because it is the first known use of C-AFM to map conductivity at surfaces and attempt to correlate this with local corrosion.

- Characterization of biofilms at surfaces using Mott-Schottky analysis and EIS. This accomplishment is significant because it is the first known application of Mott-Schottky analysis for examining biofilms at surfaces.

- Tabulation of Tafel parameters into a database. This accomplishment is significant because it allows one to analyze large amounts of "biocorrosion" data in a statistical manner, which is very important given the variances in microorganism behavior.

- Extension of the biocorrosion task to examining the corrosion of Ni-Cr-Mo alloys for Yucca Mountain project. This accomplishment is significant because it demonstrates that the capabilities developed with ESR funding are applicable to DOE activities.

- Laboratory monitoring of biocorrosion using EN. This accomplishment is significant because EN is a real-time measurement and can be readily implemented in service environments.

- Potential implementation of EN surveillance system in INTEC SNF pools and dry storage environments. This accomplishment is significant because it links INEEL R&D with INEEL Operations, and because it is a realizable field-employable solution arising from ESR funding.

- Presentation of research results at the Gordon Conference on Electrochemistry held in Santa Barbara, CA. This accomplishment is significant because it provided important potential collaboration with Prof. Patrick Unwin and Dr. Julie MacPherson (University of Warwick in the United Kingdom).

- Presentation of research results at the Gordon Conference on Localized Corrosion held in New London, NH. This accomplishment is significant because it demonstrated the success of the biocorrosion task over 2 years, and has led to active collaborations.

- Invited presentation of Biocorrosion task at DOE-BES Corrosion Contractors' Meeting in Upton, NY. This accomplishment is significant because it demonstrated recognition of the INEEL Biocorrosion task within DOE, and it may lead to future funding.

FY 2001 accomplishments were as follows:

- We presented three papers at international symposia detailing our work in the area of localized corrosion.

- Three journal articles were accepted for print. One of which, dynamical SECM manuscript, constituted a seminal work in the field of localized corrosion.

- Successful marketing of techniques developed within the Biocorrosion task to other programs.

FY 2000 accomplishments are as follows:

- Collaboration with ANL-W provided a means to test for microbial growth on actual SNF cladding hulls with strong radiation fields.

- We completed preliminary studies using the SRET.

- A very detailed study laying the foundation for future investigation of drying processes was initiated.

- The surface protein structure of D. radiodurans was examined and we acquired high-resolution in vivo AFM images of the HPI layer within this bacteria. A manuscripts was published in peer literature documenting this result.

- Presentation of results both at regional and national meetings has been a goal during FY 2000. In all, we delivered nine presentations, two of which were invited.

FY 1999 accomplishments were as follows:

- Several species of bacteria were isolated, cultured, and identified from SNF pools at the INTEC.

- The radiation resistance of bacteria isolated form spent fuel storage pool was assessed using high energy irradiation at the Idaho State University linear accelerator facility. A correlation was observed between radiation tolerance and gram positive bacteria.

- Improved methods were developed to maintain sterility in control chambers for long periods of time in coupled electrochemical corrosion cells.

- The SRET analysis enabled imaging localized electrochemical activity on Al 6061 surfaces as a function of microbial environment.

Conclusions

Local corrosion is a problem that requires more detailed understanding than is presently available. The research conducted by the Biocorrosion task has attempted to develop unique research capabilities that will allow an acquisition of data that should provide this better understanding. Biocorrosion requires the level of understanding provided by the research capabilities developed within this project. Most important is that future Biocorrosion research rely on well-defined (representative) sampling techniques rigorous statistical treatments of data than those presented in the peer-review literature. Microorganisms can both evolve and adapt to many environmental variations, and therefore one must not concentrate upon discrete observations but on a statistical treatment of data to predict behavior.

Publications

Accepted or Published

Boxley, C. J., H. S. White, T. E. Lister, P. J. Pinhero, "Electrochemical Deposition and Re-oxidation of Au at Highly Oriented Pyrolytic Graphite. Stabilization of Au Nanoparticles on the Upper Plane of Step Edges", *Journal of Physical Chemistry B* (accepted 8/2002).

Lister, T. E., P. J. Pinhero, "Measurement of Corrosion Dynamics Using Scanning Electrochemical Microscopy", *2002 Electrochemical Society Proceedings* (accepted 10/2002).

Lister, T. E., R. E. Mizia, P. J. Pinhero, "In Situ of Corrosion Events in Austenitic Steels by Scanning Electrochemical Microscopy", *Corrosion* (accepted 10/2002).

Lister, T. E., R. E. Mizia, P. J. Pinhero, "Scanning Electrochemical Microscopy Study of Corrosion Dynamics on Type 304 Stainless Steel", *Electrochemical and Solid State Letters* 5, B33 (2002).

Mizia, R. M., T. E. Lister, P. J. Pinhero, C. V. Robino, J.N. Dupont, "Microstructure and Corrosion Performance of Neutron Absorbing Ni-Cr-Mo-Gd", *Corrosion* (accepted 10/2002).

Pinhero, P. J., T. E. Lister, and R. E. Mizia, "Development of an Electrochemical Noise Surveillance System for Determining Compliance of INEEL High Level Waste Tanks to Corrosion Standards", *Corrosion* (accepted 10/2002).

Pinhero, P. J., T. E. Lister, T. L. Trowbridge, R. E. Mizia, "Analysis of Local Defects in Surface Films on Commercial Alloys Using Conductive

Atomic Force Microscopy (C-AFM)", *Corrosion* (accepted 10/2002).

Wright, R. N., T. E. Lister, W. D. Swank, P. J. Pinhero, "Corrosion Performance of HVOF Sprayed C22 Coatings", *Journal of Thermal Spray Technology* 11 (in print 12/2002).

Submitted or In Preparation

Pinhero, P. J., T. E. Lister, "Conductive Atomic Force Microscopy of Inclusions in Al 6061-T6 Alloys", in preparation.

Presentations

Lister, T. E., poster, Gordon Research Conference on Electrochemistry, Santa Barbara, CA (2/11/2002 – 2/15/2002).

Pinhero, P. J., poster, Gordon Research Conference on Localized Corrosion, New London, NH (7/22/2002 – 7/26/2002).

Pinhero, P. J., oral, DOE Corrosion Contractors Meeting, Upton, NY (8/16/2002 – 8/17/2002).

REFERENCES

1. C. H. Paik, H. S. White, R. C. Alkire, *J. Electrochem. Soc.* 147, 4120 (2000).
2. T. E. Lister, P .J. Pinhero, *Electrochem. Solid State Lett.* 5, B33 (2002).
3. P. Zahumensky, S. Tuleja, J. Janovec, V. Magula, *Corrosion* 57, 874 (2001).
4. R. Nishimura, I. Katim, Y Maeda, *Corrosion* 57, 852 (2001).
5. M. T. Shehata, V. Moore, D. E. Parsons, J. D. Boyd, *Microstructural Science* 12, 329 (1983).
6. S. Jonsson, S. Malm, Scand. *J. Metallurgy* 7, 18 (1978).
7. E.G. Webb, T. Suter, R.C. Alkire, *J. Electrochem. Soc.* 147, B186 (2001).
8. C. A. Zimmerman, "Corrosion Evaluation of ICPP High-Level Waste Storage Tanks, WINCO-1064,Idaho National Engineering Laboratory, April 1989.

Corrosion of Neutron Absorbing Materials

Patrick J. Pinhero, Ph.D., Tedd E. Lister, Ph.D., and Ronald E. Mizia

SUMMARY

The INEEL, through the National Spent Nuclear Fuel Program, is developing corrosion resistant, neutron absorbing structural alloys for nuclear criticality control. These alloys will be used as inserts in the DOE standard canister that will be used to store highly enriched DOE Spent Nuclear Fuel (SNF) in interim (at the INEEL) and long-term storage in the Yucca Mountain Repository. The alloy composition is based on the Ni-Cr-Mo system with gadolinium (Gd) additions. Gd was chosen due to its high thermal neutron absorption properties. The current metallurgical development program has shown that the Gd will be present in the alloys as a nickel, Gd-rich, intermetallic second phase. Preliminary corrosion tests showed that the gadolinide, which intersects the metal surface, may be susceptible to localized corrosion. This would remove some amount of Gd from the structural alloy in some postulated repository solutions. These solutions would contact the SNF and the neutron absorbing structural alloy after breach of the repository waste package. The requirement is that Gd stay in place in the breached canister and continue to retard nuclear criticality. This report describes a corrosion test program that defines the corrosion performance of a simulated gadolinide under a range of postulated repository chemistry conditions.

PROJECT DESCRIPTION

DOE is tasked with the management and disposal of DOE-owned spent nuclear fuel (SNF). The SNF management approach is to package SNF in the DOE standard canister that will hold it during interim storage, transportation, and final disposal at the proposed national repository located at Yucca Mountain, Nevada. The standard canister will need a corrosion-resistant alloy for neutron-absorbing structural inserts for criticality control because of the fuel enrichment and total quantity of fissile material in some DOE SNF. Criticality control for enriched SNF in repository disposal is particularly problematic because the SNF may become more reactive as it degrades from its initial geometry and product form. These structural inserts will also provide SNF geometry control. The structural inserts and DOE standard canister are shown in Figure 1.This alloy must be corrosion resistant under the projected storage conditions so as not to leach out the neutron-absorbing element (neutron poison). The time of greatest significance is when the repository's aqueous environment reaches the inside of the canister after the outer waste package barriers are breached. This is termed the "fully-flooded" condition. Other technical requirements are that this alloy be weldable, have acceptable mechanical properties for American Society of Mechanical Engineers (ASME) code approval, and be produced using ingot metallurgy techniques.

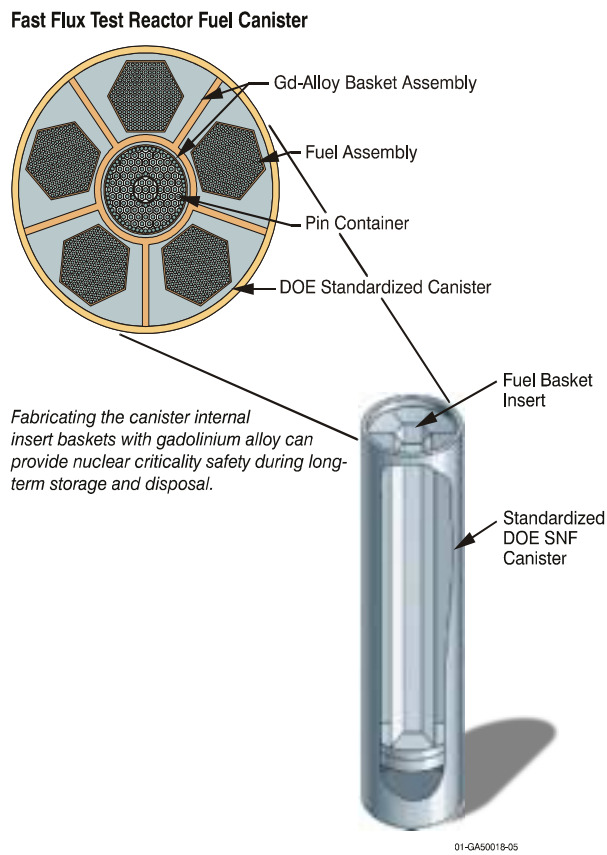

Figure 1. DOE Standard Canister with neutron absorbing structural insert.

An alloy development program is underway under the National Spent Nuclear Fuel Program (NSNFP) that includes the INEEL, Sandia National Laboratory, and Lehigh University. The basic workflow of the program is shown in Figure 2. It consists of defining the alloy system for alloying with Gd, studies of primary melting and secondary refining, thermomechanical processing and testing of mechanical and corrosion resistance properties. This program initially studied 316L austenitic stainless steel alloyed with varying levels of Gd. 316L stainless steel was initially chosen because it has known corrosion properties, and stainless steels have been alloyed with boron for criticality control. The use of boron-containing stainless steel was ruled out because of the lower thermal neutron absorption properties of boron. The microstructure, mechanical properties, and corrosion resistance of these alloys have been described elsewhere.[1–3] These studies showed that Gd has no solubility in the austenitic matrix of 316L stainless. The study of 316L-based alloys was discontinued due to hot workability problems (low hot ductility) associated with the low liquation temperature and extended melting temperature range of the $(Fe, Ni, Cr)_3Gd$ secondary, intermetallic phase associated with these alloys.

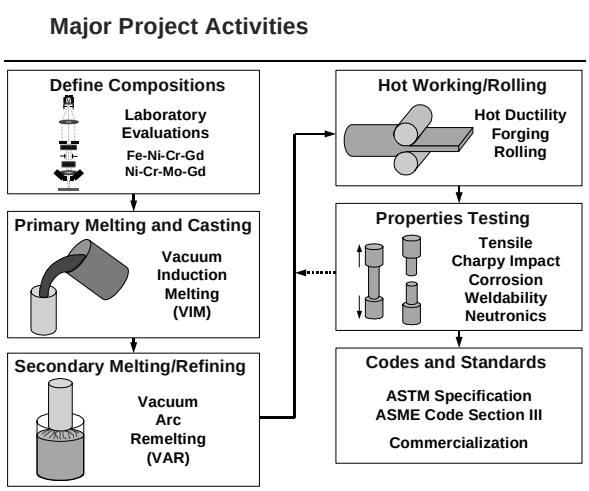

Figure 2. Project workflow.

The alloy development program then shifted to using the Ni-Cr-Mo alloy system as an intermetallic base. These alloys are used to fabricate components that will be used to resist aggressive aqueous environments. The Alloy 22 (UNS N06022) material specified for the Yucca Mountain Waste Package Outer Barrier (10,000-year life) is an alloy of this type. The first Ni-Cr-Mo-Gd trial ingot showed that when you add Gd to a Ni-Cr-Mo matrix, the resultant alloy solidifies with the formation of a primary austenite matrix and a terminal, eutectic-like secondary-phase constituent as shown in Figure 3. As with the stainless alloys, this intermetallic phase will affect the mechanical properties and corrosion resistance of these alloys.

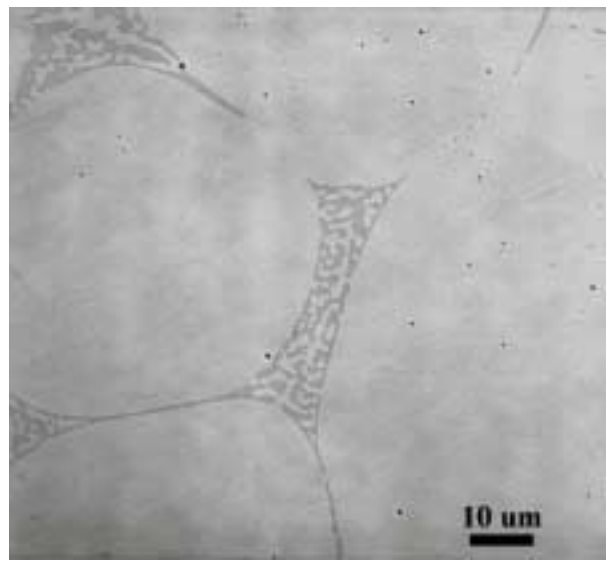

Figure 3. LOM photomicrograph of Ni-based Gd alloy, as cast.

Earlier work with borated stainless steels[4] showed that the ductility of the alloy would decrease with an increased volume fraction of the boron-rich second phase. To balance the goals of maximizing Gd loading, adequate corrosion performance, and meeting the ASME code requirements we are investigating control of the size, shape and distribution of the Gd-rich second phase. The techniques being proposed are: control the initial melt chemistry, molten metal secondary refining techniques such as vacuum arc remelting, and thermomechanical processing treatments.

RESULTS

Ingot/Plate Preparation

Four ingots were produced by the vacuum induction melt (VIM) technique and vacuum cast

into 60 lb ingots with the chemistries shown in Table 1. Heat M322 was produced by VIM with a 300 lb initial melt that was vacuum cast into two 10 cm (3.9 in) diameter equal length round bars. One of these bars was vacuum arc remelted (VAR) under approximately 130 Pa (1 torr) He pressure into a 14.3 cm diameter ingot weighing approximately 64 kg (140 lb). Table 2 shows the results of chemical analysis of the original and VAR ingots. All ingots were hot rolled to a plate approximately 1.5 cm (0.6 in.) thick by 15 cm (6 in.) wide. The ingots were homogenized at 1,160°C (2,125°F) +/- 14°C (25°F) for 16 hours prior to rolling, and then reheated between rolling passes as necessary. Following rolling, the plate was solution annealed for four hours at 1,160°C (2125°F) +/- 14°C (25°F) and quenched with water.

Figure 4 shows light optical micrographs (LOM) of the HV9810A plate in the three principal orientations: rolling plane, transverse to the rolling direction, and longitudinal to the rolling direction. The composition of the second phase (light gray) of the rolled plate was measured with Electron Microprobe Analysis (EPMA) and electron back-scattered diffraction (EBSD). EBSD analysis identified the second phase as a Ni_5Gd intermetallic mixed with other dissolved elements such as Cr, Mo, and Fe. This Gd-rich phase is referred to as a gadolinide. The gadolinide composition was similar in all ingots (see Table 2).

Comparison of these images with the microstructure of a cast ingot (see Figure 3) shows that the shape of the gadolinides evolves during hot rolling. Gd oxides (Gd_2O_3) are also apparent in all three orientations and are visible as small black specs distributed throughout the matrix and occasionally within the gadolinide constituent. Qualitatively, the gadolinides become flattened out intervals up to and exceeding those expected in

Table 1. Chemistries of VIM ingots.

Element	Heat HV9810	Heat HV9812	Heat HV 9813	Heat HV9814
Al	0.042	0.056	0.303	0.055
C	0.011	0.006	0.010	0.009
Co	<0.1	<0.1	<0.1	<0.1
Cr	16.21	21.27	22.64	22.33
Cu	0.004	0.003	0.030	0.06
Fe	0.15	2.02	0.16	0.09
Gd	1.58	1.98	1.82	1.93
Mg	Not reported	Not reported	Not reported	Not reported
Mn	0.10	0.10	0.10	0.10
Mo	14.16	12.01	15.02	0.57
N	0.005	0.007	0.007	0.007
Nb	Not reported	Not reported	Not reported	Not reported
Ni	66.50	59.97	60.77	75.67
O	0.013	0.014	0.021	0.019
P	0.01	0.01	0.01	0.01
S	0.002	0.001	0.002	0.002
Si	0.03	0.04	0.04	0.05
Ti	0.004	0.004	0.005	0.003
W	0.01	2.98	0.13	0.005

Table 2. Results of chemical analysis of Heat M 322.

Element	As Cast Concentration (wt%)	After VAR Concentration (wt%)
Al	0.04	0.005
B	0.0015	<0.001
C	0.005	<0.01
Co	0.01	<0.001
Cr	15.91	14.93
Cu	0.04	<0.001
Fe	0.01	0.028
Gd	2.37	2.38
Hf	0.004	<0.01
Mg	0.0023	<0.001
Mn	0.01	<0.001
Mo	15.30	14.71
N	0.0024	0.0016
Nb	0.006	0.005
Ni	bal	bal
O	0.0004	0.0022
P	0.001	<0.005
S	0.0002	<0.001
Si	0.001	<0.01
Ta	0.002	<0.01
Ti	0.004	<0.005
V	0.003	<0.001
W	0.04	0.015
Zr	0.008	0.001

in the rolling plane and elongated in the rolling direction. The gadolinide constituent is generally distributed as discrete small particles, although these are often aligned along specific planes parallel to the rolling plane. The effect of the VAR secondary refinement of Heat M322 is shown in Figure 5. The Gd level in this alloy is much higher than in HV9810 (2.38% vs. 1.58%). The elongated stringer-like structures of the gadolinides in HV9810 were transformed into a more circular structure where the alignment is not so pronounced.

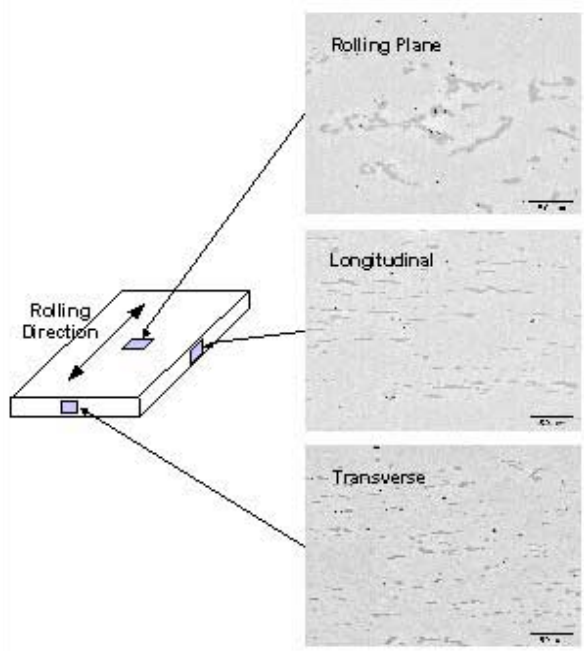

Figure 4. LOM of heat HV 9810A.

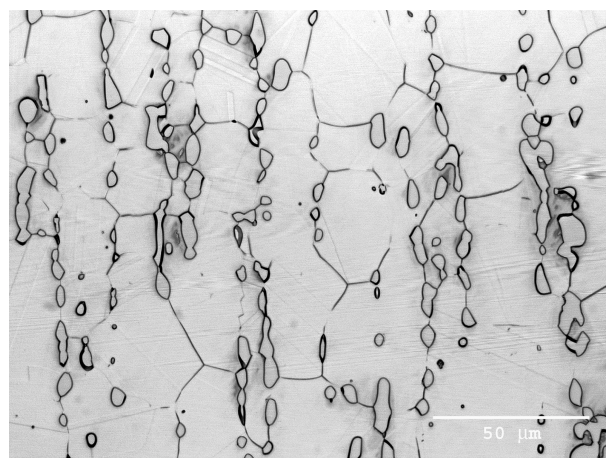

Figure 5. LOM of heat M322.

Mechanical Properties

The requirements for the mechanical property measurements for acceptance of new materials for use in nuclear applications are defined in ASME Boiler and Pressure Vessel Code, Section III, Division 3,[5] and the requirements of various ASME Code Technical Subgroups of Sections II and III. The requirements are defined as tensile testing and Charpy V-Notch (CVN) impact testing. The tests must be conducted at temperature service, and must be statistically valid. Testing must be conducted in two orientations

(longitudinal and transverse) relative to the plate rolling direction. For the Ni-Cr-Mo-Gd alloys currently under development, the temperature range for this testing has been determined to be 23—400°C (tensile tests) and -40–400°C (CVN tests) through analysis of standardized canister performance when loaded with DOE SNF.

Mechanical properties testing was performed in accordance with American Society for Testing and Materials (ASTM) Specifications E 8 and E 23, respectively.[6,7] Heat identity was maintained by insuring only one alloy plate was machined.

The test matrix was based on ASME Code Case N-510 for borated stainless steel,[8] and included tests over a range of temperatures for both test sample orientations. Replicate tension tests were conducted over the same temperature ranges. Testing of the tensile and CVN samples was conducted with calibrated test equipment. The initial strain rate for the tension tests was 0.005/min, and the 0.2% offset yield strength. Ultimate tensile strength, total elongation, and reduction of area at fracture were determined.

Tensile and CVN test samples were machined in two orientations from the finished alloy plate per ASME guidelines (see Figure 6). After the test samples were received, a random sample of 20% of the machined test articles from the heat HV9810 were found to be within tolerance.

Table 4 presents a summary of tensile properties for HV9810 and HV9814 at 23 and 350°C. The strength values for the HV9810 alloy are similar to those expected for commercial Ni-Cr-Mo corrosion resistant alloys, and will be suitable for repository applications. The strength values for HV9814 are lower. The CVN testing data for HV9810 is shown in Table 5. The ASME Boiler and Pressure Vessel Code requirements[9] for impact toughness in nuclear applications call for minimums of 20 J (15 ft-lb) impact energy and 0.38 mm (0.015 inch) lateral expansion, and it is clear that the longitudinal orientation for the HV9810 alloys easily meets this requirement. Impact toughness in the transverse orientation is marginal in this respect. For these alloys, impact toughness is controlled by the particle shape and spatial distribution, as well as volume fraction.

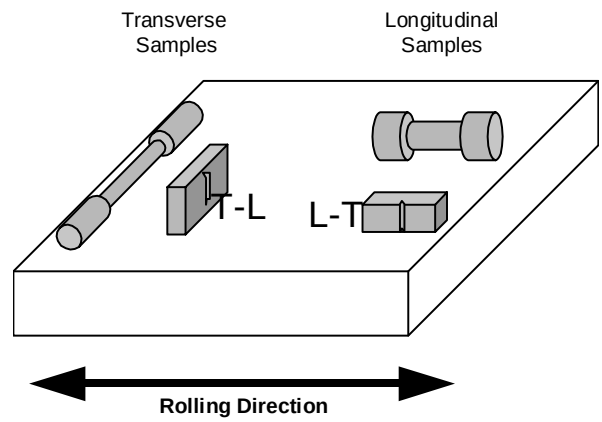

Figure 6. Orientation of tensile and CVN test samples.

Corrosion Testing

Corrosion properties of Ni-Cr-Mo-Gd alloy heats HV9810 and M322 were evaluated using two electrochemical methods: cyclic polarization (CP) and potentiostatic (PS) polarization. The following chemistries were tested: 0.1 M HCl, (30°C), 0.028 M NaCl (30°C), and Yucca Mountain J-13 chemistry.[10] The acidic chloride was chosen for known localized corrosion initiation and is a bounding case for early waste package failure. The J-13 solution is considered to be in-drift, water chemistry at the end of the regulatory period (10,000 years)[11] and is shown in Table 6.

Samples were machined from plate approxi-mately 15.24 mm thick for heats HV9810, HV9814, and M322. The cylindrical specimens were 6.3 mm diameter by 48 mm long for heats HV9810 and HV9814, and 6.3 × 42 mm long for heat M322. The differences were due to the final plate layout for machining of all mechanical test and corrosion samples. The specimens were degreased by sonication in acetone, then ethanol. An initial mass was measured, then mounted in a modified Stern-Makrides electrode assembly. The clean, mounted specimen was placed into a freshly purged corrosion cell as specified by the ASTM G5 standard[12] and fitted with two graphite rod auxiliary electrodes, a saturated calomel electrode (SCE) reference connected through a luggin capillary, and a gas purge. The cell contained 1 L of test solution. The entire assembly was thermo-statically maintained at 30.0°C in a water bath.

Table 4. Summary of tensile properties for HV9810 and 9814.

0.2% Offset

Alloy	Orientation	Temperature, °C (°F)	Yield Strength[a] Mpa (ksi)	Tensile Strength[a] Mpa (ksi)	Uniform Strain[a] (%)	Total Strain[a] (%)	RA[a] (%)
HV9810	Long	23 (75)	372 (54.0)	814 (118.1)	41.7	44.4	88.4
HV9810	Trans	23 (75)	380 (55.1)	789 (114.5)	32.6	33.3	28.8
HV9810	Long	350 (660)	276 (40.0)	709 (102.9)	36.9	39.7	41.2
HV9810	Trans	350 (660)	289 (41.9)	703 (102.0)	33.3	35.1	31.4
HV9814	Long	23 (75)	262 (38.0)	656 (95.1)	33.8	37.0	37.1
HV9814	Trans	23 (75)	270 (39.2)	628 (91.1)	22.2	>22.4[b]	12.7
HV9814	Long	350 (660)	202 (29.3)	572 (82.9)	35.4	39.4	39.9
HV9814	Trans	350 (660)	208 (30.2)	559 (81.1)	30.4	35.7	26.5

a. Average of three tests per condition.

b. All failures outside of gauge length.

Table 5. Summary of Charpy impact values for Heat 9810.

Alloy	Orientation	Temperature, °C (°F)	Impact Energy,[a] J (ft-lb)	Lateral Expansion,[a] mm (inch)
HV9810	Long	-40 (-40)	34.4 (25.4)	0.66 (0.026)
HV9810	Trans	-40 (-40)	18.4 (13.6)	0.39 (0.016)
HV9810	Long	23 (73)	33.8 (24.9)	0.68 (0.027)
HV9810	Trans	23 (73)	19.8 (14.6)	0.45 (0.018)
HV9810	Long	150 (302)	38.9 (28.7)	0.73 (0.029)
HV9810	Trans	150 (302)	21.0 (15.5)	0.50 (0.020)
HV9810	Long	300 (572)	44.9 (33.1)	0.70 (0.028)
HV9810	Trans	300 (572)	28.9 (21.3)	0.53 (0.021)
HV9810	Long	450 (842)	50.6 (37.3)	0.67 (0.027)
HV9810	Trans	450 (842)	32.4 (23.9)	0.57 (0.023)

a. Average of two tests per condition.

Table 6. Well J-13 chemistry.

Ion	Well J-13 Water Concentration (mg/L)
Na^+	45.80
K^+	5.04
Ca^+	13.0
Mg^+	2.01
Cl	7.14
NO_3	8.78
SO_4	18.4
F	2.18
HCO_3	128.9

The CP test follows the requirements of ASTM G 61.[13] In summary, the corrosion potential was measured for 50 minutes prior to the CP scan. CP scans were acquired from the equilibrated corrosion potential to +1.0 V vs. SCE. The potential sweep rate was 0.6 V/hour. PS testing of a duplicate specimen, prepared in the same manner as the CP tests, was performed at 0.20 V vs. SCE in all solutions for 50 hours. The value of 0.20 V was selected because it is the lowest potential where pronounced corrosion activity occurs in Cl-containing media (see Figure 7A). It is believed that this potential corresponds to dissolution of the surface-exposed gadolinide phase.

Following corrosion testing, microstructural changes were documented with scanning electron microscopy (SEM). Both secondary electron (SE) and backscattered electron (BSE) imaging provide information about the topography and secondary phases, respectively. In addition to imaging, energy dispersive spectra (EDS) were also acquired to provide information about the chemistry of each phase. Dual beam Focused Ion Beam (FIB) SEM, courtesy of Sandia National Laboratory, was also used to cross section through secondary phases and corroded areas. SEM of FIB cross-sectioned samples was completed at the INEEL.

A comparison of CP scans for HV9810 and HV9814 alloys in 0.1 M HCl is shown in Figure 8A. In the forward sweep, both alloys show significant currents initially but the HV9810 alloy, which contains more Mo, passivates in comparison to the HV9814 alloy. In the reverse sweep, both alloys display some passivation, with the current density of the HV9810 alloy being much lower. In the second cycle of HV9810 (not shown), the current density remained lower than the initial sweep, indicating a passivation of the surface. For comparison, the current at a Ni-Cr-Mo Alloy 4 (UNS N06455) specimen was tested. As expected for Ni alloys, very low current was observed up to the transpassive region. Figure 8B shows the effect of Gd content. The M322 alloy possesses a higher Gd content and displays a higher current density across most of the potential range. Thus a higher Gd content results in a higher corrosion current. Figure 9 is a BSE micrograph of the HV9810 alloy before performing corrosion measurements, Figure 10 is one after. It is clear that the secondary Gd-rich phase (bright phase) is absent following the corrosion experiment. Additionally, the pitting features appear to be similar to the Gd-rich phase microstructures. It is clear from CP experiments that the surface passivates for the Ni-Cr-Mo-Gd following the initial forward sweep. The evidence points to a removal of the Gd phase exposed to the surface followed by a reduction in the current due to the stability of the remaining primary phase.

Corrosion testing was also performed in J-13 simulant (see Reference 9). Figure 11 shows the CP results. This solution is a much less aggressive, and low currents are observed for both Ni-Cr-Mo-Gd alloys and the borated Type 304 SS. The M322 alloy did show some hysteresis in the return sweep, the HV9810 did not show that behavior. PS tests at 0.2 V were performed for HV9810 and M322 alloys as shown in Figure 7. Measurements in 0.1 M HCl showed a large initial current spike that decayed to less than 0.1 mA/cm^2 by the end of the test. SEM images of both alloys are similar to those from CP experiments with the Gd-rich phase preferentially attacked. In J-13 solution, the current at 0.2 V was four orders of magnitude lower in value than in 0.1 M HCl. The microscopy (not shown) appears the same as the untreated alloy (Figure 10), with no attack of the secondary phase.

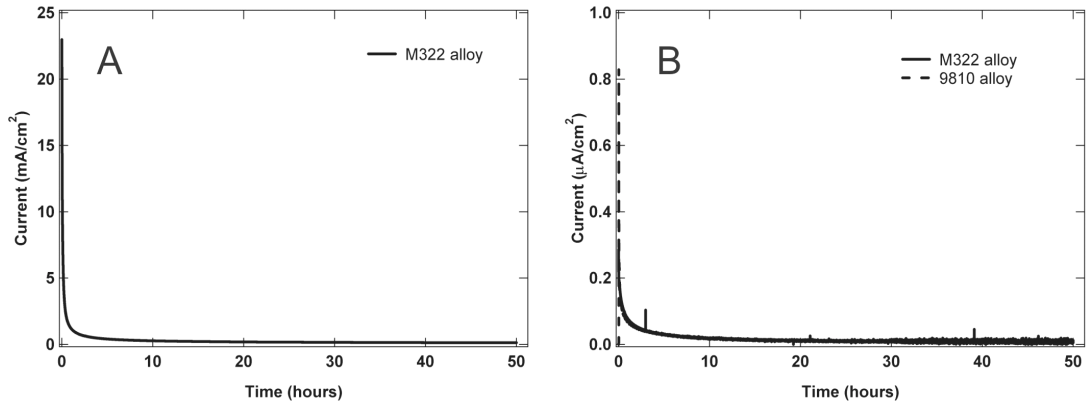

Figure 7. Constant potential results, 200 mV vs. SCE, 30°C: (A) 0.1 M HCl B+; (B) J-13.

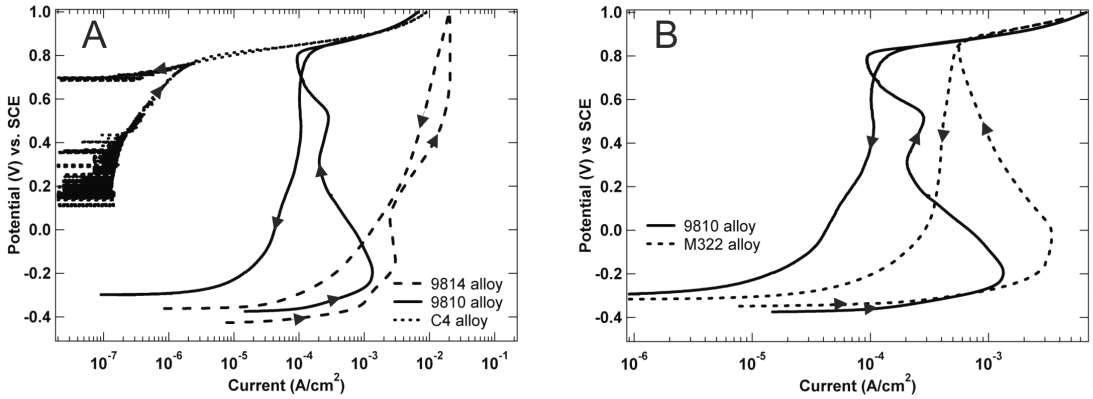

Figure 8. CPP test results in 0.1 M HCl at 30°C.

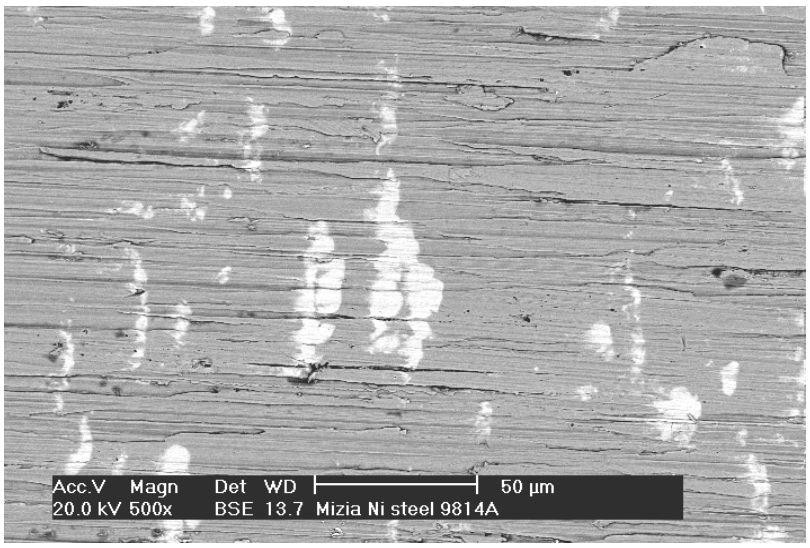

Figure 9. Corrosion sample surface, SEM- BSE, 9810, unexposed, gray particles are $(Ni, Cr)_5Gd$, black particles are Gd_2O_3.

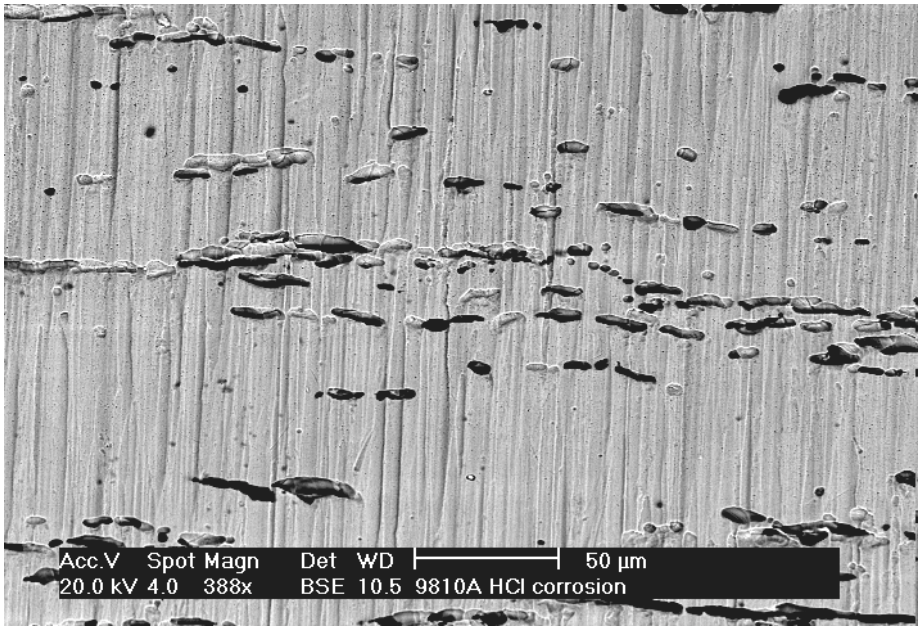

Figure 10. SEM image, BSE, heat 9810 after exposure to 0.1 M HCl at 30°C, $(Ni, Cr)_5Gd$ and Gd_2O_3 on surface removed.

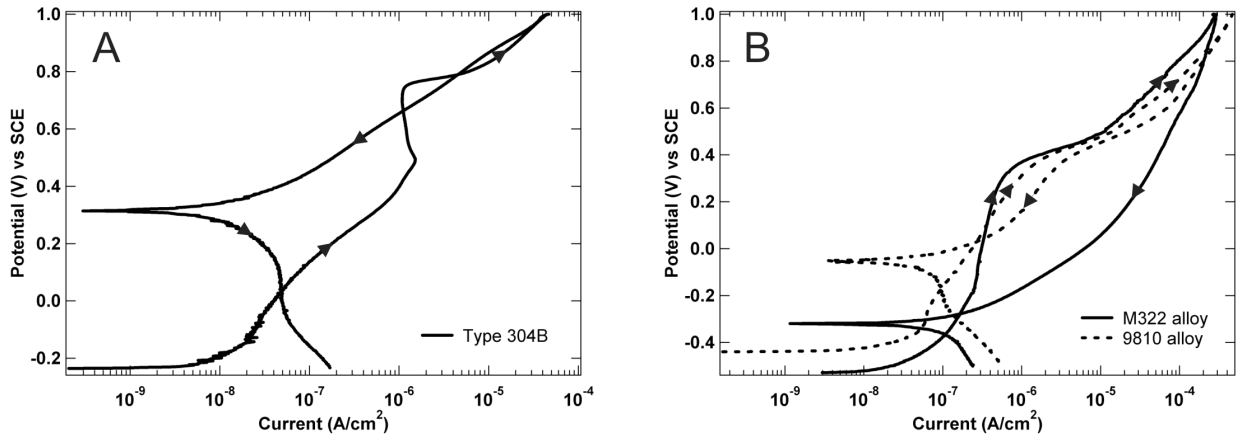

Figure 11. CPP test results in J-13 at 30°C.

Further investigation of the attack on the Gd-rich phase was probed by selectively cross-sectioning in situ using the dual beam FIB/SEM. Figure 12 shows a SE image of the FIB milled corroded area. In this image the gadolinide appears to be subjected to crevice attack as evidenced by the hollowed morphology, both to the side and beneath the Gd-rich particle.

Conclusions and Discussion

One concern relates to the transverse ductility and impact energy as some of these values are below minimum ASME Code acceptable levels. The ductility of similar alloys such as borated stainless steel, which consists of similar brittle second phase particles in a ductile matrix, have been shown to drop with an increasing amount of the second phase. In the case of the Ni-Cr-Mo-Gd alloys under development here, increases in the amount of Gd results in a decrease in alloy ductility. This has implications for meeting the minimum mechanical properties. The mechanical property performance (Charpy Impact) may be affected by our adherence to the standard commercial practices used for fabricating

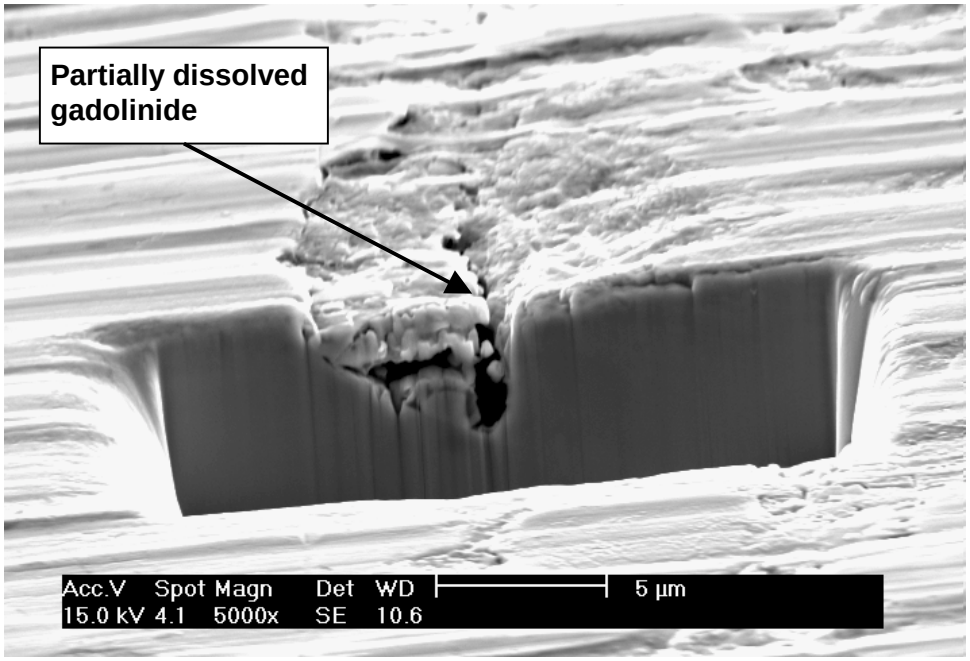

Figure 12. FIB image of partially dissolved gadolinide, after exposure to 0.1 M HCl at 30°C.

Ni-Cr-Mo alloys. We are constrained by the fact that our ingots (6 in. diameter) do not receive the same amount of hot work that a common commercial size ingot (18–24 in. diameter) would receive in being reduced to a plate product with an approximate 1/2 in. thickness. As a result, the amount of secondary phase (gadolinide) refinement due to hot working may be less in our pilot size ingots than in full-scale commercial ingots. Thus, we may be in the unusual situation of having our small-scale results being overly conservative as compared to what may be obtainable with large-scale commercial practice. We are therefore evaluating methods to replicate large-scale hot working procedures in smaller ingots, while at the same time maximizing the alloy mechanical properties.

The corrosion resistance of these alloys will be dependent on the amount of Gd addition, which will determine the amount of the gadolinide that will be present in the alloy matrix. The gadolinide that intersects the surface exposed to aqueous solutions simulating the Yucca Mountain environment might be preferentially attacked and removed, but the underlying Ni-Cr-Mo matrix will then repassivate, and the corrosion rate will drop off to an extremely low rate.

ACCOMPLISHMENTS

This project was initiated in March 2002. In the ensuing 7-month period several key accomplishments were achieved. A successful inter-institutional collaboration was initiated between the INEEL, Sandia National Laboratory, and Lehigh University. This collaboration has produced a peer-reviewed manuscript that was recently accepted for publication. This has initiated interest from potential external funding sources.

Publications

Mizia, R. M., T. E. Lister, P. J. Pinhero, C. V. Robino, J. N. Dupont, "Microstructure and Corrosion Performance of Neutron Absorbing Ni-Cr-Mo-Gd," *Corrosion* (accepted 10/2002).

REFERENCES

1. *Development of Gadolinium-Containing Stainless Steels,* DOE/SNF/REP-066, Idaho National Engineering and Environmental Laboratory, January 2001.

2. R. E. Mizia, P. J. Pinhero, T. E. Lister, J. N. DuPont and C. V. Robino, "Corrosion Performance of A Gadolinium-Containing Stainless Steel," *Paper 138, Corrosion 2001, NACE International, Houston, TX.*

3. J. N. Dupont, C. V. Robino, and R. E. Mizia, "Development of Gadolinium Containing Stainless Steels fro Nuclear Criticality Control," *TMS 2000 Fall Meeting, TMS Society, St. Louis, MO*.

4. C. V. Robino and M. J. Cieslak, *Fusion Welding of Advanced Borated Stainless Steels*, SAND93-3981, UC-704, Sandia National Laboratory, February 1994.

5. ASME Boiler and Pressure Vessel Code, Section III, Division 3, *Containment Systems and Transport Packaging for Spent Nuclear Fuel and High-Level Radioactive Waste*, The American Society of Mechanical Engineers, New York, NY, 2002.

6. ASTM E8-01, *Standard Methods for Tension Testing of Metallic Materials,* American Society for Testing and Materials, West Conshohocken, PA. (2002).

7. ASTM E23-02, *Standard Test Methods for Notched Bar Impact Testing of Metallic Materials,* American Society for Testing and Materials, West Conshohocken, PA. (2002).

8. Case N-510-1 *Borated Stainless Steel for Class CS Core Support Structures and Class 1 Component Supports, Section III, Division I,* The American Society of Mechanical Engineers, New York, NY, 1994.

9. Boiler & Pressure Vessel Code, Section III, Division 3, Containment Systems and Transport Packaging for Spent Nuclear Fuel and High-level Radioactive Waste, The American Society of Mechanical Engineers, New York, NY.

10. J. Harrar, J. Carley, W. Isherwood, and E. Raber, "Report of the Committee to Review the Use of J-13 Well Water in Nevada Nuclear Waste Storage Investigation", UCID-21867, Lawrence Livermore National Laboratory, January 1990.

11. *In-Package Chemistry for Waste Forms, ANL-EBS-MD-000056, REV00,* US DOE Office of Civilian Radioactive Waste Management, March 15, 2001.

12. G5-94, *Standard Reference Test Method for Making Potentiostatic and Potentiodynamic Anodic Polarization Measurements,* American Society for Testing and Materials, West Conshohocken, PA. (2002).

13. G 61-86, *Standard Test Method for Conducting Cyclic Potentiodynamic Polarization Measurements for Localized Corrosion Susceptibility of Iron-, Nickel-, or Cobalt-Based Alloys*, American Society for Testing and Materials, West Conshohocken, PA. (2002)

Near-Surface Engineered Environmental Barrier Integrity

S. J. Piet, R. P. Breckenridge, and project team: J. Beller, D. Burns, L. Chambers, G Geesey, D. Glenn, J. Jacobson, T. Kaser, D. Kunerth, T. Luther, P. Martian, R. Martineau, G. Matthern, E. Mattson, T. McGonigle (Idaho State University), R. Podgorney, I. Porro, and J. Seymour (Montana State University), R. Soto, E. Steffler, A. Stormberg, G. Stormberg, R. Versteeg, and G. White

SUMMARY

Society has and will continue to generate hazardous wastes, which pose risks that must be managed. Risk for exceptionally toxic, long-lived, and feared waste is controlled through deep burial, such as at Yucca Mountain. Some wastes are recycled, destroyed, or treated, while others are stored at or near the ground level (in someone's back yard). Most of these "back-yard" storage sites include a surface barrier (cap) to prevent downward water migration, but some hazards from these caps will persist indefinitely. Indeed, some caps only years old have not shown adequate performance. As society and regulators have demanded additional proof that caps are robust against more threats and for longer time periods, they have become increasingly complex and expensive. As has been found in other industries, increased complexity will eventually increase the difficulty in estimating performance, in monitoring system/component performance, and in repairing or upgrading barriers as risks are managed. We need an approach that will lead to simpler, less expensive, longer-lived, more manageable caps.

The objective of this project, which started in April 2002, is to catalyze a Barrier Improvement Cycle (iterative learning and application), making Remediation System Performance Management (doing the right maintenance neither too early nor too late) possible. The knowledge and capabilities gained will help verify the adequacy of past remedial decisions, improve barrier management, and enable improved solutions for future decisions. We believe it will be possible to develop simpler, longer-lived, less expensive caps that are easier to monitor, manage, and repair. The project plan is to (a) improve the knowledge of degradation mechanisms in times shorter than service life, (b) improve modeling of barrier degradation dynamics, (c) develop sensor systems to identify early degradation, and (d) provide a better basis for developing and testing new barrier systems.

This project combines selected exploratory studies (benchtop and field scale) with the coupled effects of accelerated aging testing at intermediate mesoscale, the testing of new monitoring concepts, and the modeling of dynamic systems. The emphasis on mesoscale (coupled) tests, accelerated effects testing, and dynamic modeling separates this project from other efforts, simultaneously building on that body of knowledge. We are examining the performance of evapo-transpiration, capillary, and grout-based barriers. To date, we can report new approaches to the problem, provide a few preliminary results, and are building new experimental and modeling capabilities.

PROJECT DESCRIPTION

Introduction

The world faces tough challenges in assuring that contaminated materials are isolated and that risks to humans and the environment are maintained legally acceptable, over long time periods. The removal and treatment of wastes at many contaminated sites is technically difficult, expensive, and hazardous, exposing workers and the environment to chemical and radiological contamination. New approaches that include "robust containment and stabilization technologies will be a key factor in the success of DOE's strategy to manage subsurface contamination… DOE's management commitment potentially extends for many thousands of years."[1]

In 1997 the National Research Council reviewed barrier technologies for containment of contaminants, concluding that, "barriers such as surface caps and subsurface vertical and horizontal

barriers will be needed as important components of remediation strategies."[2] They identified the following issues:

- Existing barrier performance data are inadequate; we should learn more how existing barriers are performing.

- Knowledge to predict lifetimes of selected barrier materials and resultant barrier systems is inadequate.

- All ecological and engineering factors need to be considered to predict and enhance long-term performance.

The National Research Council then reviewed the long-term management of DOE legacy waste sites in 2000, citing the need for a much broader, more systematic approach for contaminant reduction, isolation, and stewardship.[3] Their report stated that "the objective is to achieve a barrier system that is as robust as reasonably achievable," given the current limitations. They went on to say that, "the most important consideration in the use of engineered barriers and waste stabilization approaches in waste management is the fact that there is limited experience with most, if not all, of the systems being considered." They concluded that improvements are needed to enhance scientific and engineering understanding of barrier materials and designs.

More recently, the Nuclear Regulatory Commission staff has said that longevity assumptions in current barrier performance assessments "…have no basis in the scientific and technical literature and experience."[4]The Environmental Protection Agency has studied barriers, [5, 6] concluding that data from barriers in service is often not adequate to know if the barrier is providing adequate protection; worse, rarely is there information on the internal condition of the barrier. RCRA and CERCLA caps are often designed for 30-year lifetimes, yet often the hazards will remain toxic. On what basis will cap lifetimes be extended or barriers be upgraded?

DOE studied alternative cap designs at the field scale,[7] yet, many questions remain regarding the short-term (few years) behavior of those caps; long-term behavior is even less understood. The workscope of this project intended to complement the existing alternative cap studies. Meanwhile, DOE is designing caps with long lifetimes, such as the INEEL CERCLA Disposal Facility (ICDF) designed for 1,000 years.[8] Caps are an integral part of DOE's cleanup strategy.[9,10]

To illustrate the challenge, consider the dominant barrier monitoring approach—sample ground water. Finding ground water contamination means that the barrier system has failed, and failed so long ago that contamination has migrated to ground water, thereby expanding the volume to be remediated (at higher cost). The effectiveness of ground water monitoring is weaker when there is a thick unsaturated (vadose) zone between barrier and ground water. In more arid systems, this zone can be hundreds-of-meters thick (hence long transport times), and can have localized preferential flow paths that may be difficult to detect by a finite set of monitoring wells. Newer cap and barrier systems include the use of a leak collection and detection layer under the barrier. (This is generally impractical if the barrier is installed above buried waste without moving the waste.) This reduces the time between system-level failure and detection, but the barrier system has still failed before detection. The trend in other industries is to detect degradation prior to failure to decrease lifecycle cost, extend lifetimes, increase performance, etc.

The development of barrier analytical models have focused on hydrologic models with limited evaluation of other mechanisms of contaminant transport and barrier changes over time. We have not found a peer-reviewed model that defines "failure" and associated processes and events controlling the aging of barrier systems, barrier components and materials, and resulting mobilization and transport of contaminants.

Most accelerated aging barrier work has focused on single components acted on by a single force, such as freezing/thawing, erosion, etc. The testing standards also focused on single components; standards for accelerated aging of barrier systems were not identified. Most work has centered on answering single questions such as: What is the effect of freeze/thaw of geosynthetic

clay liners? We did not find any coordinated laboratory or mesoscale accelerated tests focused on validating analytical models estimating the changing integrity of barriers.

To meet these needs, the INEEL is working to improve understanding in the linkages between how classical engineering can be merged with scientific principles from areas such as ecology, chemistry, materials, sensors, and hydrology. This focus will use an ecological engineering approach to help us improve the way barriers are designed and managed,[11] and better understand and evaluate possible long-term changes in barrier performance. This work will improve understanding of what constitutes degradation, improve experimental capabilities of understanding of long-term degradation processes, establish a dynamic model of long-term degradation, and suggest improved ways to monitor degradation before system-level failure.

What We Need: Remediation System Performance Management

Most environmental remediation problems are multifaceted, thus require multicomponent solutions. For example, closure of even simple landfills requires design and construction of caps, liners, leachate collection systems, and monitoring systems. Remediation of more complicated contaminated sites can also require design and construction of pump and treat systems, vapor vacuum extraction systems, and various in situ and ex situ treatment and disposal operations. The components of a remedial system must work together to protect human health and the environment, so analysis of remedial action effectiveness must focus on the system as a whole rather than a single component.

This distinction has important implications. For example, systems that incorporate multiple barriers to water and contaminant movement (caps, grouts, liners, thick vadose zones, long distances to receptors, etc.) can be designed to allow leakage through each barrier. As long as the system as a whole meets regulatory requirements, one or more of the barriers can fail without causing an unacceptable system response. Under a systems analysis focus, degradation modes for each component must be investigated to identify positive and negative feedback effects on neighboring components. Furthermore, experiments that are designed to test various components of a remedial system must consider physical processes that are controlled by neighboring components. For example, investigation of vapor phase contaminant release from a treated waste form might have to consider the transport enhancement effects of effects of vapor vacuum extraction and the diffusion retardation effects of an extensive cap. Tests of a physical process in isolation may produce incomplete or erroneous data.

Figure 1 illustrates the concept of remediation system performance management,[12] with the following elements:

- Determine how remedial systems will degrade and eventually fail. For our purposes, system failure occurs only if or when regulatory dose limits are exceeded.
- Identify the indicators of degradation.
- Design a monitoring system that is guaranteed to detect the degradation indicators.
- Incorporate positive feedback loops that will allow systems to self-heal to the maximum extent possible (beneficial dynamic processes compensate for harmful processes).

Although this project is working toward such an integrated system, we caution that it does not have the objective nor resources to substantially increase data monitoring, collection, and analysis of field data for the hundreds of caps already in service. We do see this project as encouraging and enabling such a development.

The first of the four elements is the most critical, since a clear understanding of how a system will fail is needed before effective mitigating measures can be planned. Its just that analysis of remedial systems can be complicated.

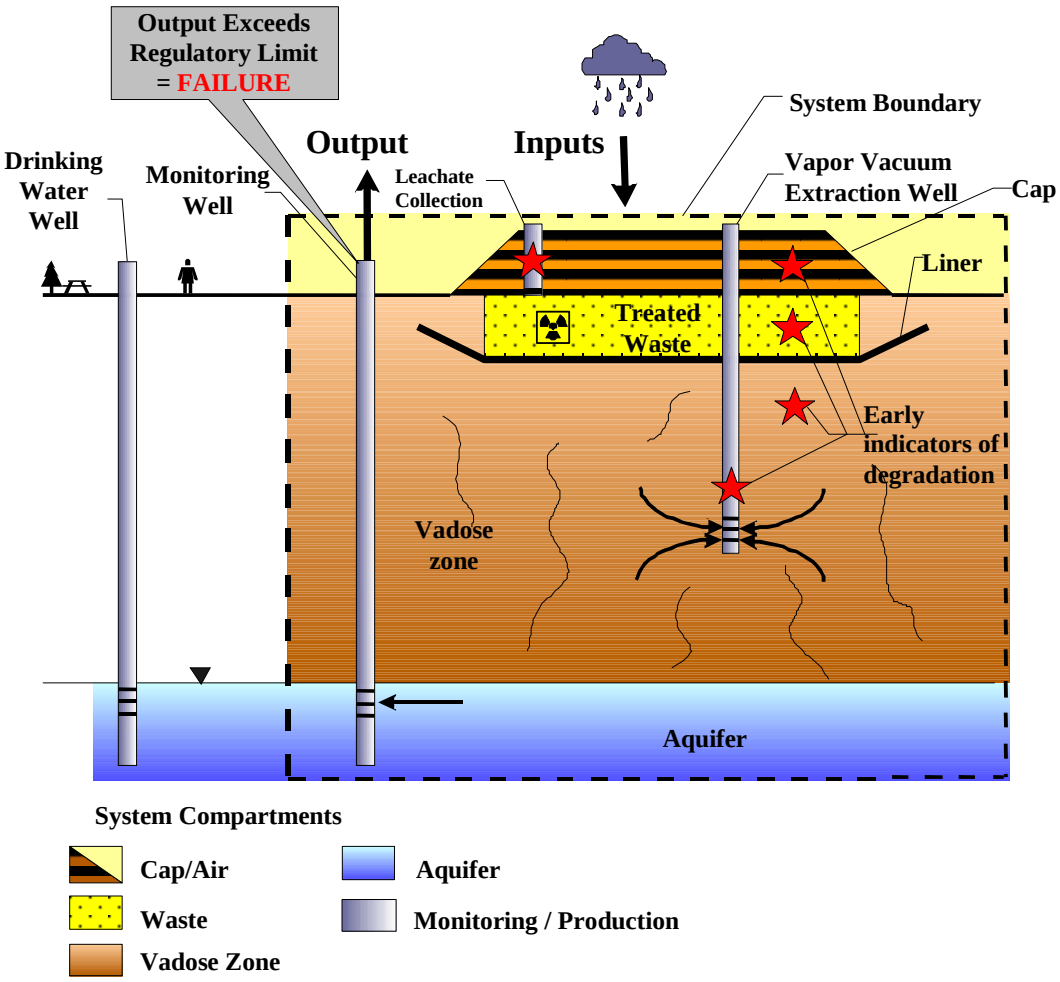

Figure 1. Remediation system performance management.

Certain questions must be answered before completing a list of degradation indicators:

- What is failure?
- What may cause system-level failure?
- What is the probability of occurrence for each contributing event or process?

Likewise, positive and negative feedbacks caused by varying modes for components must be investigated before a complete understanding of the potential for system failure can be developed.

Clarification of system failure enables the other three, interrelated elements. For example, the types and placement of the detectors to be used in a monitoring system are dependent on the physical indicators that must be measured. Yet, limits on detector sizes, sensitivities, cost, and placement restrict the type of indicators that can be selected for monitoring. Similarly, monitoring system response might be required before self-healing steps can be taken. The monitoring system should determine if a response has occurred and measure its degree of effectiveness.

There are at least two benefits to emphasizing system performance analysis during the design of remedial actions. First, evidence suggests that, in complex systems, simplifying component design tends to improve system performance; complicating component design tends to hurt system performance. If this evidence holds for remediation systems, it could support development of simpler and less expensive cap and waste treatment designs. Second, designing remedial

investigations using a systems analysis perspective will improve efficiency of the investigations and reduce the cost of rework. Investigations that consider all variables impacted by operation of a remedial system will avoid shortcomings that result from consideration of only a subset of important variables.

Getting There: Barrier Improvement Cycle

Our analysis of past work and future cleanup strategies suggests that a more comprehensive, systematic approach is needed to continuously improve barrier performance prediction, design, and management/maintenance (see Figure 2). Fortunately, much of the needed knowledge, models, and monitoring techniques exist. This project is aimed at providing additional parts to enable a barrier improvement cycle. Accordingly, the project combines:

- Selected data from the field—specifically looking at microbial behavior as microbes are central to ecology and apparently understudied at present. Plant ecology is extremely important to barrier performance, and it is likely to change over the life of a cap. Changes in plant ecology, microbial ecology, water balance, and soil-building processes are interrelated.

- Tests at multiple physical scales to bridge the gap between field and benchtop tests. This mesoscale regime allows examination of coupling among effects, control of those effects, and sometimes acceleration of effects.

- Dynamic modeling of barrier degradation processes—building on existing hydrological models that assume the barrier structure is static (weather inputs are dynamic).

- Selected exploration of new, noninvasive monitoring techniques that may lead to field deployment. (They also help diagnose tests within the project.)

- Integration of the above parts.

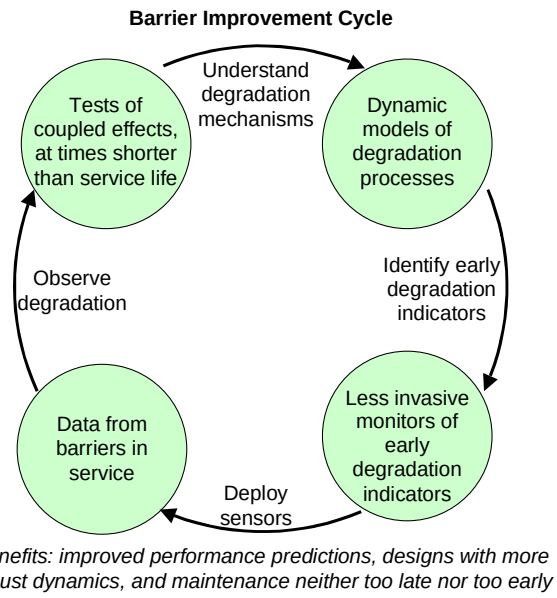

Figure 2. Using knowledge of dynamic processes and mesoscale tests (coupled effects, acceleration) to better predict performance, improve design, and improve maintenance.

These efforts, combined with other past and present work, will increase our understanding of how engineered environmental barriers evolve over time. The project complements the emphasis of other programs on field and bench top studies by emphasizing testing at intermediate scales (mesoscale) where coupling of effects can be observed and sometimes accelerated, and modeling of dynamic processes.

Product improvement cycles similar to Figure 2 are found in many other industries. Indeed, the practicality and effectiveness of such cycles are improving as the information age makes it easier to collect and process data and as the understanding of degradation processes is combined into appropriate dynamic models. "Complex systems foreshadow their failure with subtle changes in performance."[13] To avoid the mistakes of replacing components too early or too late: "Ultimately, improvements and cost reductions in sensors and computing power will enable remote maintenance and diagnostics to move to consumer products. Refrigerators, washers and other appliances will receive instructions and report operating conditions over the Internet."[13]

Similar concepts are being developed in medicine, looking ever earlier for patterns that would indicate new diseases (or bioterror attacks). Similarly, at the individual level, for decades doctors have stressed the value of early detection of illnesses. The likelihood of cure goes up, and the cost tends to go down, as illnesses are detected earlier in individual patients. In contrast, the tendency in barrier monitoring (consistent with regulations) is to only detect contamination in ground water, by which time the barrier has failed, contamination has spread, and further cleanup has become more difficult (if not impossible). We describe this as detecting dead patients (barriers) years after they died (failed). Might it be cost effective and more protective of the public to detect barrier degradation prior to failure?

Similar trends exist at nuclear power plants, where an understanding of system and component aging has allowed a 50% increase in the authorized lifetime (40–60 years) of at least 10 U.S. nuclear power plants. Increased understanding, modeling, and monitoring of degradation has resulted in better power plant maintenance and billions of dollars of economic benefit from extending power plant lifetime.

If this type of improvement cycle can be envisioned and implemented for engines, aircraft, consumer products, medicine, nuclear power plants, etc., why not barriers that protect people from chemical and radiological hazards?

Rationale for Approach

A wealth of information on cap design exists. However, performance data are less available and usually in the form of knowledge derived from a combination of the following:

- Field data from existing barriers regarding effects of stressors since construction (a few decades of experience)
- Field studies of new surface cap designs (Reference 7)
- Small-scale laboratory data on individual effects
- Performance assessments for the deep geological waste disposal projects, which are isolated from the near-surface environmental changes that drive many of the degradation mechanisms critical to near-surface barriers.

One approach to assessing long-term barrier performance is to use experience gained at field sites. Except for applied water simulating precipitation, the effects on barrier performance are usually limited by the rates that natural environmental processes associated with the barrier occur, such as the number of freeze/thaws per year. This approach provides limited understanding of a barrier's performance at a different site, under different climatic conditions, or with a modified design at a similar site.

Another approach is to conduct small-scale, short-duration, single-effect tests such as ultraviolet degradation of synthetic materials, freeze/thaw cycling on concrete, etc. The long-term aggregate effect of these processes is typically modeled by linearly combining the effects of the individual processes. Such an approach does not address the dynamically coupled effects of these processes that can affect long-term barrier performance. This limitation is increasingly important, as barriers become more complex with multiple layers and functions.

These approaches have not been sufficient to establish understanding of the relevant dynamic processes for the entire system. In fact, current barrier models and regulations assume that barriers can be designed, built, and perform at a nearly constant rate over a fixed time. After the design life of the barrier has been expended, its performance is assumed inconsequential. Monitoring of such barriers generally takes place by detecting barrier system failure rather than barrier degradation. (In some places, caps are visually inspected for signs of erosion or subsidence, which could lead to barrier system failure.) The current methodology is to design a barrier for some fixed lifetime, reach agreement with regulators to determine performance requirements, and monitor for barrier system failure rather than monitor the internal performance of the barrier prior to failure (see Figure 3a).

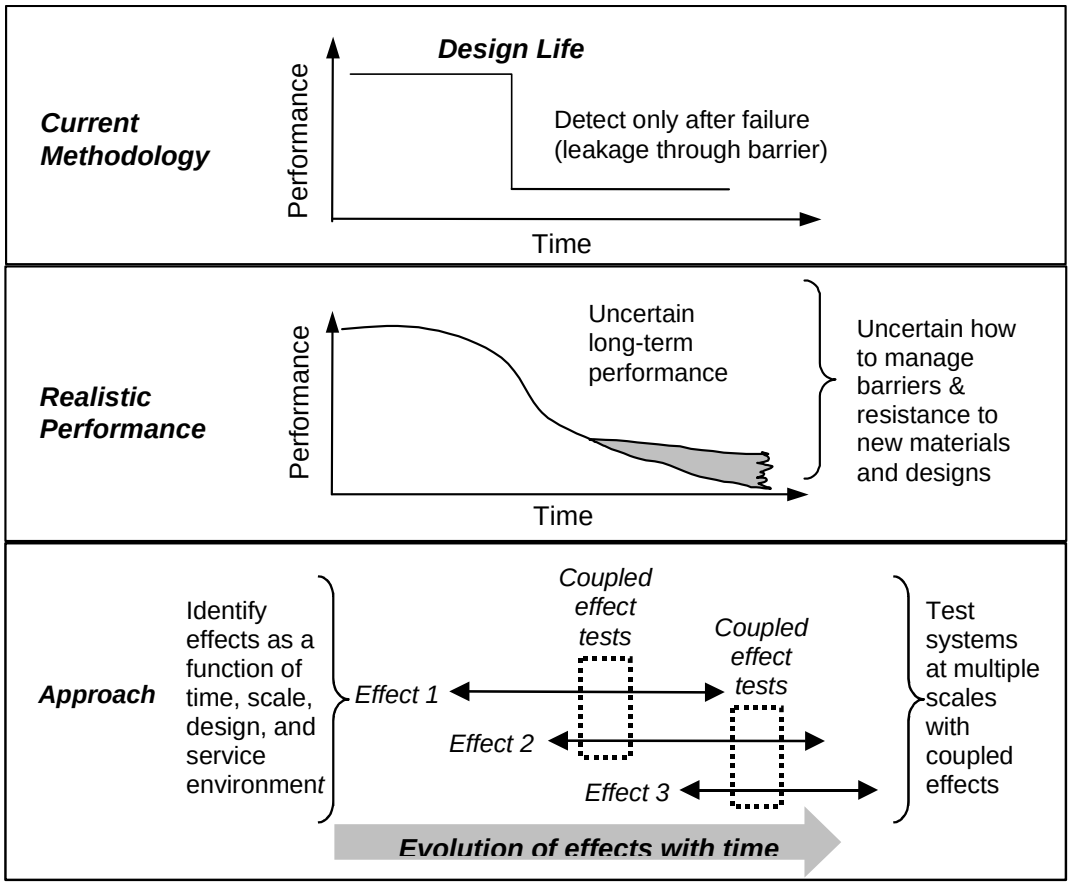

Figure 3. Evolution of barrier performance approaches: (a) current methodology for designing and regulating near-surface barriers, (b) more realistic expectation of how barriers evolve; uncertainties grow with time, (c) practical approach to studying how barriers degrade with time.

The way barriers really perform rarely follows the simple step-function pattern in Figure 3a. Barrier performance generally degrades gradually (see Figure 3b). The short-term performance (less than 10 years) of barriers is fairly well understood and currently the focus of numerous studies. We hypothesize that the uncertainty of barrier performance is embedded in slowly developing coupled processes. These will change the barrier structure and performance. Indeed, the relative importance of processes likely changes as the barrier itself evolves. The identification of these processes and their coupling are not fully understood. Furthermore, the quantitative analysis of the interaction between these processes and their effects has not been performed.

We use a holistic approach to evaluate the performance of barriers for hazardous waste management. This approach will evaluate individual effects on barriers, how individual effects couple, and the relative importance of effects as a function of time. By considering coupled interactions, we hope to significantly advance the understanding of barrier performance and build important new R&D capabilities. The coupled approach is illustrated in Figure 3c.

We considered the range of potential stressors, degradation mechanisms, and effect. We then considered which effects can be tested at what physical scale and with what degree of "acceleration," (see Table 1). We considered which effects might combine to determine which combination of effects should be tested together. The result is a mosaic of tasks, described below. We initiated tests at specific physical scales (see Table 2) for mechanisms that may influence earthen cap performance, with some supplemental tasks for grout and geosynthetic clay liners (GCL).

Table 1. Factors considered in assessing which testing scales are appropriate for each degradation process.

Consideration	Field	Mesoscale (28 m^3), EBTF	Mesoscale (0.3 m^3) BADTL	Benchtop
Which effects are possible to test at this physical scale	All that occur during the period of service, but determining the role of each effect is difficult and some-times impossible	Possible to test most effects	Impractical to test plant or animal intrusion	
Which effects can be controlled	Only control of precipitation is possible (over a limited area)	Can control precipitation, animals, and plants	Practical to control temperature, water influx, soil moisture, mechanical disturbances, colonization of microbes, etc.	
Which effects can be accelerated?	Only control of precipitation is possible	Acceleration of water flux possible, but not biological	Acceleration of most effects (individually and combined) is possible	Acceleration of most effects (individually) is possible
Relative ease of monitoring effects	Low	Generally high		High
Relative duration	Service time (decades)	Years	Months to years	Weeks to months
Relative cost	High cost for many years	Intermediate costs		Low

EBTF = Engineered Barrier Test Facility

BADTL = Barrier Accelerated Degradation Testing Lab

Table 2. Project test matrix showing which processes are being tested at which physical scales.

Degradation processes	Field	Mesoscale (28 m^3), EBTF	Mesoscale (0.3 m^3) BADTL	Benchtop
Microbial influence on soil formation and water transport	Cores		Being considered for future work	Analyze cores
Plant intrusion		Coupled effects (precipitation accelerated)		
Animal intrusion				
Precipitation and wet/dry cycles			Coupled and accelerated effects	
Freeze/thaw cycles				GCL & Grout long-term data
Shake/subside/stress changes				

Understanding Surface Cap Issues (Task 1)

The purpose of this component is to develop a better understanding of the impacts of various forces on the integrity of caps and barriers. Our initial tasks focus on biological phenomena, especially in capillary barriers. Better understanding at normal exposure rates is necessary before knowing the importance of the effects and whether it is needed and possible to accelerate effects.

Effects of Soil-Forming Processes on Surface Caps (Subtask 1.1)

Surface caps for the disposal of radioactive or hazardous wastes are often constructed of homogenized subsoil material from the local area.

Over time, these materials are subjected to natural soil-forming processes caused weathering and the activities of plants and animals. These processes result in the development of strata within the cap material, which may ultimately influence cap performance. The objective of this subtask is to evaluate the changes in the vertical distribution of carbon (C) and phosphorus (P) concentrations in soil cores collected from the Protective Cap Biobarrier Experiment (PCBE) site, and to compare these features with those of soil cores collected from a nearby, undisturbed (mature) site. Organic C (see Figure 5) and available P (see Figure 6) play an important role in the structure and function of the soil ecosystem).[14]

The PCBE was established in 1993 to examine different surface cap designs under different vegetation types and moisture regimes.[15] Because these caps have been in place for 8 years, they in effect provide an example of accelerated soil forming processes. The comparison will provide vital insight into plant-soil interactions within the surface cap and how these interactions progress over time. Ultimately, this information will help with the current assessment of impacts on surface caps due to plant/soil interactions, and enhance models used to predict cap performance.

During September 2001, 144 soil cores were collected at the PCBE site, which is located on the Experimental Field Station at the INEEL. In June 2002, 24 soil cores were collected from an undisturbed site located about 0.5 miles north of EBR1. In each subplot (PCBE site) or plot (undisturbed site), a soil core was collected from beneath a sagebrush canopy and a bunchgrass canopy and in an open area adjacent to that plant. Each soil core was collected to a depth of 15 cm and was cut into segments at certain distances from the surface, which are as follows: 1.25 cm, 2.5 cm, 3.75 cm, 5.0 cm, 7.5 cm, and 12.5 cm, yielding a total of 1,008 samples. Organic C will be determined according to the tube digestion/ heating block method,[16] a modification of the Walkley-Black method,[17] which has been found to improve the recovery of organic C. For plant-available soil P, samples have been extracted with a buffered alkaline solution of sodium bicarbonate,[18] and the solution will be analyzed using an inductively coupled plasma atomic emission spectroscopy (ICP/AES) analyzer.

Capillary Bench Scale NMR Summary (Subtask 1.2)

This subtask expands the capability of nuclear magnetic resonance (NMR) imaging at the micrometer and millimeter scale, to improve understanding of how microbiological growth in subsurface material influences how water moves through complex flow paths that approach those anticipated to develop in caps over centuries. The imaging technique will be evaluated for its potential to relate the impact of bacterial accumulation in preferential flow paths on water flow properties such as dispersion coefficient, local mean velocity, and propagators relevant to spatial and temporal correlations. The objective of this subtask is to establish NMR microimaging capability to noninvasively measure transport in fractures relevant to barrier performance and assess the impact of microbial growth on fracture transport. Toward this end, imaging capabilities on the NMR system in the INEEL Chemistry division were established and synchronized with the Montana State University Department of Chemical Engineering NMR microimaging system. The INEEL system is a wide-bore system allowing samples up to 25 mm; the MSU narrow-bore system has stronger magnetic field gradients and a maximum sample

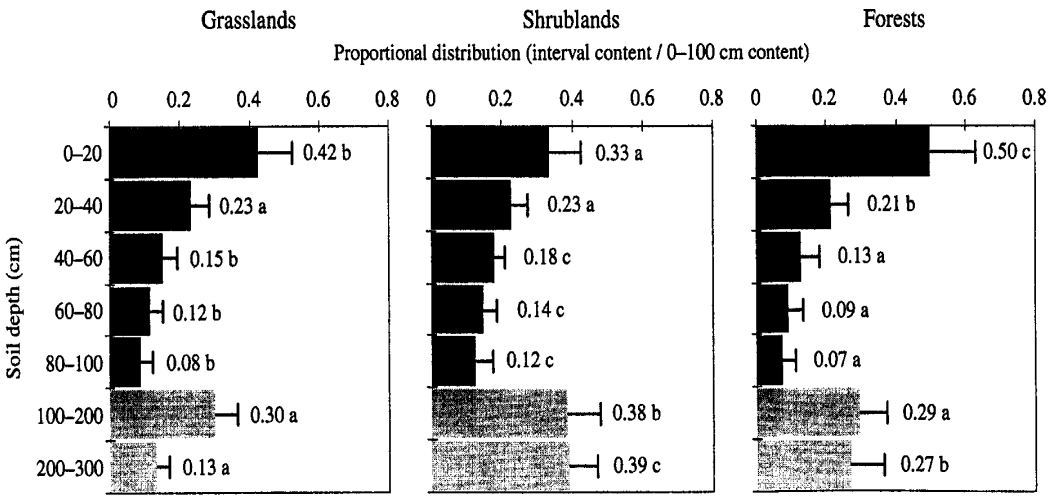

Figure 5. Profiles of soil organic carbon distributions associated with dominant plant functional types (mean + SD). Grasslands are dominated by grasses and other herbaceous plants; shrublands include brush, shrub steppe, and scrub vegetation; forests are dominated by trees, including woodlands. Black bars indicate the proportional total organic carbon distribution in the first soil meter in 20-cm intervals. These values come from averaging the actual proportional values of individual soils. Bars in the first meter sum to one. Gray bars indicate the proportion of additional carbon in the 100–200 cm and 200–300 cm layers; the number to the right shows their contribution relative to the first meter. Values below the first meter were obtained from a smaller number of soils. Letters indicate significant differences among vegetation types at each depth interval (*t* test, $P < 0.05$) (used with author's permission).[19]

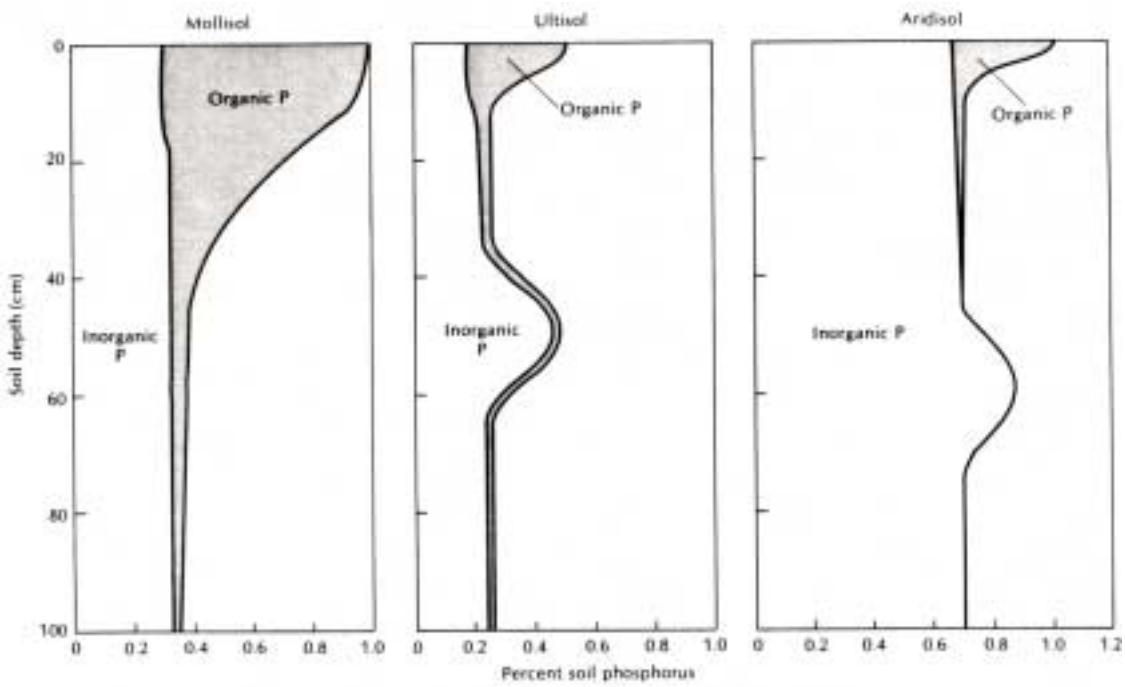

Figure 6. Phosphorus content of representative soils of three soil orders. Organic phosphorus makes up a high proportion of the soil phosphorus in the Mollisol and a much lower proportion in the others. The Aridisol has high phosphorus content because little of the inorganic phosphorus compounds has been leached from the soil. The higher content in the subsoil is due to fixation by Fe, Al oxides (Ultisol) and by calcium compounds (Aridisol).[20]

size of 10 mm. The difference in sample size will allow for the testing of issues related to scale-up of mathematical flow and transport models. NMR microimaging allows spatial resolution of chemical and dynamic information. Spatial resolution is limited to about 20 μm; however, chemical and dynamic information on the molecular nanometer scale, by means of magnetic relaxation, chemical shift or molecular diffusion is available within the 20-μm region.

The capabilities of the systems were established using well characterized, spatially heterogeneous samples. The first was a water sample with 1.15–1.17 mm internal diameter capillary tubes in a 10-mm sample tube at the INEEL, and a 5-mm sample tube at MSU. Figure 7 shows a cross sectional image of the capillaries used to calibrate the magnetic field gradients. The bright regions are the ^{1}H signal from the protons in the water while the dark rings are the glass, which gives no NMR signal. The image is a cross section of the sample tube obtained by selecting a 1.5 mm slice and spatial encoding 256 × 256 points with a field of view of 1.0 cm. The spatial resolution is 39.06 mm/pixel. This verifies the magnetic field gradients are calibrated as the capillaries are circular and 30 pixels = 1.17 mm in diameter. Analogous results have been obtained on the MSU system. As noted above, a primary strength of NMR microimaging is the sensitivity to molecular scale information within spatially localized regions. In this way, information such as pore size or microbial cell distribution on scales smaller than the image resolution can be obtained. Figure 8 shows diffusion weighted NMR images of 1 mm beads filled with Vitamin E oil in olive oil. The beads have a hard shell coating about 100 μm thick that gives no NMR signal. The beads that are directly in the plane of the slice selected for imaging appear as 1 mm circles, while those not centered on the plane appear smaller since only a portion of them is imaged. Quantitative spatially resolved maps of the translational diffusion coefficient can be obtained from these images. The first image in each series in Figure 8a and b are magnetic spin-spin relaxation time, T_2, weighted. Each oil has different signal intensity due to the difference in intermolecular interactions present in each. Diffusion and relaxation time weighting as demonstrated here will allow for spatial determination of microbial activity in porous and fracture samples.

Experiments to image microbial biofilms in a 1 mm capillary and flow model porous bead pack are underway to establish the methods necessary to measure dispersion coefficient, local mean velocity, and propagators relevant to spatial and temporal correlations.

Meso and Field-Scale Testing of Microbial Effects on Capillary Barriers (Subtask 1.3)

Soil cores are being examined to study relationships between microbial growth and hydrologic properties within capillary barrier systems. This effort will evaluate two conceptual models of microbial distribution. The first model assumes that the microbes are uniformly distributed throughout the surface layer of the capillary barrier. The second conceptual model hypothesizes that the fine/coarse media interface will exhibit enhanced growth. Such fundamental understanding should clarify whether microbial effects are positive (increase resistance to water infiltration such as by plugging) or negative (decrease resistance by changing surface tension).

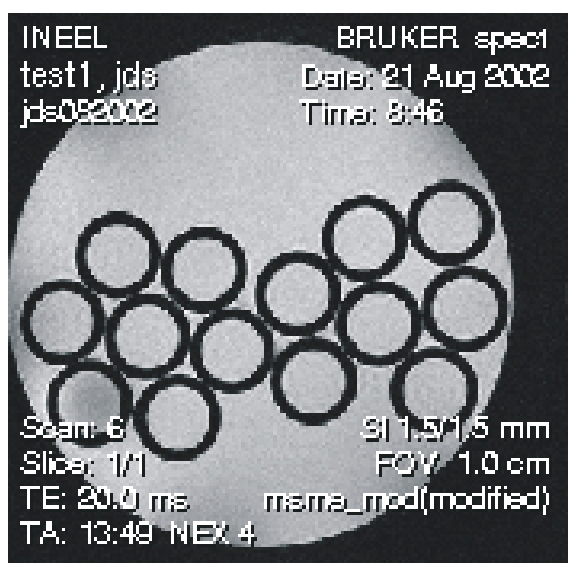

Figure 7. NMR image of 1.15–1.17 mm capillary tubes in a 10 mm NMR tube filled with water taken on the INEEL 300 MHz NMR system.

(a)

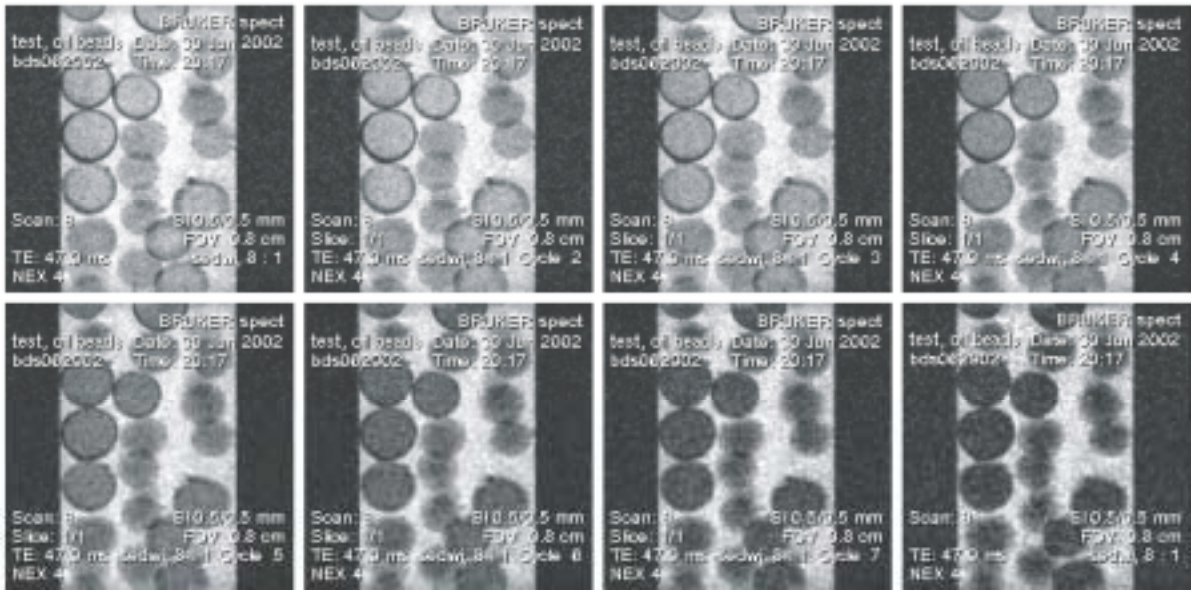

(b)

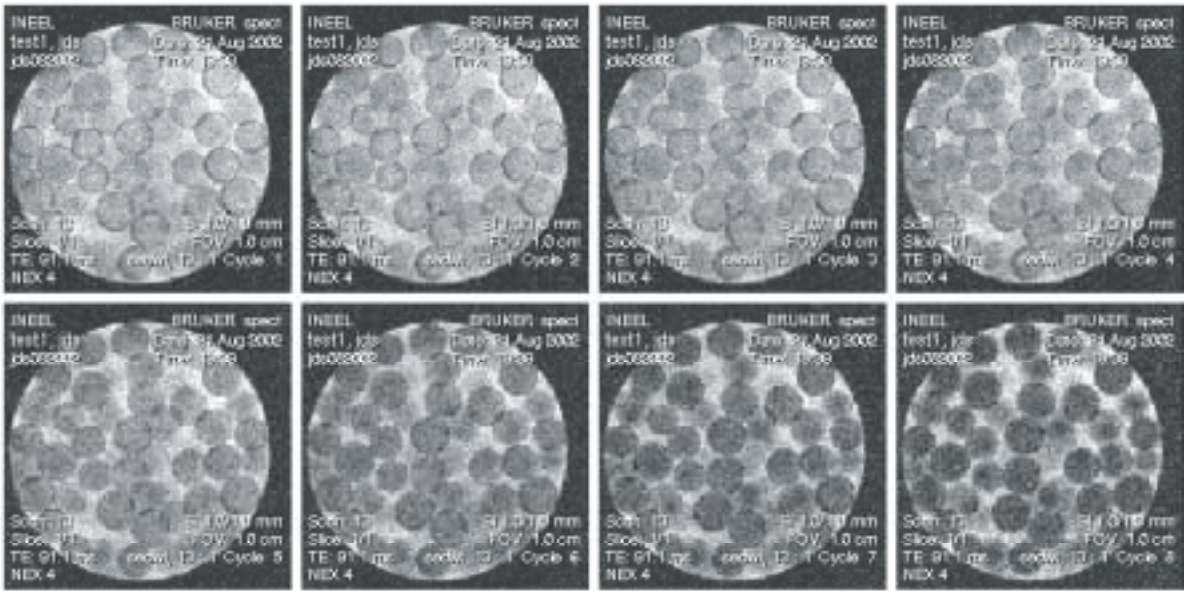

Figure 8. NMR diffusion weighted images of 1 mm vitamin E oil filled beads in olive oil. (a) Images from the MSU 250 MHz NMR system of a 500 mm thick slice of a diameter along the 5 mm sample tube axis with 128 by 128 in plane resolution over an 8 mm field of view for a spatial resolution of 62.5 μm in the first image of the series the vitamin E oil within the beads appears darker since it has a shorter T2 relaxation time than the olive oil. The signal intensity in each successive image (left to right) in the series decreases proportional to translational diffusive motion of the molecules. The faster diffusion of the vitamin E is determined from the faster rate of signal attenuation in the beads relative to the olive oil.
(b) Images of the same beads in olive oil in a 10 mm outer diameter sample tube in the INEEL 300 MHz NMR system. The image is of a 1 mm thick cross section slice of the cylindrical sample tube with 128 by 128 in plane resolution over a 10 mm field of view for a resolution of 78.1 μm. The images are diffusion weighted as in (a).

Many DOE contaminated sites cannot be effectively remediated, and will require a surface barrier to inhibit infiltration through the contaminated soil/landfill. Construction of capillary barriers is the preferred alternative in semiarid sites. Although the soil physical aspects of prototype capillary barriers have been studied extensively and are the basis for prediction of hydraulic performance, the microbial aspect of the capillary barrier has been ignored. It is hypothesized that the mixing/potential addition of organic matter in the capillary barrier surface layer and the interface of the capillary barrier (fine soil over coarse soil) creates ideal environments for microbial growth. Secondary effects of this microbial growth (effects on surface tension, wettability, physical changes of the pore size distribution, etc.) on the capillary barrier performance have not been examined. The effects of microbial growth on long-term capillary barrier performance are not accounted for in hydraulic models.

We hypothesize that the engineering design of DOE capillary surface barriers can enhance growth of microorganisms leading to secondary effects on the hydraulic properties of the soils within these barriers. Depending on the magnitude of the microorganism growth and their distribution within the barrier, the barrier performance could be enhanced or degraded. Two conceptual models of microbial distribution within capillary barriers are examined. The first model assumes that the microbes are uniformly distributed throughout the surface layer of the capillary barrier, the second model hypothesizes that the fine/coarse media interface will exhibit enhanced growth. As a consequence of microbial growth within a barrier, the unsaturated moisture characteristic relationship of the barrier layers is not only a property of the soil matrix itself, but is also dependent on the microbial magnitude and distribution. Results from this work will support the design, operational management, and long-term monitoring of waste isolation using capillary surface barriers.

The first year of this research task examined the physical and microbial distribution of existing DOE sponsored capillary barrier prototype designs in an effort to examine the potential for microorganisms to significantly affect the hydraulic performance of existing research prototype surface barriers. Core samples were collected from two INEEL sites for microbiological-hydrological-geochemical analyses. The first INEEL site was the Engineered Barrier Testing Facility (EBTF) that had two barrier designs to sample, the thick soil design and the capillary/biobarrier design (see Figure 9). These barriers were constructed in 1996. The thick soil design can be used as a base case to examine if the capillary barrier interface is a significant growth area for subsurface microbes (see Figure 10 a for CO_2 profile comparison). The second site, also at the INEEL, is the PCBE, which was built in 1993. This site had three appropriate barrier designs to study; each had natural vegetation established on its surface. In total, five barrier designs were evaluated from these two sites.

Figure 9. Mesoscale Engineered Barrier Test Facility (EBTF).

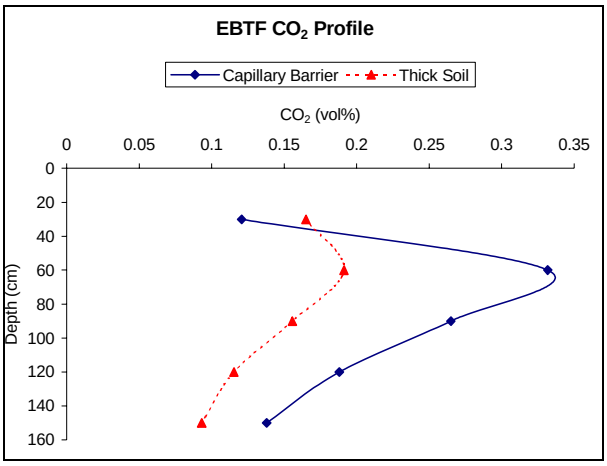

Figure 10. CO_2 profile at the EBTF capillary barrier and the thick soil barrier.

Microbial cell density and activity was plotted against depth (barrier layer, distance from root zone) to determine their distribution within the capillary barrier. Relationships between microbial biomass and activity and other physical and chemical parameters were estimated by correlation matrix analysis. The preliminary result of Phase 1 (analysis of field samples) indicate:

- Microbes do exist in capillary barriers in the range of 1 × 10+7 cells per gram.
- Under current EBTF management practices, the microbial communities do not appear to be affecting the performance of the barrier.
- The assumption of uniform one-dimensional (1-D) flow through the capillary barrier is questionable.
- Pedogenic processes appear to be taking place within the barrier affecting the hydraulic properties.
- In general, the microbial community is fairly uniform throughout the barrier; however, conventional sampling techniques may not be acceptable for microbial interfacial analyses.

Future years of this research will focus on developing quantitative relationships between microbial presence and hydraulic properties at the continuum level. A primary barrier to successful investigation of the feedbacks between flow and transport and microbial activity has been the difficulty in controlling microbial conditions over the time-scales necessary for unsaturated flow experiments. We propose to use geocentrifuge techniques to provide a solution to the time-scale problem. Microbial communities can be established in experimental packages to a desired level. These packages can then be placed in the centrifuge vastly decreasing the time necessary to evaluate the unsaturated hydraulic properties. We therefore propose to use the existing unsaturated flow apparatus (UFA) and the INEEL 2-m geocentrifuge to study the feedbacks between microbial activity and unsaturated flow and transport in environments similar to those encountered at DOE's major vadose zone waste disposal sites.

Sensing Barrier Changes (Task 2)

This task focuses on developing the science and engineering to fill technical gaps in the capabilities to sense changes in the integrity of barrier systems. These tests will be conducted at the most appropriate scale—those focusing on animal and plant intrusion are incorporated into EBTF tests; those focusing on proof-of-concept for cementitious materials are being conducted at the bench-top-scale.

Applications of Electrochemical Impedance Spectroscopy for Monitoring the Long-Term Performance of Caps and Barriers (Subtask 2.1)

The objective of this subtask is to develop electrochemical impedance spectroscopy methods for use in monitoring the long-term performance of caps and barriers. Bench-top scale testing will be carried out to provide proof-of-concept to determine if electrochemical impedance spectroscopy can be used to detect and monitor the progress of various failure modes in cementitious caps and barriers.

Impedance spectroscopy methods are based on the well-established theory of electronic ac (alternating current) circuit analysis with both instrumentation and data analysis techniques being analogous. The fundamental approach of impedance spectroscopy is the application of a

spectrum of small-amplitude sinusoidal voltage excitations to interrogate the system of interest and the measurement of that systems' response. In theory, any intrinsic property that influences the conductivity of a material permeability, porosity, ionic conductivity, etc.) can be examined by impedance measurements.

Techniques based on impedance spectroscopy offer the possibility of providing a reliable and cost-effective means of characterizing and monitoring cap/barrier integrity. The development of such techniques directly addresses DOE long-term stewardship need for low-maintenance, long-lived, noninvasive sensors.

This subtask is designed to provide proof-of-concept experiments to determine if electrochemical impedance spectroscopy can be used to detect and identify failure modes in caps and barriers. Because it is likely that many engineered caps and barriers will be constructed using cementitious materials, initial impedance studies are being carried out on concretes and cement composites (Figure 11).

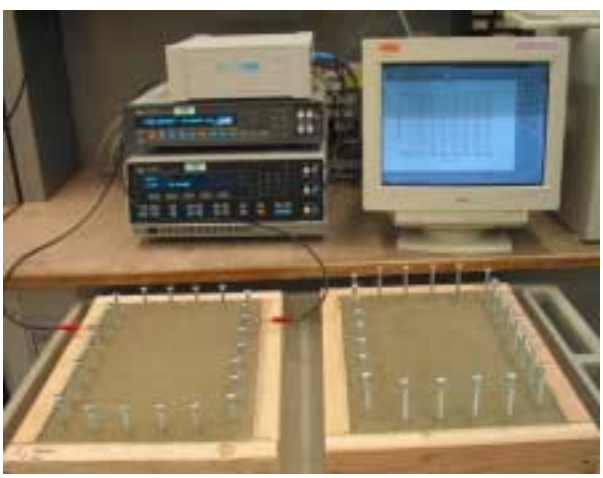

Figure 11. Electrochemical Impedance equipment and concrete slabs with imbedded electrodes.

This study will provide the knowledge base necessary for the complete interpretation of the impedance spectra of cementitious systems. The data will be used to describe the various physical-chemical processes presumed to be important to these systems. Initial efforts will develop electrochemical impedance methods designed to (a) detect and monitor water intrusion into concrete, (b) detect stress/strain on a concrete slab, and (c) detect deterioration of cap integrity due to microcracking.

Less Invasive Monitors of Early Degradation Indicators (Subtask 2.2)

The objective of this subtask is to explore three ideas that facilitate some of the above testing tasks, and that may lead to field deployable monitors:

- Animal and plant intrusion by noninvasive techniques—tested at the EBTF mesoscale.
- Soil moisture, temperature, and pressure by a wireless sensor platform—tested in the field.
- Degradation by electrical impedance spectroscopy—tested at the benchtop scale.

Monitoring of Animal and Plant Intrusion Monitoring by Nonintrusive Techniques. The subtask is evaluating the use of nonintrusive techniques to better understand animal and plant intrusion dynamics. Three nonintrusive techniques are being studied at the EBTF:

- Tracers, which if validated could be used in actual caps in service;
- Ground penetrating radar, which could be used as needed in service;
- Electromagnetic induction, as a proof of principle.

Integration of the soil tracer study with the two geophysical techniques allows us to crosscheck results among the three methods. When integrated with the EBTF testing described above, these studies provide the opportunity to evaluate the techniques under different environmental (precipitation) and surface cover conditions.

A trapping survey performed last year near the EBTF indicates that deer and pocket mice are the most abundant rodent species available at the periphery of those sites, followed by chipmunk, kangaroo rat and ground squirrel.[21] Since deer mice will be used for this study, a protocol was

written to ensure that all the safety issues of handling rodents that are potential Hanta virus carriers were taken into consideration. This protocol follows the guidance and regulations established by the Center for Disease Control and Prevention. In addition, a detailed protocol was prepared by Stoller Corporation describing proper handling and maintenance of rodents in semi-captivity; this protocol is in the process of being presented to local veterinaries for review. Finally, a method developed by Washington State University in collaboration with Stoller Corporation to motivate rabbits to dig into the soil will be tested with the mice.[22] In the spring of 2003 we will place pregnant females in the plots. The pregnant females disposition for digging and nesting, along with the placement of PVC shallow holes, should accelerate the construction of tunnels and burrows in the testing plots.

The mixture of sand/soil is such that in the event of animal intrusion, detection will be evident by the presence of soil tracers brought to the surface of the cap as a result of burrowing. Colored sand was selected since it can be thoroughly mixed with a variety of soils commonly used in caps designed with natural materials. This type of sand is nontoxic and insoluble in water. It also has good stability and weatherability. Before placing the colored sand, we tested the amount needed to be incorporated with the soil mix, and determined an appropriate proportion suitable for easy detection. To test the proportion of sand/soil required, we prepared a titration of different colored sands mixed with the soil and asked a group of volunteers to identify the samples, indicating color of the sand and difficulty in detecting the grains. Based on their responses, we selected the three easiest colors to identify—pink, green and blue. We found the best proportion of sand/soil to be roughly 1–1.5%. The colored sand has been placed in the fine soil in layers of 22 mm. The pink sand was placed at 1.48 m deep, green sand at 1.0 m, and blue sand at 0.58 m. The capillary break is 1.5 m deep. Results will be available in late 2003.

An automated imaging system and different sensors including ground penetrating radar and electromagnetic induction will be set in place. This effort will use time-lapse 4-D geophysics, to collect multiple data sets at fixed 3-D spatial coordinates, remove the complexity of the background, and produce time-dependent changes in physical properties (density, electromagnetic) denoting penetrations in the soils. The design has the following characteristics:

- The gantry system will ride over all plots and retreat into a protected housing. We chose a design where the acquisition unit and motors ride over the rack because weather conditions at the site are such that continued exposure of electronics would be detrimental to a rack and pinion system. The only exposed component of the gantry system will be an anodized aluminum rail. The design was completed and system components have been received.

- The gantry system and geophysical instrumentation can be controlled remotely. It is modular and allows for integrating multiple instruments in a straightforward way. System deployment is weather dependent. A software program was developed to continuously pull weather data from the Internet and write it to a local database where it can be used to interpret results and make decisions on data collection. Another element is integration with a remotely controllable camera that will allow researchers to get real time access to site conditions.

- Data processing, visualization, and interpretation software must drive the whole system. We have identified appropriate visualization software (EVS) and designed a software infrastructure, driven by a centralized piece of controller software (written in Labview/Visual C).

Remote Monitoring of Soil Moisture, Temperature, and Pressure by a Wireless Sensor Platform. Unusual changes in soil moisture, temperature, and pressure could signal that the cap was not performing as anticipated, that degradation could be occurring. Typical monitoring techniques require electrical power and signal transmission lines, thereby necessitating invasive and costly lines to and from the sensors. It would be helpful to develop a sensor platform that could provide information without such complications.

The INEEL has previously developed a versatile micropower sensor interface platform for the purpose of periodic, remote sensing of environmental variables like subsurface moisture, temperature, or radiation (see Figure 12).[23] The key characteristics of the platform architecture are that the components are passive thereby requiring no internal power source and that it communicates with a reader via short-range telemetry. Other attributes include the potential for a long service life and compact size that makes it well suited for retrofitting existing structures. Functionally, the sensor package is read by a short-range inductive coil that both activates/powers the sensor platform and detects the sensor output via a radio frequency signal generated by the onboard programmable interface/controller microchip. Inherent to this approach is an operational depth limit and power budget in which sensors must function. Operational depths will be limited to the distance the induction field can be projected into the ground as defined by the electrical/physical characteristics of the antenna systems and electromagnetic properties of the soil. The practical operating depth is about two meters. (This illustrates that thicker caps are generally more difficult to monitor.) Almost any low power sensor can be integrated that fits within the operating parameters of the analog to digital converters in the controlling microchip and the platform's power budget.

This subtask provided for the installation of the sensor platforms at the Gilt Edge Gold Mine in South Dakota, providing an opportunity to install and demonstrate the capabilities of the INEEL wireless sensor platform. Sensor packages were assembled, transported to the site, and buried in the gravel layer below the liner. The liner is presently being put into place and covered with topsoil. Three sensor packages were assembled and installed. Assuming the sensor platforms survived final barrier construction, they will be demonstrated at a later date.

Acceleration and Coupling of Processes (Task 3)

This task explores acceleration and coupling of bench-top and mesoscale processes, and will have several subtasks that will be worked together to ensure consistent approaches to accelerated aging.

Figure 12. Sensor platform installed a the Gilt Edge Mine.

Effects of Long-Term Freeze-Thaw Cycling on the Hydraulic Integrity of Geosynthetic Clay Liners (Subtask 3.1)

Geosynthetic clay liners (GCLs) are geocomposites that typically consist of a thin layer of dry bentonite between two layers of geotextiles or attached with an adhesive to a geomembrane.[24] An important issue or concern in areas of the country with cold climates is whether freeze-thaw cycling affects the hydraulic integrity of GCLs. Laboratory studies on GCLs have shown that they retain their hydraulic characteristics when subjected to short-term or limited freeze-thaw cycling.[25] Given that evaporation ponds, landfills, and other cap/barrier structures are being constructed with anticipated or required functional life spans of tens or even hundreds of years, some regulatory agencies are requiring overly conservative designs to make up for the lack of long-term data.

There is an identified need for a better understanding of the long term physical and hydraulic properties of GCLs. The objective of this research is to test and determine the performance and hydraulic integrity for a variety of commercially geosynthetic clay liners when subjected to long-term freeze-thaw cycling.

The scope of the present phase of the research is to perform laboratory freeze-thaw tests of three GCL materials using a flexible wall permeameter. Samples of three commercially available GCLs have been obtained from CETCO, including those to be used in current designs at the INEEL. These are Bentomat ST (see Figure 13), which will be used for the INEEL CERCLA Disposal Facility (ICDF) evaporation ponds, Bentomat DN (see Figure 14), which will be used for ICDF landfill and evaporation ponds, and Claymax 600CL, which will be used for comparison with previous studies. Current literature reports freeze-thaw testing of GCLs that regularly perform up to 20 cycles of freeze-thaw. The current research will increase the number of cycles to at least 150 (time permitting up to 300) to provide a sound base for future design and regulatory decisions.

The general approach will be to measure the hydraulic conductivity of the test specimens prior to freezing and thawing in order to establish base hydraulic conductivities, and then measure hydraulic conductivity after a given number of freeze-thaw cycles. Hydraulic conductivity tests will be performed on 70 mm diameter test specimens in a flexible wall permeameter. After determining the test specimen's hydraulic conductivity, it will be placed in a freezer for 24 hours to freeze the GCL. The GCL will then be allowed to thaw for 24 hours before being either retested or refrozen.

Experimental Approach. The general experimental approach will be to measure the hydraulic conductivity of the test specimens prior to freezing and thawing to establish base hydraulic conductivities. We will then measure hydraulic conductivity after a given number of freeze-thaw cycles. Hydraulic conductivity tests will be performed on 70 mm diameter test specimens in a flexible wall permeameter. After determining the test specimen's hydraulic conductivity, it will be placed in a freezer for 24 hours to freeze the GCL. The GCL will then be allowed to thaw for 24 hours prior to being either retested or refrozen.

A literature search was conducted to ensure that comparable long-term studies had not already been done and to determine the protocols and methods used so that our research could be performed in a similar manner for comparability purposes. The task has been completed.

The methodologies used to conduct the freeze/thaw cycling and the hydraulic conductivity tests are a compilation from several different sources, including ASTM,[26-28] Geosynethic Research Institute's GCL-2 Test procedure for determining hydraulic conductivity of GCLs,[29] and operating instructions for the system.[30]

Laboratory procedures have been developed per ASTM standards (see experimental approach). This involved reviewing several applicable standards and then developing a single procedure. This task is complete.

A working assumption for the laboratory tests is that three freeze-thaw cycles will equal one calendar year. The hydraulic conductivity will be measured after the number of freeze-thaw cycles representing 0 (control), 1, 3, 5, 7, 10, 15, 25, 50, 75, and 100 years. A total of three individual specimens of each of the specific GCLs will be measured for the total number of freeze-thaw cycles. This will make for a total of 99 individual samples (33 of each GCL).

The second phase of the research will be to evaluate the effects of repeated freeze-thaw cycling at the bench top or mesoscale. The general approach will be to incorporate GCLs into a typical evaporation pond liner design in a $3 \times 3 \times 3$ ft freeze-thaw chamber. The entire system will then be subjected to repeated freeze-thaw cycling and the GCLs hydraulic conductivity measured. This data will be compared with the laboratory-scale data.

A three-cell flexible wall permeameter was procured, tested, and calibrated and is now being used to perform hydraulic conductivity measurements on test samples. Two bench-scale (mesoscale) $3 \times 3 \times 3$ ft freeze-thaw chambers were procured and arrived at the INEEL on August 29, 2002. These chambers are now being prepared for use.

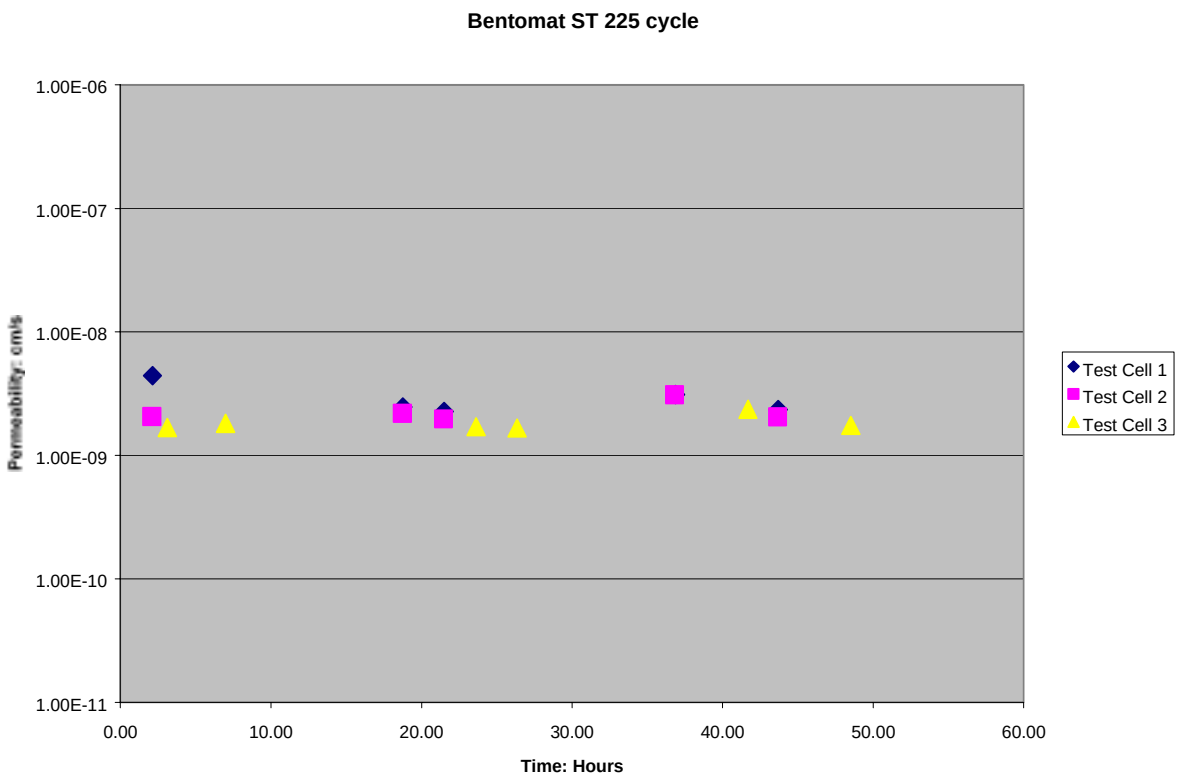

Figure 13. Initial hydraulic conductivity baseline data of the Bentomat-ST liner material.

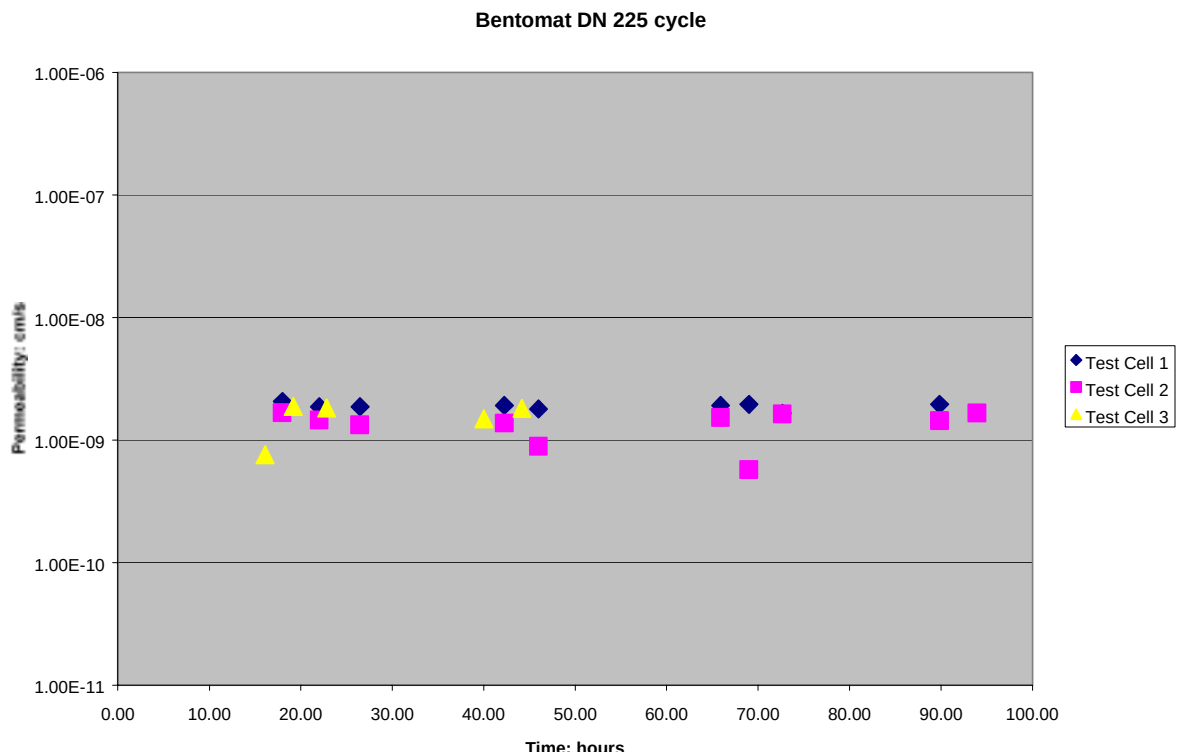

Figure 14. Initial hydraulic conductivity baseline data of the Bentomat-DN liner material.

Long-Term Performance of Grout (Subtask 3.2)

This subtask investigates the degradation of grout material and surrogate waste materials as a result of thermal cycling with and without water at bench-scale. The PI is working closely with INEEL EM personnel to determine what grout systems are most likely to be used at the INEEL and design the tests based on these grout systems. The task lead is working with the Capillary Barrier Profile Changes, Mesoscale Testing of Mechanical Effect and Long-Term Performance of GCL subtasks to develop a consistent approach to freeze-thaw testing. A consistent approach to mesoscale design for cap and barrier testing is also being refined.

An acceleration of process study is evaluating the engineered material grout with direct relevance to INEEL cleanup needs. This study is initially focused on bench-top scale, but we will proceed to larger-scale, multiple-effects as appropriate. Because the INEEL has a cold, semiarid climate, freeze/thaw cycles are particularly important relative to grout mechanical stability.

The objectives of this work are to characterize the negative effects of freeze thaw cycles on the mechanical integrity of grout systems. Simplified cement based materials are being used to establish baseline experimental data to compare directly with formulations slated for deployment. A range of sample sizes are being used to determine optimal test procedures in addition to identifying geometry-sensitive processes. Figure 15 shows the range of specimen sizes currently being used. The material response to freezing with and without water will provide the science based data to justify a specific implementations of grout.

An 11 ft^3 environmental chamber will be used for all bench scale testing. A high heat capacity chamber will be used to conduct precise thermal tests of grout and related materials under controlled conditions. The complete progression of damage accumulation will be characterized by sample sectioning at known damage states. These data will then be used to refine a test matrix involving remotes sensing capabilities and to make direct durability evolutions of specific grouts.

Figure 15. Range of grout specimen geometries being used for bench scale durability testing.

Preliminary finite element models have been created to approximate the mechanical effects of freezing water within cement based materials with large metallic waste forms. Early models show the thermal effects of a water reservoir in concrete that experiences freezing. Simulations of modest temperature changes results in significant stresses that predict grout failure. Figure 16 shows preliminary mesh (2a) and contour plots (2b) of thermally induced stresses in response to water-grout interactions during temperature changes..

Acceleration/Performance—Accelerated Precipitation Effects on Coupled Processes (Subtask 3.3)

The objective of this subtask is to determine the accelerated precipitation effects on coupled processes and interaction among (a) cap performance, (b) vegetation, (c) soil microbiology, and (d) small animal burrowing. Accelerated testing will be implemented by artificially increasing the precipitation level experienced by the test caps, based on the fact that water is a significant driver of processes in the cap. Increased levels of precipitation will represent possible future (worst-case) environmental conditions. The subtask is designed to test the hypothesis that cap performance resulting from the multiple interactions among soil cap processes and accelerated environmental conditions differs from cap performance observed under single-effects testing.

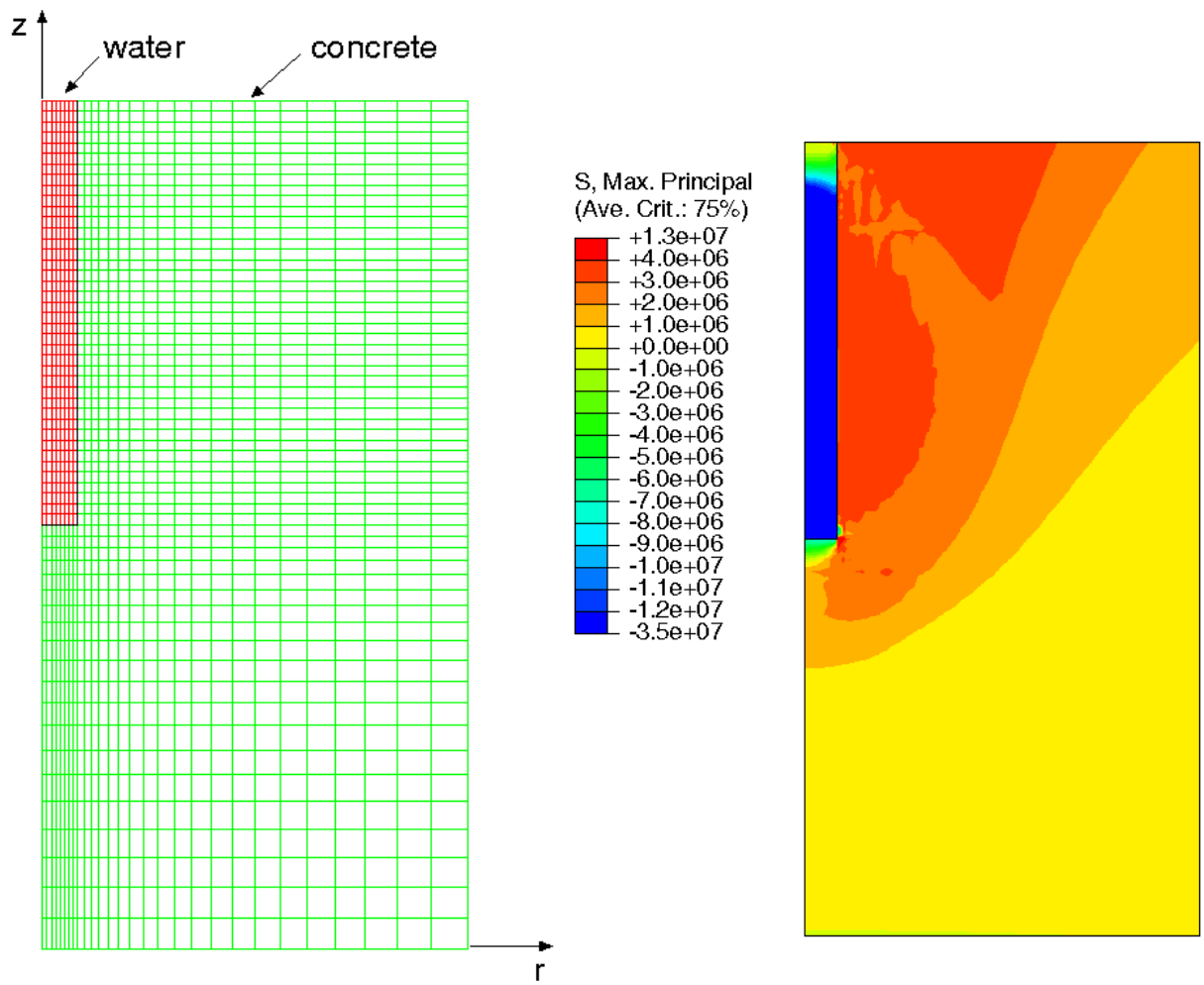

Figure 16. Preliminary mesh with water-grout combination (a). Contours illustrate the regions and magnitude of thermally induced stresses in response to freezing water (b).

This work will be conducted at the EBTF. Mockups of an evapo-transpiration storage-type soil cap will be constructed and instrumented to measure soil moisture, soil moisture tension, soil temperature, and drainage. Overall soil cap performance will be evaluated in terms of the cap's water balance. Test plot vegetation and soil microbial populations also will be assessed.

This subtask is integrated with subtask 2.2 by providing the test caps and supporting the small mammals. Integration with the geophysical techniques study also provides the opportunity to evaluate the geophysical techniques under different environmental (precipitation) and surface cover conditions. Although the focus of the geophysical techniques subtask is on biointrusion detection, data collected from Subtasks 2.2 and 3.3 also will be used to explore correlations between geophysical measurements and soil physical and hydraulic properties in the caps.

This subtask also provides the opportunity to retrieve vadose zone monitoring instruments that have been buried since 1996. During the dismantling of existing test plots at the EBTF in preparation for building the new test plots, heat dissipation sensors and thermocouple psychrometers will be retrieved and recalibrated. The new calibrations will be compared to the original calibrations. The objective of this facet of the subtask is to determine how buried instrument calibrations change over time, and how these changes affect interpretations of cap performance.

The JSA for dismantling and reconstructing the test cells at the EBTF was approved to allow work to begin July 1, 2002. An industrial vacuum truck was subcontracted to help remove soil and dismantle the EBTF test plots from the previous experiment. Dismantling of all six test cells was completed. Heat dissipation sensors and thermocouple psychrometers from the previous experiment were recovered during dismantling for the buried instrument recalibration study (Figure 17). All six test cells were backfilled to about the 4-ft level to begin the cell reconstruction. All existing cell wall penetrations that will not be used in the new test plot configuration were sealed. Five new penetrations were drilled through the test cell side walls. Plywood "floors" used to provide support and protection for the cell geomembrane liners were installed. Dividing walls used to create two test plots in each test cell were installed. Plumbing systems for test plot drains were installed and tested for water flow continuity.

Figure 17. Buried instrument retrieval during dismantling of previous experiment test plots at the EBTF. The instruments will be recalibrated to evaluate calibration stability over time under field conditions.

The geomembrane liners used to seal the bottom of the test plots were installed. The calibration of new TDRs and heat dissipation sensors for installation in the test plots was completed (under subcontract). Thermocouples recovered from the previous experiment were checked for proper function in preparation for installation in the new test plots. Instrument towers for buried instruments are being constructed and installed as test plot construction progresses (See Figure 18). The automated data acquisition system has been designed and will be installed as soon as the instrumentation in the test plots is installed. Test plot reconstruction should be completed in September; initial data collection from the test caps will commence immediately thereafter. Establishment of vegetation on selected test plots is scheduled for October.

Figure 18. Colored sand and instrument tube tower used for biointrusion monitoring studies at EBTF plots.

Acceleration/Performance—Capillary Barrier Profile Changes, Mesoscale Testing of Mechanical Effects (Subtask 3.4)

The objective of this subtask is to evaluate the susceptibility of capillary barriers to degradation over time in response to various stressors such as freezing/thawing cycles, wetting/drying cycles, shaking, and the interaction of these stressors. The study is based on the hypothesis that repeated exposure of the barrier to these stressors will alter the physical structure of the barrier, thus altering the barrier's hydraulic properties and affecting subsequent performance. This study seeks to accelerate the application of the stressors to address long-term performance concerns. To do this requires the test barrier to be subjected to numerous cycles in a relatively short time. The application of stressors also needs to be applied in a manner that will mimic field conditions. Translation of these requirements to testing at the field- or EBTF-scale is difficult, if not impossible, so this subtask focuses on the use of mesoscale test barriers that provide the ability to manipulate the environment to evaluate accelerated effects on barriers.

A test matrix outlining the experimental treatments and interactions to be explored in this subtask was developed. Independent Hazard Review documentation to carry out this subtask was developed, submitted, and approved.

Dr. Hilary I. Inyang visited the INEEL and was briefed on the objectives and proposed experimental methods. He provided feedback on the experimental treatment matrix and methods leading to a reevaluation of the test matrix. Numerical modeling of treatment effects on the mesoscale experimental barriers was performed to aid the experimental design and help determine equipment and material needs. Orders were placed for apparatus needed to implement the stressor treatments.

The next smaller scale is ~1 m^3. Compared to EBTF, we lose the ability to have colonies of animals, and therefore, cannot test animal intrusion. However, we gain ability to manipulate the environment to evaluate accelerated effects on barriers. We will build upon the data for capillary barriers at the field scale (Reference 7) and EBTF scale. However, we wish to use this mesoscale to explore behavior in long-term data and help provide data to support analytical predictions. Specific mechanisms to be evaluated include seismic/subsidence activity, freeze-thaw, and water infiltration at mesoscale.

Modeling of Barrier Degradation Dynamics (Task 4)

Our approach to modeling involves different scales, but the different scales refer to the dimensionality and sophistication of the models, not physical size. The long-term multiyear objective of this effort to develop a suite of models that incorporates stressors and effects that assesses and predicts barrier risk as a function of time. The models need to be able to assess uncertainties in a probabilistic sense and provide insights to the value of information; for example, by reducing the uncertainty in parameter X, we reduce the uncertainty in calculated risk by Y at a future time period Z. Often the nature and amount of uncertainty change with time as the barrier evolves and the relative importance of stressors/effects therefore changes. This will guide both R&D and operational management of barriers and complement and enhance existing risk/uncertainty analyses (Reference 31).

4-D Hydrology Performance Assessment Model Development (Subtask 4.1)

The objectives of this task are to begin development of an all inclusive barrier simulation code for evaluating the performance of hazardous waste landfill barriers. The code will be developed using modularity, and will potentially incorporate barrier failure mechanisms identified in other work performed under the "Barrier Material Performance Prediction and Accelerated Effects Testing" subtask. These mechanisms may include changes in material properties due to microbial activities, leaching and deposition, freezing and thawing, erosion, and other yet to be identified mechanisms.

There are currently no multidimensional codes available to simulate the full range of physics

occurring in hazardous waste landfill barriers. The current codes available for simulating evapo-transpiration and the physics of unsaturated flow (capillarity) are 1-D. Quasi 2-D models that include the effects of surface runoff and lateral flow in drainage layers are available, but do not rigorously solve the unsaturated flow problem. Instead they use a mass routing approach by applying continuity to available pore water and the evaporative demand. There are numerous multidimensional models available that rigorously solve the unsaturated flow problem, but they only offer simple surface boundary conditions and do not include atmospheric energy and water transfer at the surface from continually changing atmospheric conditions. Furthermore, the current 1-D barrier and multidimensional unsaturated flow codes use the Darcy flow assumption, which neglects the convective components in the momentum equations. The validity of Darcy type flow is questionable for many subsurface environments such as fractured material and surface water/subsurface interactions.

The theory for water, energy, and contaminant transport in unsaturated porous media is based on the well understood principles of Richard's equation, which describes unsaturated liquid water flow; Fick's Law, which describes water vapor movement; Fourier's Law, which describes conductive heat flow in the soil profile; the convection-diffusion equation, which describes energy movement with the pore water; and the advection-dispersion equation, which describes contaminant transport in the subsurface.

Alternatively, water movement in a porous medium can be described by the conservative form of the Navier-Stokes equations. The Navier-Stokes equations will reduce to Richard's Equation when the convective components are neglected. This the case for most flow in a porous medium because the velocity is very small and inertial forces play a very minor role. The advantage of employing the Navier-Stokes equations is that the code will have a wider range of applicability and could include overland water flow and atmospheric conditions into the computational domain.

The governing equations for fluid flow are solved by simulation codes using one of three general methods: analytical, finite difference, and finite element. Analytical techniques use classical mathematical methods to obtain explicit solutions to the partial differential equations, and often can only be applied to simplified cases. Finite difference methods replace the partial derivative in the governing equations with a quotient of two finite differences resulting in a series of algebraic equations. Finite element methods use a technique similar to the finite difference method in that the governing equations are reduced to a series of algebraic equations upon discretization. However, the finite element method uses an integral form of the governing equation and interpolation functions for estimating variable values across discrete elements.

Ground water simulation codes cannot be used as tools with confidence until they are thoroughly tested. Three types of analysis are used in testing a newly developed code: verification, validation, and benchmarking. Verification is accomplished by comparing simple analytical solutions to those predicted by the simulation code. This verification process has two main objectives: to verify that the computational algorithms can accurately solve the governing equations, and to determine if the code is fully operational and no major programming errors persist. Often the analytical solutions available for comparison exist for very simple problems. Thus, even if the numerical model successfully duplicates the analytical model, the code still may fail in complex "real world" situations. To determine how well the code will handle complicated boundaries and soil heterogeneities, the code can be validated by modeling a field experiment. However, the data from appropriate field experiment may not be available. In this situation, the code may be bench marked by comparing the results to another code that has already been carefully tested.

Computational fluid dynamics (CFD) from the mechanical engineering discipline has made much progress in the past few years in developing new numerical techniques, and ground water models are often a decade or more behind the current "state of the art." One very interesting technique used within CFD is adaptive mesh refinement. Adaptive mesh refinement is most useful for physical problems that have variations in scale.

When solving these problems numerically, high grid resolution is needed to adequately solve the equations. However, there are often also large portions of the domain where high levels of refinement are not needed at different simulation times. Using a highly refined mesh over the entire simulation region and over the entire simulation time may represent a waste of computational effort. By locally refining the mesh only where needed at any time during the simulation, adaptive mesh refinement allows concentration of effort where it is needed in local high gradient areas. The progression of an infiltration event into dry soil is an example of a variable scale problem. At the leading edge of the infiltration front, the matric potential gradient is very large and requires a very fine mesh to adequately solve the problem. However between infiltration events, the gradient can be very uniform and a very fine computational mesh is not needed. Furthermore, new computational meshes will be needed if erosional processes have changed material layer thickness.

The approached used to develop a barrier simulation code that can simulate the full range of physics occurring in near-surface barriers is a multiyear effort that includes the following activities: (1) survey the available barrier simulation codes; (2) survey the state-of-the-art computational techniques used in hydrology and other fields such as computational fluid dynamics; (3) identify the state of the art computational techniques amenable to unsaturated/saturated ground-water flow and contaminant/energy transport simulation in near surface barriers and select a preferred method; (4) develop the simulation code using this method in a progressive sequence starting with a 1-D code and continuing to a 2-D and 3-D; and (5) verify, validate, and benchmark the code with analytical models, experimental results, and comparisons with other codes, respectively.

Path Forward. A new ground water model employing the conservative form of the Navier-Stokes equations is proposed to simulate subsurface and near-surface flows. It would be an "all-phase" model that would be composed of three basic phases: liquid, gas, and solid porous matrix. Multiple components could exist in each of the phases, such as water vapor and air in the gaseous phase. The Navier-Stokes equations would govern all three phases. The solid porous matrix can be viewed as an unmovable third phase. However in the solid porous matrix, the Navier-Stokes equations reduce to a thermal energy equation. The proposed model would extend beyond the current ground water models by full inclusion of overland water flow and atmospheric conditions into the computational domain. The model will contain the following features:

- Governing equations are multiphase, multi-component variable density Navier-Stokes equations in multiple spatial dimensions.

- Model will employ the Pressure-Corrected Implicit Continuous Eulerian-Finite Element Method (PCICE- FEM) scheme developed here at the INEEL. This scheme is a semi-implicit, pressure-based algorithm capable of high-order accurate transient and steady-state simulations.

- Reactive physics capable of simulating an arbitrary number of components and phases (liquid and/or vapor reactants).

- Extensive phase change physics for the liquid water-water vapor and air mixture to include evaporation, condensation, and freezing at the free surface and in the solid porous matrix.

- Model capability includes simulating the atmosphere near the free surface to include barometric pressure, temperature, absolute humidity (water vapor-air mixture), and heat flux.

- Full thermal energy resolution in the liquid, gaseous, and solid porous matrix phases to include energy transport due to the fluid mass transport, reactive heat generation, and atmospheric conduction and radiation.

- The model incorporates the Ergun drag model for porous material. Whereas Darcy's approximation assumes that the pressure gradient is proportional to velocity (permeability coefficient), the Ergun model combines permeability with the nonlinear inertial effects (velocity-based).

There are two major areas of improvement that may be realized by employing the Navier-Stokes equations versus Richard's equation for simulating flows in near surface environments. The most obvious advantage is the wider range of applicability obtained with the system of Navier-Stokes equations over Richard's equation. Richard's equation is restricted to porous material. The coefficient matrix for Richard's equation becomes singular for porosities of 1 (continuous fluid) or 0 (impermeable solid matrix). A Navier-Stokes solution is applicable across a full range of material, from continuous fluid to impermeable solids. The second advantage comes from the widely different numerical approaches required to solve the two forms of governing equations. Spatial discretization of Richard's equation results in a nonlinear system of equations in the form of $AY = b$, where $A = f(x,y,Y)$. The pressure-based scheme employed in the PCICE-FEM scheme also requires a system of equations to be solved in the form of $AY = b$. However, the system of discretized equations is linear in nature as the coefficient matrix A is only a function of the spatial integration terms, $A = f(x,y)$, and not the dependent variable Y. Thus, the proposed model is only required to solve $AY = b$ once per time step versus several times per time step for an iterative nonlinear Richard's formulation.

Development of a 1-D finite element code based upon the PCICE-FEM scheme to simulate two-phase flow in a solid porous matrix was begun this fiscal year. Building on the FY 2002 work, FY-2003 tasks are as follows:

- Submit a peer-reviewed manuscript to Water Resources Research detailing the one-dimensional finite element code's governing hydrodynamic theory, numerical scheme, and numerical results. This manuscript will include the benchmark of the 1-D finite element code with a conventional unsaturated ground water model and validation with an unsaturated column flow experimental from the literature. Alternatively, the 1-D model could validated with results from the ESRA capillary barrier experiment.

- Develop a 2-D multiphase code employing the PCICE-FEM scheme. Extending the 1-D code to 2-D. This task will include benchmarking and validation of the 2-D code by comparing the numerical results with an existing multi-dimensional code and with empirical results obtained with 2-D unsaturated experiments documented in the literature. It is also hoped that INEEL experimental fracture flow results will be available for code validation.

- Develop a transient multidimensional adaptive gridding module to be spawned by the flow solver to resolve high changes in flow variable gradients.

Preliminary ET Dynamic Model (Subtask 4.2)

This subtask is exploring barrier performance/degradation dynamics.[32] One aspect is the design and evaluation of relatively simple but very flexible system dynamic models to explore the dynamics of barrier performance. This research provides a tool to map out the underlying feedback loop structure of the system and explore the relationships between the various components. This modeling is designed to explore the structure and behavior of the system, whereas more sophisticated models are strong tools for exploring sensitivities to parameter uncertainties.

System dynamics is an analytical approach that examines complex nonlinear feedback loop systems through the study of the underlying system structure. A thorough understanding of the structure of these complex systems can lead to an explanation of their performance over time and in response to both internal and external perturbations. By understanding a system's underlying structure, predictions can be made relative to how the system will react to change.

A system dynamics model is a visual representation of a system. This visualization of the components and connections is one of the assets of this modeling technique. The visual model defines, through a graphical interface, a series of differential equations, which define the behavior of the system over time. The software that we are using in this modeling exercise is Stella© Research. The calculations are performed using numerical integration. Although the

interface makes the modeling look superficial and almost trivial, there is a very sophisticated mathematical engine that does the calculations. Using this modeling technique it is possible to model very complicated systems.

System dynamics models are descriptive in nature. All the elements in the model must correspond to actual entities in the real world. The decision rules in the model must conform to actual practice and real-world phenomenon such that adjusting an element in the model corresponds to a physical change in the real system. Our intentions for the model are threefold:

1. To have visual diagram of the system from which to engage discussions on the various elements of the model and elicit input from interested parties.

2. To gain insights into the dynamics of the movement of moisture in the soil and to identify core structure of the system.

3. To develop a tool for the analysis of long-term performance.

Illustrative Model Description (as a learning tool only). The first barrier model we are developing (still under development) is a single-layer soil cap with a vegetative cover. The model tracks the soil moisture content in the cap as well as deep drainage into the waste level. The change in moisture in the cap layer is dependent on the inflow of moisture from precipitation, run-on and irrigation, field capacity of the soil, current moisture level of the soil, and extraction from evapo-transpiration and deep drainage.

The model has four basic components: stocks, flows, constants/auxiliaries, and connectors. Figure 18 shows a diagram of a generic single layer cap model, illustrating how these four components are combined. The **Stocks**,

, accumulate quantities of material, in this case, moisture. The **flows**, 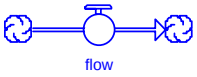

, physically change the quantities of the stocks. The direction of the arrow defines whether it is an inflow into the stock or an outflow from the stock. Inflows would include precipitation, irrigation and run-on. Outflows would include runoff, deep drainage, evaporation, and transpiration.

Auxiliaries/Constants,

, contain information that feeds into the stocks or flows. The **Connectors**, →, symbolize a relationship between two elements in the model and the direction of the arrow indicates the direction of the influence. The precision of the model depends on the exactness of the data as well as the ability to capture the relationships that are important to the behavior of the system. This simple model could mimic the general behavior of an ET cap, but would be too generic to be of much use. How complicated the model becomes depends on how precisely we want to model all the physical elements in the system. However, the basic model gives us a focal point to begin to discuss each of the physical components (inflows, outflows, evapo-transpiration, etc.) and how they are connected in the model.

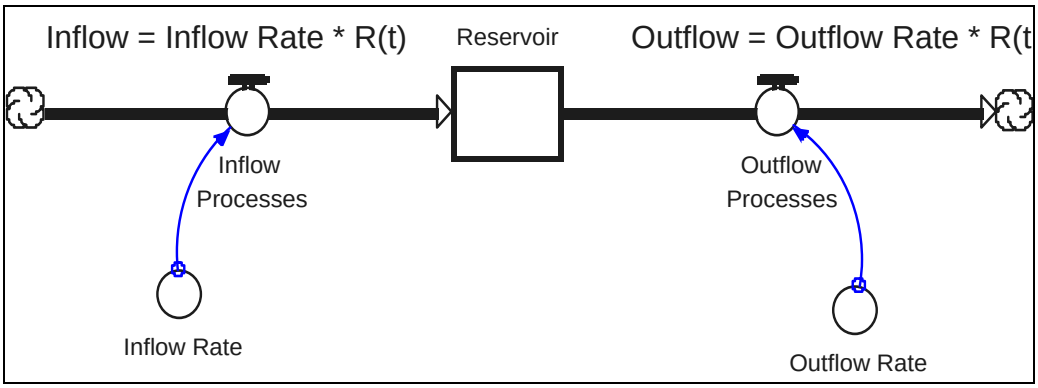

Figure 18. Generic system diagram for cap moisture content.

Figure 19 shows the way we have elected to model the moisture content in the cap. We have divided the cap into several different layers to track the moisture movement through the cap. The top layer, closest to the surface, is the evaporative layer. This layer is relatively thin (~20 cm) and for heavy rains quickly becomes saturated and drains into the deeper layers of the cap. The moisture remaining after percolation is predominantly removed through evaporation. The moisture removal process in the lower layers is dominated by transpiration and wicking, and, in cases of heavy infiltration, deep drainage. Movement of the moisture down through the soil is modeled using the Green-Ampt equations. Evaporation and transpiration are modeled using the FAO modified Penman-Monteith equations. We are currently working on a set of equations to map the wicking process, and a plant root growth submodel to further refine the transpiration rates.

The capillarity effect (wicking) would move moisture from the wetter lower layers back up towards the surface as the surface areas are dried by evaporation and transpiration. The capillary effect of drawing moisture back up is effected by soil type, moisture content, and height.

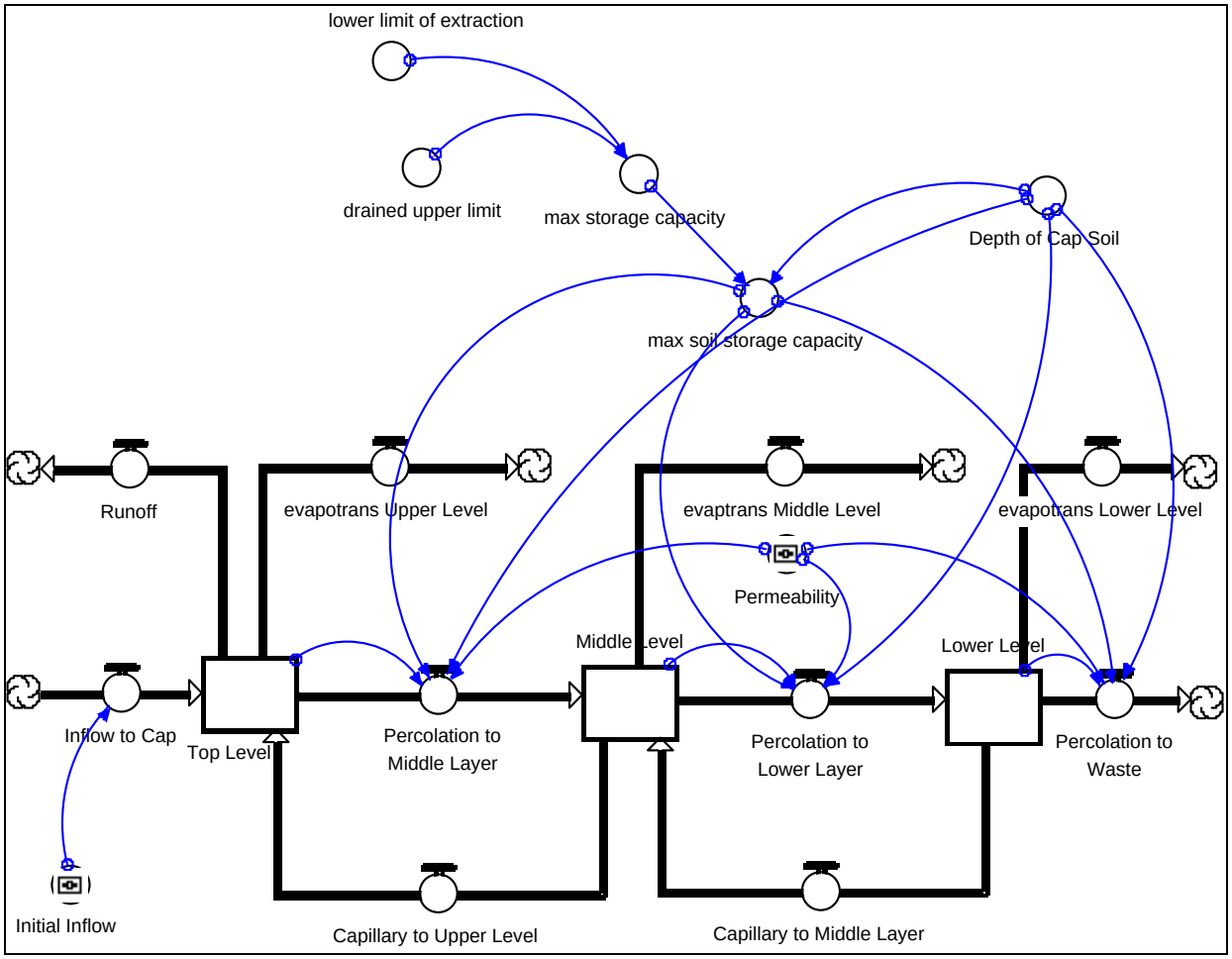

Figure 19. Display of the preliminary model for the ET Cap. The rectangle boxes are stocks that hold quantities, in this case, moisture content of the soil. The cap layer is divided into 3 sections to capture the movement through the soil. Each of the stocks have flows that move moisture both in and out of the stock (percolation, evapo-transpiration, etc.).

The transpiration effect is governed by the root density component of the model. The higher the root density, the more transpiration occurs up to the point where the soil moisture reaches the lower limit of extraction, whereas transpiration from that zone ceases to occur. The root density will increase if there is sufficient moisture in the soil to sustain the current amount of plant life. If the moisture levels drop below the necessary amount to sustain the current amount of plants, the plant root density decreases; thus, a lower ability to remove moisture from the soil.

The model has a runoff component based on the slope and amount of precipitation. The current model has a slope component that can be adjusted but for current analysis the slope is set at zero. Currently, all precipitation is assumed to move into the top layer of the cap.

The model keeps track of current moisture content in each of the different layers and total drainage from the bottom of the cap into the waste zone. Graphs are used to display the moisture levels throughout the simulation period. The user can track the inflow of moisture, see the effects on the moisture content in the various layers, and see the effect of the drying cycle through the evapotranspiration process

The system operates on a system of feedback loops. Excess moisture in the soil (above the current transpiration capacity) causes an increase in plant growth, which increases plant root density, which increases transpiration, which reduces the excess moisture in the soil until the two elements (transpiration and moisture) are in equilibrium.

The amount of moisture the soil can hold will depend on the type of soil and the depth of the cap. We will be able to adjust both of these parameters to test the performance levels and cap depth of different soils. In addition, different plant species have different transpiration rates and capacities, which will affect the performance of the cap. The model will allow the user to select the variety of plants on the cap.

Some plants will send roots down very deep, others will keep their roots relatively close to the surface. This difference changes the performance of the ET component in terms of transpiration and rooting into the waste zone.

The model has a flight simulator front end (see Figure 20) that allows the user to experiment with different cap designs and environmental parameters, and run the simulation to see the effects on cap performance. The user can change a variety of parameters form cap thickness, precipitation, initial soil moisture, elevation, latitude, average wind speed, and average temperature. The cap depth is a user-defined value that defaults to 3 m. The user can select a cap as thin as 0.5 m or as thick as 6 m. We chose 0.5 m as the lower boundary because this is the minimum allowed under EPA's current requirements for RCRA Subtitle D landfill caps. The interface allows the user to adjust various options by adjusting slide bars, dial knobs, and graphical inputs. When the user is ready to test a cap design they click on the run button. The results appear on the chart on the interface.

Figure 21 shows a trial run where there is an initial inflow of 100 mm of precipitation into a cap that is 2.2 m thick with a moderate permeability level. The results show the sharp increase in moisture content of the top layer (#1, blue line) and then a steady drop as the moisture percolates from the top layer down into the middle layer. The middle layer shows a gradual increase in moisture content until it creeps slightly above the storage capacity (#4, green line). At that point moisture begins to percolate from the middle layer into the third layer. The moisture content for the third layer rises slightly but doesn't reach the storage capacity. By the tenth day, the system has reached equilibrium. The top and middle layers are at field capacity level but the third layer is still below the field capacity. In this case, the cap had sufficient capacity to store the influx of moisture to prevent any drainage into the waste layer.

This is a simple preliminary model that does not include all the components needed to evaluate the long-term structural integrity of a cap design. We included it here to trigger discussion about the various components already captured in the model and those missing that should be included. Even in this simplistic stage, the model can test some simple cap designs and give insight as to the complex behavior of ET Caps.

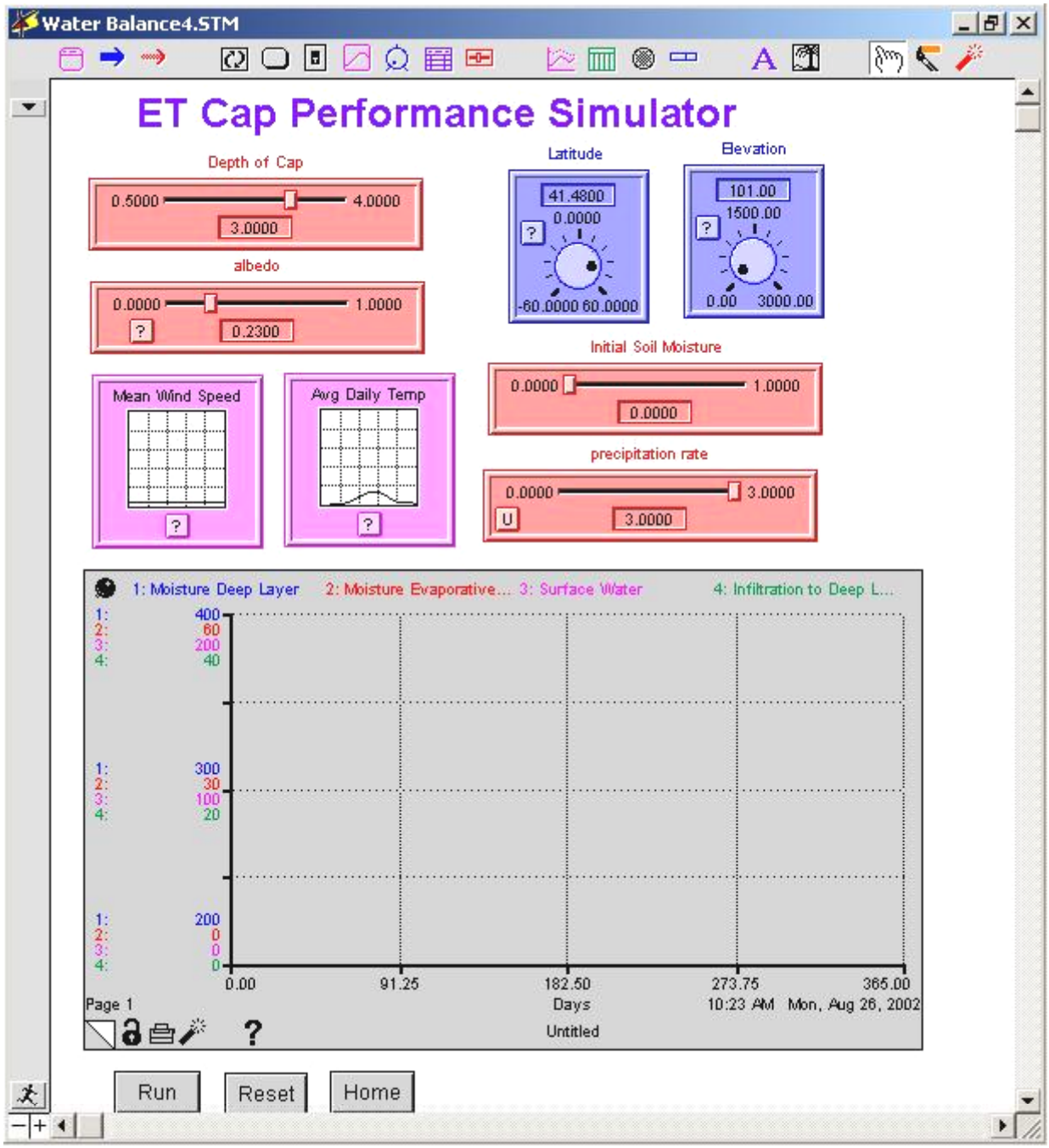

Figure 20. Display of the cockpit with slide bars and click buttons for operation.

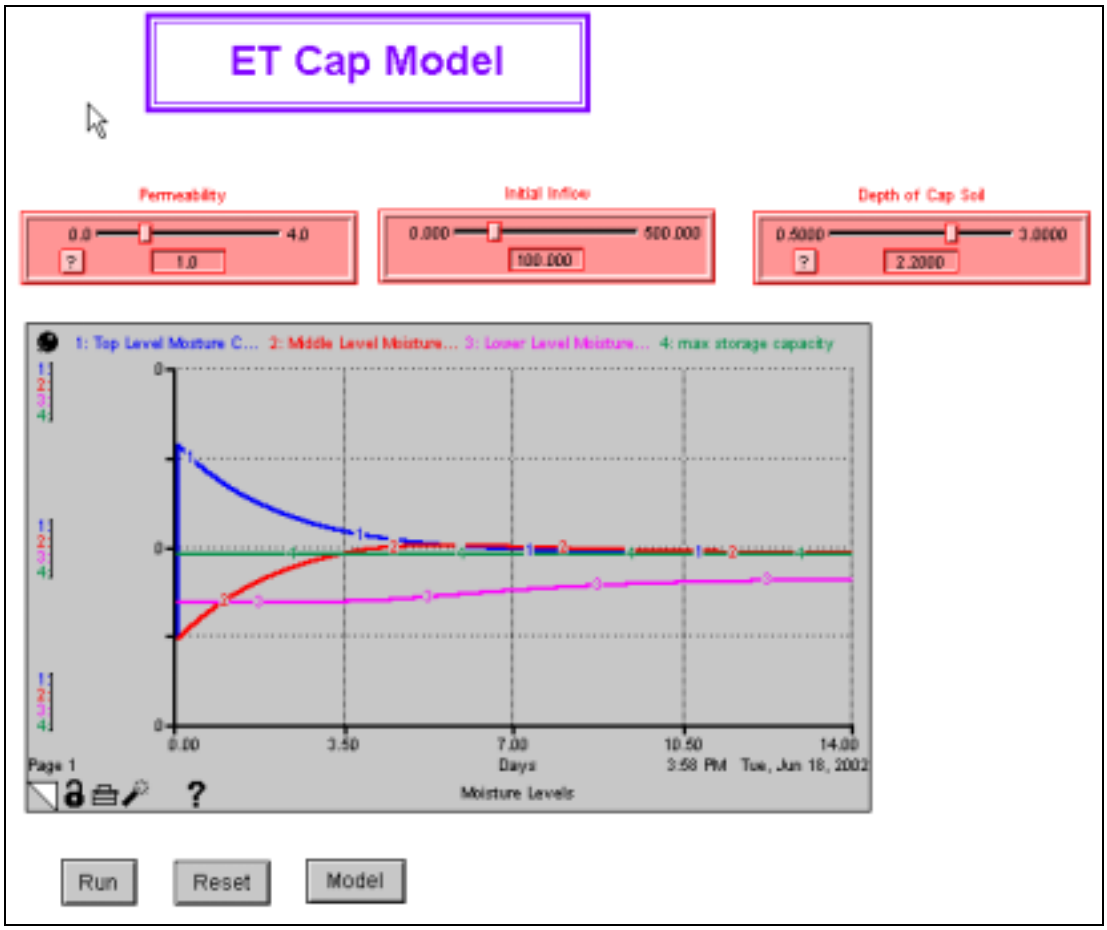

Figure 21. Preliminary ET dynamic model.

Overarching Technical Constraints (Task 5)

Near Surface Engineered Barriers Technical Constraints (Subtask 5.1)

This subtask focused on defining a sound technical basis from which to build the INEEL's program in Near Surface Engineered Environmental Barriers. It focused on defining the technical issues that limit the application of barrier technologies, which included clearly defining the state of the technology, the technical limitations and constraints, and recent and ongoing research. Gaps in technology and science were identified and attempts will be made to prioritize them. This effort builds on existing efforts that have been performed by both the Environmental Protection Agency[5,6] and DOE.[7] Our first focus was on defining the overall focus of the Near Surface Engineered Environmental Barriers effort. We accomplished this through discussions with personnel from EM Operation's at the INEEL, Miamisburg Environmental Management Subtask (Mound), Savannah River Site, Oak Ridge Operations Office, and the Grand Junction Office. We also evaluated the DOE Environmental Management Program's revised strategy (see Reference 9) to better understand their revised approach to clean-up across the complex. There was a fairly consistent need among Sites to be able to determine the integrity of existing barriers and for demonstrating the long-term integrity of proposed barriers. This was selected as the focus for developing the technical constraints document. The science and engineering needed to better ensure the present and long-term integrity of caps and barriers can be accomplished by (see Figure 22) (a) understanding the processes that affect the cap and barrier integrity, (b) sensing changes in the barrier, (c) accelerating the aging

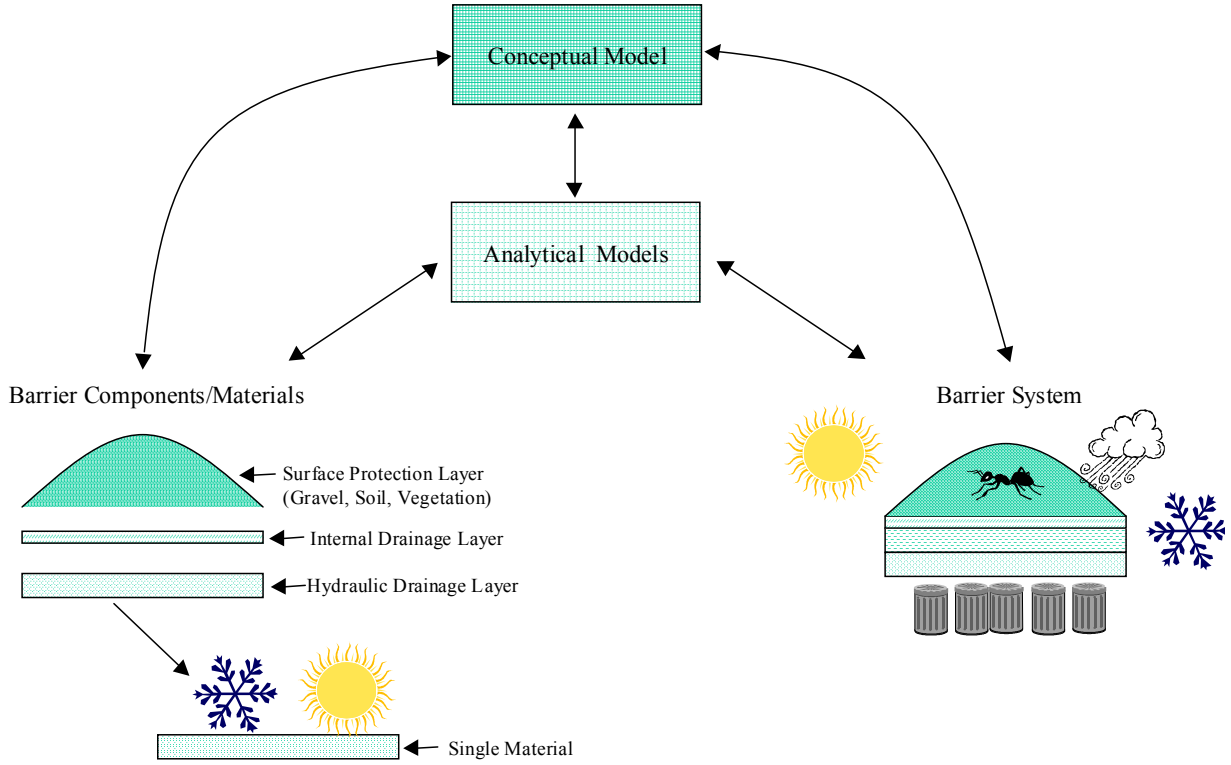

Figure 22. Accelerated aging of barrier materials and systems supports the validation of analytical models and the testing of the conceptual model and its hypothesis.

process and determining barrier performance, and (d) modeling. Within each of these functions, the impacts of natural phenomena, including weathering, biological, geological, chemical, radiological, and catastrophic impacts and the combined effects were considered.

Accelerated Aging (Subtask 5.2)

One measure of the success of new containment systems is their ability to maintain integrity over long periods of time. Models validated with experimental data can be used to extrapolate natural processes. This subtask focused on defining the present state-of-the-art for accelerated aging of containment materials to provide data for model validation.

This subtask focused on gathering information through searches on the worldwide Web, literature searches through the INEEL Technical Library, and recently published conference proceedings. Laboratories that presently perform accelerated testing were also identified. This subtask also identified existing capabilities of laboratories to perform accelerated testing of materials likely to be used in barrier systems. The subtask identified gaps and opportunities for the INEEL relative to unique accelerated testing capabilities.

This subtask also examined state-of-the-art studies, both real and simulated, of the accelerated aging of materials used in caps and barriers (referred to in this report as barriers). In the searches of published literature and worldwide Websites, we found that a relatively small quantity of data had been gathered on accelerated aging of materials anticipated or actually used for caps and barriers for radioactive material. Thirteen major categories of materials were identified:

- Asphalt
- Clay
- Concrete
- Grout
- Metal
- Microbe
- Rock
- Sand

- Soil
- Synthetic
- Vegetation
- General
- Other

The term "general" includes the general references to multilayer and RCRA designs. The term "other" includes nontraditional barrier materials.

The review of materials only identified 29 of 136 reports that address research studies on accelerated aging of materials. Field demonstrations were not considered accelerated aging tests for the purpose of this study unless they specifically addressed an aspect of accelerated aging. The subtask also identified 15 organizations that presently perform accelerated testing of the materials of concern.

At the time of this report, the task to identified gaps and opportunities for the INEEL to unique accelerated testing capabilities has not been completed.

Scientific Data Management System (Subtask 5.3)

This effort is designed to develop capabilities in the conceptual design of a system capable of accessing existing data sources, acquire and organize relevant data, enter data or findings from research to assess the performance and/or integrity of surface or near-surface barriers.

Activities. The activities conducted to develop of the data management approach are described in this section.

A survey was conducted among the organizations likely to have developed such a system (EPA, NRC, DOE, DOD, NSF). This survey showed the existence of numerous studies and reports on this type of research but no searchable databases were found. This may seem surprising at first; however, the variety of interests and designs being pursued by the above organizations and the lack of consistency in terminology and testing methodology prevent the integration of the body of knowledge into a single tool available to all. An analysis of the potential users of this system was performed and the following are some of the most prominent groups:

- Scientific community at large
- Regulators and State officials
- Civic and environmental groups
- Affected individuals.

An evaluation of the information contained in the system determined it would likely:

- Pertain to existing caps and barriers, which through operation, monitoring, and maintenance activities, could provide insights to the relative performance of those barriers.
- Be the results of research activities being conducted by the scientific community involved with the design of such caps and barriers. By analyzing this information it is possible that trends would develop and a step improvement be realized in the approach to both design and performance evaluation methods.

A survey of related tools already available or in the development stage was conducted to evaluate the potential value of using all or parts of them to save time and money in the development of such a data management system. This survey resulted in a number of databases dealing with other features of the same sites where these caps and barriers may exist. For example, the INEEL developed a database for the Long Term Stewardship Program in FY 2001 and 2002, which contains information on the DOE sites, location, contaminants, stakeholders, volumes, end-state, etc. This database provides a solid footing to further develop it and include the additional information about those sites related to the performance of the caps and barriers in them.

Development of a prototype was initiated. Figures 23 and 24 show screenshots of the interface that will eventually enable the user to:

- Find out what has been done to date

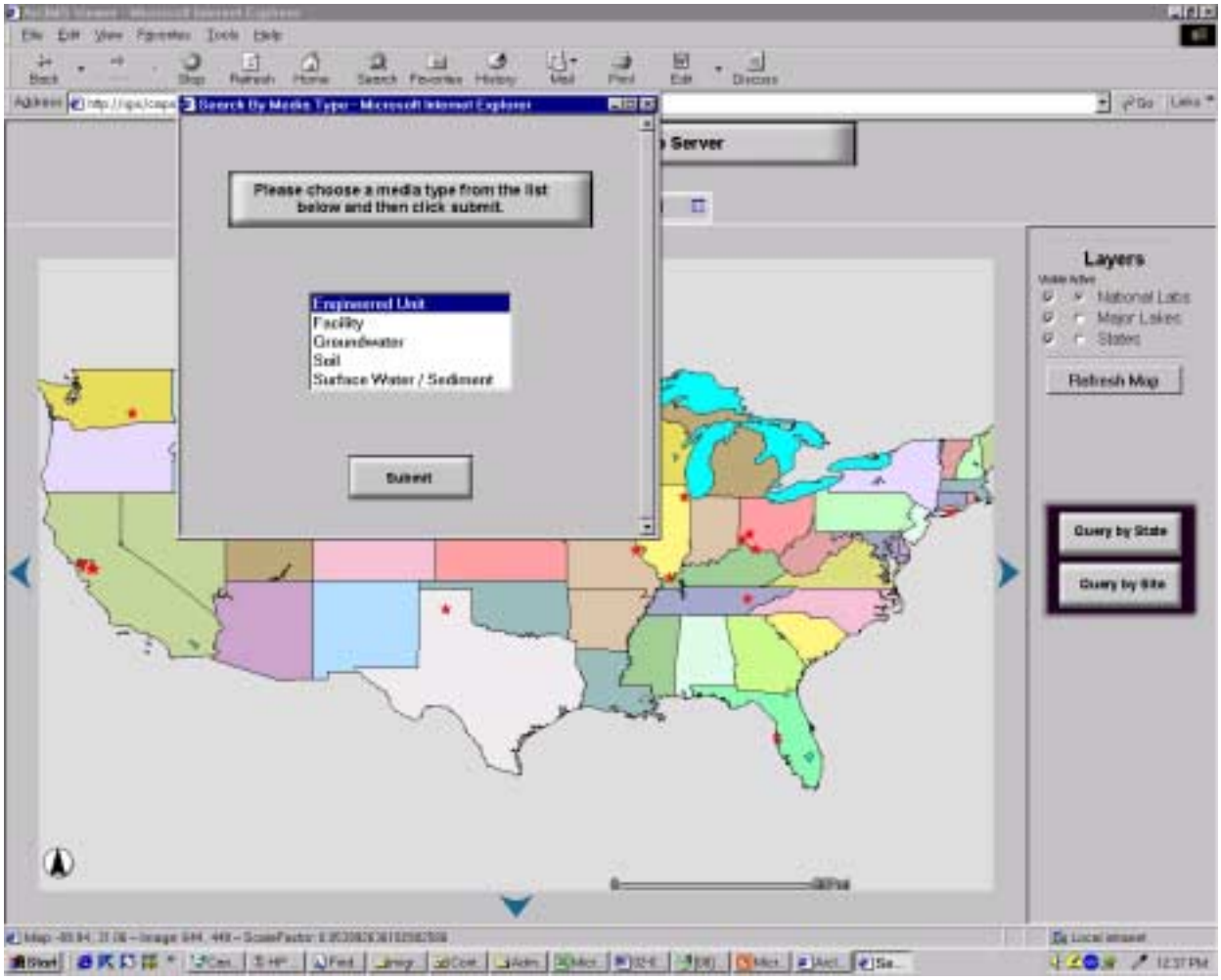

Figure 23. Clicking on contaminants by media type presents a choice of media types.

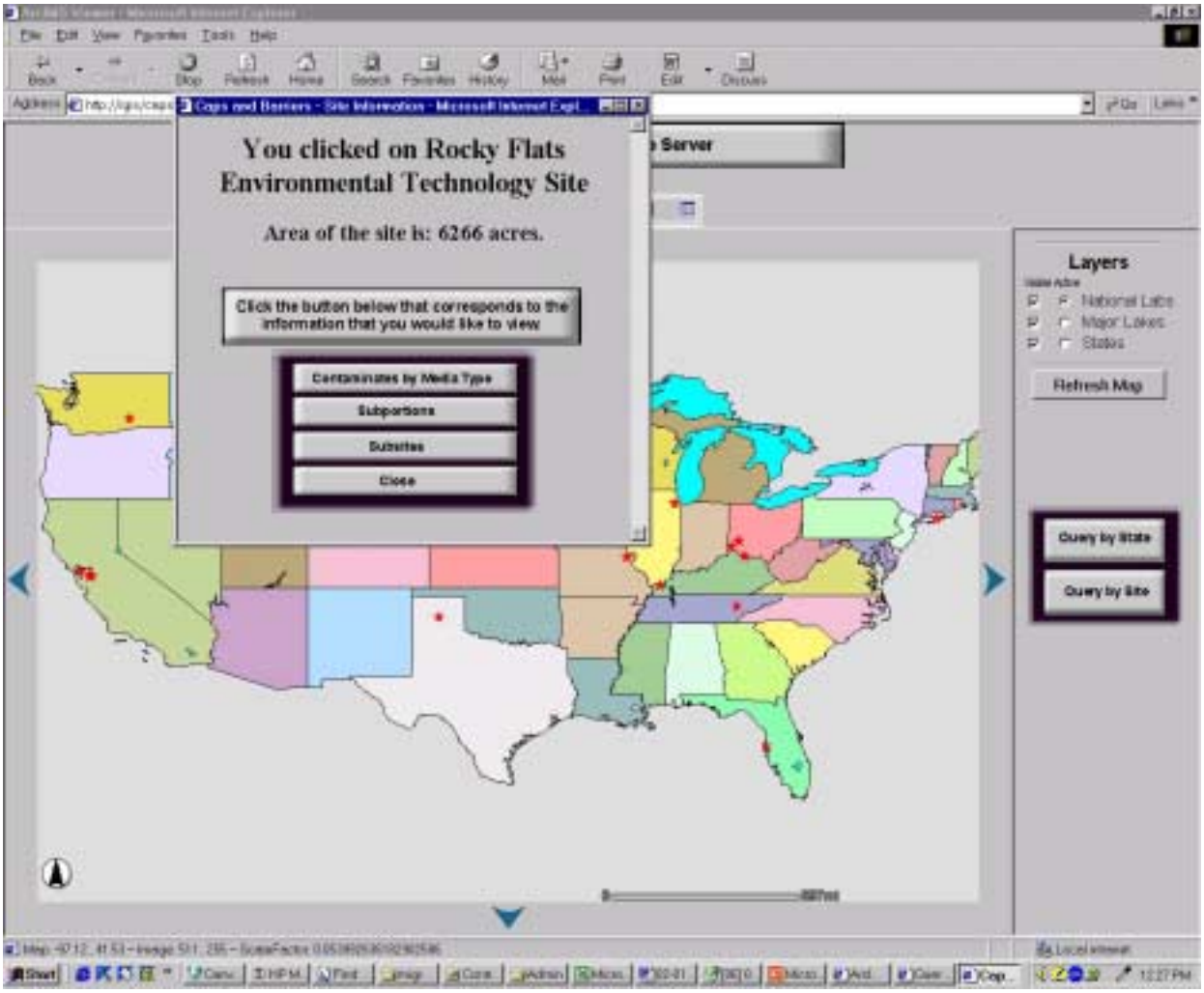

Figure 24. Query by site.

- Who is performing any tests for what, when the results would be available, etc.

- What approach has been taken and found to be good/bad in the design of tests to evaluate performance of caps in a "wet" environment, semi-arid climate, etc.

- What indicators of performance have been determined to yield reliable information to establish a strong correlation between cause and effect, which would lead to the identification of failure mechanisms—the beginning of the true understanding of the science behind the engineering of caps and barriers.

Path Forward. The importance of integrating the body of knowledge into a single repository cannot be overemphasized. Most of the information available (although scattered) deals with the effects of cap failure after the fact. We typically detect cap failure by analyzing for contaminants under the cap through ground-water testing. However, there is very little testing of the non-contaminated section of the disposal unit, the cap. The research the INEEL is currently performing on caps and barriers may be one of the few works toward that goal. Being able to share that information with others and solicit similar input from other institutions would result in a valuable resource with which to design better caps and barriers in the future.

In FY 2003 and beyond, the objectives would be to develop the skeleton of the data management system and make it functional over the web, acces-

sing related information residing in the identified databases and providing a user interface to enter data from tests performed at the INEEL and elsewhere.

Project Level Path Forward

The research and capabilities built in this project will benefit DOE by improving confidence in existing barriers, providing improved technical basis for managing existing barriers, and improving the basis for designing and testing new barriers. DOE is quickly driving toward achieving as much cleanup as possible by 2012. Caps and barriers at many DOE facilities will play a major role in cleanup strategies, and need to be designed with maximum integrity to minimize future risk. Designers would like to increase the use of engineered materials to improve performance or reduce over-conservatism. The avoidance of using engineered materials is a factor in using separate layers for each function. Sometimes that is optimal, but, we observe that surface caps are becoming thicker, partially as a result. When designing a new facility, it is often practical (but expensive) to dig deeper so that the cap top does not project too far above the surrounding terrain, thereby increasing risk of exposure to wind and water erosion (see Figure 25). This is generally impractical when applying a surface cap as part of closure of an existing contaminated site. Excess conservatism in addressing some factors can lead to increased vulnerability to others, such as wind.

Specifically, the project incorporates research that will benefit near-term cleanup operations such as final design of the ICDF, cleanup and closure at the INEEL Subsurface Disposal Area (SDA), and the Idaho Nuclear Technology and Engineering Center (INTEC). All of these sites will eventually be capped. The ICDF cap will, and SDA and INTEC caps may, include evapo-transpiration and capillary barrier functions. (A surface cap is likely needed even for portions of the SDA where buried waste will be removed; residual hazards will remain and water should not be allowed to infiltration into the rest of the SDA.) Portions of the SDA and INTEC will probably have grout and even concrete caps. For example, the Waste Calcining Facility at INTEC has been entombed (filled with grout) and capped with concrete.

Similar examples exist throughout the DOE Complex and private sector. The duration of hazards is often long. This project will help provide the basis for managing and improving performance of these barriers.

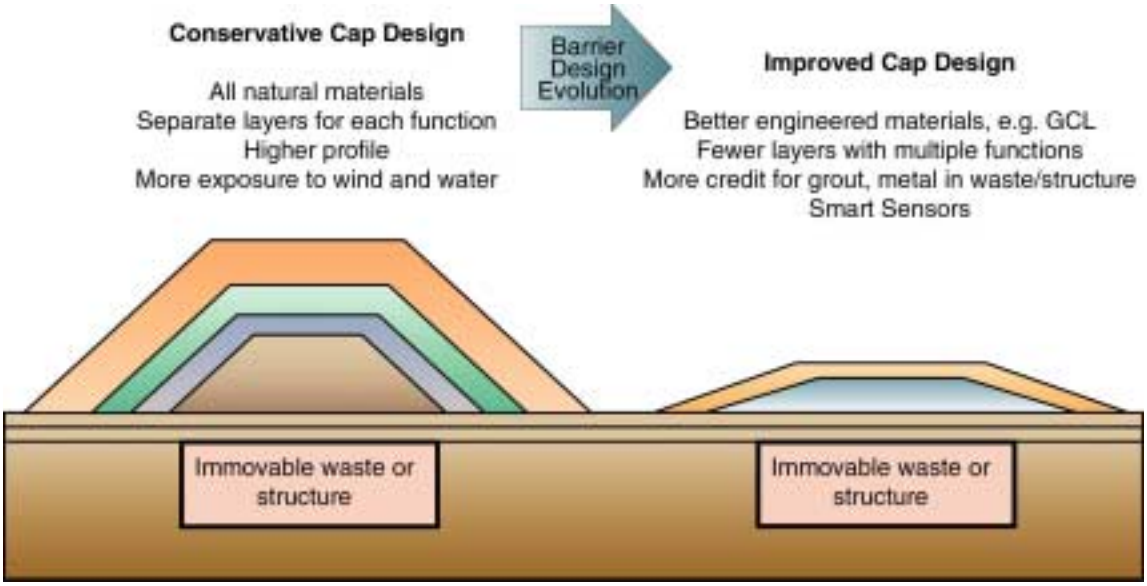

Figure 25. Improved confidence in long-term barrier performance will improve barrier design.

ACCOMPLISHMENTS

Our accomplishments during FY 2002 are as follows:

- Samples are being processed so they can be analyzed for organic C and P. The tube digestion/heating block has been applied to approximately 20% of the samples, but the organic C calculations are yet to be done. About 40% of the available P samples have been completely processed and are in cold storage until they can be analyzed using the ICP/AES. (Subtask 1.1)

- A two-channel flow cellhas been successfully imaged on the INEEL NMR imaging instrument. This is a major accomplishment, since we were not initially certain that an image could be obtained through the flow cell's epoxy matrix. Work is now focusing on determination of the resolution that can be obtained with the instrument. (Subtask 1.2)

- Preliminary data for the first set of PCBE caps are coming available, but there is not sufficient data yet to draw conclusions on microbial-hydrological interactions. The hydrologic data suggests that some compaction of the caps has occurred. (Subtask 1.3)

- Preliminary experiments have been conducted to determine whether or not impedance spectroscopy can detect and monitor water intrusion into a fully cured slab of concrete. While analysis of the data is not yet complete (to be completed with Final), indications are that impedance spectroscopy is extremely sensitive to water permeating into and through a concrete slab. (Subtask 2.1)

- Samples of three commercially available GCLs have been obtained from CETCO, including those to be used in current designs at the INEEL. These include Bentomat ST, which will be used for the ICDF evaporation ponds, Bentomat DN, which will be used for ICDF landfill and evaporation ponds, and Claymax 600CL, which will be used for comparison with previous studies. (Subtask 3.1)

- We developed a working relationship with the INEEL ICDF operations staff, and temperature monitoring instrumentation has been installed in conjunction with the construction of the ICDF evaporation ponds. Project integration with operations has occurred and involves installing thermistors in the base materials of the INEEL ICDF evaporation pond in order to monitor actual field conditions throughout the winter. This will provide representative data on the depth, maximum and minimum temperatures, and the duration of freezing in the field. This information will then be used in developing the freeze-thaw regime for the bench scale (mesoscale) tests. This task is currently being performed; several thermistors have been installed.

- The environmental chamber is operational and preliminary experiments have been completed. Commercial "neat" grout and 5,000 psi concrete are being evaluated for experimental baseline comparisons. The grout formulation GMENT 12 is currently identified as the material to be deployed for INEEL grout work. Four 55-gal drums are on site and available for testing. Appropriate hardware has been ordered for GMENT 12 high-shear mixing. (Subtask 3.2)

- Analytical models are being used to predict the progression of bulk fracture. Statistical models are being evaluated in an effort to explain complete fracture of a block as a function of freeze damage. It is anticipated that with experimental damage evolution data, this statistical model will approximate the time for discrete fractures to coalesce in the presence of water driven freeze-thaw material failure and predict the time required to generate through-thickness fractures. This effort is very preliminary however shows promise in addressing time domain predictions of degradation. (Subtask 3.2)

- The survey of available barrier simulation codes as part of the 4-D modeling activities identified a multidimensional code has

recently been released. The VADOSE/W software (Geo-Slope, 2002) simulates the interaction of the meteorological conditions, the ground surface, the vadose zone, and the local ground-water regime. However, the model is limited to 2-D and is based on Richard's equation. The Richard's equation formulation limits the code to simulating fluid movement in a porous medium only. The survey of available barrier simulation codes compiled. (Subtask 4.1)

- The modeling literature search revealed a growing trend to model subsurface flows with multiphase governing hydrodynamic equations because the Darcy assumption's validity is questionable for many flow features in near-surface environments. A Darcy formulation is only valid for flow through a porous medium. This formulation is not valid for individual fracture or macropore-scale simulations. Free surface influences, such as the atmosphere or surface water must be simplified and treated as a boundary condition in the Darcy formulation. A ground water model employing the conservation of mass, momentum, and energy equations would be valid for simulating porous medium and nonporous medium and the interaction between the two domains. The survey of "State of the Art" computational techniques and recommended approach for development of a comprehensive barrier simulation code is included in Appendix B. The path forward is summarized in the next section.

Publications

Geesey, G. G., A. L. Neal, P. A. Suci, B. M. Peyton, A Review of Spectroscopic Methods for Characterizing Microbial Transformations of Minerals, *J. Microbiol. Meth.*, Vol. 51, 2002, pp. 125–139.

Hilary I. Inyang and S. J. Piet, Chapter 3.0, Damage and System Performance Prediction, chapter of book on waste containment barrier systems sponsored by EPA, DOE, and DuPont corporation, in press.

Presentations

Chambers, L. S., T. P. McGonigle, G. J. White, C. J. Holst, "Soil forming Processes and their Effects on Surface Caps," poster presentation by summer fellowship student at the U.S. DOE sponsored *Scientific Summary Poster Presentation, August 2002, INEEL, Idaho Falls, ID*.

Piet, Dr. Steven J., "Near Surface Engineered Environmental Barrier Integrity," GIEES-Duke Energy Seminar Announcement, Sepember 23, 2002.

Piet, Steven J. and Robert P. Breckenridge, *Near-Surface Engineered Environmental Barrier Integrity, Spectrum2002 Conference, Reno Nevada, August 2002.*

REFERENCES

1. National Research Council Board on Radioactive Waste Management, *Research Needs in Subsurface Science*, National Academy Press, Washington D.C., 2000.

2. National Research Council, Committee on Remediation of Buried and Tank Wastes, *Barrier Technologies for Environmental Management*, National Academy Press, Washington D.C., 1997.

3. National Research Council, Committee on Remediation of Buried and Tank Waste, *Long-Term Institutional Management of U.S. Department of Energy Legacy Waste Sites*, National Academy Press, Washington D.C., 2000.

4. Nuclear Regulatory Commission, Office of Nuclear Regulatory Research, "Radionuclide Transport in the Environment Research Program Plan," March 2002.

5. Environmental Protection Agency, "Evaluation of Subsurface Engineered Barriers at Waste Sites," EPA 542-R-98-005 (1998), www.clu-in.org.

6. L. Pearlman, "Subsurface Containment and Monitoring Systems: Barriers and Beyond,"

National Network of Environmental Management Studies Fellow, U.S. Environmental Protection Agency, Technology Innovation Office, 1999, www.clu-in.org or www.epa.gov/tio/products/intern/pearlman/finalpap.htm.

7. Department of Energy, *Alternative Landfill Cover," Subsurface Contaminants Focus Area and Characterization, Monitoring, and Sensor Technology Crosscutting Program, Innovative Technology Summary Report*, DOE/EM-0558 2000.

8. "INEEL CERCLA Disposal Facility Remediation Design/Construction Work Plan/Title II Design (Draft Final Title II)," DOE/ID-10848, Revision 1, Draft Final, April 2002.

9. Top to Bottom Review Team, "A Review of the Environmental Management Program United States Department of Energy," Department of Energy, February 4, 2002.

10. *Environmental Management Performance Management Plan for Accelerating Cleanup of the Idaho National Engineering and Environmental Laboratory*, Predecisional Draft, DOE/ID-11006, Department of Energy, June 2002.

11. W. J. Mitsch and S. E. Jorgensen, *Ecological Engineering*, John Wiley & Sons, NY, NY 1989.

12. Concept provided by INEEL Environmental Restoration Operations (2002), unpublished.

13. R. Pool, "If It Ain't Broke, Fix it," Technology Review 104 (7), (2001), pp. 64-69.

14. E. A. Paul and F. E. Clark, *Soil Microbiology and Biochemistry*, *2nd Edition*, New York, Academic Press, 1996, pp. 340.

15. J. E. Anderson and A. D. Forman, *The Protective Cap/Biobarrier Experiment A study of Alternative Evapo-transpiration Caps for the Idaho National Engineering and Environmental Laboratory*, prepared for the U.S. Department of Energy Idaho Field Office, Environmental Surveillance, Education and Research Program, Contract DE-AC07-00ID13658 by Stoller Corporation (STOLLER-ESER-46), Idaho Falls, ID, 2000, pp. 291.

16. D. L. Heanes, "Determination of total organic C in soils by an improved chromic acid digestion and spectrophotometric procedure," *Communications in Soil Science and Plant Analysis*, Vol. 15, 1984, p. 1191.

17. A. Walkley and I. A. Black, "An Examination of the Degtjareff Method for Determining Soil Organic Matter and a Proposed Modification of the Chromic Acid Titration Method," *Soil Science*, Vol.37, 1934, p. 29.

18. S. R. Olsen and L. E. Sommers, "Phosphorus," in A. L. Page, R. H. Miller, and D. R. Keeney (eds.), *Methods of Soil Analysis*, Madison, WI, American Society of Agronomy, 1982, pp. 403–430.

19. E. G. Jobbágy and R. B. Jackson, "The Vertical Distribution of Soil Organic Carbon and Its Relation to Climate and Vegetation," *Ecological Applications*, Vol. 10, 2000, p. 423.

20. N. S. Brady, *The Nature and Properties of Soils, tenth edition*, New York, MacMillan Publishing Company, 1990.

21. A. I. Stormberg and J. A. Cook, *Use of Genetic Markers as a Screening Tool for Ecological Risk Assessment at the INEEL: Microsatellite Mutation Rate of Burrowing Mammals*, report within M. C. Thelen, ed., Laboratory-Directed Research and Development for FY 2001, INEEL/EXT-03-00421, INEEL (2002).

22. R. Sayler and L. Shipley, *The First Experimental release of Idaho Pigmy Rabbits at the INEEL*, Progress Report No.1, Department of Natural Resource Science, Washington State, Pullman, WA 99164 (2002).

23. D. L. Miller and S. J. Piet, "Environmental Systems Research Candidates Final Report," FY 2000–2001, INEEL/EXT-01-01403, 2002.

24. R. D. Hewitt and D. E. Daniel, "Hydraulic Conductivity of Geosynthetic Clay Liners after Freeze-Thaw," *Journal of Geotechnical and Geoenvironmental Engineering* Vol. 123 (4), 1997, pp. 305-313.

25. L. C. Wong and M. D. Haug, "Cyclical Closed-System Freeze-Thaw Permeability Testing of Soil Liner and Cover Materials," *Can. Geotech. J.*, Vol. 28(6), 1991 pp. 784-793.

26. ASTM, "Standard Test Methods for Measurement of Hydraulic Conductivity of Saturated Porous Materials Using a Flexible Wall Permeameter," D 5084-00, 2000.

27. ASTM, "Standard Test Method for Measurement of Index Flux through Saturated Geosynethic Clay Liner Specimens Using a Flexible Wall Permeameter," D 5887-99, 1999.

28. ASTM, "Standard Test Method for Determining the Effect of Freeze-Thaw in Hydraulic Conductivity of Compacted or Undisturbed Soil Specimens Using a Flexible Wall Permeameter," D 6035-96, 1996.

29. R. M. Koerner, "Designing with Geosynethics," 4th Edition, Prentice Hall, New Jersey, 1998 p. 759/

30. Operating Instructions - Tri-Flex 2 Permeability Test System, Ele International, Pelham, Alabama (undated)

31. Cliff Ho, et al., "Development of a Risk-Based Performance-Assessment Method for Long-Term Cover Systems – Application to the Monticello Mill Tailings Repository," Sandia National Laboratories, SAND2001-3032, 2001.

32. S. J. Piet, J. J. Jacobson, P. Martian, R. Martineau, and R. Soto, "Modeling and Simulation of Long-Term Performance of Near-Surface Barriers," Waste Management 03, 2003.

Alternative Waste Stabilization Technologies

D. Gombert, J. Richardson, J. Roach, and N. Soelberg

SUMMARY

This project proposes a radically different technology for converting radioactive waste into glass for final disposal. This technology, known as the cold crucible induction melter (CCIM), has the potential to significantly simplify and reduce the cost of waste stabilization around the world. Its potential applications also include high-temperature (>1,300°C), high-purity, and very corrosive melts (alumina, zirconia, ruby-glasses, and custom-design specialty glasses). Due to its range of capability and readily adaptable design for remote operation, the CCIM technology could serve as the next generation concept for converting highly-radioactive waste into glass for final disposal. The CCIM is essentially a noncontact melting design, and should have a design life many times greater than current designs, thereby reducing capital and maintenance costs significantly.

This project is dedicated to fully characterizing and extending the capabilities of the CCIM technology, while establishing a flexible prototype system at the INEEL. Project activities include designing a state-of-the-art variable frequency, variable-power unit capable of processing both liquid and solid feeds, verifying the theoretical modeling done in another project, and proof testing new crucible/induction coil configurations.

The activities conducted during FY 2002 resulted in the design and fabrication of the prototype system.

PROJECT DESCRIPTION

Background

The United States and Europe currently use joule heated melter (JHM) technology to convert highly- radioactive waste into glass for final disposal. This technology passes electricity between water or air-cooled electrodes submerged in a molten pool of glass in a brick-lined chamber. Although fairly reliable, this technology is inherently limited by the susceptibility to corrosion and melting of the refractory bricks and metal electrodes. In addition, the glass chemistry must be carefully controlled or it can exacerbate material problems that lead to electrical short-circuiting and glass leaks, which have caused failures in test melters.

Specialty glass manufacturers in the United States and Europe currently use induction melting for high-purity or high-temperature processing, but pay dearly for expensive platinum and high-purity ceramic crucibles. Ceramic-lined melter designs can be used for less demanding process conditions or product requirements, but may suffer relatively short lifetimes due to corrosive conditions.

Recent DOE studies[1,2] supported by the Tank Focus Area (a national research and development program supported by the DOE to solve technical problems associated with disposition of high-level waste) have identified the need for a more rugged glass melter with a wider operating range. Russian researchers also point out that a new melter concept will be needed to process some of the unique high activity waste still in storage and unsuitable for processing with the current JHMs at Mayak.[3]

During FY 2002, in collaboration with Russian colleagues and the University of Montana, a new test facility was designed and fabricated at the INEEL for the new CIMM technology. The facility has a novel stainless steel segmented crucible with bottom and side drains, powered by a 60 kWe high-frequency power supply.

The CCIM inductively heats the melt inside a water-cooled, segmented crucible that is essentially transparent to the magnetic field. This allows the molten material to be maintained at temperatures above 2,000°C while contained within the solid shell or “skull” of the feed composition. The skull isolates the melt from the crucible, eliminating the need for glass-contact

refractory and electrodes, as well as the corrosion and temperature limitations of those materials.

The remainder of this section describes the CCIM modeling basis and designs for the following systems: induction power, mechanical, offgas, cooling, and instrument and control.

Modeling

Modeling will provide needed design information and insight into melter system operation. CCIM electromagnetic thermal fluid modeling supports two issues: Engineering design of pilot- or full-scale CCIM waste processing systems, and furthering our understanding of how to configure and operate a CCIM to maintain final waste form quality.

The FY 2002 CCIM modeling effort was funded by another program, which was funded some months before the melter design effort began. Consequently, it only indirectly benefited the project during FY 2002 by providing the baseline technical capability to enable initiation of the CCIM prototype design project. The modeling capability will be used subsequently to provide valuable design and operating input as the ESRA project proceeds.

Performance Requirements

FY 2002 project activities focused on (a) developing and validating computer-based models representing energy deposition, temperature, and residence time for various melter configurations and waste formulations, and (b) the model basis for the design of the power deposition and control system for the pilot scale system.

These models will help meet the following objectives:

1. Understand energy deposition, temperature profile, and residence time for axially symmetric single-frequency configuration

2. Identify operating conditions regimes acceptable for waste treatment (time, temperature, waste loading, etc.)

3. Control system schema, including dynamic response, linearization, and load presented to power supply

4. Identify scaling factors and develop methodology to scale designs

5. Determine offgas processing requirements and how they are affected by melter operational characteristics (waste constituents and forms, profiles, cold cap, reflux wall temperature, etc.)

6. Assess external inductor melter geometries such as elliptical, cruciform, etc.

7. Assess multiple-inductor geometries, including focused inductors (stirring by convection) and gimbaled inductor geometry

8. Understand multiple frequency responses

9. Establish crucible cooling geometries including defined wall gradients (hot reflux, vertical and horizontal gradients)

To date, objectives 1, 2, 3, 4, and 5 comprise the basis for a high confidence-level baseline design, and objectives 5 (future work), 6, 7, 8, and 9 comprise optimization of baseline and can be performed and adopted during the design and construction phases of an operational CCIM facility project.

Strategy/Engineering Approach

The INEEL has developed two complimentary models. The first is a bulk electrical properties model being developed jointly by the INEEL and Montana Tech, which represents the melt as a single load conductance presented across the primary induction coil. This model, called the lumped parameter LOAD model, provides a single measurable melter parameter that can be used as the basis for feedback control. It assumes axial symmetry and computes inductive energy deposition while accounting for varying resistivity with temperature. It is also represented as an equivalent circuit simulation using a finite difference algorithm. The second is a finite element model that simulates the internal state and processes in the melt, such as temperature profiles,

convection, and inactive regions. This model, which is being reviewed and revised with the help of the Electrotechnical Institute in St. Petersburg, Russia, accounts for inductive energy deposition and temperature variation of density, electrical resistivity, thermal conductivity, and specific heat; also, the energy required for dissolution of inputs and losses through the cold cap.

Lumped Parameter LOAD Model

The objective of the lumped parameter LOAD model was to develop a representation that results in a single-load resistance term across the primary inductor of an induction melter that can be measured with external instruments. The hypothesis is that a known melter state can be maintained without the need for online measurements within the melt itself by measuring and controlling this value.

Lumped parameter model development is based on several key assumptions:

1. Cylindrical symmetry, regardless of the thermodynamics of the heated medium, with temperature variation only in the radial direction.

2. Thermodynamic and electrical effects can be modeled separately because electrical induction is occurring during time periods more that four orders of magnitude faster than thermal. The resulting thermodynamic and electrical calculated values are then coupled.

3. One can take full advantage of the assumption of symmetry and independence and model the thermal effects as a nonlinear diffusion equation with variation only in the radial dimension. The computed temperature distribution feeds into the electrical model to allow temperature corrections of electrical conductivity.

The electromagnetic model accounts for energy deposition in the melt by induction. Each computed cell of the thermodynamic model is assumed to be at its individual cell temperature. The electrical model adjusts the electrical conductivity of the thermodynamic cell based on cell temperature by taking each thermodynamic cell and representing it as a number of electrical cells that compute power. The power in each cell is computed from a simple Ohm's Law relationship where V_{cell} is the potential seen by the specific electrical cell that has been corrected for skin depth. R_{cell} is the characteristic resistance of the specific electrical cell.

The overall result is a very simple lumped parameter circuit where the melt is characterized as conductance of the melt volume, or Gmelt.

Finite Element Model

As noted above, a second model was developed using finite element techniques. We used the commercial finite element heat transfer and computational fluid dynamics code FIDAP to compute the electromagnetic field and heat transfer for the finite element model of the CCIM. The model is based on a previous JHM model developed at the INEEL. The model calculates the magnetic vector potential, which has real and imaginary components. A modified magnetic vector potential is calculated from the following equations in axi-symmetric form:

$$\frac{\partial^2 \phi_c}{\partial r^2} + \frac{\partial^2 \phi_c}{\partial z^2} - \frac{1}{r}\frac{\partial \phi_c}{\partial r} = \mu_0 \sigma_e \omega_e \phi_s$$

$$\frac{\partial^2 \phi_s}{\partial r^2} + \frac{\partial^2 \phi_s}{\partial z^2} - \frac{1}{r}\frac{\partial \phi_s}{\partial r} = -\mu_0 \sigma_e \omega_e \phi_i - \mu_0 r J_\theta \qquad (1)$$

Capabilities of System

At their current state of development, both the lumped parameter model and the finite element model generate useful results. Figure 1 illustrates the energy and temperature profiles generated by the lumped parameter model. Note the melt temperature has stabilized. The increase in temperature near the wall results from energy deposition primarily occurring near the walls where the inductive field is strongest.

Figures 2 and 3 show finite element model examples of the real magnetic vector potential and the nondimensional temperature.

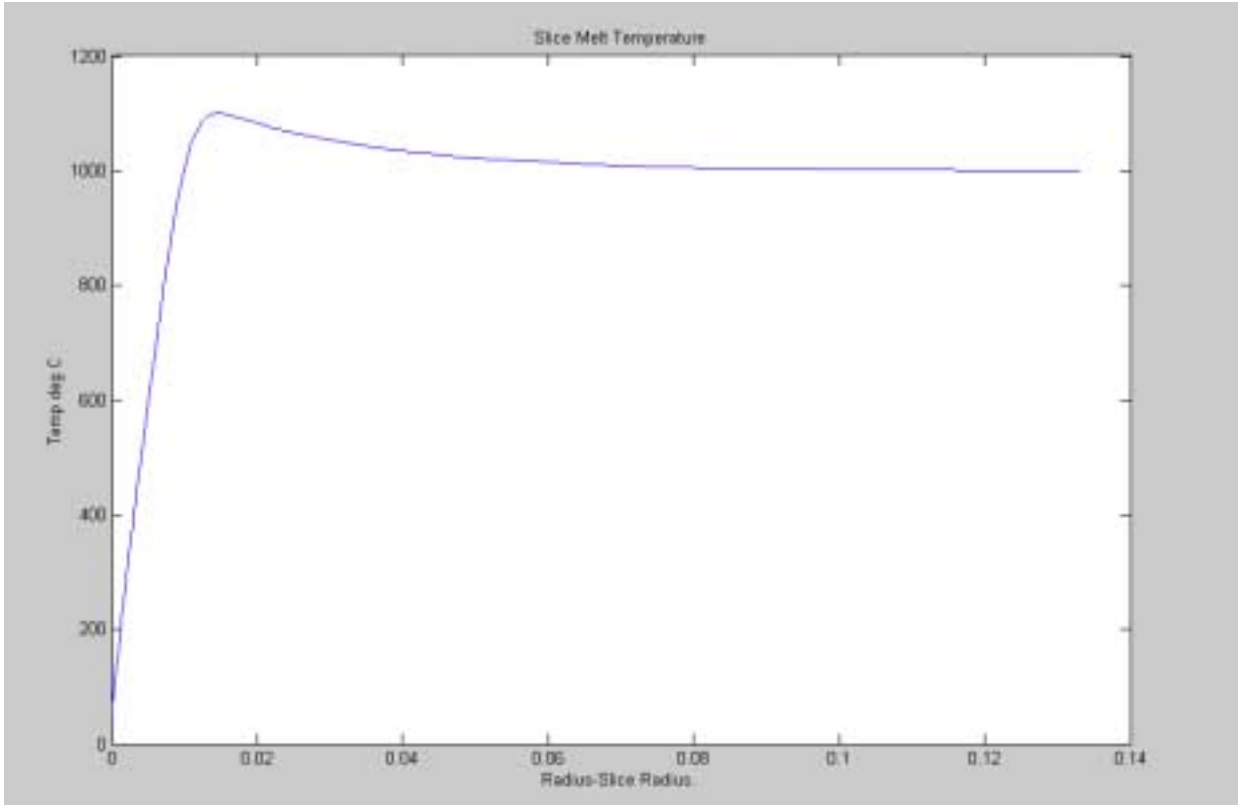

Figure 1. Lumped parameter model melt temperature profile.

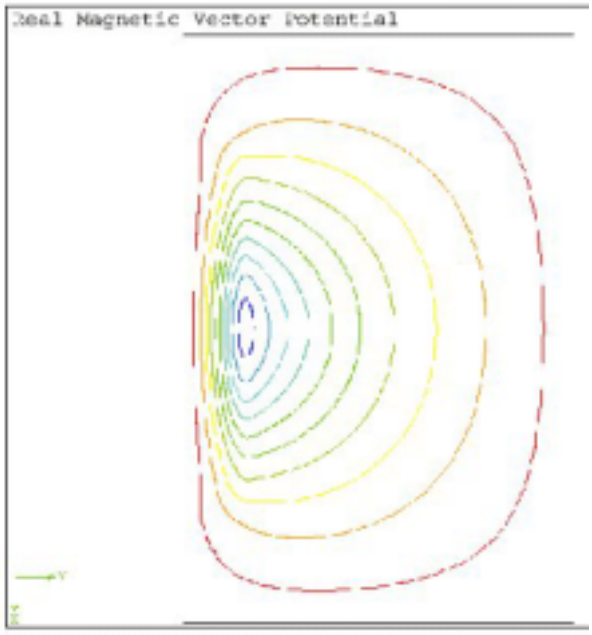

Figure 2. Finite element calculated real magnetic vector potential profile.

Figure 3. Finite element calculated nondimensioned temperature profile.

Induction Power System

Performance Requirements

The induction power system consists of three major components: a radio frequency generator, a coil transfer relay, and a primary induction coil. The system configuration and each component perform distinct functions and must respond to certain design requirements to ensure overall system performance. Thermodynamic calculations, systems issues, safety concerns, and operational considerations are all factored into system performance requirements. The primary requirements for the CCIM Induction Power System are:

- Nominal maximum output power 60 kW.
- Ability to operate at output powers between 10 kW and 60 kW.
- Ability to inductively conduct energy into molten glass inside cold crucible of specified diameter.
- Frequency range: 200–400 kHz, 2.0–4 MHz; ± 10%.
- Continuous operation.
- Output power control: manual via panel control, and 4–20 mA current input control signal.
- Interlock automatic shutdown and binary voltage outputs: tube and coil internal coolant, access panel interlock, and power system status.
- Shutdown: provide remote "red switch" emergency shutdown capability via open or closure contact input. Design shall allow parallel or series connection of one or more additional remote emergency shutdown switches. Generator shutdown response time shall be <1 second.
- Dynamic response: rise-time response of less than 2 seconds.

Strategy/Engineering Approach

Design of the Electromagnetic Induction Power System followed a series of specific intermediate designs and calculations. First, the electrical power of the radio frequency generator power was specified based on desired melter throughput and calculated heat loss. These same calculations yielded desired external crucible diameter and desired height of melter volume. Second, a design basis value of melt resistivity was selected. A survey of various sources of data on borosilicate glasses at nominal operating temperatures of 1,050–1,250°C revealed a range of resistivity values of 2 ohm/cm to 10 ohm/cm. A value of 6 ohm/cm was selected as the design basis for the CCIM prototype melter.

The next step in the design of the electromagnetic induction power system was to determine an appropriate operating frequency that provides an optimal melter throughput. It has been determined empirically[4] that for cylindrical melters the diameter should be approximately a factor of 3.8 times the skin depth (represented as δ) at the nominal frequency of operation. The skin depth is calculated:

$$\delta = 5*10^3 (\rho/\mu f)^{1/2} \qquad (2)$$

where

ρ	=	electrical resistivity in ohm-cm of the melt
μ	=	magnetic permeability of the melt
f	=	frequency of the energy being applied in hertz.

Accounting for the 3.8 factor and rearranging, optimal frequency of operation can be determined with:

$$f = 3.6*10^8 (\rho/\mu d^2) \qquad (3)$$

where d represents the diameter of the melted volume.

After specification of the power level, physical diameter, coil height, and computation of the optimal operating frequency, it is possible to calculate the number of amp-turns of the primary inductor. The approach used in the CCIM prototype design was outlined by Baker[5] in a classical induction melter paper published in 1957. Briefly, we performed the following procedure:

1. Calculate the total magnetic flux using previously determined values for power, diameter, resistivity, height, and magnetic permeability of molten glass.

2. Calculate the coil voltage for various numbers of coil turns using the total flux value, and accounting for skin depth within the coil material.

3. While accounting for external reluctance, compute coil current for each turn's configuration.

4. Select the number of turns compatible with physical constraints and current capability of the radio frequency source and transfer relay.

These calculations resulted in the selection of a six-turn active coil configuration.

The next step in the process was the physical design of the primary induction coil. The total inductance and leakage inductance of two-coil geometries were measured: a single six-turn coil, and two three-turn coils in parallel. The former operates at higher voltage, and the latter operates at higher total current. Both provide the same number of amp-turns calculated from the coil design procedure outlined in the previous paragraph. Both coils were considered candidates, with final choice dependent upon selection of a commercial radio frequency power generator, and its ability to generate and deliver energy at the nominal operating frequency to one or both coils with their respective total inductances.

Finally, an energy-transfer system was designed. Conventional melters use a fixed primary inductor and vary the vertical position of the crucible within the induction field to focus the energy deposition depending on operations such as startup, feeding, and glass pouring. This involves using a piston or screw device, but moving parts are undesirable for a prototype of a production radiological melter. The final design for the coil to be used in a radioactive environment will be a focus of future research.

Upon completion of coil design, an RF generator was specified. Technical specifications resulting from the above calculations included power level and output current, induction frequency and load inductance, and interface compatibility with the novel coil energy transfer system.

Description

Following the above calculations, we completed the detailed engineering design and implementation of an electromagnetic induction power system. Major components include a Taylor-Winfield Thermionic C-6000 radio frequency generator, a coil transfer relay, and the induction coil.

The Thermionic C-6000 electronic induction radio frequency generator (RFG) consists of three major subsystems including a high frequency generator chassis, an enclosed plate transformer unit, and a control workstation (see Figure 4). The high frequency generator chassis contains a twin-tube tuned-grid tuned plate Class C oscillator operating at a nominal output power of 60 kWe (see Figure 5).

Figure 4. C-6000 high frequency generator chassis and control panel.

Figure 5. Tuned-grid tuned-plate oscillator.

The ITT F-5771 power triodes each have a plate dissipation of 22-1/2 kWe when operating in Class C mode. Also contained in the generator chassis is a primary de-ionized water circulation system that provides cooling for the tube anodes, high voltage oil-filled capacitors, and power inductors. Cabinet air is cooled as necessary via a water-to-air heat exchanger. The secondary system consists of a propylene glycol circulation loop to an external chiller unit. The enclosed plate transformer supplies a nominal 15-kV, 3-phase power to the generator chassis. 480-V input to the plate transformer is switched by a variable duty-cycle phase-controlled firing system in the generator chassis. The 15 kV transformer output, which is rectified with a 3-phase, full-wave bridge in the chassis, is subsequently filtered to provide low-ripple direct current to the triode oscillator. Varying the angle of the firing system allows programming the plate voltage to the triodes, thus controlling output power. The control workstation is a stand-alone panel providing front panel monitoring of power, plate and grid current, anode voltage, and interlock status.

During the design process it was determined that the output capacitance of the three 750 pF vacuum capacitors installed in the C-6000 is compatible with two three-turn inductors in parallel, which is one of the two primary inductor candidate configurations identified and characterized earlier. These capacitors can be seen in Figure 6. The resulting frequency of oscillation is within 5% of the optimal induction frequency, and both the current and coil voltage are well within the capabilities of the C-6000 unit as currently configured. The induction coil is made from 0.95 cm (3/8 in.) copper tubing with a nominal a nominal internal diameter of 30 cm.

Figure 6. Inductor power transfer relay.

Capabilities of System

The electromagnetic induction power system provides induction power of 60 kWe at a nominal frequency of approximately 2.6 MHz. Power is adjustable via the control panel or 4–20 mA computer interface continuously over the range of 10–60 kWe. Maximum design power output is 75 kWe. Overpower interlocks prevent this power from being obtained without readjustment. The generator can be reconfigured to provide full power at a single frequency over a frequency range of 200–400 kHz and 2–4 MHz. This range can be extended above 4 MHz, but full output power is not guaranteed. Similarly, the induction coil can be reconfigured to transfer energy over these frequency ranges. Efficiency will vary, however, as throughput rates are optimized only at frequencies related to melt resistivity. The generator is capable of providing power to a wide variety of inductor designs. Note that operation between 400 kHz and 2 MHz is prohibited for commercial operation in the U.S.

Functionality is included to continuously monitor operating parameters within the power supply system and provide automatic shut down under preset conditions. In addition, multiple and redundant safety interlocks are provided to protect operators.

Mechanical System

The key mechanical components of the CCIM system include the crucible, the glass drain system, and the offgas lid. Extensive structural support components have been designed, fabricated, and procured as necessary for the primary crucible and ancillary systems; however, these are not discussed in this report.

Cold Crucible

Performance Requirements

The cold crucible must provide containment for the material fed into the induction field, while cooling the walls to provide thermal insulation for maintaining structural integrity. The cooling fluid used for this system is de-ionized water. As a result, the cooling system must provide adequate temperature control for the crucible walls while ensuring that the cooling water does not reach its boiling temperature. This must be accomplished while maximizing the energy deposition from the induction coil into the melt chamber formed by the crucible. Several factors impact the energy deposition into the melt, including crucible materials of construction, crucible wall configuration to minimize eddy current paths, crucible wall configuration to provide an efficient induction energy path, crucible bottom configuration to minimize eddy current paths, and relationship of the induction coil geometry to the crucible geometry. The crucible must also accommodate the glass drain systems that are necessary. Similarly, the crucible must provide appropriate interface with the offgas lid and associated feed, offgas, and other penetrations.

Strategy/Engineering Approach

The basic geometry of the crucible is determined by three main factors: the power level of the high-frequency generator, the relative magnetic permeability of the melt, and the electrical resistivity of the melt. These two material properties—magnetic permeability and resistivity—are particularly critical in optimizing the overall system efficiency, because they drive the coil geometry and operational frequency for a given power level. Nominal values for the material properties were selected that are expected to be representative of the waste surrogates that will be processed in the CCIM, based on previous research that has been conducted within the DOE, as well as by the Russian scientists with whom the INEEL is collaborating. Specifically, the relative magnetic permeability is assumed to be unity, and the resistivity is assumed to be between 6 ohm-cm. Additionally, a 60 kWe high-frequency generator was purchased, thus establishing the values for the three critical parameters. Since the power that is deposited into the melt is strongly dependent on the ratio of the diameter of the melt volume to skin depth (d/δ), and the skin depth is determined by the permeability, resistivity, and frequency of operation, an iterative approach was used to arrive at a nominal optimal diameter of 10.5 in. (26.7 cm) for the melt chamber. This in turn determined the overall crucible height of 16.0 in. (40.6 cm), which provides appropriate clearance from the induction coil to minimize eddy current losses. Industry practice typically uses one coil radius as a rule of thumb for adequate clearance from the top or bottom of the coil.

Several key differences in design philosophy exist between Russian collaborators and INEEL engineers due to application requirements. For example, the Russians typically drain melted glass from the side of the crucible, near the middle of its length. They operate with a two-turn or three-turn coil, melt in a concentrated zone in the middle and drain from that zone, creating a “marsh” area below the coil that is an unpredictable mixture of unmelted glass, waste material, slag, and molten product. This zone cannot be drained and always remains in the crucible. Additionally, the offgas system used in the Russian applications is generally not as rigorous as DOE systems, which greatly simplifies their offgas system interface requirements.

This crucible is designed to accommodate both a bottom drain and lower side drain for pouring melted glass. The details of the glass draining systems are discussed below; however, their design configurations determined the crucible configuration, particularly at the bottom manifold.

As previously discussed, the greatest energy flux into the melt occurs within the skin depth,

which is measured from the inside diameter of the induction coil. Consequently, the efficiency of the system is maximized when the space between the inside diameter of the coil and the outside diameter of the melt cylinder is minimized. For this project, the crucible is constructed of 0.50 in. (1.27 cm) diameter cooling tubes. This size was considered to be the smallest that could be reasonably machined and welded into a useable assembly based on the designated crucible diameter. One key factor that impacts this choice is the necessity to maintain a fixed separation between the individual cooling tubes for their entire length to reduce the eddy current losses, thus increasing the energy deposition into the melt volume. Experimental results by U.S. and Russian researchers show that the crucible wall should be constructed using at least 24 sections with nominal separation gaps of 1–2 mm to allow efficient energy deposition. Comparative testing of 4-segment versus 24-segment crucibles showed projected increased melt rates of over 90% at 60 kWe.[6]

Materials of construction are a key consideration when optimizing an induction melter system. The material commonly used in industry for water-cooled induction heating systems is copper. This is due to the low electrical resistivity of copper and the high thermal conductivity. As a comparison, nominal values for electrical resistivity of copper versus 304 stainless steel at 20°C are 1.7×10^{-6} ohm-cm and 60×10^{-6} ohm-cm, respectively. Similarly, the thermal conductivity values at 20°C are 340 W/m-K versus 14 W/m-K, respectively. However, for applications involving treatment of radioactive waste streams, the secondary products generated during processing can be highly corrosive and materials such as stainless steel, Inconel, or Hastelloy alloys are more suitable, regardless of the electrical losses. Although virtually all of the laboratory scale crucibles being operated by Russian scientists at the Khlopin Radium Institute and the Electro Technical University are constructed of copper tubing, the units at the Radon Production Association facility, which are used to process actual radioactive waste, use all stainless steel construction.

The most important function of the crucible is to provide adequate cooling to maintain a slag layer to protect the crucible materials while not allowing the cooling water to be overheated and boil. Analysis of the overall heat balance for the crucible, mating offgas lid, and bottom drain are fairly complex, even for steady-state operations. Simplifications were made for the initial design that provide conservatism. Beginning with Fourier's Law:

$$Q = -k\nabla T \tag{4}$$

$$q = -k(\partial T/\partial x + \partial T/\partial y + \partial T/\partial z) \tag{5}$$

Combining this with the energy conservation equation (heat diffusion) yields:

$$\partial/\partial x(k\partial T/\partial x) + \partial/\partial y(k\partial T/\partial y) + \partial/\partial z(k\partial T/\partial z) + q' = \rho c_p \partial T/\partial t \tag{6}$$

For one dimensional steady state analysis of a radial system, a thermal resistance approach can be used. The governing equation is then:

$$q = (T_1 - T_{4,\infty})/\{[\ln(r_2/r_1)/2\pi k_{melt}] + [\ln(r_3/r_2)/2\pi k_{slag}] + [\ln(r_4/r_3)/2\pi k_{ss}] + [1/2\pi r_4 L h_{water}]\} \tag{7}$$

where

$T_{4,\infty}$ = temperature of melt

T_1 = bulk temperature of cooling water

r_1 = distance from crucible centerline to centerline of skin depth

r_2 = distance from crucible centerline to interface between melt and slag layer

r_3 = distance from crucible centerline to interface between slag layer and cooling tube wall

r_4 = distance from crucible centerline to interface between tube wall and cooling water

k_{melt} = average thermal conductivity of melt

k_{slag} = average thermal conductivity of slag

k_{ss} = average thermal conductivity of stainless steel

h_{water} = convection coefficient of water flowing in cooling tubes

Physical Description

The crucible designed for this project is constructed of 304 stainless steel. It consists of three primary components: the lower manifold, the cooling tubes, and the upper manifold. The lower manifold, which provides the supply and return lines for the cooling water, is a 11.75 in. (29.8 cm) diameter by 2.0 in. (5.08 cm) deep hollow disk segmented into eight separate sections. The manifold is segmented because the lowest active coil of the inductor is only approximately 1.00 in. (2.54 cm) above the upper plate of the lower manifold. This is part of an innovative energy deposition scheme that concentrates the induction energy to appropriate locations during various operational phases. Invention Disclosure Record 146 has been submitted documenting this novel approach. The contact surfaces between the segments are coated with a nonconductive high-temperature ceramic that provides electrical isolation. This approach helps minimize the eddy current losses in the lower manifold. Each pie-shaped segment consists of two chambers. The lower chamber is larger volume than the upper chamber, which ensures constant, full flow in the upper chamber and cooling tubes, which are in contact with the melt surfaces. The lower manifold also includes a specially designed bottom drain interface slot that provides for efficient location, ease of maintenance of sacrificial components (the drain tube), peripheral cooling, and ease of replacement of the bottom drain.

The upper manifold is a 0.87 in. (2.2 cm) deep doughnut shaped hollow disk with a 16.5 in. (41.9 cm) outside diameter, and a 10.5 in. (26.7 cm) inside diameter. The configuration of the upper manifold is designed to provide an appropriate interface surface with the offgas lid and to provide an inside volume the same as the cooling tubes to ensure full flow and minimize accumulation of air/steam bubbles in the cooling system. The upper surface of the manifold has 0.375 in. (0.965 cm) diameter by 1.5 in. (3.81 cm) long threaded studs welded on a 15.5 in. (39.4 cm) diameter bolt circle for mating with the offgas lid. The flow chamber is internally segmented to provide flow control for the cooling water. The upper manifold also contains relief valves to ensure that the crucible could never be over-pressurized due to blockage and steam build-up.

The cooling section consists of sixty 0.50 in. (1.27 cm) diameter by 16 in. (40.6 cm) long tubes attached into the upper and lower manifolds on a 10.75 in. (27.3 cm) diameter centerline, providing a nominal longitudinal tube spacing of 1.5 mm. Four additional cooling tubes located directly above the bottom drain complete the circle to form the complete melt chamber; however, these are actually part of the side drain and are described below. The isolation gap between the individual cooling tubes will be sealed from the outside using a ceramic putty specifically formulated for such applications. The putty will be placed on the outside because the crucible will be under slight vacuum due to the offgas system and this will minimize flaking into the melt. Figure 7 shows the crucible assembly during welding.

Figure 7. Crucible assembly.

Capabilities

As designed, the crucible meets all of the performance requirements identified above. During operation, the crucible will contain up to 3.75 gallons (14.2 liters) of melt, while maintaining appropriate temperatures in the crucible walls. Based on calculations, the crucible will be able to effectively function at full power of the generator (60 kW) and up to 2,000°C. The designed residence time of the water in the crucible will result in a heat flux into the cooling water at this operating level, which will only increase the temperature by about 20°C. At nominal operating levels (20 kW) only a 7°C increase is expected. These calculations are consistent with actual experience in the Russian melters, although they are different configurations.

The induction coil will be separated from the crucible by a 0.125 in. (0.31 cm) thick fused quartz tube, thus providing only 0.63 in. (1.6 cm) dead space between the coil and melt volume, using over 77% of the skin depth energy.

Glass Drain System

The glass drain system actually consists of a bottom drain and a side drain. The bottom drain is the primary drain mechanism; however, the initial crucible design will include a side drain during testing of the bottom drain operation.

Performance Requirements

Above all, the glass drain system must be able to evacuate the entire volume in the crucible. Large quantities of residual waste/glass/slag mixtures in the bottom are not acceptable. The glass drain system must have adequate temperature control to heat to 1,000°C during draining and below 350°C at other times. The drain assembly must be able to provide quick response to minimize heat-up and cool-down times, thus offering efficient operation for research and field operations. Heat up from ambient to 1,000°C should be accomplished within 5 minutes. The materials of construction must be able to withstand these operational temperatures and be resistant to the erosion of molten glass. The assembly must also be designed such that thermal expansion can be accommodated without impact to the components. The design must be easily adaptable to remote operation, offering ease of installation and maintenance.

Strategy/Engineering Approach

The majority of the energy from an induction coil is deposited into the skin depth, thus providing a uniform flux, and the most predictable conditions. Based on this, the bottom drain was designed to provide draining from the middle of the skin depth zone. Pouring from this area will provide the greatest control over the temperature and resulting viscosity of the melt.

Because erosion is a major problem in glass drain systems, the drain tube is considered a sacrificial component in this design. Consequently, the configuration of the drain tube was designed such that it contains no threaded components and is easily removed and replaced without disassembly of any other systems. The internal configuration of the drain tube has been designed to provide clean pouring with minimum wicking. It is also designed to provide maximum flexibility in adapting the drain orifice to the melt viscosity as necessary.

High operational temperatures such as 1,000°C are difficult to reliably achieve in ambient air with traditional nichrome-type heaters. Additional induction heating can be used, but this adds complexity to the overall design of the drain. However, because the drain is located in the skin depth zone and is a solid conductive material, the induction field will couple with the bottom drain system, augmenting the heating system for the drain. Significant advances have been made using advanced ceramics and vapor deposition techniques to manufacture heaters that can achieve and operate at the temperatures required for a molten glass drain system. A novel heating sleeve was designed and manufactured using these advanced technologies for the CCIM project. Resistance heating is accomplished by introducing an electric current into a pyrolitic graphite trace that is vapor deposited onto a boron-nitride ceramic substrate.

In addition to the bottom drain, a side drain system was designed into the crucible configuration. The side drain is located at the

bottom of the side of the crucible in the same proximity as the bottom drain to allow complete evacuation of the melt. This is considered a back-up system and will not be used if the bottom drain works as designed, but is deemed necessary until the bottom has been proven since it is an innovative design (an IDR has been submitted) that is yet to be tested.

Physical Description

The bottom drain assembly is constructed almost entirely of Inconel 693. This is a relatively new alloy that provides comparable corrosion resistant while offering much better machining capability than Inconel 690, the more commonly used material for these applications. This material selection allowed complexities in the configuration of internal components to be more effectively manufactured. The bottom drain is a 2.5 in. (6.35 cm) diameter assembly that consists of five main components: outer guide sleeve, cooling spool, drain tube, heating sleeve, and bottom retainer. The assembly will be held in place in the crucible by close fit into an interface slot with a retainer lip on the crucible assembly. Contact with the walls of this interface slot provide cooling for the outer guide sleeve, where additional valve controlled cooling air is provided as needed to achieve desired temperatures. The heating sleeve is designed to provide 1.5 kW, which, coupled with the induction energy, is expected to be able to heat the drain tube to the necessary temperature within the desired time frame.

The internal configuration of the drain assembly has been designed to provide maximum heating capacity while minimizing cool-down time. Although an external mechanical sliding closure has been provided, this may prove to be unnecessary, as will the side drain system. Unique combinations of water and air cooling with induction and resistance heating provide an innovative approach for effectively draining glass from an induction melter system. Invention Disclosure Record 149 has been submitted on the bottom drain design. Figure 8 is a photograph of the assembled bottom drain.

The side drain assembly is also constructed using Inconel-693 (the components that are in contact with molten glass). It is comprised primarily of an air-cooled plug that can be manually lowered and raised, allowing molten glass to flow over the guide plate into a common container. To accomplish this, four of the cooling

Figure 8. Bottom drain assembly.

tubes must stop short of the lower manifold. For that reason, they are actually a separate assembly with an independent cooling water supply. The cooling water is provided through ports that pass through holes in the guide plate. These four tubes form a continuous circuit and are attached to the upper manifold for structural stability, but do not penetrate into the water chamber. The side drain is designed with a curved surface on the upper contact surface (on the cooling tube loop) to provide a single line for the closure seal. This minimizes the possibility of the side drain being blocked due to slag such that it cannot be closed. Figure 9 shows the components that constitute the side drain assembly.

Figure 9. Side drain components.

Capabilities

The bottom drain will be the primary glass drain mechanism. It will be capable of achieving temperatures up to near 1,500°C due to the innovative combined heating scheme. For nominal pouring applications of 1,000°C, the drain tube will be able to heat up from ambient temperature in less than 2.5 minutes, assuming 50% efficiency. The internal components of the bottom drain include heat transfer enhancing features that are designed to provide 86% efficiency at a nominal convection coefficient of 100 W/m^2-K, which is easily achievable using compressed air flow (forced convection). This allows for rapid cooling of the drain tube such that flow shut-off can be achieved within 2 minutes.

Offgas Lid

The requirements for offgas control drove many features of the offgas lid, as well as the crucible assembly. These instances will be identified as appropriate.

Performance Requirements

To minimize acid reflux on the crucible and in the offgas system, the offgas temperature in the offgas plenum must be maintained at 600°C. The offgas lid must be capable of maintaining a slight vacuum (1 in. wc) while minimizing air in-leakage and providing the ability to control the amount of air in-leakage to 5 scfm. The offgas must also provide disengagement distance equal to approximately one crucible diameter from the surface of the melt to minimize particulate and ejecta entering the primary offgas duct. This requirement, coupled with the requirement to provide one coil radius clearance from the upper coil of the inductor to the bottom of the upper manifold, was used to determine the overall lid height.

The offgas lid materials must be able to operate in a high-temperature, high-corrosive environment, and maintain structural integrity.

The offgas lid must provide interface to the crucible, the offgas system, dry feed system, liquid feed system, view ports, and thermowells for thermocouple access.

Strategy/Engineering Approach

The internal physical dimensions of the offgas lid were easily determined due to the coil and melt surface clearance requirements, along with the crucible interface configuration. Corresponding external dimensions would then be determined in accordance with the amount of refractory needed. However, one of the primary benefits of a cold crucible system is the absence of refractory in the melter. Unfortunately, most offgas lids for melters contain a layer of refractory to provide insulation as well as corrosion protection for the material. This limits the application of the CCIM system, and defeats the purpose of some of the research being conducted for this project. Therefore, an innovative design was developed for the offgas lid that eliminates all refractory while protecting the materials and maintaining outer temperatures at 50°C, or less. A series of heat shields are used to form chambers within the offgas lid, some of which are air cooled. This design is proprietary and has been documented in Invention Disclosure Record 130; therefore, only limited information can be provided on its configuration. The design was developed by modeling the lid for radiant heat transfer using a wide-band exponential model for a CO_2-H_2O-Soot offgas composition at 600°C. A method that approximates the inside of such a chamber using a speckled furnace gray model was employed. Additionally, an extensive literature search was performed to locate experimental values for emissivity of various materials at various temperatures and in various conditions. The analysis showed that the design goals could be met with this approach if a convection coefficient of 195 W/m^2-K could be achieved in one chamber, which is quite possible using compressed air forced convection. Therefore, this is the basis of the offgas lid design.

Since no refractory is used, the inner materials must be protected from the corrosive environment that can be generated when processing certain types of waste. To that end, a high-temperature advanced ceramic material was identified that has been formulated to match the thermal expansion of Hastelloy that can be easily applied to the structure. This coating was also accounted for in the thermal analysis model, since it impacts the emissivity of the material. This coating will be

applied to the inner most layer in closest proximity to the melt surface. All penetrations into this space will be seal welded to ensure that the offgas cannot enter into the cooled chambers and precipitate. The top of the offgas lid was also angled to minimize hot spots that generally occur at corners in heated ducts.

Physical Description

The offgas lid is a chambered "tophat" design with angled upper corners and a mating flange forming the "brim" of the tophat (see Figure 10). The complete outer shell, including the bottom flange is constructed of 304 stainless steel, while the inner shields, inner flange, and penetration tubes are of Hastelloy. The conical portion on the top is angled such that three 2.0 in. (5.08 cm) view ports can be used to view the entire melt surface and crucible walls above the melt line. The primary interface is a 5.5 in. (14.0 cm) duct that connects to the offgas system. The offgas lid also includes a 2.0 in. (5.08 cm) dry feed port, 1.0 in. (2.54 cm) wet feed port, and four 1.0 in. (2.54 cm) thermowell ports for thermocouple applications. All interface ports are flanged as appropriate to interface with mating systems. The offgas lid assembly has a 10.5 in. (26.7 cm) inside diameter and is 6.0 in. (15.2 cm) high on the inside. The bottom flange is an 18.0 in. (45.7 cm) diameter ring with mating holes for the crucible upper manifold bolts located on a 15.5 in. (39.4 cm) diameter bolt circle. It also contains eight cooling air supply and return ports located around the perimeter just above the bottom flange. A flexible gasket material will be applied between the interface surfaces to help minimize air in-leakage.

Capabilities

When operational, the offgas lid will be able to maintain the offgas plenum temperature at or above 600°C, while maintaining the outer shell at below 50°C, based on model calculations, allowing full access during operation. Operational temperatures above the nominal 1,200°C will require additional air in-leakage and increased cooling air flow, which are designed to be valve controllable for the specific need. The heated cooling air will be vented to the offgas system to provide needed preheated air for entry into the HEPA filters in the system.

When the assembly is complete, including all flanged port connections, the offgas lid will weigh less than 100 lbs (37.3 kg) and will be easily installed and removed. The disengagement length from the melt surface to the centerline of the primary offgas duct will always be greater than 10.0 in. (25.4 cm); however, during feeding, which is the most critical time, it will typically be 12.0 in. (30.5 cm) or more.

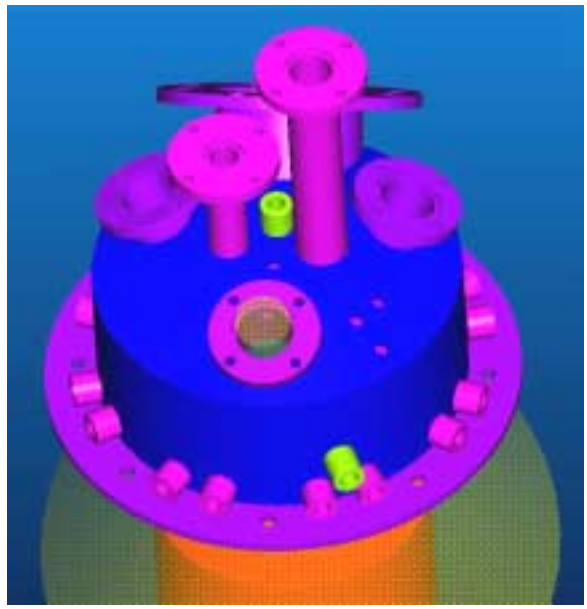

Figure10. Offgas lid components.

Feed System

Performance Requirements

The feed system must be capable of adding various types of industrial glass compositions as well as simulated DOE waste into the CCIM. The system must support a full range of testing, including foreseeable corrosive solutions, chemical additives, and fritted glasses. The feed may be introduced to the melter continuously or in batches, and slurries may be used requiring continuous agitation.

Strategy/Engineering Approach

The feed systems for the CCIM were designed to handle solids, liquids, and slurries. Separate

systems convey dry or wet materials all the way to the melter plenum. The feed lines drop straight into the melter, precluding holdup, and the feed lines may each be isolated. The solid feed system has been designed to handle glass frit, glass forming chemicals, and granular or powdered sugar (used as a chemical reducing agent). The stainless steel liquid feed system will handle most corrosive nitric acid based solutions. A mixer located in the feed tank will maintain any slurries used as a feed as in suspension.

The solid feed system consists of a K-tron Twin Screw Volumetric Feeder (Model K2 MV-T35). A variety of feeder screws can accommodate various bulk materials. The various screws can provide solids feed rates from 1.25–2,500 L/hr (1.7–3,400 kg/hr). All parts in contact with the material being fed are stainless steel. An oversized feed hopper (60 L) will assure that the nominal solids feed rate of 3–10 kg/hr can be maintained for several hours without recharging the feeder.

The liquid feed system has the capacity to feed a solution or slurry through stainless steel lines to the CCIM at a rate up to 20 L/hr using a Masterflex L/S pump. The feed tank has a capacity of 200 L. An impeller in the tank provides mixing to maintain the feed as a homogenous liquid or suspended slurry. The solution is pumped through a line and recirculated back to the feed tank providing a constant feed supply to the feed pump, and helping mix. The feed pump for the liquid system is capable of pumping up to 204 L/hr.

The feeds will be deposited in the center of the melt in line with a view port and monitoring camera. This will allow studies on maximizing melter throughput, and visual observation of surface cover and turbulence.

Offgas System

The CCIM offgas treatment system is designed to provide the necessary control of offgas emissions from the CCIM as well as a test bed for evaluating offgas system unit operations. The offgas system is a smaller-scale working model of a full offgas system that would be required in a full-scale waste treatment facility to meet the Hazardous Waste Combustor (HWC) Maximum Achievable Control Technology (MACT) standards.

The CCIM test system, when co-located with other potential test systems such as the laboratory-scale steam reformer or the autocatalytic diesel reformer, can use shared and co-funded offgas components. The CCIM offgas system may also be used for other, specifically offgas system-related research or demonstrations for NO_X, particulate, or mercury control studies. The system described below is the complete offgas system that would be used for CCIM, steam reformer, or other tests where a nonradioactive simulant of sodium bearing waste (SBW), including such hazardous components as Cd, Pb, Hg, and nitric acid is used.

The FY 2002 ESRA funds did not provide the full offgas system described below. While the full system as described is now being designed, procured, and installed, progress to date does not include the full offgas system. The progress to date, with ESRA and limited other funding expended at the end of FY 2002, is summarized below.

Performance Requirements

The offgas system is designed to meet the following performance requirements:

- Control a slight vacuum in the CCIM plenum space during operation.
- Enable testing and demonstration of the complete treatment system model, including evaluations of offgas composition, flowrate, and conditions, and evaluations of the performance of key offgas system unit operations, including NO_x reduction, organics oxidation, acid gas scrubbing, particulate filtration, and mercury control.
- Control specific air pollutants in the CCIM offgas to levels expected to be required to meet applicable regulations based on the assumption that the HWC MACT standards would apply to a CCIM system designed to treat sodium bearing waste.
- Assure worker and facility protection during testing from various hazards in the feed or

offgas, including high temperatures, particulate matter, Cd, Hg, NO_x, and CO.

Strategy/Engineering Approach

Several options exist for offgas systems designed to meet requirements such as the HWC MACT standards. Various options for high-performance offgas systems for mixed waste treatment are grouped into four general approaches[7]:

- Dry systems (partial cooling, dry particulate filtration, and dry acid gas scrubbing)
- Dry-wet systems (partial cooling, dry particulate filtration, and then wet acid gas scrubbing)
- Wet-dry systems (total quench and wet scrubbing for both particulate and acid gases, followed by dry final particulate filtration)
- Entirely wet systems (total quench and wet scrubbing for both particulate and acid gases).

Dry offgas systems avoid any liquid secondary waste streams, which is a requirement at some facilities. Acid gas scrubbing is accomplished by dry adsorption of acid gases onto hydrated lime sorbent that is injected upstream of the baghouse and collected in the baghouse. But entirely dry offgas systems require operator control and maintenance associated with sometimes problematic dry sorbent feed systems that is undesired in mixed waste systems where worker exposure to radioactivity and radioactive contamination are important concerns.

In a dry-wet system, particulate (including most of the toxic metals and radionuclides) is removed from the offgas to form a dry secondary stream that may be recycled to the primary treatment device or immobilized for final disposal. Acid gases are removed by wet scrubbing following the particulate removal. The dry-wet system may use lower temperature baghouses or high-temperature filters for the initial particulate control, followed by wet acid gas scrubbing. Some designs include reheating and final dry filtration downstream of the wet scrubber, and so could also be correctly called dry-wet-dry systems. Dry systems require higher temperature (up to 800°C) filtration or partial, controlled offgas cooling to more traditional baghouse filtration temperatures below 200°C. Higher temperature filtration and partial, controlled cooling are not well demonstrated for mixed waste treatment applications.

The offgas in a wet-dry system is rapidly cooled and all contaminants, including PM, radionuclides, toxic metals, and acid gases are wet scrubbed. These produce a single secondary aqueous mixed waste with some suspended and dissolved matter. After wet scrubbing, the offgas is reheated (to prevent moisture condensation in downstream control equipment) and dry-filtered to remove trace-level particulate and other contaminants.

Entirely wet systems are commonly used in many thermal processes including hazardous waste incineration and some mixed waste incineration systems such as the Toxic Substances Control Act Incinerator (TSCAI) facility. Wet systems do not include post-scrubbing reheating and HEPA filtration, a standard for most radioactive and mixed waste handling and treatment processes.

Each of the four general types of offgas systems has several distinct advantages and disadvantages because of the differences in how each type addresses particulate and acid gas control. After consideration of these advantages and disadvantages, a wet-dry system model was selected for the CCIM test system. Wet-dry systems have been used more widely in mixed waste treatment systems than any other approach. Wet-dry systems provide very high and redundant removal efficiencies for pollutants subject to the HWC MACT standards.

The following goals and constraints were considered for the offgas system:

- Sizing calculations considered the offgas flowrate and conditions, not just for the CCIM, but also the steam reformer test system being designed for evaluate steam reforming for SBW.
- Functional and operating requirements for each component were defined based on both the CCIM and steam reformer test systems.

- Equipment is designed to enable sampling access prior to and after each major component, and to allow quantitative cleaning and recovery of material captured in each component following each run.
- The equipment downstream of the quench unit, starting with the scrubber, must be located so that quenched offgas from an adjacent test system such as the steam reformer can enter the scrubber.
- Test systems such as the CCIM and the steam reformer will not operate simultaneously and will share the offgas system downstream of the quench unit.
- A new stack will be procured and installed.

System Description

The CCIM offgas system is shown in Figure 11. Primary components of this system, starting at the CCIM lid, are:

- Heated duct to the thermal reaction chamber
- thermal reaction chamber
- Offgas quench section
- Wet scrubber system
- Offgas reheater
- Offgas HEPA filter
- Activated carbon bed for mercury capture
- Induced draft fan

CCIM Pilot Test Green Offgas System
21 June 2002

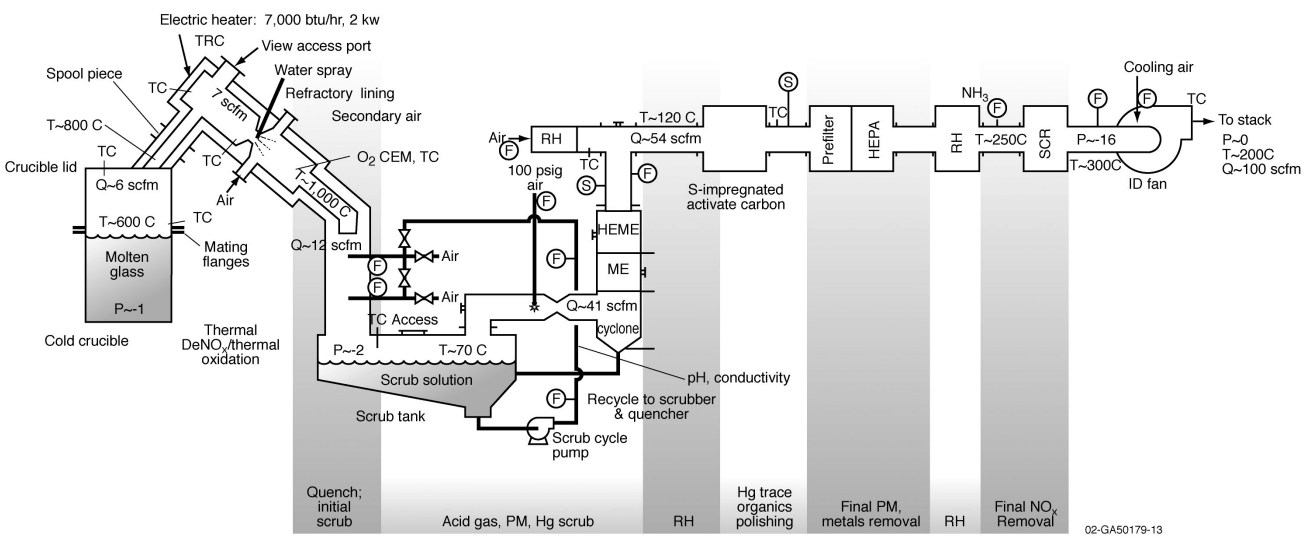

Legend:

S	=	Sample points	Q	=	Flowrate, scfm
TC	=	Thermocouple	ME	=	Mist Eliminator
PS	=	Pressure Sensor	HEME	=	High Efficiency ME
DP	=	Differential pressure indicator	PM	=	Particulate Matter
F	=	Flow indicator	CEM	=	Continuous Emission Monitor
pH	=	pH sensor	RH	=	Electric reheater
NG	=	Natural gas	SCR	=	Selective catalytic NO_x reduction
C	=	Conductivity	HEPA	=	High-efficiency particulate air
T	=	Temperature, C	TRC	=	Thermal reaction chamber
P	=	Pressure, H_2O			

Figure 11. CCIM offgas system.

Heated Duct to the TRC. The heated inconel duct enables flow of offgas from the melter to the thermal reaction chamber. Often in traditional joule heated melters, this duct includes a "film cooler" designed to blend air or steam with the melter offgas to minimize deposition of particulate matter in the melter offgas on the interior walls of this duct, eventually plugging the duct. For the CCIM test system, this duct is heated using a high-temperature electric resistance heating element to heat the duct wall to at least 800°C. This will cause any particulate depositions to melt enough to flow out of the end of the tube and back into the melter. This also avoids dilution of the melter offgas typically by a factor of 5–10 times, thereby minimizing the downstream offgas flowrate and sizes of downstream offgas equipment.

Thermal Reaction Chamber. The TRC performs nonselective, noncatalytic, thermal NO_x reduction similar to more traditional fossil-fired staged combustion, except that heat required to heat and maintain the gas at NO_x reduction reaction temperatures (around 1,000°C) is provided by electric heating. This design is described in INEEL Invention Disclosure Record 142.[8] The heated duct at the inlet of the TRC preheats the melter offgas to about 730°C. The offgas is further heated in the first stage of the thermal reaction chamber by an electric tube heater to a maximum of about 1,150°C. The tube heater has a maximum temperature rating of 1,200°C. The tube heater and the reaction chamber are sized and configured to provide adequate heat transfer surface area, mixing, and residence time to heat and maintain the gas at design temperature for at least 2-seconds residence time. Methane is added to react with oxygen and NO_x in the inlet gas. NO_x reduction reaction products include N_2, CO, CO_2, and H_2O. The stoichiometry is maintained oxygen-deficient in order to favor NO_x-reduction reactions. Because of the reducing stoichiometry, this section is called the reducing section.

The second stage of the TRC includes evaporative cooling of a water spray into the offgas to cool the NO_x-reduced offgas to about 840°C. The cooled gas exit temperature is the highest temperature that results in an acceptable gas temperature downstream of the oxidizer section.

In the oxidizer section, air is added to provide oxygen for complete oxidation of CO and other products of incomplete combustion (PICs) that were formed or remain in the reducing section offgas. The oxidizer section is designed consistent with typical efficient thermal oxidizer designs, with a residence time of at least 2 seconds at a gas temperature of at least 1,000°C. The temperature is controlled to avoid exceeding 1,000°C by the water spray in stage two, to avoid excessive thermal NO_x formation.

Offgas Quench Section. Following thermal oxidation the offgas is cooled (quenched) by water spray evaporation to the adiabatic dewpoint of the offgas with the added evaporated water. This section is constructed of Hastelloy steel to tolerate the initially high offgas temperature and to provide good resistance to corrosion at both high and low temperatures.

Wet Scrubber System. Immediately following the temperature quench stage, the offgas will pass through a wet scrubber designed to remove acid gases and some of the residual particulate matter. The scrubber system includes the high performance scrubber itself, the scrub tank that collects and holds scrub solution, a demister, a high-efficiency mist eliminator (HEME), and the scrub solution recirculation system. The recirculation system includes a pump, valves, and piping to recirculate scrub solution to the spray quench nozzles in the offgas quench section, to the scrubber, and to demister and HEME washing nozzles.

The scrubber is a high performance scrubber, using added energy input in the form of atomizing air and pressurized scrub solution to (a) aerosolize and mix the scrub solution with the offgas for efficient acid gas and particulate scrubbing, and (b) provide some suction on the offgas as it flows through the scrubber. This is different from most traditional venturi scrubbers, which use energy from sometimes high pressure drop of the offgas itself to aerosolize and mix the scrub solution with the offgas. Avoiding high offgas pressure drops in the offgas system is desired to minimize high vacuums that cause:

- higher ambient air in leakage,

- higher adiabatic water dewpoint temperatures and higher water content in the offgas
- higher volatility of mercury and other more volatile species
- higher induced draft fan requirements.

Offgas Reheater

After the HEME, the offgas is reheated and slightly diluted by blending with preheated air to raise the offgas mixture temperature above its dewpoint. This reheat design is unique compared to other designs that simply use electric or steam-heated elements to directly heat the offgas. In this design, the offgas is indirectly heated by first preheating ambient air to about 500°C, and then mixing the preheated air with the offgas. This design is better for mixed waste systems because the heating elements are not exposed to the offgas, and because the offgas temperature does not need to be raised as high as otherwise, because the moisture content of the offgas is lowered slightly by dilution from the air. The amount of dilution is small, typically well under 10%.

Offgas HEPA Filter

The HEPA filter removes particulate matter from the offgas downstream of the reheater. The amount of particulate matter remaining in the offgas at this point is low, because most of the particulate matter is removed in the quench and scrubber sections. A new prototype HEPA filter designed for easier replacement in a mixed waste system will be evaluated in this test system.

Activated Carbon Bed for Mercury Capture

The granular activated carbon bed is a packed bed of 1.5–3 mm sulfur-impregnated activated carbon particles. Sulfur-impregnated activated carbon has been determined in several studies at the INEEL and elsewhere[9,10,11] to be the best technology for capturing mercury, regardless of speciation, in mixed waste offgas. Several remaining issues relating to mercury capture with sulfur-impregnated carbon that can be evaluated in this test system include (a) potential capture efficiencies and loading based on bed design and operating parameters, (b) capture of other potential trace-level pollutants including volatile and semivolatile organic compounds, dioxins, and halogen compounds, and (c) leachability and stabilization characteristics of spent carbon.

Induced Draft Fan

The induced draft (ID) fan provides the motive force to draw the offgas from the steam reformer through the offgas system. Since offgas flow rates may vary widely under different test conditions, the ID fan will be equipped with a variable speed controller, flow/pressure control dampers, and upstream, damper-controlled addition of ambient air to augment and control the total gas flowrate and vacuum.

Offgas System Capabilities

Capabilities and functional requirements for each offgas system component are summarized below:

- Reduce NO_2 levels in the offgas to less than 100 ppmv; reduce NO levels to less than 1,000 ppmv.
- Meet all HWC MACT standards.
- Operate stably within temperature, excess oxygen, and offgas composition requirements, with a 50% increase in the offgas flowrate and with a turndown in the outlet offgas to 10%, of the design offgas flowrate.
- Rapidly cool, within less than 1 second, the hot thermal oxidizer offgas to the offgas dewpoint. The rapid cooling minimizes catalytic dioxin/furan formation by limiting the residence of the offgas in the catalytic dioxin-forming temperature range of 200–400°C.
- Achieve 99.95% removal of Hg from the offgas, when the input total Hg concentration is about 40,000 ug/wscm, regardless of whether the Hg is present in the gas as elemental Hg or $HgCl_2$.
- Use engineered or administrative controls to avoid occurrence of fires in the carbon bed.

Progress To Date

Progress as of the end of Fiscal Year 2002 on the design, procurement, and installation of the full offgas system, with ESRA funding and limited other funding, include:

- *A full mass and energy balance of the complete system*: this has been completed. This mass and energy balance documents assumptions and calculations leading to design and operating conditions, equipment sizes, and amounts and kinds of added air, water, and energy.
- *Heated duct to the TRC*: This has been designed, procured, and received.
- *TRC*. This has been designed, components procured, and is in fabrication at the IRC machine shop.
- *Offgas Quench Section*. This has been designed, components procured, and is in fabrication at the IRC machine shop.
- *Wet Scrubber System*. Design is underway for this system.
- *Offgas Reheater*. This has been designed, procured, and received.
- *Offgas HEPA Filter*. Design is underway for this system.
- *Activated Carbon Bed for Mercury Capture*. Design is underway for this system.
- *Induced Draft Fan*. Design is underway for this system.

Cooling System

Performance Requirements

The cooling system must keep the RF generator cooled within normal operating parameters, and the crucible cooled to within the tolerances of the materials of construction. Temperatures greater than 100°C may be considered, but the ramification to pressure vessel design and code stamp become significant to a research prototype that may be significantly altered or changed out in short time. The emergency cooling system must provide sufficient cooling to safeguard operating personnel and prevent significant equipment damage.

Strategy/Engineering Approach

The RF generator and the cold crucible are heated components of the CCIM system that both require cooling but with specific characteristics. The RF generator has factory set coolant requirements to remove the waste heat generated. It requires coolant temperatures below 80°F for the system to be operable, and is designed to shut down at higher temperatures. In a loss of power event, the generator will shut off due to lack of power. In all shut-off events, the generator will be in a safe condition with no residual heat damage potential and with no continued input of energy into the glass melt. The RF generator does not need special emergency event cooling.

The cold crucible does not have the low coolant temperature requirements of the RF generator. It would also be inefficient to maintain the crucible with coolant below 80°F because it would be excessively cool. A higher operating temperature for the crucible would allow advantageous options in the cooling system design. Due to this characteristic contrast between the main components to be cooled, two separate cooling systems will be used, one for each component.

The materials of construction of the crucible and the thermal mass of the melt it contains necessitates an emergency cooling system. The high temperatures of the melt present the possibility of unacceptable warping or melting and possible failure of the crucible. If a power or cooling system failure occurs, an emergency system will be required to remove the residual heat of the glass melt to lower the temperature of the glass, and maintain allowable crucible and coolant temperatures. Thus an uninterruptable cooling supply will be required to take over the regular operation of the crucible cooling system when triggered by operation controls in the event of a primary coolant system failure or a power failure. This will be accomplished by using normally open solenoid valves powered closed in the primary

cooling loop to permit recirculation of the cooling water. When triggered, these valves open to permit the pressurized building water supply to cool the crucible. In an unlikely emergency with no power and no facility water, a cooling reservoir is available to gravity flow water to cool the system. The reservoir has been sized to lower the bulk temperature of the glass in the crucible to 200°C. The system is designed such that as the gravity flow system empties and the head pressure decreases such that equilibrium is reached, drain valves on the supply and return manifolds will be opened, evacuating the crucible and removing any potential for boiling the water.

Description

The heat generated by the RF generator is primarily due to inefficiencies of the generator itself. For 120 kWe feed to the generator at peak load, the generator must dissipate approximately 50% of the input power as heat. There is a primary and secondary loop used to cool the generator. The primary loop circulates water through the generator to a liquid-liquid heat exchanger. This loop is internal to the facility and requires no freeze protection. The secondary loop circulates a water and propylene glycol coolant from the liquid-liquid heat exchanger to the outdoor water chiller. The coolant was selected for freeze protection of the secondary loop. All coolant is recirculated, generating no secondary waste. A water chiller is used to maintain the primary coolant loop below the shutoff temperature of the generator.

Heat is removed from the crucible to maintain the crucible in a safe condition when containing a glass melt. The crucible must be cooled to maintain the desired operational properties of a cold crucible. There are primary, secondary, and emergency cooling loops for the crucible. The primary loop circulates water through the crucible to a liquid-liquid heat exchanger. The primary loop is completely internal to the facility and does not require freeze protection. The secondary loop circulates water and propylene glycol coolant from the liquid-liquid heat exchanger to an outdoor air-cooled radiator. The coolant was selected for freeze protection of the secondary loop. All coolant is recirculated, generating no secondary waste. An air-cooled radiator was selected because of the relatively high operating temperature of the primary loop. This higher temperature allows for the needed temperature difference to cool with a radiator in forced ambient air. The cooling water in the crucible can absorb close 50 kWe at maximum power, which will increase the water temperature by approximately 20°C, based in the designed flow rate and residence time. The heat exchanger is sized to manage this heat load.

The emergency cooling system (see Figure 12) is supplied by the building demineralized water supply to minimize impacts to the system in a power failure. Two 250 gallon water tanks are available to gravity flow water through the crucible to lower the melt temperature below the boiling point of water if no facility water is available. The gravity flow rate and volume have been calculated to prevent steam generation during emergency cooling, and to prevent crucible failure and damage. In the event steam is generated, the crucible has been designed with pressure relief valves to safely reduce pressure, precluding overpressure induced crucible damage.

Instrumentation and Control

Performance Requirements

The CCIM prototype system will be controlled manually using a computer-based control console. Feed, crucible, induction power, offgas, and cooling systems are all controlled in this manner. There are four basic requirements for the CCIM control and instrument display system:

- Remote-manual operation of all controls necessary for normal nonemergency operation Icon, slider-bar, or menu driven operator control input
- Simultaneous near real-time display of all instrument values and control states
- Real time video display of crucible side-wall and upper melt surface.

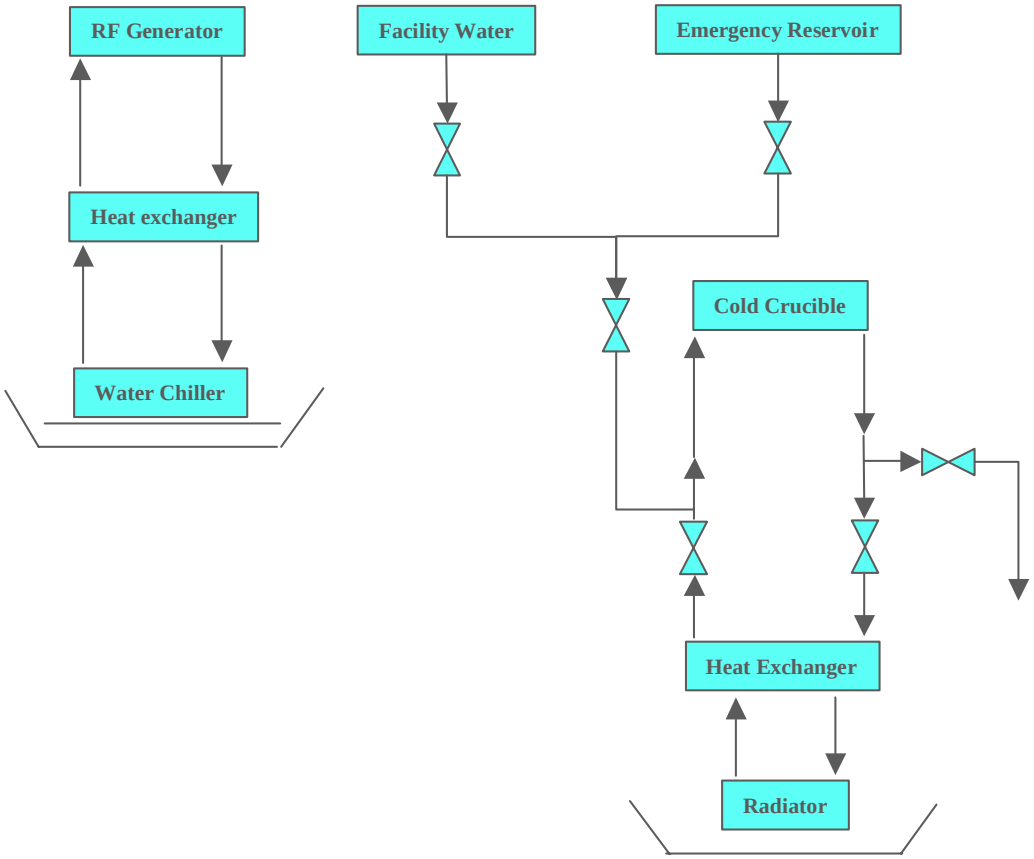

Figure 12. Cooling system schematic.

In addition, the control system design must provide for future addition of automated control, interlocks, and programmed alarm and emergency response functions.

The CCIM instrumentation system includes a variety of instruments. Parameters measured include temperature, voltage, fluid flow, and several specialized instruments. All requirements include signal conditioning and any software algorithms. Cooling system temperature measurements must be accurate within 1°C at nominal operating temperature. Offgas and melt measurements need be within 2% of nominal values. Flow measurements must be within 5% of nominal values. Because of uncertainties associated with measurement application, there is only an accuracy requirement of 1% receiving and displaying of the output of the optical pyrometer, and an accuracy specified for the instrument itself. The instrumentation system shall provide operator controlled archiving capability of all or some of the measured parameters at a specified time interval.

Another required provision is for real-time video monitoring of the crucible side-wall and a view of the upper melt surface. Required features include real-time simultaneous monitoring and recording of all inputs with a time and date stamp.

Strategy/Engineering Approach

Early in the design process the engineering design team decided to base the control and instrument system around a line of commercially available industrial-grade data acquisition and control components. The strategy was that a single manufacturer could be selected that could provide both hardware and software components which could then be readily configured into an integrated control and instrumentation system. The desirable features of such a system include availability of interface cards for all plant instruments and

control functions, and the ability to configure these interface cards with software. Similarly, such a system would provide an integrated environment to configure the screen displays and controls.

Because there is a requirement that instrument values and control status be displayed simultaneously in near real time, a piping and instrumentation diagram (P&ID) display strategy was adopted so that information display format would be intuitive as much as possible. The intent was to apply this philosophy where both hardware and software interfaces made it practical.

The design team also decided to standardize instruments and hardware interfaces as much as possible to minimize spare parts requirements and to simplify the design process as much as possible.

System Description

The prototype CCIM control and instrument system consists of multiple components or subsystems. These are the control computer, LabVIEW software, P&ID displays, the Instrument Interface, plant instruments, the Control Interface, plant controls, and a video monitoring system. Each of these is briefly described below.

The control computer used in the CCIM prototype is a 1.8 GHz Pentium 4 with 512 MB of random access memory and a 40 GB hard drive. The unit is configured with a read/write CD intended for archive and data logging. Populated output slots include RS-232, one GPIB interface, and a multifunction input/output to communicate with the National Instruments analog chassis in the Instrument Interface. Also included is a parallel port interface to a HP-990cxi printer.

The software package consists of National Instruments LabVIEW Full Development System Version 6.1. LabVIEW allows the user to quickly develop user interfaces to give interactive control over the software system. Two tool kits were also purchased to complement LabVIEW, a PID Control tool kit and Automation Symbols tool kit. The PID Control tool kit adds proportional, integral, and derivative, as well as fuzzy logic control functions to assist in quickly developing programs for automated control. The Automation Symbols toolkit adds a library of process symbols such as pumps, piping, and tanks to enhance the operator interface.

The control and instrumentation system includes four 17-in. color monitors and one 21-in. color monitor for engineering development and P&ID display. A high-level summary P&ID with limited control and instrument icons is presented on the 21-in. monitor, with detailed engineering values presented on the remaining four smaller monitors. The information is allocated as follows:

- Crucible and feed systems
- Offgas systems
- Cooling
- Induction power system.

Figure 13 shows the 21-in. monitor display. The instrument interface consists of an National Instruments SCXI-1001, 12 slot chassis. Interface modules installed the chassis provide signal conditioning, reference, and transducer level-shifting for thermocouple temperature measurements, voltage measurements, current detection. Switched outputs provide low-current ac switching to drive relays and triac interfaces that include the following:

1. 128 general purpose +/-10 V voltage inputs that are used to measure voltage and thermocouple output as well as 0–20 mA current loops.
2. 32 general purpose 0–42 V voltage inputs that will be used to measure plate current and voltage outputs from the radio frequency generator.
3. 32 binary switched 240 Vac, 200 mA triac switches, used to operate solid-state relays.
4. 32 binary high-voltage inputs. These are currently not used.
5. Eighteen 4–20 mA output channels to drive continuously variable control functions. These interfaces will provide input reference to the RF generator Allen-Bradley controller and drain valve heater control.

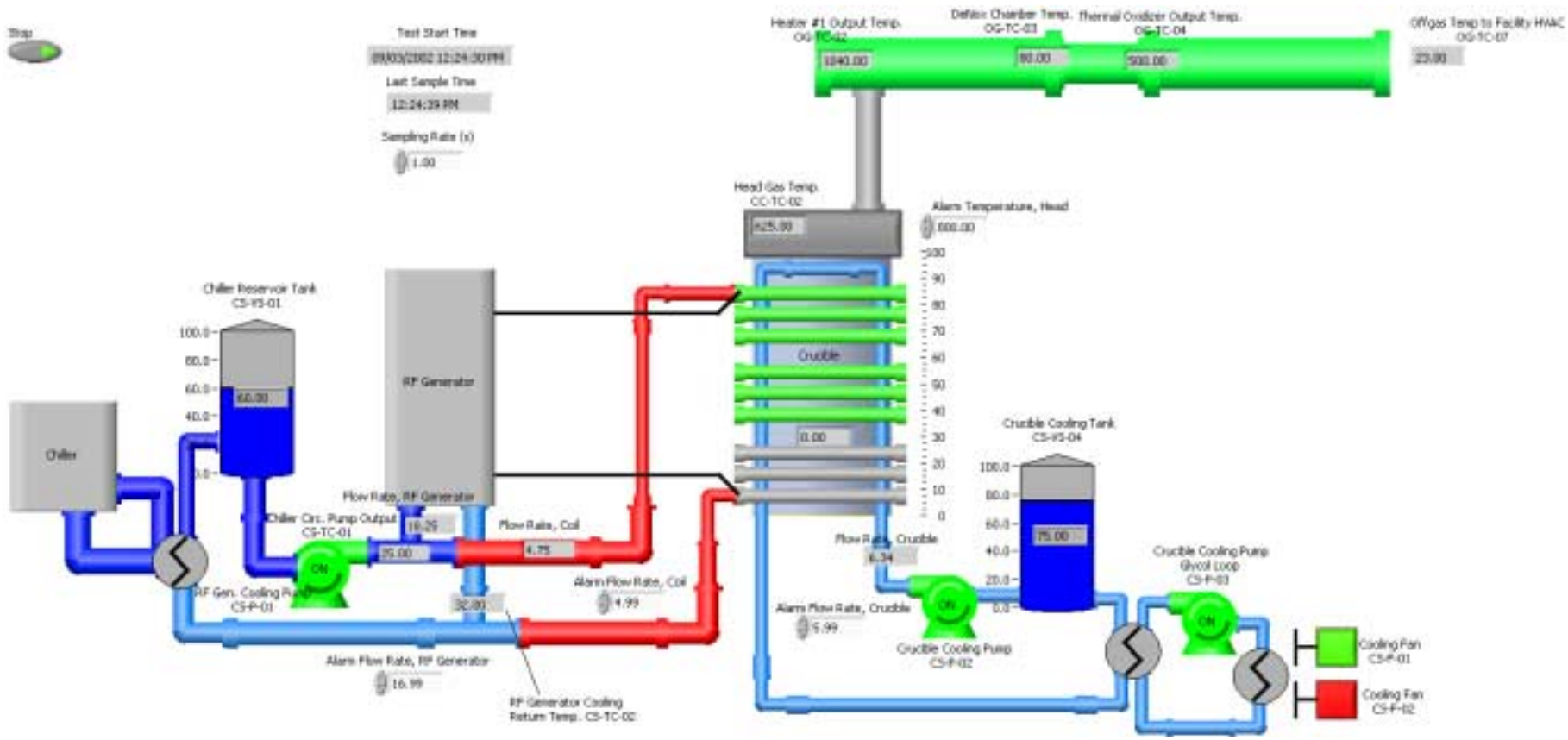

Figure 13. P&ID display.

There are a total of 37 plant instruments. The current design contains 22 type K thermocouples and two turbine flow meters that are monitored by the computer. The RF generator monitor panel provides instrumentation performing monitoring and display of generator anode voltage, anode current, grid current, and state of interlocks. Instruments are provided to measure coolant flow, accumulator tank level, secondary coolant temperature, anode over-current, and anode over-voltage. Manually read instruments in the CCIM prototype include four crucible segment coolant flows, one side drain valve coolant flow, RF generator secondary coolant system temperature and pressure, and crucible heat pressure. Additional computer interfaced and manual measurements are being added as experimental work proceeds.

There are four types of control outputs from the computer. Directly provided are IEEE-485 serial digital communications interfaces to the offgas heater system and RS-232 serial digital interface to the optical pyrometer. These connect directly to output cards in the control computer respectively. Binary outputs from a National Instruments SCXI-1163R optically isolated digital output module are connected as switched 120 Vac. These outputs have 200 mA capacity, which is insufficient to operate contactors and valves. The control interface consists of 32 RS3-1A40-22 solid state power relays manufactured by NTE Electronics. Each relay consists of a power Triac with optically isolated gates. Input requirement is 120 Vac 2 mAs and output capacity is 240 Vac 40 amps. Figure 14 illustrates the array of solid state power relays making up the panel. An additional interface panel has also been constructed providing eight more channels to accommodate future expansion of the control system.

The SCXI-1163R optically isolated digital output card gives the operator the ability to turn various plant devices ON/OFF by using the user interface icons on the computer screen. The 32 solid-state relays mentioned in the previous paragraph will be used to directly run the equipment, or in cases where the current surge may be above 40 A, they will run power contactors capable of handling a higher current surge. The power for 27 devices will be controlled by the screen inputs, including seven pumps, four fans,

Figure 14. Control Interface Panel.

and 10 valves for the cooling, feed, and offgas systems. Power is also controlled in this fashion for three motors in the feed system and three heaters in the offgas system. There are currently five 4–20 mA outputs. These outputs will drive the input reference for the RF generator and the input for the heater on the drain valve. The remaining three outputs will provide reference for variable speed fans on the offgas and feed system and a variable position valve that controls the rate of flow of the liquid slurry into the crucible.

As noted earlier, there is a requirement to remotely observe both the crucible side wall and the top of the melt. The video monitoring system performs these functions. It consists of three remotely powered television cameras and a video processing and display console. A Sony micro-camera monitors the crucible side-wall. It is a concentric in-line unit with an approximate diameter of five-eights in. that attaches to the structure inside the crucible barrier. A second tripod-mounted camera has remote focus and zoom, and is installed to monitor through an access window so that the top of the melt can be observed. A third general-purpose tripod-mounted camera is supplied with remote focus and pan-tilt-zoom features. It can be used for a wide variety of test applications such as views of the liquid and dry feed tanks. The video console contains a 13-in. color monitor, a time and date display generator, a quad splitter that allows one or all three cameras to be displayed, and an industrial-grade video recorder (see Figure 15).

Figure 15. CCIM video console.

Capabilities of System

The Instrumentation and Controls (I&P) system provides 192 input channels and 50 output channels. These channels will accommodate additional sensors as the design of the melter increases in complexity. There are currently two additional slots on the National Instrument analog chassis for future growth, or to add additional chassis in series. This gives the system the ability to expand and add more input and output channels as the melter design changes. The digital I/O card that communicates between the PC and the chassis will sample at a rate of 333 thousand samples per second. This gives the I&C system the ability to sample each channel at 650 samples per second. The LabVIEW software is also flexible and will give the operator the ability to add and remove functions quickly as the needs and design change. The I&C system can also be configured to make the melt process automated by adding control loops and automated alarms that will induce a set response based on set alarm values.

Future Research and Development

Induction melting is well known in industry and widely applied for production of metals and some specialty glasses, but within the relatively narrow field of radioactive waste vitrification, the technology is somewhat of an enigma that has frustrated its implementation. Generally, the papers on vitrification of radioactive waste using the CCIM technology that have been published in the last decade have been by vendors, and details are proprietary, which does not overcome this lack of comfort with the design concept. Further, the cold-crucible concept is new to many decision makers, and demonstration of the technology in an open, interactive form is paramount to realistic evaluation prior to considering the technology for implementation.

In this project, researchers at the INEEL are collaborating with Russian and university colleagues to develop modeling capabilities to bridge the many gaps between theory and operation. Soon the INEEL concepts for the electrical and mechanical designs and preliminary modeling results will be submitted for publication and peer review. In the coming months, the INEEL will be verifying modeling results with practical testing, and refining the designs based on these results. This test bed will be available for inspection and external evaluation testing geared toward quantifying a detailed energy balance, offgas emissions, and power input per unit of product. Novel designs for crucible and coil concepts will also be explored.

Plans for research and development in CCIM technology are targeted toward three objectives:

1. Verification of theoretical modeling to improve our understanding of CCIM design and controlling phenomena

2. Establishing a design basis, including characterization of the technology's capabilities, validation of the prototype design calculations, and identification of key operating parameters and interactions

3. Improvement of the current designs with innovations in crucible/coil materials, configuration, and interaction.

The LDRD funded theoretical modeling has extended the basic relationships for energy deposition versus applied frequency and melt resistivity using heat transfer theory and available thermodynamic data for glasses. The goals are to establish a basis for efficient design (melting a homogenous glass at maximum throughput) and establishing a basis for control algorithms. Power consumption is a significant concern, particularly for industrial applications, but is still secondary to glass quality and production rate. A modeling capability that would allow visualization of the temperature profile and potentially the mixing characteristics in the melt for a variety of crucible/coil configurations would allow a virtual design process to narrow the range of hardware to be fabricated for actual testing. This would accelerate the development process and reduce overall costs. The potential benefits are quite significant when one considers the investment in melter development over last 25 years by the DOE. The models developed to date will be used to predict the performance of the melter prototype(s) and evaluated against actual performance data.

As stated above, one of the primary impediments to implementing the CCIM technology is establishing a firm nonproprietary design basis for evaluation by potential customers. This includes:

- Specific productivity versus melter size (kg–glass/hr)
- Specific energy consumption (kw/kg-glass)
- A detailed energy budget
- Cooling requirements
- Fabrication cost and complexity
- Offgas source term.

In addition, a more general evaluation on overall performance is needed including:

- General performance characteristics on startup and shutdown
- Stability during varied process conditions (feeding, pouring, idling)
- Response to slurry feeding
- Corrosion and reflux of acids above the melt
- Bottom draining initiation, control, and termination
- Buildup of undesirable species.

Internal to the ESRA Project and the development of INEEL capabilities is the comparison of operating data to the initial design calculations, including:

- Electrical efficiencies
- Coil performance
- Thermal budget
- Heat transfer coefficients.

As many as three crucible/coil configurations will be investigated in FY 2003.

Improvement of current state-of-the-art waste stabilization technology designs is the last focus of this R&D effort. The current designs include innovations in crucible, coil, and drain systems for which invention disclosure documents have been filed. The planned testing will provide data to evaluate these designs and to refine the ideas. There are obvious areas of potential improvement including simplification or elimination of moving, energy management rather than accepting heat loss, and melt homogenization without mechanical mixing. FY 2003 activities will provide significant data in these areas, and define the potential for industrial involvement in the development process.

ACCOMPLISHMENTS

In FY 2002, the project submitted inspection disposition reports on novel coil, drain, and thermal reaction chamber designs. Detailed system designs were completed. Fabrication of prototypes for the crucible and glass drain systems was

completed, as was the control system. The secondary cooling systems were installed and the main facility modifications were completed. Testing will begin in early FY 2003. Collaboration and detailed design reviews, with Russian and University collaborators, were completed.

Publications

Submittal to Nuclear Technology is pending.

Presentations

Gombert, D., et al, "Cold-Crucible Design Parameters for Next Generation HLW Melters," *WM'02 February 24-28, 2002, Tucson, AZ.*

Gombert, D. "Melters – Why, How, What?" invited seminar, *International Conference on Incineration and Thermal Treatment Technologies IT3 Conference, New Orleans, LA,* May 2002.

Richardson, J., et al, "Modeling of Cold Crucible Induction Heated Melters" *Spectrum Conference, Reno, NV*, June 2002.

REFERENCES

4. J. M. Perez, et al., *High Level Waste Melter Study Report*, PNNL-13582, July 2001.

5. J. Ahearne, et al., *High-Level Waste Melter Review Report*, TFA-0108, July 2001

6. A. S. Polyakov, et al., "Strategy of Active Waste Management in the Russian Federation," A. A. Bochvar, All Russian Scientific Research Institute of Non-Organic Materials, Moscow, Russia, *Nuclear Engineering and Design*, Vol. 173, 1997, pp. 269–275.

7. D. Venable and T. P. Kim, "Radio Frequency Heating Fundamentals and Applications," Westinghouse Electric Corporation, 1946, p. 379

8. R. M. Baker, "Design and Calculation of Induction-Heating Coils," *Proceedings of the IRE*, March 1957, pp. 31–40

9. P. G. Clites, "The Inductoslag Melting Process," *Bulletin 673*, U.S. Department of the Interior, 1982.

10. C. H. Oh, *Hazardous and Radioactive Waste Treatment Technologies Handbook*, edited by Chang Ho Oh, CRC Press, Washington, D.C., May 2000.

11. N. R. Soelberg and B. D. Raivo, "Electrically Heated Thermal Reaction Chamber," Invention Disclosure Record 142, INEEL, August 29, 2002.

12. A. Chambers, M. Knecht, N. Soelberg, D. Eaton, D. Roberts, and T. Broderick, "Mercury Emissions Control for Mixed Waste Thermal Treatment," *1998 International Conference on Incineration and Thermal Treatment Technologies, Salt Lake City, UT,* May 12–16, 1998.

13. INEEL, *WERF MACT Feasibility Study Report*," INEEL/EXT-98-01166, November 1998.

14. N. R. Soelberg, A. Chambers, M. A. Knecht, D. Eaton, and K. Liekhus, *MACT System Integration Study*, INEEL/EXT-99-00340, June 1999.

Non-Ideal Solution Thermodynamics

Randall LaViolette, Michael McIlwain, Dean Peterman, and Jill Scott (INEEL)
Donald Schreiber (Western Michigan State)

SUMMARY

Thermodynamic modeling of the behavior of complex waste solutions is fast becoming a powerful means of providing data for informed decision-making and selection of alternatives for management of chemical processes and products. The objective of this project is to develop a variety of approaches for estimating Pitzer parameters. These parameters are needed to describe high-level waste physical properties, component solubilities, and chemical reactivity. We are fabricating an isopiestic measurement apparatus to test the accuracy of various prediction approaches.

Molecular dynamics (MD) and quantum mechanics (QM) activities have included the testing of commercial algorithms for accuracy and validity for published test ionic solutions. QM calculations on nitrate and aluminum ions were performed to understand the hydration configuration around the species, obtain interaction potentials, and explore the potential of water displacement/competition. Depending on the number of species considered, MD simulations can require quite extensive modeling run times in order to correctly represent the system of interest. One way of reducing the computation time is to develop a simple interaction potential for water and all other atoms in the system. Another approach was to employ massively parallel codes for the MD simulation.

Multicomponent Pitzer parameter estimation is being pursued to augment direct modeling of the properties of high ionic strength solutions. The Pitzer ion-interaction model relies on experimentally determined Pitzer parameters, when available for single component systems. Progress to date indicates that ion size and acidity are valuable for predicting the shape of the desired trend.

Experimental measurement capability is being established to validate predictions being supplied by the modeling and empirical tasks. Water activities are determined in this isopiestic apparatus by measurement of mass transfer of water between samples. The current state of apparatus development is such that we can now plan for testing and calibration.

PROJECT DESCRIPTION

Task 1: Modeling

The modeling of non-ideal solutions is the primary activity of this task. Three subactivities are concurrently being performed. The first seeks to validate the COMPASS® empirical force field for ionic solution thermodynamics and structure and develop theories for transferring simulation results into thermodynamic properties.

The COMPASS® library consists of parameters for a general interatomic empirical force field for atoms and molecules. These parameters and the force field are designed to be transferable, and include bond, van der Waals, and electrostatic interactions up to four-body systems. With the appropriate force field, one may simulate the dynamics of a dense liquid (neat or solution) by integrating Newton's equations of motion. One may take averages along equilibrated trajectories (translation in x, y, and z coordinates) to obtain mechanical (e.g., energy, pressure), structural (e.g., pair correlation), and dynamical (e.g., velocity autocorrelation, diffusion coefficient) properties. For validation purposes, one compares these results and their respective uncertainty with experimental and theoretical values to test the hypothesis that COMPASS® provides force fields capable of providing usable results for our planned studies. These calculations are demanding, even for our best resources; one typical trajectory of medium length (40 ps) on the SGI Origin 3800 requires 4–8 hours.

Summarizing the results so far, COMPASS® provides values for mechanical and structural properties consistent with accepted values.

Nevertheless, the final test consists of obtaining entropies and free energies or chemical potentials from these results. These cannot be read directly from the simulation results, but must be first transformed by theory. The second subactivity seeks the identification and selection of the theory.

The simplest relation between the mechanical energy and the free energy requires an integration of the former over a wide range of temperatures to obtain the latter. However, that approach turns out to be computationally unfeasible for ionic solutions, so we turned to more sophisticated theories that allow us to calculate the free energy from computer simulation results. There are several competing approaches; the simplest is based on the Pratt-Chandler perturbation theory for solutions.[1] In their approach, the structure (pair correlation functions) rather than the energy is the central quantity. Integration of the differences between pair correlation, with and without the solute, provides the free energy. Consequently, much of our effort this summer has been the calculation of pair correlation functions for various temperatures and concentrations of ionic solutes in water with the COMPASS® force field. Preliminary results suggest that COMPASS® provides a model in good agreement with experimental results, but these will be further verified with work expected to continue into FY 2003.

The third subactivity seeks to find a speedier alternative for the computer simulations and the COMPASS® force fields, which are demanding calculations, complicated, and require special treatment of the long-range forces. One researcher developed a new model for waste that employs only short ranged forces. This was accomplished by adding three-body interactions that partly screen nontetrahedral neighbors to two-body interactions that accurately reproduce the oxygen-oxygen pair correlation function. Further refinement showed that this combination could be reduced to an anisotropic pair potential. Preliminary results have been encouraging. Not only has the pair correlation been made to agree with accepted results, but the more demanding angle correlation function has as well. Of course, it is not possible to study hydrogen exchange, for example, with this model. Although further study is required, this new model could reduce the computational burden by as much as two orders of magnitude, running at the same speed as a liquid of Lennard-Jones atoms, for example. Although novel, this model will soon be a candidate for publication.

The second subactivity is pursuing a different empirical force field (consistent-valence force field [CVFF]) to calculate mechanical and structure properties of water containing various dissolved ions. The first step in the process was to equilibrate the initial amorphous configuration by calculating 1 ns (nanosecond) trajectories. These were time-consuming calculations requiring approximately 380 hours of computation. Oxygen-oxygen pair correlation functions derived from the resulting trajectories were comparable to correlations produced (flexible hydrogen-oxygen bond with four or five point charge distributions) by TIP4P and TIP5P models.[2,3] Similar trajectories were prepared for one molal nitrate ion, one molal aluminum ion, one molal hydronium ion, and one molal aluminum nitrate.

In the future, we plan to calculate trajectories for a range of temperatures for each one of these cases to determine the solution-free energy. Individual species free energy or chemical potential should be derived by difference.

Since the calculation of 1 ns trajectories is a computationally intensive activity, an ongoing effort seeks to examine the possibility of importing various molecular dynamics codes that can be operated in a massively parallel computer configuration. Based on examination of a number of possibilities, a code developed by the University of Groningen in the Netherlands called GROMACS was selected.[4,5] GROMACS is widely used to model biological molecules in water. The model has the flexibility of using fixed water models, such as (inflexible hydrogen-oxygen bond and single point charge) SPC and TIP3P, or the user may define the specific properties of water to be employed in the calculation. The user can also incorporate force fields for elements not presently included in the data sets. The current status of establishing GROMACS at the INEEL is that the code has been compiled for a UNIX operating system and shown to produce satisfactory results for supplied test cases. Efforts are currently

underway to develop force-field parameters for aluminum and nitrate nitrogen. Comparison calculations are to be performed with the CVFF and COMPASS approaches to determine applicability.

Quantum Mechanical Modeling

Currently, we are running our calculations with Gaussian 98W using GaussView for MS Windows as the interface. Most of the calculations were carried out at the B3LYP (molecular orbital basis set) level of theory. Because computations have proved to be computer intensive, we have acquired a site license for the UNIX version of Gaussian 98. The sitewide version of Gaussian 98 has been received and is currently being installed on a Beowulf cluster, which should enable complex, intensive computations in the future.

Consultation with Dr. J. B. Wright at Natick, who recently completed a study comparing different solvation modeling schemes with experimental data, has revealed that we are better off ignoring the solvation gradient calculation methods currently available.[6] Instead, he suggested that we use the presence of 32 H_2O molecules as the baseline for simulating complete solvation. At this level of solvation, parameters, such as partial charges, structure, etc., should be relatively constant. These values will then be used to set the parameters for calculations using the MSI software for modeling systems with multiple ion types in solution.

Hydration of Nitrate and Nitric Acid

Initially, we modeled the nitrate (NO_3^-) with H_2O system. Our work is consistent with that of previous published results.[7] From a detailed examination of the interaction of $NO_3^- + H_2O$ in various configurations, the B3LYP bases set calculations were shown to closely match experimental results. In our work, we have been using B3LYP 6-311 (d,p) calculations to investigate the complete hydration of NO_3^-.

While the nitrate/water system provides a basis for future calculations, to be more appropriate for the sodium-bearing waste, it is important to look at the effect that excess protons have on hydration and activity. Therefore, we have also been studying the following systems:

- Nitric Acid with H_2O
- Nitrate + Hydronium ion with H_2O.

Ideally, these systems should provide complementary results because the initial proton transfer steps should be the mirror image of each other. After the initial proton transfer step, the results are expected to be the same.

Compared to the nitrate and water system, our initial calculations indicate that the presence of the additional proton in the above systems plays a dominant role in the solvation structure around the nitrate ion, as a sequence of proton transfers leads to formation of a series of hydrogen bonds. With six H_2O molecules, it appears that the proton is part of a hydrogen bonding network composed of four water molecules, $H_9O_4^+$ (see Figure 1).

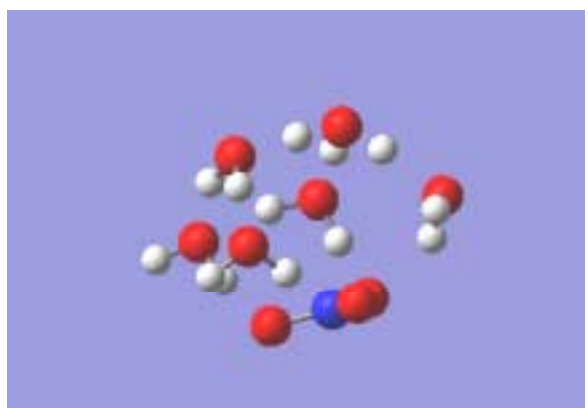

Figure 1. Hydration of NO_3^- with six water molecules.

However, the bond distances suggest that two of the water molecules are more closely associated with the proton, which indicates that the proton may exist more like a Zundel ion, H_5O_2+.[8] This observation is consistent with experimental results obtained by Zawada and Dryjanski that suggest that the structure of the hydrated proton in nitric acid is $H^+ \cdot 2H_2O$, similar to other acid solutions.[9] Zawada and Dryjanski noted that, unlike the data for the other acids, the nitric acid data initially suggested that the proton was hydrated by three water molecules forming $H_7O_3^+$. However, they corrected the data for the absorption due to nitrate,

which reduced the number of hydrating waters to less than three. To determine whether the proton in nitric acid solution should be treated as H_5O_2+, $H_7O_3^+$ or $H_9O_4^+$, it will be necessary to perform the calculations with the second solvation sphere.

Aluminum Hydration and Interaction with Nitrate Ion

We have also recently initiated an investigation of the effect of nitrate ion on the hydration of aluminum ion, Al^{3+}. The goal is to determine how nitrate ion can affect the hydration of Al^{3+}, especially if water is scarce.

Calculations for the first hydration sphere of aluminum ion at the B3LYP 6-311 (d,p) level are in good agreement with literature values.[10,11] Both show that 6 H_2O molecules coordinate equally around Al^{3+} forming $Al(H_2O)_6^{3+}$ (see Figure 2). The second hydration sphere has not been calculated using Gaussian 98 for Windows because computational time on a single PC was prohibitive. However, the second hydration sphere is considered crucial to the overall evaluation because the energy to transfer hydrogens from the first to the second hydration shell is expected to be quite small.[10]

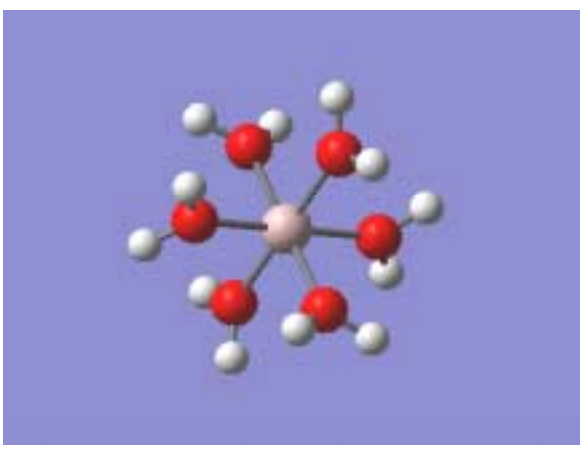

Figure 2. First solvation sphere of Al^{3+} with 6 H_2O molecules.

When a single nitrate ion (NO_3^-) interacts with $Al(H_2O)_6^{3+}$, the nitrate ion forms hydrogen bonds with two of the coordinating water molecules to form $Al(H_2O)_6^{3+}\cdot NO_3^-$ (See Figure 3).

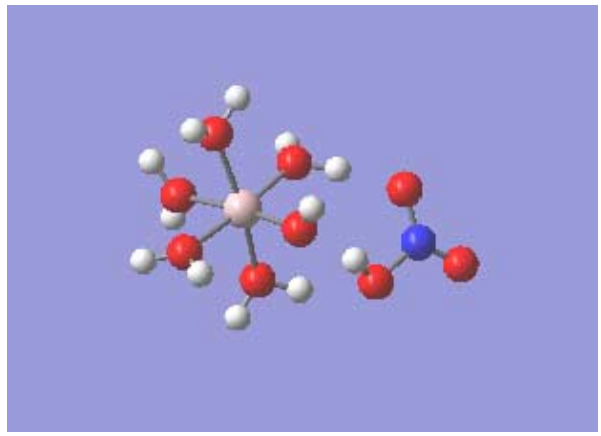

Figure 3. Interaction of NO_3^- with $Al(H_2O)_6^{3+}$.

The hydrogen bonding of the nitrate to the two waters causes the bond length of the water oxygen to the Al^{3+} to shorten (e.g., from 1.937 to 1.760 Å). However, the Al—O_{H2O} bond length for the waters not hydrogen bonded to nitrate lengthen (e.g., 1.937 to 1.980 Å). The addition of further nitrate ions continues to distort the first hydration sphere; however, the full effect cannot be determined until all of the waters in the second hydration sphere can be accounted for in the calculations. The addition of the second hydration sphere waters is expected to mitigate some nitrate ion effects.

If the aluminum ion is under coordinated by one water molecule forming $Al(H_2O)_5^{3+}$ (Figure 4) and is allowed to interact with NO_3^-, then the nitrate ion not only occupies the uncoordinated site, but also displaces another water molecule to form $Al(H_2O)_4(NO_3)^{2+}$ as illustrated in Figure 3.

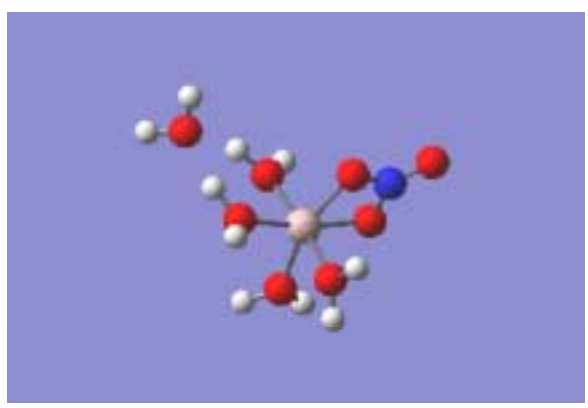

Figure 4. Interaction of NO_3^- with $Al(H_2O)_5^{3+}$.

Comparison of the energetics for $Al(H_2O)_6^{3+}$, $Al(H_2O)_6^{3+}\cdot NO_3^-$, and $Al(H_2O)_4(NO_3)^{2+}$ are not

complete at this time because such a comparison would require an equivalent system (e.g., same number and type of all atoms). These calculations will be performed when it is practical to include the second hydration shell. Additionally, future calculations will include identifying transition states for the water displacement reactions.

Based on current results for the nitrate/nitric acid and aluminum/nitrate systems, it will be important to investigate the concerted effects that Al^{3+}, NO_3^-, H^+, and H_2O exert on each other for determining partial charges, hydration, energetics, and activities.

Task 2: Multicomponent Pitzer Parameters

The primary objective of this task is to develop a model for predicting the chemical and physical behavior of high-level waste during remediation. The model selected for this purpose was the semi-empirical Pitzer's Ion-interaction Model.[11] This model has been widely used for the prediction of non-ideal solution behavior. Pitzer's model does an excellent job of predicting the solubility of minerals over a wide range of conditions for systems where the parameters are available.[12,13,14] Although there are numerous systems where the parameters are available, there are others where they are not.[15] For example there is little data for the aluminum and fluoride ions, two ions found in significant concentration in some high-level wastes. The aim of this project was to develop a system using the Pitzer Ion-interaction Model. This system would rely on experimentally determined Pitzer parameters when available, and parameters predicted from theoretically based empirical relations when not available.

The first activity of this task was to develop theoretically based empirical equations for the prediction of Pitzer's binary (single salt) parameters. The Pitzer model uses empirical parameters based on virial coefficients. The model equations were originally written in terms of Excess Gibbs Free Energy, but other equations can be derived by the appropriate differentiation (Reference 15). The Pitzer equation for the activity coefficient of single electrolyte system is:

$$\ln \gamma_c = f^{\gamma} |z_M z_X|/2 + 2 (\nu_M \nu_X/\nu)\, m\, B^{\gamma}_{MX} + 2 [(\nu_M \nu_X)^{3/2}/\nu]\, m^2\, C^{\gamma}_{MX} \quad (1)$$

$$f^{\gamma} = -A_{\phi} * [I^{1/2} / (1 + b * I^{1/2}) + 2 / b * \ln(1 + b * I^{1/2})] \quad (2)$$

$$B^{\gamma}_{MX} = \beta^{(0)} + \beta^{(1)} / (\alpha^2 * I) [1 - (1 + \alpha I^{1/2} - 0.5\, \alpha^2 I) \exp(-\alpha I^{1/2})] \quad (3)$$

The "I" is the molal ionic strength, "m" is the molality, "$\beta^{(0)}$", "$\beta^{(1)}$" and "C" are the empirical parameters obtained when the equations are fit to the data. The "α" and "b" are constants that have the values of 2.0 $kg^{1/2}\ mol^{-1/2}$ and 1.2 $kg^{1/2}\ mol^{-1/2}$ respectively. For 2:2 electrolytes a third term is added to equation (3) with the same form as the second term but with a $\beta^{(2)}$ and α_2 instead of the original parameters. For 2:2 equations the α in the second term is also replaced by a α_1. The values of the α_1 and α_2 are 1.4 $kg^{1/2}\ mol^{-1/2}$ and 12 $kg^{1/2}\ mol^{-1/2}$ respectively. The empirical terms are related to the virial coefficients by the following equations:

$$B^{\gamma}(I) = 2\, \lambda_{MX} + I\, \lambda'_{MX} + (\nu_M/2\nu_X)\, (2\, \nu_{MM} + I\, \nu_{MM}) + (\nu_X/2\nu_M)\, (2\, \lambda_{XX} + I\, \lambda'_{XX}) \quad (4)$$

$$C^{\gamma}_{MX} = [9 / (\nu_X \nu_M)^{1/2} / 2)(\nu_M\, \mu_{MMX} + \nu_X\, \mu_{MXX}) \quad (5)$$

The symbols λ and μ are second and third virial coefficients for the subscripted interactions. Any system used for predicting Pitzer parameters must be consistent with the basic theory on which Pitzer's Model is based.

Our original idea, based on a suggestion by Pitzer and Mayorga,[16] was to fit the $\beta^{(0)}$ parameters as function of ion size. This method would be consistent with the basic theory. We thought that this would work well since there were a large number of parameters available. For best results we decided to group the salts according to charge type and counter ion. We then planned to use a second suggestion by Pitzer and Mayorga (Reference 16), which was that the $\beta^{(1)}$ should be proportional to the $\beta^{(0)}$ parameter. Again for the best correlation, this relation would be obtained for a particular charge type and counter ion. After initial attempts, simply fitting the parameters by themselves did not give us the quality prediction we expected. Our concern was that the $\beta^{(0)}$, $\beta^{(1)}$,

and C parameters for a given salt were too interdependent, so we decided to start with the original data.

We reformulated the equations by replacing the parameters, $\beta^{(0)}$, $\beta^{(1)}$, and C with polynomials that were functions of ionic radii. By doing this we hoped to disconnect the interdependence of the parameters of a particular salt resulting in an improved fit. We then fit these equations to the data provided in Robinson and Stokes review.[17] This is the same data that Pitzer and Mayorga originally used (Reference 16). This method also resulted in a weighting based on the amount of experimental data and not just the number of salts. Again, in accordance with theory, the data were separated into data files of each charge groups (the 1:1 salts, 2:1 salts, etc.) and each data file fit separately. The polynomials used in these fits were functions of both cation and anion radii. While the results of these fits were better than those obtained from the fits of the original Pitzer parameters, they were not of the quality that we desired. We then decided to fit the equations, now only a function of cationic radii, to data of salts of a particular anion and charge type. For example, all the 1:1 chloride salts were fit together. The quality of these fits was significantly improved over the fits of all of single charge type together. In these fits we used crystallographic ionic radii reported by Shannon.[18] In cases where there were radii for multiple structures of a particular cation, we used the hexadentate radius. The general form of the equations we used are given below.

$$\beta^{(0)} = b_{01} + b_{01} * r + b_{03} * r \quad (6)$$

$$\beta^{(1)} = b_{11} + b_{12} * r + b_{13} * r \quad (7)$$

$$\beta^{(2)} = b_{21} + b_{22} * r + b_{23} * r \quad (8)$$

$$C^{\gamma} = c_1 + c_2 * r + c_3 * r \quad (9)$$

Where "r" is the radius of the cation and the parameters b_{01}, b_{02}, b_{03}, etc., are the coefficients of the fits. We next examined the ability of these polynomials to represent the data of the individual salts. In most cases the equations reproduced the shape and were within an acceptable accuracy. We did however note some problems, especially with the 1:1 salts. We realized that our fits were being affected by the data of the acid form of the anions. Since, in most cases, there were significant amounts of data for the acids, and the radius of the hydrogen ion was very suspect, we decided to remove all the acid data from the anion data bases and refit the equations to the new data sets. We then put the data for all of the acids into a single data file and fit Pitzer's equations with radii polynomials to this new set. In the case of the acid fit, anionic radii were used. The removal of the acid data resulted in improved fits of the 1:1 salts. We settled on these resulting parameters, which are presented in Table 1 along with the fit's standard deviation. From Table 1 it can be seen that not all of the parameters were needed for every fit. Also in future applications when we do not have an anion equation for the salt of interest we will use the global fit of that charge group (1:1). It should also be pointed out that we are still accumulating data from the literature as we search for mixed salt systems, so we still may be able to add additional anion fits.

Next, we wanted to compare the predictions of the equations to data that was not used in the fits. Figures 5–7 demonstrate the ability of the equations to predict activity coefficients for electrolytes of different charge types. The electrolytes used were chloric acid (Figure 5), cobalt (II) chloride (Figure 6), and thallium (III) nitrate (Figure 7). You can see from the plots that the equations do a very good job at moderate concentrations. In the case of cobalt (II) chloride and chloric acid, although the equations represent the general shape of the data, they do have significant deviation at molalities above 3 molal. Finally, we have begun fitting similar radii based polynomials for the ternary parameters to the common ion mixture data. Once we have equations for these mixing parameters we will use the equations of all the parameters for predictions of mineral solubility and compare our results to the data from the literature.

Table 1. Coefficients for $\beta^{(0)}$, $\beta^{(1)}$, $\beta^{(2)}$, and C^{γ} for Anions of Salts with Different Charge Types.

		b_{01}	b_{02}	b_{03}	b_{11}	b_{12}	b_{13}	c_1	c_2	c_3	□
	Acids	3.15014	-0.03253162	0.0000883		-0.00001036	0.00001299	1.911467	-0.02089996	0.00005661	0.051
	Anion	b_{01}	b_{02}	b_{03}	b_{11}	b_{12}	b_{13}	c_1	c_2	c_3	□
1:1	F^-	-0.15199	0.00150362			0.00166713					<0.001
	C^{l-}	0.60596	-0.00719546	0.0000222		0.00672615	-0.0000329	0.007367		-0.00000022	0.002
	Br^-	0.47328	-0.00245032					-0.067619	0.00037301		0.001
	I^-	0.26380	-0.00107819			0.00757378	-0.0000457	-0.013941			0.004
	$NO3^-$	0.48720	-0.00390493		2.16051	-0.03186233	0.0001234	0.092001	-0.00191209	0.00000929	0.005
	$ClO3^-$	0.41986	-0.00340437		0.29734	-0.00027980					<0.001
	$BrO3^-$	0.32896	-0.00290075			0.00141849					<0.001
	OH^-	-0.05941	0.00145969		-0.60784	0.00491493					0.003
	$H_2ASO_4^-$	0.00853	-0.00050886		0.95444	-0.00534962					<0.001
	$H_2PO_4^-$	0.14766	-0.00176827			0.00099894			0.00007096		0.003
2:1	Cl^-	0.57235	-0.00234048			0.01243079					0.029
	Br^-	0.72231	-0.00208686		2.29424			0.075104	-0.00066155		0.005
	I^-	0.82042	-0.00187154			2.43767726		0.075144	-0.00070624		0.001
	$NO3^-$	-5.21886	0.11613106	-0.0005927	20.12575	-0.33495471	0.0015154	2.976494	-0.05972360	0.00029287	0.021
	$ClO3^-$	1.10094	-0.00456161		2.83838	-0.00326280					0.002
1:2	CO_3^{2-}	-0.27105	0.00294523		0.80171	0.00876828					0.001
	SO_4^{2-}	0.06761			1.40715			0.107807	-0.00089303		0.015
	HPO_4^{2-}	-0.31880	0.00259589		2.32552	-0.00549701					<0.001
	CrO_4^{2-}	0.26815	-0.00112610		1.85604	-0.00164180					<0.001
3:1	Cl^-	1.58136	-0.00643702		6.52418	0.01464025		-0.219665	0.00170086		0.004
	NO_3^-	0.91157			-14.24703	0.52259824	-0.0030660	-0.618696	0.01882401	-0.00014247	0.001
1:3	AsO_4^{3-}	-0.55912	0.00688779		4.45961	0.03183370					<0.001
	PO_4^{3-}	-0.77808	0.00760268		8.53592						<0.001
	Anion	b_{01}	b_{02}	b_{03}	b_{11}	b_{12}	b_{13}	b_{21}	b_{22}	b_{23}	
2:2	SO_4^{2-}	0.51965	-0.00260437			0.02338953		95.780715	-1.28010397		0.010

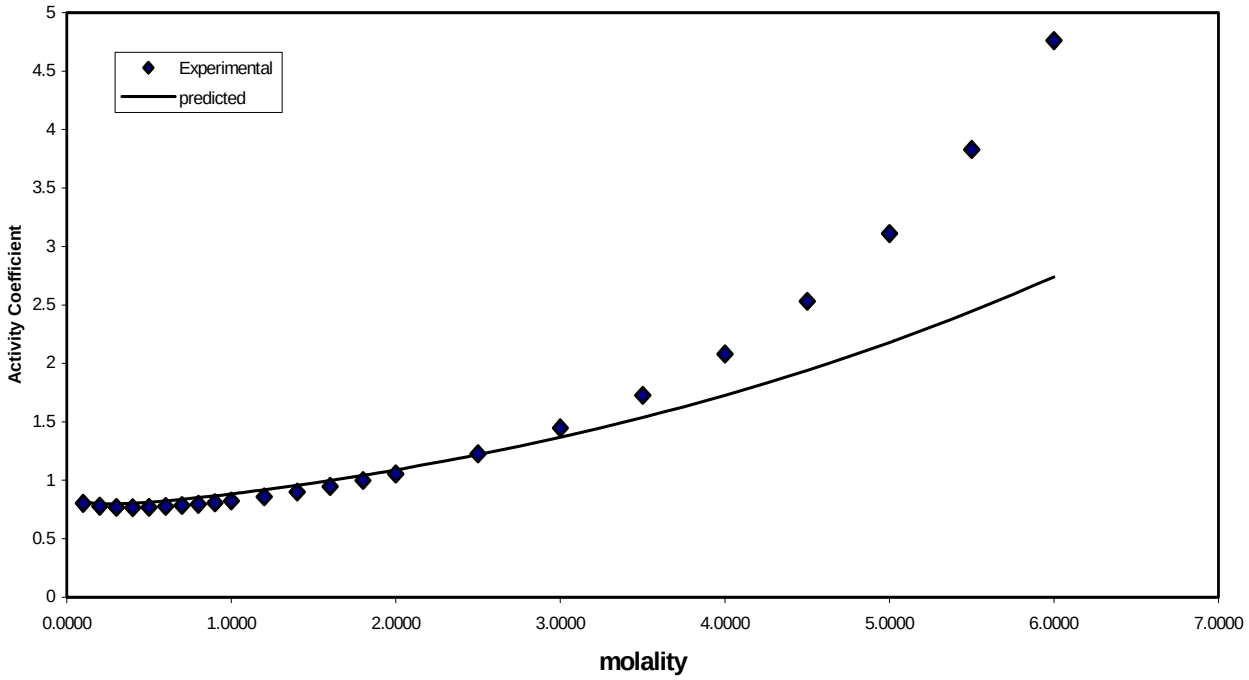

Figure 5. Predicted and experimental activity coefficients of $HC20_3$.

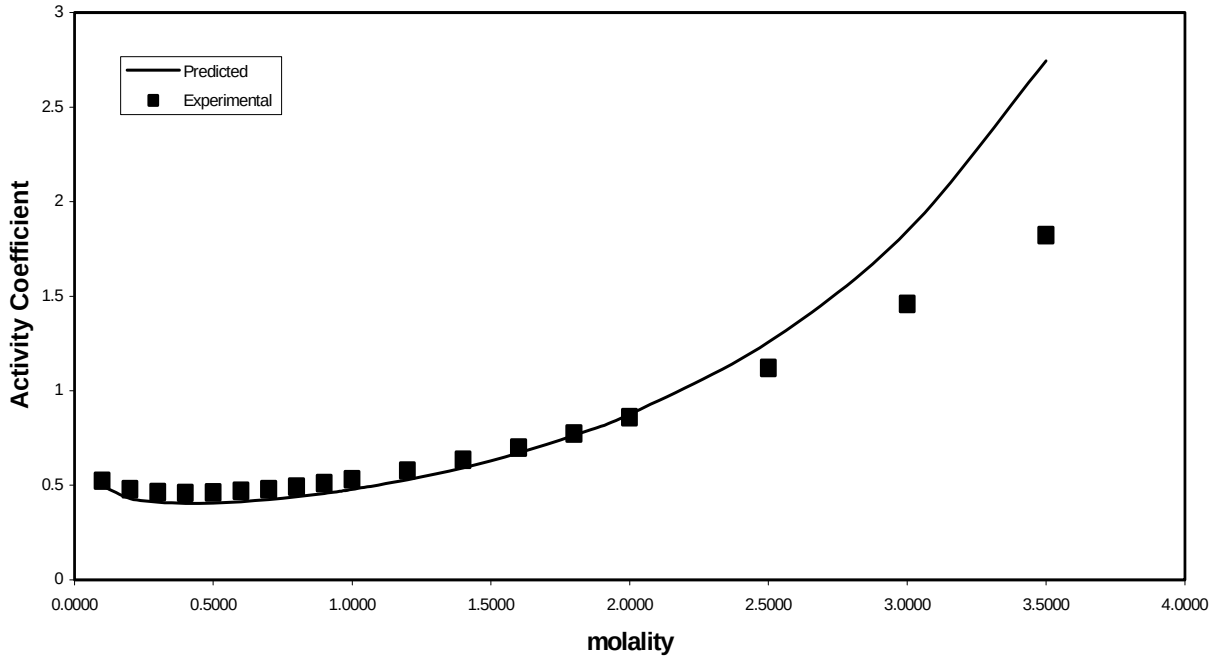

Figure 6. Predicted and experiment activity coefficients for $CoC1_2$.

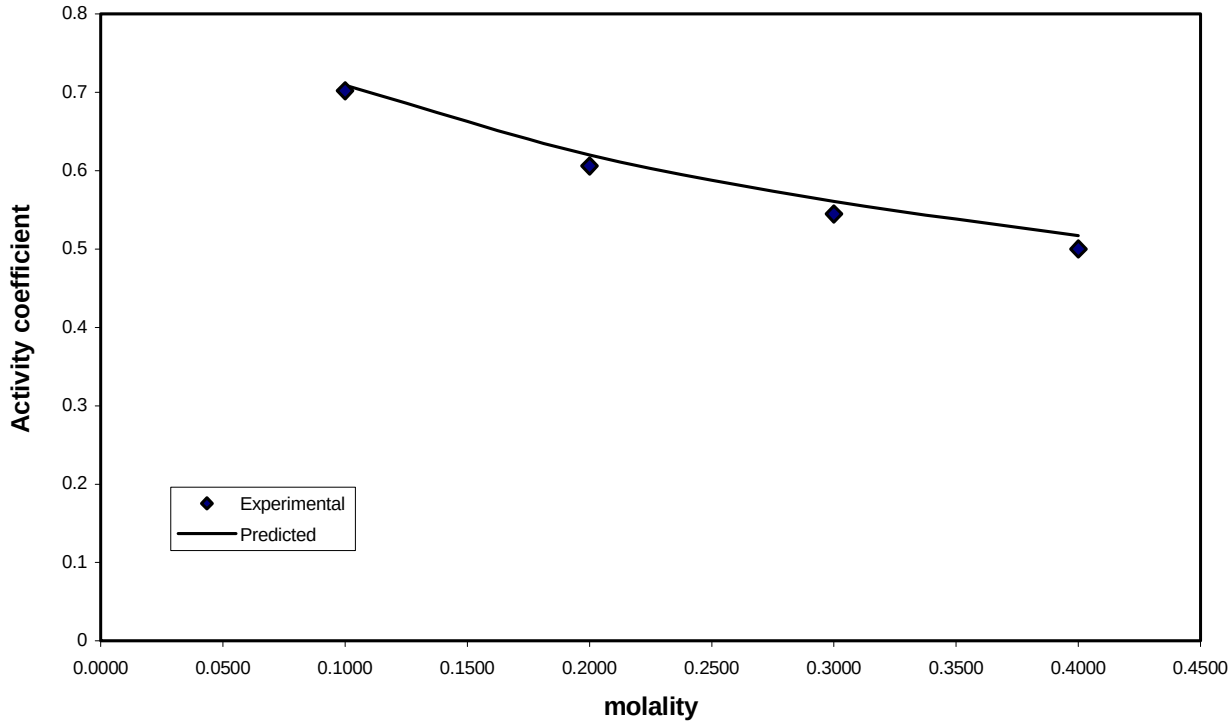

Figure 7. Predicted and experiment activity coefficients for $TIN0_3$.

Task 3: Experimental Measurements

Thermodynamic modeling of the behavior of complex waste solutions is fast becoming a powerful means of providing data for informed decision-making and selection of alternatives for management of chemical processes and products. Legacy wastes from processing of nuclear materials for defense and power production are present in large quantities at a number of DOE sites, notably Savannah River, Hanford, West Valley, and the Idaho National Engineering and the INEEL. Processes to treat, transport, and safely dispose of these wastes are in operation and/or under development at these and other locations. Difficulties in handling these hazardous materials pushes projected processing costs into the tens or hundreds of billions of dollars. More accurate process simulation for alternative treatment evaluation and process optimization offers hope of substantial cost savings.

Reliable thermodynamic models for solutions involving electrolytic species must properly account for non-idealities. Apparent stoichiometric concentrations in mass-action expressions such as equilibrium constants must be replaced with activities with respect to known standard states. This is typically accomplished through use of activity coefficients. Thus, to produce reasonable estimates from thermodynamic calculations, reliable values for the activity coefficients of both the solutes and the solvent are essential.

The primary goal of the experimental effort is to determine osmotic coefficients and mean activity coefficients for aqueous electrolyte solutions of interest to the INEEL. This requires working with solutions of varying ionic strength (up to ~10 *m*) and high (>1 M H^+) acidity. Many methods for measuring the activity coefficients of electrolyte solutions have been reported in the literature.[19] In general, the activity coefficients may be determined for the solutes in solution or for the solvent. Measurement of the activity coefficients of individual components of the solution requires a direct technique, such as measuring the electromotive force (emf) of an electrochemical cell or the solubility limit for a component in the solution. The emf measurements are limited to electrolytes for which a useful

electrochemical half-cell exists and the solubility limit measurements are most useful for species at or near their saturation concentration in solution. The activity coefficient of the solvent may be determined by techniques such as freezing-point depression or boiling point elevation measurements, vapor pressure measurements, and isopiestic measurements. Freezing-point depression or boiling-point elevation and vapor pressure measurements allow for very precise determination of solvent activity coefficients, but suffer from the necessity of complete degassing of solutions and very precise control of temperature. The isopiestic technique is much less susceptible to temperature variations and applies to solutions having electrolyte concentrations >0.1 $mol \cdot kg^{-1}$.

The osmotic coefficients determined from the isopiestic equilibrations are directly related to the activity of the solvent. In the case of a binary solution, the measured osmotic coefficient is used with the Gibbs-Duhem equation to calculate the activity coefficient of the solute (Reference 17). the added degree of freedom for ternary solutions due to the second solute requires the use of a thermodynamic model such as the Pitzer ion interaction model to calculate constituent activity coefficients.[20]

There are many literary examples dealing with the use of the isopiestic technique to determine the solvent activity of binary (a single salt and water)[21,22,23,24] and ternary (two salts and water)[25,26,27] solutions. In general, the isopiestic technique requires that several different solutions held in separate sample containers come to thermodynamic equilibrium by transferring solvent molecules through a common vapor phase. The sample containers are placed in a large vessel, which is evacuated to the vapor pressure of the solvent and allows for the exchange of solvent molecules between the various samples. The sample cups (material of construction is platinum) are held in a large copper block to minimize the temperature gradients experienced by the different sample solutions. After the sample solutions in the isopiestic apparatus have come to thermodynamic equilibrium (activities of the solvent in each sample are identical), each solution is weighed and its molality calculated. By using at least one isopiestic reference solution (one for which the activity of the solvent is a known function of molality) during the equilibration, the solvent activity in the test samples can be determined from the molality of the reference solution. By performing the isopiestic equilibrations over a wide range of molalities, the activity coefficients of the solvent can be determined over a range of electrolyte concentrations.

Current Activities

To date, research activities have centered on the design and construction of the isopiestic apparatus. Platinum was chosen as the material for the sample containers. The cups have been received. Copper blocks are used to hold the platinum sample containers in the isopiestic chambers. The copper blocks have been fabricated and are currently being gold plated to provide some protection from corrosive nature of the vapors generated by the test solutions.

The design and construction of the major parts of the experimental apparatus, the water bath and the isopiestic chambers, is complete (see Figure 8). The isopiestic chambers (four were constructed) are constructed from Hastelloy® C-22 (see Figure 9). This material was chosen because of its superior fluoride ion corrosion resistance relative to more common stainless-steel alloys.

Figure 8. Interior of the water bath used for isopiestic equilibrations. The rack holds and rocks the isopiestic chambers and rock the chambers insuring effective mixing of the test solutions.

Figure 9. Photograph of a stainless steel (Hastelloy® C-22) isopiestic chamber. The valve in the lid is used for purging and evacuating the atmosphere inside the chamber.

Since the isopiestic technique relies on the exchange of solvent molecules through a common vapor phase and vapor phase composition is a strong function of temperature, accurate temperature control (at least ±0.005°C) is an absolute necessity for the successful application of the isopiestic technique. In addition, some experiments may require several weeks or more to reach isopiestic equilibration. Therefore, temperature accuracy and long-term temperature stability are equally important.

The water bath is constructed from 18-gauge stainless steel and insulated with rigid fiberglass insulation (approximately R-20). The bath is cooled with a copper coil connected to a closed-loop refrigerated bath (Neslab RTE-211) and heated with an immersion heater (Watlow, Firerod Immersion Heater, 1,000 W, 120 V). A high precision water bath temperature controller (Hart Scientific, Model 2100) is used to control the output of the heater. The temperature of the water bath is monitored with a calibrated thermocouple thermometer (Hart Scientific, Model 1504). An example of the temperature stability achievable with this system is shown in Figure 10.

While the standard deviation of the mean temperature of the water bath is significantly less than 0.005°C (see Figure 3), a better indication of the temperature stability is provided by the maximum variation in the value of the measured bath temperature. For the data in Figure 10, the maximum variation is approximately 0.003°C. The water bath is clearly operating well within the required design specification of ±0.005°C.

Future Work

The construction the experimental apparatus was a time-consuming, although necessary task. With the completion of the apparatus, experimental efforts will transition to the determination of activity coefficients of electrolytes in non-ideal solutions. In order to accomplish this task, the performance of the isopiestic apparatus (time required for equilibrations, presence of temperature gradients within the chamber, etc.) must be determined. These experiments are currently being planned and should be completed during this calendar year. Following the completion of these initial measurements, work will center on the measurement of activity coefficients for electrolyte species of interest to the INEEL. Several examples include mercurous and mercuric chloride in sodium nitrate/nitric acid solution, hydrofluoric acid in sodium nitrate/nitric acid solution. This is not a complete list of species to be investigated and the list is subject to revision as better information concerning potential problem species in the INEEL tank wastes become available.

ACCOMPLISHMENTS

Thus far we have:

- Performed molecular dynamic simulations of potassium chloride, calculated physical and thermodynamic properties, and found good correlation with published data.
- Performed quantum mechanical calculations of nitrate and water and aluminum ion and water.
- Performed equilibrated molecular dynamic simulations of aluminum ion in water, nitrate ion in water, sodium in water, hydronium in water, and determined pair-correlation functions for each.

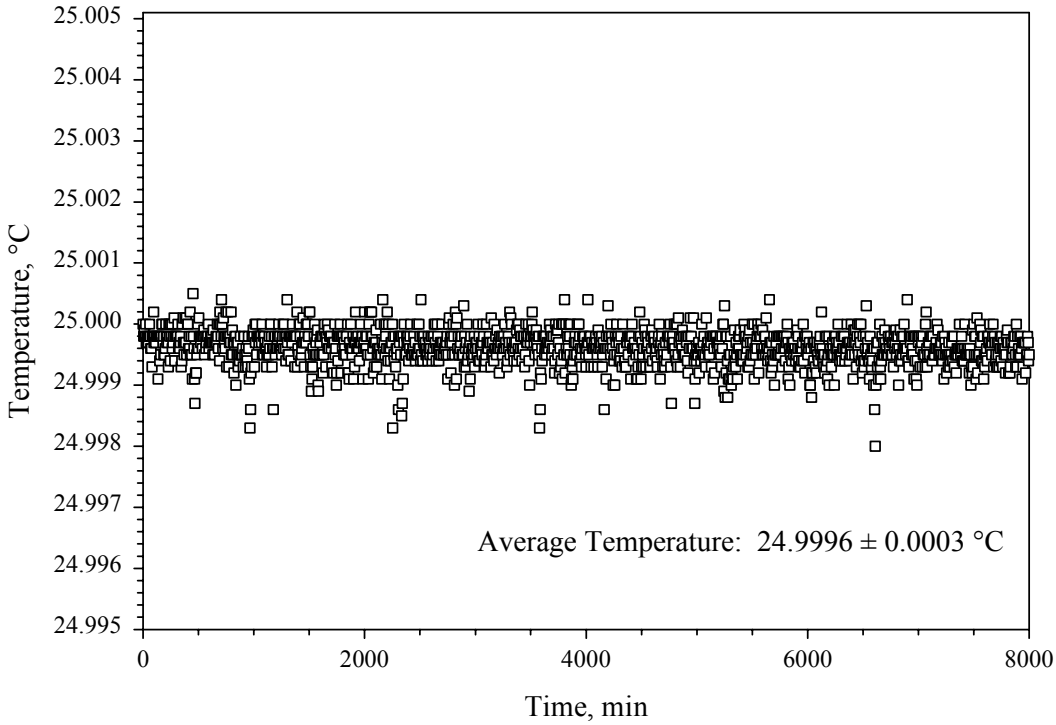

Figure 10. Plot of the temperature stability of the isopiestic water over an extended period of time.

- Imported a parallel code for molecular dynamic simulation to reduce computation time.
- Estimated Pitzer parameters using polynomials that were a function of ionic radii, were used to calculate activity coefficients, and produced good fits to experimental data at moderate concentrations.
- Fabricated an isopiestic apparatus.

REFERENCES

1. D. Chandler and L. R. Pratt, *J. Chem Phys*, Vol. 65, 1976, p 2925.
2. P. L. Moore Plummer, *J. Mol. Structure (Thermochem)*, Vol. 417, 1997, pp.35–47.
3. M. W. Mahoney and W. L. Jorgensen (2001) *J. Chem. Phys.*, Vol. 115, 2001, pp. 10758–10768.
4. H. J. X. Berendsen, D. van der Spoel, and R. van der Drunen, (1995) *Comp. Phys. Comm.*, Vol. 91, 1995, 43–56.
5. E. Lundahl, B. Hess, and D. van der Spoel, (2001) *J. Mole. Mod.*, Vol. 7, 2001, pp. 306–317.
6. J. B. Wright, Private communication, June 2002.
7. C. Ebner, R. Sansome, and M. Robst, *Int. J. Quantum Chem*, Vol. 70, 1998, pp. 877–886.
8. I. Kampschulte-Scheuing and G. Zundel, (1970) *J. Phys. Chem.*, Vol. 74, 1970, p. 2363.
9. E. Wasserman, J. R. Rustead, and S. S. Zantheas, *J. Chem. Phys*, Vol. 106(23), 1997, p. 9769.
10. M. I. Lubin, E. J. Bylaska, and J. H. Weare, *Chem. Phys.* Lett., Vol. 322(6), 2000, pp. 447–453.
11. K. S. Pitzer, 1973), *J. Phys. Chem.*, Vol. 77, 1973, pp. 268–277.
15. C. E. Harnie and J. H. Weare, *Geochim. Cosmochim. Acta.*, Vol. 44, 1980, pp. 981–997.

16. C. R. Paige, W. A. Kornicker, O. E. Hielman Jr., and W. J. Snodgrass, Vol. 56, 1992, pp. 1165–1173.

17. S. M. Sterner, I. Chou, R. T. Downs, and K. S. Pitzer, *Geochim. Cosmoschim. Acta.*, Vol. 56, 1992, pp. 2295–2309.

18. K. S. Pitzer, *Ion-Interaction Approach: Theory and Data Correlation*," *in Activity Coefficients in Electrolyte Solutions*, 2nd ed., K. S. Pitzer Ed., CRC Press, Boca Raton, Florida, 1991.

19. K. S. Pitzer and G. Mayorga, *J. Phys. Chem.*, Vol. 77, 1973, pp. 2300–2308.

20. R. A. Robinson and R. M. Stokes, *Electrolyte Solutions*, 2nd ed. Revised, Butterworths, London, 1965.

21. R. D. Shannon, *Acta. Crystallogr.*, Vol. A32, 1976, p. 751.

22. J. A. Rard and R. F. Platford, *"Isopiestic Experimental Methods," in Activity Coefficients in Electrolyte Solutions*, 2nd ed., K. S. Pitzer Ed., CRC Pres, Boca Raton, Florida, 1991.

23. J. A. Rard and D. G. Miller, *J. Chem. Eng. Data*, Vol. 32, 1987, p. 85.

24. J. A. Rard, S. L. Clegg, and D. A. Palmer, (2000) *J. Soln. Chem.*, Vol. 20, 2000. p. 1.

25. M. T. Zafarani-Moattar and M. Aria, *J. Soln. Chem*, Vol. 30, 2001, p. 351.

26. J. G. Albright, P. Rizzo, and J. Rard, *J. Chem. Thermodynamics*, Vol. 30, 1998, p. 327.

27. J. A. Rard and S. L. Clegg, , *J. Chem. Eng. Data*, Vol. 42 1997, p. 819.

28. J. Seidel, K. Rossner, and F. Kuschel, *J. Chem. Eng. Data*, Vol. 30, 1985, p. 289.

29. C. Pan and W. Argersinger, *J. Chem. Eng. Data*, Vol. 32, 1987, p. 205.

30. M. A. Flesia, M. R. Gennero de Chialvo, and A. C. Chialvo, *Fluid Phase Equil.*, Vol. 131, 1997, p. 189.

Inorganic Supports for Binding Ammonium Molybdophosphate to Produce Ion Exchange Sorbents for Removal of Cesium-137 from Acidic Nuclear Waste

Troy Tranter, Terry Todd, and Scott Herbst

SUMMARY

Ion exchange is a widely recognized technology for removing target ions from aqueous solutions. It is a relatively mature science used in a variety of industries, ranging from pharmaceuticals to water purification. It is often a preferred technology from a process engineering perspective because of its simplicity, relatively small footprint, and lower capital investment compared to other separation processes. This technology has been used in the nuclear industry for removing radionuclide metals from reactor coolant and waste streams in nuclear power generating stations. However, there is a current need to customize this technology so it can be applied to separating or partitioning radionuclides from aqueous legacy wastes associated with cold war era activities. For example, there is an urgent need to separate the high activity fission products such as ^{137}Cs and ^{90}Sr from the longer-lived transuranic (TRU) isotopes so they can be disposed of in appropriate repositories. Unlike the waste streams associated with nuclear power plants, legacy waste streams are usually the result of a dissolution process in the Highly Enriched Uranium (HEU) fuel cycle or weapons production, or from the off-gas scrub streams associated with vitrification processes used to solidify these liquid wastes. These streams are typically very acidic or very alkaline and potentially of very high ionic strength. These characteristics make this waste very problematic for any type of separation process. Consequently, a sorbent or ion exchange material designed for use with these waste streams must be unique in that it must have a very high selectivity and stability in high radiation, temperature, and acid or alkaline environments. Inorganic ion exchange materials are usually superior in their ability to satisfy these criteria, but inorganic ion exchange media typically exist as fine powders, making large-scale use impractical, unless the medium can be affixed to an appropriate matrix. The most common matrices used for the support structure are organic polymer materials. Supports of this type are very porous and provide good diffusion and hydrodynamic properties. Unfortunately, they are not compatible with high radiation fields or acceptable as final waste forms due to leachability and the potential for hydrogen gas generation resulting from radiolytic degradation of the organic matrix.

PROJECT DESCRIPTION

The objective of this research is to design a totally inorganic ion exchange material that would satisfy a niche in the treatment of legacy liquid radioactive waste. This new sorbent composite material would be used to remove radioactive cesium from highly acidic liquid waste streams, such as the sodium bearing tank waste currently stored at the INEEL. Thus, this material must be (a) amenable to use in a process to treat waste of high acidity and ionic strength, (b) highly resistant to radiolytic degradation and elevated temperatures resulting from decay heat generation, and (c) amenable to fixation by a suitable binding agent or support that will allow the formation of a bead or grain with good mechanical and hydraulic properties. This suitable binding agent must possess the same qualities of stability in high acid, oxidizing, temperature, and radiation environments. The composite material should exhibit high selectivity for cesium and provide good kinetic and hydrodynamic properties. The process for producing the material must also be capable of generating production-scale quantities at reasonable cost.

Ammonium molybdophosphate (AMP), $(NH_4)_3P(Mo_3O_{10})_4 \bullet 3H_2O$, is a yellow crystalline

inorganic compound shown to have the requisite selectivity and stability properties. It has been demonstrated by Smit and Van[1] to be highly selective for Cs, and exhibits a selectivity sequence for the alkali metals similar to other heteropolyacids of the Keggin structure ($Cs^+ > Rb^+ > K^+ > Na^+ > Li^+$). The ion exchange mechanism of AMP is reported by Buchwald and Thistlethwaite to be an isomorphous exchange of cesium ions for ammonium ions in the crystal lattice.[2] According to Smit and Van (see Reference 1), the phosphomolybdate complex ion, $(PMo_{12}O_{40})^{-3}$, consists of a hollow sphere formed by the 12 MoO_6 octahedra with the PO_4 group in the center of the crystal structure of the ammonium salt of this ion. The ammonium ions with associated water molecules are likely fit in between these spheres of negative ions, accounting for the cohesion of these ions. These researchers also report the exchange of NH_4^+ for the monovalent ions (Na^+, K^+, Rb^+, and Cs^+) with Cs being much preferred over the others. This selectivity for Cs over other cations and excellent distribution coefficient in HNO_3 systems, up to 10 N, has been demonstrated by Suss and Pfrepper.[3] In 1961, work by Wilding proved the effectiveness of AMP for Cs removal from acidic and highly salted nuclear waste streams, and showed no significant decrease in Cs distribution coefficient in the presence of 10 g/L Na and K.[4] Wilding's work also showed no appreciable effect on Cs sorption from HNO_3 concentrations up to 1.5 M and distribution coefficient values of 1,000 or greater were obtained in most of his experiments. Kinetic studies, in batch systems, were also conducted by these researchers and indicated rapid exchange (<30 min) of Cs in the AMP (see References 3 and 4.) Krtil and Chavko also found very rapid kinetics for Cs in AMP,[5] reporting that the Cs uptake practically did not vary with time and that equilibrium was established almost immediately.

Irradiation studies with electron doses up to 1 MGy were conducted by Rao et al.[6] The results of this research show detectable changes in the physicochemical structure of AMP at high radiation dose (1 MGy) without decrease in Cs capacity or distribution coefficient in HNO_3 systems.

As mentioned earlier, for AMP to be practical in a process scale, it must be fixed with a binding agent, substrate, or support that will allow it to be used in a packed bed with reasonable flow rate and minimal pressure drop, such as acceptable hydrodynamics. Current state-of-the-art for synthesizing an engineered form of AMP involves combining this exchange material with an organic support. Sebesta presents the merits of various techniques for fixing inorganic sorbents into engineered forms and discusses a new technique of combining AMP with an inert binding polymer, polyacrylonitrile (PAN), to create a composite absorber.[7] Further reports by Sebesta et al. show excellent Cs selectivity and removal from acidic radioactive wastes as well as good mechanical and physical characteristics of the composite.[8,9,10] This AMP-PAN composite was further evaluated by Tranter et al. and Todd et al.,[11,12] in which the high Cs capacity and selectivity of AMP-PAN was verified via bench scale column tests using simulated acidic waste and actual radioactive tank waste. The efficacy of the AMP-PAN for Cs removal was demonstrated at semiscale with simulated waste by Herbst et al.[13]

Although the AMP-PAN composite provides excellent Cs separation, there is a valid concern that this material will breakdown after prolonged exposure to high radiation, high temperature, or both. Also, the organic PAN binding material is not compatible with many treatment processes proposed for stabilizing highly radioactive waste. Therefore, the Cs or AMP would have to be stripped from the support and the organic fraction disposed of as a secondary waste. Consequently, there is a pressing need for the development of a totally inorganic AMP composite (AMP fixed on an inorganic support) that would provide reasonable kinetics and hydrodynamic performance. This new composite would maintain the excellent performance of the AMP exchanger while eliminating the stability concerns associated with an organic binder. The development and testing of such a composite material is the focus of this research and development effort. It should be noted that, even though the AMP-PAN composite material has questionable properties of long term stability, a substantial amount of data exist regarding the equilibrium and dynamic behavior of this material. Thus, the documented performance

of the AMP-PAN composite is used as a benchmark for assessing the efficacy of the newly developed inorganic AMP composite exchanger.

During FY 2002, we investigated:

- Methods for impregnating glass crystalline microspheres with AMP
- AMP-ZrHP composite selectivity
- Preliminary studies for AMP-cenosphere equilibrium capacities
- Preliminary studies for AMP-censophere dynamic behavior.

Impregnation of Glass Crystalline Microspheres with AMP

Glass Crystalline Microspheres (Cenospheres)

The glass microcrystalline material, to be used as a substrate, was initially developed as a high surface area sorbent media as part of a collaborative research effort between the Khlopin Radium Institute (KRI), St. Petersburg, Russia, the Institute of Chemistry and Chemical Technologies (ICCT), Krasnoyarsk, Russia and the Idaho National Engineering and Environmental Laboratory (INEEL).[14] The material, termed Gubka, or "sponge" in Russian, is an open-cell glass crystalline porous material (see Figure 1) that is produced from hollow glass crystalline microspheres, commonly known as cenospheres, formed as small mineral slag particles in fly ash from coal combustion. The cenosphere sizes typically range from 0.1 to 0.5 mm in diameter. Average compositions of the cenospheres include primarily the minerals common in glass, including up to 65 wt% silicon oxide, 25 wt% aluminum oxide, and lower amounts of iron, calcium, magnesium, potassium, and titanium oxides ranging from <1 to 5%.

The method of preparation includes separating the cenospheres into fractions based on size, density, magnetic or nonmagnetic, and perforated or nonperforated characteristics. The cenosphere walls can be further treated with acids to form an increased number of perforations, allowing the interior volume of individual cenospheres to be more accessible to radioactive solutions. The porous matrix consists of two types of porous openings: intraglobular pores in the cenosphere walls of 0.1–30 μm, and interglobular pores between the cenospheres of 20–100 μm. Selected cenosphere fractions can be molded and agglomerated by sintering with or without a binder at high temperatures. Thus, the porous blocks or beads can be formed or engineered to desired size and shape based upon hydrodynamic and kinetic specifications.

Depending on the cenosphere fractions selected, sintering conditions, and additional treatments, the material is formed with a total open-cell porosity ranging from 40–90%. The cenospheres have an apparent density of 0.3–0.6 g/cm^3 and a compressive strength in the range of 1.2–3.5 MPa. The cenosphere material is chemically stable in concentrated nitric, hydrochloric, sulfuric, and phosphoric acids at boiling temperatures.[14–16] The raw material for producing the cenospheres exists in abundance as fly ash waste in both Russia and the U.S., and is commercially available in both countries.

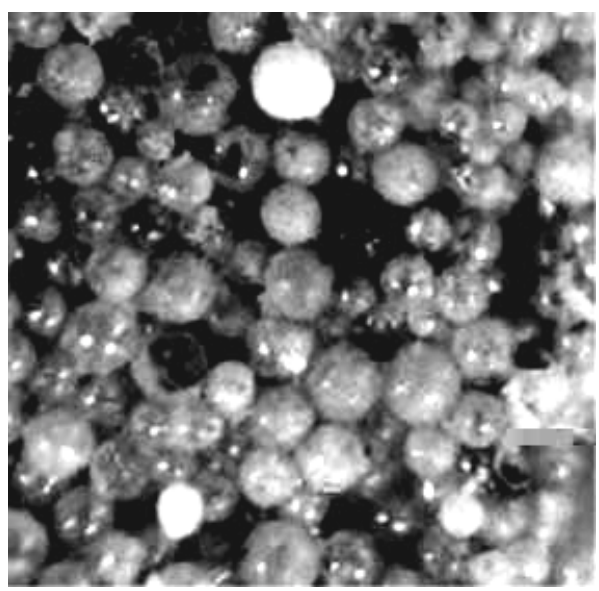

Figure 1. Optical micrograph (60x) of the censosphere porous matrix.

Incorporation of AMP into Gubka Matrix

Only the perforated cenospheres are used for AMP impregnation; these perforations are necessary to provide a diffusion pathway for the cesium to reach the AMP inside the spheres. The feasibility of loading the AMP compound into the hollow perforated cenospheres has been demonstrated. Two techniques to accomplish this were investigated. The first technique entails loading the soluble form of the AMP salt into the inside of the hollow censospheres under vacuum. This is possible because AMP dissolves in NH_4OH alkaline solution. The loaded cenospheres are dried for 8 hours at 120°C. The material is then loaded once again under vacuum with 4 M HNO_3. This precipitates the AMP salt inside the cenospheres. The excess AMP solid is rinsed from the interstitial void space within the matrix with approximately 20 void volumes of 2 M HNO_3. Three impregnation cycles are performed to obtain a maximum AMP loading of approximately 35 wt%. Good reproducibility between sets was obtained by this method. The second technique entails synthesizing the AMP salt from its precursors inside the hollow cenospheres. The cenospheres are initially loaded under vacuum with a solution of NH_4OH and $(NH_4)_6Mo_7O_{24}$ in mixture of citric and nitic acid. The cenospheres are then immersed in an aqueous solution of $(NH_4)HPO_4$ which diffuses into the spheres and precipitates AMP. Improvements to the second technique are still being investigated since the diffusion process by the current method is slow, taking much longer than the recrystallization approach to obtain acceptable mass loadings.

A collaboration with the ICCT Institute in Krasnoyarsk, Russia was also initiated to have scientists at this institute study methods for cenosphere impregnation. These researchers obtained AMP mass loadings of approximately 35 wt% using similar techniques. Figure 2 is an optical photograph of AMP crystals inside the cenosphere obtained by direct synthesis.

A cross-section of an AMP loaded cenosphere (see Figure 3) clearly shows the thick layer of AMP crystal deposition inside the cenosphere. This AMP was loaded into the cenosphere via the recrystallization technique described above.

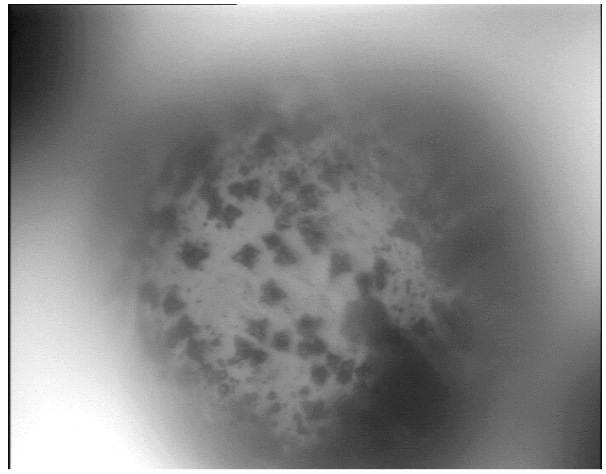

Figure 2. AMP crystals inside cenosphere (350).

Error! Objects cannot be created from editing field codes.

Figure 3. Cross section of AMP [illegible] cenosphere (recrystallization method).

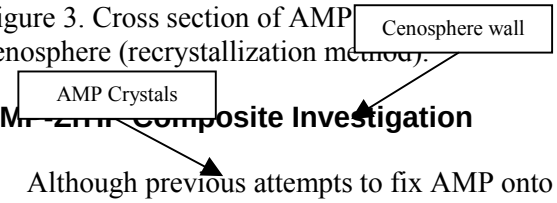

AMP-ZrHP Composite Investigation

Although previous attempts to fix AMP onto an inorganic bead or substrate have had limited success, one available engineered form of AMP is on ZrHP. This material has been developed and produced in very limited quantities at Oak Ridge National Laboratory (ORNL). The hexamethylenetetramine (HMTA)/urea internal gelation technology developed by Collins et al.,[17–19] provides a method of preparing inorganic ion exchange materials in an engineered form as microspheres. Using this technology, these researchers have prepared small quantities of AMP-ZrHP in bead form with up to 50 wt% loadings of AMP. Data from one unpublished dynamic column test preformed by INEEL researchers suggest that this material may have Cs loading capacities similar to AMP-PAN. However, these data indicate that the kinetics are substantially slower than those of AMP-PAN. Nonetheless, as with the AMP-cenosphere composite previously discussed, it is anticipated that the kinetics would be acceptable for intended waste treatment applications. It is also expected that the AMP-ZrHP composite adsorber would meet the requisite stability criteria as specified earlier. The primary concern with this material is the potential absorption of the TRU elements by

the ZrHP in nuclear waste treatment applications. This would be detrimental in that the exchange material could then become TRU waste, which would greatly complicate and limit disposal options. However, at the time of this writing, AMP-ZrHP is the only other engineered form of AMP of which the authors are aware. Thus, it was included in this evaluation.

Tests were performed to determine the affinity of the AMP-ZrHP for adsorption of selected TRU isotopes from acidic media. Several sets of batch contacts were performed using known amounts of AMP-ZrHP sorbent and simulated sodium-bearing waste (SBW) feed solutions spiked with ^{238}Pu, ^{241}Am, and ^{237}Np. These isotopes were chosen because they are the predominant (based on activity) TRU isotopes in the actual SBW tank waste stored at the INEEL. The composition of the simulated SBW solution used for these experiments and subsequent experiments discussed below is shown in Table 1.

The solid and liquid phases were placed in test tubes and mixed for 48 hours to allow equilibration between phases. The phases were then separated and the liquid phase was analyzed by liquid scintillation spectrometry (LSC) to determine the amount of TRU present. The concentration of TRU isotopes in the solid phase was then calculated by material balance. The distribution coefficient (K_d) was determined for each system according to the following formula:

$$K_d = \frac{(C_o - C_e)}{(C_e)} * \frac{V}{M} \qquad (1)$$

where

C_0 = Initial concentration of the ion in solution before contacting sorbent.

C_e = Final equilibrium concentration of ion in solution after contacting sorbent.

V = mLs of solution

M = Grams of sorbent material contacted.

The resulting K_d values are listed in Table 2. Although the K_d values given in Table 2 are not extremely high, they do indicate that the sorbent material would be well over 10,000 nCi/g for Plutonium and neptunium in the sorbent phase if the feed were actual SBW tank solution.

Table 1. Average composition of SBW tank simulant.

Component	(M)
Ag	3.0E-05
B	1.95E-02
Ca	6.1E-02
Cd	3.32E-03
Cr	5.4E-03
Cs	1.29E-05 to 2.76E-05
Fe	2.5E-02
Hg	1.60E-03
K	2.0E-01
Mn	1.2E-02
Mo	7.3E-04
Na	1.9E+00
Pb	1.4E-03
Sr	2.0E-05
Zr	9.0E-03
Al	7.0E-01
SO4	3.0E-02
PO4	2.04E-02
F	6.8E-02
Cl	3.05E-02
HNO3	1.8

Therefore, it is not likely that this material would be a suitable candidate for removing cesium from waste solutions containing high concentrations of TRU isotopes.

Table 2. Transuranic distribution coefficients in simulated INEEL tank waste for ZrHP-AMP composite.

Spike	Feed	Weight (g)	Vol. (mL)	Vol/ Mass	Kd
^{238}Pu	Simulated Tank Waste	0.50	15.0	30	87

^{238}Pu	Simulated Tank Waste	1.00	15.0	15	112
^{237}Np	Simulated Tank Waste	0.50	15.0	30	24
^{237}Np	Simulated Tank Waste	1.00	15.0	15	12
^{241}Am	Simulated Tank Waste	0.50	15.0	30	2
^{241}Am	Simulated Tank Waste	1.00	15.0	15	1

AMP-Cenosphere Equilibrium Capacity

Batch contacts were performed with the AMP-cenosphere composite using the SBW simulant shown in Table 1 to generate an equilibrium isotherm for the system. The simulant was spiked with NIST traceable ^{137}Cs to a concentration of approximately 500 Bq/mL to facilitate analysis via gamma spectrometry. The feed solution was allowed to equilibrate with the tracer for 24 hours prior to beginning the experiment. Batch experiments were initiated by quantitatively weighing and transferring amounts of dry AMP-cenosphere composite into 20 mL borosilicate glass test tubes. Fifteen mL aliquots of feed solution were then quantitatively dispensed into each test tube containing known weights of the AMP-cenosphere composite. The tubes were attached to a mixing wheel (ROTO-TORQUE Model 7637-01) and the solid and liquid fractions were mixed for contact times of 24 ± 1 hours at ~15 rotations per minute. Tests were performed at ambient temperature (23°C ± 2°C). After the 24-hour contact period, the tubes were removed from the mixer and centrifuged for 5 minutes. Aliquots (5 mL) were removed from the aqueous fraction and filtered through a Gelman® Acro disk (0.45 µm) syringe filter to remove any solids suspended in the liquid. No visible suspended solids were present before or after filtering. Analysis of the aqueous feed and equilibrated fractions were done by gamma spectrometry using a high purity germanium (HPGe) detector (Oxford CP80210) coupled to a (SUN® Microsystems, Sparc 10) computer workstation. Total measure-ment uncertainties varied as a function of analyte concentration, but were typically within ±5%. The analyte concentration in the solid phase was then calculated by material balance.

Ion exchange equilibria can be characterized from the equilibrium isotherm. The isotherm is a graphical representation, which in theory, covers experimental conditions at a given temperature. Any set of experimental conditions (temperature, solution concentration, sorbent concentration, etc.) corresponds to one point on the isotherm surface. Historically, many theoretical models have been proposed to describe equilibrium in solid-fluid systems. Explicit equations that treat the solid as a flat surface or that assume pore filling have been derived.[20] Many early attempts to model ion exchange equilibria involved fitting empirical equations to experimental results. These equations were usually modifications of mass action law or adsorption isotherms of Langmuir or Freundlich. Although derived from different models and assumptions, most of these equations will provide a reasonable fit to experimental isotherm data by suitable choice of constants.[21] For this analysis, the classical Langmuir isotherm equation was used to fit the equilibrium data. The Langmuir equation is:

$$q = Q_o \cdot \frac{K \cdot c}{(1 + K \cdot c)} \qquad (2)$$

where

q = the equilibrium concentration of the ion (Cs) in the sorbent phase

Q_o = the asymptotic maximum concentration of the ion (Cs) in the solid phase

c = the equilibrium concentration of the ion (Cs) in the liquid phase

K = the equilibrium constant for the ion (Cs) between the solid and liquid phases.

The equilibrium isotherm curve presented in Figure 4 was generated by plotting equilibrium liquid phase Cs concentration in milligrams Cs/L against equilibrium solid phase concentration in milligrams Cs/g AMP (dry weight).

Visual inspection of the data shows that the curve becomes linear in the regions of very high and very low equilibrium concentrations. Unlike other classical models, such as Fruendlich, the Langmuir equation becomes linear in these concentration regions which makes it an intuitive choice for these data. The Langmuir model is also a convenient choice because it gives the asymptotic maximum solid phase capacity (Q_0) which can be compared with values obtained from other sorbents. The determination coefficient (r^2) resulting from the fit to these data was 0.99 and the Q_0 value is 61 mg Cs/L, which is in reasonable agreement with the value of 72 mg Cs/L obtained for AMP-PAN with SBW simulant (see Reference 11). Visual inspection of the plot also shows that the overall curve is nonlinear and concave downward. The nonlinear aspect agrees with previous work wherein AMP-PAN was reported as highly selective for Cs. This, by definition, necessitates a nonlinear isotherm. Isotherm curves that are concave downward throughout are designated as type I or "favorable," while those that are concave upward throughout are termed "unfavorable."[22] The designations favorable and unfavorable refer to sorbent behavior for target ion up-take. As with previous work using AMP-PAN (see Reference 11), this is a good indicator that the AMP-cenosphere composite will behave favorably when used in a dynamic mode to remove Cs.

The combined effects of equilibrium and mass transfer will determine the shape or pattern of the exchange boundary, and thus the breakthrough curve, when the fluid and solid are contacted in a fixed-bed system. Because of this, confirmation of favorable equilibrium is very important because it usually indicates that a constant pattern front (CPF) or "self sharpening" boundary will develop in a fixed-bed contactor, provided mass transfer takes place at a reasonable rate. As described by Helfferich,[23] the sharp exchange boundary results from the fact that the counter ion in the feed, in this case Cs, is much preferred by the ion exchanger under favorable equilibrium. The sharpening of the exchange boundary means the boundary "wave" or exchange zone will maintain a steady state shape or CPF as it moves through the bed during the loading cycle, and will occupy a relatively small portion of the total column at any given time.[24]

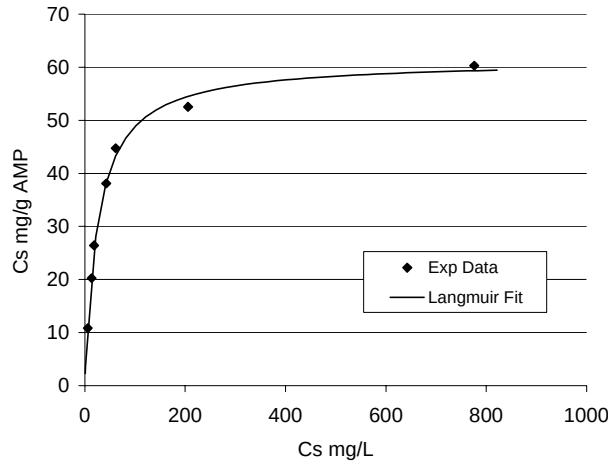

Figure 4. Cesium equilibrium isotherm for AMP-cenospheres and simulated SBW.

AMP-Cenosphere Dynamic Column Experiments

In order to assess the applicability and efficiency of the AMP-cenosphere composite for Cs removal in a fixed bed system, small scale column tests must be performed to obtain kinetic and loading capacity data. These data are obtained by generating complete breakthrough curves at various combinations of flow rate and bed volume. These column data can then be used to elucidate column capacity and kinetic parameters, which, under appropriate conditions, can be used for actual process column design. In FY 2002, the dynamic studies were initiated by generating a complete breakthrough curve using a small column (2.3 cm^3 bed volume) and SBW simulant feed solution spiked with a known quantity of ^{137}Cs tracer. Similar to the batch tests described above, the simulated SBW was allowed to equilibrate with the Cs tracer for 24 hours to ensure complete isotopic equilibration between radioactive ^{137}Cs and stable ^{133}Cs. The column used for the test had a 9.5 mm inside diameter with a maximum possible bed height of 48 mm. The inlet, outlet, and base of the column were stainless steel with the bed portion made of trans-parent Plexiglas which allowed visual inspection of the bed throughout the test. The column was designed to operate in an up-flow or down-flow configuration; this test was performed in down-flow mode. An air-free bed was obtained in the test by using a careful and consistent technique for

loading the sorbent bed into the column. First a solution of 0.1 N HNO_3 was pumped through the associated tubing to the column inlet until all air bubbles were removed. The tubing to the column inlet was then closed and the column was loaded with the desired amount of dry AMP-cenosphere composite sorbent. A vacuum was established inside the column using a small laboratory size vacuum pump. The outlet tubing from the column was closed and the inlet opened allowing the 0.1 N HNO_3 to flood the column and bed material. This vacuum loading technique ensures that the inside of the cenospheres are fluid filled, which is necessary to establish a medium for mass transport into the AMP containing portion of the cenospheres. This technique also eliminates any air present in the column, which helps to prevent channeling during column operation. Several bed volumes (BV) of the acid solution were pumped through the column to calibrate the flow rate and then the influent was switched to the SBW simulant reservoir and the start time was recorded. The feed was pumped through the column by a valveless metering pump (FMI Lab Pump Model QVG-50). A consistent flow rate set at 5 mL/hour was maintained by controlling the pump with a 10-turn potentiometer (FMI Stroke Rate Controller Model V100).

The feed rate was consistent throughout the test. Column effluent samples were collected at constant intervals throughout the run by using a fraction collector (Eldex Model UFC), which enabled discreet fraction collection at preset time intervals. The collected samples were analyzed by gamma spectrometry to determine the amount of ^{137}Cs in the column effluent. The total Cs concentration was then calculated using the known ratio of radioactive to stable Cs in the feed solution. Figure 5 shows the experimental bench-scale column. The column was visually monitored during the test and air bubbles or bed disruptions were not observed.

A cesium breakthrough curve was generated from the test by plotting the volume of feed processed against the fractional breakthrough, which is defined as the Cs concentration in the effluent (C) divided by the Cs feed concentration or Cs concentration in the influent (C_0) (see Figure 6). The bed volume for the test was 2.3 cm^3 with an AMP amount of 30 wt%, which equals a total of 0.55 grams of AMP in the bed.

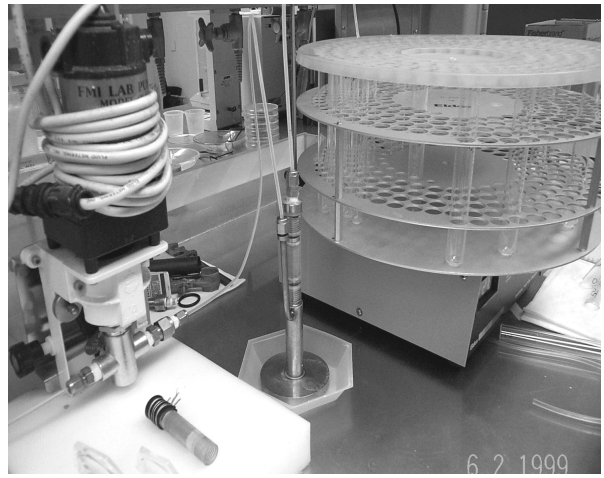

Figure 5. Experimental bench scale column.

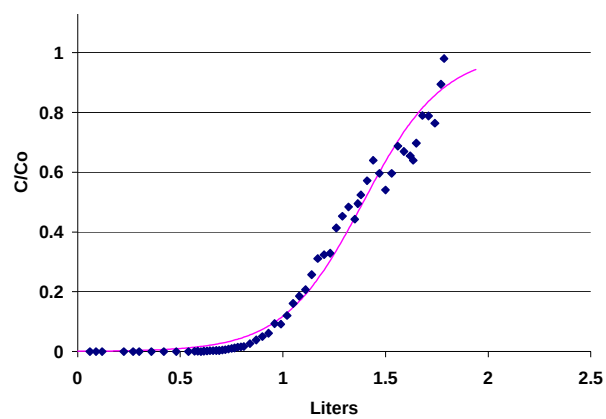

Figure 6. Cesium breakthrough curve, AMP-cenosphere sorbent and SBW simulant.

In Figure 6, the experimental data obtained from the dynamic column test are shown as individual points, whereas the solid line represents a fit to these data using a simplified second order kinetic model developed by Thomas.[25] These data were fit reasonably well with this model which takes the form:

$$\frac{C_o}{C} = 1 + e^{\frac{k_1}{F}(q_o M - C_o V)} \tag{3}$$

where

C = effluent concentration, mg/L

C_0 = feed concentration, mg/L

k_1 = overall rate constant, L/h-mg

F = volumetric flowrate, L/h

q_0 = maximum sorbent phase concentration, mg/g

M = mass of sorbent, g

V = throughput volume, L.

The total Cs capacity of a given mass of sorbent for a given feed and specified throughput volume can then be calculated from the following relationship:

$$\frac{M\ C}{M\ AMP} = \int_0^v \frac{(C_o - C)dv}{M} \qquad (4)$$

where the variables are as defined previously.

Substitution of the Cs concentration from Equation 3 into the relationship of 4 results in:

$$\frac{M\ C}{M\ AMP} = \int_0^v C_0 - \frac{C_0}{1 + e^{\frac{k_1}{F}(q_0 M - C_0 v)}} dv \qquad (5)$$

Evaluating this integral numerically using a volume corresponding to 100% column exhaustion results in 4.3 mg of Cs removed from the SBW simulant per gram of AMP. It is interesting to note that when the cesium concentration value in the SBW simulant (1.7 mg/L) is used in the Langmuir relationship from Equation 3, it predicts an equilibrium solid phase concentration of 3.8 mg of Cs per gram of AMP. With reasonable kinetics, the sorbent should be at equilibrium with the feed at full exhaustion, which is indicated by the close agreement between the batch and dynamic Cs capacity numbers. It should also be noted that the equilibrium value for the target ion in the solid phase is a function of the target ion concentration in the feed. Therefore, the sorbent capacity would be much higher for a feed with increased Cs concentration. However, the Cs feed concentration chosen for the current dynamic experiment was selected because it represents the average value of the Cs expected in the actual SBW composite solution.

Potential Applications of the New Technology

During FY 2002, several contacts were made regarding potential uses of the new sorbent impregnated cenosphere technology. A contract was signed with the Australian Nuclear Sciences and Technology Organization (ANSTO) in which the INEEL will provide new technology and design consultation for the upgrade of their medical isotope production facility. As part of this agreement, the new AMP-cenosphere material is one of the candidate sorbents that will be tested for removing ^{137}Cs from highly acidic and radioactive solutions resulting from irradiated ^{235}U target dissolution. This will provide the INEEL with a valuable test bed for the new technology, and may lead to future licensing agreements.

The Idaho Tank Farm Project group has agreed to include the AMP-cenosphere material as one of the possible candidates for removing Cs from INEEL acidic waste solutions. As part of this, they have agreed to fund some preliminary engineering studies with the newly developed material in FY 2003.

Contacts were initiated with Diversified Technologies Co. from Oak Ridge Tennessee. They were very interested in the new technology for possible applications in treating waste water at nuclear power generating stations. Follow-up discussions are planned with company representatives during FY 2003.

ACCOMPLISHMENTS

- Two techniques for impregnating the inside of hollow glass cenospheres have been developed, which provide AMP mass loadings of up to 35 wt%. The methods are the recrystallization of the AMP from a NH_4OH alkaline solution and the direct synthesis of the AMP salt from ammonium paramolybdate and monosubstituted ammonium phosphate.

- Batch studies have been completed using ZrHP as an inorganic support for AMP. The

tests did not include an assessment of Cs capacity, as the primary concern was whether or not the ZrHP binder would show an affinity for the adsorption of transuranic isotopes. These tests confirmed that the binder did show a moderate degree of adsorption for isotopes of Pu, Am, and Np. As previously mentioned, this is very undesirable since the SBW currently stored and the INEEL contains substantial quantities of isotopes of these elements. The batch experiments indicated that the degree of transuranic sorption by the ZrHP binder would result in the bed material far exceeding the limits for a TRU waste, which would make disposal of the material much more costly and problematic. Therefore, the work in FY 2003 will focus primarily on the development of the AMP-cenosphere technology.

- Equilibrium batch contact experiments were completed with the AMP-cenosphere composite and simulated SBW. An isotherm generated from these data was shown to be Type I with very favorable selectivity for Cs uptake. These data were fit very well by an isotherm model of the classical Langmuir form. This will simplify calculation of the equilibrium concentration terms for both the solid and liquid phases when enough data are obtained to begin numerical solutions of the rigorous transport equations, which will be necessary for column design and scale-up. It was also shown that the asymptotic maximum Cs capacity of the AMP-cenosphere composite agreed very favorably with those previously calculated for AMP-PAN, which has been chosen as the comparative benchmark for this study. Additional isotherms will be generated in FY 2003 to obtain data at different temperatures of feed composition concentrations, and further quantify the equilibrium behavior of the new composite.

- A dynamic column experiment has been completed at bench-scale using the AMP-cenosphere composite and simulated SBW. The results of this test were very promising, indicating acceptable kinetic behavior and a dynamic capacity similar to AMP-PAN. The column data were fit with a second order kinetic model, the solution of which was nearly coincident with the experimental data. The column Cs capacity derived from the numerical integration of this model agreed very well with the value predicted by the Langmuir isotherm, which provides an initial validation of both models. The kinetic model can now be used to design and predict the behavior of future column tests, resulting in reduced experimental time and cost. A full range of dynamic column experiments are planned for FY 2003 at both bench and semiscale. These experiments are necessary to obtain the data needed to elucidate various diffusion parameters, which are necessary to properly describe and predict mass transport properties.

- A collaboration was established with scientists at the V. G. Khlopin Radium Institute in St. Petersburg, Russia and the Institute of Chemistry and Chemical Technologies in Krasnoyarsk, Russia. Each of these institutes possess unique capabilities and expertise for performing various physical tests on highly radioactive materials. They also have access to facilities that can be used for performing pilot-scale testing of the newly developed sorbent on actual radioactive waste solutions, which could potentially be used for a much lower cost than similar facilities in the U.S. The collaboration has also resulted in intellectual property for both the U.S. and Russian laboratories, as patents on the selective sorbent impregnated cenosphere technology are currently being filed in both countries.

Patents

T. J. Tranter, et al., “Ion-Selective Glass Crystalline Microspheres by Impregnation with Selective Sorbents,” Invention Disclosure, DOE Case No. S-97,170. Has been elected by DOE and the Russian Ministry of Atomic Energy and is currently in the filing process in both countries.

Publications

Accepted or Published

Tranter, T. J., A. S. Aloy, N. V. Sapozhnikova, A. A. Tretyakov, A. G. Anshits, D. A. Knecht, T. A. Todd, and J. Macheret, "Porous Crystalline Silica (Gubka) as a Inorganic Support Matrix for Novel Sorbents," accepted for *Scientific Basis for Nuclear Waste Management,* February 2002.

Submitted or In Preparation

Aloy, A. S., N. V. Sapozhnikova, S.V. Podeynitstin, A.G. Anshits, T. J. Tranter, T. A. Todd, "Porous Crystalline Silica (Gubka) as Inorganic Support Matrix for Specific Extractants" submitted for publication in *Nuclear Technology*.

Tranter, T. J., T. A. Todd, R. S. Herbst, "Ammonium Molybdophosphate (AMP) Impregnated Censospheres as an Inorganic Ion Exchange Media for Separating Cesium from Acidic Nuclear Waste Streams" in preparation from submittal to *Solvent Extraction and Ion Exchange*.

Presentations

Aloy, A. S., N. V. Sapozhnikova, S. V. Podeynitstin, A. G. Anshits, T. J. Tranter, T. A. Todd, "Porous Crystalline Silica (Gubka) as Inorganic Support Matrix for Specific Extractants" presented at *Spectrum '02 Conference, Reno, Nevada*, August 2002.

Knecht, D.A., T.J. Tranter, J. Macheret, A. Meyer, D. Yesso, T. Daniels, A.S. Aloy, N.V. Saphozhnikova, A.S. Anshits, O.M. Sharonova, A.A. Tretyakov, "Deployment of Porous Crystalline Matrix (Gubka) for Stabilizing Radioactive Standard Solutions at Fernald," *Proceedings of Waste Management 2002, Tucson AZ*, February 2002.

Tranter, T. J., "Progress with AMP-Cenosphere Composite for Selective Cesium Removal" presented at *Joint U.S.- Russian Workshop, Reno Nevada*, August 2002.

Tranter, T. J., A. S. Aloy, N. V. Sapozhnikova, A. A. Tretyakov, A. G. Anshits, D. A. Knecht, T. A. Todd, and J. Macheret, "Porous Crystalline Silica (Gubka) as a Inorganic Support Matrix for Novel Sorbents," presented at *Material Research Society Conference, Boston, MA*, Nov 2001.

REFERENCES

1. J. Smit and R. Van, "Ammonium Salts of the Heteropolyacids as Cation Exchangers," *J. Nature,* May 31, 1958, p. 1530.

2. H. Buchwald and W. P. Thistlethwaite, "Some Cation Exchange Properties of Ammonium 12-Molybdophosphate," *J.Inorg. Nuc. Chem.,* Vol. 5, 1957, p. 341.

3. M. Suss and F. Pfrepper, "Investigation of the Sorption of Cesium from Acidic Solutions by Various Inorganic Sorbents," *Radiochimica Acta*, Vol. 29, 1981, pp. 33-40.

4. M. W. Wilding, *Cesium Removal From Acidic Radioactive Waste Solutions*, IDO-14544, Idaho Falls, Idaho, 1961.

5. J. Krtil and M. Chavko, "Ion-Exchange Properties of Ammonium Salts of Heteropoly-Acids: VII. Sorption of Cs-137 and Rb-86 on Acid and Normal Ammonium and Thallous Salts of Phosphotungstic and Phosphomolybdic Acid," *J. Chromatog*, Vol. 27, 1967, pp. 460.

6. K. L. N. Rao, J. P. Shukla, and B. Venkataramani, "Electron Irradiation Studies on Ammonium Molybdophosphate," *J. Radioanal. Nuc.Chem., Articles*, Vol. 189(1), 1995, pp. 107–114.

7. F. Sebesta, "Methods of Modification of Properties of Inorganic Ion-Exchangers for Application in Column Packed Beds," *J. Radioanal. Nuc. Chem*., Vol. 220(1), 1997, pp. 77–88.

8. Sebesta, F., John, J., and Motl, A., "Phase II Report on the Evaluation of Polyacrylonitrile (PAN) as a Binding Polymer for Absorbers Used to Treat Liquid Radioactive Wastes,"

SAND96-1088, Sandia National Laboratories, Albuquerque, New Mexico, 1996.

9. F. Sebesta, J. John, and A. Motl, *Development of Composite Ion-Exchangers and Their Use in Treatment of Liquid Radioactive Wastes*, Czech Technical University of Prague, July 1996.

10. F. Sebesta, J. John, and A. Motl, *Evaluation of PAN-Based Inorganic-Organic Composite Absorbers for Chemical Separations Applications at DOE Sites*, Technical University of Prague, June 1997.

11. T. J. Tranter, R. S. Herbst, T. A. Todd, A. L. Olson, H. B. Eldredge, "Evaluation of Ammonium molybdophosphate-Polyacrylonitrile (AMP-PAN) as a Cesium Selective Sorbent for the Removal of Cs-137 from Acidic Nuclear Waste Streams," *Advances in Environmental Research*, Vol. 6, 2001, pp. 107–121.

12. T. A. Todd, K. N. Brewer, D. J. Wood, P. A. Tullock, N. R. Mann, L. G. Olson, "Evaluation and Testing of Inorganic Ion Exchange Sorbents for the Removal of Cesium-137 from Actual Idaho Nuclear Technology and Engineering Center Acidic Tank Waste," *Separation Science and Technology*, Vol. 36 (5&6), 2001, pp. 999–1016.

13. R. S. Herbst, J. D. Law, T. A. Todd, D. J. Wood, T. G. Garn, E. L. Wade, *Integrated AMP-PAN, TRUEX, and SREX Flowsheet Test to Remove Cesium, Surrogate Actinide Elements, and Strontium from INEEL Tank Waste Using Sorbent Columns and Centrifugal Contactors*, Bechtel BWXT Idaho, INEEL/EXT-2000-00001, January 2000.

14. A. S. Aloy, A. G. Anshits, D. A. Knecht, T. J. Tranter, A. A. Tretyakov, and J. Macheret, "Development and Testing of a New Porous Crystalline Matrix (Gubka) for Stabilizing Actinide Solutions," *Scientific Basis for Nuclear Waste Management XXIII,* Vol. 608, 2000, pp. 637–642.

15. D. A. Knecht, T. J. Tranter, A. S. Aloy, A. G. Anshits, A. A. Tretyakov, and J. Macheret, "Progress in Development of Porous Crystalline Matrix (Gubka) for Stabilizing Liquid Waste Solutions," *Proceedings of Waste Management 2001, Tucson AZ,* March 2001.

16. A. G. Anshits, A. S. Aloy, A. A. Tretyakov, D. A. Knecht, T. J. Tranter, O. M. Sharanova, T. A. Vereshchagina, I. D. Zykova, N. V. Sapozhnikova, A. V. Strelnikov, and J. Macheret, "Development and Characteristics of a New Porous Crystalline (Gubka) Matrix for Stabilizing Radioactive and Hazardous Solutions," *Scientific Basis for Nuclear Waste Management XXIV,* Vol. 663 (2001).

17. J. L. Collins, D. J. Davidson, C. W. Chase, B. Z. Egan, D. D. Ensor, R. M. Bright, and D. C. Glasgow, *Development and Testing of Ion Exchangers for Treatment of Liquid Wastes at Oak Ridge National Laboratory*, ORNL/TM-12315, Oak Ridge National Laboratory, March 1993.

18. J. L. Collins, B. Z. Egan, K. K. Anderson, C. W. Chase, J. E. Mrochek, J. T. Bell, G. E. Jernigan, *Evaluation of Selected Ion Exchangers for the Removal of Cesium from MVST W-25 Supernate*, ORNL/TM-12938, Oak Ridge National Laboratory, April 1995.

19. J. L. Collins, "Method of Preparing Hydrous Titanium Oxide Spherules and Other Gel-Forms Thereof," U.S. Patent 5,821,186, October 1998.

20. R. H. Perry and D. W. Green, *Perry's Chemical Engineers' Handbook,* McGraw-Hill, New York, 7th ed., 1997 pp. 16–12, 16–13.

21. F. Helfferich, *Ion Exchange,* McGraw-Hill, New York, 1962, p. 194.

22. S. Brunauer, L. S. Deming, W. E. Deming, E. Teller, "On a Theory of the van der Waals Adsorption of Gases," *J. Am. Chem. Soc.,* Vol. 62, 1940, p. 1723.

23. F. Helfferich, *Ion Exchange*, McGraw-Hill, New York, 1962, pp. 424–425.

24. P. A. Schweitzer, *Handbook of Separation Techniques for Chemical Engineers,* McGraw-Hill, New York, 3rd ed., pp. 544–546.

25. H. C. Thomas, "A Problem in Kinetics." *Anals of the New York Academy of Science,* Vol. 49, 1948, p. 161.